

# THIS WEEK



## EDITORIALS

**WORLD VIEW** A new bombing campaign against physicists and nanotechnology **p.373**

**CHEMISTRY** Unlikely reaction could turn nanotubes into nanoreactors **p.374**

**2080 ALL TROUT** Failing fishy future forecast as global warming takes hold **p.374**

## Spoils of war

*Conflict poisons both land and sea, and lost natural resources lead to more violence. Ecology is an unlikely objective during wartime, but one that can help to secure peace.*

**W**hy is the cancer rate on the Puerto Rican island of Vieques higher than that in the surrounding Caribbean? And where did the bands of toxic mercury in the soils of Slovenia come from? An answer to both is warfare. Massive amounts of noxious munitions have been dumped off Vieques during training exercises by the US navy, and are linked to illnesses. And the mercury is a chemical legacy of artillery barrages along the Soca Front during the First World War.

Active fighting burns and crushes whole landscapes. Even greater harm can come from the chaos that surrounds war. When rules and regulations fall by the wayside, natural resources are plundered and poaching is rife. Deforestation rates have soared as successive conflicts have raged in Afghanistan, and Pakistani 'timber mafias' have looted valuable woods from the region.

Enter the warfare ecologists. By studying warfare's effects on the environment, and the environment's effects on war, these researchers hope to short-circuit the cycles of violence leading to natural-resource crises leading to violence. A paper on page 438 links El Niño weather events to civil conflicts, showing that the connections can be strong.

It is clear that humanity at the beginning of the twenty-first century is much better at violent conflict than at planet management. Certainly, the US Department of Defense's budget is 100 times that of the National Science Foundation. Inevitably, there is criticism that those who promote warfare ecology are simply looking to tap fat military budgets.

How can these ecologists respond to this cynicism? They can research the interplay between ecosystems and international aid and relief, and suggest smart technological fixes, such as solar panels in refugee camps, which improve safety there. After a war, they can restore ecosystem services necessary for continued peace, from clean water to locally grown food. And they can promote 'peace parks', protected areas that span borders, preserve nature, provide a feel-good common cause for local and national governments and create economic opportunities through tourism.

But there are troubling aspects to warfare ecology. Peter Smallwood, a biologist at the University of Richmond, Virginia, who has worked to establish a peace park in Afghanistan, points out that such projects are so enthusiastically supported by soldiers trying to win hearts and minds that they can blur the lines between civilian and military acts.

It is also an uncomfortable truth that war can be a boon to ecosystems and rare species. War zones, military bases and weapons labs around the world serve as de facto protected areas, many of which are now managed with biodiversity in mind. The demilitarized zone between North and South Korea has become a haven for endangered species such as red-crowned cranes (*Grus japonensis*). In Colombia, jungle areas held by guerrilla fighters are safe from development.

This does not mean that warfare ecologists must wish for conflicts to continue. Instead, they can prepare for peace, by partnering with conservation organizations to raise funds that can be mobilized when war zones open up.

The current financial climate sees even sacrosanct defence budgets feeling the pinch, and ecological research and nature protection could be among the early casualties. But warfare ecology should and will go on. Ecologists are used to making do, and there is always a war somewhere.

The field can be a grey area in which to work: a nebulous zone between propaganda and peacemaking, between mitigating harm and being seen as applying a public-relations gloss to violence. But ecology is most relevant to society when it studies the intersection between humans and the environment. And along with romance and music and endless curiosity, war remains one of humanity's most characteristic activities. ■

## Go with the flow

*Technology to track the path of a raindrop points the way to better environmental awareness.*

**I**t might seem impossible to get lost in the modern world with its ubiquity of digital maps, but there is more than one way to be lost. Truly knowing where you are goes beyond pinpointing your position. It means knowing where your water comes from and where it goes, where your electricity is generated and where your rubbish ends up. It means being aware of what plants and animals live nearby and what kind of soil lies beneath your feet.

For example, an undergraduate at a rainy Butler University in Indianapolis, Indiana, can use his or her smartphone to instantly calculate a route to the nearest Starbucks coffee shop. But chances are that he or she remains ignorant of how the rain flows through the city on its way to the White River, the Mississippi and, finally, the Gulf of Mexico.

Enter Raindrop, a phone application that combines sewer and watercourse maps with the software that makes getting a caffeine fix so easy. Tap the map and watch the path of a single raindrop flow from your location through streams, culverts and pipes into the river. The app, due to launch next month, was funded by the US National Oceanic and Atmospheric Administration and put together by a team led by ecologist Timothy Carter at Butler. It is currently limited to Indianapolis, but similar efforts could be designed for other cities.

A better appreciation of watercourses and other hidden networks can only strengthen human connections to ecosystems, biogeochemical cycles and resource flows, and will arguably make people more likely to support science and environmental causes. Making available the data that science and society produce in these innovative ways can help people to find themselves — even if they had no idea that they were lost. ■



## Stand up against the anti-technology terrorists

Home-made bombs are being sent to physicists in Mexico. Colleagues around the world should ensure their own security, urges **Gerardo Herrera Corral**.

**M**y elder brother, Armando Herrera Corral, was this month sent a tube of dynamite by terrorists who oppose his scientific research. The home-made bomb, which was in a shoe-box-sized package labelled as an award for his personal attention, exploded when he pulled at the adhesive tape wrapped around it. My brother, director of the technology park at the Monterrey Institute of Technology in Mexico, was standing at the time, and suffered burns to his legs and a perforated eardrum. More severely injured by the blast was his friend and colleague Alejandro Aceves López, whom my brother had gone to see in his office to share a cup of coffee and open the award. Aceves López was sitting down when my brother opened the package; he took the brunt of the explosion in his chest, and shrapnel pierced one of his lungs.

Both scientists are now recovering from their injuries, but they were extremely fortunate to survive. The bomb failed to go off properly, and only a fraction of the 20-centimetre-long cylinder of dynamite ignited. The police estimate that the package contained enough explosive to take down part of the building, had it worked as intended.

The next day, I, too, was sent a suspicious package. I have been advised by the police not to offer details of why the package was judged of concern, but it arrived by an unusual procedure, and on a Sunday. It tested positive for explosives, and was taken away by the bomb squad, which declared a false alarm after finding that the parcel contained only books. My first reaction was to leave the country. Now, I am confused as to how I should respond.

As an academic scientist, why was my brother singled out in this way? He does not work in a field that is usually considered high-risk for terrorist activity, such as medical research on animals. He works on computer science, and Aceves López is an expert in robotics. I am a high-energy physicist and coordinate the Mexican contribution to research using the Large Hadron Collider at CERN, Europe's particle-physics laboratory; I have worked in the field for 15 years.

An extremist anarchist group known as Individuals Tending to Savagery (ITS) has claimed responsibility for the attack on my brother. This is confirmed by a partially burned note found by the authorities at the bomb site, signed by the ITS and with a message along the lines of: "If this does not get to the newspapers we will produce more explosions. Wounding or killing teachers and students does not matter to us."

In statements posted on the Internet, the ITS expresses particular hostility towards nanotechnology and computer scientists. It claims that nanotechnology will lead to the downfall

of mankind, and predicts that the world will become dominated by self-aware artificial-intelligence technology. Scientists who work to advance such technology, it says, are seeking to advance control over people by 'the system'. The group praises Theodore Kaczynski, the Unabomber, whose anti-technology crusade in the United States in 1978–95 killed three people and injured many others.

The group's rhetoric is absurd, but I urge colleagues around the world to take the threat that it poses to researchers seriously. Information gathered by Mexican federal authorities and Interpol link it to actions in countries including Spain, France and Chile. In April this year, the ITS sent a bomb — similar to the one posted to my brother — to the

head of the Nanotechnology Engineering Division at the Polytechnic University of Mexico Valley in Tlaxiaco, although that device did not explode. In May, the university received a second parcel bomb, with a message reading: "This is not a joke: last month we targeted Oscar Camacho, today the institution, tomorrow who knows? Open fire on nanotechnology and those who support it!"

The scientific community must be made aware of such organizations, and of their capacity for destruction. Nanotechnology-research institutes and departments, companies and professional associations must beef up their security procedures, particularly on how they receive and accept parcels and letters.

I would like to stand up and speak in this way because I believe that terror should not succeed in establishing fear and imposing conduct that takes us far from the freedom we enjoy. I would like the police to take these events seriously; they

are becoming a real threat to society. I would also like to express my solidarity with the Monterrey Institute of Technology — the institution that gave me both financial support to pursue my undergraduate studies and high-level academic training.

To oppose technology is not an unacceptable way to think. We may well debate the desirability of further technical development in our society. Yet radical groups such as the ITS overlook a crucial detail: it is not technology that is the problem, but how we use it. After Alfred Nobel invented dynamite he became a rich man, because it found use in mining, quarrying, construction and demolition. But people can also decide to put dynamite into a parcel and address it to somebody with the intention of killing them. ■

**Gerardo Herrera Corral** is a physicist at the Research and Advanced Studies Centre of the National Polytechnic Institute of Mexico in Mexico City.  
e-mail: gherrera@fis.cinvestav.mx

I BELIEVE THAT  
**TERROR**  
SHOULD NOT  
SUCCEED IN  
**ESTABLISHING**  
**FEAR**  
AND  
**IMPOSING**  
**CONDUCT.**

➔ **NATURE.COM**  
Discuss this article  
online at:  
[go.nature.com/oitlya](http://go.nature.com/oitlya)



# SEVEN DAYS

The news in brief

## POLICY

### Racial bias at NIH?

The US National Institutes of Health (NIH) is investigating whether its reviewers are racially biased, after an agency-funded study found that black scientists were less likely to win funding for grant applications than white scientists were, even when educational background, nationality, training and other variables were taken into account. "The situation is not acceptable," says NIH director Francis Collins. The study was published on 18 August (D. K. Ginther *et al. Science* **333**, 1015–1019; 2011), together with a commentary in which Collins committed the NIH to action. See [go.nature.com/dpnb31](http://go.nature.com/dpnb31) for more.

### Lab safety at Yale

US federal investigators have criticized safety standards at a machine lab at Yale University in New Haven, Connecticut, where 22-year-old undergraduate Michele Dufault died in April (see *Nature* **472**, 270–271; 2011). But Yale disputes the findings, saying that they contained "significant inaccuracies". The US Occupational Safety and Health Administration (OSHA) found faults with the lathe at which Dufault was

## NUMBER CRUNCH

# 86%

The proportion of Earth's species yet to be discovered, according to a 23 August study showing that the planet is host to between 7.4 million and 10 million species. See [go.nature.com/gbw9pg](http://go.nature.com/gbw9pg) for more.

Source: C. Mora *et al. PLoS Biol.* **9**, e1000606 (2011)



AL DIAZ/MIAMI HERALD/MCT/NEWSCOM

## Key test agreed for private spaceflight

The first flight to the International Space Station by a commercial vehicle should take place later this year. Private spaceflight company SpaceX, based in Hawthorne, California, said on 15 August that NASA

had given it a 30 November date to launch its Dragon capsule for a mission to dock with the station. The capsule, which is intended to carry astronauts in the future, will be sent to space on the company's Falcon 9 rocket (pictured).

working, and said Yale should ensure that students don't work alone. But OSHA did not fine the university over the problems because it has jurisdiction over workplace incidents only if they involve paid employees. See [go.nature.com/1uai86](http://go.nature.com/1uai86) for more.

### Zone of no return

Japan's government is expected to officially confirm this week that many people will not be allowed to return to their homes around the Fukushima Daiichi nuclear plant — probably for decades. A survey released last week by the science and education ministry found that levels of radiation are still beyond government safety limits in

most areas on the edge of a 20-kilometre exclusion zone around the plant (set up soon after the nuclear crisis began). See [go.nature.com/d4g4n2](http://go.nature.com/d4g4n2) for more.

### All change in Italy

Italian science politics is set for a shake-up after new heads were nominated for 11 research institutes on 13 August. Scientists say the changes could protect budgets and lead to more transparent recruitment. See page 386 for more.

## BUSINESS

### Melanoma hope

A cancer drug that yielded remarkable results against seemingly intractable

advanced melanoma in clinical trials (see *Nature* **467**, 140–141; 2010) was approved by the US Food and Drug Administration on 17 August. The drug, vemurafenib (Zelboraf), targets cancers that bear a particular mutation in the B-Raf protein. Regulators also approved a test to identify cancers with this mutation. Vemurafenib was developed by the biotechnology firm Plexxikon, based in Berkeley, California, and Swiss drug company Roche.

### Lymphoma drug

In another cancer drug approval last week, Seattle Genetics, based in Bothell, Washington, has been given the green light from

IBM RESEARCH the US Food and Drug Administration to sell its targeted lymphoma therapy, brentuximab vedotin (Adcetris). The drug combines an antibody that targets lymphoma cells with a poison that is released inside the cell. See page 380 for more.

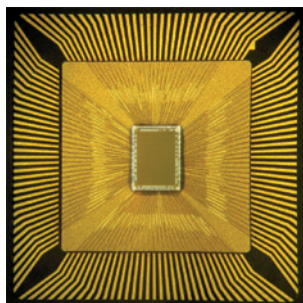
## RESEARCH

## Higgs signal fades

The Higgs boson is proving tougher to find than physicists had hoped. In July, a flurry of 'excess events' (see *Nature* 475, 434; 2011) hinted that the Higgs was popping up inside the Large Hadron Collider, the particle accelerator at CERN, Europe's high-energy physics lab near Geneva, Switzerland. But data presented on 22 August at the Lepton Photon 2011 conference in Mumbai, India, show the signal fading. That means that the excess "is probably just a statistical fluctuation", says Adam Falkowski, a theoretical physicist at the University of Paris-South in Orsay, France. See [go.nature.com/shww4r](http://go.nature.com/shww4r) for more.

## Brainy microchips

Researchers at computing giant IBM have unveiled experimental microchips that they say emulate the brain's architecture. Conventional chips have their computational elements in the



central processing unit, with the random-access memory off to one side. But in IBM's 'cognitive computing' chips (pictured), the two are wired together, allowing signals to flit between memory and computation. Because less energy is wasted shuttling electrons around, the main benefit is decreased power consumption. The chips may also be good at crunching through problems such as pattern recognition. See [go.nature.com/7ipigl](http://go.nature.com/7ipigl) for more.

## Research for hire

A US company that encourages researchers to outsource their experiments online last week launched its eBay-like website, [scienceexchange.com](http://scienceexchange.com). Science Exchange, based in Palo Alto, California, hopes that scientists will post experiments on the website, and that other researchers and institutions with the facilities and expertise will

submit bids to do the work. Elizabeth Iorns, the company's co-founder, says that this could speed up research and use facilities more efficiently. See [go.nature.com/5tzarv](http://go.nature.com/5tzarv) for an interview with Iorns.

## Deforestation up

Deforestation in the Amazon rainforest is 15% greater than last year, according to preliminary results from coarse-resolution satellite data released by Brazil's National Institute for Space Research in São José dos Campos. The rise in the August 2010 to July 2011 season is disappointing, given the drastic cuts in deforestation that Brazil has managed since 2004. But it could have been worse: stronger enforcement seems to have countered sudden spikes of forest clearing seen earlier in the year, as farmers and loggers anticipated a weakening in Brazil's 'forest code' (see *Nature* 476, 259–260; 2011). That legislation is still being debated.

## Future space tech

NASA is putting about US\$175 million into three space missions to develop technology that might be used on future science probes, the agency announced on 22 August. A mercury-ion atomic clock to test ultra-precise timing in deep space should be ready to launch in

## COMING UP

28 AUG–1 SEPT

The American Chemical Society holds its 2011 autumn meeting in Denver, Colorado. Talks include the use of chemistry to produce cleaner air and water. [go.nature.com/mmnd5d](http://go.nature.com/mmnd5d)

31 AUGUST

Rumours from Beijing hint that China's first experimental space laboratory, Tiangong 1, may launch by the end of this month.

three years, as should a solar sail seven times larger than any yet deployed in space. A demonstration in which lasers will be used to transmit data from a spacecraft (radio waves are used at present) should launch in four years. See [go.nature.com/icw5bp](http://go.nature.com/icw5bp) for more.

## PEOPLE

## NIH resignation

The director of a soon-to-be-dissolved centre at the US National Institutes of Health (NIH) is stepping down. Barbara Alving, who has headed the National Center for Research Resources (NCRR) since 2005, announced her resignation on 16 August. It takes effect on 1 October, the start of the US government's 2012 budget year. That is also when NIH director Francis Collins hoped to have congressional approval to create a new translational medicine centre, which is expected to absorb some of the functions of the dismantled NCRR (see *Nature* 471, 15–16; 2011). But the future of this reorganization is uncertain, with Congress yet to pass an NIH 2012 spending bill.

➔ [NATURE.COM](http://NATURE.COM)

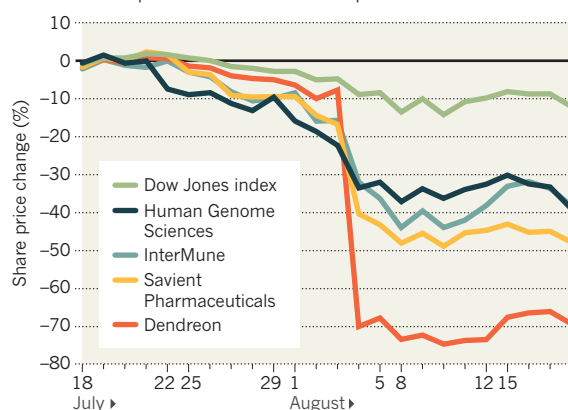
For daily news updates see: [www.nature.com/news](http://www.nature.com/news)

## TREND WATCH

Biotech company Dendreon in Seattle, Washington, reported on 4 August lower-than-expected earnings for its Provenge prostate cancer vaccine (see [go.nature.com/p1729i](http://go.nature.com/p1729i)), sending its shares, and those of some other biotech companies, into a tailspin in a volatile August market. Three other companies (see graph) that had just launched or were about to launch products were hit by worries that financial woes would drive down demand for expensive biotech medicines.

## US BIOTECH STOCKS PLUNGE IN AUGUST

In a volatile market, poor results from Dendreon seem to have dragged down the share prices of other biotech companies this month.





# NEWS IN FOCUS

**DRUGS** A watershed approval for tumour-targeting toxic antibodies **p.380**

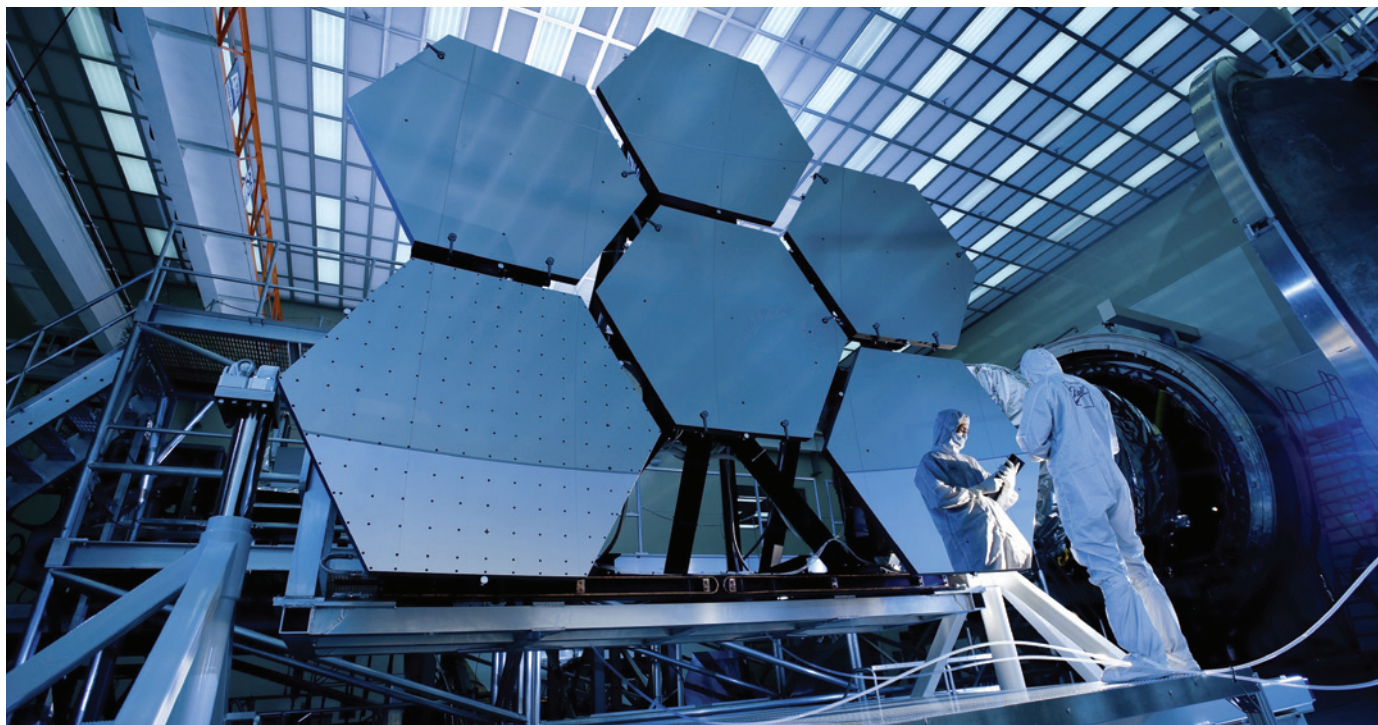
**FERTILITY** Clinics rush to offer untried egg-freezing service **p.382**

**ITALY** New heads promise to clean up science institutes **p.386**



**PROFILE** Brian Kobilka, the quiet force in protein crystallography **p.387**

NASA/MSFC/D. HIGGINBOTHAM/E. GIVEN



The James Webb Space Telescope's segmented mirror is already taking shape, but massive cost overruns have led to calls for the project to be cancelled.

## ASTRONOMY

# NASA to share telescope cost

*Budget-busting astronomy project could get extra cash from human spaceflight funds.*

BY ERIC HAND

The James Webb Space Telescope (JWST) is perilously overbudget and under threat of cancellation, but *Nature* has learned that it may be offered a financial lifeline. The flagship observatory is currently funded entirely through NASA's science division; now NASA is requesting that more than US\$1 billion in extra costs be shared 50:50 with the rest of the agency. The request reflects administrator Charles Bolden's view, expressed earlier this month, that the telescope is a priority not only for the science programme, but for the entire agency.

NASA expects that the total cost of getting the 6.5-metre telescope to the launch pad by 2018 will be about \$8 billion, around

\$1.5 billion more and three years later than an independent panel predicted in November 2010. Because in the next few years agency budgets are likely to be flat at best, scientists had feared that the JWST would end up swallowing the \$1-billion astrophysics budget whole, or at least heavily eroding the \$5-billion science-division budget. The new proposal would scrape money from other corners of the agency's \$18-billion budget, which also supports programmes such as aeronautics, technology development and human spaceflight. Matt Mountain, director of the Space Telescope

**► NATURE.COM**  
Read 'The telescope that ate astronomy'.  
[go.nature.com/pkktf3j](http://go.nature.com/pkktf3j)

Science Institute in Baltimore, Maryland, says he is glad that the agency is making the JWST a priority. "There's an

acknowledgement that the science budget can't solve this on its own," says Mountain, whose institute operates the Hubble Space Telescope and is preparing to do the same for the JWST.

The proposal to share the JWST's costs across the agency is part of a 'replan' developed by NASA after the independent panel criticized the project's management and found it to be colossally overbudget (see *Nature* 468, 353–354; 2010). The plan has been under consideration for weeks by the White House's Office of Management and Budget (OMB), which has an oversight role in setting budgets. NASA declined to comment on the cost-sharing aspects of the plan, but spokesman Trent Perrotto notes that five years of operational costs will bring the telescope's overall price tag up to \$8.7 billion. If the OMB rejects the plan, it ►



► would cast further doubt on whether the JWST will ever fly, because a House of Representatives committee has already voted, on 13 July, to cancel the telescope.

The drama surrounding the JWST is clearly on the mind of Bolden, NASA's highest official. On 2 August, before a meeting of the NASA Advisory Council began, Bolden told an assembly of dozens of advisers that the JWST is now one of the agency's top three priorities.

The first is to continue to support the development of commercial rockets able to carry people to and from the International Space Station in low-Earth orbit, a goal of companies such as Space Exploration Technologies (SpaceX) of Hawthorne, California. Second is the development of a heavy-lift rocket that can take astronauts beyond low-Earth orbit to reach objects such as nearby asteroids. Both of these activities would fall under the aegis of the Human Exploration and Operations Mission Directorate, which was formed on 12 August in a merger of the programme that operated the now-retired space-shuttle fleet and the programme that began the development of the Constellation rockets, part of the now-cancelled project to return to the Moon. That Bolden's third priority is the JWST "makes it clear that he's going to be fighting for it", says Alan Boss, an astronomer at the Carnegie Institution of Science in Washington DC and chair of a NASA astrophysics advisory subcommittee.

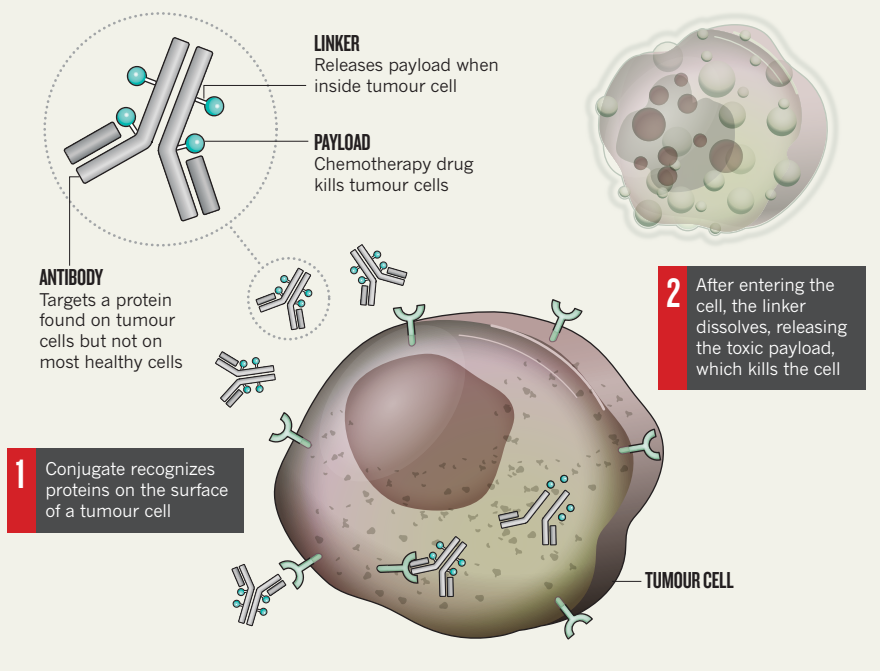
Even allowing for cost-sharing within the agency, lawmakers on Capitol Hill would have to cough up more money for NASA than recommended by the House committee if it is to turn all of Bolden's priorities into realities. In September, when Congress returns from recess, it is expected to resume the appropriations process for the 2012 fiscal year. All eyes will be on the Senate and Barbara Mikulski (Democrat, Maryland) to see how strongly she fights for the JWST project, which is being managed in her state.

If the OMB approves NASA's plan — and if lawmakers oblige by appropriating enough money — astronomers should consider themselves lucky. Some observers suggest that if the science division has to cover only half of the JWST's overruns, it could do so without delaying or cancelling any other missions.

But Brett Alexander, president of the Commercial Spaceflight Federation, says that shifting the cuts onto other parts of the agency will definitely hurt. He points out that scientists complained loudly in 2006 when money was redirected from science to support the Constellation rocket-building effort. "Now the science community may be looking for human spaceflight money to cover the science overruns," he says. ■

## SEEK AND DESTROY

Scientists say that conjugates tethering a chemotherapy drug to an antibody are on the cusp of achieving clinical success for treating certain types of cancer.



## DRUG DEVELOPMENT

# Toxic antibodies blitz tumours

*Tightly targeted cancer therapy receives marketing approval.*

BY HEIDI LEDFORD

Eventually, Clay Siegall got used to doors slamming in his face. When the cancer researcher decided to create a company that would fight cancer using weaponized antibodies, investors were sceptical. "We contacted 35, then 40, then 45 venture-capital companies," he says. "We got turned down over and over and over."

Siegall and his partners kept trying, and 13 years later the investors who eventually bet on Siegall's company, Seattle Genetics, of Bothell, Washington, are getting their reward. On 19 August, the US Food and Drug Administration (FDA) approved the company's lead therapy, an antibody engineered to deliver a poisonous payload directly into lymphoma cells. The hope is that such antibodies, called antibody-drug conjugates, will sidestep the punishing toxicities of classical chemotherapies, which run loose in the bloodstream and kill healthy cells in addition to their targets.

Tim Illidge, an oncologist at the University of Manchester, UK, says that the approval is a "game-changer" for a promising class of drugs that has struggled to gain a foothold since it was first described in a 1964 *Nature* paper<sup>1</sup> (see 'A long time coming'). "We're essentially in a renaissance of the antibody-drug conjugate," he says.

Unembellished, or 'naked', antibodies are already used to treat cancer because of their unparalleled ability to target proteins found on the surface of tumour cells. Their high profit margins and strong patent protections have pharmaceutical companies clamouring for more. Siegall says that Seattle Genetics toyed with naked antibodies, too. "But by and large," he says, "most naked antibodies just don't have a strong, potent ability to knock out tumour cells."

Enter antibody-drug conjugates, which do have that knock-out punch. Their power comes from their payloads: lethal drugs tethered to the antibody that remain harmless until

the conjugate releases them inside cancer cells (see 'Seek and destroy').

But for decades, developers have struggled to get the crucial elements to work together: the antibody, the drug it carries and the linker that binds the two. Seattle Genetics' conjugate, Adcetris (brentuximab vedotin), seems to have overcome the hurdles; it combines a synthetic poison called vedotin with an antibody that targets CD30, a protein found on many lymphoma cells.

In July, an FDA advisory committee voted unanimously in support of accelerated approval for Adcetris after Seattle Genetics reported that 94% of the 102 people with Hodgkin's lymphoma in a trial of the treatment saw their tumours shrink, and 73% achieved partial or complete remission. "This drug is wildly active," said panellist Mikkael Sekeres, an oncologist at the Cleveland Clinic in Ohio, after the vote.

The accelerated approval means that the drug can now be prescribed by doctors while Seattle Genetics conducts follow-up clinical studies. Mark Monane, a senior analyst at the investment-banking firm Needham & Company in New York, predicts that the drug will bring in up to US\$400 million a year in sales.

Janice Reichert, an analyst at the Tufts Center for the Study of Drug Development in Boston, Massachusetts, expects more approvals to follow. Between 2000 and 2005, only six antibody-drug conjugates entered the clinic for the first time, she says. From 2005 to 2009, 15 more joined their ranks. Now, 25 are currently in cancer clinical trials — more than at any other time. Two have reached late-stage clinical trials: trastuzumab emtansine, a breast-cancer therapy jointly developed by biotechnology firms Genentech, based in South San Francisco, and ImmunoGen in Waltham, Massachusetts; and inotuzumab ozogamicin, a lymphoma therapy developed by Pfizer in New York.

Pitfalls remain. The only other conjugate to ever win accelerated approval from the FDA, a different version of Pfizer's lymphoma therapy, was pulled from the market last year after further tests showed that the drug offered no benefits over standard chemotherapy. Many

blame the failure on a linker that fell apart in the bloodstream, boosting toxicity and limiting the dose that could be used. Seattle Genetics had to pull one of its antibodies from clinical trials for similar reasons, says Siegall. As a result, the company developed a linker that is degraded by the enzymes that are most active inside the cell.

ImmunoGen, Seattle Genetics' main competitor, has struggled to find the right drug to couple to its antibodies. For years, the company attempted to use ricin, a toxin produced by castor beans. But ricin triggered a dangerous immune response. ImmunoGen now steers clear of complex proteins and picks small-molecule poisons that are less likely to attract the attention of the immune system.

A lingering problem for the field is a lack of control over how many drug molecules attach to each antibody. More control would help standardize each dose and lessen the potential toxicity of the treatment. A method developed by researchers at Genentech, a subsidiary of Swiss drug firm Roche, seemed to have conquered the problem but has not yet been tested clinically<sup>2</sup>. Unexpected toxicities led the company to shelve the technique for the time being, says Paul Polakis, Genentech's director of cancer targets. "It's like a game of whack-a-mole," he sighs. "You knock out one toxicity and another shows up."

Although antibody engineers still have work to do in optimizing the design, the approval of Adcetris means they have a bellwether to watch. The improving fortunes in the field, which culminated in last week's approval, have finally brought Siegall the investor attention that eluded him for so long. Seattle Genetics has partnered with 11 outside firms, bringing in \$150 million in new capital. More than a quarter of that was raised in the past year. "I'm happy to say I no longer have to convince investors that this is a productive field," he says.

All of this leaves those who have followed the technology marvelling at its reversal of fortune. "When I first became interested in the field in the early 1990s, there was a lot of despondency," says Illidge. "And now look at it. Everything has changed." ■

1. DeCarvalho, S., Rand, H. J. & Lewis, A. *Nature* **202**, 255–258 (1964).
2. Junutula, J. R. et al. *Nature Biotechnol.* **26**, 925–932 (2008).

**"It's like a game of whack-a-mole. You knock out one toxicity and another shows up."**

## A LONG TIME COMING

For nearly half a century, researchers have been trying to capture the therapeutic potential of antibody-drug conjugates, which combine the tumour-killing power of a drug with the tumour-seeking ability of an antibody.

**1964**

Researchers create the first antibody-drug conjugates<sup>1</sup>.

**1981**

The Dana Farber Cancer Institute in Boston, Massachusetts, spins out ImmunoGen to focus on conjugates.

**1986**

US regulators approve the first therapeutic 'naked' antibody.

**1998**

Seattle Genetics is founded and focuses on conjugates.

**2000**

US regulators approve Pfizer's Mylotarg (gemtuzumab ozogamicin) for treatment of leukaemia.

**2010**

Pfizer withdraws Mylotarg after finding no significant benefit to patients.

**2011**

Regulators approve Seattle Genetics' Adcetris for some forms of lymphoma.



BUSINESS WIRE

**MORE ONLINE**

### TOP STORY



Ancient Egyptians used 'hair gel' [go.nature.com/tode8u](http://go.nature.com/tode8u)

### OTHER NEWS

- Climate change will hit genetic diversity [go.nature.com/snmuiy](http://go.nature.com/snmuiy)
- End of an era for research subs at Harbor Branch Oceanographic Institute [go.nature.com/key4od](http://go.nature.com/key4od)
- Chilean sea bass certified 'green' aren't necessarily so [go.nature.com/vsub7u](http://go.nature.com/vsub7u)

### ON THE BLOG



Up in smoke: cannabis genome sequenced [go.nature.com/645me9](http://go.nature.com/645me9)

P. LANDMANN/GETTY IMAGES





L. VAN LIESHOUT/AFP/GETTY

Freezing eggs in liquid nitrogen to extend women's reproductive years is becoming commonplace, but data are lacking about outcomes from older eggs.

## FERTILITY

# Growth of egg freezing blurs 'experimental' label

*Older women who use the procedure are not treated as trial participants despite unknowns.*

BY ALISON MOTLUK

The first thing that Alison Hopkins did after finishing her PhD was freeze 14 of her eggs. She knew she wanted children, but she was 38 and didn't have a partner. "It buys you time, it eliminates any pressure," she says. "I thought it was a really good insurance policy."

For such women, however, egg freezing is "a shot in the dark," says Hopkins' fertility specialist, John Jain, who heads Santa Monica Fertility in California. Very few of the older women who have frozen eggs to beat the clock have tried to use them, says Jain. He estimates that, worldwide, fewer than ten babies have been born from eggs frozen for women aged 38 or over. And no one knows how successful the freezing and thawing of older eggs will be — despite the fact that most women now seeking the service are over 38.

These uncertainties are reflected in the recommendations of the American Society for Reproductive Medicine (ASRM) — the advisory body to the fertility industry — but not in the practises of its members, even some of those who formulate the guidelines. The

ASRM states clearly that oocyte cryopreservation should not yet be offered to older women as a way of extending their fertility. It also says that all egg freezing should be considered experimental, and be performed as part of a research project governed by an institutional review board (IRB), which is supposed to monitor, review and approve the research.

ASRM practice-committee chair Samantha Pfeifer of Penn Health for Women in Radnor, Pennsylvania, says that there are still many unanswered questions. "How successful will this be for someone in her late thirties?" she asks. "That has not been evaluated in any randomized controlled trials." There is also debate about what technique works best. Some of the chemicals used in the freezing process are toxic to embryos, and no one knows how much the eggs absorb. Moreover, there has been no systematic follow-up of children born from frozen eggs.

**"There may be some damage to cell organelles after thawing, which an older, unhealthier egg probably cannot recover from."**

Oocyte cryopreservation was originally explored to help women with cancer, because treatments such as chemotherapy can cause sterility. But, according to Briana Rudick, a fertility specialist at Columbia University in New York, the biggest demand is now from women electing to delay motherhood. Although Eric Widra, a member of the ASRM's practice committee, says that "almost nothing" is known about how well older eggs will freeze and thaw, the clinic he works for, Shady Grove Fertility in Washington DC, offers egg freezing to older women. It bills the procedure as a woman's chance to "lock in her fertility potential for future use", which is at odds with ASRM practice committee guidelines.

Although most fertility doctors go through the motions of doing research, such as getting IRB approval, many do not consider the procedure experimental, or their clients research subjects. "I completely reject their experimental designation," says Nicole Noyes at the New York University Langone Medical Center. She argues that egg freezing is now well established and has a high rate of success, and that in clinics with a proven track record it should not be



singled out as needing special oversight.

Yet calling the procedure experimental without genuinely treating it as such leaves women with all the downsides of experimental science but few of the protections, says Gerald Schatz, vice-president of Citizens for Responsible Care and Research, a non-profit organization that works to improve standards for human research subjects. If it's really research, he says, there should be a carefully designed trial every time, results should be reported, fees should be reduced and there should be safety monitoring. The results should help to shape standard medical practice.

But the industry is a competitive one. And Pfeifer points out that many centres do not feel compelled to share their results. "That's unfortunate," she says, "because if everybody did, we'd know how it's going." This lack of transparency contrasts sharply with that for *in vitro* fertilization, for which the results of all cycles must be reported to the US Centers for Disease Control and Prevention in Atlanta, Georgia, either directly or through the Society for Assisted Reproductive Technology (SART), a sister organization to the ASRM. "We don't have the same transparency for egg freezing," says Widra, chair of the SART practice committee.

### SHORT ON SCIENCE

Unlike new drugs or medical devices, which must be approved by the US Food and Drug Administration before they can be marketed, advances in medical techniques need no such mandate. Fertility treatments have been among the quickest to leap from lab to clinic. "There's a history of moving forward quickly in reproductive medicine," says Laura Shanner, a bioethicist at the University of Alberta in Edmonton, Canada. "There are endemic problems of poorly done, poorly structured research." Neither intra-cytoplasmic sperm injection (ICSI) — a technique that injects sperm directly into an egg — nor pre-implantation genetic diagnosis, for instance, went through lengthy testing in humans before being marketed.

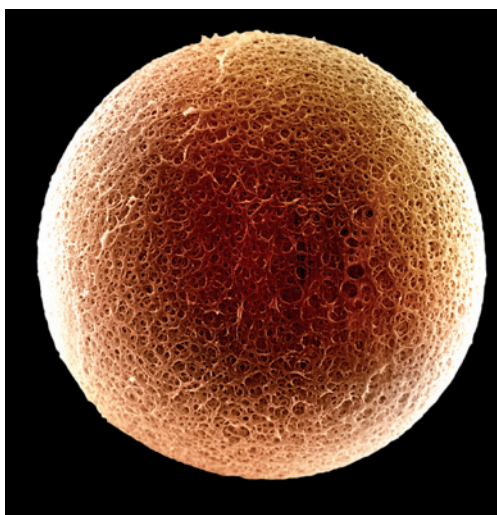
The controversies surrounding egg freezing are not limited to the United States. In the United Kingdom, the Royal College of Obstetricians and Gynaecologists and the British Fertility Society issued a joint statement in 2009 warning that women should not look to egg freezing for non-medical reasons, but numerous clinics now offer the service. In the Netherlands, members of parliament voted in April to end a ban on non-medical egg freezing, allowing women up to age 45 to freeze their eggs.

Human eggs, which are large, aqueous and permeable, are tricky to freeze. One of two current methods, 'slow-freezing', involves dehydrating the egg using chemical cryoprotectants, then cooling it slowly to induce the formation of ice outside it. The egg is then cooled further

to between about  $-30^{\circ}\text{C}$  and  $-40^{\circ}\text{C}$  before being plunged into liquid nitrogen. Unless great care is taken, ice crystals form inside the cell and destroy it. However, advances during the past few years have significantly increased success rates, and now as many as 50–90% of eggs can survive slow-freezing and thawing (J. Boldt *Reprod. BioMed.* <http://dx.doi.org/10.1016/j.rbmo.2010.11.019>; 2011).

'Vitrification', a newer method, involves treating the egg with a higher concentration of cryoprotectants, then immediately plunging it into liquid nitrogen. When done properly, the solution within and surrounding the egg turns into a glass-like substance, which avoids the formation of damaging ice crystals. Between 80% and 95% of vitrified eggs survive.

Potential concerns with both techniques are that the cryoprotectants can be toxic to the egg, and that freezing and thawing might affect the egg's meiotic spindle, although spindles are generally thought to reform several hours after thawing.



Being large and aqueous, human eggs are hard to freeze.

Although some doctors expect that older eggs will survive freezing and thawing just as well as younger ones, many are not so sure. "Every embryologist will tell you that good quality eggs won't suffer from freezing, but older eggs may not do so well," says Claudio Benadiva at the University of Connecticut Health Center in Farmington. Rudick argues that, for this reason, older women should be included in studies. "There may be some damage to cell organelles after thawing, which a healthy egg can probably recover from, but an older, unhealthier egg probably cannot recover from," she says.

Worldwide, it is estimated that fewer than 2,000 people have been born from frozen eggs, about 400 of them in the United States. A substantial number have been born in Italy, where the

freezing of embryos was not permitted until recently, but egg freezing was allowed. Only four babies had been born from frozen eggs by the end of March 2009 in the United Kingdom, according to the latest figures from the Human Fertilisation and Embryology Authority.

Importantly, almost all of the children were conceived from the eggs of young women, many of whom were egg donors. "You shouldn't assume a 42-year-old will have the same success as a younger woman," says Pfeifer. According to [clinicaltrials.gov](http://clinicaltrials.gov), only a few of the registered trials evaluating oocyte cryopreservation even allow healthy women over the age of 37 into the studies, and none of them is studying older women in particular. The ASRM says that it wants more data on egg freezing at all ages. "We would like to see larger studies," says Widra. "We'd like reproducibility."

### COUNTING THE COST

Despite the absence of data, fees for egg freezing can be high. The charge for hyperstimulating the ovaries, retrieving eggs and cryopreserving them can exceed US\$10,000. Keeping them frozen will add another \$500 or so a year, and thawing them costs around \$1,000. Cryopreserved eggs must be inseminated using ICSI, which costs around \$1,200 a session. All told, a single attempt at a child could cost close to \$20,000. Even with fresh eggs, a single *in vitro* fertilization attempt gives women aged 38–40 only a 22% chance of a live birth. By age 43 or 44, that drops to just 5%. How much freezing and thawing will reduce those odds by no one can say.

Rudick recommends caution to women of all ages seeking to freeze their eggs. Her research shows that many clinics that offer egg freezing have limited experience in thawing the cells, let alone turning them into babies. In spring 2009, Rudick contacted every clinic in the United States, 64% of which responded. Of the 140 that provided data on their egg-freezing service and outcomes, 45 had never thawed a client's frozen eggs (B. Rudick *et al. Fertil. Steril.* **94**, 2642–2646; 2010). At least 30 clinics had no live births from the eggs that they had thawed, and 11 more had achieved only one live birth. Only 8 respondents had managed 10 or more live births, she told *Nature*.

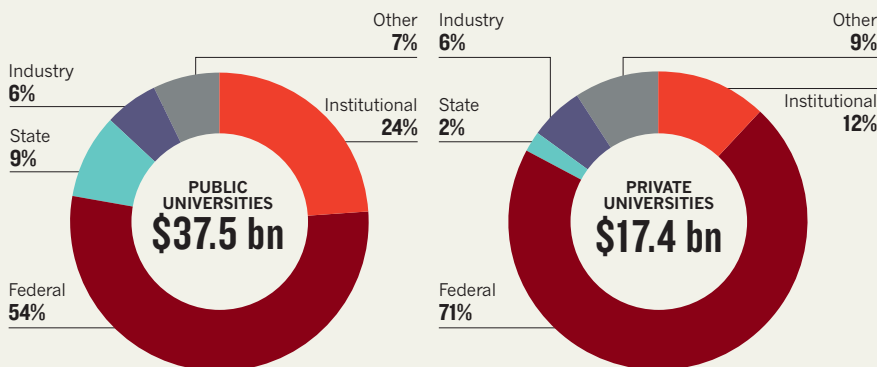
Nevertheless, for those women who calculate that a slim chance of having a child is better than none at all, the debate over how the procedure is designated and documented may be a minor concern in the face of an overriding hope. Before undergoing the procedure, Hopkins says, she researched it extensively. She was not surprised to hear that only a few children have been born from eggs the same age as hers, but is undaunted by the uncertainties surrounding the technology. "I don't see it as experimental," she says. "I'm very confident that I will end up with a live birth." ■

➔ **NATURE.COM**  
For more on fertility treatments and their regulation, see: [go.nature.com/8gyiat](http://go.nature.com/8gyiat)

SOURCE: NSF

## FOOTING THE US RESEARCH BILL

With state support falling below 10% of total research funding, public universities are increasingly relying on institutional funds, and student tuition fees in particular. The effect is less pronounced at private universities, which rely more on federal research dollars and can have large endowments.



Research and development funding source as a percentage of total (2009)

### FUNDING

# Thrift in store for US research

*Science academy panel to call for university fat trimming.*

BY EUGENIE SAMUEL REICH

When state budget woes threatened the University of California system in 2009, more than 300 leading scientists wrote to then-governor Arnold Schwarzenegger to plead for protection. It did little good: the state cut more than US\$630 million from the university's budget, forcing the institution to slash faculty members' salaries and hike student tuition fees.

The US National Academy of Sciences is finalizing a plan to spare other universities from a similar fate, or worse. Last year, after state budget cuts across the country hit many public universities, and even the wealthiest private universities saw their endowments drop by more than 20%, Congress turned to the academy for advice about how to put research universities on a stable long-term footing without costing the country too much more.

Scientists might not like the answer. *Nature* has learned that the report, scheduled for final release by the end of the year, is likely to suggest that US universities become much more efficient.

The recommendations of the 21-person panel, an influential group of researchers, business people and university administrators, are still in draft form. But members of the panel spoke to *Nature*: some in general terms, and some only on background, because draft

information is considered confidential. They suggested that their call for belt-tightening will not spare universities' most prized assets: researchers and laboratories. "There is a concern about costs," says study chairman Chad Holliday, former chief executive of chemical company DuPont and now chairman of the board of Bank of America, based in Charlotte, North Carolina.

Academic researchers might be asked to save money by sharing equipment, facilities and supervision duties — not only between research groups, but even between institutions in the same city. The panel highlights the example of multi-institutional research centres such as the US Department of Energy's Energy Innovation Hubs.

Such efforts can draw federal and state support, says Claude Canizares, vice-president for research at the Massachusetts Institute of Technology (MIT) in Cambridge, who is not a member of the panel. He points to the Massachusetts Green High Performance Computing Center, a project costing more than \$100-million, under construction in Holyoke. It has up to \$25 million in support from the state and will provide shared supercomputing facilities for MIT, Boston University, Northeastern University in Boston, Harvard University in Cambridge and the state-wide University of Massachusetts system. "We're pooling our resources," says Canizares.

As another cost-cutting measure, the panel is likely to urge state and federal governments to simplify some of the regulations that apply to research grants. "My private view is that federal oversight is well intentioned, but it can be piled on from all directions," says panel member Peter Agre, a Nobel-prizewinning molecular biologist at John Hopkins University in Baltimore, Maryland. Universities have lobbied against 'effort-reporting', for example, in which researchers are told to document how their time is spent on particular projects.

Along with the bitter medicine, the panel will also offer a recommendation that universities will welcome: a call to grant funders to pay the full indirect costs of research, or overheads. These include administration costs and building maintenance and depreciation, and generally amount to about 30 cents on the dollar.

Current US government policy is for funding agencies to pay full indirect costs, but in 1991 Congress imposed a cap of 26% on the administrative costs that institutions could recoup. Moreover, agencies sometimes claim exemptions. In 2010, for example, the National Institutes of Health said that universities could not charge overheads for genome-sequencing arrays, because the expensive devices have few administrative costs associated with them. Some private funders, such as the James S. McDonnell Foundation in St Louis, Missouri, which finances brain research, refuse to cover indirect costs at all.

The result is that universities are increasingly subsidizing grants from their own funds (see 'Footnote the US research bill'). Between 1969 and 2009, the proportion of research funding supported by institutional money rose from 10% to 20%, according to the US National Science Foundation. Public universities and all but the wealthiest private ones are increasingly taking that money from tuition fees. "The cost of research gets passed on to undergraduates," says Ronald Ehrenberg, an

**The call for belt-tightening will not spare researchers and laboratories.**

economist at Cornell University in Ithaca, New York, and a member of the panel. This erodes public support for research universities — a trend that the panel hopes to reverse with its recommendations.

The panel members are aware that allowing universities to charge more for overheads could leave less grant money available for research, and that cost-cutting on campus would squeeze research further. But their report will urge the government to target funding strategically, concentrating on research areas with the greatest potential to produce innovation and jobs, says Holliday. "We are trying to be the first in the world to leading-edge technology, because that brings the most prosperity to the American people." ■



# Italy chooses new brooms to clean up science institutes

*Incoming presidents expected to champion merit-based recruitment and efficiency drives.*

BY EDWIN CARTLIDGE

Efforts to cut nepotism and inefficiencies in Italian science may get a boost following the government's nomination of new presidents and board members for 11 of the country's public research institutes.

In a break with the past, when the government controlled the entire selection process, an independent committee of scientists has drawn up the shortlists, from which research minister Mariastella Gelmini has made the final choices. Researchers contacted by *Nature* say that the nominations, unveiled on 13 August, could lead to faster and more transparent recruitment and promotion throughout the institutes, as well as helping to protect science budgets from looming cuts.

Key nominations include Francesco Profumo, an electrical engineer and rector of the Polytechnic of Turin, who will replace particle physicist Luciano Maiani as president of the National Research Council (CNR). Giovanni Bignami, currently president of the international Committee on Space Research, will take over as president of the National Institute for Astrophysics (INAF), and Domenico Giardini, a seismologist at the Swiss Federal Institute of Technology in Zurich, will head the National Institute of Geophysics and Volcanology. All are due to take office next month.

The nominations are part of a broader initiative to give Italy's public research institutes greater independence, a plan that was originally proposed by the previous centre-left government of Romano Prodi and then passed into law by the current centre-right administration of Silvio Berlusconi at the end of 2009. The plan frees institutes to draw up their own statutes, and could, in principle, allow them to set up quicker and more transparent procedures for recruitment and promotion, says Italian physicist Renzo Rubele, a science-policy analyst at the Free University of Brussels in Belgium. Current procedures make it all too easy for politicians and senior scientists to advance the careers of junior researchers on the basis of personal acquaintance rather than merit.

**"It will not be easy to resist various pressures that seek to retain the existing structure."**



Francesco Profumo (left) and Enrico Saggese are among those slated to take over Italy's national institutes.



L: POLITECNICO DI TORINO. R: CONTRASTO/EVINE

Political pressure is most acute at the CNR, Italy's largest research organization, which has more than 4,000 researchers working in some 100 institutes, grouped into 11 departments. Established in 2003, the departments were shaped more by politics than scientific demands, says Rubele, and their number needs to be cut. The CNR's statutes, which went into effect in May, limit the number of departments to a maximum of seven. "It will not be easy to resist various pressures that seek to retain the existing structure," says Maiani, "but the cut must be made."

That responsibility now rests with Profumo. He declined to comment on departmental restructuring, but told *Nature* that one priority will be to increase the organization's annual income from European programmes and industry, potentially rising from about €450 million (US\$650 million) to around €1 billion. He also thinks that CNR researchers must be encouraged to patent more of their innovations.

Although the nominations are a visible sign of greater transparency, Rubele says that there is controversy surrounding the proposed appointment of Enrico Saggese, who is slated to remain as president of the Italian Space Agency (ASI). Saggese was made president in 2009 after being installed a year earlier by the Berlusconi government as emergency

commissioner, following the removal of the then-president, Bignami.

Saggese was previously vice-president for space activities at Finmeccanica in Rome, Italy's largest aerospace company and one of the major recipients of ASI's space procurement contracts. "ASI is often not considered scientifically as a truly independent space agency," says Rubele, "but as a means of procurement for Finmeccanica and other space-based businesses". Saggese responds that defending himself against conflict-of-interest allegations has become "boring", and argues that each president "brings his own particular experience" to the job.

Astrophysicist Pietro Ubertini of the Institute of Space Astrophysics and Cosmology in Rome, a director within the INAF, says that under the leadership of Saggese, ASI has spent a lot on applied research and not enough on pure science, but adds that at a time of great uncertainty over government funding, "it may be useful to have continuity" in the management of the agency. Saggese says, however, that ASI's funding for basic research has increased during his three years in charge, leading to a rise in both the quantity and quality of papers by Italian researchers in this field.

Rubele estimates that it will take a year to gauge the impact of the new appointees. "We will need to see what they do to the recruitment process and whether they can save their budgets from cuts," he says. "That will be a difficult exercise in the current climate." ■

➔ **NATURE.COM**  
Read more on  
European science  
policy at:  
[go.nature.com/ptxmzt](http://go.nature.com/ptxmzt)



# It's all about the structure

*For more than 20 years, Brian Kobilka worked to create a portrait of a key cell receptor. Sometimes, the slow, steady approach wins.*

BY LIZZIE BUCHEN

**B**rian Kobilka was exhausted when he stepped off the 12-hour red-eye flight from China to San Francisco, California, last May. But after a quick nap at home, he headed straight back to the airport and crammed his long frame into another plane, this time bound for Chicago, Illinois. Once there, he drove to the Advanced Photon Source at Argonne National Laboratory, a source of powerful X-ray beams used for analysing protein structures. Kobilka, a biochemist at Stanford University in California, was desperate to see the latest data from his lab's effort to make the first atomic-scale, three-dimensional image of a key cell-surface receptor locked with its protein partner. The image marked the last leg of an intellectual journey that he had started some 20 years before.

Nearly every function of the human body, from sight and smell to heart rate and neuronal communication, depends on G-protein-coupled receptors (GPCRs). Lodged in the fatty membranes that surround cells, they detect hormones, odours, chemical neurotransmitters and other signals outside the cell, and then convey their messages to the interior by activating one of several types of G protein. The G protein, in turn, triggers a plethora of other events. The receptors make up one of the largest families of human proteins and are the targets of one-third to one-half of drugs. Working out their atomic structure will help researchers to understand how this central cellular-communication system works, and could help drug-makers to design more effective treatments.

The structure and workings of GPCRs have been overriding obsessions of Kobilka for most of his professional life. For much of this, he had little company, as the proteins were widely considered too complex and unwieldy to be stabilized as crystals, a prerequisite for structural

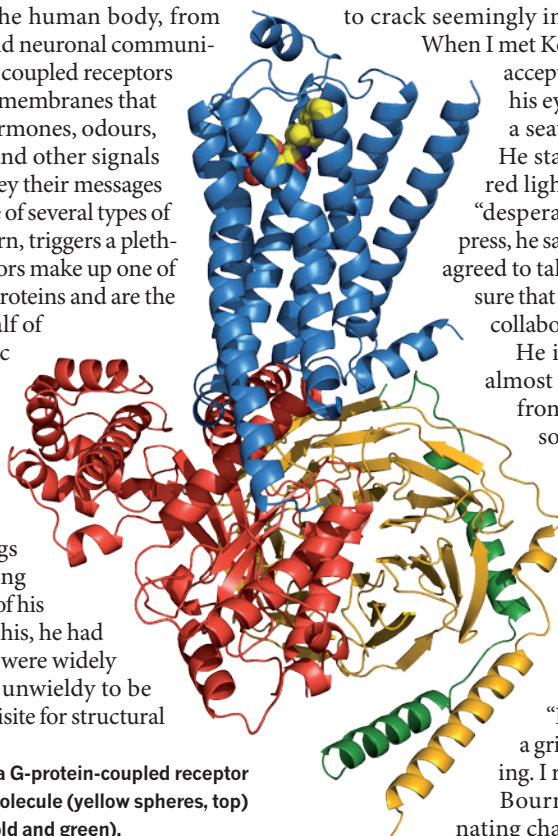
analysis by X-ray crystallography. But his determination has finally started to pay off. In 2007, his team solved the first high-resolution structure of a GPCR that binds to a hormone<sup>1-3</sup>; in January this year he did the same for the receptor poised to activate its G-protein<sup>4</sup>; and last month, he published the results from Chicago, the first structure of any GPCR in the act of turning on its G protein<sup>5</sup>.

The latest accomplishment has many in the field buzzing about a Nobel prize. "But if they do give it to him, it'll be the devil to get him to Stockholm," says Henry Bourne, a professor emeritus at the University of California, San Francisco, who worked on G proteins and has known Kobilka since the 1980s. Kobilka loathes the limelight, and is renowned as much for his shy modesty as his ability to crack seemingly impossible protein structures.

When I met Kobilka at his Stanford office, he accepted a quick handshake, averting his eyes, and reluctantly offered me a seat across from him at his desk. He stared anxiously at the glowing red light on my voice recorder. He is "desperately fearful" of talking to the press, he says, his voice breaking, and only agreed to talk because he "wanted to make sure that the contributions of my lab and collaborators are recognized".

He is so fearful, in fact, that it is almost impossible to draw much out from him. When asked why he is so captivated by GPCRs, Kobilka struggles for an answer. "I'm just inherently fascinated by these proteins. I don't know. I just want to know how they work," he says. The only time he becomes animated is when describing the conformation of the receptor gripping its G protein. "It's a fantastic structure," he says, a grin across his face. "It's just amazing. I really enjoy talking about it."

Bourne says that "Brian is a fascinating character. He's so driven, and ►



**A fine figure:** a molecular view of a G-protein-coupled receptor (blue) turned on by a signalling molecule (yellow spheres, top) and activating a G protein (red, gold and green).

S. RASMUSSEN, A. KRUSE

enormously intense. But you don't get any feeling of — nor is there any — self-aggrandizing, pushiness, show-offiness. There is absolutely none of that. It's quite refreshing and rare."

Perhaps Kobilka's rare reticence and determination are exactly what make him so well-suited for the task of protein crystallization — a pursuit in which a complete atomic structure is the finish line, and there are few intermediate rewards. "What he did was, step by step, sneak up on it to make it work," says Bourne.

### BAKING TO BIOLOGY

Kobilka is from a small, rural community in central Minnesota. His grandfather and father were bakers; his mother decorated the cakes. Kobilka studied biology and chemistry at the University of Minnesota in Duluth, where he met his future wife, Tong Sun Thian, in biology class. "He always topped the curve," she says. "But he was also so modest and quiet, you'd never know."

Kobilka got his first taste of research when he and Tong Sun worked in a developmental biology lab at the university, and built a tissue-culture hood for the lab using scrap heavy plastic from his father's bakery. He enjoyed research, but went to medical school anyway — in rural Minnesota, he says, people who were interested in biology became doctors. Studying at Yale University in New Haven, Connecticut, Kobilka developed an interest in intensive-care medicine and the drugs used in life-or-death situations that act on GPCRs — particularly the receptors for adrenaline and noradrenaline, which open the airways and boost heart rate.

In 1984, after his residency, Kobilka applied for a fellowship with Robert Lefkowitz at Duke University in Durham, North Carolina. It was the premier lab studying receptors for adrenaline, which had become a model system for all hormone receptors. When Kobilka joined, the lab was just starting to think about how to clone the gene for the  $\beta_2$ -adrenergic receptor ( $\beta_2$ AR) and determine its genetic sequence. But the receptor was produced in such small amounts that the team was only able to collect enough protein to work out a few scraps of its likely genetic sequence. Kobilka then displayed "the first of many flashes of technological innovation," says Lefkowitz: he decided to construct a library of mammalian genomic sequences and screen it with the scraps of sequences they had. This would pull out longer clones that could be pieced together to reveal the full sequence.

The plan worked. And when the team stitched together the receptor sequence<sup>6</sup>, it held a surprise: several strings of amino acids that are typically found in cell membranes showed that the receptor snaked through the membrane seven times. It was just like rhodopsin, the light-detecting receptor in the retina that was also known to activate a G protein. At the time, there was no reason to think that these receptors were going to look the same — especially when one was turned on by light, and the other by a hormone.

"It was a real eureka moment," recalls Lefkowitz. At the time, about 30 proteins were known to turn on G proteins. "We realized, oh my god, they're all going to look like this. It's a whole family!"

That family became known as seven-transmembrane receptors, or GPCRs — and is now known to have nearly 800 members in humans. Kobilka describes the watershed cloning project with humility. "It was exciting just to be involved," he says. "It was the result of a lot of heroic work by the Lefkowitz lab."

Sometimes that self-effacement has

**NATURE.COM**  
Read more about  
GPCRs:  
[go.nature.com/rwbghq](http://go.nature.com/rwbghq)



held Kobilka back. After he left Duke, he was interviewed for a faculty position in the pharmacology department at the University of California, San Francisco. "We had him and another guy," says Bourne, who was then head of the department. "It was very clear to everyone that Brian was smart, no question. But he didn't sparkle in the slightest. He was this shy, pale, Scandinavian-looking guy. I thought, who is this guy? He's very strange, so modest, so quiet."

The other guy got the job, and Stanford snapped up Kobilka, says Bourne. "We should have hired both of them."

After his success with  $\beta_2$ AR, Kobilka was hooked. He wanted to see what the receptor looked like in three dimensions using X-ray crystallography, in which a beam of X-rays is fired at a protein crystal and the resultant diffraction pattern is used to reveal the arrangement of its atoms. It was an audacious goal. To produce an intelligible X-ray diffraction pattern, Kobilka first needed to crystallize the receptor — a formidable process of packing millions of identical copies of protein so tightly that they form a solid that looks like a microscopic shard of glass. Working out the conditions that will allow a protein to crystallize can take years, and membrane proteins such as GPCRs are the hardest of all: they must be coaxed out of the membrane intact, but it is the membrane that holds them in shape. GPCRs are also constantly shifting into various states, and most are expressed in very low quantities. To collect enough protein, Kobilka





Brian Kobilka is “inherently fascinated” with G-protein-coupled receptors and has single-mindedly sought their structures.

JONATHAN SPRAGUE/REDUX/EVINE

would need to express the  $\beta_2$ AR at about 100–1,000 times the levels at which it is normally produced in a cell. At that time, no one was close to crystallizing a GPCR and few were trying.

Crystallizing the receptor became Kobilka’s pet project because he thought it was too high risk for a postdoc or graduate student. “We used to joke that he’d come running into the lab from teaching or a meeting with a column in his hand, trying to do a binding assay to see if his latest purification had worked before he went home,” says Mark von Zastrow, one of Kobilka’s first postdocs, who now studies GPCR trafficking at the University of California, San Francisco. Kobilka had reason to rush through the workday — he had two young children at home, Tong Sun was at medical school and they had a “tremendous” mortgage. To make ends meet, he moonlighted as a doctor in the emergency department at weekends. Von Zastrow recalls poking fun at Kobilka for his seemingly futile crystallography project. “He told us, ‘You’ll see. The crystals are going to be so big, I’m going to make a ring for Tong Sun out of them.’”

As the years rolled by, Kobilka’s lab was carrying out various biochemistry and biophysics experiments aimed at getting to know the  $\beta_2$ AR more intimately, and he was inching forwards in expressing and purifying the protein. But he wasn’t noticeably closer to getting the structure. “People viewed what he was doing as dotting i’s and crossing t’s,”

says Bourne. “And for a while it was sort of that. He wasn’t getting published in fancy journals.” The team showed that GPCRs have big, floppy loops inside and outside the cell, and that the receptor writhes and squirms, adopting a variety of levels of activation<sup>7</sup>. The work only made crystallization look more impossible.

In the meantime, another GPCR crystallography effort raced ahead. In 2000, Krzysztof Palczewski and his postdoc Tetsuji Okada, then at the University of Washington in Seattle, published the crystal structure of rhodopsin, the light-sensing GPCR in the retina<sup>8</sup>. It was a significant accomplishment, but of little help to Kobilka. Rhodopsin is plentiful — a bucketful of cow eyes from the slaughterhouse gives enough pure protein for crystallography. It is also simpler and more stable than other GPCRs, and its structure was thought to be different.

In 2001, Kobilka got disheartening news. His main funding, from the Howard Hughes Medical Institute in Chevy Chase, Maryland, would not be renewed after it ran out in 2003. His lab began to struggle financially, and went “deep into the red” to support his expensive crystallization crusade. “I don’t think I ever considered giving up,” says Kobilka. “I admit that it was frustrating at times, but I enjoyed the challenge and I wanted to know the answer.” Kobilka says that one of his friends “best described my ►



persistence as ‘irrational optimism’.

Finally, in late 2004, his group managed to grow tiny crystals — too small to be analysed at Stanford’s synchrotron facility. Gebhard Schertler, a crystallographer then at the Medical Research Council Laboratory of Molecular Biology in Cambridge, UK, suggested that Kobilka take his samples to the European Synchrotron Radiation Facility (ESRF) in Grenoble, France, which had the tightly focused beamline needed to analyse such small crystals. “We were running out of money all the time,” says Schertler, now at the Paul Scherrer Institute in Villigen, Switzerland. “The measurements were all on my grants.” The crystals diffracted to a resolution of around 20 ångströms — so low that there was no discernible image. A resolution of about 4 Å is needed to see the organization of individual atoms.

Still, says Kobilka, “it was very exciting. In part it was because I was very naive. I thought we’d be able to get to 3 Å in no time.” He finally had the confidence to hire postdocs

**“That’s what makes scientists go. That moment, when we know we’ve found a new continent.”**

for the crystallography project. In 2005, he also received a financial lifeline, winning two funding streams from the US National Institutes of Health in Bethesda, Maryland. But frustration followed — the team couldn’t get the crystals to grow any bigger or diffract any better. The receptor’s changeable activation states and floppy segments — particularly one restless loop on the intracellular side of the receptor — made it very difficult to trap all the proteins in an identical conformation. The team realized that they’d have to do something radical: chop off the loose ends, and either anchor the loop in place with an antibody or replace it altogether with a protein known to crystallize well.

The antibody project, led by postdoc Søren Rasmussen, came together first. As before, they first took the crystals to Schertler, at the ESRF. “It was the greatest thing,” says Schertler. “Brian and I and our team were at the synchrotron. We were sitting in front of the machine when the measurements came in. When we first saw the pattern for 3.5 Å, everyone in the room jumped up. It was a very happy moment. That’s what makes scientists go. That moment, when we know we’ve found a new continent.” The structure, published in *Nature*<sup>1</sup>, was the second crystal structure of a GPCR, after rhodopsin.

Scientists, however, reserve their accolades for the fusion-protein project, which wasn’t far behind. Postdoc Daniel Rosenbaum found that one protein — T4 lysozyme (T4L) — looked promising for fusing to the receptor in place of the loop. And Kobilka had got in touch with Ray Stevens at the Scripps Research Institute in La Jolla, California, and his new postdoc Vadim Cherezov, who had been optimizing a fatty scaffold to lock the membrane proteins in place for crystallization. T4L and the fatty scaffold turned out to be the winning combination. Just days after the *Nature* paper, Kobilka and Stevens published back-to-back papers in *Science*<sup>2,3</sup> that solved the structure of the engineered  $\beta_2$ AR to 2.8 Å.

The trio of papers marked a milestone in structural biology, and sharply intensified the competition in what was by now a fast and aggressive field. Stevens became one such competitor, and his lab is now powering through further

GPCR structures.

But Kobilka’s heart was set on a different goal. The GPCR structures had been snapshots of receptors in an inactive state. To really understand the receptor’s workings, researchers needed to see it as it was being activated by a ligand and turning on the G protein. This project was even more technically daunting than the last. The protein complex was too big to hold in the fatty scaffold; the G protein kept falling off; and this time, the extracellular part of the receptor wouldn’t sit still for crystallization. “This was difficult enough that I wasn’t sure we were ever going to get it,” says Kobilka. “I thought it might be my retirement project.” He also knew that several other labs, particularly those studying rhodopsin, were breathing down his neck.

Kobilka reached out to all manner of experts for help, including Roger Sunahara, an expert on G proteins at the University of Michigan in Ann Arbor. The various groups developed a detergent for stabilizing the receptor with its G protein; a lipid scaffold that could support the complex; and an antibody that could hold it together. And Rasmussen was relentless, testing thousands upon thousands of crystallization conditions and ways to engineer the protein.

One morning last May, Kobilka took a quick peek down the microscope at Rasmussen’s latest effort to produce crystals. “They were already bigger than any other crystals we’d grown of the complex,” says Kobilka. “It was extremely exciting. I didn’t know if they would diffract well or not, but I had a good feeling.” But a planned trip to China meant that he couldn’t be there for the first X-ray images. “As soon as we got to the hotel in Beijing, he got online,” says Tong Sun. When he found out it was solved, “he was on cloud nine. You could tell he just wanted to go back.”

The new picture, solved to a resolution of 3.2 Å, reveals a tangled molecular threesome:  $\beta_2$ AR with a ligand clasped at one end and the G protein nested up on the other. “There’s definitely been a race, and in my opinion, Kobilka has triumphed,” says Chuck Sanders, a structural biologist at Vanderbilt University in Nashville, Tennessee. “Hopefully the field will spread out a little. This complex was the prize, and that’s been done now.”

Kobilka, of course, diverts credit to his collaborators and the “unsung heroes” of his lab, anxious that everyone should see their names in this story. His allegiance to the receptors is as resolute as ever. “The more we learn” about these proteins, he says, “the more complicated and fascinating they are.”

He is already working to understand more of the complications: what the various active states of the receptor look like, why different receptors couple to different G proteins and what happens when different ligands bind to the same receptor. He is also using other techniques, such as electron microscopy and nuclear magnetic resonance, to understand how GPCRs flex and move. “The job isn’t done yet,” he says.

Maybe not — but few would doubt now that Kobilka will finish it. “Brian ultimately reaches his goals,” says Lefkowitz. “Sometimes it takes 15 years, but he gets there.” ■

**Lizzie Buchen** is a freelance writer based in San Francisco, California.

1. Rasmussen, S. G. F. *et al. Nature* **450**, 383–387 (2007).
2. Rosenbaum, D. M. *et al. Science* **318**, 1266–1273 (2007).
3. Cherezov, V. *et al. Science* **318**, 1258–1265 (2007).
4. Rasmussen, S. G. F. *et al. Nature* **469**, 175–180 (2011).
5. Rasmussen, S. G. F. *et al. Nature* <http://dx.doi.org/10.1038/nature10361> (2011).
6. Dixon, R. A. F. *et al. Nature* **321**, 75–79 (1986).
7. Ghanouni, P. *et al. J. Biol. Chem.* **276**, 24433–24436 (2001).
8. Palczewski, K. *et al. Science* **289**, 739–745 (2000).

# DANGER ZONES

Some of the most powerful earthquakes emanate from remote ocean-floor faults. Geophysicists are now laying networks of sensors to keep tabs on these hidden killers.

BY NAOMI LUBICK

Japanese seismologists have been worried about a sea-floor fault for years. The Nankai trough off the nation's southeast coast has produced some of the most devastating earthquakes in Japanese history and is considered ripe for another. So, earlier this year, researchers went out in the ship *KAIYO* to install underwater seismic observatories that should reveal more about the fault and provide seconds of warning when the next big quake hits. In March, the ship was just depositing a batch of the sensors when the massive Tohoku-Oki earthquake broke a completely different fault, 800 kilometres to the northeast, triggering a tsunami that crippled coastal communities.

Seismologists had not thought that the Japan trench off the Tohoku coast was capable of generating such giant earthquakes, in part because they did not have enough devices on the sea floor to catch signs of the building stress. The same dearth of data exists elsewhere, wherever one tectonic plate rams into another and slides beneath it. Such subduction zones generate the planet's most powerful earthquakes, including the biggest ever recorded, a magnitude-9.5 monster off the coast of Chile in 1960. In 2004, a subduction-zone quake off the Indonesian island of Sumatra triggered a tsunami that killed more than 230,000 people. And researchers forecast that a subduction zone bordering the north-western coast of the United States is building towards a magnitude-9 shock that could happen within the next century.

The trouble for seismologists is that these major faults sit hundreds of kilometres from land and buried by thousands of metres of water, where it is difficult to place and maintain observatories equipped with the

seismometers, global-positioning-system units and other instruments that can reveal the structure of the faults and detect changes such as warping of the crust.

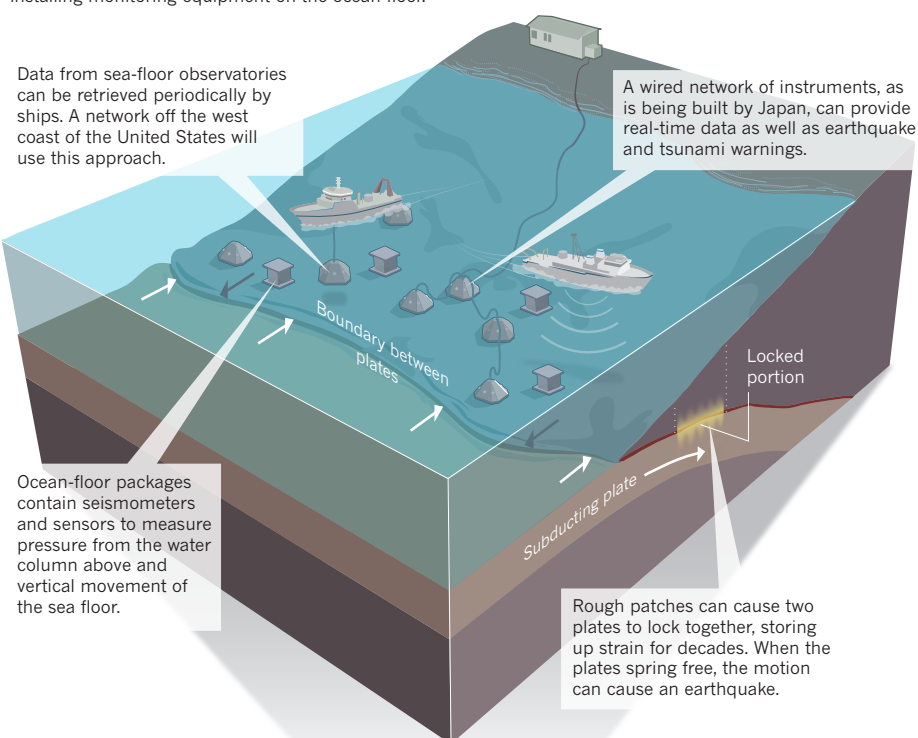
Japan has just 50 observatories offshore to watch its sea-floor faults, compared with more than 8,700 on land. Other nations are even less prepared, with few or no sensors on the sea floor, where the most dangerous parts

of subduction zones lie. Instead, they rely on measurements taken by stations on land — which provide a distant and muffled reading, much like that obtained by a cardiologist who places a stethoscope over a patient's shoe in a fruitless attempt to monitor the heart.

Researchers are now trying to get much closer to the action. The Japanese effort to wire up the Nankai trough is the most

## SENSORS ON THE SEA FLOOR

To learn more about subduction zones — regions where one tectonic plate slips beneath another, and sources of giant earthquakes — geophysicists are installing monitoring equipment on the ocean floor.





ambitious project so far, but the United States and Canada have programmes to monitor the Cascadia subduction zone, which runs from northern California to British Columbia (see 'Sensors on the sea floor'). With better data, geophysicists hope to improve their understanding of how subduction zones work and possibly identify signs of impending disasters.

"Without ocean-bottom measurements, we're always guessing," says Emma Hill, a geodesist at the Earth Observatory of Singapore who is studying quake risks off Indonesia.

### FAULTY UNDERSTANDING

Subduction zones are the recycling centres in the theory of plate tectonics, which describes the movement of the great oceanic and continental plates that make up Earth's brittle outer shell. When two plates collide, the cold, dense

waves from tremors across the globe — all of which should help to illuminate the geometry of the interface between the upper and lower plates. Pressure sensors track warping of the crust by measuring changes in the weight of the water column above. Telecommunications-grade cables connect the observatories with land stations, so researchers have access to the sensor data in real time.

Yoshiyuki Kaneda, who is leading the DONET project for the Japan Agency for Marine-Earth Science and Technology, hopes that the observatories will capture a whole earthquake cycle — from the build up of stress to the release during a great earthquake, followed by the gradual reaccumulation of stress. Researchers hope to learn, for example, how major earthquakes start and what kind of activity precedes them.

## WITHOUT OCEAN-BOTTOM MEASUREMENTS, WE'RE ALWAYS GUESSING THE QUAKE RISKS.

ocean crust sinks, and the plate with more-buoyant, crustal rock rides up over it. But the cartoon-like model — a conveyor belt with slabs of ocean rock diving beneath sheet-like continents above — is an overly simplified picture. "It's going to be complex," says Hill. "And we're still modelling it as a nice smooth plane."

Geophysicists want to know the details of what goes on where the two plates grind against each other. They suspect that the plates somehow become locked together, perhaps when seamounts or other rough features on the subducting plate catch on the underside of the upper plate. After many decades or centuries, the plates then spring free in a mammoth megathrust earthquake. In the case of the March earthquake in Japan, researchers had suspected that the boundary between the two plates was locked, but did not appreciate the risk because they lacked knowledge about the structure of the subduction zone and how stress was accumulating there.

They were more worried about the Nankai trough area, which has a 70% chance of producing a magnitude-8 quake in the next 30 years, according to Japan's official hazard forecast. As part of the Dense Oceanfloor Network System for Earthquakes and Tsunamis (DONET), geophysicists will create a network of 20 underwater observatories in the region of the trough where earthquakes are thought to originate. The DONET project, started in 2006 and to be completed this year, ran to some ¥6.3 billion (US\$82 million), excluding ship time.

The observatories contain seismometers that record vibrations emanating from quakes within the subduction zone as well as seismic

When a big quake does come, the DONET observatories should be close enough to provide early warning to Osaka, Tokyo and other cities that could soon be hit by devastating seismic waves. The pressure sensors can also give advance notice of a tsunami racing toward the coast.

### WESTERN WORRIES

US researchers have seismic worries of their own, focused on the Cascadia region. Great tremors and tsunamis have hit there before, and more than 300 years have passed since the last one. "The seismic hazard from the Cascadian subduction zone is profound," says Maya Tolstoy of Columbia University's Lamont-Doherty Earth Observatory in New York.

Tolstoy is one of the principal investigators in the Cascadia Initiative, a four-year-long programme that is installing temporary observation posts to learn about the behaviour of the massive offshore fault. Last month, the team began deploying the first of 60 such observatories on the sea floor that will enhance an existing network onshore. The project is funded in part by US\$5 million from the American Recovery and Reinvestment Act of 2009, with support from the US National Science Foundation.

Each ocean-floor device, which costs \$60,000–80,000, contains a pressure gauge and a seismometer the size of a soup can, housed in a pressure case with levelling systems and protected from currents and fishing gear by a steel hood. These observatories will not be connected by cable to the mainland. Instead, researchers will retrieve each sensor and download its data once a year before

moving it to a new spot. By pinpointing where earthquakes occur in the subduction zone, data from the Cascadia Initiative will help to resolve the location and structure of the interface between the plates — such as how rough it is and which areas remain locked, says Richard Allen of the University of California, Berkeley.

The sea-floor observations should also help to decipher unusual seismic signals that have been recorded by land-based seismometers in the Cascadia area. The land sensors picked up swarms of tiny quakes occurring roughly every 12–14 months (N. I. Gershenzon *et al. Geophys. Res. Lett.* **38**, L01309; 2011) as well as seismic events that unfold so slowly that nobody can feel the shaking, even though they release substantial amounts of energy. Researchers suspect that the signals reflect activity within the subduction zone, perhaps layers within the plates moving separately or fluids migrating deep under the surface — and hope that recordings from the offshore sensors will help them to come up with an explanation. The sensors might also be able to detect changes in the locked parts of the subduction zone.

The United States is also teaming up with Canada to install long-term sea-floor observation posts in the Cascadia area as part of the Neptune project, which will collect a wide variety of biological, oceanographic and seismic data both for basic research and for potential early warnings of hazards such as algal blooms or earthquakes. Canada is spending Can\$143 million (US\$145 million) on its part of the effort, and last year finished installing a system that includes three seismic stations, five sea-floor pressure recorders and other instruments, connected by an 800-kilometre loop of cable that transmits information to a land station. Budget problems delayed the US portion of Neptune, which began laying cable this summer for observatories to be established over the next few years.

Because installing hundreds of kilometres of fibre-optic cable is expensive, researchers are working to develop autonomous seafaring robots that are able to collect the data. One proposed project would pair wave-powered robots developed by Liquid Robotics in Sunnyvale, California, with stand-alone sea-floor sensors.

As readings pour in from the various networks of offshore sensors, researchers hope they can finally gain a more sophisticated understanding of subduction zones and the hazards they hold. Such ocean-bottom observations are "going to be the story of the next few years," says Hill. Although some projects were in the works before the March earthquake, that catastrophe has added urgency to the research. "Because of Japan," says Hill, "people's minds are on this right now." ■

**Naomi Lubick** is a freelance writer in Stockholm, Sweden.

# COMMENT

**HOMININS** Did modern humans replace Neanderthals or co-exist with them? **p.395**



**HISTORY** Sigmund Freud and William Halstead on cocaine **p.397**

**BIODIVERSITY** DNA bank needed to conserve all species, not just plants **p.399**

**OBITUARY** Jonathan Widom, genomic map-maker, remembered **p.400**

P. DUREUIL/PHOTOALTO/ALAMY



Dosed up: could excessive prescription of antibiotics be hampering children's ability to fight disease?

## Stop the killing of beneficial bacteria

Concerns about antibiotics focus on bacterial resistance — but permanent changes to our protective flora could have more serious consequences, says **Martin Blaser**.

The average child in the United States and other developed countries has received 10–20 courses of antibiotics by the time he or she is 18 years old<sup>1</sup>. In many respects, this is a life-saving development. The average US citizen born in 1940 was expected to live to the age of 63; a baby born today should reach 78, in part because of antibiotics. But the assumption that antibiotics are generally safe has fostered overuse

and led to an increase in bacterial resistance to treatments.

Other, equally serious, long-term consequences of our love of antibiotics have received far less attention. Antibiotics kill the bacteria we do want, as well as those we don't. Early evidence from my lab and others hints that, sometimes, our friendly flora never fully recover. These long-term changes to the beneficial bacteria within people's

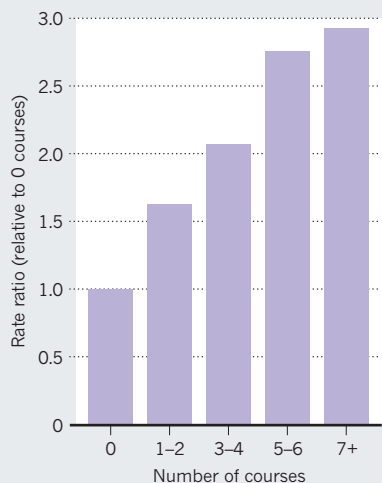
bodies may even increase our susceptibility to infections and disease. Overuse of antibiotics could be fuelling the dramatic increase in conditions such as obesity, type 1 diabetes, inflammatory bowel disease, allergies and asthma, which have more than doubled in many populations (see graph).

We urgently need to investigate this possibility. And, even before we understand the full scope, there is action we should take. ►



## TROUBLING CORRELATION

The risk of inflammatory bowel diseases in children rises with the number of courses of antibiotics taken.



► Bacteria have lived in and on animals — constituting their microbiome — since multicellular life evolved about 1 billion years ago. Hosts derive many benefits from their bacterial guests<sup>2</sup>: the *Bacteroides* species that dwell in the colon synthesize our required vitamin K; gut bacteria help us to resist invading organisms.

An oral or injectable antibiotic diffuses through the bloodstream and affects targeted pathogen and residential microbiota alike. And evidence is accumulating that our welcome residents do not, in fact, recover completely<sup>3</sup> or are replaced in the long term by resistant organisms<sup>4</sup>.

## COLLATERAL DAMAGE

In the early twentieth century, *Helicobacter pylori* was the dominant microbe in the stomachs of almost all people. By the turn of the twenty-first century, fewer than 6% of children in the United States, Sweden and Germany were carrying the organism. Other factors may be at play in this disappearance<sup>5</sup>, but antibiotics may be a culprit. For example, a single course of amoxicillin or a macrolide antibiotic, most commonly used to treat middle-ear or respiratory infections in children, may also eradicate *H. pylori* in 20–50% of cases.

In humans, eradicating *H. pylori* affects the regulation of two hormones produced in the stomach and involved in energy balance, ghrelin and leptin. And as *H. pylori* has disappeared from people's stomachs, there has been an increase in gastroesophageal reflux, and its attendant problems such as Barrett's oesophagus and oesophageal cancer. Could the trends be linked?

*H. pylori* is a risk factor for peptic ulcers and stomach cancer, but a microbe probably wouldn't have been so pervasive if it didn't

carry some benefit to its host. Indeed, large studies we performed have found that people without the bacterium are more likely to develop asthma, hay fever or skin allergies in childhood<sup>6</sup>. Stomachs that lack *H. pylori* seem immunologically quite different from those that do not, and infection of young mice with *H. pylori* protects against experimental asthma<sup>7</sup>.

There is other evidence that antibiotics cause shifts in microbial composition that may bring long-term physiological changes. For instance, as farmers have discovered, continuous, sub-therapeutic doses of many different antibacterial agents cause animals to gain weight with less food. And the earlier that antibiotics are started, the more profound the effects. In my laboratory, we have preliminary evidence in a mouse model that changes in body fat and tissue composition are associated both with low-dose antibiotic treatment that mimics farm use, and with high-dose treatment similar to those used to treat childhood infections.

The changes in our microbiome may even be fuelling the transmission of deadly organisms such as methicillin-resistant *Staphylococcus aureus*<sup>5</sup> and *Clostridium difficile*<sup>8</sup>. This is not an enormous surprise, because one of the important roles of an intact microbial ecosystem is to resist intrusions by pathogenic organisms.

To better understand the long-term effects of antibiotic use, we need to compare the microbiomes of antibiotic-using and antibiotic-free populations. We are working with Maria Gloria Dominguez Bello at the University of Puerto Rico in San Juan and her colleagues to study people living in remote regions in the Amazon who either have never received antibiotics or who have had very limited recent exposures.

If antibiotics do cause long-term physiological changes, we may not be able to wait until we fully understand the problem before changing our approaches. Knowledge gleaned from farms indicates that early life is most crucial, triggering physiological changes that are difficult to reverse later on.

Consequently, we should reduce the use of antibiotics during pregnancy and childhood. Antibiotics — particularly penicillins — are now given routinely to between one-third and one-half of all women during pregnancy or nearing childbirth in the United States and other developed countries. Babies acquire their founding bacterial

populations from their mothers while passing through the vagina at birth. So each generation — particularly the 30% or so of infants born via Caesarian<sup>9</sup> — could be beginning life with a smaller endowment of ancient microbes than the last<sup>5</sup>.

When antibiotics seem warranted — such as in the 30% of pregnant women with group B *Streptococcus*, which causes serious infection in about 1 in 200 newborns — we must better assess which mothers need to be treated, or whether a vaccine might be preferable.

## TARGETED ATTACK

Another precautionary step would be to develop specific agents to stabilize at-risk residential microbial populations, such as effective probiotics. We also need new, narrow-spectrum antibacterial agents to minimize collateral effects on the microbiota. This is an admittedly huge task, which will require providing incentives for the pharmaceutical industry to develop targeted classes of antibacterial agents and, importantly, better diagnostics that rapidly identify the problematic agent.

We may also need to start replacing what has been lost over the past 70 years. Along with receiving standard vaccinations, for instance, one day, children whose microbiome has been genotyped could be given inoculations of specific strains of *H. pylori* to reduce their chance of later developing allergies or asthma, then receive narrow-spectrum antibiotics later in life to eliminate the bacterium and lower the risks of peptic ulceration and gastric cancer.

The ease of worldwide travel is increasing our global vulnerability to pathogens, just as our ancient microbial defences are eroding. We must make use of the available technology to protect and study our bacterial benefactors before it is too late. ■

**Martin Blaser** is chair of the Department of Medicine, New York University Langone Medical Center, New York, New York 10016, USA.

e-mail: martin.blaser@med.nyu.edu

1. Sharland, M. J. *Antimicrob. Chemother.* **60** (suppl. 1), i15–i26 (2007).
2. Ley, R. E., Lozupone, C. A., Hamady, M., Knight, R. & Gordon, J. I. *Nature Rev. Microbiol.* **6**, 776–788 (2008).
3. Dethlefsen, L. & Relman, D. A. *Proc. Natl Acad. Sci. USA* **108** (suppl. 1), 4554–4561 (2011).
4. Sjölund, M., Wreiber, K., Andersson, D. I., Blaser, M. J. & Engstrand, L. *Ann. Intern. Med.* **139**, 483–487 (2003).
5. Blaser, M. J. & Falkow, S. *Nature Rev. Microbiol.* **7**, 887–894 (2009).
6. Chen, Y. & Blaser, M. J. *Arch. Intern. Med.* **167**, 821–827 (2007).
7. Arnold, I. C. et al. *J. Clin. Invest.* **121**, 3088–3093 (2011).
8. Chang, J. Y. et al. *J. Infect. Dis.* **197**, 435–438 (2008).
9. Dominguez-Bello, M. G. et al. *Proc. Natl Acad. Sci. USA* **107**, 11971–11975 (2010).

► **NATURE.COM**  
For more on  
antibiotics crisis:  
[go.nature.com/8ddj4x](http://go.nature.com/8ddj4x)



An exhibit from the Krapina Neanderthal Museum in Croatia depicts a Neanderthal family before modern humans expanded from Africa and arrived in Europe.

## PALAEOANTHROPOLOGY

# African origins

Jean-Jacques Hublin enjoys a book supporting the idea that modern humans replaced Neanderthals.

**T**he question of when, where and why modern humans emerged is the subject of intense debate, and antagonistic views have sprung up as a result. For many years, supporters of the multiregional hypothesis have suggested that modern populations in Africa, Europe and Asia (the 'Old World') descended from local archaic hominins, such as Neanderthals in Europe or late *Homo erectus* in Asia. Today, the Recent African Origin (RAO) model is more widely accepted. It argues instead that modern humans expanded out of Africa between 100,000 and 50,000 years ago, almost entirely replacing archaic Eurasian humans. The assimilation model falls in between, and implies a high rate of interbreeding between invaders and locals.

Chris Stringer was one of the first promoters of the RAO hypothesis. *The Origin of Our Species* is his latest appraisal of this model. Combining the thrill of a novel with a remarkable depth of perspective, the book offers a panorama of recent developments in palaeoanthropology, including the technical improvements that allow for more accurate dating of the fossil record and more precise reconstructions of past environments. Alongside traditional analyses of bones and stones,

Stringer guides the reader through the growing complexity of the field, which has recently extended into palaeogenetics, demography, developmental biology, experimental psychology and neurology. By drawing together a broad range of viewpoints, Stringer's original ideas will open up avenues for those who deal with genes, fossils or artefacts.

One may smile when reading how some in the field have associated early humans' first uses of red pigments with female menstruation and Palaeolithic sex strikes. But on crucial biological and behavioural issues, Stringer is careful to be more critical. Supporters of the multiregional or assimilation models were quick to take advantage of last year's sequencing of the Neanderthal genome to emphasize interbreeding between modern humans and Neanderthals. Stringer explains that current palaeogenetic evidence instead supports a scenario of almost complete replacement. The low level of hybridization observed between the two groups probably involved only a handful of interbreeding



**The Origin of Our Species**  
CHRIS STRINGER  
Allen Lane: 2011.  
352 pp. £20

events at the time when modern humans first expanded out of Africa. He is also refreshingly politically incorrect when admitting the evolutionary role of intergroup violence in the replacement processes.

The initial version of the RAO hypothesis, presented 30 years ago, proposed that modern humans emerged in a small, sub-Saharan 'Garden of Eden'. Stringer's updated picture imagines genetic contributions of populations from a much broader swathe of the African continent. He also emphasizes the role of random genetic drift, demography and cultural selection in the emergence of modern humans. Yet, in his view, the dramatic expansion that made us the first lone human species on the face of the Earth is no historical accident.

Our biological evolution, particularly that of our brain, is intimately linked to cultural and sociological changes. Neanderthals probably did not see the world as we do, and we replaced them because of our differences. Still, readers may remain unconvinced by some of Stringer's claims, in particular the chronological overlap between the first modern humans and their archaic predecessors in Africa. Whether the emergence of modern humans was sudden or gradual remains unanswered.

Stringer wisely states in his conclusion that science is not about being right or wrong, but about approaching the truth of the natural world. Although he has complied with this philosophy throughout his many writings, one must admit that he has mostly been right since the beginning. ■

**Jean-Jacques Hublin** is director of the Department of Human Evolution, Max Planck Institute for Evolutionary Anthropology, Leipzig, Germany.  
e-mail: hublin@eva.mpg.de

**NATURE.COM**  
For more on early human genetics, see:  
[go.nature.com/rtpwpl](http://go.nature.com/rtpwpl)





Natural maths: the spiral arrangement of seeds in a sunflower head follow Fibonacci's sequence.

## MATHEMATICS

# Life models

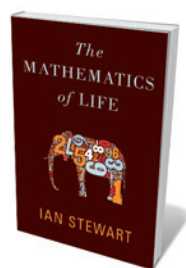
Biology is too complex to be unified by mathematics, finds **Marc Feldman**.

Ian Stewart is a prolific writer of books about mathematics. His latest volume attempts to put mathematical thinking at the centre of biology. *The Mathematics of Life* is framed around five revolutions: the microscope, the development of taxonomy, evolution, Gregor Mendel's discovery of discrete inherited traits (later found to be genes) and the structure of DNA. Mathematics, which Stewart claims unites these developments, is proposed as a sixth "biological revolution".

These five milestones were indeed major breakthroughs, but Stewart's efforts to situate mathematics at their core seem contrived. His historical style means that there is no up-to-date assessment of, or speculation about, the kind of mathematics that biologists might find useful in the future. A better survey might, for example, have considered Sewall Wright's contributions to the study of small populations or Ronald Fisher's reconciliation of genetics and biometry.

One-third of the book is essentially a fast course in biology, covering the importance of the microscope in discovering microbes; elements of plant development; the contributions of Charles Darwin, Alfred Russel Wallace and Mendel; and an introduction to DNA structure. There is an extensive section on the Fibonacci series and plant growth, but later chapters on the origin of life and astrobiology seem misplaced as these topics lack obvious mathematical underpinnings.

The tremendous progress in computational biology is barely mentioned, and behavioural biology is buried in a description of game theory rather than the



**The Mathematics of Life**  
IAN STEWART  
Basic Books: 2011.  
368 pp. \$27.99

mathematics of dynamic systems. Whereas discussions of ecosystem analysis from the 1980s and 1990s are well presented, work from the past 15 years is not: the active theoretical debate on whether ecological communities are neutral or competition-driven is not referred to. Recent theories that address species depletion and climate change are strangely neglected.

Nor does the book describe how Fisher, Wright and J. B. S. Haldane developed the mathematics of evolutionary genetics while

**"The fragmentation of biology and its maths is likely to continue for a long time."**

laying the foundations for modern data analysis. This is a missed opportunity to unify the chapters on Mendel and Darwin, biologically and

mathematically. Modern population genetics, with its wealth of stochastic processes and highly nonlinear dynamics, is ignored.

Epidemiology, one of the oldest applications of mathematics to biology, is in the chapter on plankton — in my view, a strange juxtaposition. Given the emphasis on history, the foundational 1927 work of William Kermack and Anderson McKendrick that gave rise to the modern theory of epidemics is a glaring omission. Networks, which are a hot topic in biology and social science, receive a brief but outdated treatment, whereas topological knot theory is expansively discussed as fundamental to the biology of macromolecules.

As a mathematician, it is understandable that Stewart chooses to emphasize the concept of symmetry. But the relationship between the abstract mathematics of symmetry and organismal or molecular biology seems tenuous. I would have preferred to see space devoted to the properties of deterministic or stochastic dynamic systems, for example, that are closer to the interests and needs of practising biologists. The reader is left with Stewart's personal passions rather than the big picture suggested by the book's title.

The extreme diversity between the different disciplines of biological research mitigates against a unification in terms of mathematical modelling. It is not sufficient to claim, as Stewart does, that such a unification could be built around a theory of complexity. Although Stewart's many examples of mathematical models of biological phenomena are interesting to read, each requires a different part of mathematics. The fragmentation of biology and its maths is likely to continue for a long time. ■

**Marc Feldman** is professor of mathematical and evolutionary biology at Stanford University, Stanford, California 94305, USA. e-mail: [mfeldman@stanford.edu](mailto:mfeldman@stanford.edu)

## PSYCHOLOGY

# Giants on coke

George Rousseau learns about the impact of cocaine on physicians Sigmund Freud and William Halsted.

Two eminent physicians became addicted to cocaine in the 1880s: Sigmund Freud, the founder of psychoanalysis, and William Halsted, the great US surgeon and early advocate of the aseptic technique. Each developed a dependence while seeking ways to reduce their anxieties about their careers and private lives. Now, two books explore how the addiction altered each man's life, personally and professionally.

Medical historian Howard Markel explores these parallel lives in *An Anatomy of Addiction*, and David Cohen in *Freud on Coke* valiantly interprets Freud's conscious and unconscious states without obeisance to canonical biography. Both books are gripping for their revelations about private lives in public contexts — in these cases, the lives of driven men determined to become world-class figures while under the influence.

As Markel notes, Freud is thought to have started taking cocaine as a young researcher at the Vienna General Hospital in the early 1880s, to relieve nasal lesions. Cocaine — known as coca at the time — was considered a miracle drug. Its extraordinary physiological powers were the topic, in 1885, of Freud's first medical treatise, *Über Coca*. Freud was then scraping together a living, insecure about his medical competence and his strained relationship with his politically radical father, and trying to find a niche for himself. Cocaine assuaged his stress, but addiction blinded him to the drug's medical use as an anaesthetic, even though he was convinced of its use in treating morphine addiction.

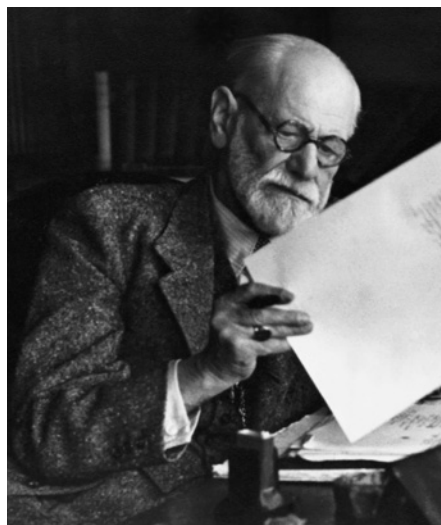
Halsted, Markel shows, became hooked on cocaine while criss-crossing continents. He sailed on ocean liners to Europe, studied medicine in Germany and was so restless that he sometimes disappeared from work and public life. In 1886, his addiction landed him in the Butler Hospital, a psychiatric institute in Providence, Rhode Island, where he was treated and released. But as his star rose he continued to take the drug, even while a leading professor at the Johns Hopkins University School of Medicine, the country's premier

**An Anatomy of Addiction: Sigmund Freud, William Halsted, and the Miracle Drug Cocaine**

HOWARD MARKEL  
Pantheon: 2011.  
352 pp. \$28.95

**Freud on Coke**

DAVID COHEN  
Cutting Edge Press:  
2011. 200 pp. £14.99



L: CORBIS; R: ALAN MASON CHESNEY ARCHIVES, JOHNS HOPKINS MED. INSTS

Psychologist Sigmund Freud (left) and surgeon William Halsted took cocaine to relieve anxiety.

medical school in Baltimore, Maryland.

Ambition and anxiety were not the only factors favourable to the development of a habit. Coca was viewed as harmless in the nineteenth century, and, as scientific researchers, Freud and Halsted had access to large quantities. They were among its first user-victims. Both saw their enslavement as just another moral defect that could be remedied by routine and prayer. But cocaine use fundamentally affected their relationships with patients, colleagues, family and friends, and was detrimental to their health. Each man's 'coke story' also raises the question of whether either would have been able to conquer a new province of knowledge without the drug.

Certainly, Freud's anxieties figure prominently in the famous 1895 dream 'Irma's injection', which became a pillar of his psychoanalytic theory. Both Markel and Cohen consider the episode to be key to understanding his addiction. The dream reflected a bizarre incident in Freud's life. His medical accomplice, Wilhelm Fliess, with Freud's blessing, had attempted to cure Freud's patient Emma Eckstein of her 'nasal reflex neurosis' by operating on her nose. Fliess botched the operation. In the dream, Irma (Emma) reproaches Freud for her condition, and he blames it on an injection given by a friend. In real life, Freud was so anxious about the effect of this case on his reputation that he took even more cocaine, affecting his

marriage and other relationships.

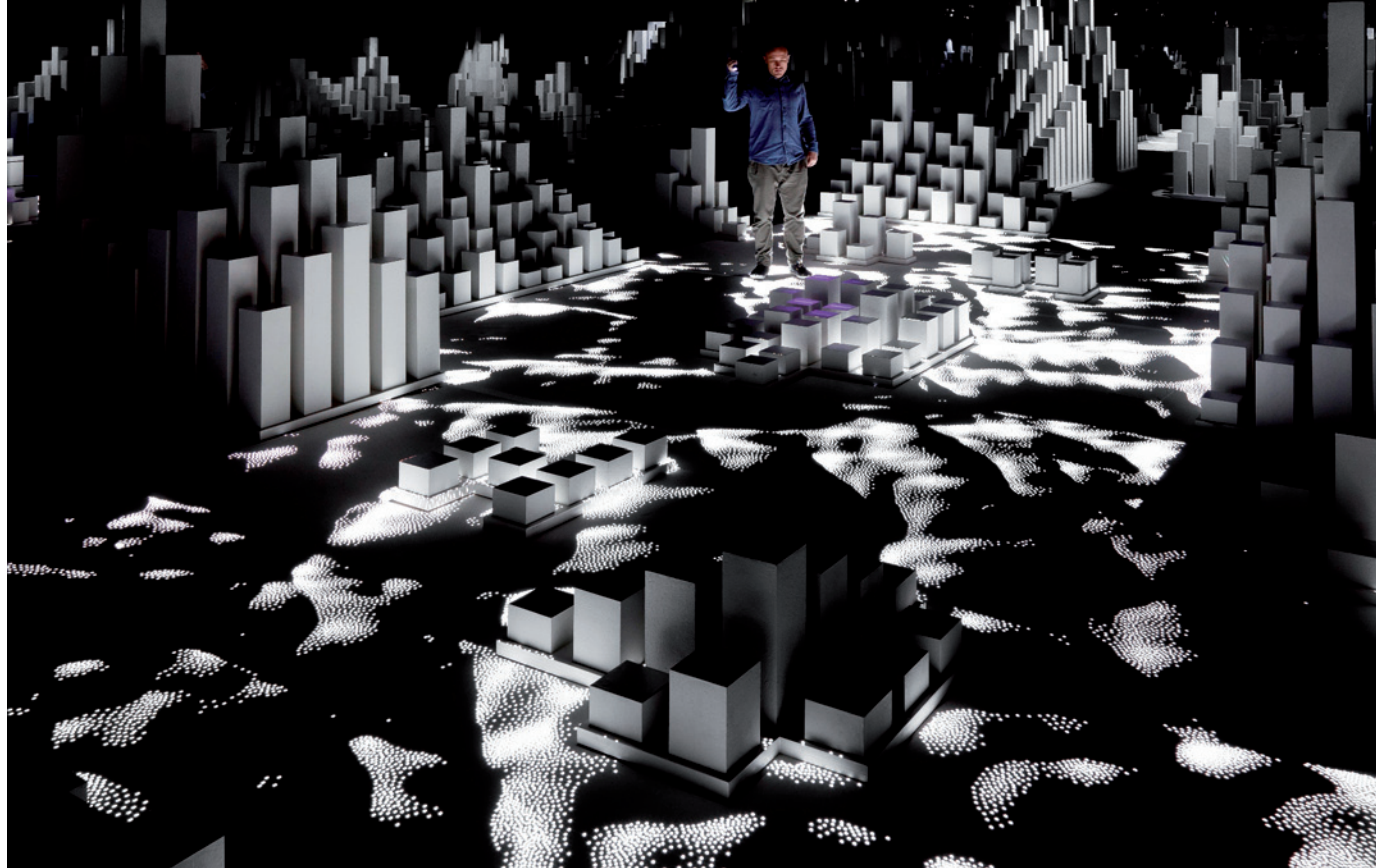
Halsted also struggled with personal relationships. Yet his addiction probably accelerated his already formidable drive, and may even have helped him to formulate insights on the urgent need for surgical antisepsis.

Both men learned to suppress and manage their addictions after making their names. Late in life, Freud — who seemed to thrive on contradiction and hypocrisy — took giant steps to cover up traces of his habit, because the truth might have cast a shadow over his central theories. Most of Halsted's hospital colleagues knew of his addiction, but nothing was said — and the man himself, as is clear in Markel's book, could not countenance the truth.

Markel brilliantly describes the paradoxes of the two lives. Cohen adroitly teases out the nuances of the Irma episode. There is also a subplot to Cohen's biography: the resistance the writer encountered from some specialists while researching his book. The reputation of the Viennese enigma remains unassailable among official biographers, but with every passing year, the weight of evidence points more clearly to the high price that Freud and his intimates paid for the 'cocaine years'. ■

**George Rousseau** is a professor of history at the University of Oxford and co-director of its Centre for the History of Childhood, Oxford, OX1 4AU, UK.  
e-mail: george.rousseau@magd.ox.ac.uk





J. ADRIAN/NATL MARITIME MUS.

*High Arctic* immerses visitors in an abstract landscape representing the Svalbard glaciers, the names of which are illuminated by the viewer's ultraviolet torch.

#### CLIMATE CHANGE

# Notes from a cold climate

**Deborah Dixon** explores an elegiac exhibition about the far reaches of the Arctic.

The Arctic is often portrayed in 'long shot' as a sublime and haunting land- and seascape. The launch of an exhibition in the glorious new Sammy Ofer wing of London's National Maritime Museum gives the top of the world real immediacy, using sound, light and sculpture to bring home the experience of venturing to this glacial region.

*High Arctic* is an interactive installation recreating the Arctic impressions of Matt Clark, creative director of London-based art and design team United Visual Artists. Clark — whose day job is producing stage shows for bands such as The Chemical Brothers — journeyed to the Svalbard ice field in 2010 with Cape Farewell, an organization that has taken tens of artists and scientists to polar locations for dialogue on climate change since 2001.

The virtual voyager's first port of call in the exhibition is a foyer documenting the Cape Farewell trip. Video screens relay interviews with team members and film clips from the voyage — of icebergs, polar bears and scientific equipment. In a darkened corridor beyond is a timeline of polar discovery, picked out by the light of ultraviolet torches given to visitors on entry. The timeline runs from 2100 back to the fourth century BC,

when the Greek geographer Pytheas of Massalia (a Greek colony; now modern Marseilles, France) travelled to the far north and described the midnight Sun and ice floes.

Other figures in polar history are noted. They include: Jonas Poole, who in the seventeenth century explored Bear Island and Spitsbergen off Norway, and established the English whaling trade; nineteenth-century explorer William Parry, who in 1827 set a record for reaching the most northerly point that stood for nearly half a century; and Nils Strindberg, the Swedish photographer who accompanied S. A. Andrée on his helium-balloon expedition in the Arctic in 1897.

These characters inspired a work by Clark's fellow voyager, British poet Nick Drake. Fragments of Drake's verse are played in a vast 40-by-15-metre room permeated by a soundscape of creaking wood, whistling wind and radio static. Arranged on the floor are more than 3,000 monolithic white forms of varying heights, grouped into 74 'islands' representing the Svalbard archipelago. These abstract representations of individual glaciers, whose names can be picked out in the

**High Arctic**  
National Maritime  
Museum, London.  
Until 13 January 2012.

ultraviolet light cast by visitors' torches, have the ghostly air of a drowned cityscape.

Further flicks of the torch reveal more information and poetic interpretations of the fragile landscape in five light 'pools'. In one, shaped like Svalbard's islands, lines of latitude and longitude shift under the beam; in others, snow flurries and drifts appear, then melt into black slicks. In yet another, squares of light calve from a cluster of small monoliths and break up under the torchlight to show the deterioration of the glaciers.

*High Arctic* is elegiac and engaging. Its sights and sounds reveal the wonder and human cost of scientific endeavour in the region. Paradoxically, the more we know, the more we realize the limits to our understanding of this remote place. As Drake's poem has it, "I staked my life and sailed into a dream;/When at last I returned home/They did not believe me./I wrote the truth in a book,/But then the book was lost..." ■

**Deborah Dixon** is a Reader in human geography at Aberystwyth University, Ceredigion, SY23 3DB, Wales, UK, and co-leader of a project investigating the emergence of art-science collaborations. e-mail: dxd@aber.ac.uk

# CORRESPONDENCE

## Invest in a DNA bank for all species

To complement its efforts to conserve nature in the wild, the Convention on Biological Diversity should develop a comprehensive and adequately funded global effort to preserve intact genomes and viable cells for every known species and for new species as they are discovered. Super-cold freezing is the current method of choice, from a whole rhino skin to a bacterium.

Freezing tissue costs US\$200–300 per species, with negligible maintenance costs. Preserving material from all the roughly 1.8 million known species would cost about \$540 million. The United States spends more than \$1 billion every four days on the war in Afghanistan. So less than \$1 billion to preserve the DNA of all known species on Earth, with whom we share billions of years of evolutionary history, seems like good value.

Keeping DNA intact for future research has the potential for cloning and for the resurrection of extinct species. Some worry that we might then do less to save life in the wild. But it does not make sense to lose genomes forever just because we lack the motivation to pursue conservation at the same time.

Plants are currently better represented in frozen collections than animals, with the best coverage for agricultural species. But seed banks collectively hold viable tissue of just a fraction of all known species. There is no shared plan or funding for an entire encyclopedia of life.

We need an inventory of what is already preserved and a plan for preserving what is not. We need shared protocols for collection and storage, and ways to ensure that countries can participate without fear of losing out on revenue from future commercial uses.

Flexible guidance on priorities

would be helpful, for example to preserve the most genetically divergent species, to address threatened species in good time, and to engage the international community in collecting and storing tissue.

**William Y. Brown** *Brookings Institution, Washington DC, USA. [wbrown@brookings.edu](mailto:wbrown@brookings.edu)*

## Learn from Ireland's knowledge economy

You highlight China's scientific investment drive (*Nature* **476**, 5; 2011). This is a reminder that nations with little experience of modern large-scale investment in science may be jumping into ill-planned knowledge-economy ventures that could have serious long-term consequences.

Take Ireland, for example. An explosion in scientific investment quickly attracted many scientists to the country and saw it climb up the international scientific rankings. Now fundamental flaws in the Irish system are showing up as the funding fades.

Having been recruited from the United States by Science Foundation Ireland (SFI), we were shocked to discover how poorly planned and disjointed the research system seems to be in Ireland. The SFI does not make clear to either the host institution or the recruited scientist that their investment in the recruit is short-term. One learns after recruitment that universities often do not want to employ researchers for longer than 4 years, to avoid commitments under the European Union's fixed-term workers' contract.

Continuous changes by the SFI to core funding programmes, combined with cronyism in the Irish university system, mean that the career structures and support needed to build a stable research environment are missing.

Many Irish researchers are discontented; some have left

or are leaving the country (D. Ahlstrom *The Irish Times* 17 December 2010). Ireland seems not to realize that it is scientists who drive research, focusing instead on large capital investments in impressive research buildings that bolster the image of an economic strategy.

Many countries try to emulate the US academic system. This is based on money, yes, but also on supporting talent through the tenure track. Ignore this and valuable government finances will be wasted and the careers of young scientists will hit a dead end. Developing a knowledge economy requires some knowledge of how to do it properly.

**Mojgan Naghavi** *Columbia University, New York, USA. [mn2034@columbia.edu](mailto:mn2034@columbia.edu)*

**Derek Walsh** *New York University, New York, USA.*

## Nanomaterials should be defined

Andrew Maynard argues against defining engineered nanomaterials for regulatory purposes (*Nature* **475**, 31; 2011). But such a definition is urgently needed, especially for particulate nanomaterials. The aim should be to identify a general class of materials for attention — whether they are benign or hazardous.

Nanomaterials have many properties not shared by their larger-scale counterparts, some of which have safety implications. More and more products containing novel nanomaterials are reaching the market.

In light of legitimate public concerns and the resultant political responses, a revision and adaptation of legislation is considered necessary. The European Cosmetic Products Regulation of 2009 and a European Parliament legislative resolution on food information adopted in July 2011 both stipulate that nanomaterial

ingredients should be strictly labelled. The European Parliament has called for the adoption of a “comprehensive science-based” definition of ‘nanomaterial’.

Maynard's point that such materials are heterogeneous is justified. However, they all have structures on the nanoscale, which modify their other properties. Size is therefore the most appropriate parameter on which to base a broad definition (see also G. Lövestam *et al.* EUR 24403 EN, European Commission Joint Research Centre; 2010). A definition is required for labelling purposes, and would assist industry and regulators in identifying where specific safety assessments might be necessary. We acknowledge that it would need revision in line with fresh scientific evidence.

**Hermann Stamm** *European Commission Joint Research Centre, Institute for Health and Consumer Protection, Ispra, Italy. [hermann.stamm@ec.europa.eu](mailto:hermann.stamm@ec.europa.eu)*

## Stats for papers let authors track impact

Your website now enables authors to access download statistics for their publications in journals of the Nature Publishing Group (see [go.nature.com/9wmgcu](http://go.nature.com/9wmgcu)), a feature I have found useful. What's more, information on median downloads for all articles in a specific journal enables me to evaluate that journal's impact in the wider scientific community.

**Si Ming Man** *University of Cambridge, Cambridge, UK. [smm77@cam.ac.uk](mailto:smm77@cam.ac.uk)*

### CONTRIBUTIONS

Correspondence may be sent to [correspondence@nature.com](mailto:correspondence@nature.com) after consulting the author guidelines at [go.nature.com/cmchno](http://go.nature.com/cmchno).



# Jonathan Widom

## (1955–2011)

Genomic map-maker and consummate teacher.

One of the fundamental paradoxes of DNA, life's most iconic molecule, is that nearly a metre of this polymer must be packed into the microscopic nucleus of every human cell while still granting access for the many biochemical and biophysical transactions needed to exploit its genetic information. Jonathan Widom rigorously and creatively applied physical and chemical principles to unravel the mystery of how genomes can at once be tightly packed and yet available for read-out. He did this over a 30-year career that ended unexpectedly and prematurely on 18 July 2011. He was 55.

Widom was born in Ithaca, New York, to parents who were, and still are, both chemists at Ithaca's Cornell University. The first of three children, who all became scientists, Widom's career reflects the intellectual curiosity fostered in his scientifically prolific home. Growing up near the Finger Lakes of upstate New York, he and his friends searched for crayfish, toads, butterflies and moths in the streams and fields, foreshadowing his future in biology. His passion for exploration, cultivated in his early days, only increased, as did the palette of topics he chose to investigate. In 1977 he obtained a bachelor's degree in chemistry, also from Cornell.

### UNPACKING DNA

Widom's lifelong interest in how organisms manage their genomes began during his graduate student days in the laboratory of Robert Baldwin at Stanford University in California. In viruses that infect bacteria, more than 10 micrometres of DNA is stuffed into a roughly 50-nanometre protein head, a process that has been likened to putting 500 metres of suspension-bridge cable into the back of a delivery truck. Widom's thesis work used electron microscopy and light scattering to test ideas about DNA packing, inspired in part by the startling observation that when surrounded by appropriate ions of opposite charge, DNA will spontaneously collapse into doughnut-shaped configurations.

After completing his PhD in 1982, he moved to the laboratory of Aaron Klug at the Medical Research Council Laboratory of Molecular Biology in Cambridge, UK. There he turned his attention to the geometry of eukaryotic DNA packing, setting the stage for the scientific questions that would dominate his career. Proteins known as histones compact DNA in eukaryotic organisms. Histones form stubby cylindrical octamers,



and each octamer wraps up nearly 150 base pairs of DNA to form a nucleosome. Widom's beautiful seminars spelled out his vision for a physically based genome science. This vision spanned from the rules governing the assembly and accessibility of individual nucleosomes all the way to what dictates nucleosome positioning genome-wide, and how this positioning governs gene expression. In recent years, this vision has been coming to fruition, largely as a result of Widom's work.

During the 1990s, one of the most important questions that Widom attacked with his "troops", as he affectionately called those working with him in his lab, was how the many proteins that copy, transcribe and repair genomic DNA reach sites within individual nucleosomes. As an independent investigator, first at the University of Illinois in Urbana-Champaign and later at Northwestern University in Illinois, he designed increasingly accurate experiments to measure the rate at which individual nucleosomes open up to render their sequestered DNA accessible. He probed the influence of packing depth and environment by burying recognition sites for DNA-cutting enzymes or fluorescent molecules at different spots within nucleosomes. He delighted in starting with simple models based on fundamental principles and seeing how far those models might go in explaining complicated biological problems.

Widom articulated the biological problem that most consumed him in recent years as: "Do nucleosomes care about their position on the genome and does the genome encode the positions of these nucleosomes?" As a prelude to answering these questions, Widom and his troops performed one of his most well-known experiments, revealing the extent to which different DNA sequences favour the formation of nucleosomes. These results sowed the seeds for his seminal genome-scale efforts to seek out the rules for nucleosome occupancy in organisms ranging from yeast to humans. At the time of his death, he and his collaborators had just introduced a groundbreaking chemical-mapping strategy using engineered histones to investigate this question and produce maps at base-pair resolution.

### LEGENDARY GENEROSITY

Jon was the best of colleagues. He was noted for his honesty, kindness and insatiable curiosity. He loved life, and everyone around him felt happier and smarter in his presence. His generosity was legendary. As a tiny but telling example, each year he and his wife Daphne bought four season tickets for the opera and took a pair of friends or colleagues to each performance. At work, he always had time to help anyone who asked, never hinting that he had his own prodigious workload.

He loved cooking and there was no better dinner companion. He read insatiably, and his resulting broad and penetrating knowledge, scientific and otherwise, often gave others the feeling that he knew more about their work than they knew themselves. His passion for exploration took him all over the world, with recent trips to India and China merging his love of food and the outdoors. For many of us, his attendance at a meeting was a prerequisite for our own.

An ancient Greek definition holds that happiness is "the exercise of vital powers along lines of excellence in a life affording them scope". Jonathan Widom had extraordinary vital powers which he exercised along lines of excellence in a way that was an inspiration to all. ■

**Rob Phillips** is a professor of biophysics and biology, California Institute of Technology, Pasadena, California 91125, USA. He was a friend and collaborator of Widom's from 2001.  
e-mail: phillips@pboc.caltech.edu

R. GRABER/NORTHWESTERN UNIV.

## FORUM Chemical engineering

# Fuel for debate

With fossil-fuel supplies set to dwindle, the race is on to find ways of making fuels from renewable sources of biomass. Two experts discuss the broad strategies — biochemical and thermochemical — that have emerged as practical approaches.

### THE TOPIC IN BRIEF

- Finding ways to make fuels from renewable sources is among the most active research areas in chemistry.
- One strategy is to use biological agents, such as enzymes or whole organisms, to catalyse processes for converting biomass into fuels, or to make fuels by photosynthesis.
- Alternatively, the thermochemical approach uses abiological, chemical means to make fuels from biomass.
- Each approach offers different advantages and challenges for the large-scale production of biofuels.

## Biochemistry for biofuels

STEPHEN MAYFIELD

Biochemical production of biofuels is already a successful and profitable business — last year more than 50 billion litres of bioethanol was produced worldwide<sup>1</sup>. Bioethanol is made by fermenting sugars derived from maize (corn) starch or sugar cane using yeast, but, from a quick back-of-the-envelope calculation, I estimate that at the present production rate, maize and sugar cane will probably at best be able to replace only about 3% of the energy currently generated by fossil fuels. And with food prices rising at an unprecedented rate (partly as a side effect of crops being grown for biofuel production), making fuel from maize and sugar cane may not be a sustainable solution to the world's energy needs.

We clearly require new sources of bioenergy that aren't tied to food or limited in supply. Perhaps the two most promising options are plant-derived lignocellulose (woody material) and algae (Fig. 1). Developing economically viable processes for making biofuels from these sources is a challenge in both cases, and the two sources each have their own scientific obstacles to overcome. For lignocellulose, the



**Figure 1 | Biomass for fuels.** **a**, Lignocellulose is found in fibrous biomass, such as this waste material from maize (corn) farming. It is most effectively converted into fuels by thermochemical processes. **b**, Algae naturally produce oils that can be used as biofuels, encouraging research into algal culturing systems.

challenge for the biochemical approach is to find a way of degrading the material into simple sugars that can then be converted into fuels by microorganisms. There are presently several research efforts aimed at solving this problem,

but progress seems to be slowing, and it may be that this is an area where thermochemical processes have real advantages.

Algae, on the other hand, produce oils (lipids) by photosynthesis that should fit almost seamlessly into our existing petroleum infrastructure<sup>2</sup>. When efforts to make biofuels from algae began a few years ago, the main hurdles were recognized to be: identifying or genetically engineering algal strains that grow rapidly and have high lipid content; developing algal crop-protection strategies; devising economic methods for harvesting algae from water and extracting oil from the harvested algae; and finding ways to efficiently turn algal oils into fuels.

Since then, algal strains have been found that are suitable for commercial biofuel production, and great strides have been made in lipid-extraction and fuel-conversion technologies (although further improvements could undoubtedly be made). Of the remaining hurdles, crop protection in algal farming is likely to be similar to that for any crop — a constant battle between the farmer and various pests and pathogens. Although advances in algal crop-protection strategies have been made, this is clearly one area that must still be properly understood and developed.

In addition, the lack of economically viable harvesting processes remains a major obstacle to commercial biofuel production from algae. Perhaps the biggest problem is that algae growing in ponds make up only 0.1% of the mass, with the remaining 99.9% being water. And the algae must be concentrated 200-fold, to 20% solids, before oil extraction can take place. Removing the excess water is a costly process. Several potential solutions to this have been proposed, including filtration systems, chemical or biological methods for aggregating cells, and even systems in which algae secrete the oils, thus removing the need for algal harvesting. But more work is needed.

I firmly believe that if we had the equivalent of a combine harvester for algae that was as efficient as harvesters are for grains, then the cost of algal biofuels would be similar to that of petroleum fuels today. In fact, the best estimates suggest that the cost of algal oil is currently only about three times that of



petroleum<sup>3,4</sup> — not bad, considering that we have had just a few years of real research investment in this field.

**Stephen Mayfield** is in the San Diego Center for Algae Biotechnology, and in the Division of Biological Sciences, University of California, San Diego, San Diego, California 92093, USA. e-mail: smayfield@ucsd.edu

The author declares competing financial interests. See go.nature.com/xmx4sx for details.

## Thermochemical solutions

P. K. WONG

Thermochemical routes to making biofuels are perhaps best exemplified by the production of fuels from lignocellulose biomass — sources of which include agricultural and forestry residues (such as wheat stalks and wood), municipal waste (paper and wood) and specially grown crops (such as *Miscanthus* grasses and poplar trees). But although lignocellulose is abundant<sup>5</sup> and cheap, its conversion to biofuels is expensive.

The logical way to make biofuels from lignocellulose is to adapt the approach used in the gas-to-liquid (GTL) or coal-to-liquid (CTL) processes for converting natural gas or coal into synthetic diesel<sup>6</sup>. The biomass-to-liquid (BTL) process involves gasifying lignocellulose — converting it into syngas, a mixture of carbon monoxide and hydrogen — by heating it in the presence of oxygen or water, typically at about 800 °C. The syngas is polymerized in a reaction called the Fischer–Tropsch synthesis (FTS) to make linear hydrocarbons known as alkanes. These are then ‘cracked’ to make the shorter alkanes (containing 12–20 carbon atoms) characteristic of diesel.

Synthetic diesel produced by BTL is more expensive than fossil diesel or diesel made by GTL and CTL, for several reasons. First, unlike the gasification of coal or the conversion of natural gas into syngas, gasification of lignocellulose generates tar, which requires costly removal to prevent the fouling of equipment and poisoning of FTS catalysts. Second, the ratio of hydrogen to carbon monoxide in biosyngas is about 1:1, but the FTS requires this to be about 2:1. To increase the ratio, an extra step is needed in which carbon monoxide is reacted with water to form hydrogen and carbon dioxide. This reduces the amount of carbon incorporated into the product from the biomass, thereby increasing the overall amount (and cost) of biomass required. Finally, BTL cannot achieve the same economy of scale as GTL and CTL because of the challenging logistics and high costs of collecting and transporting lignocellulose biomass.

Syngas can also be converted into methanol and then into gasoline<sup>7</sup> (a mixture of C<sub>5</sub> to C<sub>10</sub> alkanes). The technology for this route is proven — a commercial-scale methanol-to-gasoline plant operated successfully for about 10 years in New Zealand, using natural gas as the source of syngas. But a biomass-based methanol-to-gasoline process would require syngas to be made from biomass, and would therefore face the same problems as BTL.

Several catalytic chemical processes that do not involve syngas have also been investigated. A common goal is to increase the energy density of the fuel by eliminating oxygen from the biomass — the less oxygen there is in a fuel, the more energy is released on combustion<sup>8</sup>. Besides deoxygenation, many other reactions can be used to convert compounds obtained from biomass into fuels of suitable volatility and energy density for use in different engines. For example, small molecules can be joined together to make larger ones in oligomerization and condensation reactions, and cracking in the presence of hydrogen (hydrocracking) is useful for breaking larger compounds into smaller ones. Importantly, any hydrogen used should be derived from renewable sources to minimize carbon emissions.

### NANOTECHNOLOGY

## Smart connections

**Nanoscale devices have now been made that mimic biological connections in the brain by responding to the relative timing of signals. This achievement might lead to the construction of artificial neural networks for computing applications.**

DMITRI B. STRUKOV

The development of artificial neural networks that could rival their biological counterparts is arguably the last frontier in computing. A long-standing drawback is the lack of efficient hardware technology. Two papers — one by Kuzum *et al.*<sup>1</sup> in *Nano Letters* and the other by Ohno and colleagues<sup>2</sup> in *Nature Materials* — report the synthesis of inorganic artificial synapses that bring viable technology for artificial neural networks a step closer.

The mammalian brain outperforms computers in many computational tasks — for example, it can recognize a complex image faster and with better fidelity, and yet consumes a tiny fraction of the energy used by computers to do this. In an attempt to make computers that match the efficiency of biological information processing, artificial neural networks were conceived, the first implementations<sup>3</sup> of which appeared even before the first digital microprocessor. But although the performance of microprocessors has improved

It is currently difficult to predict which approach — biochemical, thermochemical or a hybrid of the two — will ultimately be most cost-effective for making lignocellulosic biofuels. But if the history of bioethanol is any guide, it will take years of experience in producing such biofuels before they become as cheap as fossil fuels. ■

**P. K. Wong** is at the Institute of Chemical and Engineering Sciences, Agency for Science, Technology and Research, 627833 Singapore. e-mail: pkwong@ices.a-star.edu.sg

1. www.ethanolrfa.org/pages/statistics#E
2. Hannon, M., Gimpel, J., Tran, M., Rasala, B. & Mayfield, S. *Biofuels* **1**, 763–784 (2010).
3. Davis, R., Aden, A. & Pienkos, P. T. *Appl. Energy* <http://dx.doi.org/10.1016/j.apenergy.2011.04.018> (2011).
4. Craggs, R. J., Heubeck, S., Lundquist, T. J. & Benemann, J. R. *Wat. Sci. Technol.* **63**, 660–665 (2011).
5. Somerville, C., Youngs, H., Taylor, C., Davis, S. C. & Long, S. P. *Science* **329**, 790–792 (2010).
6. Klass, D. L. *Biomass for Renewable Energy, Fuels, and Chemicals* (Academic, 1998).
7. Olah, G. A., Goeppert, A. & Prakash, G. K. S. *J. Org. Chem.* **74**, 487–498 (2009).
8. Petrus, L. & Noordermeer, M. A. *Green Chem.* **8**, 861–867 (2006).

exponentially during the past four decades, the progress of artificial neural networks has been much less remarkable.

At its most abstract, a neural network can be represented by a diagram (Fig. 1a) in which nodes corresponding to neurons are connected by lines corresponding to synapses (the junctions between neurons). In parallel, each node processes input information from the preceding nodes and then passes it to the next layer of nodes. For example, a node might add together input signals, each of which is scaled by a weight associated with the corresponding synapse; the output of the node would then depend on whether the sum of the weighted inputs is higher than the threshold value of the node. For any given structure of an artificial neural network, the overall functionality is defined by the synaptic weights, which are adjusted during learning processes.

To match the complexity of the human brain, artificial neural networks would need to contain roughly 10<sup>11</sup> nodes, with every node connected on average to 10,000 others — which equates to about 10<sup>15</sup> synapses. This

requirement for high complexity, connectivity and massive parallel information processing is what makes it so challenging to make artificial neural networks that mimic the performance of biological systems. Indeed, software simulations of neural networks on conventional computers ('von Neumann' computers, for those in the know) are very slow. Neural networks based on purpose-built integrated circuits are more efficient in terms of speed, area and power consumption, but even these are largely inadequate using current technology. For instance, the crudest artificial synapse requires more than ten transistors, which is impractical for the implementation of large networks.

Artificial synapses that address some of these challenges were reported last year<sup>4</sup>. These nanometre-scale devices consisted of thin films of amorphous silicon enriched with clusters of silver atoms, sandwiched between two metal electrodes. When a voltage bias was applied across the electrodes in one direction, silver filaments formed and/or grew in the silicon, decreasing the electrical resistivity of the device and so increasing the synaptic weight (the conductivity). When the polarity of the applied voltage bias was reversed, the silver filaments dispersed and/or shrank, increasing the resistivity and so reducing the synaptic weight.

The idea of using a resistive switching mechanism to implement artificial synapses has been around for many years<sup>3,5,6</sup>, but the devices described above<sup>4</sup> clearly demonstrated that functional artificial synapses could be made that have a nanometre-scale footprint. In a neural network, the synapses would act as 'crossbar' junctions between overlapping electrodes attached to artificial neurons (Fig. 1b), and so the footprint of the synapses is limited only by the overlapping area of two electrodes — the smaller the overlapping area, the smaller the synapses can be. Crude estimates<sup>7</sup> have shown that synapses smaller than 10 nanometres in length could be used to make artificial neural networks of sufficient complexity and connectivity to challenge the computational performance of the human brain.

Kuzum *et al.*<sup>1</sup> now show that nanoscale artificial synapses can be constructed using different materials and physical mechanisms from those used previously<sup>4</sup>. The authors made their devices using a chalcogenide glass that switches reversibly between an amorphous phase (of high resistivity) and a crystalline phase (of low resistivity) in response to electric pulses. By applying a voltage to a film of the glass, they could thus induce resistive switching in their devices. The volumes of the two phases in the film change gradually and depend on the magnitude and duration of the applied voltage pulse, so the authors were able to continuously tune the resistivity of the devices.

Because of the large number of synapses, any practical implementation of artificial

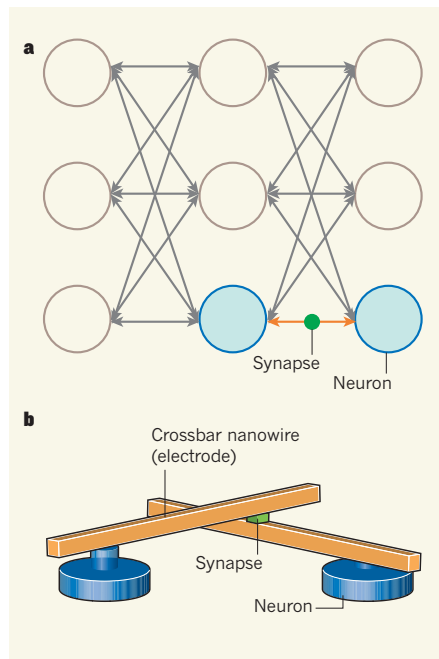


**Figure 1 | Making the connection.** **a**, Artificial neural networks that mimic the behaviour of neurons in the brain have been proposed as possible computational systems. Such networks can be represented by diagrams depicting how the artificial neurons are connected. Arrows indicate that each neuron receives and transmits signals to all the other neurons to which it is connected. All the connections incorporate artificial synapses, but for simplicity only one is shown. **b**, In reality, devices that act as artificial synapses serve as junctions for electrodes projecting from artificial neurons, as shown here for part of a nanometre-scale 'hybrid crossbar' circuit. The components shown correspond to the coloured components depicted in **a**. Kuzum *et al.*<sup>1</sup> and Ohno *et al.*<sup>2</sup> report devices that act as nanometre-scale artificial synapses.

neural networks must be able to update synaptic weights in parallel; otherwise, learning processes would be too slow. The main mechanism for efficient learning in biological neural networks was postulated<sup>8</sup> by Donald Hebb in 1949, and was eventually demonstrated experimentally<sup>9</sup> in 1998. A crucial aspect of this mechanism is that changes in synaptic weight depend on the relative timing of pulses from presynaptic and postsynaptic neurons — the weight strengthens if two neurons are activated simultaneously, but weakens when they are activated separately.

The most exciting aspect of Kuzum and colleagues' work<sup>1</sup> is the experimental demonstration that their artificial synapses can undergo Hebbian learning. In line with theoretical proposals<sup>10,11</sup>, the authors set up a synapse between two artificial neurons and used a specific sequence of voltage pulses to enforce learning. When active, the presynaptic neuron generated a sequence of high-amplitude, short-duration electric pulses followed by lower-amplitude but longer-duration pulses, whereas the postsynaptic neuron generated a single

negative pulse. The authors observed that, if the negative pulse overlapped in time with the higher-amplitude presynaptic pulses, the total bias across the synapse was large enough to enforce gradual growth of the amorphous (highly resistive) phase of the synapse. But if the postsynaptic neuron's negative pulse overlapped with low-amplitude presynaptic pulses, the total applied bias across the synapse was smaller and caused gradual crystallization of the synapse — lowering the resistivity and increasing the synaptic weight. The authors set up the system so that, if the pulses didn't overlap, no changes in conductance occurred.

Studies of biological synapses have revealed two distinct temporal modes for synaptic plasticity (the process in which synaptic weights are modulated). In short-term plasticity, changes to weights last for less than a few seconds, whereas long-term potentiation causes increases in weights that can persist for many hours<sup>12</sup>. In other words, synaptic weights decay quickly after single events in which presynaptic and postsynaptic pulses overlap; weights become permanent only after the repeated reinforcement of overlapping pulses.

Ohno *et al.*<sup>2</sup> report nanoscale artificial synapses that exhibit both short-term and long-term plasticity. The underlying mechanism is, again, resistive switching: the application of a voltage across the device results in the formation of silver filaments that bridge a nanometre-scale gap between two electrodes, lowering the resistivity of the synapse and increasing the synaptic weight. The authors observed that short-term plasticity occurs in response to intermittent voltage pulses, and propose that, under these conditions, incomplete silver bridges form — bridges the thickness of one atom that rapidly dissolve in the absence of a voltage. But when they applied rapidly repeated voltage pulses, they observed long-term plasticity. They attribute this to the formation of complete (thicker) bridges, which are more stable than the incomplete ones and persist for a longer time.

The fabrication technology used to make artificial synapses is still largely immature, resulting in variations in the properties of thin-film resistive switching devices. The amount of variation would be unacceptable in components of conventional integrated circuits. This situation is likely to change, however, given the large efforts currently being made by industry to develop digital computer memories based on crossbar junctions. Advances in crossbar-memory cells would aid the development of artificial neural networks, because similar materials and device structures are used in both technologies. The fact that neural networks are typically extremely fault tolerant<sup>7</sup> should also relax the requirement for low variation in the properties of artificial synapses. So, after decades of frustratingly slow progress, perhaps artificial neural networks are finally about to come of age. ■



**Dmitri B. Strukov** is in the Department of Electrical and Computer Engineering, University of California, Santa Barbara, Santa Barbara, California 93106, USA. e-mail: [strukov@ece.ucsb.edu](mailto:strukov@ece.ucsb.edu)

1. Kuzum, D., Jeyasingh, R. G. D., Lee, B. & Wong, H.-S. P. *Nano Lett.* <http://dx.doi.org/10.1021/nl201040y> (2011).
2. Ohno, T. *et al. Nature Mater.* **10**, 591–595 (2011).

3. Widrow, B. Tech. Rep. 1553-2; [www.isl.stanford.edu/~widrow/papers/t1960anadaptive.pdf](http://www.isl.stanford.edu/~widrow/papers/t1960anadaptive.pdf) (1960).
4. Jo, S. H. *et al. Nano Lett.* **10**, 1297–1301 (2010).
5. Thakoor, S., Moopenn, A., Daun, T. & Thakoor, A. P. *J. Appl. Phys.* **67**, 3132–3135 (1990).
6. Yang, J. J. *et al. Nature Nanotechnol.* **3**, 429–433 (2008).
7. Likharev, K. K. *Science Adv. Mater.* **3**, 322–331 (2011).
8. Hebb, D. O. *The Organization of Behavior: A*

- Neuropsychological Theory* (Wiley, 1949).
9. Bi, G. & Poo, M. J. *Neurosci.* **18**, 10464–10472 (1998).
10. Snider, G. S. in *Proc. IEEE/ACM Int. Symp. Nanoscale Architectures*, Anaheim, California, 85–92 (2008).
11. Linares-Barranco, B. & Serrano-Gotarredona, T. Preprint at <http://precedings.nature.com/documents/3010/version/1> (2009).
12. Kandel, E. R., Schwartz, J. H. & Jessel, T. M. *Principles of Neural Science* 4th edn (McGraw-Hill, 2000).

## ASTROPHYSICS

# The awakening of a cosmic monster

**Most galaxies harbour giant black holes; some are ‘silent’ whereas others produce copious amounts of radiation. The awakening of a silent monster has just been witnessed as it breaks apart and swallows a nearby star. SEE LETTERS P.421 & P.425**

DAVIDE LAZZATI

On 28 March 2011, the Swift team of astronomers was put on alert: a new  $\gamma$ -ray source had appeared in the northern sky. This was not big news for Swift, a satellite designed to look for  $\gamma$ -ray bursts (GRBs), which are a class of transient sources caused by the violent death of fast-spinning massive stars. However, as reported by Burrows *et al.*<sup>1</sup> on page 421 of this issue, continued observations of the event revealed that something entirely new had been detected. Whereas GRBs have a short-lived bright phase followed by a long, smooth decay, the source that astronomers were observing maintained a very high luminosity and a strong variability for more than a month. In addition, follow-up observations in the radio waveband, reported by Zauderer *et al.*<sup>2</sup> on page 425, showed that the new source was expanding with a velocity close to the highest speed allowed by nature: that of light. Finally, optical observations<sup>3</sup> placed the transient at the centre of a distant galaxy, drawing a completely different picture from the initial GRB interpretation.

The new source, called Swift J164449.3 + 573451, is now believed to be the electromagnetic signature of the tidal disruption of a star by the massive black hole sitting at the centre of its host galaxy. In this case, the black hole has a

mass of approximately 1 million Suns<sup>1,2</sup>, a value that is comparable to that of the Milky Way’s central black hole<sup>4</sup>. However, this is relatively light compared with the black hole family’s most massive members, which can have a mass of more than 1 billion Suns.

The tidal disruption of stars by massive black holes had been predicted theoretically<sup>5–7</sup>, and its consequences have been sparsely observed in the past<sup>8–10</sup>. However, the onset of the event itself had never previously been observed. The new observations managed to surprise

observers and theorists alike by revealing X-rays 10,000 times brighter than predicted and photons of much higher frequency than expected. The reason for these unexpected characteristics lies in the dynamics of the disruption process of the star and the accretion of stellar matter onto the black hole.

As a star wanders close to a massive black hole, the force exerted on its nearside is much greater than the force felt by its farside. As a consequence, the star is stretched, in a process analogous to the sea tides on Earth. However, if the star gets too close, the interaction becomes so strong that the star itself is destroyed. Because the stellar material carries a lot of angular momentum, it cannot ‘rain down’ on the black hole but instead forms a disk structure that slowly accretes onto it. The slow accretion leads to the emission of copious amounts of electromagnetic radiation — the awakening of the black hole.

The observations presented by Burrows *et al.*<sup>1</sup> and Zauderer *et al.*<sup>2</sup> show that the theoretical models<sup>5–7</sup> missed the fact that a high-speed (relativistic) jet is produced in the accretion process. Relativistic jets are quite common in astrophysics<sup>11,12</sup>. They consist of outflows of particles and/or electromagnetic field that are narrowly collimated around the rotational axis of a black hole (Fig. 1). In the case of Swift J164449.3 + 573451, astronomers were lucky enough to be observing the system along the jet axis. A relativistic jet pointing at us appears much brighter than one that lies orthogonal to the line of sight, owing to the relativistic collimation of its photons. In addition, as a consequence of the Doppler effect, a jet pointing at us shines at higher frequencies. For Swift J164449.3 + 573451, the jet is estimated<sup>2</sup> to be moving at a velocity of 99.5% of the speed of light. Therefore, the relatively low-luminosity optical transient that had been predicted<sup>5–7</sup> turned out to be an extremely bright source of electromagnetic radiation at all wavelengths, all

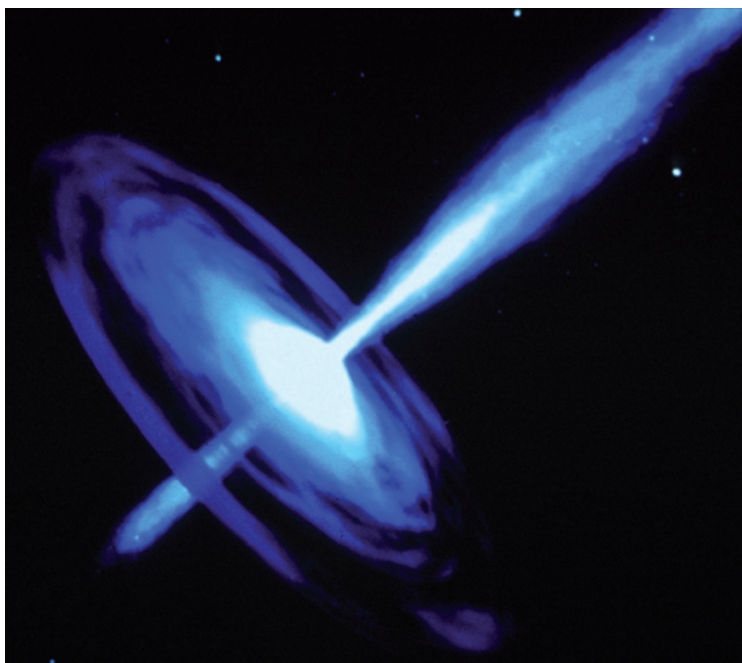


**Figure 1 | High-speed jet.** A relativistic jet, such as the one shown in this artist's impression, is an outpouring of particles and electromagnetic radiation formed when gas and stars fall into a spinning black hole. Burrows *et al.*<sup>1</sup> and Zauderer *et al.*<sup>2</sup> observed the birth of a relativistic jet at the heart of a galaxy hosting a supermassive black hole.

D. BERRY (STSC)

the way from radio waves to  $\gamma$ -ray photons.

The results of Burrows *et al.* and Zauderer *et al.* are not, however, limited to being a surprise for astrophysicists — they could also help to shed light on the conditions and physical processes in action in the centre of galaxies. As I write, orbiting satellites and telescopes on Earth are observing Swift J164449.3+573451 at multiple wavelengths to constrain its spectral and temporal evolution. If the outburst of  $\gamma$ -rays was produced by a tidally disrupted star, the new source should eventually fade when all of the stellar material has been swallowed by the black hole.

In addition, future observations are likely to reveal more outbursts of this kind. Knowing

the rate at which they occur will allow us to constrain the fraction of galaxies that harbour a massive black hole, the properties of black holes, and the density of stars in the central part of galaxies. Finally, witnessing the birth and early evolution of a new relativistic jet will give us a wealth of information on the jet-formation process itself, as well as on the way in which the jet interacts with the surrounding material as it opens a passage through the interstellar medium of its host galaxy. ■

**Daide Lazzati** is in the Department of Physics, North Carolina State University, Raleigh, North Carolina 27695-8202, USA. e-mail: dlazzat@ncsu.edu

1. Burrows, D. N. *et al.* *Nature* **476**, 421–424 (2011).
2. Zauderer, B. A. *et al.* *Nature* **476**, 425–428 (2011).
3. Levan, A. J. *et al.* *Science* **333**, 199–202 (2011).
4. Ghez, A. M., Klein, B. L., Morris, M. & Becklin, E. E. *Astrophys. J.* **509**, 678–686 (1998).
5. Rees, M. J. *Nature* **333**, 523–528 (1988).
6. Evans, C. R. & Kochanek, C. S. *Astrophys. J.* **346**, L13–L16 (1989).
7. Strubbe, L. E. & Quataert, E. *Mon. Not. R. Astron. Soc.* **400**, 2070–2084 (2009).
8. Esquej, P. *et al.* *Astron. Astrophys.* **462**, L49–L52 (2007).
9. Gezari, S. *et al.* *Astrophys. J.* **676**, 944–969 (2008).
10. Maksym, W. P., Ulmer, M. P. & Eracleous, M. A. *Astrophys. J.* **722**, 1035–1050 (2010).
11. Bridle, A. H. & Perley, R. A. *Annu. Rev. Astron. Astrophys.* **22**, 319–358 (1984).
12. Mirabel, I. F. & Rodríguez, L. F. *Nature* **371**, 46–48 (1994).

## ENVIRONMENTAL SCIENCE

# Climate for conflict

**The idea that climate influences the onset of wars is enticing, but controversial. A study now finds a convincing correlation between global climate and civil conflict in countries affected by the El Niño/Southern Oscillation. SEE LETTER P.438**

ANDREW R. SOLOW

The notion that climate can influence the course of a war is a commonplace — think of the armies of Napoleon and Hitler coming to grief in the Russian winter (Fig. 1), or the storms that broke up Kublai Khan's Mongol fleet and the Spanish Armada. But on page 438 of this issue, Hsiang *et al.*<sup>1</sup> go further by suggesting that climate can actually be a cause of war.

A growing body of work explores possible connections between climate and human conflict. In one controversial study published in 2009, Burke *et al.*<sup>2</sup> presented statistical results relating outbreaks of civil conflict in Africa to year-to-year variations in local temperature. This work has been criticized<sup>3–5</sup> — and defended<sup>6,7</sup> — on various technical grounds such as the details of the statistical model, the number of deaths required for classification as a civil conflict, and the sensitivity of

the results to the period of analysis.

Burke and colleagues' study<sup>2</sup> focused on the effect of local climate variations on civil conflict. By contrast, Hsiang *et al.*<sup>1</sup> present the first quantitative study linking civil conflict to global climate variations — specifically, those associated with the El Niño/Southern Oscillation (ENSO). The ENSO phenomenon is characterized by quasi-periodic, large-scale shifts in sea surface temperature in the eastern equatorial Pacific. Through its effects on atmospheric circulation, ENSO influences weather patterns around the world. Broadly speaking, during the warm El Niño phase of ENSO, the continental tropics tend to be warm and dry, whereas the opposite conditions tend to occur during the cold La Niña phase.

In light of the difficulty of uncovering a clear connection between civil conflict and local climate, it may seem that looking for a connection to global climate puts the cart before the horse. Hsiang *et al.*<sup>1</sup> argue otherwise. Among other things, they point out that the various economic and social factors underlying civil conflict in one country may be influenced by climate variations in others.

Hsiang and colleagues' study proceeded in two steps. In the first step, the authors used historical climate data to divide the countries of the world into two groups: 93 'teleconnected' countries, which have strong ENSO-related climate effects, including Australia, Ghana, Laos, Sudan and Trinidad; and 82 non-teleconnected ones that don't experience these effects, such as Afghanistan, Greece, Latvia, Sweden and Tunisia. In the second step, they used statistical models to see whether the rate of outbreak of civil conflict each year from 1950 to 2004 correlated with an annual index of ENSO for the two groups.

The analysis identified a statistically significant relationship between the rate of outbreak of conflicts and ENSO among the countries in the teleconnected group, but not among the others. In the teleconnected group, the rate of outbreak of civil conflict increased from an estimated 3% in La Niña years to an estimated 6% in El Niño years. By performing a comprehensive sensitivity



**Figure 1 | Napoleon's retreat.** Bitterly cold winter weather contributed to the failure of France's invasion of Russia in 1812. Hsiang *et al.*<sup>1</sup> now report that global climate can be a cause of war. (Wood engraving, after a painting by Jan Chelminski.)



analysis, Hsiang *et al.* found that their results were unaffected by modelling choices, including those involving the way in which civil conflict and ENSO conditions are measured. Although this work<sup>1</sup>, like other studies in the field, was motivated in part by interest in the effects of global climate change, the authors take pains to note that ENSO-related variability is no proxy for long-term climate change.

Careful statistical analyses such as this one<sup>1</sup>, which relate complex human behaviour to environmental factors, can be invaluable, but they need to be complemented by more detailed studies focusing on the underlying human dynamics. Hsiang *et al.* clearly understand that any effect of climate on conflict is likely to be indirect — people do not start wars simply because they are hot. One plausible hypothesis to explain the authors' findings is that the warm, dry conditions during El Niño years reduce agricultural yields, leading to conflict related to food availability.

However, as Hsiang and colleagues note<sup>1</sup>, their analysis hints at an alternative hypothesis: civil conflicts do not originate with climate variations, but they do wax and wane, possibly as part-time fighters move in and out of agriculture. Interestingly, the same possibility was proposed<sup>2</sup> to explain the earlier work of Burke *et al.*<sup>2</sup>. Whether global climate

variations give rise to new civil conflicts or modulate existing ones would seem to have somewhat different implications for improving the situation. For example, if the first theory is correct, then efforts could be made to address simmering problems that might erupt into conflict. But if the second suggestion is true, then peace-keeping efforts should focus mainly on situations that have already boiled over. Hsiang and colleagues' results should encourage a deeper look into this issue. ■

**Andrew R. Solow** is at the Woods Hole Oceanographic Institution, Marine Policy Center, Woods Hole, Massachusetts 02543, USA. e-mail: asolow@whoi.edu

1. Hsiang, S. M., Meng, K. C. & Cane, M. A. *Nature* **476**, 438–441 (2011).
2. Burke, M. B., Miguel, E., Satyanath, S., Dykema, J. A. & Lobell, D. B. *Proc. Natl Acad. Sci. USA* **106**, 20670–20674 (2009).
3. Sutton, A. E. *et al. Proc. Natl Acad. Sci. USA* **107**, E102 (2010).
4. Buhaug, H. *Proc. Natl Acad. Sci. USA* **107**, 16477–16482 (2010).
5. Buhaug, H. *Proc. Natl Acad. Sci. USA* **107**, E186–E187 (2010).
6. Burke, M. B., Miguel, E., Satyanath, S., Dykema, J. A. & Lobell, D. B. *Proc. Natl Acad. Sci. USA* **107**, E103 (2010).
7. Burke, M. B., Miguel, E., Satyanath, S., Dykema, J. A. & Lobell, D. B. *Proc. Natl Acad. Sci. USA* **107**, E185 (2010).

## DENGUE FEVER

# Mosquitoes attacked from within

**Infection with a harmless bacterium makes the mosquitoes that transmit dengue virus resistant to viral infection. The resistant population can rapidly replace the natural, susceptible population. SEE LETTERS P.450 & P.454**

JASON L. RASGON

**D**engue fever is the most prevalent mosquito-borne viral disease in humans. The virus is transmitted mainly by the mosquito *Aedes aegypti*, and so targeting this insect has been considered a viable option for controlling the incidence of the disease. In two papers in this issue (Walker *et al.*<sup>1</sup> and Hoffmann *et al.*<sup>2</sup>), a team of researchers reports an unusual approach for making *A. aegypti* almost completely resistant to infection, and thereby blocking transmission of dengue virus. Moreover, when the authors released their dengue-resistant mosquitoes into the wild, the insects replaced nearly 100% of the natural, susceptible mosquito population within a matter of months.

Around 40% of the world's population is at risk of infection with dengue virus. Every

year, the virus infects 50 million to 100 million people, causing classical dengue fever as well as more severe symptoms such as dengue haemorrhagic fever and dengue shock syndrome. In the absence of an effective vaccine, controlling dengue is limited to targeting the mosquitoes that transmit the virus<sup>3</sup>. Many mosquito-control strategies are based on suppressing or eliminating the insect population. By contrast, population-replacement strategies aim to replace the pathogen-susceptible mosquito population with a resistant one<sup>4</sup>.

The bacterium *Wolbachia* is a common endosymbiotic associate of many insects, including mosquitoes, and lives inside their cells. It is maternally inherited, and manipulates the reproduction of its invertebrate hosts in various ways to maximize the number of infected females in the next generation; this allows *Wolbachia* to spread rapidly



## 50 Years Ago

Repeated investigations by the Medical Research Council have shown no evidence of a higher incidence of lung cancer or respiratory disease among persons exposed to increased amounts of Diesel exhaust fumes ... Mr. Freeth [the Parliamentary Secretary for Science] also said that the Warren Spring Laboratory of the Department of Scientific and Industrial Research has examined methods for removing smoke from the exhausts of Diesel-propelled road-vehicles, but no device yet tested has proved satisfactory. The British Internal Combustion Engine Research Association is undertaking fundamental work on the combustion process in Diesel cylinders which it is hoped may lead to remedial measures. Mr. Freeth said it is a fact that correct setting of the injectors and their proper maintenance and operation provide a simple and effective remedy.

From *Nature* 26 August 1961

## 100 Years Ago

As a supplement to the literary and historical Biblical exhibition which has been arranged at Bloomsbury for the tercentenary of the Authorised Version, an exhibition of the animals, plants, and minerals mentioned in the Bible has been arranged in one of the bays of the Central Hall of the Natural History Museum, South Kensington ... The collection, and the guide to it, will be of special interest to those to whom the Bible plants and animals are rich in picturesque associations; but it is, of course, part of a liberal education to know that the "unicorn" was probably the extinct wild ox or aurochs, "behemoth" the hippopotamus, the "coney" the hyrax, and the "leviathan" of Job the crocodile.

From *Nature* 24 August 1911

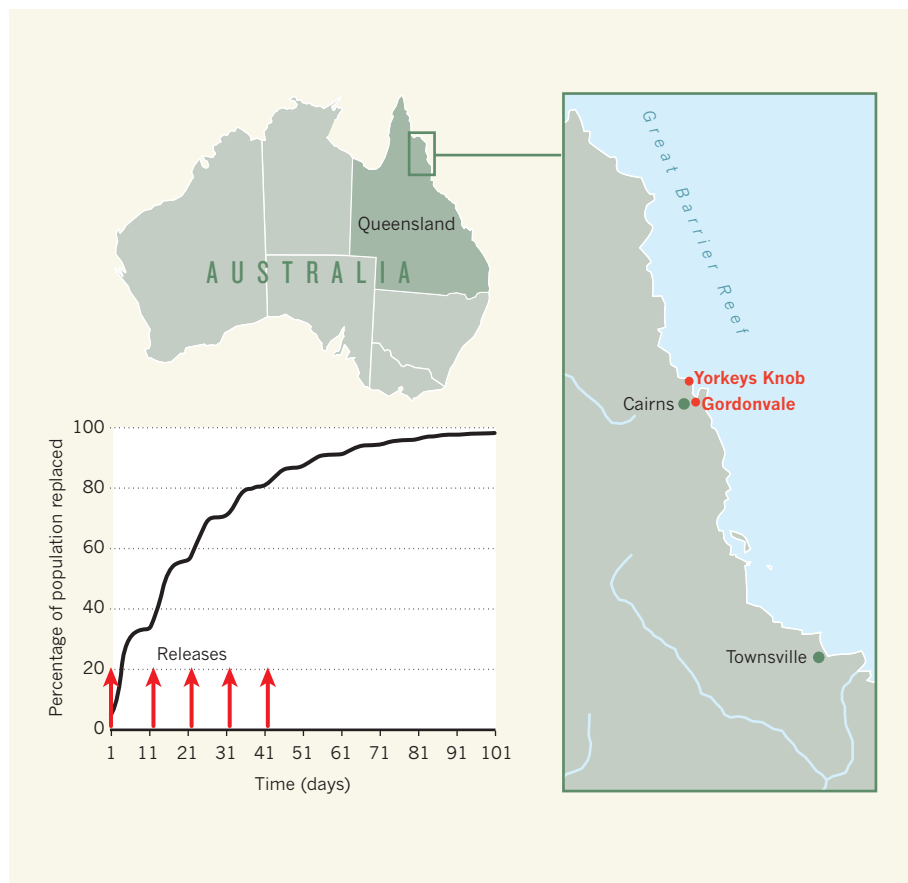


**Figure 1 | Dengue-virus control.** Hoffmann *et al.*<sup>2</sup> released *Aedes aegypti* mosquitoes infected<sup>1</sup> with the wMel strain of *Wolbachia* in two locations — Yorkeys Knob and Gordonvale — near Cairns in Queensland, Australia. After several releases, these dengue-virus-resistant mosquitoes replaced almost the entire natural, virus-sensitive *A. aegypti* population.

through populations<sup>5</sup>. Infection with the bacterium can make insects such as mosquitoes resistant to infection by many pathogens, including viruses, malaria parasites and filarial nematodes<sup>6</sup>. If *Wolbachia* is artificially introduced into an uninfected vector population, it can spread and replace the wild-type population with one in which pathogen transmission is blocked<sup>5</sup>.

Researchers showed<sup>7</sup> a few years ago that wMelPop — a virulent *Wolbachia* strain from a laboratory colony of the fruitfly *Drosophila melanogaster* — almost completely blocked dengue infection in *A. aegypti*. This *Wolbachia* strain, however, severely affected the mosquitoes' fitness, making its spread into natural *A. aegypti* populations difficult or even impossible<sup>8</sup>.

Going back to the source, Walker *et al.*<sup>1</sup> (page 450) noted that wMel, the natural, avirulent *Wolbachia* strain in *Drosophila*, can inhibit fly infection with RNA viruses. As dengue is an RNA virus, the authors reasoned that wMel might also block infection with this virus in mosquitoes, without having the virulent effects of wMelPop. Lo and behold, when they infected *A. aegypti* with wMel, the mosquitoes became highly resistant to infection by dengue virus. In experiments on caged mosquitoes,

Walker and colleagues further showed that the wMel infection could spread through laboratory mosquito populations at a rate consistent with predictions based on theoretical modelling.

Many studies would stop there. But the investigators took the astonishing next step of attempting a release of *Wolbachia*-infected mosquitoes into the wild, and, even more astonishingly, they did it in their own backyard. Queensland, Australia, has a recurring dengue problem<sup>9</sup>, and so seemed an ideal location for an initial test release.

After extensive public engagement, and development of a regulatory framework governing the release of the *Wolbachia*-infected insects, in January this year Hoffmann *et al.*<sup>2</sup> (page 454) began releasing wMel-infected mosquitoes at two locations — Yorkeys Knob and Gordonvale, both near Cairns in Queensland (Fig. 1). The authors continued to release the insects at regular intervals over the next two and a half months, with a total of roughly 150,000 mosquitoes released at each location. The frequency of *Wolbachia* infection increased extensively during the releases, but more crucially, continued to climb in both areas after releases were stopped, approaching 100% in Yorkeys Knob

and more than 80% in Gordonvale<sup>2</sup>.

Hoffmann and colleagues estimated that wMel exerts only a moderate (10–20%) fitness cost on the mosquitoes it infects. This suggested that a 'wave' of infection with this bacterial strain should eventually spread from local areas in which the infection was introduced. And spread it did — infected mosquitoes were detected several kilometres away from both release areas, probably owing to occasional long-distance movement of infected insects. Although in these experiments the infection is unlikely to increase in frequency outside the release area, but rather will be swamped by the local wild-type mosquitoes, the data suggest that long-range spread is possible<sup>2</sup>.

These studies mark the first time that a deliberate *Wolbachia*-mediated population-replacement strategy has been attempted in nature, and herald the beginning of a new era in the control of mosquito-borne diseases. The advantage of population-replacement approaches is that, once established, they are self-propagating. And because the mosquito population is simply changed rather than eliminated, effects on the ecosystem should be minimal<sup>4</sup>.

Theoretically, these strategies can also be applied to other vector-borne diseases, including malaria<sup>10</sup>. The next step will be to attempt release of *Wolbachia*-infected mosquitoes in an area with endemic, rather than sporadic, dengue transmission, such as southeast Asia or South America. It remains to be seen whether the introduction and spread of *Wolbachia* can be achieved across the highly variable worldwide range of dengue virus, and whether *Wolbachia* can provide consistent protection against viral strains of different genetic make-up. Nevertheless, these experiments<sup>1,2</sup> are a groundbreaking first step towards *Wolbachia*-mediated replacement of *A. aegypti* and so elimination of the scourge of dengue fever. ■

**Jason L. Rasgon** is in the W. Harry Feinstone Department of Molecular Microbiology and Immunology, and at the Johns Hopkins Malaria Research Institute, Johns Hopkins Bloomberg School of Public Health, Baltimore, Maryland 21205, USA.  
e-mail: jrasgon@jhsph.edu

1. Walker, T. *et al.* *Nature* **476**, 450–453 (2011).
2. Hoffmann, A. A. *et al.* *Nature* **476**, 454–457 (2011).
3. Morrison, A. C. *et al.* *PLoS Negl. Trop. Dis.* **4**, e670 (2010).
4. James, A. A. *Trends Parasitol.* **21**, 64–67 (2005).
5. Rasgon, J. L. *Adv. Exp. Med. Biol.* **627**, 114–125 (2008).
6. Iturbe-Ormaetxe, I., Walker, T. & O'Neill, S. L. *EMBO Rep.* **12**, 508–518 (2011).
7. McMeniman, C. J. *et al.* *Science* **323**, 141–144 (2009).
8. McMeniman, C. J. & O'Neill, S. L. *PLoS Negl. Trop. Dis.* **4**, e748 (2010).
9. Hanna, J. N. *et al.* *Aust. NZ J. Public Health* **30**, 220–225 (2006).
10. Hughes, G. L., Koga, R., Xue, P., Fukatsu, T. & Rasgon, J. L. *PLoS Pathog.* **7**, e1002043 (2011).



# Germ-layer and lineage-restricted stem/progenitors regenerate the mouse digit tip

Yuval Rinkevich<sup>1†</sup>, Paul Lindau<sup>1</sup>, Hiroo Ueno<sup>1</sup>, Michael T. Longaker<sup>1,2</sup> & Irving L. Weissman<sup>1,3</sup>

**The regrowth of amputated limbs and the distal tips of digits represent models of tissue regeneration in amphibians, fish and mice. For decades it had been assumed that limb regeneration derived from the blastema, an undifferentiated pluripotent cell population thought to be derived from mature cells via dedifferentiation. Here we show that a wide range of tissue stem/progenitor cells contribute towards the restoration of the mouse distal digit. Genetic fate mapping and clonal analysis of individual cells revealed that these stem cells are lineage restricted, mimicking digit growth during development. Transplantation of cyan-fluorescent-protein-expressing haematopoietic stem cells, and parabiosis between genetically marked mice, confirmed that the stem/progenitor cells are tissue resident, including the cells involved in angiogenesis. These results, combined with those from appendage regeneration in other vertebrate subphyla, collectively demonstrate that tissue stem cells rather than pluripotent blastema cells are an evolutionarily conserved cellular mode for limb regeneration after amputation.**

Although whole-body regeneration from blood and vascular structures can occur in protochordate colonial tunicates<sup>1–3</sup>, regeneration of body parts is highly restricted in vertebrates, especially in mammals<sup>4</sup>. Therefore, digit tip (fingertip or toe-tip) regrowth in mice<sup>5–9</sup> and humans<sup>10–12</sup> presents unique model systems for mammalian organ regeneration. Several hypotheses have been used to explain the mechanisms contributing to regeneration<sup>13</sup>. One hypothesis is that circulating precursors, perhaps of the mesenchymal or haematopoietic lineages, can enter damaged tissues and transdifferentiate (lineage conversion of a defined cell into another cell type) into the lost cell types<sup>14–17</sup>. Another concept is that the residual local mature cells of diverse types can dedifferentiate to form a blastema, a pluripotent class of cells (cells that may differentiate into various types of specialized cells) that can use pathways other than those used in development to form limbs and digit structures<sup>18–21</sup>; this idea has recently been emphasized as an alternative to tissue-specific stem cells having an important role in regeneration (see <http://www.nytimes.com/2010/11/09/science/09wade.html>, <http://www.nytimes.com/2010/11/09/health/09stem.html>, <http://www.nytimes.com/2010/08/06/science/06cell.html>, <http://tierneylab.blogs.nytimes.com/2009/07/02/rumsfeldian-stem-cells>, <http://www.nytimes.com/2009/03/10/science/10lab.html>). A third idea is that tissue homeostasis and regeneration derive from the kinds of tissue-specific stem cells that originally were responsible for their embryonic development<sup>22–25</sup>.

Mammalian digit tips exhibit morphological variations that contributed to the evolutionary diversification<sup>26</sup> of mammals. The digit tip is derived from multiple and distinct embryonic origins, and includes the distal bone with associated marrow cavity and haematopoietic cells, ventral (flexor) and dorsal (extensor) tendons, sweat glands with myoepithelial and luminal secreting cells and associated neurons for innervation, dermis with resident melanocytes and dendritic cells, mesenchyme with resident fibroblasts, skin epidermis with hair follicles, a nail organ composed of six specific parts (the root, nail bed, nail plate, eponychium (cuticle), perionychium and hyponychium) and is highly vascularized<sup>27</sup>. Each of these distal structures has a specific function, damage to which may result in an abnormal digit.

Newborn and adult mice are able to regrow forelimb (finger) and hindlimb (toe) digit tips after their amputation through the distal

interphalangeal joint<sup>5–9</sup>. Regeneration of the digit tip involves the integrated regrowth of multiple tissues within 2–3 months, reaching an external morphology that is cosmetically and functionally similar to normal digits. Most importantly, regeneration of the mouse distal digit shares morphological similarities with clinical cases documenting regrowth of missing distal portions of fingers in both children and adults<sup>10–12</sup>.

Here we explore the cellular source for mouse digit-tip regeneration and provide evidence that regrowth is a cumulative effort of distinct stem cells and their daughter progenitors which are germ-layer and lineage restricted.

Amputations that removed most structures of the distal digit consistently failed to regenerate (Supplementary Fig. 1a, b). Consistent with previous observations<sup>7–9</sup>, amputations with residual bone, sweat glands and nail organ remaining (amputation plane 1 and 2 (AP1/2)) showed partial to complete regrowth of distal structures after 70 days (Supplementary Fig. 1a–c and Supplementary Table 1), with histological indications of mesenchyme cells at the digit apex (Supplementary Fig. 1d–d’). Short pulse regimes of 5-bromodeoxyuridine (BrdU) revealed local proliferations within defined sites of the distal digit (Supplementary Fig. 1e–g, white arrowheads). These results indicated that digit regrowth resulted from the combined activities of tissue-resident stem cells. We tested this hypothesis via genetic fate mapping and lineage tracing of the major tissues within the digit.

## Developmental restriction of ectoderm

The contribution of the epidermis to the regenerating digit was analysed using keratin-14-CreER (K14CreER) transgenic mice<sup>28</sup>. K14CreER mice were crossed with mTmG, a double-fluorescent reporter mouse that replaces the expression of tomato red with green fluorescent protein (GFP) after Cre-mediated excision<sup>29</sup>.

K14CreER<sup>mTmG</sup> mice were injected with tamoxifen and then amputated along AP1/2 (see methods) and digits were processed for histology after 3 months. GFP expression within digits was confined to ectodermal tissues (Fig. 1a–e), including dorsal and ventral epidermis, nail plate (with eponychium and hyponychium), hair

<sup>1</sup>Stanford Institute for Stem Cell Biology and Regenerative Medicine, Stanford University School of Medicine, Stanford, California 94305-5323, USA. <sup>2</sup>Hagey Laboratory for Pediatric Regenerative Medicine, Department of Surgery, Plastic and Reconstructive Surgery, Stanford University School of Medicine, Stanford, California 94305, USA. <sup>3</sup>Ludwig Center for Cancer Stem Cell Research, Stanford University, Stanford, California 94305-5323, USA. †Present address: Institute for Stem Cell Biology and Regenerative Medicine, Lorry I. Lokey Research Building, Stanford University, Stanford, California 94028, USA.

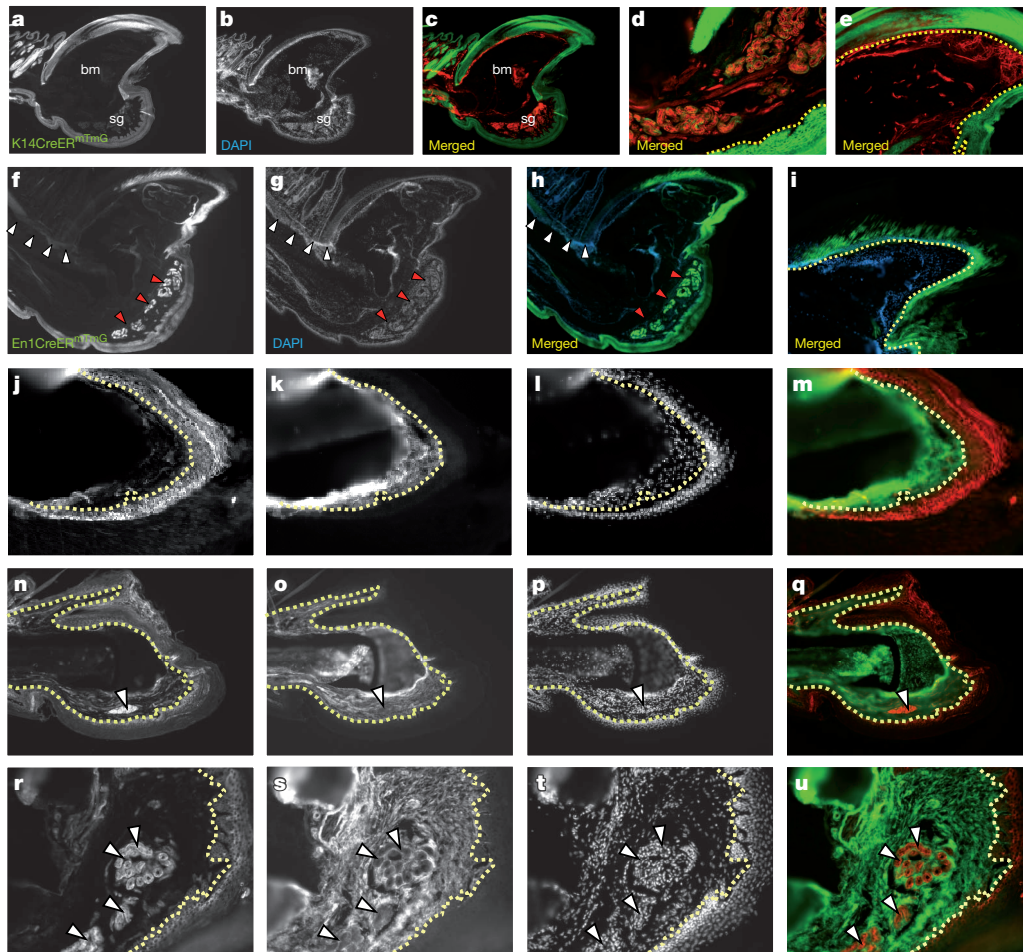


**Figure 1 | Germ-layer restriction of ectoderm/mesoderm during digit-tip regeneration.** **a–u**, Sections through a distal digit of K14CreER<sup>mTmG</sup> (**a–e**), En1Cre<sup>mTmG</sup> (**f–i**) and Prx1Cre<sup>mTmG</sup> (**j–u**) transgenic mice, 3 months after amputation. Ectoderm contributes to epidermis, nail and sweat glands and fails to contribute to mesoderm tissues (**a–i**). The dashed line outlines the border between epidermis–dermis (**d**) and nail plate–matrix (**e**, **i**). Segregation of ectoderm in En1Cre<sup>mTmG</sup> mice into dorsal and ventral fates; ventral ectoderm contributes to ventral epidermis and sweat glands (**f–h**, red arrowheads) with no contributions to the dorsal epidermis or hair follicles (**f–h**, white arrowheads). A partial contribution to nail reveals dorsal and ventral

follicles and secreting portions of sweat glands. The GFP expression was sustained, almost certainly implicating epithelial stem cells as the original tamoxifen-induced cells, as several skin turnover times had occurred over the 3-month interval. GFP expression was absent from mesoderm tissues, including bone and marrow cavity, blood vessels, tendon, nail bed, dermis and surrounding mesenchyme of the digit (Fig. 1d, e).

A similar ectoderm-specific expression of GFP emerged in regenerated digits of keratin-5-CreER<sup>mTmG</sup> (K5CreER<sup>mTmG</sup>)<sup>30</sup> transgenic mice (Supplementary Fig. 2a–e). Again, the sustained expression of GFP indicates that keratin 5, like keratin 14, is expressed in self-renewing stem cells.

Engrailed-1-Cre transgenic mice (En1Cre) were used to lineage trace the ventral ectoderm<sup>31</sup>, in a similar method. GFP expression was present within the ventral epidermis (Fig. 1f–h), duct and secreting portions of sweat glands (Fig. 1f–h, red arrowheads), and within a subset of cells of the nail plate (compare Fig. 1e to i). GFP expression was absent from the dorsal epidermis and its associated hair follicles (Fig. 1f–h, white arrowheads) and from all mesodermal tissues (Fig. 1h, i). Engrailed expression appears to be in a subset of more lineage-restricted stem cells, limited to development of ventral ectoderm and

chimaeric origins to the nail plate (**i**). This boundary is shifted compared to the published lineage mapping study, using En1CreER. Lineage tracing of Prx1Cre shows restricted GFP expression to bone, tendon and mesenchyme, with no contribution to ectoderm. Keratin 14 (K14) expression in Prx1Cre<sup>mTmG</sup> digits is mutually exclusive from GFP expression. High magnifications of nail (**j–m**), bone (**n–q**) and sweat glands (**r–u**) are shown. Dashed lines outline borders between nail plate–matrix (**j–m**) and epidermis–dermis (**n–u**). White arrowheads (**r–u**) show that sweat glands within ventral mesenchyme are GFP negative. bm, bone marrow; sg, sweat glands. Original magnification:  $\times 5$  (**a–c**, **f–h**);  $\times 10$  (**e**, **i**, **n–q**);  $\times 20$  (**d**, **j–m**, **r–u**).

to a subset of the nail plate. These results collectively show that germ-layer restriction is maintained by classes of ectodermal stem cells during digit-tip regeneration, with further restriction of ectoderm into dorsal and ventral fates and chimaeric contributions to the nail plate.

### Developmental restriction of mesoderm

The contribution of mesoderm to the regenerating digit was analysed using Prx1Cre (ref. 32) transgenic mice, in a similar method. Within regenerated digits of Prx1Cre<sup>mTmG</sup> mice, GFP expression was confined to mesodermal tissues, including bone, tendons, nail bed, dermis and mesenchyme (Supplementary Fig. 2f–j) and was absent from all ectodermal tissues (Supplementary Fig. 2i, j).

The possibility of germ-layer conversion (transdifferentiation) of mesoderm to ectoderm during digit-tip regeneration was further analysed by immunoassaying sections of regenerated digits from Prx1Cre<sup>mTmG</sup> mice for K14 protein. K14 protein was expressed in all ectoderm lineages of the digit and was mutually exclusive from GFP expression (Supplementary Fig. 2k–n). The K14–GFP border distinguished between nail plate and bed (Fig. 1j–m), between surrounding epidermis (dorsal and ventral) to digit bone and dermis (Fig. 1n–q), and between sweat glands (duct and secreting portions)



to the surrounding mesenchyme (Fig. 1r–u), demonstrating that germ-layer restriction of mesoderm and ectoderm by their respective stem and progenitor cells is maintained during regeneration of the distal digits.

We used Sox9Cre transgenic mice to lineage trace bone/cartilage precursors<sup>33</sup>, in a similar method. In line with Sox9 expression in stem cells of the skin<sup>34</sup>, GFP was expressed within all epidermal lineages of the digits (Fig. 2a–d and Supplementary Fig. 3). Within the mesoderm, GFP expression was restricted to the bone (Fig. 2a–d, dotted line; Supplementary Fig. 3a'', a''') and was absent from tendons, nail bed, dermis, vasculature and the mesenchyme surrounding the sweat glands (Supplementary Fig. 3b–c'''). As the Sox9 promoter drives Cre in these mice, and not CreER, and also because we do not know the lifespan of osteocytes, we could not conclude whether the GFP<sup>+</sup> bone cells were derived from stem or progenitor cells.

Likewise, we used scleraxisCre (ScxCre) transgenic mice crossed to the mTmG reporter to lineage trace the tendon precursors<sup>35</sup>. Within regenerated digits, GFP expression was restricted to dorsal and ventral tendons (Fig. 2e–h, dotted line), with some GFP staining also present in a distinct group of cells within the hair follicles as previously described for developing limbs<sup>35</sup>. GFP was absent from bone, blood vessels and surrounding mesenchyme and from ectodermal tissues (Fig. 2g, h).

The contribution of endothelium to the regenerating digits was assayed similarly by crossing mTmG reporter mice with Tie2Cre (ref. 36) and VE-cadherinCreER (ref. 37) transgenic mice.

In line with published work<sup>30</sup>, GFP<sup>+</sup> blood vessels were abundant within the distal regenerated digits of Tie2Cre<sup>mTmG</sup> mice. GFP expression was restricted to blood cells and blood vessels within nail bed, the dermal/hypodermal border and surrounding the sweat glands (Fig. 2i–l, white arrowheads). GFP expression was absent from other mesodermal tissues, and all ectodermal tissues (Fig. 2k, l). A restricted expression of GFP to blood vessels also emerged within regenerated digits of VE-cadherinCreER<sup>mTmG</sup> mice treated with tamoxifen before amputation (Fig. 2m–p, white arrowheads).

Specificity of the GFP to endothelium was confirmed by immunostaining sections of regenerated digits from Tie2Cre<sup>mTmG</sup> mice for

the endothelial markers platelet endothelial cell adhesion molecule 1 (CD31 (also called PECAM1); Supplementary Fig. 4a–a'', white arrowheads) and pan endothelial cell antigen (PEA; Supplementary Fig. 4, b–b'', white arrowheads). Both antibodies marked blood vessels within the nail bed, sweat glands and surrounding mesenchyme and co-localized with that of GFP. We then looked at ectoderm markers of epidermis and neural fates by immunoassaying for keratin 14 (K14; Supplementary Fig. 4c–c'') and myelin basic protein (MBP; Supplementary Fig. 4d–d''), respectively, and found that they were mutually exclusive from that of GFP expression. Likewise, in digits from VE-cadherinCreER<sup>mTmG</sup> mice, GFP expression was separate from mesenchyme/fibroblast-associated (CD105, CD90, S100A4) and haematopoietic (CD45) markers (Supplementary Fig. 5), indicating an absence of endothelial contribution to these cell populations.

A similar tissue-restricted pattern was apparent during the regrowth time point (10 days after amputation) associated with the appearance of a blastema<sup>38</sup> (Supplementary Fig. 6), demonstrating that germ-layer and lineage restriction of ectoderm and mesoderm including bone, tendon and blood vessel lineages is maintained throughout regeneration of the distal digits.

### Circulating cells do not contribute to regeneration

To address haematopoietic contributions to the regenerating digits, haematopoietic stem cells (HSCs) were isolated from transgenic mice expressing the cyan fluorescent protein (CFP-HSCs) on the basis of the following surface expressions<sup>39</sup>: Lin<sup>−</sup> (CD3<sup>−</sup>CD4<sup>−</sup>CD8<sup>−</sup>B220<sup>−</sup>Mac<sup>−</sup>Gr-1<sup>−</sup>Ter119<sup>−</sup>) CD34<sup>+</sup>Flk2<sup>+</sup>Sca1<sup>+</sup>c-Kit<sup>+</sup>Slamf1<sup>+</sup> (Fig. 3a). Wild-type mice were reconstituted with 20 CFP-HSCs ( $n = 4$ ). CFP-HSC-injected mice reached full blood chimaerism (Supplementary Fig. 7), at which time digits were amputated at AP1/2 and analysed 3 months later. HSC-derived CFP cells were observed within the marrow cavity, the dermis and mesenchyme of the distal digit, and showed ubiquitous expression of the haematopoietic antigen CD45 (Fig. 3b–g, white arrowheads). We did not find any contributions of CFP-HSC-derived cells to the major tissues of the digit, including bone, tendons, nail organ, sweat glands, epidermis or blood vessels (Fig. 3d, g).

To address further the possibility of a circulatory contribution to the regenerating digits, we created pairs of genetically marked parabiotic mice that have a shared anastomosed circulatory system<sup>40</sup>. Wild-type mice were surgically conjoined to mice expressing GFP under the chicken  $\beta$ -actin promoter. Mice were left parabiosed for 1 month for full chimaerism to be established within the haematopoietic system. Then digits from wild-type mice were amputated at AP1/2 and mice were killed 3 months later. Donor-derived GFP cells were present within numerous tissues of the distal digit, including its marrow cavity, epidermis, nail matrix and mesenchyme surrounding the sweat glands (Fig. 3h–j, white arrowheads). All donor-derived GFP cells expressed the haematopoietic antigen CD45 within all sites examined (Fig. 3k–n), and failed to contribute to the major tissues of the digit. We then checked to see if donor-derived GFP cells would contribute to new blood vessel formation after parabiosis. Donor-derived GFP cells in the digits were closely associated with blood vessels but were mutually exclusive from PEA expression (Fig. 3o–r). Thus, the angiogenesis that results in vascularized digit tips must derive from local, non-haematopoietic or any other circulating endothelial precursors, consistent with our previous results in tumour angiogenesis<sup>25</sup>. These results also demonstrate that circulating cells (of any origin) do not contribute to the major tissues within the digit, and are consistent with early irradiation experiments in salamanders (Butler and O'Brien, 1942) that showed that appendage regeneration requires a local cellular source<sup>41</sup>.

### Clonal analysis of the regenerating digits

We looked at emerging clones within regenerating digit tips, using 'Rainbow' mice, a multicolour Cre-dependent marker system that harbours a four-colour reporter construct (red, yellow, green, blue;

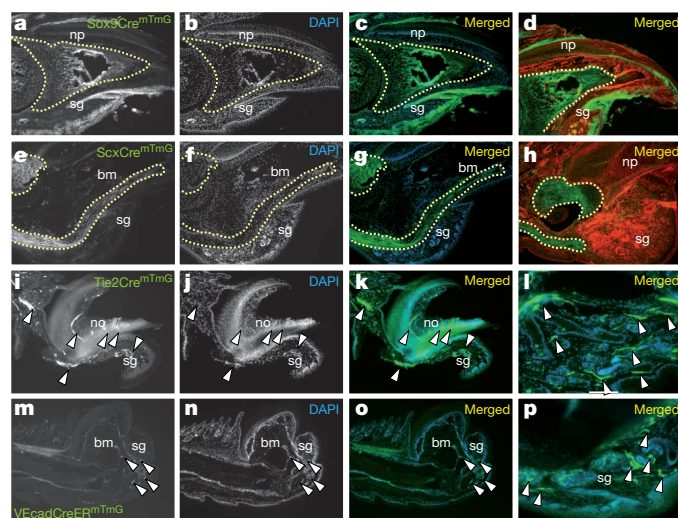


**Figure 2 | Lineage restrictions of bone, tendons and endothelium during digit-tip regeneration.** a–p, Sections through Sox9Cre<sup>mTmG</sup> (a–d), ScxCre<sup>mTmG</sup> (e–h), Tie2Cre<sup>mTmG</sup> (i–l) and VE-cadherinCreER<sup>mTmG</sup> (m–p) transgenic mice, 3 months after amputations. Lineage tracing of Sox9 shows expression within all epidermal lineages. Within mesoderm, GFP expression is restricted to the distal digit bone (a–d, outlined by a dashed line). Lineage tracing of scleraxis shows restriction of GFP to tendons (e–h, outlined by a dashed line). Lineage tracing of Tie2 and VE-cadherin shows restriction of GFP in blood cells and blood vessels of the distal digit (i–p, white arrowheads). bm, bone marrow; no, nail organ; np, nail plate; sg, sweat glands. Original magnification:  $\times 5$  (m–o);  $\times 10$  (a–k);  $\times 20$  (l, p).

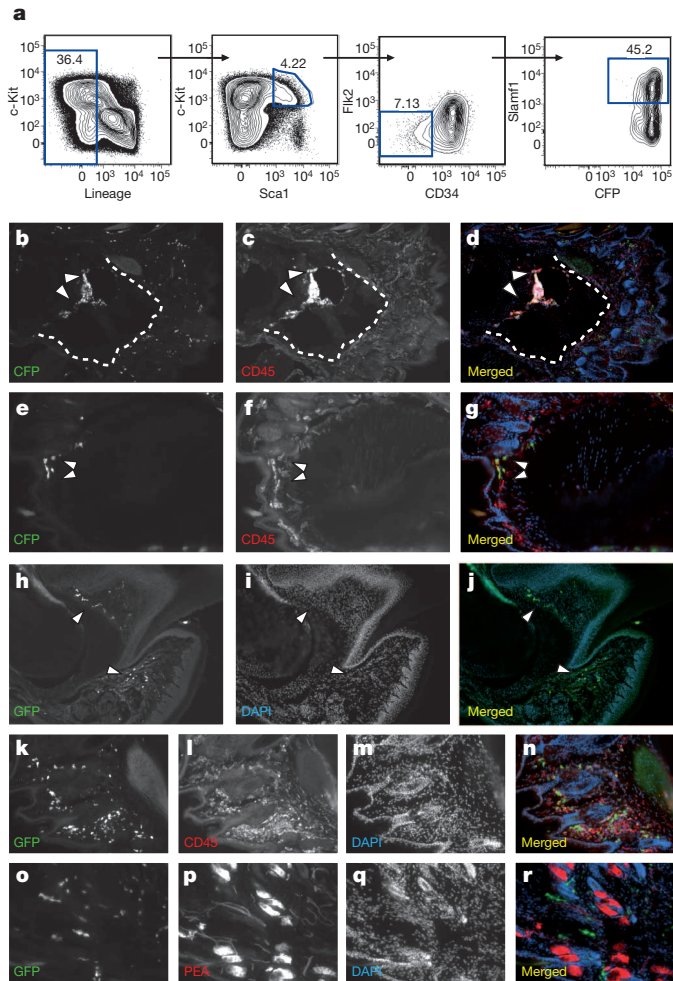


**Figure 3 | Circulating cells do not contribute to regenerating tissues of the digit tip.** **a**, Flow chart showing gating of HSCs on the basis of Lin<sup>-</sup> (CD3<sup>-</sup>CD4<sup>-</sup>CD8<sup>-</sup>Mac<sup>-</sup>Gr-1<sup>-</sup>B220<sup>-</sup>Ter119<sup>-</sup>) Flk2<sup>-</sup>CD34<sup>+</sup>Sca1<sup>+</sup>Slamf1<sup>+</sup> surface expressions (**a**). **b–g**, Sections through the digit of a host mouse that was infused with HSCs 3 months after amputation. HSC-derived cells within bone marrow (**b–d**) and dermis (**e–g**) are shown. The dotted line outlines the bone–epidermis border. **h–r**, Parabiosis between wild-type and genetically marked (GFP) littermates. **h–j**, Circulating cells within nail organ, mesenchyme surrounding sweat glands and dermis of regenerated digits (white arrowheads). **k–r**, Circulating cells within the regenerated digit express the haematopoietic marker CD45 (**k–n**) but not the endothelial marker PEA (**o–r**). Original magnification:  $\times 10$  (**b–d**, **h–j**);  $\times 20$  (**e–g**, **k–r**).

see Methods). Clonal patterns were visualized within all tissues by crossing Rainbow mice with mice harbouring an inducible Cre under the promoter of the actin gene (actinCreER). ActinCreER<sup>Rainbow</sup> offspring were injected with tamoxifen and digits were amputated at AP1/2. Mice were killed 3 months later, when digits were processed for histology. Clonal domains appeared within all regenerated tissue types (Fig. 4), with multiple clones occupying each tissue. A pattern of clonal stripes emerged from the nail bed contributing cumulatively multiple clones to the nail plate (Fig. 4a). Within the epidermis, clones expanded laterally to the basal epidermis, outwards into the stratified layer of the epidermis and inwards into dermal pegs close to the epidermis–dermis border (Fig. 4b), revealing that this new epidermis is derived from multiple expanding keratinocytes, not from hair follicles<sup>42</sup>. Within sweat glands, several clones contributed separately to the regenerating gland (Fig. 4c, white arrowheads). Blood vessels in association with the sweat glands derived from separate clones (Fig. 4d, white arrowheads), confirming our previous genetic fate mapping, and within bone, clones emerged with a restricted pattern to the proximal epiphysis, contributing laterally to new bone (Fig. 4e,

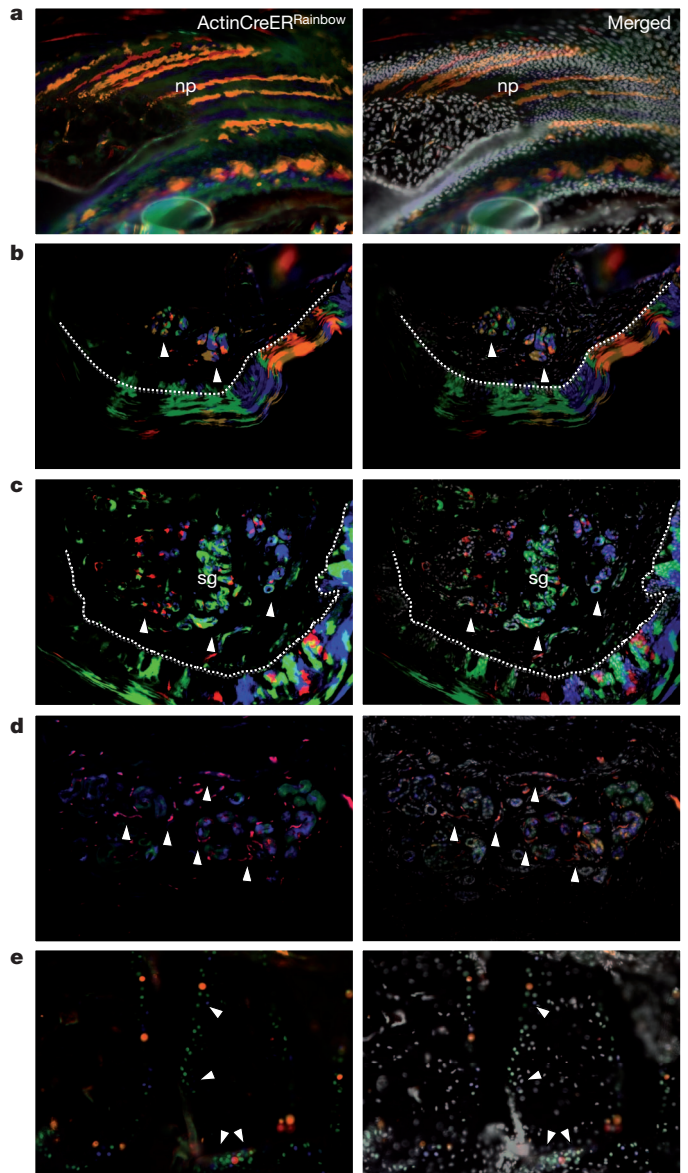


**Figure 4 | Multiple lineage-restricted clones contribute to digit-tip regeneration.** Sections through regenerated digits of actinCreER<sup>Rainbow</sup> mice. **a–c**, Expanding clones within nail (**a**), epidermis (**b**) and sweat glands (**c**). The dashed line in **b** and **c** outlines the epidermis–dermis border; white arrowheads show clones within ventral sweat glands. **d**, Sweat glands and the surrounding blood vessels (white arrowheads) are derived from separate clones. **e**, Expanding clones within the digit bone (white arrowheads). np, nail plate; sg, sweat glands. Right panels represent merged images of actinCreER<sup>Rainbow</sup> with DAPI staining. Original magnification:  $\times 20$  (**a–e**).

white arrowheads). Although we are unable at this point to indicate the contributions of fibroblasts, or rule out a pre-determined multipotent cell that contributes to bone/tendon and fibroblasts, our work with isolated bone/cartilage progenitors<sup>43</sup> and fibroblast precursors from mouse indicates that both cell types maintain lineage restriction *in vivo* and *in vitro* (Y.R., personal observations).

Early work on *Xenopus* tail regeneration revealed a similarly limited range of potential for the different stem/progenitors of the *Xenopus* tail<sup>44</sup>. In the salamander *Ambystoma mexicanum*, it was recently shown<sup>45</sup> that transplanted embryonic cells destined to form specific limb tissues maintain their embryonic fates after the amputation and subsequent regeneration of the salamander limbs. More recently, a similar fate restriction was documented in developing and regenerating zebrafish fins<sup>46</sup>. Our findings in mammals, together with those in



appendage development/regeneration of other vertebrate subphyla, attest to lineage restriction of stem/progenitor cells as an evolutionarily conserved cellular mode in which a change in cell fate or dedifferentiation to pluripotency is uncommon and negligible to regeneration, outcomes carrying significant implications for regenerative medicine.

## METHODS SUMMARY

**Mice.** Mice were maintained at the Stanford University Research Animal Facility in accordance with Stanford University guidelines. All the animals were housed in sterile micro-insulators and given water and rodent chow ad libitum.

K5CreERT2, K14CreERT2, En1Cre, VE-cadherinCreERT2 and Tie2Cre mice were obtained from The Jackson Laboratory, and a breeding colony was established. Sox9Cre and Prx1Cre mice were a gift from A. Sweet-Cordero. ScxCre mice were a gift from R. Schweitzer. mTmG mice were a gift from L. Luo.

**Digit amputations.** Amputations were conducted under the guidelines of Stanford University Administrative Panel on Laboratory Animal Care (APLAC), Protocol no. 21621. Mice (post-weaning age) were anaesthetized with intraperitoneal injection of Nembutal (pentobarbital; 50 mg kg<sup>-1</sup> body weight) or ketamine/xylazine (80 mg and 8 mg kg<sup>-1</sup> body weight, respectively). Digits were amputated using a no. 11 scalpel and allowed to heal without suturing for 2–3 months.

**Full Methods** and any associated references are available in the online version of the paper at [www.nature.com/nature](http://www.nature.com/nature).

Received 2 December 2010; accepted 30 June 2011.

- Rinkevich, B., Shlensberg, Z. & Fishelson, L. Whole-body protochordate regeneration from totipotent blood cells. *Proc. Natl Acad. Sci. USA* **92**, 7695–7699 (1995).
- Rinkevich, Y., Paz, G., Rinkevich, B. & Reshef, R. Systemic bud induction and retinoic acid signaling underlie whole body regeneration in the urochordate *Botryllodes leachi*. *PLoS Biol.* **5**, e71 (2007).
- Voskoboinik, A. *et al.* Striving for normality: whole body regeneration through a series of abnormal generations. *FASEB J.* **21**, 1335–1344 (2007).
- Sánchez Alvarado, A. Regeneration in the metazoans: why does it happen? *Bioessays* **22**, 578–590 (2000).
- Han, M., Yang, X., Lee, J., Allan, C. H. & Muneoka, K. Development and regeneration of the neonatal digit tip in mice. *Dev. Biol.* **315**, 125–135 (2008).
- Schotte, O. E. & Smith, C. B. Wound healing processes in amputated mouse digits. *Biol. Bull.* **117**, 546–561 (1959).
- Borgens, R. B. Mice regrow the tips of their foretoes. *Science* **217**, 747–750 (1982).
- Reginelli, A. D., Wang, Y. Q., Sassoon, D. & Muneoka, K. Digit tip regeneration correlates with regions of Msx1 (Hox 7) expression in fetal and newborn mice. *Development* **121**, 1065–1076 (1995).
- Neufeld, D. A. & Zhao, V. Phalangeal regrowth in rodents: postamputational bone regrowth depends upon the level of amputation. *Prog. Clin. Biol. Res.* **383A**, 243–252 (1993).
- Illingworth, C. M. Trapped fingers and amputated fingertips in children. *J. Pediatr. Surg.* **9**, 853–858 (1974).
- Rosenthal, L. J., Reiner, M. A. & Bleicher, M. A. Nonoperative management of distal fingertip amputations in children. *Pediatrics* **64**, 1–3 (1979).
- Vidal, P. & Dickson, M. G. Regeneration of the distal phalanx. A case report. *J. Hand Surg.* **18**, 230–233 (1993).
- Morgan, T. H. *Regeneration* (Macmillan, 1901).
- Bratincsák, A. *et al.* CD45-positive blood cells give rise to uterine epithelial cells in mice. *Stem Cells* **25**, 2820–2826 (2007).
- Faustman, D. L. *et al.* Comment on papers by Chong *et al.*, Nishio *et al.*, and Suri *et al.* on diabetes reversal in NOD mice. *Science* **314**, 1243a, doi:10.1126/science.1129811 (2006).
- Djouad, F., Bouffi, C., Ghanam, S., Noël, D. & Jorgensen, C. Mesenchymal stem cells: innovative therapeutic tools for rheumatic diseases. *Nature Rev. Rheumatol.* **5**, 392–399 (2009).
- Zaidi, N. & Nixon, A. J. Stem cell therapy in bone repair and regeneration. *Ann. NY Acad. Sci.* **1117**, 62–72 (2007).
- Brookes, J. P. & Kumar, A. Appendage regeneration in adult vertebrates and implications for regenerative medicine. *Science* **310**, 1919–1923 (2005).
- Tamura, K., Ohgo, S. & Yokoyama, H. Limb blastema cell: a stem cell for morphological regeneration. *Dev. Growth Differ.* **52**, 89–99 (2010).
- Christen, B., Robles, V., Raya, M., Paramonov, I. & Belmonte, J. C. Regeneration and reprogramming compared. *BMC Biol.* **8**, 5 (2010).
- Tsonis, P. A. Stem cells and blastema cells. *Curr. Stem Cell Res. Ther.* **3**, 53–54 (2008).
- Weissman, I. L. Stem cells: units of development, units of regeneration, and units in evolution. *Cell* **100**, 157–168 (2000).
- Wagers, A. J., Sherwood, R. I., Christensen, J. L. & Weissman, I. L. Little evidence for developmental plasticity of adult hematopoietic stem cells. *Science* **297**, 2256–2259 (2002).
- Wagers, A. J. & Weissman, I. L. Plasticity of adult stem cells. *Cell* **116**, 639–648 (2004).
- Purhonen, S. J. *et al.* Bone marrow-derived circulating endothelial precursors do not contribute to vascular endothelium and are not needed for tumor growth. *Proc. Natl Acad. Sci. USA* **105**, 6620–6625 (2008).
- Hamrick, M. W. Development and evolution of the mammalian limb: adaptive diversification of nails, hooves, and claws. *Evol. Dev.* **3**, 355–363 (2001).
- Said, S., Parke, W. & Neufeld, D. A. Vascular supplies differ in regenerating and nonregenerating amputated rodent digits. *Anat. Rec. A* **278**, 443–449 (2004).
- Vasioukhin, V., Degenstein, L., Wise, B. & Fuchs, E. The magical touch: genome targeting in epidermal stem cells induced by tamoxifen application to mouse skin. *Proc. Natl Acad. Sci. USA* **96**, 8551–8556 (1999).
- Muzumdar, M. D., Tasic, B., Miyamichi, K., Li, L. & Luo, L. A global double-fluorescent Cre reporter mouse. *Genesis* **45**, 593–605 (2007).
- Indra, A. K. *et al.* Temporally-controlled site-specific mutagenesis in the basal layer of the epidermis: comparison of the recombinase activity of the tamoxifen-inducible Cre-ER<sup>T2</sup> and Cre-ER<sup>T2</sup> recombinases. *Nucleic Acids Res.* **27**, 4324–4327 (1999).
- Kimmel, R. A. *et al.* Two lineage boundaries coordinate vertebrate apical ectodermal ridge formation. *Genes Dev.* **14**, 1377–1389 (2000).
- Logan, M. *et al.* Expression of Cre recombinase in the developing mouse limb bud driven by a Prx1 enhancer. *Genesis* **33**, 77–80 (2002).
- Akiyama, H. *et al.* Osteo-chondroprogenitor cells are derived from Sox9 expressing precursors. *Proc. Natl Acad. Sci. USA* **102**, 14665–14670 (2005).
- Nowak, J. A., Polak, L., Pasolli, H. A. & Fuchs, E. Hair follicle stem cells are specified and function in early skin morphogenesis. *Cell Stem Cell* **3**, 33–43 (2008).
- Pryce, B. A., Brent, A. E., Murchison, N. D., Tabin, C. J. & Schweitzer, R. Generation of transgenic tendon reporters, ScxGFP and ScxAP, using regulatory elements of the scleraxis gene. *Dev. Dyn.* **236**, 1677–1682 (2007).
- Forde, A., Constien, R., Gröne, H. J., Hämmerling, G. & Arnold, B. Temporal Cre-mediated recombination exclusively in endothelial cells using Tie2 regulatory elements. *Genesis* **33**, 191–197 (2002).
- Monvoisin, A. *et al.* VE-cadherin-CreERT2 transgenic mouse: a model for inducible recombination in the endothelium. *Dev. Dyn.* **235**, 3413–3422 (2006).
- Fernando, W. A. *et al.* Wound healing and blastema formation in regenerating digit tips of adult mice. *Dev. Biol.* **350**, 301–310 (2011).
- Forsberg, E. C., Bhattacharya, D. & Weissman, I. L. Hematopoietic stem cells: expression profiling and beyond. *Stem Cell Rev.* **2**, 23–30 (2006).
- Wright, D. E., Wagers, A. J., Gulati, A. P., Johnson, F. L. & Weissman, I. L. Physiological migration of hematopoietic stem and progenitor cells. *Science* **294**, 1933–1936 (2001).
- Liversage, R. A. in *A History of Regeneration Research: Milestones in the Evolution of a Science* (eds Dinsmore, C. E.) (Cambridge Univ. Press, 1991).
- Ito, M. *et al.* Wnt-dependent *de novo* hair follicle regeneration in adult mouse skin after wounding. *Nature* **447**, 316–320 (2007).
- Chan, C. K. *et al.* Endochondral ossification is required for haematopoietic stem-cell niche formation. *Nature* **457**, 490–494 (2009).
- Gargioli, C. & Slack, J. M. Cell lineage tracing during *Xenopus* tail regeneration. *Development* **131**, 2669–2679 (2004).
- Kragl, M. *et al.* Cells keep a memory of their tissue origin during axolotl limb regeneration. *Nature* **460**, 60–65 (2009).
- Tu, S. & Johnson, S. L. Fate restriction in the growing and regenerating zebrafish fin. *Dev. Cell* **20**, 725–732 (2011).

**Supplementary Information** is linked to the online version of the paper at [www.nature.com/nature](http://www.nature.com/nature).

**Acknowledgements** We thank A. Mosley for assistance with animal care and parabiosis experiments; A. Sweet-Cordero for providing Sox9Cre and Prx1Cre mice; R. Schweitzer for providing ScxCre mice; and L. Luo for providing mTmG reporter mice. We thank D. Montoro for assistance with histochemical stains and G. Paz for assistance with figure preparations. This work was supported in part by a grant from the California Institute of Regenerative Medicine (RC1 00354) and from the Smith Family Trust (to I.L.W.), the Oak Foundation and the Hagey Laboratory for Pediatric Regenerative Medicine (to M.T.L.). Y.R. is supported by a Human Frontier Science Program (HFSP) Long Term Fellowship, and the Machiah Foundation Fellowship.

**Author Contributions** Y.R. and I.L.W. designed the experiments. Y.R. performed the regeneration experiments, imaged and analysed the data from all regeneration experiments. H.U. provided the Rainbow reporter mice for part of the experiments. M.T.L. provided the histochemical stains for part of the experiments. Y.R. and P.L. performed the HSC transplantations and analysed the data. Y.R. and I.L.W. wrote the manuscript.

**Author Information** Reprints and permissions information is available at [www.nature.com/reprints](http://www.nature.com/reprints). The authors declare no competing financial interests. Readers are welcome to comment on the online version of this article at [www.nature.com/nature](http://www.nature.com/nature). Correspondence and requests for materials should be addressed to Y.R. ([ryuval@stanford.edu](mailto:ryuval@stanford.edu)).

## METHODS

**Mice.** Mice were derived and maintained at the Stanford University Research Animal Facility in accordance with Stanford University guidelines. All the animals were housed in sterile micro-insulators and given water and rodent chow ad libitum.

K5CreERT2, K14CreERT2, En1Cre, VE-cadherinCreERT2 and Tie2Cre transgenic mice were obtained from The Jackson Laboratory and a breeding colony was established. Sox9Cre and Prx1Cre mice were a gift from A. Sweet-Cordero. ScxCre mice were a gift from R. Schweitzer. mTmG reporter mice were a gift from L. Luo.

**Digit amputations.** Amputations were conducted under the guidelines of Stanford University Administrative Panel on Laboratory Animal Care (APLAC), Protocol no. 21621. Mice (post-weaning age) were anaesthetized with intraperitoneal injection of Nembutal (pentobarbital; 50 mg kg<sup>-1</sup> body weight) or ketamine/xylazine (80 mg and 8 mg kg<sup>-1</sup> body weight, respectively). Digits 1–5 were amputated at proximal or distal levels using a no. 11 scalpel and allowed to heal without suturing for 2–3 months.

**Generation of Rosa26-Rainbow mice.** lox2272-loxN-loxP-NheI-EcoRI sequence was introduced into the EcoRI site of pCAGGS. Fluorescent cDNAs, EGFP, mCherry, mOrange and mCerulean (Addgene) were subcloned into an expression vector, pCAGGS. The fluorescent cDNAs together with 3' globin enhancer and polyA sequences of the pCAGGS vector were PCR amplified and loxP (for mCherry), loxN (for mOrange) or lox2272 (for mCerulean) sequences at 5' non-coding region of the cDNA, and NheI at 5' and XbaI at 3' sites were attached to the fragments. The resulting NheI-XbaI fragments were subcloned into the NheI site of lox2272-loxN-loxP-pCAGGS sequentially in the following order (loxP-mCherry, loxN-mOrange, lox2272-mCerulean, and EGFP). The whole construct from the CAG promoter to the polyA sequence downstream of mCherry was cut out and subcloned into the Rosa26-1 neo vector. The vector was introduced into R1 ES cells and the knockin ES clone was established, and mice were generated.

**Mice genotyping.** The following primers and PCR conditions were used for genotyping: Cre, 5'-CGGTCGATGCAACGAGTGATGAGG-3' and 5'-CCAGA GACGGAAATCCATCGCTCG-3'; 94 °C for 10 min, 94 °C for 30 s, 56 °C for

1:30 min, 72 °C for 1.5 min, repeat 35 cycles, 72 °C for 8 min. mTmG, 5'-CTCTG CTGCCTCCTGGCTTCT-3', 5'-CGAGGCGGATCACAAGCAATA-3' and 5'-TCAATGGGCGGGGTCGTT-3'; 94 °C for 3 min, 94 °C for 30 s, 61 °C for 1 min, 72 °C for 1 min, repeat 35 cycles, 72 °C for 2 min.

**Tamoxifen injections.** 4-Hydroxytamoxifen (Sigma) was prepared by dissolving in absolute ethanol to a stock concentration of 100 mg ml<sup>-1</sup> using extensive vortexing. Tamoxifen stock solution was further emulsified in corn oil (Sigma) at 1:10. Before injection, the tamoxifen/oil suspension was sonicated in a sterile glass vial in an ultrasonic bath sonicator. 1–2.5 mg tamoxifen was injected intraperitoneally with a tuberculin syringe and 25-gauge needle.

**HSC transplantation.** Transplantation and engraftment of HSCs into mice was carried out as previously described<sup>41</sup>.

**Histology and tissue analysis.** For fixation, tissues were placed in 2% paraformaldehyde for 12–16 h at 4 °C, then decalcified in 0.4 M EDTA in PBS (pH 7.2) at 4 °C for 2 weeks. Samples were prepared for embedding by soaking in 30% sucrose in PBS at 4 °C for 24 h. Samples were removed from the sucrose solution and tissue blocks were prepared by embedding in Tissue Tek O.C.T (Sakura Finetek) under dry ice to freeze the samples within the compound. Frozen blocks were mounted on a MicroM HM550 cryostat (MICROM International GmbH) and 5–8-µm-thick sections were transferred to Superfrost/Plus adhesive slides (Fisher brand). Representative sections were stained with Movat's modified pentachrome stain, haematoxylin and eosin stain and aniline blue stain as previously described<sup>44</sup>.

**Immunohistochemistry.** Immunostaining was performed using the following primary antibodies KI67 (Abcam), CD31 (Abcam), CD90 (eBioscience), CD105 (eBioscience), PEA (BD Pharmingen), cytokeratin 5 (Abcam), cytokeratin 14 (Covance), CD45 (Biolegend), MBP (Abcam), S100A4 (Abcam).

Briefly, slides were blocked for 30 min in 10% BSA with 2% goat serum followed by incubation with primary antibody for 12–16 h. For immunoassaying on sections from mTmG mice, Alexa Fluor 647 conjugated antibody was used as secondary 1:1,000 for 1 h (Invitrogen), and was visualized in the far-red channel (Cy5). Fluorescent and bright-field images were taken with a Leica DM4000B microscope (Leica Microsystems) and RETIGA 2000R camera (QImaging Scientific Cameras).



# Structure of the membrane domain of respiratory complex I

Rouslan G. Efremov<sup>1†</sup> & Leonid A. Sazanov<sup>1</sup>

Complex I is the first and largest enzyme of the respiratory chain, coupling electron transfer between NADH and ubiquinone to the translocation of four protons across the membrane. It has a central role in cellular energy production and has been implicated in many human neurodegenerative diseases. The L-shaped enzyme consists of hydrophilic and membrane domains. Previously, we determined the structure of the hydrophilic domain. Here we report the crystal structure of the *Escherichia coli* complex I membrane domain at 3.0 Å resolution. It includes six subunits, NuoL, NuoM, NuoN, NuoA, NuoJ and NuoK, with 55 transmembrane helices. The fold of the homologous antiporter-like subunits L, M and N is novel, with two inverted structural repeats of five transmembrane helices arranged, unusually, face-to-back. Each repeat includes a discontinuous transmembrane helix and forms half of a channel across the membrane. A network of conserved polar residues connects the two half-channels, completing the proton translocation pathway. Unexpectedly, lysines rather than carboxylate residues act as the main elements of the proton pump in these subunits. The fourth probable proton-translocation channel is at the interface of subunits N, K, J and A. The structure indicates that proton translocation in complex I, uniquely, involves coordinated conformational changes in six symmetrical structural elements.

Complex I (NADH:ubiquinone oxidoreductase) is one of the largest known membrane proteins. It provides about 40% of the proton flux during proton-motive force generation for the synthesis of ATP by the mitochondrial respiratory chain<sup>1–5</sup>. Many mutations in subunits of complex I have been associated with human neurodegenerative diseases<sup>5,6</sup>. Complex I is a major source of reactive oxygen species in mitochondria: these can damage mitochondrial DNA and are considered to be causative agents in Parkinson's disease<sup>7</sup> and ageing<sup>8</sup>. Mitochondrial complex I consists of 45 subunits (980 kDa in total)<sup>9</sup>. The simpler prokaryotic enzyme usually consists of 14 'core' subunits (about 550 kDa in total) that are conserved from bacteria to humans<sup>1,2,5,10</sup>. It contains equivalent redox components and has a similar L-shaped structure to that of mitochondrial complex I (refs 2, 5, 11). The high degree of sequence conservation of core subunits indicates that the mechanism of complex I is probably the same throughout all species.

The complete atomic structure of this molecular machine is currently unknown. Structures of the *Thermus thermophilus* complex I hydrophilic domain<sup>12,13</sup> have established the electron-transfer pathway from NADH to the primary electron acceptor flavin mononucleotide, and then through seven conserved iron-sulphur clusters to the putative quinone binding site at the interface with the membrane domain (which lacks covalently bound prosthetic groups). The three largest hydrophobic subunits of complex I, NuoL, M and N (*E. coli* nomenclature), are homologous to each other and to Na<sup>+</sup>/H<sup>+</sup> antiporter complex (Mrp) subunits<sup>14,15</sup>. They are likely to participate in proton translocation. We previously determined the arrangement of  $\alpha$ -helices in the membrane domain of *E. coli* complex I, but the limited resolution (3.9 Å) prevented sequence assignment<sup>11</sup>.

Understanding how the transfer of two electrons from NADH to ubiquinone is coupled to the translocation of four protons (the current consensus value) across the membrane remains a major question in complex I research<sup>1–3,5</sup>. 'Direct' (redox-driven) and 'indirect'

(conformation-driven) mechanisms have been proposed<sup>2,3,5,16</sup>. Recently published structures revealed an unexpected structural element, helix HL, extending along nearly the entire length of the membrane domain<sup>11,17</sup>: this may act as a connecting element, coordinating conformational changes<sup>11</sup>. A greater understanding requires a knowledge of the atomic structure of the membrane domain.

## Structure determination and overall architecture

A new P1 crystal form was obtained with protein purified in the detergent cymal-7. After extensive optimization, the diffraction extended to 2.7 Å in the best direction. The crystallized fragment contains six subunits, NuoL, M, N, A, J and K (222 kDa in total), but lacks NuoH, which dissociates readily from the complex<sup>11,18</sup>. Multiwavelength anomalous diffraction (MAD) data sets were collected from SeMet-derivatized protein (Supplementary Table 1). Multi-crystal density averaging and modification led to experimental electron density maps of excellent quality (Supplementary Fig. 1). The model was refined to 3.0 Å resolution with  $R = 23.2\%$  and  $R_{\text{free}} = 28.3\%$  (Supplementary Table 1), and includes 1,952 residues (out of 2,038, Supplementary Table 2). A cymal-7 molecule, fragments of lipid aliphatic chains and several well-ordered internal water molecules are also included.

The model contains 55 transmembrane helices (TMs) (Fig. 1 and Supplementary Movie 1). Subunits NuoA, J and K form an 11-helix bundle near the interface with the hydrophilic domain, and the antiporter-like subunits NuoN, M, and L follow, as proposed earlier<sup>11</sup>. The distal subunit NuoL contains a carboxy-terminal extension that starts with TM15, followed by helix HL and ending with TM16, harboured at the interface with subunits NuoJ, K and N. Sequence conservation is high for the membrane core of all subunits (Supplementary Fig. 3), underlining its functional significance. Helix HL is poorly conserved, as might be expected for a mostly mechanical element, with the exception of residues contacting other subunits

<sup>1</sup>Medical Research Council Mitochondrial Biology Unit, Wellcome Trust/MRC Building, Hills Road, Cambridge CB2 0XY, UK. <sup>†</sup>Present address: Max-Planck Institute for Molecular Physiology, Otto-Hahn Strasse 11, Dortmund 44227, Germany.

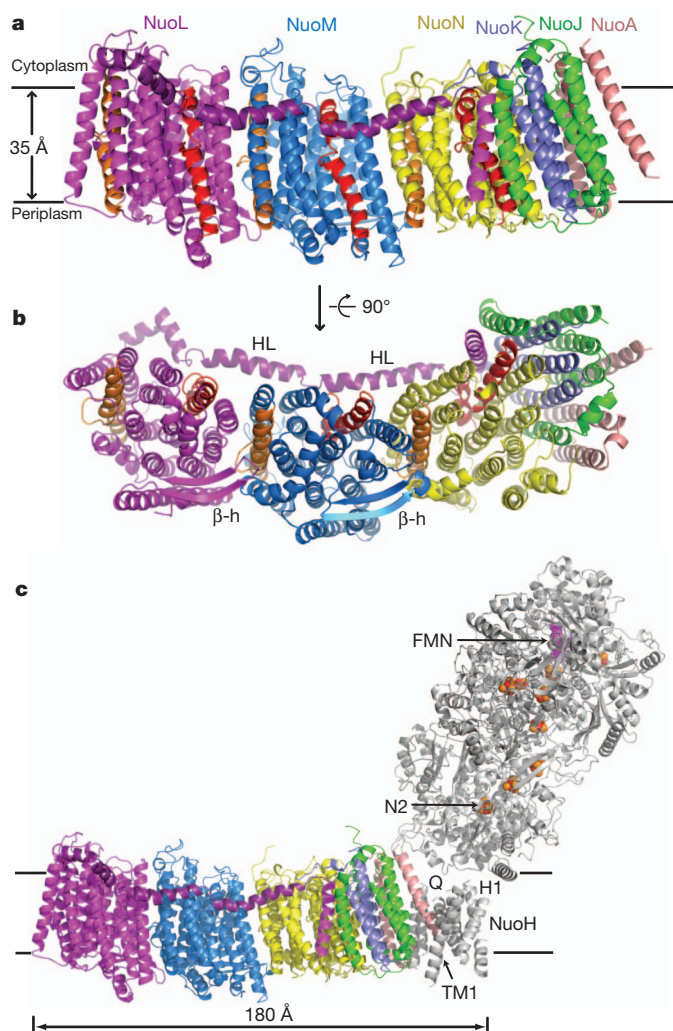


**Figure 1 | Architecture of the membrane domain of *E. coli* complex I.** Cartoon representation of the atomic model. **a**, Side view in the membrane plane. **b**, View from the periplasm into the membrane. Subunits are coloured as indicated by the labels. Discontinuous helices are shown in red (TM7) and orange (TM12). Connecting elements, helix HL and  $\beta$ -hairpins ( $\beta$ -h), are labelled. The position of the lipid bilayer is estimated as in Supplementary Fig. 4. **c**, Side view of the structure, aligned with the membrane domain of the entire complex I from *T. thermophilus* (PDB code 3M9S)<sup>11</sup>. Subunits that are not present in the *E. coli* structure are shown in grey. Flavin mononucleotide (FMN) is shown as magenta spheres; iron-sulphur clusters are shown as red-orange spheres, with cluster N2 labelled. Helix TM1 from subunit Nqo8/NuoH, helix H1 from Nqo6/NuoB and the probable quinone-binding site (Q) are indicated.

(Supplementary Fig. 3b), indicating that this helix is similarly arranged across species. The polar residues of amphipathic helix HL face the cytoplasm and apolar residues point to the membrane (Supplementary Fig. 4), indicating that helix HL resides at the surface of the lipid bilayer. The periplasmic surface of the membrane domain is mostly negatively charged and the cytoplasmic surface is positively charged, in agreement with the positive-inside rule<sup>19</sup>. Lipid bilayer boundaries are clearly visualized by the belts of solvent-exposed Tyr and Trp residues<sup>20</sup> and by the hydrophobicity of surface-exposed residues (Supplementary Fig. 4).

### Fold of antiporter-like subunits

Subunits NuOL, M and N contain 14 structurally conserved helices (Fig. 2a–c, Supplementary Fig. 5 and Supplementary Table 3). The fold differs from the bioinformatic prediction<sup>21</sup>. Sequential transmembrane helices contact each other, except for TM8 and TM9,

and TM13 and TM14. The two discontinuous helices observed previously<sup>11</sup> are TM7 and TM12. They are interrupted in the middle of the bilayer by an extended loop of 5–7 residues. The tips of these loops contain a proline that is conserved between all three antiporter-like subunits: M(Pro 239)\* in TM7 and M(Pro 399)\* in TM12 (the prefix indicates the subunit name; asterisks indicate residues conserved between all three antiporter-like subunits). As in other transporters<sup>22,23</sup>, such helices are likely to participate in proton or ion transport by introducing some flexibility and charge to the middle of the membrane.

TMs 1, 2 and 14 form a lipid-facing layer at the opposite side of the domain from helix HL and are the least conserved in sequence and in structure (Supplementary Figs 3 and 5). TMs 2 and 3 are connected at the periplasmic surface by an extended  $\beta$ -hairpin. The core of the subunits is formed by the well-conserved helices 4–13. Their arrangement has internal symmetry: TMs 4–8 can be superimposed on TMs 9–13 by a rotation of about 180° along the axis lying in the membrane plane and directed along the long axis of the domain, followed by a shift along this axis (Fig. 2c–f and Supplementary Movie 2). Thus, the two halves of the core, each containing five TMs, are related, uniquely, by symmetry along a pseudo-two-fold screw axis. Symmetry-related sets of helices in transporters may span the membrane in a parallel or antiparallel fashion, but have always been found in face-to-face arrangements, with substrate binding sites located near the symmetry axis at the domain interface<sup>22</sup>. However, in case of complex I antiporter-like subunits, the interface is formed by face-to-back contact, presenting a novel arrangement of symmetry-related helices. This places discontinuous helices 7 and 12 far apart, so that they cannot interact directly, in contrast to the situation in other transporters. It is likely that antiporter-like subunits have evolved by gene duplication<sup>22</sup>, even though the sequences of the two inverted domains (Fig. 2c–e) have diverged (Supplementary Table 3).

At the centre of each antiporter-like subunit, TM8 is partly unwound in the middle and contains a kink with no proline residues, similar to the  $\pi$ -bulge in bacteriorhodopsin<sup>24</sup>. The secondary structure is markedly disrupted near the kink (residues L(253–258), M(259–264) and N(242–247)), indicating flexibility. Such  $\pi$ -bulges (or  $\pi$ -helices<sup>25</sup>) are normally found at protein functional sites<sup>25</sup>, indicating a mechanistic importance for the kink in TM8.

Two well-studied, essential charged residues that are conserved from Mrp antiporters to complex I (refs 15, 26) are found in the middle of TM5 (L(Glu 144), M(Glu 144) and N(Glu 133); termed Glu TM5 here), and in the middle of TM7 (L(Lys 229), M(Lys 234) and N(Lys 217); Lys TM7). Lys TM7 is the last residue of the periplasmic half of discontinuous TM7 (TM7a), and its  $\epsilon$ -amino group points inside the putative proton channel (termed here the first channel), formed by TMs 5–8. Notably, Glu TM5 is wedged at the interface of TMs 5 and 6, and is exposed both to this channel and to the cavity at the interface with the adjacent subunit. The Glu TM5 carboxyl group can interact electrostatically with the Lys TM7 amino group, which is about 5–6 Å away. An invariant Trp from TM7b (M(Trp 243)\*) stabilizes the link between the two halves of TM7. The negative helix-dipole charge here may be partly compensated by N(Trp 247), M(His 248) and L(His 254).

The area near the second discontinuous helix, TM12, harbours many conserved polar residues in the middle of the membrane, so is also of clear functional importance. In NuOL and NuON, an invariant, essential<sup>27,28</sup> lysine (L(Lys 399) and N(Lys 395)) lies at the beginning of the periplasmic half of TM12 (TM12b) in a position approximately symmetrical to Lys TM7 (Fig. 2d, e). It may interact with, and stabilize, the negatively charged C terminus of TM12a. In NuOM, a similar position is occupied by an invariant Glu 407. Here, the negative dipole moment may be stabilized by the invariant His 322. Notably, Glu 407 is replaced by an invariant lysine in the homologous MrpD subunit of antiporters. The side chain of this Lys or Glu (termed Lys/Glu TM12) is exposed in a large cavity between TMs 10–13. Thus, unexpectedly, a second putative proton channel is present here, related by inverted



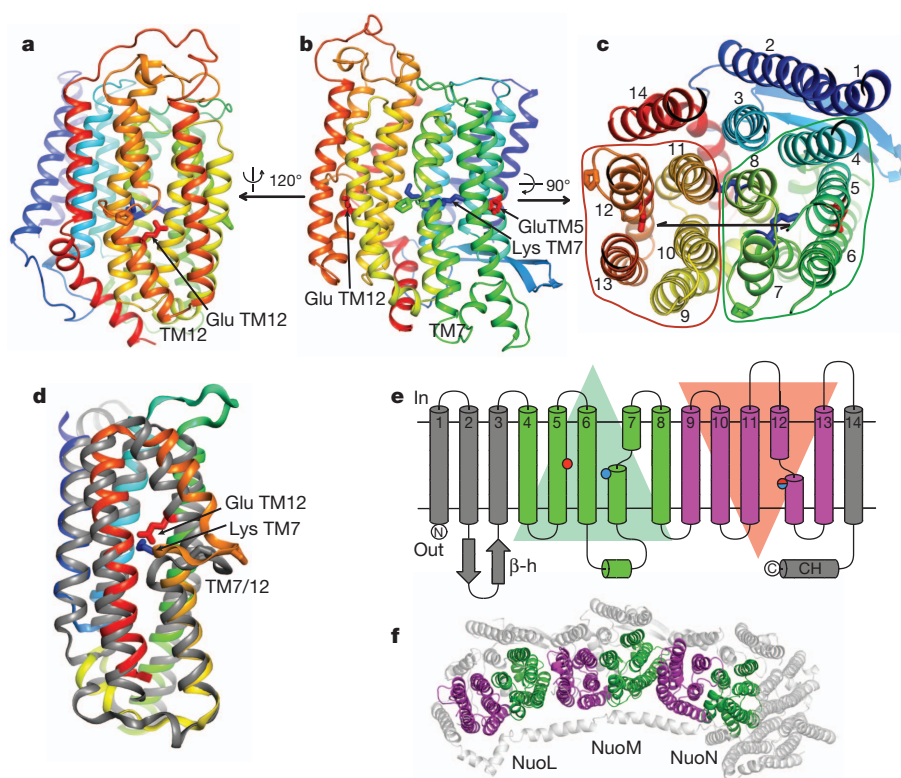


**Figure 2 | Fold of antiporter-like subunits.** The fold is illustrated using subunit NuoM. **a**, Side view, cytoplasmic side up, centred on TM12. **b**, Side view centred on TM7, coloured blue to red from N to C terminus. Essential charged residues are shown as sticks (Glu TM5 and Lys TM7 from channel 1, Glu TM12 from channel 2 and the connecting M(Lys 265) from TM8). Conserved prolines from intra-helical loops are also shown. **c**, View from the cytoplasm into the membrane. TM helices are numbered. Two inverted repeats are circled and the

pseudo-two-fold symmetry screw axis that relates them is shown. **d**, Overlay of the two symmetry-related domains (TMs 9–13, in grey, over TMs 4–8). **e**, Topology diagram of antiporter-like subunits. Two inverted repeats of the conserved core are shown in green and magenta. Crucial charged residues (Glu TM5, Lys TM7 and Lys/Glu TM12) are indicated. **f**, Structural repeats in the membrane domain, seen from the cytoplasm. TMs 4–8 are highlighted in green and TMs 9–13, in magenta.

symmetry to the first channel. Additionally, N(Lys 395) is exposed to the cavity between NuoN and NuoM, and M(Glu 407) is partially exposed to the cavity between NuoM and NuoL, similarly to Glu TM5.

Searches using either complete subunits or the repeating domain revealed no structural analogues in the protein data bank (PDB), confirming that the fold is novel. Homologous subunits in Mrp antiporters, chloroplast Ndh complexes and membrane-bound hydrogenases, not yet structurally characterized, are likely to share the same core fold.

### Fold of subunits NuoK, NuoJ and NuoA

In contrast to NuoL, M and N, the smaller subunits interact extensively, with large surface areas buried at interfaces. They also form more hydrogen bonds and salt bridges to their neighbours (Supplementary Table 4), ‘gluing’ together this end of the membrane domain.

NuoK spans the membrane with three linearly arranged  $\alpha$ -helices, connected by short loops (Supplementary Fig. 6a). NuoK interacts extensively with NuoN (Fig. 1b), consistent with the presence of the analogous MrpC subunit in antiporters<sup>29</sup>. The C terminus of NuoK extends between helix HL and NuoN, forming many inter-subunit links. NuoK can be aligned with TMs 4–6 of antiporter-like subunits (and also with TMs 9–11, but with low sequence identities) (Supplementary Table 3). Notably, conserved K(Glu 36) aligns to Glu TM5, indicating that NuoK and the antiporter-like subunits might share an ancestor.

Subunit NuoJ has an unusual non-globular fold: three linearly arranged amino-terminal TM helices border NuoK, and TMs 4 and 5 are separated at the opposite sides of the domain (Supplementary Fig. 6b). Thus, NuoJ interweaves between NuoK, A and N, stabilizing

the complex. TM3 of NuoJ contains in its middle a  $\pi$ -bulge/kink (residues 59–62), similar to TM8 in NuoL, M and N, so this helix is probably flexible and mechanistically important.

Subunit NuoA consists of three linearly arranged TM helices at the edge of the domain, interacting with NuoJ, N and K (Supplementary Fig. 6c). Its outer surface, including the conserved A(Asp 79) in the middle of the membrane, probably interacts with NuoH (Fig. 1c). A conserved loop between TM1 and TM2 is not resolved in the structure and probably interacts with the hydrophilic subunit NuoD<sup>11</sup>. The probable quinone-binding site is formed at the interface of subunits NuoH, J and A with the hydrophilic domain<sup>11</sup> (Fig. 1c).

### Interactions between subunits

About half of the total subunit surface area is buried away from the solvent (Supplementary Table 4), consistent with the relative stability of the domain. However, interactions between antiporter-like subunits are not extensive. They mainly involve two helices from each subunit (TM5 and 6 and TM12 and 13), and are mostly hydrophobic, with very few hydrogen bonds (Supplementary Table 4). Crevices between subunits are likely to be filled with lipids, some of which are ordered and modelled here.

Helix HL stabilizes the complex. It is tightly anchored to NuoN, J and K by L(TM16), which also contacts N(TM7). HL contacts NuoM near M(TM7), where HL is unwound, allowing for strong interactions via the backbone and side chains (Fig. 3 and Supplementary Table 4). In a similar fashion, helix HL forms hydrogen bonds to the main body of the domain near TM7 of NuoL and N. These contacts involve conserved M(Lys 173)\*, M(Asp 246)\* and M(Tyr 317)\*, and a semi-conserved residue, M(His 241).

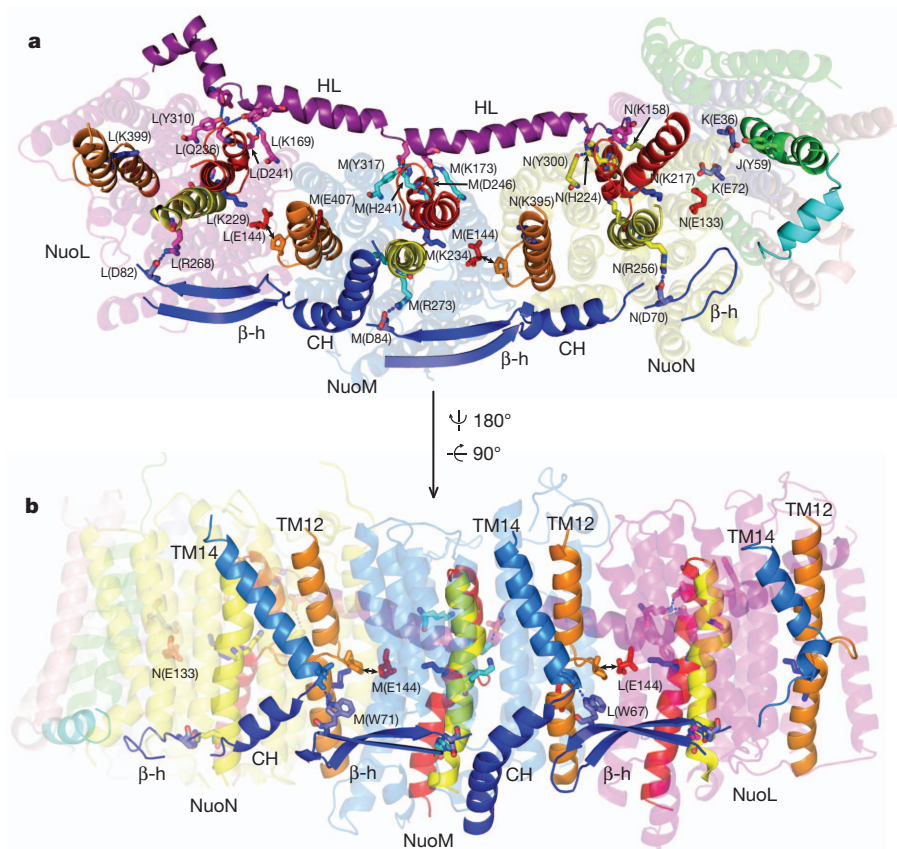


**Figure 3 | Connecting elements and interactions between subunits.** **a**, View from the periplasm. Helix HL is in purple and the  $\beta$ -hairpin-helix element  $\beta$ H (consisting of hairpins  $\beta$ -h and helices CH) is in blue. The contacting helix from NuoJ (preceding TM5 of NuoJ) is in cyan. Helices that are probably involved in conformational changes are shown in red (TM7 in NuoL, M and N), orange (TM12), yellow (TM8) and green (TM3 in NuoJ). Essential charged residues are shown as sticks and labelled (prefix indicates subunit). Also shown are

conserved residues involved in contacts between antiporter-like subunits and helix HL, as well as between the  $\beta$ -hairpins and TM8. Putative hydrogen bonds are indicated. Potential interactions between Glu TM5 and a conserved proline from the TM12 loop are indicated by arrows. **b**, View in the membrane, with TM14 also shown (light blue). Tryptophan residues forming hydrogen bonds to the backbone at the C terminus of TM14 are indicated.

Notably, an additional element connecting antiporter-like subunits is present on the opposite side of the domain from helix HL. The extended and well-ordered (thus probably rigid)  $\beta$ -hairpins from neighbouring subunits contact each other via a stretch of C-terminal amphipathic helices termed CH (Fig. 3). This notable  $\beta$ -hairpin-helix element (termed the  $\beta$ H element) extends over the entire length of the antiporter-like subunits and contributes to the stability of the complex, because the only polar interactions between NuoM and NuoN are via the tip of the NuoM  $\beta$ -hairpin (there are also similar interactions between NuoM and NuoL; Supplementary Table 4). Predictions of secondary structure indicate that there are  $\beta$ -strands of similar length between TMs 2 and 3 in most other species, so the  $\beta$ -hairpin and second connecting element are likely to be common features.

### Proton translocation pathways in subunits NuoL, M and N

The central positions of Lys TM7 and Lys TM12 in both channels, close to the breaks in TM7 and TM12, and the severe effects of their mutations (Supplementary Table 6), indicate that in complex I, unusually, lysine rather than carboxylate residues have a central role in the proton pump (one exception is M(Glu 407)). Examination of potential pathways (Supplementary Discussion, section 1) shows that none of the channels is solvent-accessible on both sides of the membrane.

In the first channel, the cavity surrounding Lys TM7 is about  $70 \text{ \AA}^3$  and is lined by 2–5 polar residues (Fig. 4a–c and Supplementary Table 5). It is closed from the periplasm by large hydrophobic residues but is open to the cytoplasm via a network of polar residues. Cavities between

subunits L and M, and M and N, are blocked from the periplasm but may be accessible from the cytoplasm, possibly allowing an additional (but less likely; Supplementary Discussion, section 1) protonation route for Lys TM7, by ‘side-entry’ near Glu TM5.

The cavity in the second channel, near Lys/Glu TM12, is markedly larger and more hydrophilic than that in the first one (up to  $200 \text{ \AA}^3$ ,  $\sim 10$  polar residues; Fig. 4a–c and Supplementary Table 5). Access to the cytoplasm is closed but the periplasm is accessible via short polar networks.

Many conserved charged and polar residues in the middle of the membrane connect the two channels in each subunit (Fig. 4, Supplementary Fig. 8 and Supplementary Table 5). Notably, in NuoM and NuoN, central positions in this connection are occupied by invariant essential residues<sup>28,30,31</sup> N(Lys 247) and M(Lys 265), found near the TM8  $\pi$ -bulge. NuoL also contains an invariant residue, His 254, near this position.

Thus, in all antiporter-like subunits, unusually, two half-closed symmetry-related channels are linked, forming a single continuous proton translocation pathway through each subunit. Consistently, all the observed water molecules are either in the channels or in the connection (Fig. 4). Other pathways seem to be unlikely (Supplementary Discussion, section 2).

### The fourth proton translocation pathway

An additional channel is apparent at the interface of subunits NuoN, K, J and A. A cavity of  $\sim 130 \text{ \AA}^3$  between NuoN and NuoK can accommodate water molecules coordinated by K(Glu 72), N(Thr 160) and N(Ser 156)



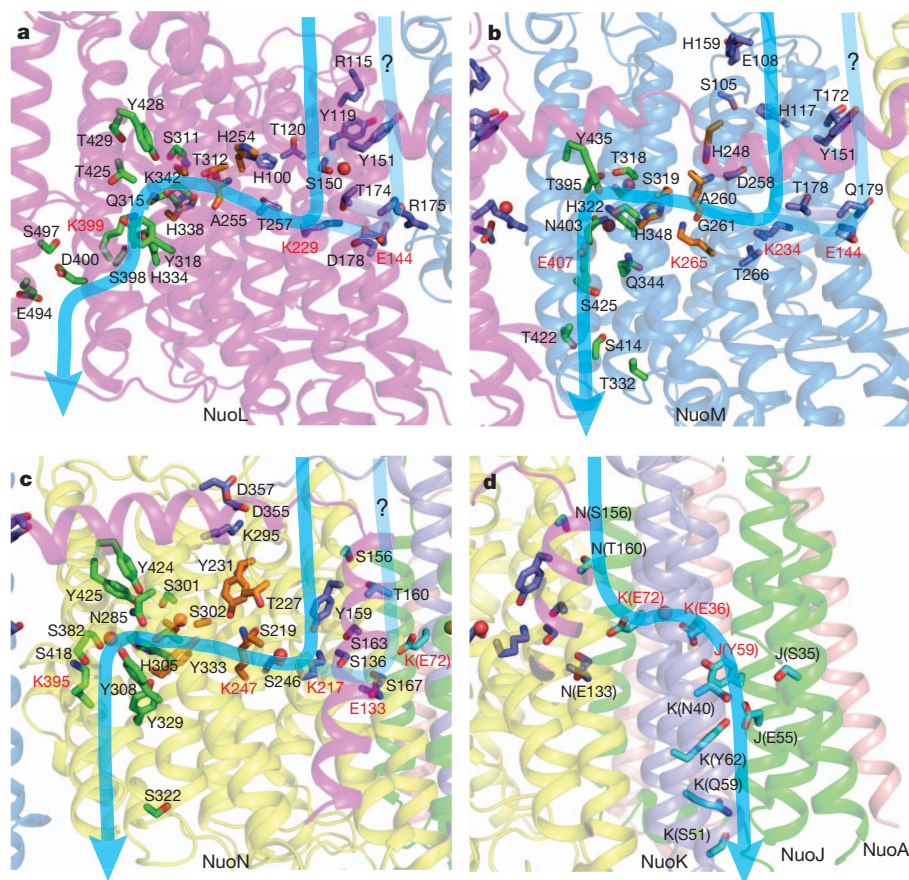


**Figure 4 | Proton translocation channels.** **a–c**, Putative channels in the antiporter-like subunits. Polar residues lining the channels are shown as sticks, with carbon in dark blue for the first channel, in green for the second channel and in orange for connecting residues. **d**, Channel at the interface of subunits NuoN, K and J, with polar residues in cyan. All views are in a similar orientation to Fig. 1a. Approximate proton translocation paths are indicated by blue

arrows. Additional, less likely, input channels at the interfaces of subunits are paler in colour and labelled '?'. Essential charged residues are labelled in red. Water molecules resolved in the structure are shown as red spheres. Alanine and glycine from the  $\pi$ -bulge in TM8 may coordinate water molecules via exposed backbone carbonyls.

(Fig. 4d). Space for the cavity is provided by an invariant residue, K(Gly76). Access to the periplasm is blocked by large hydrophobic residues but the cytoplasm is accessible with only a short constriction near K(Leu83). Indeed, the structure shows a water molecule in the middle of the bilayer, between the conserved, essential residues<sup>32,33</sup> K(Glu36) and K(Glu72). From K(Glu36), the continuation of the pathway is apparent at the interface of TMs 2 and 3 from NuoK and NuoJ, reaching the periplasm. Several small cavities here may contain water molecules coordinated by conserved polar residues (Fig. 4d). An alternative 'sideways' pathway from K(Glu36) to the periplasm through invariant A(Glu81) to A(Glu102) can be considered, but is less likely, requiring a more extended network of water molecules.

### Mechanism of proton translocation

There is no evidence in the structure for any potential electron carriers in the membrane domain, for the existence of quinone-binding sites in antiporter-like subunits, or for a different role of NuoN (Supplementary Discussion, section 4), as has been discussed in the literature<sup>34–36</sup>. Structural features combine to indicate strongly that complex I operates purely by a conformation-driven mechanism.

Conformational changes in the hydrophilic domain, which occur upon reduction<sup>13</sup>, can be transmitted to the membrane-domain subunits NuoH, A, J and K (Supplementary Discussion, section 3). Helix HL can relay these changes to TM7 in NuoL, M and N, leading to protonation of Lys TM7 upon closer approach of Glu TM5. Recent studies have confirmed the essential coupling role of this helix<sup>37,38</sup> (Supplementary Discussion, section 4).

The structure indicates that conformational changes in both half-channels of the antiporter-like subunits are coordinated not only by helix HL, but by several connecting elements, acting in concert to achieve tight coupling of proton translocation events. HL can drive TM7 in the first channel, and, on the opposite side of the domain, the  $\beta$ H element can drive TM12 in the second channel. The two channels can interact both within subunits (via TM8, which contains an invariant connecting Lys or His near its flexible kink) and also between subunits, because the intra-helical loop of TM12 is in close contact with Glu TM5 on the neighbouring subunit. Furthermore, Glu TM5 can also interact electrostatically with Lys/Glu TM12 from a neighbouring subunit, because both residues are exposed to the inter-subunit cavities.

We suggest the following translocation cycle via antiporter-like subunits (Fig. 5), assuming that Lys TM7 is protonated and that Lys/Glu TM12 is deprotonated in the oxidized state (meaning the state of iron-sulphur cluster N2 and a nearby cluster<sup>13</sup>, because most clusters are reduced during turnover<sup>39</sup>). Conformational changes upon reduction move Glu TM5 away from Lys TM7, forcing lysine to donate its proton into the link between the two half-channels and eventually to Lys/Glu TM12, which becomes protonated owing to local conformational changes, either with or without help from Glu TM5 from the neighbouring subunit. Upon return to the oxidised-state conformation, Glu TM5 moves back, Lys TM7 is protonated from the cytoplasm, reloading the pump, and Lys/Glu TM12 ejects its proton into the periplasm. Overall, three subunits translocate three protons.

In the fourth putative channel, a notable feature indicating conformational coupling is the  $\pi$ -bulge on TM3 of NuoJ, which contains a

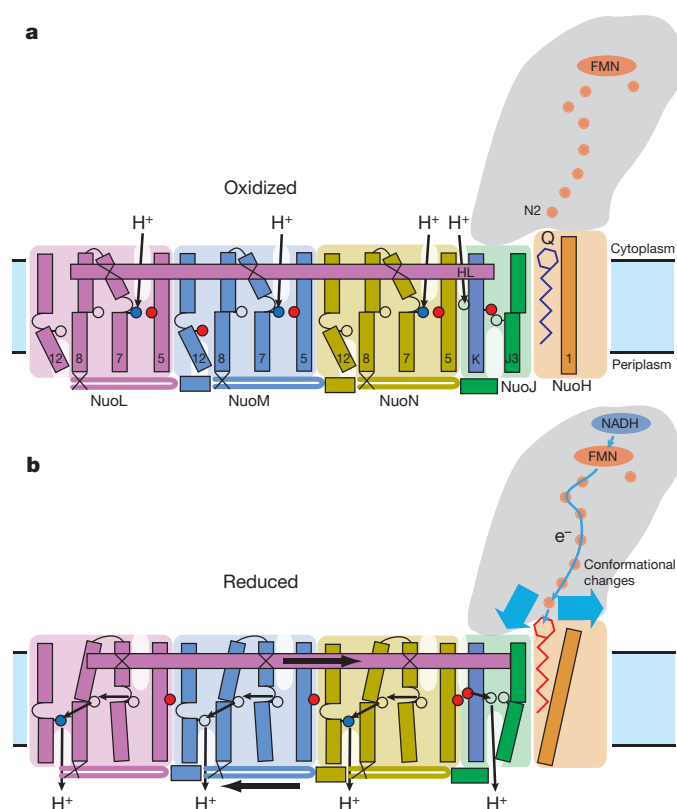


**Figure 5 | Proposed mechanism of complex I.** **a**, Oxidized state. **b**, Reduced state. Conformational coupling between electron transfer and proton translocation is mediated by helix HL (cytoplasmic side) and the  $\beta$ H element (periplasmic side). TM helices are numbered. Crucial charged residues (Glu TM5, Lys TM7, Lys/Glu TM12 and Lys/His TM8 from Nuol, M and N, as well as K(Glu 72) and K(Glu 36), interacting with J(Tyr 59)) are indicated by red or empty circles (Glu) and empty or blue circles (Lys) for unprotonated or protonated residues, respectively. In Nuol, M and N, Lys TM7 from the first half-channel is assumed to be protonated in the oxidized state. Upon reduction, it donates its proton to the connecting Lys/His TM8 and then on to Lys/Glu TM12 from the second half-channel. Lys/Glu TM12 ejects its proton into periplasm upon return from the reduced to the oxidized state. A fourth proton per cycle is translocated at the interface of Nuon, K and J.

residue that is invariant and important for activity<sup>40,41</sup>, J(Tyr 59), forming a hydrogen bond to K(Glu 36), a central residue of this channel. TM3 is the most conserved helix in Nuoj (Supplementary Figs 3a and 8) and is a hotspot for human mitochondrial disease mutations (Supplementary Table 7). Conformational changes, propagating from the nearby hydrophilic domain, can move the flexible TM3 of Nuoj and J(Tyr 59), resulting in the protonation/deprotonation of K(Glu 36) and the translocation of the fourth proton (Fig. 5). Because the four channels that are present in the structure account for the measured  $H^+/e^-$  stoichiometry<sup>42</sup>, any additional direct coupling, as proposed recently<sup>43,44</sup>, is unlikely.

Our knowledge of the structure of the core subunits of complex I is now nearly complete (except for subunit Nuoh). The effects of many mutations, including those causing human diseases, can now be understood (Supplementary Tables 6–8). This molecular machine has one of the most intricate architectures among known protein structures. The redox energy of NADH, binding at the tip of the hydrophilic domain, is eventually used in the membrane domain, at distances of up to  $\sim 300$  Å away. Our previously published analogy of the ‘steam engine of the cell’ is emphasized by the presence of several connecting elements, including helix HL, which are powered by the redox energy of electron transfer and which drive six symmetrical structural domains, plus one asymmetrical domain, resulting in a very effective proton pump.

## METHODS SUMMARY

The membrane domain of *E. coli* complex I was purified as previously described<sup>11</sup>, except that the detergent cymal-7 was used. Protein was crystallized in the presence of lipids using polyethylene glycol (PEG) 4000 and sodium tartrate as the precipitant at pH 4.8, with the additives 0.15% sodium cholate and 0.1 M NDSB-256 (non detergent sulfobetaine-256). Diffraction was improved by a slow increase of PEG 4000 concentration to 30%, by dialysis at 4 °C.

Diffraction data were collected from cryo-cooled crystals (100 K) on beamline ID29 at the European Synchrotron Radiation Facility (ESRF) and X06SA at the Swiss Light Source (SLS). Crystallographic phases were obtained using selenomethionine-labelled protein. Electron density was improved by multi-crystal averaging and density modification. The folds of individual subunits and sequence register at the initial steps of model building were determined using the positions of anomalous density peaks from Se atoms, directionality of helices and density connectivity. A combination of manual and automatic model building was used. Data collection and refinement statistics are presented in Supplementary Table 1.

**Full Methods** and any associated references are available in the online version of the paper at [www.nature.com/nature](http://www.nature.com/nature).

Received 2 March; accepted 24 June 2011.

Published online 7 August 2011.

- Walker, J. E. The NADH:ubiquinone oxidoreductase (complex I) of respiratory chains. *Q. Rev. Biophys.* **25**, 253–324 (1992).
- Yagi, T. & Matsuno-Yagi, A. The proton-translocating NADH-quinone oxidoreductase in the respiratory chain: the secret unlocked. *Biochemistry* **42**, 2266–2274 (2003).
- Brandt, U. Energy converting NADH:quinone oxidoreductase (complex I). *Annu. Rev. Biochem.* **75**, 69–92 (2006).
- Ohnishi, T. Iron-sulfur clusters/semiquinones in complex I. *Biochim. Biophys. Acta* **1364**, 186–206 (1998).
- Sazanov, L. A. Respiratory complex I: mechanistic and structural insights provided by the crystal structure of the hydrophilic domain. *Biochemistry* **46**, 2275–2288 (2007).
- Schapiro, A. H. Human complex I defects in neurodegenerative diseases. *Biochim. Biophys. Acta* **1364**, 261–270 (1998).
- Dawson, T. M. & Dawson, V. L. Molecular pathways of neurodegeneration in Parkinson's disease. *Science* **302**, 819–822 (2003).
- Balaban, R. S., Nemoto, S. & Finkel, T. Mitochondria, oxidants, and aging. *Cell* **120**, 483–495 (2005).
- Carroll, J. et al. Bovine complex I is a complex of 45 different subunits. *J. Biol. Chem.* **281**, 32724–32727 (2006).
- Yip, C. Y., Harbour, M. E., Jayawardena, K., Fearnley, I. M. & Sazanov, L. A. Evolution of respiratory complex I: “supernumerary” subunits are present in the alpha-proteobacterial enzyme. *J. Biol. Chem.* **286**, 5023–5033 (2011).
- Efremov, R. G., Baradaran, R. & Sazanov, L. A. The architecture of respiratory complex I. *Nature* **465**, 441–445 (2010).
- Sazanov, L. A. & Hinchliffe, P. Structure of the hydrophilic domain of respiratory complex I from *Thermus thermophilus*. *Science* **311**, 1430–1436 (2006).
- Berrisford, J. M. & Sazanov, L. A. Structural basis for the mechanism of respiratory complex I. *J. Biol. Chem.* **284**, 29773–29783 (2009).
- Fearnley, I. M. & Walker, J. E. Conservation of sequences of subunits of mitochondrial complex I and their relationships with other proteins. *Biochim. Biophys. Acta* **1140**, 105–134 (1992).
- Mathiesen, C. & Hagerhall, C. Transmembrane topology of the Nuol, M and N subunits of NADH:quinone oxidoreductase and their homologues among membrane-bound hydrogenases and bona fide antiporters. *Biochim. Biophys. Acta* **1556**, 121–132 (2002).
- Friedrich, T. Complex I: a chimaera of a redox and conformation-driven proton pump? *J. Bioenerg. Biomembr.* **33**, 169–177 (2001).
- Hunte, C., Zickermann, V. & Brandt, U. Functional modules and structural basis of conformational coupling in mitochondrial complex I. *Science* **329**, 448–451 (2010).
- Baranova, E. A., Holt, P. J. & Sazanov, L. A. Projection structure of the membrane domain of *Escherichia coli* respiratory complex I at 8 Å resolution. *J. Mol. Biol.* **366**, 140–154 (2007).
- von Heijne, G. Membrane protein structure prediction. Hydrophobicity analysis and the positive-inside rule. *J. Mol. Biol.* **225**, 487–494 (1992).
- Yau, W. M., Wimley, W. C., Gawrisch, K. & White, S. H. The preference of tryptophan for membrane interfaces. *Biochemistry* **37**, 14713–14718 (1998).
- Vik, S. B. The transmembrane helices of the L, M, and N subunits of Complex I from *E. coli* can be assigned on the basis of conservation and hydrophobic moment analysis. *FEBS Lett.* **585**, 1180–1184 (2011).
- Vinothkumar, K. R. & Henderson, R. Structures of membrane proteins. *Q. Rev. Biophys.* **43**, 65–158 (2010).
- Screpanti, E. & Hunte, C. Discontinuous membrane helices in transport proteins and their correlation with function. *J. Struct. Biol.* **159**, 261–267 (2007).
- Luecke, H., Schobert, B., Richter, H. T., Cartailler, J. P. & Lanyi, J. K. Structure of bacteriorhodopsin at 1.55 Å resolution. *J. Mol. Biol.* **291**, 899–911 (1999).
- Cooley, R. B., Arp, D. J. & Karplus, P. A. Evolutionary origin of a secondary structure:  $\pi$ -helices as cryptic but widespread insertional variations of  $\alpha$ -helices that enhance protein functionality. *J. Mol. Biol.* **404**, 232–246 (2010).



26. Morino, M. *et al.* Single site mutations in the hetero-oligomeric Mrp antiporter from alkaliphilic *Bacillus pseudofirmus* DF4 that affect  $\text{Na}^+/\text{H}^+$  antiport activity, sodium exclusion, individual Mrp protein levels, or Mrp complex formation. *J. Biol. Chem.* **285**, 30942–30950 (2010).
27. Nakamaru-Ogiso, E. *et al.* the membrane subunit NuoL (ND5) is involved in the indirect proton pumping mechanism of *Escherichia coli* complex I. *J. Biol. Chem.* **285**, 39070–39078 (2010).
28. Amarneh, B. & Vik, S. B. Mutagenesis of subunit N of the *Escherichia coli* complex I. Identification of the initiation codon and the sensitivity of mutants to decylubiquinone. *Biochemistry* **42**, 4800–4808 (2003).
29. Mathiesen, C. & Hagerhall, C. The 'antiporter module' of respiratory chain complex I includes the MrpC/NuoK subunit—a revision of the modular evolution scheme. *FEBS Lett.* **549**, 7–13 (2003).
30. Euro, L., Belevich, G., Verkhovskaya, M. I., Wikstrom, M. & Verkhovskaya, M. Conserved lysine residues of the membrane subunit NuoM are involved in energy conversion by the proton-pumping NADH:ubiquinone oxidoreductase (complex I). *Biochim. Biophys. Acta* **1777**, 1166–1172 (2008).
31. Torres-Bacete, J., Nakamaru-Ogiso, E., Matsuno-Yagi, A. & Yagi, T. Characterization of the NuoM (ND4) subunit in *Escherichia coli* NDH-1: conserved charged residues essential for energy-coupled activities. *J. Biol. Chem.* **282**, 36914–36922 (2007).
32. Kao, M. C., Nakamaru-Ogiso, E., Matsuno-Yagi, A. & Yagi, T. Characterization of the membrane domain subunit NuoK (ND4L) of the NADH-quinone oxidoreductase from *Escherichia coli*. *Biochemistry* **44**, 9545–9554 (2005).
33. Kervinen, M., Patsi, J., Finel, M. & Hassinen, I. E. A pair of membrane-embedded acidic residues in the NuoK subunit of *Escherichia coli* NDH-1, a counterpart of the ND4L subunit of the mitochondrial complex I, are required for high ubiquinone reductase activity. *Biochemistry* **43**, 773–781 (2004).
34. Fisher, N. & Rich, P. R. A motif for quinone binding sites in respiratory and photosynthetic systems. *J. Mol. Biol.* **296**, 1153–1162 (2000).
35. Ohnishi, T., Nakamaru-Ogiso, E. & Ohnishi, S. T. A new hypothesis on the simultaneous direct and indirect proton pump mechanisms in NADH-quinone oxidoreductase (complex I). *FEBS Lett.* **584**, 4131–4137 (2010).
36. Nakamaru-Ogiso, E., Sakamoto, K., Matsuno-Yagi, A., Miyoshi, H. & Yagi, T. The ND5 subunit was labeled by a photoaffinity analogue of fenpyroximate in bovine mitochondrial complex I. *Biochemistry* **42**, 746–754 (2003).
37. Steimle, S. *et al.* The role of subunit NuoL for proton translocation by the respiratory complex I. *Biochemistry* **50**, 3386–3393 (2011).
38. Michel, J., Deleón-Rangel, J., Zhu, S., Van Ree, K. & Vik, S. B. Mutagenesis of the L, M, and N subunits of complex I from *Escherichia coli* indicates a common role in function. *PLoS ONE* **6**, e17420 (2011).
39. Krishnamoorthy, G. & Hinkle, P. C. Studies on the electron transfer pathway, topography of iron-sulfur centers, and site of coupling in NADH-Q oxidoreductase. *J. Biol. Chem.* **263**, 17566–17575 (1988).
40. Kao, M. C. *et al.* Characterization of the membrane domain subunit NuoJ (ND6) of the NADH-quinone oxidoreductase from *Escherichia coli* by chromosomal DNA manipulation. *Biochemistry* **44**, 3562–3571 (2005).
41. Patsi, J., Kervinen, M., Finel, M. & Hassinen, I. E. Leber hereditary optic neuropathy mutations in the ND6 subunit of mitochondrial complex I affect ubiquinone reduction kinetics in a bacterial model of the enzyme. *Biochem. J.* **409**, 129–137 (2008).
42. Galkin, A. S., Grivennikova, V. G. & Vinogradov, A. D.  $\text{H}^+/2\text{e}^-$  stoichiometry in NADH-quinone reductase reactions catalyzed by bovine heart submitochondrial particles. *FEBS Lett.* **451**, 157–161 (1999).
43. Treberg, J. R. & Brand, M. D. A model of the proton translocation mechanism of complex I. *J. Biol. Chem.* **286**, 17579–17584 (2011).
44. Ohnishi, S. T., Salerno, J. C. & Ohnishi, T. Possible roles of two quinone molecules in direct and indirect proton pumps of bovine heart NADH-quinone oxidoreductase (complex I). *Biochim. Biophys. Acta* **1797**, 1891–1893 (2010).

**Supplementary Information** is linked to the online version of the paper at [www.nature.com/nature](http://www.nature.com/nature).

**Acknowledgements** This work was funded by the Medical Research Council. We thank the ESRF and the SLS for provision of synchrotron radiation facilities. We are grateful to the staff of beamlines ID29 (ESRF) and X06SA (SLS) for assistance.

**Author Contributions** R.G.E. performed research and analysed data; L.A.S. designed the project, analysed data and wrote the manuscript, with contributions from R.G.E.

**Author Information** The coordinates and structure factors have been deposited in the RCSB Protein Data Bank under accession code 3RKO. Reprints and permissions information is available at [www.nature.com/reprints](http://www.nature.com/reprints). The authors declare no competing financial interests. Readers are welcome to comment on the online version of this article at [www.nature.com/nature](http://www.nature.com/nature). Correspondence and requests for materials should be addressed to L.A.S. ([sazanov@mrc-mbu.cam.ac.uk](mailto:sazanov@mrc-mbu.cam.ac.uk)).

## METHODS

**Protein purification, crystallization and post-crystallization treatment.** Complex I from *E. coli* was purified from strain BL21(DE3) as previously described<sup>45</sup>. The membrane and hydrophilic domains were separated<sup>11</sup> by treatment with a high concentration of  $Mg^{2+}$ : purified complex I ( $2.5\text{ mg ml}^{-1}$ ) was incubated in 20 mM Bis-Tris (pH 6.0), 5% (v/v) glycerol, 400 mM  $MgCl_2$ , 12.5 mM NaCl, 0.5 mM  $CaCl_2$  and 0.25% (w/v) *n*-dodecyl- $\beta$ -maltoide (Glycon) for 2 h on ice. The protein solution was diluted tenfold with buffer A (20 mM Bis-Tris (pH 6.0), 0.02% cymal-7 (Anatrace)), loaded onto a Mono-S HR 5/5 column and eluted with a 25 ml gradient, from 10% to 70%, of buffer B (1 M NaCl in buffer A). Fractions containing the membrane arm were pooled, concentrated in 100-kDa MWCO concentrators (Ultracel-100K, Amicon), diluted tenfold with 10 mM sodium acetate (pH 4.8), 50 mM NaCl and 0.02% cymal-7, and concentrated to  $10\text{--}11\text{ mg ml}^{-1}$ .

Before crystallization, lipids (1,2-dimyristoleoyl-*sn*-glycerol-3-phosphocholine with *E. coli* polar lipids at a 3:1 ratio (w/w), Avanti Polar Lipids) were added to the protein to  $2\text{ mg ml}^{-1}$  final concentration. Crystals were grown by the sitting drop method, mixing protein at 1:1 (v/v) ratio with 0.1 M sodium acetate (pH 4.8), 0.3 M sodium tartrate (pH 5.0), 9% (w/v) PEG 4000, 0.15% sodium cholate and either 0.1 M NDSB-256 or 0.4% nonyl-glucoside from Detergent Screen HT (Hampton Research). Crystals grew at 22 °C as thin plates of up to 200  $\mu\text{m}$  in length and 20–40  $\mu\text{m}$  in thickness. They were harvested after 3 weeks to 4 months, and initially diffracted to 7 Å resolution. To improve diffraction properties, crystals were slowly cooled to 4 °C, placed into micro-dialysis buttons, and mother liquor was exchanged by dialysis for 0.1 M sodium acetate (pH 4.8), 0.15 M sodium tartrate (pH 5.0), 30% PEG 4000, 0.1% sodium cholate and 12.5% glycerol over a period of 5 days.

For selenomethionine labelling, a feedback inhibition method<sup>46</sup> was applied during cell growth on M9-derived minimal media with 0.6% malate (optimized for maximal yield of complex I) as a carbon source. Purification and crystallization conditions were identical to those for native protein except for the addition of 10 mM tris(2-carboxyethyl)phosphine (TCEP, Thermo Scientific) to crystallization solutions.

Because the crystals were obtained at low pH and it is known that *E. coli* complex I dissociates into hydrophilic and hydrophobic domains after prolonged incubation at pH outside the 5.5–6.5 range<sup>47</sup>, we assayed the purified enzyme for NADH:Q activity at pH 4.8. The activity is lower than at optimal pH<sup>45</sup>, but is still substantial ( $\sim 4\text{ }\mu\text{mol}$  NADH oxidised per min per mg protein). It is still fully inhibited by piericidin A, indicating that enzyme is functional and that there are no drastic effects of pH on the conformation of the entire complex or individual domains.

**Data collection and processing.** Data were collected at 100 K with an ADSC Q210 detector at beamline ID29 at the European Synchrotron Radiation Facility and a Marmosaic 225 detector on the high-resolution diffractometer of beamline X06SA at the Swiss Light Source. Image data were processed with MOSFLM and SCALA from the CCP4 suite<sup>48</sup>.

**Model building and refinement.** Crystals grew in space group *P1* with two molecules in the unit cell and 70% solvent content. As is the case with orthorhombic crystals<sup>11</sup>, triclinic crystals were non-isomorphous and diffracted anisotropically, with the worst diffraction along the *a* axis and comparable resolution along axes *b* and *c*; the *c* axis being systematically slightly better. Using the Diffraction Anisotropy Server (<http://services.mbi.ucla.edu/anisocore/>)<sup>49</sup>, the best native data set was anisotropically scaled and truncated to 3.4 Å, 3.0 Å and 3.0 Å resolution, where the *F*/ $\sigma$  ratio drops to  $\sim 2.6\text{--}2.8$  along the *a*\*, *b*\* and *c*\* axes, respectively (scaling 2, Supplementary Table 1), resulting in better-quality electron density maps. As a control, the final model was also refined against non-truncated raw data at 3.2 Å resolution, with excellent statistics (scaling 1, Supplementary Table 1). Crystal packing resembles that observed previously in space group *P2*<sub>1</sub>*2*<sub>1</sub>*2*<sub>1</sub>, with strong interactions between hydrophilic surfaces and no visible side contacts, explaining the weaker diffraction along the *a* axis (Supplementary Fig. 2). It is possible that side contacts are mediated by poorly ordered lipids.

Several anomalous diffraction data collected from selenomethionine-containing crystals were used for phasing (Supplementary Table 1). Despite challenges presented by anomalous data collection in the *P1* space group, several good quality MAD data sets were obtained using a low-intensity beam and, in some cases, inverse-beam geometry. Initially, the positions of more than 140 Se atoms in the unit cell were determined and refined automatically in PHASER<sup>50</sup>, using molecular replacement (MR) phases from the backbone model of the membrane fragment of *E. coli* complex I (PDB code 3M9C, ref. 11). The correspondence of the Se positions with peaks on the anomalous difference map was verified manually. When such maps were calculated with phases improved by density modification, the positions of 80 Se atoms per molecule were revealed. Experimental MAD phases calculated with these Se atoms in SHARP<sup>51</sup> gave a figure of merit of 0.23 in the resolution range between 20 Å and 3.5 Å, with the anomalous phasing power from peak, inflection and remote data sets being 0.608, 0.368 and 0.195, respectively. Isomorphous phasing power for inflection and remote data sets was 0.158 and 0.198, respectively.

Phases were improved and extended by multi-crystal averaging with histogram matching and solvent flattening in the CCP4-suite program DMmulti. The molecular masks and transformation matrices were obtained from MR solutions. Four data sets were used: two from two *P1* crystals (one native and one with Se MAD phases, Supplementary Table 1), and two phased data sets in the *P2*<sub>1</sub>*2*<sub>1</sub>*2*<sub>1</sub> space group from our previous study (Supplementary Table 1 in ref. 11, crystals Native1 with TaBr1 MAD phases and Native3 with TaBr3 SAD phases). Additionally, a solvent-flipped map was calculated in CNS<sup>52</sup> using MAD data from a single SeMet-containing crystal. The maps were of excellent quality; they had better connectivity in DMmulti maps and, occasionally, better side-chain density in CNS maps, so both maps were used during model building.

Individual subunit folds and sequence register at the initial steps of model building were deduced on the basis of Se atom positions, directionality of helices determined using the 'find\_helices\_strands' procedure in PHENIX<sup>53</sup>, and local density averaging in O (ref. 54), as well as density connectivity. An initial model was built by combining manual building in O and Coot v.0.6.1 (ref. 55) with automatic model building in Buccaneer v.1.5 (ref. 56). The model was rebuilt manually during cycles of refinement. The structure was refined in PHENIX. A subset of 2% of structure factors was omitted from refinement and used for cross-validation (calculation of *R*<sub>free</sub>). Simulated annealing was used in the early stages; secondary structure and non-crystallographic symmetry restraints were used throughout the refinement and TLS (translation, libration and screw-rotation displacements parametrization) was used during the final refinement. For initial refinement, Se MAD experimental or blurred phases from multi-crystal averaging were used, whereas final refinement was only against native data. Several well ordered internal water molecules were modelled on the basis of their well defined electron density, presence of coordinating residues and low B-factor upon refinement. The final model includes 1,952 residues, one cymal-7 molecule, eight water molecules and nine fragments of lipid aliphatic chains. The structure was validated in PROCHECK<sup>57</sup> and MOLPROBITY<sup>58</sup> and was found to be of better-than-average quality for the resolution. As calculated with PROCHECK, 87.0/12.3/0.3/0.0% of residues are in preferable/allowed/generously allowed/disallowed Ramachandran regions, respectively.

**Bioinformatics.** Searches for structural analogs in the PDB were performed using the SSM server ([www.ebi.ac.uk/msd-srv/ssm/cgi-bin/ssmserver](http://www.ebi.ac.uk/msd-srv/ssm/cgi-bin/ssmserver)). In the case of NuoK and NuoA, as expected for small transmembrane proteins, similar folds could be found in the PDB, but without any significant sequence similarity. Structure-based multiple sequence alignments were performed in CLUSTALW v1.83 (ref. 59) with the profile alignment option. Homology models of the 14 conserved TM helices of Mrp subunits A and D from *Bacillus subtilis* and *Bacillus pseudofirmus* were built with MODELLER 9v7 (ref. 60) using structures of the *E. coli* subunits NuoL and NuoM, respectively, as templates. Sequences for modelling were aligned with CLUSTALW, using 30 sequences for NuoL or NuoM in addition to Mrp sequences and the structure-based profile alignment option. Figures were prepared in PyMol.

45. Sazanov, L. A., Carroll, J., Holt, P., Toime, L. & Fearnley, I. M. A role for native lipids in the stabilization and two-dimensional crystallization of the *Escherichia coli* NADH-ubiquinone oxidoreductase (Complex I). *J. Biol. Chem.* **278**, 19483–19491 (2003).
46. Van Duyn, G. D., Standaert, R. F., Karplus, P. A., Schreiber, S. L. & Clardy, J. Atomic structures of the human immunophilin FKBP-12 complexes with FK506 and rapamycin. *J. Mol. Biol.* **229**, 105–124 (1993).
47. Leif, H., Sled, V. D., Ohnishi, T., Weiss, H. & Friedrich, T. Isolation and characterization of the proton-translocating NADH: ubiquinone oxidoreductase from *Escherichia coli*. *Eur. J. Biochem.* **230**, 538–548 (1995).
48. Collaborative Computational Project 4. The CCP4 suite: programs for protein crystallography. *Acta Crystallogr. D* **50**, 760–763 (1994).
49. Strong, M. et al. Toward the structural genomics of complexes: crystal structure of a PE/PPE protein complex from *Mycobacterium tuberculosis*. *Proc. Natl Acad. Sci. USA* **103**, 8060–8065 (2006).
50. McCoy, A. J. et al. Phaser crystallographic software. *J. Appl. Cryst.* **40**, 658–674 (2007).
51. de La Fortelle, E. & Bricogne, G. Maximum-likelihood heavy-atom parameter refinement for multiple isomorphous replacement and multiwavelength anomalous diffraction methods. *Methods Enzymol.* **276**, 472–494 (1997).
52. Brunger, A. T. Version 1.2 of the crystallography and NMR system. *Nature Protocols* **2**, 2728–2733 (2007).
53. Adams, P. D. et al. PHENIX: building new software for automated crystallographic structure determination. *Acta Crystallogr. D* **58**, 1948–1954 (2002).
54. Jones, T. A. & Kjeldgaard, M. Electron-density map interpretation. *Methods Enzymol.* **277**, 173–208 (1997).
55. Emsley, P. & Cowtan, K. Coot: model-building tools for molecular graphics. *Acta Crystallogr. D* **60**, 2126–2132 (2004).
56. Cowtan, K. The Buccaneer software for automated model building. 1. Tracing protein chains. *Acta Crystallogr. D* **62**, 1002–1011 (2006).
57. Laskowski, R. A., MacArthur, M. W., Moss, D. S. & Thornton, J. M. PROCHECK: a program to check the stereochemical quality of protein structures. *J. Appl. Cryst.* **26**, 283–291 (1993).



58. Chen, V. B. *et al.* MolProbity: all-atom structure validation for macromolecular crystallography. *Acta Crystallogr. D* **66**, 12–21 (2010).
59. Thompson, J. D., Higgins, D. G. & Gibson, T. J. CLUSTAL W: improving the sensitivity of progressive multiple sequence alignment through sequence weighting, position-specific gap penalties and weight matrix choice. *Nucleic Acids Res.* **22**, 4673–4680 (1994).
60. Eswar, N. *et al.* Comparative protein structure modeling using Modeller. *Curr. Protoc. Bioinformatics* **Ch. 5**, Unit 5.6 (2006).

# Relativistic jet activity from the tidal disruption of a star by a massive black hole

D. N. Burrows<sup>1</sup>, J. A. Kennea<sup>1</sup>, G. Ghisellini<sup>2</sup>, V. Mangano<sup>3</sup>, B. Zhang<sup>4</sup>, K. L. Page<sup>5</sup>, M. Eracleous<sup>1</sup>, P. Romano<sup>3</sup>, T. Sakamoto<sup>6,7,8</sup>, A. D. Falcone<sup>1</sup>, J. P. Osborne<sup>5</sup>, S. Campana<sup>2</sup>, A. P. Beardmore<sup>5</sup>, A. A. Breeveld<sup>9</sup>, M. M. Chester<sup>1</sup>, R. Corbet<sup>6,7,8</sup>, S. Covino<sup>2</sup>, J. R. Cummings<sup>6,7,8</sup>, P. D'Avanzo<sup>2</sup>, V. D'Elia<sup>10</sup>, P. Esposito<sup>11</sup>, P. A. Evans<sup>5</sup>, D. Fugazza<sup>2</sup>, J. M. Gelbord<sup>1</sup>, K. Hiroi<sup>12</sup>, S. T. Holland<sup>6,7,13</sup>, K. Y. Huang<sup>14</sup>, M. Im<sup>15</sup>, G. Israel<sup>16</sup>, Y. Jeon<sup>15</sup>, Y.-B. Jeon<sup>17</sup>, H. D. Jun<sup>15</sup>, N. Kawai<sup>18,19</sup>, J. H. Kim<sup>15</sup>, H. A. Krimm<sup>6,7,13</sup>, F. E. Marshall<sup>7</sup>, P. Mészáros<sup>1</sup>, H. Negoro<sup>20</sup>, N. Omodei<sup>21,22</sup>, W.-K. Park<sup>15</sup>, J. S. Perkins<sup>6,7,8</sup>, M. Sugizaki<sup>19</sup>, H.-I. Sung<sup>17</sup>, G. Tagliaferri<sup>2</sup>, E. Troja<sup>7</sup>, Y. Ueda<sup>12</sup>, Y. Urata<sup>23</sup>, R. Usui<sup>18</sup>, L. A. Antonelli<sup>10,16</sup>, S. D. Barthelmy<sup>7</sup>, G. Cusumano<sup>3</sup>, P. Giommi<sup>10</sup>, A. Melandri<sup>2</sup>, M. Perri<sup>10</sup>, J. L. Racusin<sup>7</sup>, B. Sbarufatti<sup>3</sup>, M. H. Siegel<sup>1</sup> & N. Gehrels<sup>7</sup>

Supermassive black holes have powerful gravitational fields with strong gradients that can destroy stars that get too close<sup>1,2</sup>, producing a bright flare in ultraviolet and X-ray spectral regions from stellar debris that forms an accretion disk around the black hole<sup>3–7</sup>. The aftermath of this process may have been seen several times over the past two decades in the form of sparsely sampled, slowly fading emission from distant galaxies<sup>8–14</sup>, but the onset of the stellar disruption event has not hitherto been observed. Here we report observations of a bright X-ray flare from the extragalactic transient Swift J164449.3+573451. This source increased in brightness in the X-ray band by a factor of at least 10,000 since 1990 and by a factor of at least 100 since early 2010. We conclude that we have captured the onset of relativistic jet activity from a supermassive black hole. A companion paper<sup>15</sup> comes to similar conclusions on the basis of radio observations. This event is probably due to the tidal disruption of a star falling into a supermassive black hole, but the detailed behaviour differs from current theoretical models of such events.

Swift J164449.3+573451 was discovered when it triggered the Swift<sup>16</sup> Burst Alert Telescope<sup>17</sup> (BAT) on 28 March 2011. Subsequent analysis of BAT data taken before the on-board trigger shows that the outburst was first detected on 25 March 2011 (Supplementary Fig. 1). The Swift X-Ray Telescope<sup>18</sup> (XRT) measured a source position<sup>19,20</sup> of right ascension (J2000) 16 h 44 min 49.92 s, declination (J2000) +57° 35′ 00.6″, with a 90% confidence error circle radius of 1.4 arcsec. Subsequent optical<sup>21</sup> and radio<sup>15</sup> observations showed that a variable radio source was located at the centre of a galaxy within the XRT error circle. Optical spectroscopy<sup>21</sup> measured a redshift of 0.354, corresponding to a luminosity distance  $D$  of  $5.8 \times 10^{27}$  cm (calculated as  $L = 4\pi D^2 F$ , where  $L$  is luminosity and  $F$  is flux).

We performed broad-band follow-up observations using  $\gamma$ -ray, X-ray, ultraviolet, optical and near-IR (NIR) telescopes. The flares seen by the BAT are closely tracked with better sensitivity in the 0.3–10-keV band by the XRT (Fig. 1). The X-ray light curve is complex and highly variable, with peak isotropic luminosities exceeding  $10^{48}$  erg s<sup>−1</sup> (Fig. 2), implying accretion onto a compact object. The integrated isotropic X-ray power (over the 50 days following the first BAT trigger)

is  $\sim 2 \times 10^{53}$  erg (1–10 keV). We have found no statistically significant periodic or quasi-periodic signals in the XRT data. Details of our observations and data analysis are given in Supplementary Information section 1.

Swift J164449.3+573451 has not been previously detected at any wavelength and is not present in any sky catalogues. X-ray flux upper limits from observations by ROSAT, XMM-Newton, MAXI and Swift between 1990 and 24 March 2011 are 2–4 orders of magnitude lower than the peak X-ray fluxes measured by Swift (Fig. 2), and the ROSAT upper limits are an order of magnitude below the lowest flux in the first 50 days after the first BAT trigger.

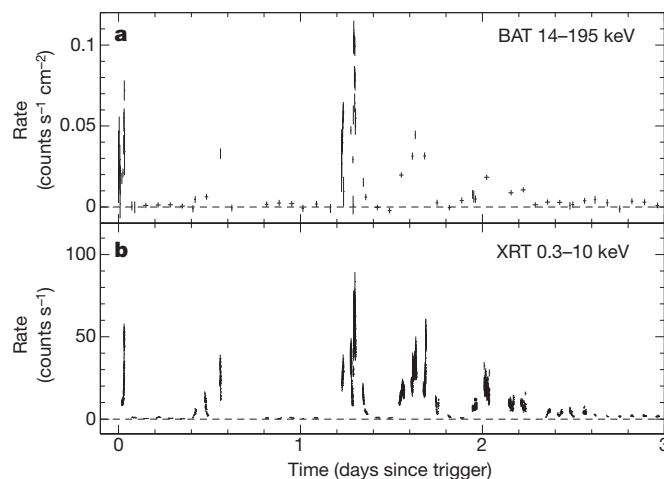


**Figure 1 | Swift BAT and XRT light curves for the first three days of observations.** **a**, BAT light curve (14–195 keV). **b**, XRT light curve (0.3–10 keV). The horizontal axis is time in days since the first BAT on-board trigger on 28 March 2011. The BAT and XRT count rates track each other closely, with episodes of bright flaring (up to 200 mCrab in the BAT) in the first few days after the first BAT trigger. The source brightness then dropped dramatically, with an average BAT count rate of  $0.0020 \pm 0.0005$  counts cm<sup>−2</sup> s<sup>−1</sup> between 2 and 18 April 2011. Data gaps are caused by times when the source was not being observed. Error bars, 1 $\sigma$ .

<sup>1</sup>Department of Astronomy and Astrophysics, The Pennsylvania State University, 525 Davey Laboratory, University Park, Pennsylvania 16802, USA. <sup>2</sup>INAF – Osservatorio Astronomico di Brera, Via Biancamano 46, 23807 Merate, Italy. <sup>3</sup>INAF – Istituto di Astrofisica Spaziale e Fisica Cosmica, Via U. La Malfa 153, I-90146 Palermo, Italy. <sup>4</sup>Department of Physics and Astronomy, University of Nevada, Las Vegas, Nevada 89154, USA. <sup>5</sup>Department of Physics and Astronomy, University of Leicester, University Road, Leicester LE1 7RH, UK. <sup>6</sup>CRESST, Greenbelt, Maryland 20771, USA. <sup>7</sup>NASA Goddard Space Flight Center, Greenbelt, Maryland 20771, USA. <sup>8</sup>University of Maryland, Baltimore County, 1000 Hilltop Circle, Baltimore, Maryland 21250, USA. <sup>9</sup>University College London / Mullard Space Science Laboratory, Holmbury St Mary, Dorking RH5 6NT, UK. <sup>10</sup>ASI Science Data Center, via Galileo Galilei, 00044 Frascati, Italy. <sup>11</sup>INAF – Osservatorio Astronomico di Cagliari, località Poggio dei Pini, strada 54, I-09012 Capoterra, Italy. <sup>12</sup>Department of Astronomy, Kyoto University, Oiwake-cho, Sakyo-ku, Kyoto 606-8502, Japan. <sup>13</sup>Universities Space Research Association, 10211 Wincopin Circle, Suite 500, Columbia, Maryland 21044-3432, USA. <sup>14</sup>Academia Sinica Institute of Astronomy and Astrophysics, Taipei 106, Taiwan. <sup>15</sup>Center for the Exploration of the Origin of the Universe, Department of Physics and Astronomy, FPRD, Seoul National University, Shillim-dong, San 56-1, Kwanak-gu, Seoul, Republic of Korea. <sup>16</sup>INAF – Osservatorio Astronomico di Roma, via Frascati 33, I-00040 Monteporzio Catone, Italy. <sup>17</sup>Korea Astronomy and Space Science Institute (KASI), 776 Daedeokdae-ro, Yuseong-gu, Daejeon 305-348, Republic of Korea. <sup>18</sup>Department of Physics, Tokyo Institute of Technology, 2-12-1 Ookayama, Meguro-ku, Tokyo 152-8551, Japan. <sup>19</sup>MAXI team, RIKEN, 2-1 Hirosawa, Wako, Saitama 351-0198, Japan. <sup>20</sup>Department of Physics, Nihon University, 1-8-14 Kanda-Surugadai, Chiyoda-ku, Tokyo 101-8308, Japan. <sup>21</sup>W. W. Hansen Experimental Physics Laboratory, Kavli Institute for Particle Astrophysics and Cosmology, Department of Physics, Stanford University, Stanford, California 94305, USA. <sup>22</sup>SLAC National Accelerator Laboratory, Stanford University, Stanford, California 94305, USA. <sup>23</sup>Institute of Astronomy, National Central University, Chung-Li 32054, Taiwan.



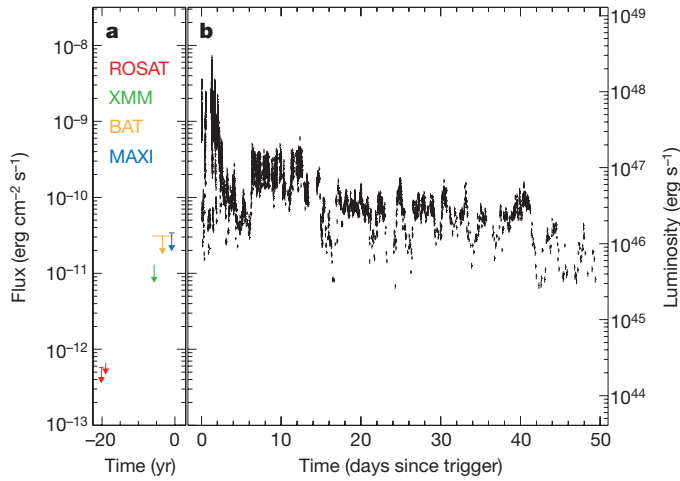


**Figure 2 | Swift XRT light curve of Swift J164449.3+573451 for the first 7 weeks of observations.** **a**, Historical  $3\sigma$  X-ray flux upper limits from the direction of Swift J164449.3+573451, obtained by sky monitors and serendipitous observations over the past 20 years. The time axis for this panel is in years before the BAT on-board trigger on 28 March 2011. The horizontal bars on each upper limit indicate the time interval over which they were calculated, and are placed at the value of the  $3\sigma$  upper limit. All flux limits are calculated for the 1–10 keV band. (The BAT upper limit measured in its native energy band is about three orders of magnitude lower than the peak flux measured by the BAT during the early flares). **b**, XRT light curve in the 1–10 keV band. The X-ray events were summed into time bins containing 200 counts per bin and count rates were calculated for each time bin. Time-dependent spectral fits were used to convert count rates to absorption-corrected fluxes in the 1–10 keV band. The right-hand axis gives the conversion to luminosity of the source, assuming isotropic radiation and using  $H_0 = 71 \text{ km s}^{-1}$ ,  $\Omega_m = 0.27$  and  $\Omega_\Lambda = 0.73$ . Following nearly 3 days of intense flaring with peak fluxes over  $10^{-9} \text{ erg cm}^{-2} \text{ s}^{-1}$  and isotropic luminosities of  $\sim 10^{48} \text{ erg s}^{-1}$ , Swift J164449.3+573451 decayed over several days to a flux of about  $5 \times 10^{-11} \text{ erg cm}^{-2} \text{ s}^{-1}$ , then rose rapidly to  $\sim 2 \times 10^{-10} \text{ erg cm}^{-2} \text{ s}^{-1}$  for about a week. It has been gradually fading since. Details of the upper limits and XRT light curve are given in Supplementary Information section 1. Vertical error bars,  $1\sigma$ . Time bin widths are smaller than the line width of the vertical error bars.

Swift J164449.3+573451 is unlike any previously discovered extragalactic X-ray transient.  $\gamma$ -ray bursts reach similar peak fluxes and luminosities, but fade much more rapidly and smoothly than Swift J164449.3+573451. The broad class of active galactic nuclei cover the range of luminosities that we measured for Swift J164449.3+573451 ( $3 \times 10^{45}$  to  $3 \times 10^{48} \text{ erg s}^{-1}$ ), but no individual active galactic nucleus has been observed to vary by more than about two orders of magnitude. Supernovae have much lower luminosities (X-ray luminosity  $L_X < 3 \times 10^{41} \text{ erg s}^{-1}$ ). Some Galactic transients (such as supergiant fast X-ray transients) vary by similar amounts<sup>22</sup>, but their luminosities are 10 orders of magnitude lower than that of Swift J164449.3+573451. This source appears to be without precedent in its high energy properties.

Our X-ray and NIR observations provide limits on the mass of the accreting black hole. The most rapid observed variability is a  $3\sigma$  doubling in X-ray brightness over a timescale of  $\delta t_{\text{obs}} \approx 100 \text{ s}$ . This constrains the size of the black hole under the assumption that the central engine dominates the variability. For a Schwarzschild black hole with mass  $M_{\text{bh}}$  and radius  $r_s$ , the minimum variability timescale in its rest frame is  $\delta t_{\text{min}} \approx r_s/c \approx 10.0(M_6) \text{ s}$ , where  $M_6 \equiv (M_{\text{bh}}/10^6 M_\odot)$  and  $M_\odot$  is the solar mass. At  $z = 0.354$ , this gives:

$$M_{\text{bh}} \approx 7.4 \times 10^6 \left( \frac{\delta t_{\text{obs}}}{100} \right) M_\odot \quad (1)$$

where  $\delta t_{\text{obs}}$  is in seconds. Much smaller masses are unlikely, as they would lead to shorter timescale variability. However, short timescale

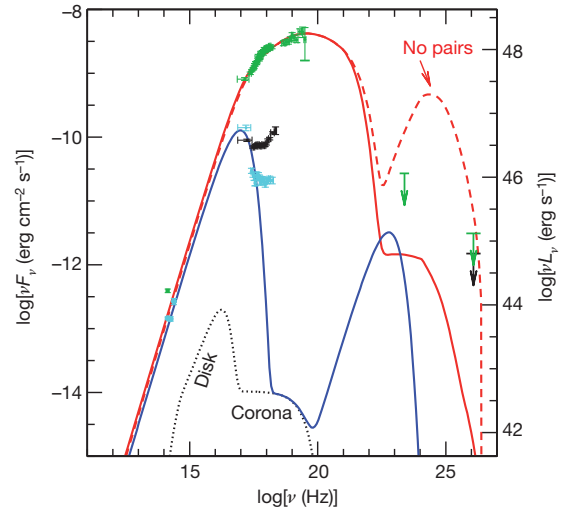


**Figure 3 | The spectral energy distribution of Swift J164449.3+573451.** The green data points (and upper limits) are from the early bright flaring phase; cyan data points are from the low state at 4.5 days; black data points (and upper limit) are from roughly 8 days after the first BAT trigger. Error bars,  $1\sigma$ . The NIR fluxes were dereddened with  $A_V = 4.5$ , and the X-ray data were corrected for absorption by  $N_H = 2 \times 10^{22} \text{ cm}^{-2}$ . Upper limits from the Fermi LAT ( $2 \times 10^{23} \text{ Hz}$ ) and from VERITAS<sup>29</sup> ( $10^{26} \text{ Hz}$ ) are also shown. The solid red curve is a blazar jet model<sup>30</sup> dominated by synchrotron emission, fitted to the spectral energy distribution of the brightest flares. On the low frequency side, the steep slope between the NIR and X-ray bands requires suppression of low-energy electrons, which would otherwise overproduce the NIR flux. This requires a particle-starved, magnetically dominated jet. On the high frequency side, the LAT (95%) and VERITAS (99%) upper limits require that the self-Compton component (red dashed line labelled ‘no pairs’) is suppressed by  $\gamma$ – $\gamma$  pair production, which limits the bulk Lorentz factor in the X-ray emitting region to be  $\Gamma \lesssim 20$ . The model includes a disk/corona component from the accretion disk (black dotted curve), but the flux is dominated at all frequencies by the synchrotron component from the jet. The blue curve shows the corresponding model in the low X-ray flux state. The kink in the X-ray spectrum in the low and intermediate flux states suggests that a possible additional component may be required; it would have to be very narrow, and its origin is unclear. Further details, including model parameters and two alternative models, are presented in Supplementary Information section 2.

variability can also be produced in a jet with substructure, in which case this constraint may underestimate the black hole mass. We obtain an independent constraint on the black hole mass from the relation between the mass of the central black hole,  $M_{\text{bh}}$ , and the luminosity of the galactic bulge,  $L_{\text{bulge}}$ . This gives an upper limit of  $\sim 2 \times 10^7 M_\odot$  (see Supplementary Information section 2.1 for details). We conclude that the dimensionless black hole mass,  $M_6$ , is likely to be between 1 and 20.

For a black hole of this size, the peak isotropic X-ray luminosity exceeds the Eddington luminosity,  $L_{\text{Edd}} = 1.3 \times 10^{44} M_6 \text{ erg s}^{-1}$ , by several orders of magnitude. If the radiation were truly isotropic, radiation pressure would halt accretion and the source would turn off. This contradiction provides strong evidence that the radiation pattern must be highly anisotropic, with a relativistic jet pointed towards us.

In addition to the X-ray observations discussed above, we obtained photometry in the uvw2, uvm2, uvw1, u, b, v, R, J, H and Ks bands with the Swift UVOT, LOAO, BOAO, TNG, UKIRT, CFHT and Maidanak Observatory telescopes (Supplementary Fig. 5). We used our broad-band data set to construct spectral energy distributions at several key time periods in order to constrain models of the emission mechanism (Fig. 3). The spectral energy distributions show that the broad-band energy spectrum is dominated by the X-ray band, which accounts for 50% of the total bolometric energy output in the high/flaring X-ray state. The optical counterpart of the transient X-ray source is not detected in optical or ultraviolet bands, but is detected strongly in

the NIR, indicating substantial extinction by dust in the host galaxy. We measure an extinction of  $A_V \approx 4.5$  (Supplementary Information section 1.2.3), which corresponds to a neutral hydrogen column density of  $N_H \approx 1 \times 10^{22} \text{ cm}^{-2}$  for the Galactic interstellar medium gas-to-dust ratio<sup>23</sup>; this is in rough agreement with the measured intrinsic X-ray absorption (Supplementary Fig. 11).

The spectral energy distribution constrains the possible emission mechanism. We assume that the NIR and X-ray photons originate in the same emission region, an assumption that is consistent with the NIR and X-ray spectral slopes. The optical-to-X-ray slope then requires a magnetically dominated, particle-starved jet. Although not shown here, we interpret the radio emission<sup>15</sup> as an external shock in the gas surrounding Swift J164449.3+573451. Details of our modelling are given in Supplementary Information sections 2.3–2.7.

This luminous, relativistic jet is probably powered by the tidal disruption of a star, which can explain the increase by four orders of magnitude in the X-ray flux from this supermassive black hole, the slow decay in flux following the initial outbursts, and the inferred mass accretion amounting to a substantial fraction of a solar mass (Supplementary Information section 2.2). It is not surprising for such an event to produce an X-ray jet<sup>6,24</sup>. If the accretion is powered by the tidal disruption of a star, we can estimate the jet beaming factor based on the expected statistics of tidal disruption events. The Swift BAT, with a field of view of  $\sim 4\pi/7$  sr and a duty cycle of  $\sim 75\%$ , has detected one such event in  $\sim 6$  years at a peak flux that would have been detectable to redshift  $z \approx 0.8$ . The all-sky rate of Swift J164449.3+573451-like events is therefore  $R_{4\pi} \approx 1 \text{ yr}^{-1}$ , with a 90% confidence interval<sup>25</sup> of  $0.08\text{--}3.9 \text{ yr}^{-1}$ . Taking into account the volume rate of tidal disruption events and the galaxy number density, and assuming that  $\sim 10\%$  of such events produce relativistic jets, we estimate that the fraction of tidal disruption events with jets pointed towards us must be  $\sim 10^{-3}$  (Supplementary Information section 2.9.1; a similar conclusion was obtained by the companion paper<sup>15</sup>). This jet solid angle can be achieved by a bulk Lorentz factor of  $\Gamma \approx 10\text{--}20$  or a jet opening angle of  $\theta_j \approx 5^\circ$ .

Our observations of Swift J164449.3+573451 provide a unique data set for studying the onset of jet activity from a supermassive black hole, and are consistent with a prediction that a low-density, magnetically dominated jet might be formed during the super-Eddington phase of a tidal disruption event<sup>6</sup>. However, little theoretical work has been published discussing observational signatures of the onset of such a jet. Instead, tidal disruption models have concentrated on emission from the stellar surface, the accretion disk and the surrounding medium: an X-ray or  $\gamma$ -ray thermal flare is expected from the surface of the star as it is crushed by the strong gravitational gradient of the black hole<sup>5,7</sup>, with peak luminosity of  $< 10^{44} \text{ erg s}^{-1}$  and a duration of tens of seconds; a phase of super-Eddington accretion of bound debris, accompanied by a wind that interacts with the surrounding medium<sup>6,26</sup>, will radiate in the ultraviolet–NIR<sup>6</sup> or X-ray<sup>26</sup> bands with luminosity  $\lesssim 10^{44} \text{ erg s}^{-1}$ ; and at late times the bolometric luminosity from the accretion disk may undergo a steady decline that traces the mass accretion rate of post-disruption debris<sup>2,27,28</sup>,  $\frac{dM}{dt} \propto (t - t_0)^{-5/3}$ , where  $(t - t_0)$  is the time since the stellar disruption. Detailed multi-band light curve models of emission from the accretion disk in tidal disruption events suggest that the X-ray emission should be characterized by a broad, smooth X-ray light curve peaking at  $L_X \approx 3 \times 10^{44} \text{ erg s}^{-1}$  weeks to months after the stellar disruption for a  $10^6\text{--}10^7 M_\odot$  black hole<sup>26</sup>, in sharp contrast to our observations. The dramatic differences between these model predictions and our observations are probably due to the bright jet in Swift J164449.3+573451, which dominates the much fainter emission from the wind and disk. Long-term monitoring of Swift J164449.3+573451 will help to distinguish between competing models of this event, and will show whether emission from the jet follows the expected  $t^{-5/3}$  decay of the mass accretion rate from fallback of stellar debris.

Received 25 April; accepted 18 July 2011.

1. Rees, M. J. Tidal disruption of stars by black holes of  $10^6\text{--}10^8$  solar masses in nearby galaxies. *Nature* **333**, 523–528 (1988).
2. Evans, C. R. & Kochanek, C. S. The tidal disruption of a star by a massive black hole. *Astrophys. J.* **346**, L13–L16 (1989).
3. Ulmer, A. Flares from the tidal disruption of stars by massive black holes. *Astrophys. J.* **514**, 180–187 (1999).
4. Bogdanović, T., Eracleous, M., Mahadevan, S., Sigurdsson, S. & Laguna, P. Tidal disruption of a star by a black hole: observational signature. *Astrophys. J.* **610**, 707–721 (2004).
5. Guillochon, J., Ramirez-Ruiz, E., Rosswog, S. & Kasen, D. Three-dimensional simulations of tidally disrupted solar-type stars and the observational signatures of shock breakout. *Astrophys. J.* **705**, 844–853 (2009).
6. Strubbe, L. E. & Quataert, E. Optical flares from the tidal disruption of stars by massive black holes. *Mon. Not. R. Astron. Soc.* **400**, 2070–2084 (2009).
7. Brassart, M. & Luminet, J. Relativistic tidal compressions of a star by a massive black hole. *Astron. Astrophys.* **511**, A80 (2010).
8. Brandt, W. N., Pounds, K. A. & Fink, H. The unusual X-ray and optical properties of the ultrasoft active galactic nucleus Zwicky 159.034 (RE J1237+264). *Mon. Not. R. Astron. Soc.* **273**, L47–L52 (1995).
9. Komossa, S. & Bade, N. The giant X-ray outbursts in NGC 5905 and IC 3599: Follow-up observations and outburst scenarios. *Astron. Astrophys.* **343**, 775–787 (1999).
10. Donley, J. L., Brandt, W. N., Eracleous, M. & Boller, T. Large-amplitude X-ray outbursts from galactic nuclei: a systematic survey using ROSAT archival data. *Astron. J.* **124**, 1308–1321 (2002).
11. Esquej, P. et al. Candidate tidal disruption events from the XMM-Newton slew survey. *Astron. Astrophys.* **462**, L49–L52 (2007).
12. Gezari, S. et al. UV/optical detections of candidate tidal disruption events by GALEX and CFHTLS. *Astrophys. J.* **676**, 944–969 (2008).
13. Gezari, S. et al. Luminous thermal flares from quiescent supermassive black holes. *Astrophys. J.* **698**, 1367–1379 (2009).
14. Maksym, W. P., Ulmer, M. P. & Eracleous, M. A tidal disruption flare in A1689 from an archival X-ray survey of galaxy clusters. *Astrophys. J.* **722**, 1035–1050 (2010).
15. Zauderer, B. A. et al. The birth of a relativistic outflow in the unusual  $\gamma$ -ray transient Swift J164449.3+573451. *Nature* doi:10.1038/nature10366 (this issue).
16. Gehrels, N. et al. The Swift gamma-ray burst mission. *Astrophys. J.* **611**, 1005–1020 (2004).
17. Barthelmy, S. D. et al. The Burst Alert Telescope (BAT) on the SWIFT Midex mission. *Space Sci. Rev.* **120**, 143–164 (2005).
18. Burrows, D. N. et al. The Swift X-Ray Telescope. *Space Sci. Rev.* **120**, 165–195 (2005).
19. Goad, M. R. et al. Accurate early positions for Swift GRBs: enhancing X-ray positions with UVOT astrometry. *Astron. Astrophys.* **476**, 1401–1409 (2007).
20. Evans, P. A. et al. Methods and results of an automatic analysis of a complete sample of Swift-XRT observations of GRBs. *Mon. Not. R. Astron. Soc.* **397**, 1177–1201 (2009).
21. Levan, A. J. et al. An extremely luminous panchromatic outburst from the nucleus of a distant galaxy. *Science* **333**, 199–202 (2011).
22. Romano, P. et al. Two years of monitoring supergiant fast X-ray transients with Swift. *Mon. Not. R. Astron. Soc.* **410**, 1825–1836 (2011).
23. Bohlin, R. C., Savage, B. D. & Drake, J. F. A survey of interstellar H I from  $L\alpha$  absorption measurements. II. *Astrophys. J.* **224**, 132–142 (1978).
24. Grindlay, J. E. in *X-ray Timing 2003: Rossi and Beyond* (eds Kaaret, P., Lamb, F. K. & Swank, J. H.) 413–422 (Am. Inst. Phys. Conf. Ser., Vol. 714, 2004).
25. Kraft, R. P., Burrows, D. N. & Nousek, J. A. Determination of confidence limits for experiments with low numbers of counts. *Astrophys. J.* **374**, 344–355 (1991).
26. Lodato, G. & Rossi, E. M. Multiband light curves of tidal disruption events. *Mon. Not. R. Astron. Soc.* **410**, 359–367 (2011).
27. Phinney, E. S. in *The Center of the Galaxy* (ed. Morris, M.) 543–553 (IAU Symp., Vol. 136, 1989).
28. Lodato, G., King, A. R. & Pringle, J. E. Stellar disruption by a supermassive black hole: is the light curve really proportional to  $t^{-5/3}$ ? *Mon. Not. R. Astron. Soc.* **392**, 332–340 (2009).
29. Aliu, E. et al. VERITAS observations of the unusual extragalactic transient Swift J164449.3+573451. *Astrophys. J.* (in the press); preprint at <http://arXiv.org/abs/1107.1738>.
30. Ghisellini, G. & Tavecchio, F. Canonical high-power blazars. *Mon. Not. R. Astron. Soc.* **397**, 985–1002 (2009).

**Supplementary Information** is linked to the online version of the paper at [www.nature.com/nature](http://www.nature.com/nature).

**Acknowledgements** We acknowledge support from the following funding agencies: NASA, NSF and DOE (US); the UK Space Agency; ASI, INAF and INFN (Italy); the Autonomous Region of Sardinia; MEXT, KEK and JAXA (Japan); CRI/NRF/MEST (Korea); NSC and Academia Sinica (Taiwan); CEA/Irfu, IN2P3/CNRS and CNES (France); and the K. A. Wallenberg Foundation, the Swedish Research Council and the National Space Board (Sweden). We thank the Swift, Fermi and MAXI operation teams; and we thank A. Read for help with the most recent XMM slew data. We acknowledge the contribution of pre-publication upper limits by the VERITAS Collaboration. Finally, we acknowledge the use of public data from the Swift and Fermi data archives (<http://heasarc.nasa.gov/docs/swift/archive/> and <http://fermi.gsfc.nasa.gov/ssc/>, respectively), as well as data supplied by the UK Swift Science Data Centre at the University of Leicester. E.T. is a NASA Postdoctoral Fellow.



**Author Contributions** D.N.B., J.A.K. and M.E. composed the text, using inputs from the other co-authors. Theoretical interpretation was provided by G.G., B.Z., M.E. and P.M., with contributions by A.D.F., S. Campana and N.G.; J.A.K., V.M., K.L.P., J.P.O., P.R., S. Campana, A.P.B., V.D'E., P.E., P.A.E. and G.I. processed and analysed the Swift XRT data. T.S., J.R.C. and H.A.K. processed and analysed the Swift BAT data. Swift UVOT data were processed and analysed by A.A.B., M.M.C., S.T.H. and F.E.M. Ground-based optical/NIR data were obtained with the TNG, BOAO, LOAO, CFHT, UKIRT and Maidanak Observatory telescopes, and were provided, reduced and analysed by S. Covino, P.D'A., D.F., K.Y.H., M.I., H.D.J., Y.J., Y.-B.J., J.H.K., W.-K.P., H.-I.S., G.T., Y. Urata and L.A.A. Fermi LAT data analysis was performed by R.C., N.O., J.S.P. and E.T.; K.H., N.K., H.N., M.S., Y. Ueda and R.U. processed and analysed the MAXI data. A.D.F. provided liaison with the

VERITAS Collaboration. J.M.G. and P.G. provided analysis of ROSAT archival data, and J.P.O. provided analysis of archival XMM data. All authors discussed the results and commented on the manuscript.

**Author Information** Swift data are available from the NASA HEASARC (<http://swift.gsfc.nasa.gov/docs/swift/archive/>) or from mirror sites in the UK ([http://www.swift.ac.uk/swift\\_portal/archive.php](http://www.swift.ac.uk/swift_portal/archive.php)) and Italy (<http://swift.asdc.asi.it/>). Reprints and permissions information is available at [www.nature.com/reprints](http://www.nature.com/reprints). The authors declare no competing financial interests. Readers are welcome to comment on the online version of this article at [www.nature.com/nature](http://www.nature.com/nature). Correspondence and requests for materials should be addressed to D.N.B. ([burrows@astro.psu.edu](mailto:burrows@astro.psu.edu)).

# Birth of a relativistic outflow in the unusual $\gamma$ -ray transient Swift J164449.3+573451

B. A. Zauderer<sup>1</sup>, E. Berger<sup>1</sup>, A. M. Soderberg<sup>1</sup>, A. Loeb<sup>1</sup>, R. Narayan<sup>1</sup>, D. A. Frail<sup>2</sup>, G. R. Pettipas<sup>1</sup>, A. Brunthaler<sup>3</sup>, R. Chornock<sup>1</sup>, J. M. Carpenter<sup>4</sup>, G. G. Pooley<sup>5</sup>, K. Mooley<sup>4</sup>, S. R. Kulkarni<sup>4</sup>, R. Margutti<sup>6</sup>, D. B. Fox<sup>7</sup>, E. Nakar<sup>8</sup>, N. A. Patel<sup>1</sup>, N. H. Volgenau<sup>9</sup>, T. L. Culverhouse<sup>9</sup>, M. F. Bietenholz<sup>10,11</sup>, M. P. Rupen<sup>2</sup>, W. Max-Moerbeck<sup>4</sup>, A. C. S. Readhead<sup>4</sup>, J. Richards<sup>4</sup>, M. Shepherd<sup>4</sup>, S. Storm<sup>12</sup> & C. L. H. Hull<sup>13</sup>

Active galactic nuclei, which are powered by long-term accretion onto central supermassive black holes, produce<sup>1</sup> relativistic jets with lifetimes of at least one million years, and the observation of the birth of such a jet is therefore unlikely. Transient accretion onto a supermassive black hole, for example through the tidal disruption<sup>2,3</sup> of a stray star, thus offers a rare opportunity to study the birth of a relativistic jet. On 25 March 2011, an unusual transient source (Swift J164449.3+573451) was found<sup>4</sup>, potentially representing<sup>5,6</sup> such an accretion event. Here we report observations spanning centimetre to millimetre wavelengths and covering the first month of evolution of a luminous radio transient associated with Swift J164449.3+573451. The radio transient coincides<sup>7</sup> with the nucleus of an inactive galaxy. We conclude that we are seeing a newly formed relativistic outflow, launched by transient accretion onto a million-solar-mass black hole. A relativistic

outflow is not predicted in this situation, but we show that the tidal disruption of a star naturally explains the observed high-energy properties and radio luminosity and the inferred rate of such events. The weaker beaming in the radio-frequency spectrum relative to  $\gamma$ -rays or X-rays suggests that radio searches may uncover similar events out to redshifts of  $z \approx 6$ .

On the discovery<sup>4</sup> of Swift J164449.3+573451 by NASA's Swift satellite, and the identification of a galaxy at a redshift<sup>6</sup> of  $z = 0.354$  within Swift's X-ray localization region (radius,  $1.4''$ ), we initiated radio observations of the transient on 2011 March 29.36 UT with the Expanded Very Large Array (EVLA) at a frequency of 5.8 GHz and discovered an unresolved source with a flux density of  $310 \pm 7 \mu\text{Jy}$ . Astrometric matching demonstrated that the radio source coincides with the galaxy nucleus (Fig. 1), as was subsequently confirmed<sup>6</sup> with other data. A follow-up EVLA observation 0.9 d later revealed that the

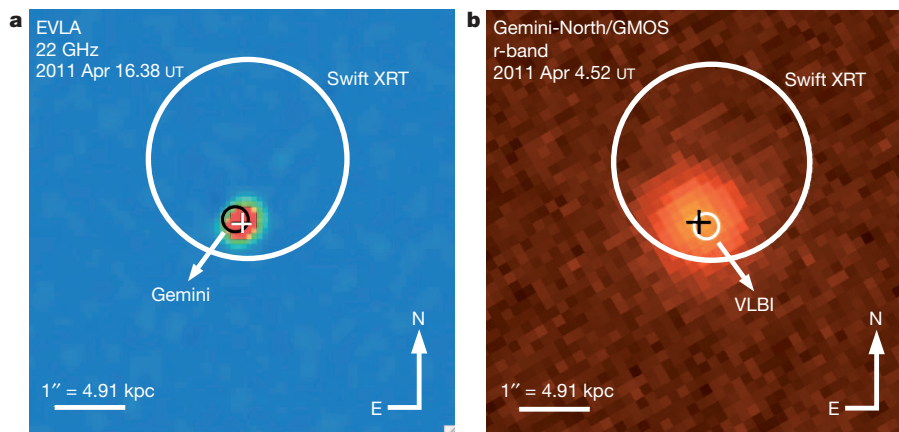


**Figure 1 | Radio and optical images of Swift J164449.3+573451 and its host galaxy reveal a positional alignment between the transient and the centre of the galaxy.** **a**, Radio image from the EVLA at a frequency of 22 GHz. The most precise radio position, from very-long-baseline interferometry (VLBI) is  $\alpha_{J2000} = 16\text{ h } 44\text{ min } 49.93130\text{ s}$ ,  $\delta_{J2000} = +57^\circ 34' 59.6893''$  ( $\pm 0.1\text{ mas}$ ; Supplementary Information). **b**, Optical r-band image obtained on 2011 April 4.52 UT with the Gemini-North 8-m telescope and astrometrically aligned to the Two-Micron All-Sky Survey (2MASS) catalogue using 14 common objects, with a resulting root mean squared uncertainty of 0.13 arcsec in each coordinate (68% confidence level). The galaxy's optical centroid is located at  $\alpha_{J2000} = 16\text{ h } 44\text{ min } 49.942\text{ s}$ ,  $\delta_{J2000} = +57^\circ 34' 59.74''$  ( $\pm 0.01\text{ arcsec}$ ). The Swift X-ray Telescope (XRT) error circle (large white circle), with a radius of 1.4 arcsec (90% confidence level), contains the galaxy, but cannot be used to

locate the X-ray transient position. However, the radio position relative to the astrometric solution of the Gemini image has an uncertainty of only 0.18 arcsec (68% confidence level; this uncertainty is dominated by the astrometric match of the optical image to the 2MASS catalogue, not by the radio position itself) and leads to an offset of  $0.11 \pm 0.18\text{ arcsec}$ , corresponding to a physical scale of  $0.5 \pm 0.9\text{ kpc}$  at  $z = 0.354$ . The radio transient position is therefore consistent with an origin in the nucleus of the host galaxy. In **a**, the radio centroid is marked by cross hairs, and the galaxy optical centroid (with an uncertainty of 0.18 arcsec due to 2MASS astrometric solution) is marked by the small black circle. In **b**, The galaxy optical centroid is marked by cross hairs, and the radio position (with an uncertainty of 0.18 arcsec due to 2MASS astrometric solution) is marked by the small white circle.

<sup>1</sup>Harvard-Smithsonian Center for Astrophysics, 60 Garden Street, Cambridge, Massachusetts 02138, USA. <sup>2</sup>National Radio Astronomy Observatory, PO Box 0, Socorro, New Mexico 87801, USA. <sup>3</sup>Max-Planck-Institut für Radioastronomie, Auf dem Hügel 69, 53121 Bonn, Germany. <sup>4</sup>Department of Astronomy, California Institute of Technology, Pasadena, California 91125, USA. <sup>5</sup>Mullard Radio Observatory, Cavendish Laboratory, Cambridge CB3 0HE, UK. <sup>6</sup>INAF Osservatorio Astronomico di Brera, via Bianchi 46, Merate 23807, Italy. <sup>7</sup>Department of Astronomy, Pennsylvania State University, University Park, Pennsylvania 16802, USA. <sup>8</sup>School of Physics & Astronomy, Tel Aviv University, Tel Aviv 69978, Israel. <sup>9</sup>California Institute of Technology, Owens Valley Radio Observatory, Big Pine, California 93513, USA. <sup>10</sup>Hartebeesthoek Radio Astronomy Observatory, PO Box 443, Krugersdorp 1740, South Africa. <sup>11</sup>Department of Physics and Astronomy, York University, Toronto, Ontario M3J 1P3, Canada. <sup>12</sup>Department of Astronomy, University of Maryland, College Park, Maryland 20742, USA. <sup>13</sup>Department of Astronomy, University of California, Berkeley, California 94720, USA.



source brightened to  $530 \pm 10 \mu\text{Jy}$ , thereby conclusively linking the X-ray/ $\gamma$ -ray transient and the galaxy. The galaxy shows no evidence<sup>6</sup> for an active nucleus (AGN; Supplementary Fig. 1), and the lack of previous X-ray/ $\gamma$ -ray activity argues<sup>4</sup> against the transient originating in an active galactic nucleus flare.

We carried out additional observations at multiple frequencies spanning 1–345 GHz using several centimetre-wave and millimetre-wave facilities (Supplementary Table 1). The spectral energy distribution (SED) in this frequency range on 2011 March 30 UT (time since initial transient event,  $\Delta t \approx 5$  d) is well described by a power law with  $F_\nu \propto \nu^{1.3 \pm 0.1}$  up to  $F_\nu(345 \text{ GHz}) = 35 \pm 1 \text{ mJy}$ . The steep power law requires self-absorbed synchrotron emission. The weak near-infrared variability<sup>6</sup> indicates that  $F_\nu(2.5 \mu\text{m}) \approx 0.1 \text{ mJy}$ , and the lack of optical variability leads<sup>6</sup> to an upper bound of  $F_\nu(0.64 \mu\text{m}) \leq 2 \mu\text{Jy}$ . The SED therefore peaks in the millimetre band, with a best-fit rest-frame peak frequency and flux density of  $\nu_p \approx 6 \times 10^{11} \text{ Hz}$  and  $F_{\nu,p} \approx 80 \text{ mJy}$ , respectively (Fig. 2). The non-detection of optical variability requires significant rest-frame extinction, of  $A_V \geq 3 \text{ mag}$ , further supporting a nuclear origin. Subsequent SEDs at  $\Delta t \approx 10, 15$  and  $22 \text{ d}$  show significant evolution, with  $\nu_p \propto t^{-1.3}$  and  $F_{\nu,p} \propto t^{-0.8}$  (Fig. 2).

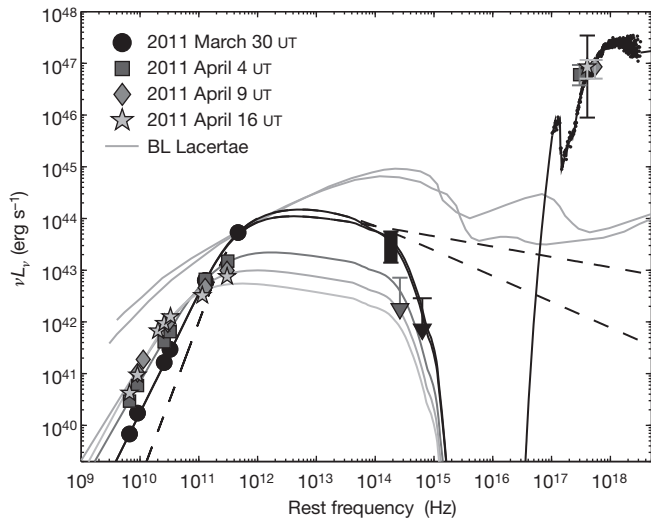


**Figure 2 | SEDs (luminosity,  $\nu L_\nu$ ; frequency,  $\nu$ ) of Swift J164449.3+573451 from radio to X-rays point to synchrotron emission from a relativistic outflow.** Our radio observations cover decimetre to millimetre wavelengths at 5, 10, 15 and 22 d after the initial  $\gamma$ -ray detection (errors of 1 s.d. are smaller than the symbol sizes). The near-infrared (NIR) luminosity on March 30 can only be constrained within a factor of five owing to the unknown contribution from the host galaxy; on April 4, the NIR upper limit is inferred from a Hubble Space Telescope image<sup>6</sup>. Only an upper bound is available on the optical luminosity (black triangle), owing to the lack<sup>6</sup> of variable emission. The flux in the soft-X-ray band is highly variable on March 30, but is more quiescent at 10, 15 and 22 d (extrema marked by vertical bars and mean brightness marked by solid symbols, with points at 10 and 15 d shifted slightly in frequency for clarity). The radio, NIR and optical data are well modelled by an evolving synchrotron spectrum (solid lines) with a large rest-frame optical extinction of  $A_V \geq 3 \text{ mag}$ . The synchrotron curves for the March 30 SED are for two values of the synchrotron cooling frequency:  $\nu_c \approx 2 \times 10^{13} \text{ Hz}$  (steeper optically thin slope) and  $\nu_c \approx 2 \times 10^{18} \text{ Hz}$  (shallower optically thin slope). This model cannot explain the large X-ray luminosity, which remains nearly constant while the radio spectrum is evolving strongly. A representative model for the X-ray spectrum (data, black dots; model, black line) includes power-law ( $F_\nu \propto \nu^{0.9}$ ) and black-body ( $k_B T \approx 1 \text{ keV}$ , where  $k_B$  is Boltzmann's constant and  $T$  is the temperature) components with significant absorption (hydrogen column density,  $N_H \approx 2 \times 10^{22} \text{ cm}^{-2}$ ), in agreement with the large optical extinction. Shown for comparison is the SED of the canonical blazar BL Lacertae in two separate states (varying in peak frequency and flux of the synchrotron component), normalized to the luminosity of Swift J164449.3+573451 at 345 GHz. The blazar SED provides a poor match.

For synchrotron sources, there is a well-defined minimum energy, achieved<sup>8</sup> near equipartition between the fractional energies in the relativistic electrons ( $\epsilon_e$ ) and the magnetic fields ( $\epsilon_B$ ). This condition defines<sup>9</sup> the equipartition angular radius,  $\theta_{\text{eq}} = 110 d_{\text{L,Mpc}}^{-1/19} F_{\nu,p,\text{mJy}}^{9/19} \nu_{p,\text{GHz}}^{-1} \mu\text{as}$ , where  $d_{\text{L,Mpc}}$  is the luminosity distance in megaparsecs,  $F_{\nu,p,\text{mJy}}$  is the peak flux in millijanskys and  $\nu_{p,\text{GHz}}$  is the frequency of peak flux expressed in gigahertz. From the March 30 UT SED, we find that  $\theta_{\text{eq}} \approx 1 \mu\text{as}$  (equipartition linear radius,  $r_{\text{eq}} \approx 1.5 \times 10^{16} \text{ cm}$ ), corresponding to mildly relativistic expansion with a Lorentz factor of  $\Gamma \approx 2$ . A more detailed model that accounts<sup>10</sup> for relativistic effects leads to similar results:  $r_{\text{eq}} \approx 1 \times 10^{16} \text{ cm}$  and  $\Gamma \approx 1.2$  (Supplementary Information). From the observed SED temporal evolution, we find that the source continues to expand relativistically with nearly constant velocity (Supplementary Information). By extrapolating the linear trend in radius, we find a formation epoch in the range 2011 March 23–26 UT, in excellent agreement with the initial  $\gamma$ -ray detection on 2011 March 25 UT (Supplementary Fig. 2). This provides independent evidence for a newly formed relativistic outflow.

An angular size of a few microarcseconds will inevitably lead to variability in the low-frequency radio emission due to interstellar scintillation, with the amplitude of modulation depending<sup>11</sup> on the ratio of the source size ( $\theta_s$ ) to the Fresnel scale ( $\theta_F$ ). For the line of sight to Swift J164449.3+573451, the maximum modulation ( $m_p \approx 1$ ) is expected<sup>12</sup> at  $\nu_0 \approx 10 \text{ GHz}$ , for  $\theta_s \approx \theta_F \approx 1 \mu\text{as}$ . The observed modulation inferred from our detailed radio light curves is tens of percent at 5–7 GHz and a few percent at 15 GHz (Fig. 3), leading to a projected radius of  $\theta_s \approx 5 \mu\text{as}$ , or  $\Gamma \approx 5$ . This provides independent evidence for a relativistic outflow. Our radio observations with VLBI at a frequency of 22 GHz place an upper bound of  $r \leq 0.8 \text{ pc}$  on the size of the radius from the accretion site, consistent with the synchrotron and scintillation analyses and providing an upper bound on the lifetime of the event of  $\leq 1.7 \text{ yr}$  for an expansion with  $\Gamma \approx 2$  (Supplementary Information).

The mean X-ray luminosity during the four radio epochs exceeds the synchrotron peak by a factor of  $\sim 10^3$  and therefore requires a distinct origin (Fig. 2). One potential mechanism to generate the large X-ray luminosity is inverse Compton scattering of radio synchrotron photons by the relativistic electrons (synchrotron self-Compton (SSC)), but from the relativistic model we find a predicted SSC X-ray luminosity of only  $\sim 2 \times 10^{45} \text{ erg s}^{-1}$  (Supplementary Information). Similarly, although order-of-magnitude variations in brightness are seen in the X-rays, our detailed radio light curves do not reveal the coincident variations that would be expected for SSC (Fig. 3). We therefore conclude that the X-ray emission is dominated by a distinct, more compact emission region, most likely at the base of the outflow.

Having established the birth of a relativistic outflow, coincident with the nucleus of the host galaxy, we now briefly describe a model to power the outflow through transient accretion<sup>5</sup> onto a supermassive black hole (SMBH). The host galaxy luminosity,  $M_B \approx -18.2 \text{ mag}$ , implies<sup>13</sup> a modest SMBH mass of  $\sim 10^6$  solar masses ( $M_\odot$ ). The duration of the bright early phase in the X-ray light curve,  $\sim 10^5 \text{ s}$ , coincides with the debris fallback time for a solar-mass star tidally disrupted at a pericentre distance of  $R_p \approx 13 (M_{\text{SMBH}}/10^6 M_\odot)^{-5/6}$  Schwarzschild radii. The most-highly bound stellar debris is expected to feed the black hole at an initial rate<sup>14</sup> of  $\sim 0.5 M_\odot/10^5$ . With a radiative efficiency of  $\geq 1\%$  at  $\sim R_p$ , this can account for the observed X-ray luminosity. However, this luminosity is  $\sim 10^3$  times the Eddington limit for a  $\sim 10^6 M_\odot$  black hole, leading inevitably to a highly collimated outflow, the origin of the radio-emitting relativistic outflow found here.

We conclude with several key implications of our results. First, our initial estimate of the energy,  $E_K \approx 3 \times 10^{50} \text{ erg}$  at  $\Delta t \approx 22 \text{ d}$  (Supplementary Table 2), corresponds to the Eddington luminosity of a  $10^6 M_\odot$  black hole, lending support to the tidal disruption scenario and suggesting that the X-ray/ $\gamma$ -ray emission is collimated by a factor of  $\sim 10^3$ . Long-term radio monitoring will test this result by providing

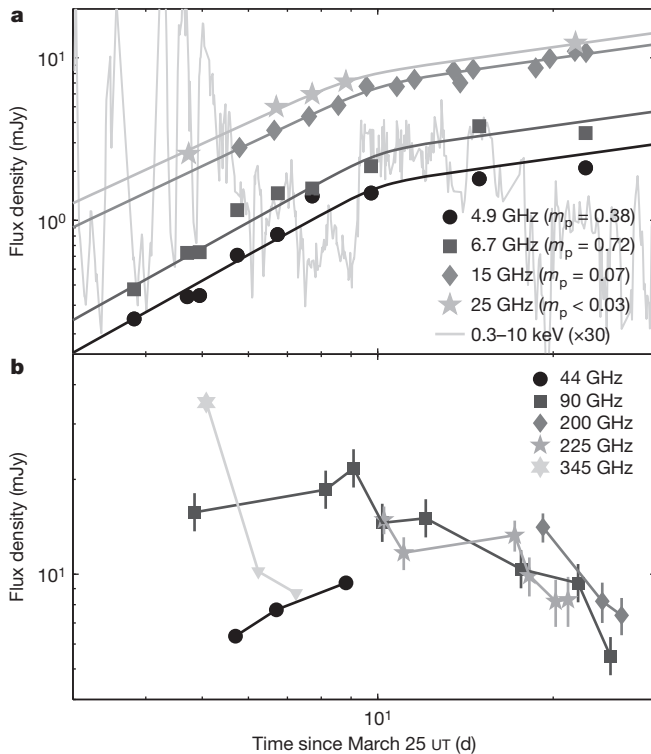


**Figure 3 | Radio light curves of Swift J164449.3+573451 at 5–345 GHz reveal interstellar scintillation.** **a**, Light curves at 5–25 GHz (error bars are smaller than symbols; Supplementary Information). These data are from the EVLA, the Arcminute Microkelvin Imager Large Array and the Owens Valley Radio Observatory 40-m telescope. The lines are broken power-law fits to the 5–25-GHz light curves, using 2011 March 25 UT as the initial time. The low-frequency light curves show significant interstellar scintillation, with the strongest modulation at 6.7 GHz. To calculate the expected interstellar scintillation, we use the NE2001 galactic free-electron density model<sup>12</sup>. For the line of sight to Swift J164449.3+573451 (galactic latitude,  $l = 86.7111$ ; galactic longitude,  $b = 39.4415$ ), the scattering measure is  $2.2 \times 10^{-4} \text{ kpc m}^{-20/3}$ . With a scattering screen distance of  $\sim 1 \text{ kpc}$ , the transition from weak to strong scattering occurs<sup>11</sup> at  $\nu_0 \approx 10 \text{ GHz}$ , and the Fresnel scale is  $\theta_{F,0} \approx 1 \mu\text{as}$  (sizes are given as radii). At frequencies above  $\nu_0$ , the modulation index is given by  $m_p \propto (\nu/\nu_0)^{-17/12} (\theta_s/\theta_{F,0})^{-7/6}$ . For frequencies below  $\nu_0$ , refractive scale scintillation leads to  $m_p \propto (\nu/\nu_0)^{17/30} (\theta_s/\theta_{F,0})^{-7/6}$ , where the refractive scale is  $\theta_r = \theta_{F,0}(\nu/\nu_0)^{-11/5}$ . By comparing these results with the observed modulation, we infer a size of  $\theta_s \approx 5 \mu\text{as}$ . Also shown is the Swift X-ray light curve<sup>4</sup> binned on a timescale of 15 min and multiplied by a factor of  $1.3 \times 10^{10}$  to fit on the same flux density scale as the radio data. The strong X-ray variability during the first 10 d is not accompanied by similar order-of-magnitude fluctuations in the radio bands, pointing to a distinct origin for the radio and X-ray emission. **b**, Light curves at 44–345 GHz from the EVLA, the Combined Array for Research in Millimeter-wave Astronomy and the Submillimeter Array (error bars, 1 s.d.). These frequencies are mainly in the decline phase and therefore provide information on the peak of the synchrotron spectrum (Fig. 2). Upper limits at 345 GHz are marked by triangles.

precise, beaming-independent calorimetry<sup>15,16</sup> of the true amount of energy released. Continued radio observations will also uniquely probe the density structure near a previously dormant SMBH as the ambient medium is swept up by the relativistic outflow. From the existing data, we find that  $n_e \propto r^{-2.4}$ , where  $n_e$  is the electron number density (Supplementary Information).

Second, with continued expansion, we expect that VLBI observations will resolve the radio source on a timescale of  $\sim 2 \text{ yr}$ , and directly confirm the relativistic expansion; from the observed flux density evolution, we predict a peak of a few millijanskys at a frequency of several gigahertz on this timescale, which is within the reach of the Very Long Baseline Array.

Third, from the detection of a single such event in six years of Swift operations, we infer a rate of  $\sim 0.1 \text{ Gpc}^{-3} \text{ yr}^{-1}$ , which is much lower than the predicted<sup>17,18</sup> tidal disruption rate ( $\sim 10^2\text{--}10^3 \text{ Gpc}^{-3} \text{ yr}^{-1}$ ) and upper limits from current radio surveys<sup>19</sup> ( $\leq 10^3 \text{ Gpc}^{-3} \text{ yr}^{-1}$ ). This suggests that the properties of Swift J164449.3+573451 are exceedingly rare; if it is due to jet collimation then the implied beaming fraction is  $\sim 10^3$ , consistent with the ratio of the observed X-ray luminosity to the Eddington limit and the radio-inferred energy.

Finally, past searches<sup>20–22</sup> for tidal disruption events have focused on the expected<sup>14</sup> bright optical/ultraviolet and soft-X-ray emission, but the large optical extinction and associated soft-X-ray absorption in Swift J164449.3+573451 suggest that radio observations may provide a cleaner signature. This is particularly true if the X-ray/ $\gamma$ -ray emission is beamed by a factor of  $\sim 10^3$ . Using the EVLA and the Atacama Large Millimeter Array, similar events are detectable to  $z \approx 6$ .

Received 22 April; accepted 12 July 2011.

1. Begelman, M. C., Blandford, R. D. & Rees, M. J. Theory of extragalactic radio sources. *Rev. Mod. Phys.* **56**, 255–351 (1984).
2. Hills, J. G. Possible power source of Seyfert galaxies and QSOs. *Nature* **254**, 295–298 (1975).
3. Rees, M. J. Tidal disruption of stars by black holes of  $10^6\text{--}10^8$  solar masses in nearby galaxies. *Nature* **333**, 523–528 (1988).
4. Burrows, D. N. *et al.* Discovery of the onset of rapid accretion by a dormant massive black hole. *Nature* doi:10.1038/nature10374 (this issue).
5. Bloom, J. S. *et al.* A possible relativistic jetted outburst from a massive black hole fed by a tidally disrupted star. *Science* **333**, 203–206 (2011).
6. Levan, A. J. *et al.* An extremely luminous panchromatic outburst from the nucleus of a distant galaxy. *Science* **333**, 199–202 (2011).
7. Berger, E. *et al.* GRB 110328A / Swift J164449.3+573451: radio-optical/NIR astrometry. *GCN Circ.* **11854** (2011).
8. Readhead, A. C. S. Equipartition brightness temperature and the inverse Compton catastrophe. *Astrophys. J.* **426**, 51–59 (1994).
9. Chevalier, R. A. Synchrotron self-absorption in radio supernovae. *Astrophys. J.* **499**, 810–819 (1998).
10. Kumar, P. & Narayan, R. GRB 080319B: evidence for relativistic turbulence, not internal shocks. *Mon. Not. R. Astron. Soc.* **395**, 472–489 (2009).
11. Goodman, J. & Narayan, R. Fitting formula for flux scintillation of compact radio sources. *Astrophys. J.* **636**, 510–527 (2006).
12. Cordes, J. M. & Lazio, T. J. W. NE2001. A new model for the galactic distribution of free electrons and its fluctuations. Preprint at (<http://arxiv.org/abs/astro-ph/0207156>) (2003).
13. Greene, J. E. & Ho, L. C. A new sample of low-mass black holes in active galaxies. *Astrophys. J.* **670**, 92–104 (2007).
14. Strubbe, L. E. & Quataert, E. Optical flares from the tidal disruption of stars by massive black holes. *Mon. Not. R. Astron. Soc.* **400**, 2070–2084 (2009).
15. Frail, D. A., Waxman, E. & Kulkarni, S. R. A 450 day light curve of the radio afterglow of GRB 970508: fireball calorimetry. *Astrophys. J.* **537**, 191–204 (2000).
16. Shivers, I. & Berger, E. A. Beaming-independent estimate of the energy distribution of long gamma-ray bursts: initial results and future prospects. *Astrophys. J.* **734**, 58–65 (2011).
17. Wang, J. & Merritt, D. Revised rates of stellar disruption in galactic nuclei. *Astrophys. J.* **600**, 149–161 (2004).
18. van Velzen, S. *et al.* Optical discovery of stellar tidal disruption flares. Preprint at (<http://arxiv.org/abs/1009.1627>) (2010).
19. Bower, G. C. Constraining the rate of relativistic jets from tidal disruptions using radio surveys. *Astrophys. J.* **732**, L12–L15 (2011).
20. Komossa, S. & Bade, N. The giant X-ray outbursts in NGC 5905 and IC 3599: follow-up observations and outburst scenarios. *Astron. Astrophys.* **343**, 775–787 (1999).
21. Gezari, S. *et al.* UV/optical detections of candidate tidal disruption events by GALEX and CFHTLS. *Astrophys. J.* **676**, 944–969 (2008).
22. Cenko, S. B. *et al.* PTF10iqa: a short-lived, luminous flare from the nuclear region of a star-forming galaxy. *Mon. Not. R. Astron. Soc.* (submitted); preprint at (<http://arxiv.org/abs/1103.0779>) (2011).

**Supplementary Information** is linked to the online version of the paper at [www.nature.com/nature](http://www.nature.com/nature).

**Acknowledgements** E.B. is supported in part by funds from NASA. A.L. is supported in part by NSF and NASA grants. R.M. acknowledges support from a Swift ASI grant and from the Ministry of Universities and Research of Italy. E.N. is partly supported by IRG and ISF grants. The EVLA and the Very Long Baseline Array are operated by the NRAO, a facility of the NSF operated under cooperative agreement by the AUI. The SMA is a joint project between the SAO and the ASIAA, and is funded by the Smithsonian Institution and the Academia Sinica. CARMA development and operations are supported by the NSF under a cooperative agreement, and by the Associates of the California Institute of Technology, the University of Chicago and the states of California, Illinois and Maryland. The AMI arrays are supported by the University of Cambridge and the STFC. This work is partly based on observations with the 100-m telescope of the MPIfR at Effelsberg.



This work made use of data supplied by the UK Swift Science Data Centre at the University of Leicester.

**Author Contributions** B.A.Z. and E.B. designed and coordinated the radio observations and analysis among all instruments reported here. B.A.Z. and D.A.F. performed EVLA observations, data reduction and analysis. G.R.P. observed the source with the SMA, and along with N.A.P. reduced and analysed the SMA observations. CARMA observations were set up, reduced and analysed by B.A.Z., J.M.C. and S.R.K. Fast-response CARMA observations were facilitated by N.H.V. and T.L.C., with the first CARMA observation made by S.S. and C.L.H.H. R.C. implemented and analysed MMT and Gemini optical observations. K.M. performed observations with the OVRO 40-m telescope and analysed results, with advice from S.R.K., A.C.S.R., J.R., M.S. and W.M.-M. G.G.P. performed observations with the AML Large Array and

analysed the results. A.M.S., A.B., M.F.B. and M.P.R. planned observations with the VLBA and the MPIfR. A.B. reduced the VLBI data. R.M. analysed and modelled the X-ray data. A.L., R.N. and E.N. provided the theoretical model for a tidal disruption event. The paper was put together by B.A.Z. and E.B., with the primary text written by E.B. and portions of Supplementary Information written by E.B., B.A.Z., R.C., K.M. and A.B. D.B.F. provided feedback on the manuscript. All authors discussed the results and commented on the manuscript.

**Author Information** Reprints and permissions information is available at [www.nature.com/reprints](http://www.nature.com/reprints). The authors declare no competing financial interests. Readers are welcome to comment on the online version of this article at [www.nature.com/nature](http://www.nature.com/nature). Correspondence and requests for materials should be addressed to B.A.Z. ([bzauderer@cfa.harvard.edu](mailto:bzauderer@cfa.harvard.edu)) or E.B. ([eberger@cfa.harvard.edu](mailto:eberger@cfa.harvard.edu)).

# Role of sulphuric acid, ammonia and galactic cosmic rays in atmospheric aerosol nucleation

Jasper Kirkby<sup>1</sup>, Joachim Curtius<sup>2</sup>, João Almeida<sup>2,3</sup>, Eimear Dunne<sup>4</sup>, Jonathan Duplissy<sup>1,5,6</sup>, Sebastian Ehrhart<sup>2</sup>, Alessandro Franchin<sup>5</sup>, Stéphanie Gagné<sup>5,6</sup>, Luisa Ickes<sup>2</sup>, Andreas Kürten<sup>2</sup>, Agnieszka Kupc<sup>7</sup>, Axel Metzger<sup>8</sup>, Francesco Riccobono<sup>9</sup>, Linda Rondo<sup>2</sup>, Siegfried Schobesberger<sup>5</sup>, Georgios Tsagkogeorgas<sup>10</sup>, Daniela Wimmer<sup>2</sup>, Antonio Amorim<sup>3</sup>, Federico Bianchi<sup>9,11</sup>, Martin Breitenlechner<sup>8</sup>, André David<sup>1</sup>, Josef Dommen<sup>9</sup>, Andrew Downard<sup>12</sup>, Mikael Ehn<sup>5</sup>, Richard C. Flagan<sup>12</sup>, Stefan Haider<sup>1</sup>, Armin Hansel<sup>8</sup>, Daniel Hauser<sup>8</sup>, Werner Jud<sup>8</sup>, Heikki Junninen<sup>5</sup>, Fabian Kreissl<sup>2</sup>, Alexander Kvashin<sup>13</sup>, Ari Laaksonen<sup>14</sup>, Katrianne Lehtipalo<sup>5</sup>, Jorge Lima<sup>3</sup>, Edward R. Lovejoy<sup>15</sup>, Vladimir Makhmutov<sup>13</sup>, Serge Mathot<sup>1</sup>, Jyri Mikkilä<sup>5</sup>, Pierre Minginette<sup>1</sup>, Sandra Mogo<sup>3</sup>, Tuomo Nieminen<sup>5</sup>, Antti Onnela<sup>1</sup>, Paulo Pereira<sup>3</sup>, Tuukka Petäjä<sup>5</sup>, Ralf Schnitzhofer<sup>8</sup>, John H. Seinfeld<sup>12</sup>, Mikko Sipilä<sup>5,6</sup>, Yuri Stozhkov<sup>13</sup>, Frank Stratmann<sup>10</sup>, Antonio Tomé<sup>3</sup>, Joonas Vanhanen<sup>5</sup>, Yrjö Viisanen<sup>16</sup>, Aron Vrtala<sup>7</sup>, Paul E. Wagner<sup>7</sup>, Hansueli Walther<sup>9</sup>, Ernest Weingartner<sup>9</sup>, Heike Wex<sup>10</sup>, Paul M. Winkler<sup>7</sup>, Kenneth S. Carslaw<sup>4</sup>, Douglas R. Worsnop<sup>5,17</sup>, Urs Baltensperger<sup>9</sup> & Markku Kulmala<sup>5</sup>

**Atmospheric aerosols exert an important influence on climate<sup>1</sup> through their effects on stratiform cloud albedo and lifetime<sup>2</sup> and the invigoration of convective storms<sup>3</sup>. Model calculations suggest that almost half of the global cloud condensation nuclei in the atmospheric boundary layer may originate from the nucleation of aerosols from trace condensable vapours<sup>4</sup>, although the sensitivity of the number of cloud condensation nuclei to changes of nucleation rate may be small<sup>5,6</sup>. Despite extensive research, fundamental questions remain about the nucleation rate of sulphuric acid particles and the mechanisms responsible, including the roles of galactic cosmic rays and other chemical species such as ammonia<sup>7</sup>. Here we present the first results from the CLOUD experiment at CERN. We find that atmospherically relevant ammonia mixing ratios of 100 parts per trillion by volume, or less, increase the nucleation rate of sulphuric acid particles more than 100–1,000-fold. Time-resolved molecular measurements reveal that nucleation proceeds by a base-stabilization mechanism involving the stepwise accretion of ammonia molecules. Ions increase the nucleation rate by an additional factor of between two and more than ten at ground-level galactic-cosmic-ray intensities, provided that the nucleation rate lies below the limiting ion-pair production rate. We find that ion-induced binary nucleation of H<sub>2</sub>SO<sub>4</sub>–H<sub>2</sub>O can occur in the mid-troposphere but is negligible in the boundary layer. However, even with the large enhancements in rate due to ammonia and ions, atmospheric concentrations of ammonia and sulphuric acid are insufficient to account for observed boundary-layer nucleation.**

The primary vapour responsible for atmospheric nucleation is thought to be sulphuric acid. However, theory suggests that peak concentrations in the boundary layer ( $10^6$ – $10^7$  cm<sup>-3</sup>; ref. 8) are usually too low for the binary nucleation of H<sub>2</sub>SO<sub>4</sub>–H<sub>2</sub>O to proceed. Furthermore, after nucleation there is generally insufficient H<sub>2</sub>SO<sub>4</sub> to grow the clusters to cloud condensation nucleus sizes (more than 50 nm), so organic species are primarily responsible for particle growth<sup>9,10</sup>. Nucleation of sulphuric acid particles is known to be enhanced by the presence of ternary species such as ammonia<sup>11–13</sup> or organic compounds<sup>14</sup> such as amines<sup>15–17</sup> or oxidized organic compounds<sup>18,19</sup>. Ions are also expected to enhance nucleation<sup>20–24</sup>, and ion-induced nucleation has been observed

in the atmosphere<sup>25,26</sup>. Because the primary source of ions in the global troposphere is galactic cosmic rays (GCRs), their role in atmospheric nucleation is of considerable interest as a possible physical mechanism for climate variability caused by the Sun<sup>27,28</sup>.

Here we address three issues that currently limit our understanding of atmospheric nucleation and its influence on climate<sup>7</sup>. First, quantitative measurements of the roles of ions and ternary vapours are lacking. Second, the nucleation mechanism and the molecular composition of the critical nucleus have not been directly measured. Third, it remains an open question whether laboratory measurements are able to reproduce atmospheric observations: recent experiments have concluded that atmospheric concentrations of H<sub>2</sub>SO<sub>4</sub> and H<sub>2</sub>O without ternary vapours are sufficient<sup>29</sup> or insufficient<sup>19</sup> to explain boundary-layer nucleation rates.

We present here the first results from the CLOUD experiment at CERN (see Methods, Supplementary Information and Supplementary Fig. 1 for experimental details). The measurements, obtained at the CERN Proton Synchrotron, represent the most rigorous laboratory evaluation yet accomplished of binary, ternary and ion-induced nucleation of sulphuric acid particles under atmospheric conditions.

The nucleation rates ( $J$ , cm<sup>-3</sup> s<sup>-1</sup>) are measured under neutral ( $J_n$ ), GCR ( $J_{\text{GCR}}$ ) and charged pion beam ( $J_{\text{ch}}$ ) conditions, corresponding to ion-pair concentrations of about 0, 400 and 3,000 cm<sup>-3</sup>, respectively. A typical sequence of  $J_n$ ,  $J_{\text{GCR}}$  and  $J_{\text{ch}}$  measurements is shown in Supplementary Fig. 2 and is described in the Supplementary Information. Both  $J_{\text{GCR}}$  and  $J_{\text{ch}}$  comprise the sum of ion-induced and neutral nucleation rates, whereas  $J_n$  measures the neutral rate alone. The nucleation rates are shown in Fig. 1 as a function of [H<sub>2</sub>SO<sub>4</sub>] at 248, 278 and 292 K. As the temperature is reduced, lower H<sub>2</sub>SO<sub>4</sub> concentrations are sufficient to maintain the same nucleation rates, as a result of the decrease in the H<sub>2</sub>SO<sub>4</sub> saturation vapour pressure. Apart from contaminants (see below), the only condensable vapours present in the chamber for these data are H<sub>2</sub>SO<sub>4</sub> and H<sub>2</sub>O. The experimental results are slightly higher than model calculations<sup>30</sup> based on thermochemical data for charged H<sub>2</sub>SO<sub>4</sub>–H<sub>2</sub>O clusters<sup>23</sup> under  $J_{\text{ch}}$  ionization conditions, but they show similar curvature and slope.

The presence of ions from ground-level GCR ionization ( $J_{\text{GCR}}$  curves) enhances the neutral nucleation rate roughly twofold at 292 K and

<sup>1</sup>CERN, CH-1211 Geneva, Switzerland. <sup>2</sup>Goethe-University of Frankfurt, Institute for Atmospheric and Environmental Sciences, 60438 Frankfurt am Main, Germany. <sup>3</sup>SIM, University of Lisbon and University of Beira Interior, 1749-016 Lisbon, Portugal. <sup>4</sup>University of Leeds, School of Earth and Environment, LS2-9JT Leeds, United Kingdom. <sup>5</sup>University of Helsinki, Department of Physics, FI-00014 Helsinki, Finland. <sup>6</sup>Helsinki Institute of Physics, University of Helsinki, FI-00014 Helsinki, Finland. <sup>7</sup>University of Vienna, Faculty of Physics, 1090 Vienna, Austria. <sup>8</sup>Ionicon Analytik GmbH and University of Innsbruck, Institute for Ion and Applied Physics, 6020 Innsbruck, Austria. <sup>9</sup>Paul Scherrer Institut, Laboratory of Atmospheric Chemistry, CH-5232 Villigen, Switzerland. <sup>10</sup>Leibniz Institute for Tropospheric Research, 04318 Leipzig, Germany. <sup>11</sup>University of Milan, Department of Inorganic, Metallorganic, and Analytical Chemistry, 20133 Milan, Italy. <sup>12</sup>California Institute of Technology, Division of Chemistry and Chemical Engineering, Pasadena, California 91125, USA. <sup>13</sup>Lebedev Physical Institute, Solar and Cosmic Ray Research Laboratory, 119991 Moscow, Russia. <sup>14</sup>University of Eastern Finland, FI-70211 Kuopio, Finland. <sup>15</sup>NOAA Earth System Research Laboratory, Boulder, Colorado 80305, USA. <sup>16</sup>Finnish Meteorological Institute, FI-00101 Helsinki, Finland. <sup>17</sup>Aerodyne Research Inc., Billerica, Massachusetts 01821, USA.



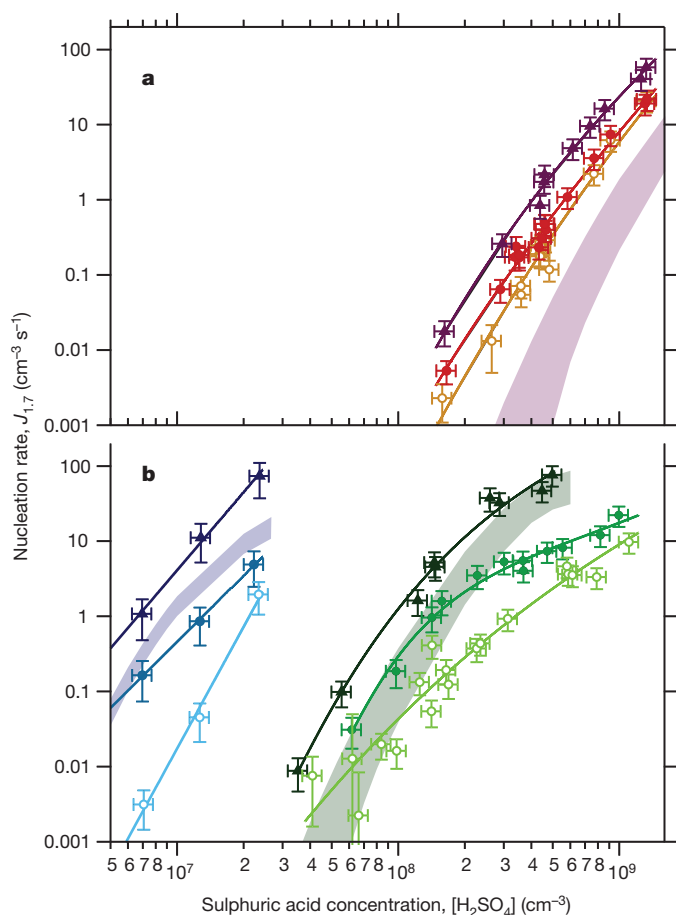


**Figure 1 | Plots of nucleation rate against  $\text{H}_2\text{SO}_4$  concentration.** Neutral, GCR and charged (pion beam) nucleation rates are shown at 1.7 nm diameter,  $J_{1.7}$ , as a function of sulphuric acid concentration at 38% relative humidity. **a**, Rates at 292 K; **b**, rates at 248 K (blue) and 278 K (green). The  $\text{NH}_3$  mixing ratios correspond to the contaminant level ( $<35$  p.p.t.v. at 278 and 292 K;  $<50$  p.p.t.v. at 248 K). Triangles,  $J_{\text{ch}}$ ; filled circles,  $J_{\text{GCR}}$ ; open circles,  $J_{\text{n}}$ . The predictions of the PARNUC model<sup>30</sup> for binary  $\text{H}_2\text{SO}_4$ – $\text{H}_2\text{O}$  charged nucleation,  $J_{\text{ch}}$ , are indicated by the coloured bands. The fitted curves are drawn to guide the eye. The error bars indicate the estimated total statistical and systematic 1 $\sigma$  measurement uncertainties, although the overall factor 2 systematic scale uncertainty on  $[\text{H}_2\text{SO}_4]$  is not shown.

more than tenfold at 278 and 248 K. The enhancement factor is up to five times larger at the higher ion-pair concentrations typical of the upper troposphere (Fig. 2, and  $J_{\text{ch}}$  curves in Fig. 1). Overall, we find that the nucleation rate varies with negative ion concentration,  $[\text{ion}^-]$ , as  $J = J_{\text{n}} + k[\text{ion}^-]^p$ , with  $p = 0.7$ – $1.0$  (Fig. 2). Our measurements show evidence of saturation of  $J_{\text{GCR}}$  and  $J_{\text{ch}}$  by their convergence with  $J_{\text{n}}$  at high nucleation rates (Fig. 1), where almost every negative ion gives rise to a new particle<sup>21</sup>. However, even with ion enhancement, our measurements show that binary nucleation of  $\text{H}_2\text{SO}_4$ – $\text{H}_2\text{O}$  will proceed at extremely low rates in the atmospheric boundary layer. In contrast, in the cooler mid-troposphere and perhaps at lower altitude in some polar regions, ion-induced binary nucleation can proceed at ambient acid concentrations<sup>23</sup>.

CLOUD has measured the molecular composition of nucleating charged clusters from monomers up to stable aerosol particles, and has time-resolved each step of their growth. Example mass spectra are shown in Supplementary Fig. 3. The ion-induced nucleation measurements in Fig. 1 exclusively involve negative clusters, containing the  $\text{HSO}_4^-$ ,  $\text{HSO}_5^-$  or  $\text{SO}_5^-$  ion (Supplementary Fig. 4 shows an example of a nucleation event). However, at higher ammonia concentrations (see below) we have also observed positively charged nucleation, involving the  $\text{NH}_4^+$  ion.

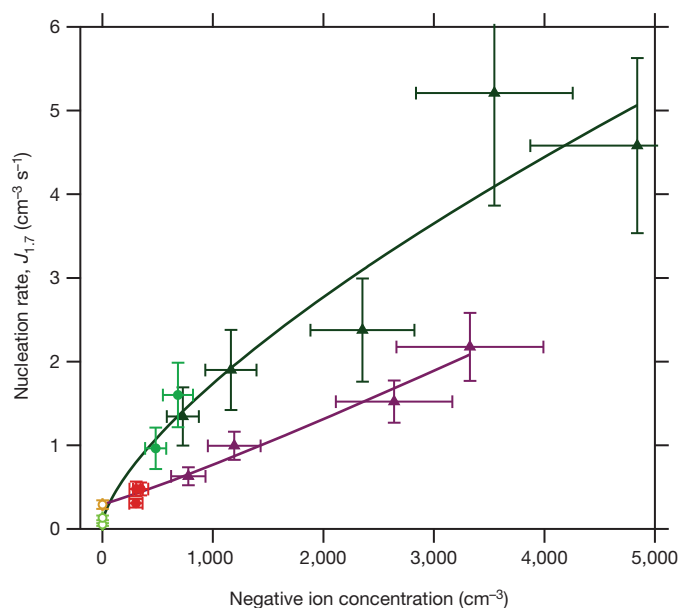


**Figure 2 | Plots of nucleation rate against negative ion concentration.** Nucleation rates as a function of negative ion concentration at 292 K and  $[\text{H}_2\text{SO}_4] = 4.5 \times 10^8 \text{ cm}^{-3}$  (purple line), and at 278 K and  $[\text{H}_2\text{SO}_4] = 1.5 \times 10^8 \text{ cm}^{-3}$  (green line). Triangles,  $J_{\text{ch}}$ ; filled circles,  $J_{\text{GCR}}$ ; open circles,  $J_{\text{n}}$ . All measurements were made at 38% relative humidity and 35 p.p.t.v.  $\text{NH}_3$ . Neutral nucleation rates,  $J_{\text{n}}$ , were effectively measured at zero ion pair concentration (ion or charged-cluster lifetime  $<1$  s). The curves are fits of the form  $J = j_0 + k[\text{ion}^-]^p$ , where  $j_0$ ,  $k$  and  $p$  are free parameters. The error bars indicate only the point-to-point 1 $\sigma$  errors; the nucleation rates and ion concentrations each have estimated overall scale uncertainties of  $\pm 30\%$ .

The chemical composition of nucleating clusters containing up to  $n = 20$  sulphuric acid molecules, including the  $\text{HSO}_4^-$  ion, is shown in Fig. 3. At 292 K the clusters above  $n = 4$  are found always to be accompanied by additional nitrogen-containing molecules, comprising  $\text{NH}_3$ , amines (mainly dimethylamine and ethylamine) and urea (Fig. 3c, d). Although these ternary vapours were not intentionally added to the chamber—at least initially—they are crucial to the nucleation. The measured contaminant mixing ratios of ammonia and total amines were less than 35 parts per trillion by volume (p.p.t.v.) and less than 50 p.p.t.v., respectively. It is notable that the nucleating  $\text{H}_2\text{SO}_4$  clusters included only nitrogen-containing bases, even though a broad spectrum of gas-phase contaminants was identified in the chamber. A clear progression is observed from almost pure binary nucleation at 248 K to pure ternary nucleation at 292 K; both binary and ternary nucleation contributed at 278 K. From the molecular measurements, the binary fraction (or upper limit) can be determined for each  $J_{\text{ch}}$  measurement. After application of these corrections, there is excellent agreement between the experimental binary  $J_{\text{ch}}$  values and the model predictions shown in Fig. 1.

Further measurements were made with  $\text{NH}_3$  intentionally added to the chamber. The nucleation rates were highly sensitive to small additions of ammonia up to about 100 p.p.t.v., with evidence of saturation at higher mixing ratios (Fig. 4). In some cases the saturation also resulted from the ionization rate limits of about  $4 \text{ cm}^{-3} \text{ s}^{-1}$  for GCRs and  $80 \text{ cm}^{-3} \text{ s}^{-1}$  for the pion beam. The onset of positively charged nucleation was observed at about 900 p.p.t.v.  $\text{NH}_3$  at 292 K and at 300 p.p.t.v.  $\text{NH}_3$  at 278 K, which contributed to a further rise of  $J_{\text{GCR}}$  and  $J_{\text{ch}}$ . With additional  $\text{NH}_3$  the nucleating clusters revealed a distinctive increase in the  $\text{NH}_3$  molecular content (compare Fig. 3c with Fig. 3d). These observations provide clear experimental evidence that the nucleation rates are strongly limited by the availability of  $\text{NH}_3$  at mixing ratios below 100 p.p.t.v., and further strengthen our argument that binary nucleation is not significant in the global boundary layer.

The negative cluster ion spectra (Fig. 3) show strong, quasi-stable peaks corresponding to the charged pure monomer, dimer and trimer

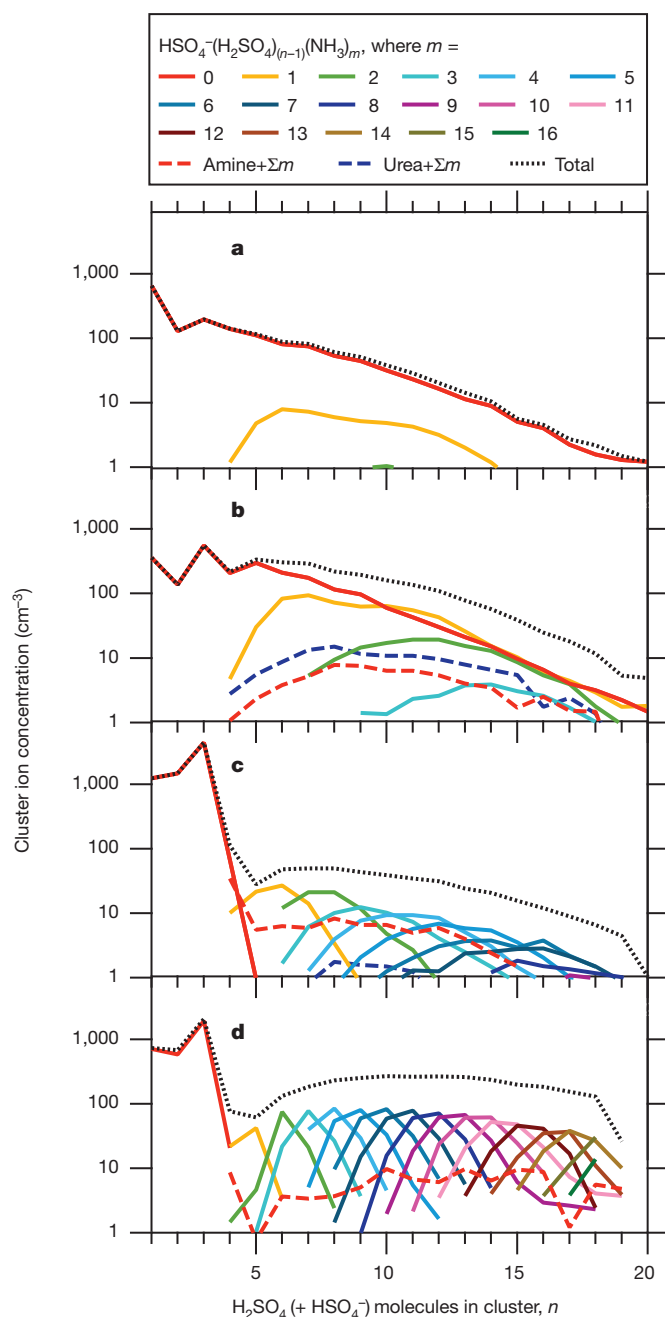


**Figure 3 | Ion cluster composition.** **a–d**, The chemical composition of charged nucleating clusters at 248 K (<35 p.p.t.v.  $\text{NH}_3$ ) (**a**), 278 K (<35 p.p.t.v.  $\text{NH}_3$ ) (**b**), 292 K (<35 p.p.t.v.  $\text{NH}_3$ ) (**c**) and 292 K (230 p.p.t.v.  $\text{NH}_3$ ) (**d**). The cluster spectra are averaged over the steady-state nucleation period. To simplify the figures, only the overall envelopes are shown for organic species. The concentrations are approximately corrected for detection efficiency.

of sulphuric acid. Here ‘pure’ implies only  $\text{H}_2\text{SO}_4$  and  $\text{H}_2\text{O}$ , although we point out that no water molecules were detected because they were lost by collisional dissociation or rapid evaporation from the sulphuric acid clusters on entering the vacuum of the instrument. At 292 K, pure acid clusters with  $n \geq 4$  were highly suppressed, showing that the charged pure tetramer was unstable and evaporated rapidly. The clusters grew by a striking stepwise accretion of  $\text{NH}_3$  molecules, each stabilizing a distinct additional number of acid molecules, depending on the ammonia concentration. Figure 3d shows how the cluster maintained a strict 1:1 molar ratio of ammonia and sulphuric acid as it grew, suggesting that the most stable growth path involved ammonium bisulphate ( $\text{NH}_4^+\text{HSO}_4^-$ ) cluster formation. All clusters showed this

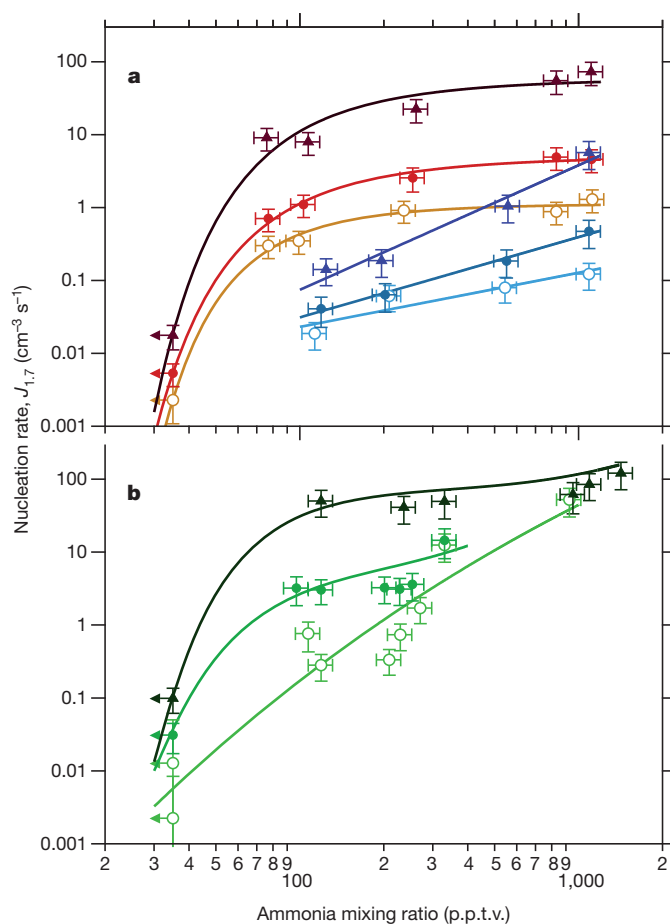


**Figure 4 | Plots of nucleation rate against  $\text{NH}_3$  concentration.** Nucleation rates are shown as a function of ammonia mixing ratio. **a**, At 292 K and  $[\text{H}_2\text{SO}_4] = 1.5 \times 10^8 \text{ cm}^{-3}$  (curves) and  $4.3 \times 10^7 \text{ cm}^{-3}$  (straight lines); **b**, at 278 K and  $[\text{H}_2\text{SO}_4] = 6.3 \times 10^7 \text{ cm}^{-3}$ . All measurements were made at 38% relative humidity. Triangles,  $J_{\text{ch}}$ ; filled circles,  $J_{\text{GCR}}$ ; open circles,  $J_n$ . The fitted lines are drawn to guide the eye. The bars indicate  $1\sigma$  total errors, although the overall ammonia scale uncertainty of a factor 2 is not shown.

1:1 molar ratio above 100 p.p.t.v. ammonia—and a decreased  $\text{NH}_3$  content below. The observed change in the nucleation rate from a strong to weak  $\text{NH}_3$  dependence at some value below 100 p.p.t.v. (Fig. 4) is therefore explained as a transition from  $\text{NH}_3$ -limited to  $\text{NH}_3$ -saturated nucleation (that is, where each acid molecule condensing on the cluster is immediately stabilized by an ammonia molecule, thereby suppressing its evaporation). Quantum chemical calculations indicate that  $\text{NH}_3$  and amines bind strongly to neutral acid clusters<sup>31</sup>, indicating that ternary nucleation of neutral clusters above  $n = 1$  may proceed by the same mechanism as that observed for charged clusters above  $n = 4$ , after which the negative charge becomes sufficiently shielded to allow  $\text{NH}_3$  to bind. We term this stepwise stabilization of  $\text{H}_2\text{SO}_4$  clusters the base-stabilization nucleation mechanism.

The CLOUD measurements address a long-standing controversy in atmospheric nucleation, namely whether binary nucleation of sulphuric acid and water vapour can account for new particle formation in the boundary layer. Figure 5 presents a comparison of our GCR nucleation rates with atmospheric observations of boundary-layer nucleation<sup>8,32,33</sup> and recent laboratory experiments<sup>19,29</sup>. We find that ion-induced binary nucleation proceeds at a significant rate in the cool temperatures of the free troposphere at atmospheric concentrations of sulphuric acid, and may be an important process when ternary vapour concentrations are low. Some fraction of these particles may be transported downwards and could constitute an important source in the remote marine boundary layer. In contrast, we show that binary



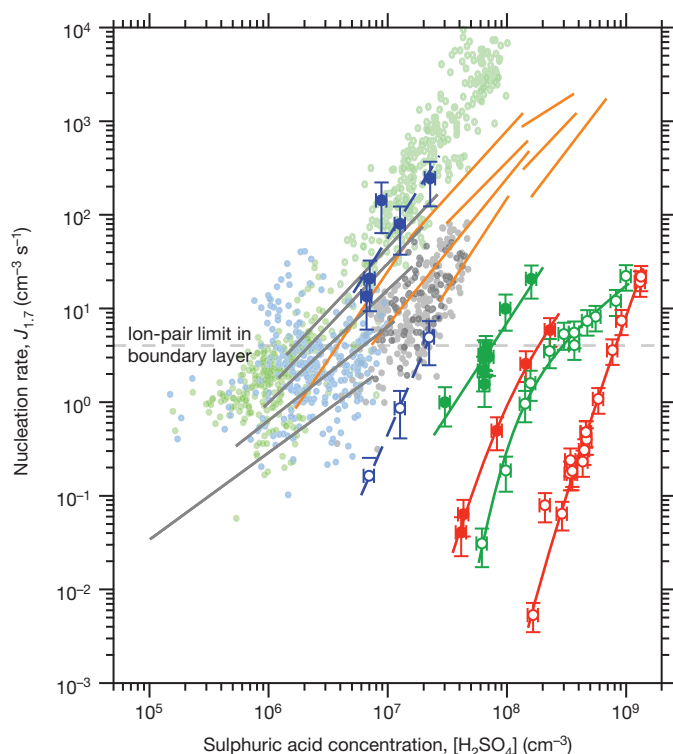


**Figure 5 | Nucleation rate comparison.** Comparison of CLOUD data with measurements of the nucleation rate of new particles as a function of  $[H_2SO_4]$  in the atmospheric boundary layer (pale filled circles<sup>8,33</sup> and pale open circles<sup>32</sup>) and with recent laboratory experiments at room temperature (grey<sup>19</sup> and orange<sup>29</sup> lines). The CLOUD data (large, darker symbols and lines) show the galactic cosmic ray nucleation rates,  $J_{\text{GCR}}$ , measured at 248 K (blue), 278 K (green) and 292 K (red) and at  $NH_3$  mixing ratios of <35 p.p.t.v. (open green and red circles), <50 p.p.t.v. (open blue circles), 150 p.p.t.v. (filled blue and green circles) and 190 p.p.t.v. (filled red circles). The bars indicate  $1\sigma$  total errors, although the overall factor 2 scale uncertainty on  $[H_2SO_4]$  is not shown. The measurements at 278 and 292 K bracket the typical range of boundary-layer temperatures, whereas those at 248 K reflect exceptionally cold conditions. Ion-induced nucleation in the boundary layer is limited by the ion-pair production rate to a maximum of about  $4 \text{ cm}^{-3} \text{ s}^{-1}$ .

nucleation within the boundary layer is negligible in all except the coldest conditions, so additional species are required. It has been reported<sup>29</sup> that  $H_2SO_4$  at atmospheric concentrations can explain atmospheric nucleation rates in most locations even without the clear participation of ammonia or organic substances. In view of the CLOUD results, we consider it likely that the result in ref. 29 was affected by the presence of ternary vapours below the detection limits of the experiment.

Under the conditions studied so far in CLOUD (no intentional addition of organic vapours), essentially all nucleating sulphuric acid clusters at 292 K include nitrogen-containing bases or amides:  $NH_3$ , amines or urea. However, for typical boundary-layer ammonia mixing ratios, below about 1 p.p.b.v., ternary nucleation of  $NH_3$ – $H_2SO_4$ – $H_2O$ , with or without ions, is unable to explain atmospheric observations (Figs 4 and 5). This implies that other species, most probably organic compounds<sup>18,19</sup>, are necessary for boundary-layer nucleation.

The CLOUD experiment provides direct measurements of the molecular composition from single molecule to stable aerosol particle. This has provided new insight into how the ternary nucleation of sulphuric acid particles in the region of the critical cluster proceeds by a base-stabilization mechanism: the clusters grow by a stepwise accretion of basic molecules, each stabilizing a distinct additional number of acid molecules in the cluster, depending on the vapour concentrations.

The CLOUD measurements have also quantified the enhancement of ion-induced nucleation compared with neutral nucleation.

Ground-level GCR ionization substantially increases the nucleation rate of sulphuric acid and sulphuric acid–ammonia particles, by between twofold and tenfold or more, provided that the nucleation rate lies below the limiting ion-pair production rate. Although we have not yet duplicated the concentrations or complexities of atmospheric organic vapours, we find that ion enhancement of nucleation occurs for all temperatures, humidities and cluster compositions observed so far. Ion-induced nucleation will manifest itself as a steady production of new particles that is difficult to isolate in atmospheric observations because of other sources of variability but is nevertheless taking place and could be quite large when averaged globally over the troposphere. However, the fraction of these freshly nucleated particles that grow to sufficient sizes to seed cloud droplets, as well as the role of organic vapours in the nucleation and growth processes, remain open questions experimentally. These are important findings for the potential link between galactic cosmic rays and clouds.

## METHODS SUMMARY

CLOUD is designed to study the effects of cosmic rays on aerosols, cloud droplets and ice particles, under precisely controlled laboratory conditions. The CLOUD chamber and gas system have been built to the highest technical standards of cleanliness and performance. Owing to its large volume ( $26 \text{ m}^3$ ) and highly stable operating conditions, the chamber allows nucleation rates to be reliably measured over a wide range from 0.001 to well above  $100 \text{ cm}^{-3} \text{ s}^{-1}$ . The loss rate of condensable vapours onto the walls of the chamber ( $0.0015 \text{ s}^{-1}$ ) is comparable to the condensation sink rate onto ambient aerosols under pristine atmospheric boundary-layer conditions. The experiment has several unique aspects, including precise control of the ‘cosmic ray’ beam intensity from the CERN Proton Synchrotron, the capability to create an ion-free environment with an internal electric clearing field, precise and uniform adjustment of the  $H_2SO_4$  concentration by means of ultraviolet illumination from a fibre-optic system, and highly stable operation at any temperature between 300 and 183 K. The contents of the chamber are continuously analysed by a suite of instruments connected to sampling probes that project into the chamber.

**Full Methods** and any associated references are available in the online version of the paper at [www.nature.com/nature](http://www.nature.com/nature).

**Received 9 September 2010; accepted 24 June 2011.**

1. IPCC. *Climate Change 2007: the Physical Science Basis. Contribution of Working Group I to the Fourth Assessment Report of the Intergovernmental Panel on Climate Change* (Cambridge Univ. Press, 2007).
2. Feingold, G. & Siebert, H. in *Clouds in the Perturbed Climate System* (eds Heintzenberg, J. & Charlson, R.J.) 319–338 (MIT Press, 2009).
3. Rosenfeld, D. *et al.* Flood or drought: how do aerosols affect precipitation? *Science* **321**, 1309–1313 (2008).
4. Merikanto, J., Spracklen, D. V., Mann, G. W., Pickering, S. J. & Carslaw, K. S. Impact of nucleation on global CCN. *Atmos. Chem. Phys.* **9**, 8601–8616 (2009).
5. Spracklen, D. V. *et al.* Contribution of particle formation to global cloud condensation nuclei concentrations. *Geophys. Res. Lett.* **35**, L06808, doi:10.1029/2007GL033038 (2008).
6. Pierce, J. R. & Adams, P. J. Can cosmic rays affect cloud condensation nuclei by altering new particle formation rates? *Geophys. Res. Lett.* **36**, L09820, doi:10.1029/2009GL037946 (2009).
7. Zhang, R. Getting to the critical nucleus of aerosol formation. *Science* **328**, 1366–1367 (2010).
8. Kerminen, V.-M. *et al.* Atmospheric nucleation: highlights of the EUCAARI project and future directions. *Atmos. Chem. Phys.* **10**, 10829–10848 (2010).
9. Boy, M. *et al.* Sulphuric acid closure and contribution to nucleation mode particle growth. *Atmos. Chem. Phys.* **5**, 863–878 (2005).
10. Wang, L. *et al.* Atmospheric nanoparticles formed from heterogeneous reactions of organics. *Nature Geosci.* **3**, 238–242 (2010).
11. Ziereis, H. & Arnold, F. Gaseous ammonia and ammonium ions in the free troposphere. *Nature* **321**, 503–505 (1986).
12. Coffman, D. J. & Hegg, D. A. A preliminary study of the effect of ammonia on particle nucleation in the marine boundary layer. *J. Geophys. Res.* **100** (D4), 7147–7160 (1995).
13. Ball, S. M., Hanson, D. R., Eisele, F. L. & McMurry, P. H. Laboratory studies of particle nucleation: initial results for  $H_2SO_4$ ,  $H_2O$ , and  $NH_3$  vapors. *J. Geophys. Res.* **104**, 23709–23718 (1999).
14. Zhang, R. *et al.* Atmospheric new particle formation enhanced by organic acids. *Science* **304**, 1487–1490 (2004).
15. Murphy, S. M. *et al.* Secondary aerosol formation from atmospheric reactions of aliphatic amines. *Atmos. Chem. Phys.* **7**, 2313–2337 (2007).
16. Berndt, T. *et al.* Laboratory study on new particle formation from the reaction  $OH + SO_2$ : influence of experimental conditions,  $H_2O$  vapour,  $NH_3$  and the amine

- tert-butylamine on the overall process. *Atmos. Chem. Phys.* **10**, 7101–7116 (2010).
17. Smith, J. N. *et al.* Observations of aminium salts in atmospheric nanoparticles and possible climatic implications. *Proc. Natl Acad. Sci. USA* **107**, 6634–6639 (2010).
  18. Zhang, R. *et al.* Formation of nanoparticles of blue haze enhanced by anthropogenic pollution. *Proc. Natl Acad. Sci. USA* **106**, 17650–17654 (2009).
  19. Metzger, A. *et al.* Evidence for the role of organics in aerosol particle formation under atmospheric conditions. *Proc. Natl Acad. Sci. USA* **107**, 6646–6651 (2010).
  20. Arnold, F. Multi-ion complexes in the stratosphere—implications for trace gases and aerosol. *Nature* **284**, 610–611 (1980).
  21. Raes, F., Janssens, A. & Van Dingenen, R. The role of ion-induced aerosol formation in the lower atmosphere. *J. Aerosol Sci.* **17**, 466–470 (1986).
  22. Turco, R. P., Zhao, J.-X. & Yu, F. A new source of tropospheric aerosols: Ion-ion recombination. *Geophys. Res. Lett.* **25**, 635–638 (1998).
  23. Lovejoy, E. R., Curtius, J. & Froyd, K. D. Atmospheric ion-induced nucleation of sulfuric acid and water. *J. Geophys. Res.* **109**, D08204, doi:10.1029/2003JD004460 (2004).
  24. Sorokin, A. & Arnold, F. Laboratory study of cluster ions formation in  $\text{H}_2\text{SO}_4$ – $\text{H}_2\text{O}$  system: implications for threshold concentration of gaseous  $\text{H}_2\text{SO}_4$  and ion-induced nucleation kinetics. *Atmos. Environ.* **41**, 3740–3747 (2007).
  25. Eichkorn, S., Wilhelm, S., Aufmhoff, H., Wohlfrom, K. H. & Arnold, F. Cosmic ray-induced aerosol-formation: first observational evidence from aircraft-based ion mass spectrometer measurements in the upper troposphere. *Geophys. Res. Lett.* **29**, 1698–1701 (2002).
  26. Lee, S. H. *et al.* Particle formation by ion nucleation in the upper troposphere and lower stratosphere. *Science* **301**, 1886–1889 (2003).
  27. Svensmark, H. & Friis-Christensen, E. Variation of cosmic ray flux and global cloud coverage—a missing link in solar-climate relationships. *J. Atmos. Sol. Terr. Phys.* **59**, 1225–1232 (1997).
  28. Kirkby, J. Cosmic rays and climate. *Surv. Geophys.* **28**, 333–375 (2007).
  29. Sipilä, M. *et al.* The role of sulfuric acid in atmospheric nucleation. *Science* **327**, 1243–1246 (2010).
  30. Kozil, J. & Lovejoy, E. R. A semi-analytical method for calculating rates of new sulfate aerosol formation from the gas phase. *Atmos. Chem. Phys.* **7**, 3447–3459 (2007).
  31. Kurtén, T., Loukonen, V., Vehkamäki, H. & Kulmala, M. Amines are likely to enhance neutral and ion-induced sulfuric acid–water nucleation in the atmosphere more effectively than ammonia. *Atmos. Chem. Phys.* **8**, 4095–4103 (2008).
  32. Kuang, C., McMurry, P. H., McCormick, A. V. & Eisele, F. L. Dependence of nucleation rates on sulfuric acid vapor concentration in diverse atmospheric locations. *J. Geophys. Res.* **113**, D10209, doi:10.1029/2007JD009253 (2008).
  33. Paasonen, P. *et al.* Connection between new particle formation and sulfuric acid at Hohenpeissenberg (Germany) including the influence of organic compounds. *Boreal Environ. Res.* **14**, 616–629 (2009).

**Supplementary Information** is linked to the online version of the paper at [www.nature.com/nature](http://www.nature.com/nature).

**Acknowledgements** We thank CERN for supporting CLOUD with important technical and financial resources, and for providing a particle beam from the CERN Proton Synchrotron. We also thank J.-L. Agostini, S. Atieh, J. Baechler, D. Bloess, G. Bowden, A. Braem, T. Callamand, A. Castel, L.-P. De Menezes, G. Favre, L. Ferreira, L. Gatignon, D. Gregorio, M. Guinchard, E. Ivanova, F. Josa, I. Krasin, R. Kristic, A. Kuzmin, O. Maksumov, S. Mizin, R. Richter, R. Sitals, A. Vacca, R. Veenhof, A. Wasem and M. Wilhelmsson for their contributions to the experiment. This research has received funding from the EC Seventh Framework Programme under grant agreement no. 215072 (Marie Curie Initial Training Network, 'CLOUD-ITN') and ERC-Advanced Grant 'ATMNUCLE' no. 227463, the German Federal Ministry of Education and Research (project no. 01LK0902A), the Swiss National Science Foundation (project nos 206621\_125025 and 206620\_130527), the Academy of Finland Center of Excellence program (project no. 1118615), the Austrian Science Fund (FWF; project nos P19546 and L593), and the Russian Academy of Sciences and Russian Foundation for Basic Research (grant N08-02-91006-CERN).

**Author Contributions** J.A. performed the nucleation rate analysis. S.S. conducted the API-TOF analysis. J.A., F.B., M.B., A. Downard, E.D., J. Duplissy, S.E., A.F., S.G., D.H., L.I., W.J., J.K., F.K., A. Kürten, A. Kupc, K.L., V.M., A.M., T.N., F.R., L.R., R.S., S.S., Y.S., G.T. and D.W. conducted the data collection and analysis. J.A., K.S.C., J.C., E.D., S.E., L.I., E.R.L. and F.S. performed the modelling. J.K. wrote the manuscript. U.B., K.S.C., J.C., J.K., M.K., J.H.S. and D.R.W. did data interpretation and editing of the manuscript. All authors contributed to the development of the CLOUD facility and analysis instruments, and commented on the manuscript.

**Author Information** Reprints and permissions information is available at [www.nature.com/reprints](http://www.nature.com/reprints). The authors declare no competing financial interests. Readers are welcome to comment on the online version of this article at [www.nature.com/nature](http://www.nature.com/nature). Correspondence and requests for materials should be addressed to J.K. ([jasper.kirkby@cern.ch](mailto:jasper.kirkby@cern.ch)).



## METHODS

The CLOUD chamber (Supplementary Fig. 1) is a 3-m-diameter electropolished stainless steel cylinder of 26.1 m<sup>3</sup>. After tests with a pilot experiment<sup>34</sup>, the chamber and gas supply are designed to achieve the highest standards of cleanliness and temperature stability. To stimulate photolytic reactions—in particular the oxidation of SO<sub>2</sub> to H<sub>2</sub>SO<sub>4</sub> in the presence of O<sub>3</sub> and H<sub>2</sub>O—the contents of the chamber are irradiated by ultraviolet radiation in the range 250–400 nm, introduced by means of 250 optical fibre vacuum feedthroughs installed on top of the chamber. The chamber temperature is controlled by precisely regulating the temperature of the air circulating in the space between the chamber and its surrounding thermal housing. Experiments can be performed at temperatures between 300 and 183 K. In addition, the chamber can be raised to 373 K for bakeout cleaning. The temperature stability of the chamber is about ±0.01 K, with no observable change when the ultraviolet lights are turned on at full power. The nominal operating pressure is one atmosphere. However, rapid adiabatic expansions of up to 200 mbar can be generated to operate in a classical cloud chamber mode for the creation and growth of droplets and ice particles.

Pure air, free of condensable vapours, is obtained from the evaporation of cryogenic liquid N<sub>2</sub> and liquid O<sub>2</sub>, mixed in the ratio 79:21, respectively. The air is humidified with a Nafion humidifier using water stabilized to ±0.01 K and purified by recirculation through a bank of Millipore Super-Q filters and irradiated with ultraviolet radiation to suppress biological activity. Ozone is added to the inlet air by ultraviolet irradiation (less than 200 nm). Trace gases such as SO<sub>2</sub> or NH<sub>3</sub> are obtained from gas cylinders containing 100 p.p.m.v. and 1% concentrations, respectively, in pressurized N<sub>2</sub>. Each trace gas is diluted with pure air to the required concentration before entering the chamber, and has an individual circuit, with an isolation valve at the chamber, to avoid cross-contamination or reactions with other gases outside the chamber. To suppress contamination from plastic materials, the gas piping is made from stainless steel, and all chamber seals and most gas seals are metal (gold-coated to render them chemically inert). To compensate for sampling losses, there is a continuous flow of fresh gases into the chamber of 85 l min<sup>-1</sup>, resulting in a dilution lifetime of 5 h.

The chamber can be exposed to a 3.5 GeV/c secondary π<sup>+</sup> beam from the CERN Proton Synchrotron, spanning the galactic cosmic-ray intensity range from ground level to the stratosphere. The beam is defocused to a transverse size of about 1.5 × 1.5 m<sup>2</sup> at the chamber. The horizontal and vertical beam profiles and rates are measured with a plastic scintillator hodoscope. An ionization-counter array, located nearby but outside the beam region, monitors the ambient flux and angular distribution of galactic cosmic rays. Two stainless steel fans are mounted inside the chamber, and coupled magnetically to flexible drives connected to motors located outside the thermal housing. The fans produce a counter-flow inside the chamber, to rapidly mix the fresh gases and the ions generated by the pion beam, and ensure good uniformity. To study neutral nucleation, the beam is turned off and an internal electric field of up to 20 kV m<sup>-1</sup> is applied by means of two transparent field cage electrodes. This rapidly (in about 1 s) sweeps out the background ions produced by galactic cosmic rays. The electrodes are supported on partly conducting ceramic insulators to eliminate surface charges and stray electric fields when the high voltage is set to zero.

The contents of the chamber are continuously analysed by instruments connected to sampling probes that project 0.5 m into the chamber. The chamber instrumentation for the results reported here comprise a chemical ionization mass spectrometer (CIMS) for H<sub>2</sub>SO<sub>4</sub> concentration, an atmospheric pressure interface time-of-flight (Api-TOF) mass spectrometer for molecular composition of positive and negative ions up to 2,000 Th (thomson units; 1 Th = 1 Da/e)<sup>35</sup>, a condensation particle counter (CPC) battery at 2.5–12-nm thresholds (mobility diameters), a di-ethylene glycol CPC (DEG-CPC) at 2.0 nm threshold<sup>36</sup>, a scanning particle size magnifier (PSM) in the threshold range 1.3–2 nm<sup>37</sup>, a radial differential mobility analyser (rDMA) in the size range 2–10 nm<sup>38</sup>, a scanning mobility particle sizer (SMPS) in the size range about 10–100 nm, a neutral cluster and air ion spectrometer (NAIS)<sup>39</sup>, a small-ion counter (Gerden counter), trace gas analysers (O<sub>3</sub> and SO<sub>2</sub>), a proton transfer reaction time-of-flight (PTR-TOF) mass spectrometer for organic vapour concentrations<sup>40</sup>, two instruments for NH<sub>3</sub> measurements (a long-path absorption photometer (LOPAP) and a proton transfer reaction mass spectrometer (PTR-MS)<sup>41</sup>), and instruments to measure chamber conditions (dewpoint, ultraviolet intensity, temperature and pressure). A central data acquisition (DAQ) system controls the operating conditions of the experiment, collects and backs up the data from the instruments, provides multi-user access for monitoring the performance of the instruments and chamber, and provides real-time physics analysis using the combined data from multiple instruments.

The Api-TOF<sup>35</sup> measures the ion cluster mass spectra in the chamber. Chemical species are identified from their exact mass signatures and isotopic fractions.

Owing to the high mass resolution ( $\Delta m/m = 3 \times 10^{-4}$ ) and accuracy ( $\delta m/m < 2 \times 10^{-5}$ ) of this instrument, unambiguous identification of the constituent chemical species is achieved for almost all charged clusters up to a mass/charge limit of 2,000 Th. This excludes water molecules, which are lost by collisional dissociation or rapid evaporation from the sulphuric acid clusters on entering the vacuum of the instrument. Previous measurements have established that water molecules are indeed present in these charged clusters<sup>42</sup>. In contrast, the evaporation of ammonia and amine molecules from acid clusters in the Api-TOF is thought to be small. This is supported by the sharp cluster maxima seen in Fig. 3d.

Examples of raw Api-TOF spectra during nucleation events without additional NH<sub>3</sub> at 292 K are shown in Supplementary Fig. 3. The negative-ion spectrum shows strong peaks corresponding to the charged monomer, dimer and trimer of sulphuric acid ( $A_n^-$ ,  $n = 1$ –3, where A represents H<sub>2</sub>SO<sub>4</sub> or the HSO<sub>4</sub><sup>-</sup> ion); higher sulphuric acid clusters ( $n > 3$ ) are predominantly accompanied by an additional species that is either NH<sub>3</sub>, dimethylamine or ethylamine. In contrast, the positive-ion spectrum shows no evidence for any sulphuric acid molecules, but shows pure water clusters, H<sub>3</sub>O<sup>+</sup>(H<sub>2</sub>O)<sub>*n*</sub>,  $n \leq 3$ , and a broad range of organic compounds, of which strong lines are usually produced by protonated pyridine (C<sub>5</sub>H<sub>5</sub>N.H<sup>+</sup>), urea (CH<sub>4</sub>N<sub>2</sub>O.H<sup>+</sup>), dimethylamine and ethylamine (C<sub>2</sub>H<sub>7</sub>N.H<sup>+</sup>), and C<sub>3</sub>H<sub>8</sub>N<sub>2</sub>O.H<sup>+</sup>, which corresponds to dimethylurea or other compounds (mostly amides).

The nucleation rates are obtained from the formation rates,  $dN_d/dt$  (where the subscript *d* refers to the detection threshold diameter of the particle counter), measured with a TSI 3776 CPC (50% detection threshold diameter  $d = 2.5$  nm), DEG-CPC (2.0 nm) and PSM (1.7, 1.9 and 2.1 nm)<sup>43,44</sup>. The nucleation rates are determined at the critical size (taken to be 1,200 Da, or about 1.7 nm mobility diameter) from measurements made with particle counters at thresholds between 2 and 2.5 nm, because the PSM was not available for the entire campaign. To determine the nucleation rates, the measured formation rates are corrected for losses between 1.7 nm and the detection size threshold. This requires experimental measurements of the wall loss rates and particle growth rates. Other losses, such as coagulation and dilution losses are also accounted for, but are negligible. The corrections are calculated with a kinetic model (AeroCLOUD) and are cross-checked analytically<sup>43,44</sup>. The nucleation rates are independently verified by direct measurements with the PSM at 1.7 nm threshold, where available.

Neutral nucleation rates are measured with zero beam and with the field cage electrodes set to ±30 kV. This completely suppresses ion-induced nucleation because, under these conditions, small ions are swept from the chamber in about 1 s. For ion-induced nucleation to produce a critical cluster that is not removed by the electric field, the primary negative ion from a traversing ionizing particle must, within 1 s, reach an H<sub>2</sub>SO<sub>4</sub> molecule, which grows beyond the critical size and is then neutralized by ion-ion recombination before reaching an electrode or the chamber wall. In the presence of the electric field, the recombination lifetime alone is estimated to exceed  $5 \times 10^4$  s, so ion-induced nucleation can be completely excluded as a background to the measured neutral nucleation rates.

The error on *J* has three components, which are added together in quadrature to provide the total error indicated in Fig. 1: first, a statistical measurement error derived from the scatter of the particle counter measurements, evaluated separately for each nucleation event; second, an estimated ±50% uncertainty on the modelled correction factor,  $J_{1.7}/J_d$ , where  $J_d$  is the nucleation rate at size *d*, obtained after correcting  $dN_d/dt$  for detection losses, and third, an estimated ±30% systematic uncertainty on  $J_d$  estimated from the run-to-run reproducibility of  $dN_d/dt$  under nominally identical chamber conditions.

When the chamber is operated below 292 K, the particle counters and certain other detectors are cooled to about 280 K to minimize cluster evaporation on entering the warm instrument from a cold chamber and sampling probe. However, we caution that the measurements presented here at low temperatures are subject to uncorrected evaporation effects due to relatively warm instruments.

The overall experimental uncertainty on [H<sub>2</sub>SO<sub>4</sub>] measured by the CIMS is estimated to be −50%/+100%, on the basis of three independent measurements: particle growth rate, the depletion rate of [SO<sub>2</sub>] by photo-oxidation, and an external calibration source. However, the run-to-run relative experimental uncertainty on [H<sub>2</sub>SO<sub>4</sub>] is smaller, typically ±10%. The concentrations of SO<sub>2</sub>, O<sub>3</sub> are measured with calibrated instruments and are known to ±10%. The overall uncertainty on the NH<sub>3</sub> mixing ratio is estimated to be −50%/+100%. Ammonia mixing ratios are measured with a PTR-MS and LOPAP. Although the former is more sensitive (5 p.p.t.v. lower detection limit compared with 35 p.p.t.v. for the LOPAP), the sampling probe of the LOPAP has a higher efficiency, resulting in a higher overall sensitivity for the LOPAP. Because liquid water

is used in its sampling probe, the LOPAP only provides measurements above 273 K.

34. Duplissy, J. *et al.* Results from the CERN pilot CLOUD experiment. *Atmos. Chem. Phys.* **10**, 1635–1647 (2010).
35. Junninen, H. *et al.* A high-resolution mass spectrometer to measure atmospheric ion composition. *Atmos. Meas. Tech.* **3**, 1039–1053 (2010).
36. Iida, K., Stolzenburg, M. R. & McMurry, P. H. Effect of working fluid on sub-2 nm particle detection with a laminar flow ultrafine condensation particle counter. *Aerosol Sci. Technol.* **43**, 81–96 (2009).
37. Vanhanen, J. *et al.* Particle size magnifier for nano-CN detection. *Aerosol Sci. Technol.* **45**, 533–542 (2011).
38. Brunelli, N. A., Flagan, R. C. & Giapis, K. P. Radial differential mobility analyzer for one nanometer particle classification. *Aerosol Sci. Technol.* **43**, 53–59 (2009).
39. Kulmala, M. *et al.* Towards direct measurement of atmospheric nucleation. *Science* **318**, 89–92 (2007).
40. Graus, M., Müller, M. & Hansel, A. High resolution PTR-TOF: quantification and formula confirmation of VOC in real time. *J. Am. Soc. Mass Spectrom.* **21**, 1037–1044 (2010).
41. Norman, M., Hansel, A. & Wisthaler, A.  $O_2^+$  as reagent ion in the PTR-MS instrument: detection of gas-phase ammonia. *Int. J. Mass Spectrom.* **265**, 382–387 (2007).
42. Froyd, K. D. & Lovejoy, E. R. Experimental thermodynamics of cluster ions composed of  $H_2SO_4$  and  $H_2O$ . 2. Measurements and *ab initio* structures of negative ions. *J. Phys. Chem. A* **107**, 9812–9824 (2003).
43. Kerminen, V.-M. & Kulmala, M. Analytical formulae connecting the ‘real’ and the ‘apparent’ nucleation rate and the nuclei number concentration for atmospheric nucleation events. *J. Aerosol Sci.* **33**, 609–622 (2002).
44. Kulmala, M. & Kerminen, V.-M. On the formation and growth of atmospheric nanoparticles. *Atmos. Res.* **90**, 132–150 (2008).



# A young source for the Hawaiian plume

Alexander V. Sobolev<sup>1,2,3</sup>, Albrecht W. Hofmann<sup>2,4</sup>, Klaus Peter Jochum<sup>2</sup>, Dmitry V. Kuzmin<sup>2,5</sup> & Brigitte Stoll<sup>2</sup>

Recycling of oceanic crust through subduction, mantle upwelling, and remelting in mantle plumes is a widely accepted mechanism to explain ocean island volcanism<sup>1</sup>. The timescale of this recycling is important to our understanding of mantle circulation rates. Correlations of uraniumogenic lead isotopes in lavas from ocean islands such as Hawaii or Iceland, when interpreted as model isochrons, have yielded source differentiation ages between 1 and 2.5 billion years (Gyr)<sup>2–5</sup>. However, if such correlations are produced by mixing of unrelated mantle components<sup>6</sup> they will have no direct age significance. Re–Os decay model ages take into account the mixing of sources with different histories<sup>7,8</sup>, but they depend on the assumed initial Re/Os ratio of the subducted crust, which is poorly constrained because of the high mobility of rhenium during subduction<sup>9</sup>. Here we report the first data on <sup>87</sup>Sr/<sup>86</sup>Sr ratios for 138 melt inclusions in olivine phenocrysts from lavas of Mauna Loa shield volcano, Hawaii, indicating enormous mantle source heterogeneity. We show that highly radiogenic strontium in severely rubidium-depleted melt inclusions matches the isotopic composition of 200–650-Myr-old sea water. We infer that such sea water must have contaminated the Mauna Loa source rock, before subduction, imparting a unique ‘time stamp’ on this source. Small amounts of seawater-derived strontium in plume sources may be common but can be identified clearly only in ultra-depleted melts originating from generally highly (incompatible-element) depleted source components. The presence of 200–650-Myr-old oceanic crust in the source of Hawaiian lavas implies a timescale of general mantle circulation with an average rate of about 2 (±1) cm yr<sup>–1</sup>, much faster than previously thought.

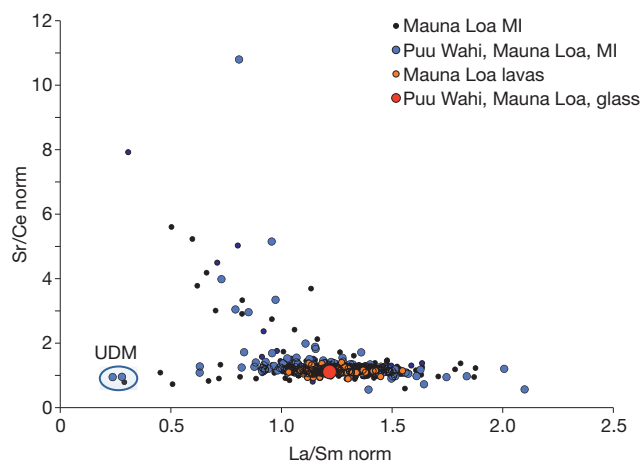


**Figure 1** | Compositions of lavas and melt inclusions in olivine phenocrysts from recent (younger than 50 kyr) eruptions of Mauna Loa volcano, Hawaii. Data for Puu Wahi lava and melt inclusions (MI) are from this study; other melt inclusions are from ref. 13 and unpublished data of A.V.S. UDM inclusions are outlined. Compositions of Mauna Loa lavas are from the GEOROC database (<http://georoc.mpch-mainz.gwdg.de/georoc/>). All ratios are normalized to primitive mantle<sup>31</sup>.

Melt inclusions in highly magnesian olivine are commonly used as proxies for parental melts<sup>10</sup>. In addition, melt inclusions provide unique information on the isotope heterogeneity of the mantle sources of ocean island basalts<sup>11,12</sup>. Compositions of melt inclusions in olivine (Supplementary Figs 1 and 2) from lavas of the largest Hawaiian shield volcano, Mauna Loa, vary considerably<sup>13</sup> (Fig. 1). Both La/Sm and Sr/Ce ratios of melt inclusions have very large (tenfold) variations, and this heterogeneity is much greater than those displayed by Mauna Loa bulk lava compositions. About 2–3% of melt inclusions are strongly depleted in the highly incompatible elements Th, U, Ba, Rb, K, Sr, Nb, Ta, Cl, B, Pb, S, Zr, Hf and the light rare-earth elements (Figs 1 and 2 and Supplementary Table 2). Here we will call these inclusions ‘ultra-depleted melts’ (UDMs). In contrast with typical Mauna Loa melts, UDMs are also slightly depleted in the moderately incompatible elements Ti, Nd, Sm and Al and are enriched in SiO<sub>2</sub>, but are similar in contents of heavy rare-earth elements, Y, Sc and Ca (Fig. 2, Supplementary Fig. 3 and Supplementary Table 2). Strontium is significantly depleted relative to Pr, Nd and Sm. UDM inclusions have been reported in association with ‘normal’ inclusions in the same olivine grains<sup>13</sup>. In such an association, inclusions of mixed composition are commonly present. Mauna Loa UDMs have been interpreted<sup>13</sup> as instantaneous melts produced by near-fractional melting of Hawaiian source by a process that is similar to that described for mid-ocean-ridge UDM<sup>14</sup>. The isotope data presented here disprove this interpretation, showing that these UDMs also have significantly different source compositions from those of other parental melts.

Strontium and lead isotopic compositions of melt inclusions in olivine phenocrysts from a single Mauna Loa lava (see Supplementary Figs 1 and 2 for inclusion images) were measured by laser ablation inductively coupled plasma mass spectrometry (LA-ICP-MS; see

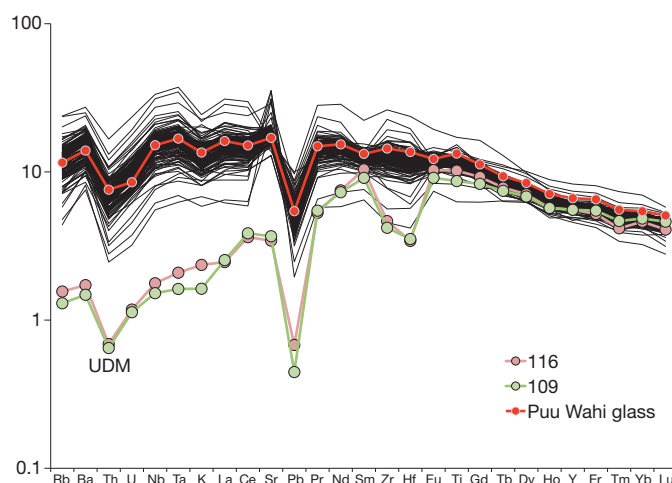


**Figure 2** | Primitive mantle<sup>31</sup> normalized concentrations of incompatible elements in melt inclusions in euhedral olivine crystals from a single sample (K97-15b) of Puu Wahi scoria cone, Mauna Loa, Hawaii. Ultra-depleted melt inclusions are labelled UDM.

<sup>1</sup>ISTerre, University Joseph Fourier, Grenoble 1 and CNRS, BP 53, 38041 Grenoble, France. <sup>2</sup>Max Planck Institute for Chemistry, Postfach 3060, 55020 Mainz, Germany. <sup>3</sup>V. I. Vernadsky Institute of Geochemistry and Analytical Chemistry, Russian Academy of Sciences, Moscow 119991, Russia. <sup>4</sup>Lamont Doherty Earth Observatory, Palisades, New York 10964, USA. <sup>5</sup>V. S. Sobolev Institute of Geology and Mineralogy, Siberian Branch of Russian Academy of Sciences, Novosibirsk 630090, Russia.

Methods for sample description and analytical details). In total, 138 inclusions were analysed for Sr isotopes, and 106 inclusions for Pb isotopes. Both Sr and Pb isotopic compositions of melt inclusions vary markedly, much more than in Hawaiian lavas overall. But their averages are nevertheless similar in compositions to those of matrix glass and of typical recent Mauna Loa lavas (Fig. 3). The range of variation is markedly higher for melt inclusions trapped in the most magnesian olivines (Supplementary Fig. 4). This is consistent with the interpretation that melt inclusions in early-formed olivine phenocrysts yield information on the compositions of unmixed parental melts, whereas lavas and inclusions in more evolved olivines are mixtures of these melts<sup>10,13</sup>. Clear evidence of such mixing is presented by the most radiogenic melt inclusions with  $^{87}\text{Sr}/^{86}\text{Sr} > 0.7060$ . These inclusions consistently fit mixing trajectories for almost all incompatible elements and Sr isotopes, thus strengthening confidence in the reliability of the isotope data (Supplementary Fig. 5). UDMs represent the endmember of such mixing combining highly radiogenic Sr ( $^{87}\text{Sr}/^{86}\text{Sr} = 0.7081 \pm 0.0006$ ,  $2\sigma$ ), much higher than the value of typical Mauna Loa melts ( $^{87}\text{Sr}/^{86}\text{Sr} \approx 0.7038$ ), with Rb/Sr ratios (0.010–0.013) that are unusually low for Mauna Loa (Fig. 3a). Lead isotope compositions of UDMs are also significantly more radiogenic than those of typical Mauna Loa melts (Fig. 3b; note that the lowest  $^{207}\text{Pb}/^{206}\text{Pb}$  ratios correspond to the most radiogenic Pb). These data clearly suggest that the UDMs could not have been produced from any typical Mauna Loa source by any melting process. Instead, the source rock must contain a component with highly radiogenic Sr and Pb, but must at the same time be strongly depleted in incompatible elements. Alternatively, this component might have been introduced by some type of contamination of the primary melt. Next we discuss possible sources.

Before presenting our preferred interpretation, namely source contamination by ancient sea water before subduction, we discuss alternative explanations. In general, the highly radiogenic Sr of Mauna Loa UDMs might be explained by one of the following processes, all of which have significant drawbacks.

First, direct input of recycled continental crust could in principle explain highly radiogenic Sr, but this is completely inconsistent with the extremely low concentrations of Rb, Ba, K, U and Pb, as well as their high Ce/Pb (50–80) and Nb/U (41–46) ratios<sup>15</sup>.

Second, continental Sr might be transferred to the mantle source during subduction more indirectly by the percolation of crustal fluids without necessarily causing trace-element enrichment, if the mantle lithology is a depleted harzburgite containing no clinopyroxene. This process requires that, in addition to Sr, all other incompatible elements including Sc, Ca and Al in UDMs come from a clinopyroxene-free harzburgite source. However, this contradicts the relatively high contents of moderately incompatible elements (Ti, Al, Ca and rare-earth elements heavier than Sm) in UDMs that are similar to those of typical Mauna Loa melts (Fig. 2 and Supplementary Fig. 3), because harzburgites are typically depleted in all these elements. Additional observations that are very difficult to reconcile with any continental source, even in a markedly 'fractionated' form, are as follows: the very low Pb concentrations and high Ce/Pb ratios, as well as high Nb/U and Nb/Th ratios, are the opposite of what would be expected from a metasomatic (fluid) transfer of a sedimentary signature from a subducted slab or from recycled sediments (see Supplementary Information); and other ratios of trace elements of similar incompatibility (Ba, Rb, Th, U and Nb) are similar (though not identical) to those of oceanic basalts, in particular Hawaiian basalts, but quite different from those of continental materials.

Third, the radiogenic Sr might be derived directly or indirectly from modern sea water. Producing UDM by contamination with typical Mauna Loa melt is highly unlikely because such a contamination process cannot result in tenfold lower concentrations of most incompatible elements. Seawater assimilation would be somewhat more plausible if it affected the original, highly depleted melt (rather than normal Mauna Loa melt). Perhaps the most efficient mechanism for this would be the assimilation of recent aragonitic carbonate containing a high concentration of radiogenic Sr and depleted in all incompatible elements<sup>16</sup>. This process could add radiogenic Sr without significantly changing most of the incompatible-element budget of the melt. However, it would also increase Sr and Ca concentrations considerably. For example, a typical Mauna Loa melt with  $^{87}\text{Sr}/^{86}\text{Sr} = 0.7040$  would require the assimilation of about 5% high-Sr carbonate to match the isotopic composition of UDM. This would result in a sixfold increase in Sr concentration of UDM if the carbonate contaminant contained 1,000 p.p.m. Sr, with  $^{87}\text{Sr}/^{86}\text{Sr} = 0.7090$ . This implies an unreasonably

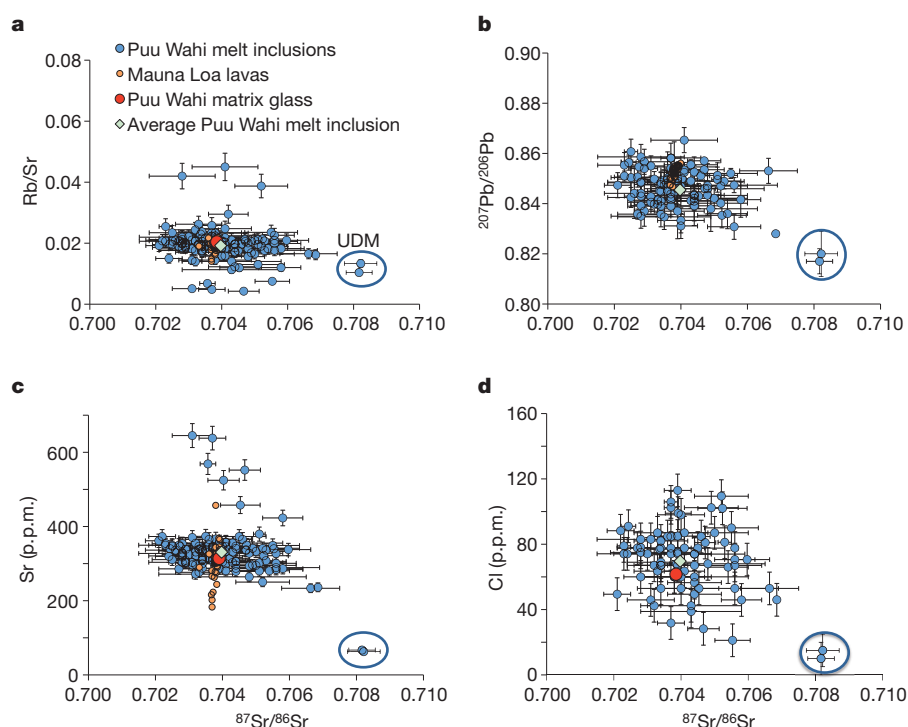


**Figure 3** |  $^{87}\text{Sr}/^{86}\text{Sr}$  ratios in melt inclusions and matrix glass in euhedral olivine crystals of sample (K97-15b), Puu Wahi scoria cone, Mauna Loa, Hawaii. **a–d**,  $^{87}\text{Sr}/^{86}\text{Sr}$  ratios are plotted against Rb/Sr (**a**),  $^{207}\text{Pb}/^{206}\text{Pb}$  (**b**), Sr (**c**) and Cl (**d**). Compositions of bulk Mauna Loa lavas from the GEOROC database are shown (in orange) for comparison. The compositions of average UDM inclusions are outlined. Error bars indicate s.e.m.



large negative Sr anomaly (half the primitive mantle value of Sr) in the initial, uncontaminated melt. Also, this process must increase the CaO content of the UDMs by at least 1.5 wt%, which is not observed (see Supplementary Fig. 3). Alternatively, seawater Sr might enter the melt by assimilation of highly altered ocean crust (including sediment). This could explain highly radiogenic Sr (Fig. 4) and low concentrations of incompatible elements, as well as more radiogenic Pb<sup>17</sup>. However, this should also incorporate other seawater-specific components, particularly B, Cl and K, because these elements are strongly enriched in altered crust<sup>18</sup>. But this is inconsistent with the extremely low concentrations of Cl (10–15 p.p.m.), B (0.3–0.4 p.p.m.) and K<sub>2</sub>O (0.05–0.07 wt%) in the UDMs (Fig. 3d and Supplementary Table 2). Even if one assumes that these volatile elements were extracted from the assimilated crustal rocks by previous high-temperature metamorphism, this process still seems unlikely. To raise the originally low <sup>87</sup>Sr/<sup>86</sup>Sr ratio of the melt to the highly radiogenic value observed, the amount of such assimilated material would have to be large. Such extensive assimilation would also affect concentrations of Ca, the heavy rare-earth elements, Y and Sc, all of which are relatively high and very similar in UDMs and typical Mauna Loa lavas (Fig. 2, Supplementary Fig. 3 and Supplementary Table 2). Alumina is slightly depleted in UDMs in comparison with Mauna Loa melts (Supplementary Fig. 3), and this also precludes the assimilation of any plagioclase-saturated, high-Al rocks, typical of oceanic crust. Similarly, we can rule out the assimilation of seawater-altered Hawaiian lavas, because of their high incompatible-element enrichment.

Reaction with altered harzburgites and their partial melting may also deliver highly radiogenic modern seawater Sr to depleted Mauna Loa

melt. But this process will also affect concentrations of Ni, Mn and Fe, which is not the case (Supplementary Fig. 8).

An additional argument against contamination by the present-day lithosphere beneath Hawaii is derived from the fact that this lithosphere is slightly more than 90 Myr old. At the time that it was created, sea water had a <sup>87</sup>Sr/<sup>86</sup>Sr ratio of 0.7074 or less (ref. 19), just below the lower limit of UDM Sr (Fig. 4). Because seawater Sr is introduced into the altered crust almost entirely during the first 3 Myr after crust formation<sup>20</sup>, it is highly unlikely that Sr contamination derived from 90-Myr-old lithosphere can account for the observed composition (<sup>87</sup>Sr/<sup>86</sup>Sr ≥ 0.7075) of the UDMs.

Because none of the above processes provides a satisfactory explanation for the presence of highly radiogenic Sr and Pb in the UDM, we suggest that the radiogenic Sr was introduced through direct or indirect contamination by ancient sea water before subduction and recycling. In this case, other indicators of sea water or seawater alteration, K, B and Cl, should easily be removed from the system by mobilization during subduction<sup>21</sup>. In addition, Ca, Al, rare-earth elements, Sc and Y in the melt would be constrained by the mineralogy of the mantle residue, specifically by the presence of garnet and high-Ca pyroxene. However, Sr in ancient sea water was, during most of Earth's history, much less radiogenic than Sr in the UDMs, except for one specific time window, namely the period between 200 and 550 Myr ago<sup>19,22</sup> (Fig. 4). According to other estimates<sup>23</sup> this period may be extended at maximum to 650 Myr. Therefore, if the effect is indeed caused by recycled seawater Sr, this sea water is unlikely to be older than 650 Myr old.

We propose that Mauna Loa UDMs reveal one of the recycled end-member compositions similar to ultra-depleted mid-ocean-ridge basalt (MORB)<sup>14</sup> or gabbros<sup>24</sup> with Sr extensively exchanged with, and dominated by, seawater Sr because of its initially low content (see model in Methods). This explanation is also consistent with the strong negative Zr anomaly in Mauna Loa UDMs, which is a common feature of ultra-depleted MORB as well<sup>14</sup>. Highly depleted gabbro-norites crystallized from remelted material of this kind possessing <sup>87</sup>Sr/<sup>86</sup>Sr up to ~0.708 have been reported in oceanic crust exposed in the Oman ophiolite<sup>25</sup>. The Sr isotopes of the other recycled rocks (typical gabbros or normal MORBs) indicated by the compositions of melt inclusions (Fig. 3) were less affected by seawater alteration because of their higher Sr contents and/or different positions in the crust<sup>18</sup>. The Sr-rich component of Mauna Loa lavas is particularly unradiogenic (<sup>87</sup>Sr/<sup>86</sup>Sr < 0.7030; see Fig. 3c), in agreement with its origin from recycled oceanic plagioclase-cumulate gabbros<sup>13</sup>. Alternatively, seawater Sr might be introduced into the subduction 'package' by means of serpentinites or carbonate veins that are ubiquitous in the oceanic crust. Particularly when precipitated at low temperatures, they preserve the Sr isotopic composition of sea water<sup>16</sup>. We further suggest that all these recycled materials have been processed during subduction to remove most of the additional Cl, B, Rb and K introduced by sea water.

Previous estimates of recycling times in mantle plumes have mostly relied on Pb isotopes. If an initially homogeneous source is differentiated (for example, by melting) into subsystems with variable U/Pb ratios, these subsystems evolve to a linear isochron in <sup>207</sup>Pb/<sup>204</sup>Pb–<sup>206</sup>Pb/<sup>204</sup>Pb space. Such linearly correlated Pb isotopes are widespread in oceanic basalts and have frequently been interpreted as isochrons corresponding to recycling ages ranging from 1.0 to 2.5 Gyr (ref. 2). However, they might also simply represent mixing lines between unrelated reservoirs<sup>6</sup>. It has been pointed out<sup>26</sup> that the isochron interpretation fails when Th/U ratios inferred from the slope of <sup>208</sup>Pb/<sup>204</sup>Pb–<sup>206</sup>Pb/<sup>204</sup>Pb correlations are inconsistent with observed Th/U ratios in the rocks, and it was concluded that the Pb isotope correlations for Mauna Kea must represent mixing lines rather than isochrons.

All Mauna Loa olivine phenocrysts possess Ni excess and Mn deficiencies, which suggests the involvement of melts from olivine-free reaction pyroxenite and peridotite sources in proportions of about

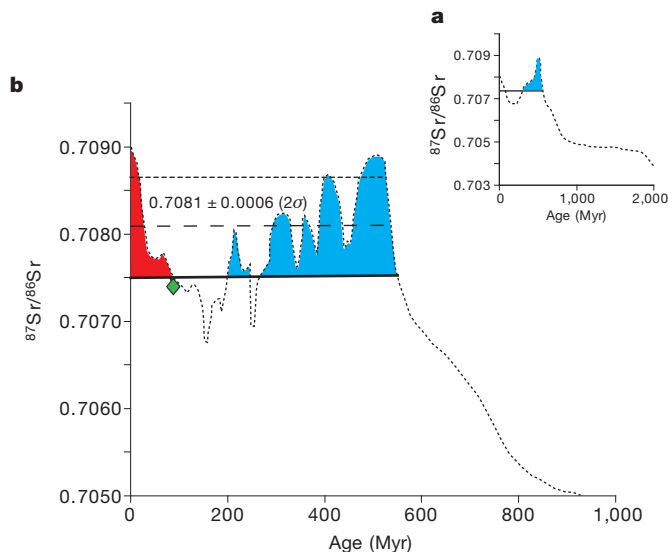


**Figure 4** | <sup>87</sup>Sr/<sup>86</sup>Sr ratios of the two most radiogenic Mauna Loa melt inclusions superimposed on the time evolution of Sr isotopic composition of sea water. **a**, Seawater evolution for the past 2 Gyr (ref. 22). **b**, Detailed Sr evolution for the past 1 Gyr (refs 19, 22). The green diamond indicates seawater composition at 90 Myr (ref. 19) corresponding to the age of lithosphere under the Big Island, Hawaii. The horizontal dashed line represents the pooled average <sup>87</sup>Sr/<sup>86</sup>Sr ratio of 21 analyses of two UDM inclusions. The dotted line and heavy black line indicate the upper and lower limits of range of two standard errors of the average <sup>87</sup>Sr/<sup>86</sup>Sr, respectively. We suggest that the radiogenic Sr in UDMs is derived from ancient sea water in the Mauna Loa source (see the text). The blue field represents the acceptable age range for the recycled seawater component. We reject ages marked by the red field because we have ruled out recent seawater contamination (see the text). We consider the lower limit of the shown range (<sup>87</sup>Sr/<sup>86</sup>Sr = 0.7075, indicated on both panels) to be a minimum estimate for the composition of the seawater component in the Mauna Loa source, because its isotopic composition must have been diluted by less radiogenic components from the original unaltered basalt and source peridotite. The most likely age of recycled seawater Sr is in the range 200–550 Myr, but it may be extended to 650 Myr (ref. 23).

60:40, respectively<sup>27,28</sup> (Supplementary information). From one-half to two-thirds of this reaction pyroxenite is derived from high-silica melt from recycled crust in the form of eclogite, with the other part being peridotite<sup>27</sup>. In total this yields 60–70% peridotite component in the source of Mauna Loa magma. However, because <sup>87</sup>Sr/<sup>86</sup>Sr in the UDMs is nearly at the maximum possible value for sea water<sup>19</sup>, this implies that most of the Sr, as well as other incompatible elements, came from the recycled crustal component. This leaves very little room for peridotite-derived incompatible elements, and thus requires that the peridotitic component was severely depleted in these elements, including Sr, so that it did not significantly affect the incompatible element budget of the final melt (see Methods and Supplementary Information for the quantitative model). Alternatively, peridotite could be moderately depleted in incompatible elements, but it would contain radiogenic Sr resulting from seawater alteration, and this would represent part of the recycled oceanic lithosphere.

Our interpretation of the UDM compositions implies an age for the recycled component in the Mauna Loa source of between 200–650 Myr, much younger than previously suggested source differentiation ages of deep mantle plumes<sup>2–5,7,8</sup>. Such a young age is consistent with a timescale of general mantle circulation with an average rate of about 1–3 cm yr<sup>−1</sup>, assuming that subducted crust was delivered to the core–mantle boundary at 2,900 km depth, and the Hawaiian plume rises from that depth.

## METHODS SUMMARY

The picritic sample K97-15b from Puu Wahi scoria cone (age 910 yr), Mauna Loa volcano, Hawaii, contains euhedral olivine grains (Fo 89–82) with naturally quenched melt inclusions and matrix glass.

Major and some trace elements in melt inclusions, glass and host olivines were determined by electron probe microanalysis on a Jeol JXA 8200 SuperProbe Electron Probe Microanalyser at the Max Planck Institute for Chemistry (MPIC) Mainz, Germany, with a 2σ relative error of 1–2%. The compositions of olivine and contents of Cl, S, Ni and Cr in inclusions were analysed by following a special procedure that allows precision and accuracy of 20–30 μg g<sup>−1</sup> (2σ error) for Ni, Ca, Mn, Al, Ti, Cr and Co, 0.02 mol% for the forsterite component in olivine<sup>28</sup>, 4 μg g<sup>−1</sup> for Cl and 20 μg g<sup>−1</sup> for S in glass.

LA-ICP-MS was used to determine trace elements in glasses of melt inclusions on an Element-2, Thermo Scientific mass spectrometer with a UP-213 New Wave Research solid-phase laser at MPIC, with a precision and accuracy of about 10–15% (2 relative standard deviations (r.s.d.)). Boron concentrations were measured by secondary-ion mass spectrometry on a Cameca Ims-3f ion probe at MPIC with an accuracy and precision of about 20% (2 r.s.d.).

*In situ* Sr and Pb isotope analyses of melt inclusions were performed at MPIC with the ICP mass spectrometer Thermo Element-2 and the New Wave UP 193 laser ablation system with a precision and accuracy of about 0.02–0.10% (1 r.s.d.) for Sr (new data and ref. 29) and 0.1% <sup>208</sup>Pb/<sup>206</sup>Pb and <sup>207</sup>Pb/<sup>206</sup>Pb (ref. 30) for one-to-three-spot analyses of melt inclusions.

Quantitative modelling suggests that highly radiogenic Sr and the chemical composition of Mauna Loa UDMs can result from recycling, melting and reacting of depleted oceanic crust altered by sea water and depleted mantle peridotite.

**Full Methods** and any associated references are available in the online version of the paper at [www.nature.com/nature](http://www.nature.com/nature).

**Received 31 July 2010; accepted 17 June 2011.**

**Published online 10 August 2011.**

- Hofmann, A. W. & White, W. M. Mantle plumes from ancient oceanic crust. *Earth Planet. Sci. Lett.* **57**, 421–436 (1982).
- Chase, C. G. Oceanic island Pb: two-stage histories and mantle evolution. *Earth Planet. Sci. Lett.* **52**, 277–284 (1981).
- McKenzie, D. *et al.* Source enrichment processes responsible for isotopic anomalies in oceanic island basalts. *Geochim. Cosmochim. Acta* **68**, 2699–2724 (2004).
- Sun, S. S. & Hanson, G. N. Origin of Ross Island basanitoids and limitations upon the heterogeneity of mantle sources for alkali basalts and nephelinites. *Contrib. Mineral. Petrol.* **52**, 77–106 (1975).
- Tatsumoto, M. Isotopic composition of lead in oceanic basalt and its implication to mantle evolution. *Earth Planet. Sci. Lett.* **38**, 63–87 (1978).
- Farnetani, C. G. & Hofmann, A. W. Dynamics and internal structure of a lower mantle plume conduit. *Earth Planet. Sci. Lett.* **282**, 314–322 (2009).
- Brandon, A. D., Graham, D. W., Waight, T. & Gautason, B. <sup>186</sup>Os and <sup>187</sup>Os enrichments and high-<sup>3</sup>He/<sup>4</sup>He sources in the Earth's mantle: evidence from Icelandic picrites. *Geochim. Cosmochim. Acta* **71**, 4570–4591 (2007).

- Sobolev, A. V., Hofmann, A. W., Brüggemann, G., Batanova, V. G. & Kuzmin, D. V. A quantitative link between recycling and osmium isotopes. *Science* **321**, 536 (2008).
- Sun, W. D., Bennett, V. C. & Kamenetsky, V. S. The mechanism of Re enrichment in arc magmas: evidence from Lau Basin basaltic glasses and primitive melt inclusions. *Earth Planet. Sci. Lett.* **222**, 101–114 (2004).
- Sobolev, A. V. Melt inclusions in minerals as a source of principal petrological information. *Petrology* **4**, 209–220 (1996).
- Saal, A. E., Hart, S. R., Shimizu, N., Hauri, E. H. & Layne, G. D. Pb isotopic variability in melt inclusions from oceanic island basalts, Polynesia. *Science* **282**, 1481–1484 (1998).
- Jackson, M. G. & Hart, S. R. Strontium isotopes in melt inclusions from Samoan basalts: implications for heterogeneity in the Samoan plume. *Earth Planet. Sci. Lett.* **245**, 260–277 (2006).
- Sobolev, A. V., Hofmann, A. W. & Nikogosian, I. K. Recycled oceanic crust observed in 'ghost plagioclase' within the source of Mauna Loa lavas. *Nature* **404**, 986–990 (2000).
- Sobolev, A. V. & Shimizu, N. Ultra-depleted primary melt included in an olivine from the Mid-Atlantic Ridge. *Nature* **363**, 151–154 (1993).
- Hofmann, A. W. in *Treatise on Geochemistry* Vol. 2 (eds Holland, H. D. & Turekian, K. K.) 61–101 (Elsevier, 2003).
- Coggon, R. M., Teagle, D. A. H., Smith-Duque, C. E., Alt, J. C. & Cooper, M. J. Reconstructing past seawater Mg/Ca and Sr/Ca from mid-ocean ridge flank calcium carbonate veins. *Science* **327**, 1114–1117 (2010).
- Muinos, S. B. *et al.* New constraints on the Pb and Nd isotopic evolution of NE Atlantic water masses. *Geochim. Geophys. Geosyst.* **9**, Q02007 (2008).
- Staudigel, H., Plank, T., White, W. M. & Schmincke, H. U. in *SUBCON: Subduction from Top to Bottom* Vol. 96 (eds Bebout, G. E. & Kirby, S. H.) 19–38 (American Geophysical Union, 1996).
- Veizer, J. *et al.* Sr-87/Sr-86, delta C-13 and delta O-18 evolution of Phanerozoic seawater. *Chem. Geol.* **161**, 59–88 (1999).
- Staudigel, H., Hart, S. R. & Richardson, S. H. Alteration of the oceanic crust: Processes and timing. *Earth Planet. Sci. Lett.* **52**, 311–327 (1981).
- Marschall, H. R., Altherr, R. & Rupke, L. Squeezing out the slab—modelling the release of Li, Be and B during progressive high-pressure metamorphism. *Chem. Geol.* **239**, 323–335 (2007).
- Shields, G. & Veizer, J. Precambrian marine carbonate isotope database: version 1.1. *Geochim. Geophys. Geosyst.* **3**, 1031 (2002).
- Halverson, G. P., Dudas, F. O., Maloof, A. C. & Bowring, S. A. Evolution of the <sup>87</sup>Sr/<sup>86</sup>Sr composition of Neoproterozoic seawater. *Palaeogeogr. Palaeoclimatol. Palaeoecol.* **256**, 103–129 (2007).
- Ross, K. & Elthon, D. Cumulates from strongly depleted mid-ocean-ridge basalt. *Nature* **365**, 826–829 (1993).
- Benoit, M., Ceuleneer, G. & Polvé, M. The remelting of hydrothermally altered peridotite at mid-ocean ridges by intruding mantle diapirs. *Nature* **402**, 514–518 (1999).
- Abouchami, W., Galer, S. J. G. & Hofmann, A. W. High precision lead isotope systematics of lavas from the Hawaiian Scientific Drilling Project. *Chem. Geol.* **169**, 187–209 (2000).
- Sobolev, A. V., Hofmann, A. W., Sobolev, S. V. & Nikogosian, I. K. An olivine-free mantle source of Hawaiian shield basalts. *Nature* **434**, 590–597 (2005).
- Sobolev, A. V. *et al.* The amount of recycled crust in sources of mantle-derived melts. *Science* **316**, 412–417 (2007).
- Jochum, K. P., Stoll, B., Weis, U., Kuzmin, D. V. & Sobolev, A. V. *In situ* Sr isotopic analysis of low Sr silicates using LA-ICP-MS. *J. Anal. At. Spectrom.* **24**, 1237–1243 (2009).
- Jochum, K. P., Stoll, B., Herwig, K. & Willbold, M. Improvement of *in situ* Pb isotope analysis by LA-ICP-MS using a 193 nm Nd:YAG laser. *J. Anal. At. Spectrom.* **21**, 666–675 (2006).
- McDonough, W. F. & Sun, S. S. The composition of the Earth. *Chem. Geol.* **120**, 223–253 (1995).

**Supplementary Information** is linked to the online version of the paper at [www.nature.com/nature](http://www.nature.com/nature).

**Acknowledgements** We thank A. T. Anderson for providing the Puu-Wahi sample, N. Groschopf for help in managing the electron probe microanalyser, A. Yasevich and O. Kuzmina for sample preparation, and G. Wörner, N. Arndt and F. Holtz for discussions. This study was funded by an Agence Nationale de la Recherche, France, Chair of Excellence grant (ANR-09-CEXC-003-01) to A.V.S. Partial support by a Gauss Professorship in Göttingen University, Germany, the Russian Foundation for Basic Research (09-05-01193a), a Russian President grant for leading Russian scientific schools (HHI-3919.2010.5), and Earth Sciences Department of Russian Academy grants to A.V.S. are also acknowledged. This is Lamont Doherty Earth Observatory contribution 7479.

**Author Contributions** A.V.S. designed the project. A.V.S. and A.W.H. conceived the interpretation and the model and wrote the paper. K.P.J. developed the analytical methods for isotope measurements by LA-ICP-MS. D.V.K. processed samples. D.V.K. and B.S. took the measurements. All authors contributed intellectually to the paper.

**Author Information** Reprints and permissions information is available at [www.nature.com/reprints](http://www.nature.com/reprints). The authors declare no competing financial interests. Readers are welcome to comment on the online version of this article at [www.nature.com/nature](http://www.nature.com/nature). Correspondence and requests for materials should be addressed to A.V.S. (alexander.sobolev@ujf-grenoble.fr).

## METHODS

**Samples.** The sample K97-15b has been collected by Alfred Anderson at Puu Wahi, from a scoria cone of 910-year-old picritic lava situated at about 3,000 m elevation on the northeast rift zone of Mauna Loa volcano, Hawaii. The melt inclusions hosted by euhedral olivine grains (Fo 89–82) of millimetre size were naturally quenched during eruption and formed fresh glass and small (a few volume per cent) low-density shrinkage bubbles (Supplementary Fig. 1).

**Isotope analyses.** *In situ* Sr and Pb isotope analyses of melt inclusions were performed at the Max Planck Institute for Chemistry in 2006, with the ICP mass spectrometer Thermo Element-2 and the New Wave UP 193 laser ablation system (wavelength 193 nm, energy density 4 J cm<sup>-2</sup>, spot sizes 50 µm (Sr) and 75–100 µm (Pb), pulse repetition rate 10 Hz)<sup>29,30</sup>. In addition, Sr was remeasured in October 2010 and February 2011 after improvements of the detection system, to reaffirm and improve the overall reliability of the Sr isotope results.

The precision and accuracy of our LA-ICP-MS method in measuring <sup>87</sup>Sr/<sup>86</sup>Sr ratios was constrained by analysing well-documented reference glasses (see Supplementary Table 1). The external precision of data obtained in 2006 was reported in ref. 29 as the standard deviation (s.d.) of sample measurements and is a strong function of Sr content of glasses (see Supplementary Fig. 6). From this equation (obtained for the reference glasses) one can predict s.d. = 0.0010 for UDMs containing 65 p.p.m. Sr. For the nine individual UDM measurements in 2006 the corresponding predicted standard error of the mean (s.e.m.) is 0.0003. These predicted values are slightly smaller than the actually observed s.d. of 0.0016 and 0.0005 for UDMs. This result is to be expected because reference glasses are significantly larger in all three dimensions than the measured inclusions and generally yield a somewhat larger number of total counts, yielding slightly higher precision.

To substantiate our results and further improve precision we reanalysed (in October 2010) the Sr isotope ratios of 21 melt inclusions, including both UDMs, using a significantly upgraded LA-ICP-MS system providing a combined effect of an improved stability and higher sensitivity. The improvements include a new multiplier system, a new ion detection unit and front-end computer of the ICP mass spectrometer, and new adjustment of the laser including cleaning of the valves and tubing in the laser ablation system. These technical improvements led to a laser fluence that was higher (about 10 J cm<sup>-2</sup> in comparison with about 4 J cm<sup>-2</sup>) and more uniform (decrease to about 2% during 4 h of operation, from about 25% before the improvements), higher counting rates (by about twofold) and lower blanks (for example, for <sup>88</sup>Sr about 70 c.p.s. in comparison with 300 c.p.s.<sup>29</sup>).

The higher precision and accuracy of the new data, for low-Sr samples, is clearly shown by new analyses of the reference glasses (Supplementary Fig. 6 and Supplementary Table 1), performed concurrently with those of the inclusions. Note that all natural reference glasses yield means of measured <sup>87</sup>Sr/<sup>86</sup>Sr ratios within one standard error of the reference value, which proves that the standard error is an appropriate measure of both precision and accuracy. The predicted maximum precision (and accuracy) of <sup>87</sup>Sr/<sup>86</sup>Sr ratios for the new measurements of UDM inclusions, estimated from these data, is s.d. = 0.0004 for an individual measurement and s.e.m. = 0.0001 for the mean of 12 measurements. A significant advance in precision of UDMs and reference glasses with similar low Sr contents is evident from Supplementary Tables 1 and 3. All reanalysed melt inclusions match the older data set very well but with better precision (see Supplementary Fig. 7). The new data for 12 individual measurements of the UDM yield <sup>87</sup>Sr/<sup>86</sup>Sr = 0.7082 ± 0.0006 (two s.e.m.). If we pool the old and the new data, we have 21 measurements yielding a virtually identical mean value of <sup>87</sup>Sr/<sup>86</sup>Sr = 0.7081 ± 0.0006 (two s.e.m.). Although the precision of the new data are somewhat better than that of the older analyses, we use the full data set of 21 analyses because the two data sets, separated by a time gap of four years, show excellent consistency.

**Analysis of major and trace elements.** Major and trace elements were determined by electron probe microanalysis on a Jeol JXA 8200 SuperProbe Electron Probe Microanalyser at MPIC, Mainz, Germany. Major-element abundances in glasses were measured at an accelerating voltage of 15 kV and a beam current of 12 nA with a reference sample of natural basaltic glass USNM111240/52 (VG2)<sup>32</sup> with a relative error of 1–2%. The compositions of olivines and Cl, S, Ni and Cr in glasses were analysed at an accelerating voltage of 20 kV and a beam current of 300 nA, by following a special protocol<sup>28</sup> that allowed 20–30 p.p.m. (2σ error) precision and accuracy for Ni, Ca, Mn, Al, Ti, Cr and Co, and 0.02 mol% for the forsterite component in olivine and 20 p.p.m. for Cl and S in glass.

Trace elements in glasses of melt inclusions were determined by LA-ICP-MS on an Element-2, Thermo Scientific mass spectrometer with a UP-213 New Wave Research solid-phase laser at MPIC, with reference to the KL-2G and NIST 612 standard glasses<sup>33</sup> (see <http://georem.mpch-mainz.gwdg.de>). Ca was used as a reference element. The typical conditions were: laser diameter 60–80 µm, energy density about 7 J cm<sup>-2</sup>, pulse repetition rate 10 Hz and ablation

time 60–80 s. The element abundances were determined with 2σ errors of no more than 5% and 10% for concentrations above 1 p.p.m. and ~0.1 p.p.m., respectively.

Boron content in glasses of melt inclusions was measured by secondary-ion mass spectrometry on a Cameca Ims3F ion microanalyser at MPIC with reference to the KL-2G and NIST 612 standard glasses by following the protocol<sup>10</sup> with a relative error commonly within 10%. The detection limit for B, estimated from <sup>11</sup>B intensity on the host olivine, was below 0.02 p.p.m.

**Modelling.** According to our model, the parental Hawaiian melts are mixtures of melts produced by the melting of olivine-free reaction pyroxenite and peridotite in which the proportion of pyroxenite-derived melt ( $X_{PX}$ ) is estimated from the olivine composition<sup>27,28</sup>. The pyroxenitic source is generated by reaction between high-Si, eclogite-derived melt and peridotite, with the proportion of reactive melt ( $\phi$ ) similar to the original amount of olivine in peridotite<sup>27</sup>. The other variables that constrain the composition of the final melt are: degrees of melting of eclogite ( $F_E$ ) and peridotite ( $F_{PE}$ ), their chemical, isotopic and phase compositions, the degree of melting of pyroxenite ( $F_{PX}$ ), melting reactions, and partition coefficients between melt and crystals. Mass conservation requires the following relations between the contents of bulk Sr, <sup>86</sup>Sr and <sup>87</sup>Sr in the final mantle-derived, primary melt (PM), peridotite (PE) and eclogite (E) for a batch melting process:

$$i_{SrPM} = i_{SrPE} \times \left[ \frac{X_{PX} \times (1 - \phi)}{F_{PX} + (1 - F_{PX}) \times K_{PX}^{Sr}} + \frac{(1 - X_{PX})}{F_{PE} + (1 - F_{PE}) \times K_{PE}^{Sr}} \right] + i_{SrE} \times \frac{\phi \times X_{PX}}{(F_{PX} + (1 - F_{PX}) \times K_{PX}^{Sr}) \times (F_E + (1 - F_E) \times K_E^{Sr})} \quad (1)$$

where  $i = 86$  or  $87$ , nd (bulk Sr)  $K_{PX}^{Sr}$ ,  $K_{PE}^{Sr}$  and  $K_E^{Sr}$  are bulk distribution coefficients for Sr or its isotopes between crystal phases and melt for pyroxenite, peridotite and eclogite, respectively.

$$^{86}Sr_j = \frac{Sr_j}{^{87}Sr_j/^{86}Sr_j + (^{84}Sr_j + ^{86}Sr_j + ^{88}Sr_j)/^{86}Sr_j} \quad (2)$$

where  $j = PM, PE$  or  $E$ , and the ratio of unradiogenic stable isotopes ( $^{84}Sr_j + ^{86}Sr_j + ^{88}Sr_j$ )/ $^{86}Sr_j = 9.43205$ .

Equation (1) for Sr, <sup>87</sup>Sr and <sup>86</sup>Sr and equation (2) for primary melt, eclogite and peridotite give six equations with nine unknowns ( $Sr_{PE}$ , <sup>87</sup>Sr<sub>PE</sub>, <sup>86</sup>Sr<sub>PE</sub>,  $Sr_{PM}$ , <sup>87</sup>Sr<sub>PM</sub>, <sup>86</sup>Sr<sub>PM</sub>,  $Sr_E$ , <sup>87</sup>Sr<sub>E</sub> and <sup>86</sup>Sr<sub>E</sub>). To resolve these equations one needs to constrain three unknowns. The seawater model presented in this paper allows a maximum <sup>87</sup>Sr/<sup>86</sup>Sr ratio of recycled eclogite of 0.7090 (first constraint), while the measured composition of the UDMs requires the minimum <sup>87</sup>Sr/<sup>86</sup>Sr ratio of the final melt to be 0.7075 (second constraint; see Fig. 4). The composition of the UDMs also allows the composition of primary UDM to be estimated by reversing olivine fractionation up to equilibrium with the most magnesian olivine for Mauna Loa (Fo 90.7; ref. 27). This yields  $Sr_{PM} = 51$  p.p.m. Sr in the primary UDM melt (third constraint).

Solving mass balance equations (1) and (2) for the above constraints and using reasonable values of  $\phi$  (0.60–0.65),  $F_E$  (0.5),  $F_{PE}$  (0.10–0.15),  $F_{PX}$  (0.45),  $X_{PX}$  (0.60),  $K_{PX}^{Sr} = 0.05$ ,  $K_{PE}^{Sr} = 0.01$  and  $K_E^{Sr} = 0.15$  (see the discussion on these parameters in ref. 27) gives a relation between contents and isotope composition of Sr in the peridotite component (Supplementary Fig. 9). Assuming a lower limit for the <sup>87</sup>Sr/<sup>86</sup>Sr ratio of peridotite of 0.7021 (extreme depletion) yields a maximum Sr content of peridotite of about 3 p.p.m., which fulfils the conditions stated above. Thus, as expected, the peridotite source should be more depleted in Sr than average depleted MORB mantle with a Sr content of 7.66 p.p.m.<sup>34</sup>. For a lower content or more radiogenic Sr in peridotite, the <sup>87</sup>Sr/<sup>86</sup>Sr in the recycled crust would be lower than 0.7090. It approaches 0.7075 (minimum allowed by the observed UDM composition) when there is no Sr in peridotite or the ratio <sup>87</sup>Sr/<sup>86</sup>Sr in peridotite is 0.7075.

The above model is somewhat oversimplified because it uses a batch melting process and considers fixed melting phase proportions in the form of constant bulk distribution coefficients. To take into account a more realistic, aggregated critical melting process and include changing phase proportions, we further use the conceptually similar but more advanced model with melting reactions and distribution coefficients explained in ref. 27. Using the above estimates for maximum Sr content in peridotite we chose for our quantitative modelling the composition of depleted abyssal harzburgite from the database<sup>35</sup> with a Sr content of 2.73 p.p.m. (model 1), and a restite after 2% of near fractional melting of depleted MORB mantle<sup>34</sup> with a Sr content of 1.96 p.p.m. (model 2). The results of modelling are shown in Supplementary Fig. 10 and Supplementary Table 4.

The composition of recycled crust was calculated to match the trace-element composition and minimum <sup>87</sup>Sr/<sup>86</sup>Sr = 0.7075 ratio of UDM primary melt. For <sup>87</sup>Sr/<sup>86</sup>Sr = 0.7021 of peridotite, the results for recycled crust are <sup>87</sup>Sr/<sup>86</sup>Sr = 0.7086



(model 1) and 0.7083 (model 2). The estimated trace-element compositions of recycled crust correspond to highly depleted oceanic crust and are reasonably close to reported compositions of depleted MORBs<sup>36,37</sup> (Supplementary Fig. 10a). The compositions of peridotites correspond to depleted abyssal harzburgite or depleted lherzolite (Supplementary Fig. 10a). We conclude that the highly radiogenic Sr and the chemical composition of Mauna Loa ultra-depleted melts can be produced by recycling, melting and reacting of depleted oceanic crust altered by sea water and depleted mantle peridotite. This peridotite may be also a part of the recycled oceanic lithosphere.

We further investigate an alternative possibility for the production of highly radiogenic Sr in ultra-depleted melt by the involvement of small amounts of continental sediments with an extremely high  $^{87}\text{Sr}/^{86}\text{Sr}$  ratio. We use the same model as model 1 but for  $^{87}\text{Sr}/^{86}\text{Sr} = 0.7025$  of recycled oceanic crust and variable amounts of sediment with the most extreme  $^{87}\text{Sr}/^{86}\text{Sr} = 0.7349$  (from Sumatra<sup>38</sup>). This yields an amount of 1.6% of such sediment in the recycled component to match  $^{87}\text{Sr}/^{86}\text{Sr} = 0.7075$  of the final melt. However, this substantially increases the concentration of highly incompatible elements such as Th and La of the final melt and significantly lowers its Nb/Th ratio (Supplementary Fig. 10d and Supplementary Table 4). We conclude that recycled continental material, even

with extremely radiogenic Sr, cannot produce the highly incompatible trace-element pattern of Mauna Loa UDMs.

32. Jarosevich, E. J., Nelen, J. A. & Norberg, J. A. Reference sample for electron microprobe analysis. *Geostand. Newsl.* **4**, 43–47 (1980).
33. Jochum, K. P. *et al.* The preparation and preliminary characterization of eight geological MPI-DING reference glasses for in-situ microanalysis. *Geostand. Newsl.* **24**, 87–133 (2000).
34. Workman, R. K. & Hart, S. R. Major and trace element composition of the depleted MORB mantle (DMM). *Earth Planet. Sci. Lett.* **231**, 53–72 (2005).
35. Niu, Y. L. Bulk-rock major and trace element compositions of abyssal peridotites: implications for mantle melting, melt extraction and post-melting processes beneath mid-ocean ridges. *J. Petrol.* **45**, 2423–2458 (2004).
36. Saal, A. E., Hauri, E. H., Langmuir, C. H. & Perfit, M. R. Vapour undersaturation in primitive mid-ocean-ridge basalt and the volatile content of Earth's upper mantle. *Nature* **419**, 451–455 (2002).
37. Bach, W., Peucker-Ehrenbrink, B., Hart, S. R. & Blusztajn, J. S. Geochemistry of hydrothermally altered oceanic crust: DSDP/ODP Hole 504B—implications for seawater–crust exchange budgets and Sr- and Pb-isotopic evolution of the mantle. *Geochem. Geophys. Geosyst.* **4**, doi:10.1029/2002GC000419 (2003).
38. Plank, T. & Langmuir, C. H. The chemical composition of subducting sediment and its consequences for the crust and mantle. *Chem. Geol.* **145**, 325–394 (1998).

# Civil conflicts are associated with the global climate

Solomon M. Hsiang<sup>1†</sup>, Kyle C. Meng<sup>1</sup> & Mark A. Cane<sup>2</sup>

It has been proposed that changes in global climate have been responsible for episodes of widespread violence and even the collapse of civilizations<sup>1,2</sup>. Yet previous studies have not shown that violence can be attributed to the global climate, only that random weather events might be correlated with conflict in some cases<sup>3–7</sup>. Here we directly associate planetary-scale climate changes with global patterns of civil conflict by examining the dominant inter-annual mode of the modern climate<sup>8–10</sup>, the El Niño/Southern Oscillation (ENSO). Historians have argued that ENSO may have driven global patterns of civil conflict in the distant past<sup>11–13</sup>, a hypothesis that we extend to the modern era and test quantitatively. Using data from 1950 to 2004, we show that the probability of new civil conflicts arising throughout the tropics doubles during El Niño years relative to La Niña years. This result, which indicates that ENSO may have had a role in 21% of all civil conflicts since 1950, is the first demonstration that the stability of modern societies relates strongly to the global climate.

The idea that the global climate might influence the peacefulness of societies<sup>1,2,11–13</sup> has motivated a growing body of research. However, much of the support for this idea is anecdotal and the two methodologies dominating quantitative work on this problem have yielded inconclusive results<sup>14</sup>. The first of these approaches correlates multi-century trends in regional climate with trends in wars<sup>15,16</sup>, but such correlations are weak<sup>16</sup> and gradual social changes over multiple centuries confound results. The second approach avoids confounding trends by correlating random changes in local annual temperature or rainfall with local civil conflicts<sup>3–7</sup>, but different statistical assumptions have yielded different results and the notion that random local temperature or rainfall shocks are analogues for global climate changes has been criticized on three grounds: (1) the global climate may affect many interacting environmental variables that influence conflict but are not adequately summarized by averages of local temperature and rainfall; (2) systematic environmental changes that occur on a planetary scale may influence markets, geopolitics or other social systems differently than location-specific weather shocks that are uncorrelated with weather in other locations; (3) predictable changes in climate and unpredictable weather shocks may generate very different social responses, even if they are otherwise identical. To circumvent these concerns, we avoid local proxies for the global climate and instead directly relate global changes in conflict risk to movements in the global climate: specifically, to the rapid annual shifts between El Niño and La Niña phases of ENSO<sup>10</sup>.

ENSO may plausibly influence multiple varieties of conflict, such as riots or genocides; however, we restrict this analysis to organized political violence. We examine the Onset and Duration of Intrastate Conflict data set<sup>17</sup>, which codes a country as experiencing ‘conflict onset’ if more than 25 battle-related deaths occur in a new civil dispute between a government and another organized party over a stated political incompatibility (see Supplementary Methods and Supplementary Table 1 for data details). Following common practice<sup>17,18</sup>, a dispute is new if it has been at least 2 years since that dispute was last active; however, individual countries may experience conflict onset in sequential years if the government has disputes with different opposition groups. We

define annual conflict risk (ACR) in a collection of countries to be the probability that a randomly selected country in the set experiences conflict onset in a given year. Importantly, this ACR measure removes trends due to the growing number of countries<sup>18</sup> (Supplementary Fig. 1).

In an impossible but ideal experiment, we would observe two identical Earths, change the global climate of one and observe whether ACR in the two Earths diverged. In practice, we can approximate this experiment if the one Earth that we do observe randomly shifts back and forth between two different climate states. Such a quasi-experiment is ongoing and is characterized by rapid shifts in the global climate between La Niña and El Niño.

To identify a relation between the global climate and ACR, we compare societies with themselves when they are exposed to different states of the global climate<sup>19</sup>. Heuristically, a society observed during a La Niña is the ‘control’ for that same society observed during an El Niño ‘treatment’. We sharpen this comparison by separating the world into two groups of countries: those whose climate is strongly coupled to ENSO and those weakly affected by ENSO. If climate influences ACR, we expect to observe the larger ENSO signal in the ACR of the former group.

Originating in the tropical Pacific, ENSO influences virtually the entire tropics by radiating waves through the atmosphere, linking climates around the globe through so-called teleconnections<sup>8,9</sup>. During an El Niño event, the continental tropics mostly become warmer and dryer, whereas effects in mid-latitudes are generally smaller and less consistent<sup>9,10</sup>. To capture this, we partition the globe into two groups based on how coupled their climates are to ENSO, separating countries into teleconnected and weakly affected groups (Fig. 1a; see also Methods, Supplementary Figs 2–5 and Methods). We identify teleconnected locations using surface temperature, instead of other variables<sup>8,10</sup>, both for theoretical reasons<sup>9</sup> and because it is less variable with broader spatial coverage. We verify that this partition preserves the well-documented structure of ENSO’s impact on countries’ average surface temperature<sup>9</sup>, precipitation<sup>8</sup>, and agricultural yields and revenues<sup>20</sup> (Supplementary Table 2 and Supplementary Fig. 6). In the analysis that follows, we base our inferences strictly on correlations over time between ENSO and ACR in the teleconnected group. We analyse ACR in the weakly affected group solely to check that there are no confounding global variables that are correlated with ENSO.

The extremes of the ENSO cycle are distinguished by anomalies of cool (La Niña) or warm (El Niño) sea surface temperature (SST) in the eastern equatorial Pacific<sup>8,10</sup>. We index ENSO by NINO3 (Supplementary Fig. 1), the SST anomaly for the grey region in Fig. 1a. Our results are insensitive to using alternative indices (Supplementary Fig. 7), but detecting ENSO impacts requires that we account for the ‘spring barrier’<sup>10</sup> by averaging NINO3 from May to December rather than over the entire calendar year (see Fig. 1b, see also Supplementary Tables 3, 4 and Methods).

We regress the conflict measure ACR on NINO3 for both groups and detect a large and significant increase in ACR associated with warmer NINO3 values only in the teleconnected group (Fig. 2a, b and Supplementary Methods). We build a linear multiple regression

<sup>1</sup>School of International and Public Affairs, Columbia University, New York, New York 10027, USA. <sup>2</sup>Lamont-Doherty Earth Observatory of Columbia University, Palisades, New York 10964, USA. †Present address: Woodrow Wilson School of Public and International Affairs, Princeton University, Princeton, New Jersey 08544, USA.

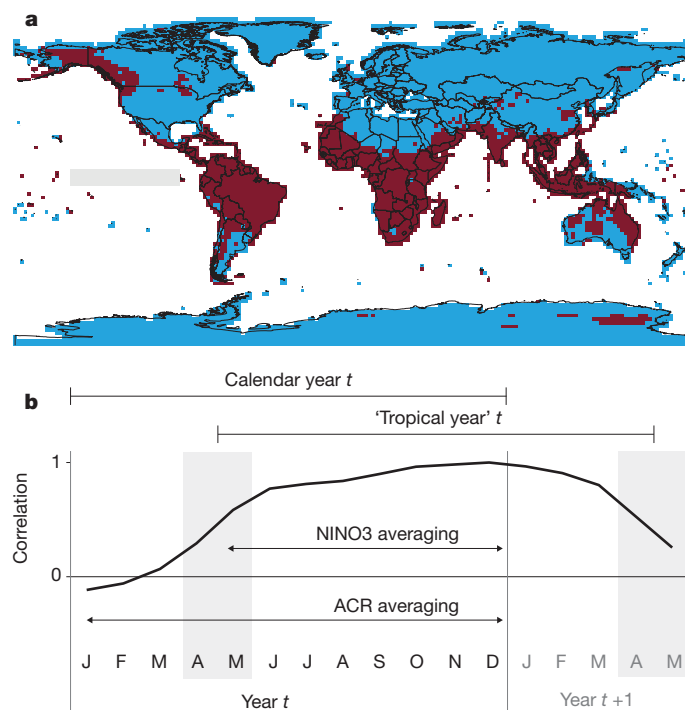


**Figure 1 | ENSO exposure over space and time.** **a**, Red (blue) indicates an ENSO teleconnected (weakly affected) pixel; NINO3 region in grey. **b**, Correlation of monthly NINO3 with NINO3 in December. The natural 'tropical year' begins in May and ends the following April at the 'spring barrier' (grey). To match monthly ENSO data with annual ACR data, an annual ENSO signal is isolated by averaging May–December NINO3.

model by including linear time trends and an additive constant to all years after 1989 (inclusive), a common technique<sup>7</sup> to account for mean shifts in ACR after the end of the Cold War (Table 1, rows 1–3). Using a non-parametric regression, we find that ACR in the teleconnected group is most responsive to strong ENSO events and is less affected by smaller deviations from the neutral state (Fig. 2b).

In the teleconnected group, ACR is 3% in the La Niña state and rises to 6% in the El Niño state, whereas ACR in the weakly affected group remains at 2% for all ENSO states (Fig. 2b). This indicates that ENSO may have affected one-fifth (21%) of all civil conflicts during this period (see Methods).

Because ENSO events occur after the April/May 'spring barrier'<sup>10</sup> (Fig. 1b), we expect conflicts triggered by ENSO to occur in the later part of the calendar year. Figure 2c, based on the subset of conflict data available at monthly resolution, shows the within-year distributions of conflict onsets for the teleconnected group in El Niño and La Niña years. The distributions of conflicts are similar early in the year, with substantial differences appearing only after ENSO events are underway.

The correlation we observe between ACR and NINO3 is robust to the battery of statistical models advanced by previous studies<sup>3,5–7</sup> (Supplementary Methods). To ensure the entrance of new countries into the sample do not drive our result, we restrict our sample to the post-colonial period<sup>5</sup> (Table 1, row 4) and estimate a country-level linear probability model<sup>5,7</sup> (row 5). We limit the sample to exclude African countries (row 6) and find that the correlation is not driven exclusively by Africa<sup>3,5,7</sup>. Further, we find that nonlinear probability models (Supplementary Fig. 8), count models (Supplementary Fig. 9) and survival models (Supplementary Table 5) produce indistinguishable results. We find the relationship persists when alternative ENSO indices are used (Supplementary Table 6). We estimate dynamic-panel and first-difference models (Supplementary Table 7) and find no evidence that patterns of serial correlation in either variable drive our results. We expand our sample to include several influential outlying observations (1946, 1948 and 1989, see Supplementary Fig. 10) and find the

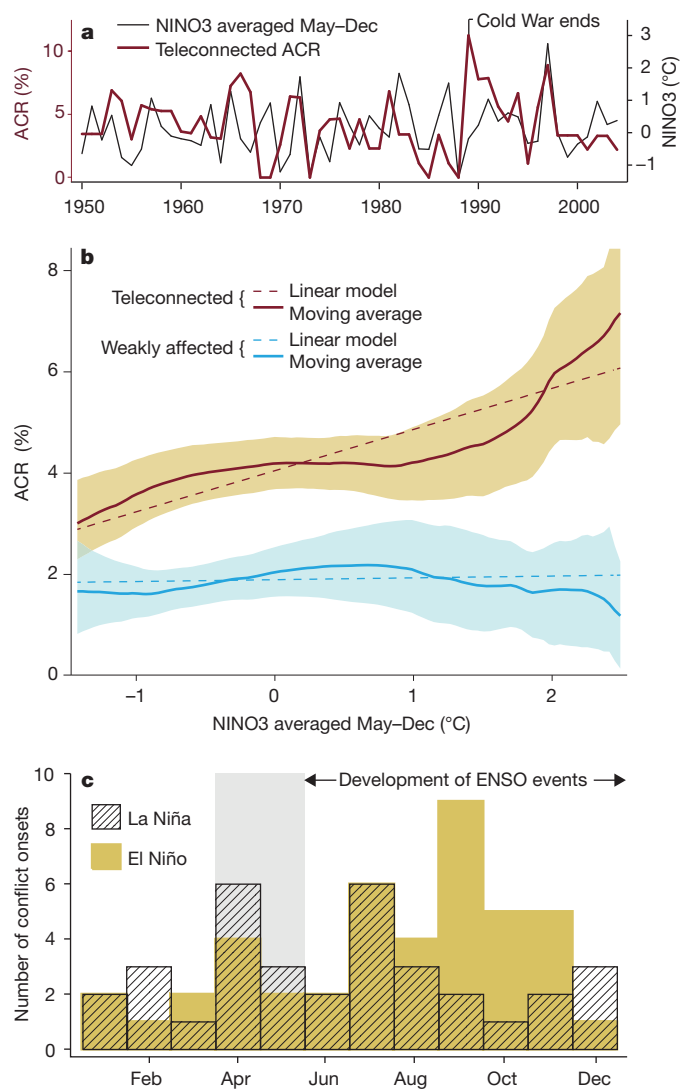


**Figure 2 | Conflict risk associated with ENSO.** **a**, Time series of NINO3 and ACR for the teleconnected group. **b**, Linear and non-parametric fit ( $n = 54$ , weighted moving average, 90% confidence intervals shaded) of ACR against NINO3. Time trends and mean shift after the end of the Cold War are removed. **c**, Solid (hatched) bars show total monthly conflict onsets in teleconnected countries during one-third of years most El-Niño-like (La-Niña-like). Monthly data are available for only half of the conflicts.

correlation persists (Supplementary Table 8). We remove country-specific constants and trends from our longitudinal model<sup>7</sup> and find our estimates unchanged (Supplementary Table 9). When we include controls for contemporaneous temperature and precipitation (Supplementary Table 10) or for lagged income, political institutions and population (Supplementary Table 11; see also Supplementary Fig. 11), we continue to find a large and significant influence of ENSO on ACR. We then estimate a model with all of the above controls, as well as controls for gender balance, urbanization, age-structure, income growth, agricultural reliance and cyclone disasters (Supplementary Table 12 and Supplementary Fig. 12) and find that our results persist across African and non-African countries. Finally, using standard definitions<sup>17</sup>, we find that neither large (more than 1,000 battle deaths) nor small ( $25 < \text{number of battle deaths} < 1,000$ ) conflicts dominate our result (Supplementary Table 13). However, we find that increasing the required peaceful period between conflicts<sup>17</sup> reduces the correlation between ENSO and large conflicts, indicating that many of the large conflicts associated with ENSO are re-occurring conflicts (Supplementary Table 13).



**Table 1 | Regression of ACR on NINO3 averaged May–December 1950–2004**

Model	Teleconnected (% °C <sup>-1</sup> )	Weakly affected (% °C <sup>-1</sup> )
(1) Group aggregate	0.76* (0.39) n = 54	0.16 (0.31) n = 54
(2) Group aggregate Linear trend	0.85** (0.40) n = 54	0.06 (0.30) n = 54
(3) Group aggregate Linear trend Post-1989 constant	0.81** (0.32) n = 54	0.04 (0.31) n = 54
(4) Same as (3) 1975–2004 only†	0.95** (0.34) n = 29	0.33 (0.45) n = 29
(5) Country-level panel Country-specific trends Country-specific constants	0.89** (0.38) n = 3,978	0.04 (0.29) n = 3,400
(6) Same as (5) Non-African countries only	0.84** (0.41) n = 2,084	-0.01 (0.29) n = 3,203

Standard errors in parentheses. 1% °C<sup>-1</sup> means the probability of conflict (ACR) rises 0.01 for each 1 °C in NINO3. 1989 dropped.

\*P < 0.1; \*\*P < 0.05.

† After 1974, the set of countries in the teleconnected group stabilized at 87–91.

El Niño might accelerate the timing of conflicts that would have occurred later. By examining years following ENSO events, we find suggestive but statistically insignificant evidence that approximately 40% of the conflicts associated with ENSO are displaced in time (Supplementary Table 14).

We evaluate the relative sensitivities of different countries by estimating a separate regression for each country ( $i$ ), decomposing ACR into a baseline component ( $\alpha_i$ ) independent of ENSO and a component ( $\beta_i$ ) that varies linearly with NINO3:  $ACR_i(t) = \alpha_i + \beta_i NINO3(t)$  (Supplementary Methods). In the teleconnected group, low-income countries are the most responsive to ENSO (that is,  $\beta$  is larger), whereas similarly low income countries in the weakly affected group do not respond significantly to ENSO (Fig. 3). Note that the dependence of baseline ACR  $\alpha$  on income is statistically indistinguishable between the two groups.

Although we observe that the ACR of low-income countries is most strongly associated with ENSO, we cannot determine if (1) they respond strongly because they are low-income, (2) they are low income because they are sensitive to ENSO, or (3) they are sensitive to ENSO and low income for some third unobservable reason. Hypothesis (1) is supported by evidence that poor countries lack the resources to mitigate the effects of environmental changes<sup>1,21,22</sup>. However, hypothesis (2) is plausible because ENSO existed before the invention of agriculture<sup>10</sup> and conflict induces economic underperformance<sup>3,18</sup>.

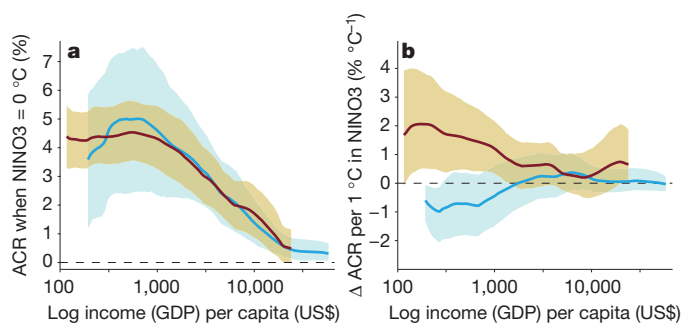


**Figure 3 | ENSO, ACR and income.** For each country  $i$ , we estimate  $ACR_i(t) = \alpha_i + \beta_i NINO3(t)$ . **a**, Baseline ACR ( $\alpha_i$ ) against log income per capita in 2007 (moving average, 90% confidence intervals shaded). Teleconnected (weakly affected) group in red (blue),  $n = 85$  ( $n = 75$ ). **b**, Same, but for the sensitivity of ACR to ENSO ( $\beta_i$ ).

Our results do not provide an estimate for the full value of a global climate state, but we can compare the global climate to income in terms of their individual associations with ACR. In a teleconnected country where average income per capita is US\$1,000 ( $\alpha_i = 4\%$ ,  $\beta_i = 1\% \text{ °C}^{-1}$ ), the 3 °C shift associated with a change from La Niña to El Niño increases ACR by 3% (Fig. 3b). This change has the same magnitude as the 3% drop in baseline ACR that is associated with increasing average income tenfold (Fig. 3a).

Because the strong ENSO events that have the greatest influence on ACR may be predictable up to 2 years in advance<sup>23</sup>, use of our findings may improve global preparedness for some conflicts and their associated humanitarian crises.

We find that the changes in the global climate driven by ENSO are associated with global patterns of conflict, but our results might not generalize to gradual trends in average temperature or particular characteristics of anthropogenic climate change. Generalizing our results to global climate changes other than ENSO will require an understanding of the mechanisms that link conflict to climate. ENSO has a proximate influence on a variety of climatological variables, each of which may plausibly influence how conflict-prone a society is. Precipitation, temperature, sunlight, humidity and ecological extremes can adversely influence both agrarian<sup>20,24</sup> and non-agrarian economies<sup>21,22</sup>. In addition, ENSO variations affect natural disasters, such as tropical cyclones<sup>25</sup>, and trigger disease outbreaks<sup>26</sup>. All of these have adverse economic effects, such as loss of income or increasing food prices, and it is thought that economic shocks can generate civil conflict through a variety of pathways<sup>1,3,18</sup>. Furthermore, altered environmental conditions stress the human psyche, sometimes leading to aggressive behaviour<sup>27</sup>. We hypothesize that El Niño can simultaneously lead to any of these adverse economic and psychological effects, increasing the likelihood of conflict. Furthermore, the influence of ENSO may exceed the sum influence of these individual pathways because it is a global-scale process that generates simultaneous and correlated conditions around the world. This is possible if non-local processes, such as increasing global commodity prices<sup>28</sup> or conflict contagion<sup>6,18</sup>, strongly influence local conflict risk. Future work will examine the relative importance of these various mechanisms.

## METHODS SUMMARY

Pixels with surface temperatures significantly and positively correlated with NINO3 for at least 3 months out of the year are coded 'teleconnected'; remaining pixels are coded 'weakly affected'. Countries are coded teleconnected (weakly affected) if more than 50% of the population in 2000 inhabited teleconnected (weakly affected) pixels. Group-level time-series regressions (Table 1, models 1–4) use a continuous variable for ACR; we drop 1989 because it is a  $3\sigma$  outlier, presumably because of the end of the Cold War. Group-level standard errors are robust to unknown forms of heteroscedasticity. Country-level longitudinal regressions (models 5 and 6) are linear probability models for conflict onset with standard errors that are robust to unknown forms of spatial correlation over distances no more than 5000 km, serial correlation over periods no more than 5 years and heteroscedasticity<sup>21</sup>. We estimate the number of conflicts associated with ENSO by assuming all conflicts in the weakly affected group were unaffected and a baseline ACR of 3% for the teleconnected group would have remained unchanged in the absence of ENSO variations. We then project the observed sequence of NINO3 realizations onto our linear conflict model ( $dACR/dNINO3 = 0.0081$ ) and find 48.2 conflicts (21%) were associated with ENSO. For additional details on methods, see Supplementary Methods and replication files in Supplementary Data.

Received 16 February; accepted 20 June 2011.

1. Homer-Dixon, T. F. On the threshold: environmental changes as causes of acute conflict. *Int. Secur.* **16**, 76–116 (1991).
2. Diamond, J. *Collapse: How Societies Choose to Fail or Succeed* (Viking, 2005).
3. Miguel, E., Satyanath, S. & Sergenti, E. Economic shocks and civil conflict: an instrumental variables approach. *J. Polit. Econ.* **112**, 725–753 (2004).

4. Levy, M. A., Thorkelson, C., Vorosmarty, C., Douglas, E. & Humphreys, M. Paper presented at the International Workshop for Human Security and Climate Change, Oslo, Norway, 21–23 June 2005.
5. Burke, M., Miguel, E., Satyanath, S., Dykema, J. & Lobell, D. Warming increases risk of civil war in Africa. *Proc. Natl Acad. Sci. USA* **106**, 20670–20674 (2009).
6. Sandholt, J. P. & Gleditsch, K. S. Rain, growth, and civil war: the importance of location. *Defence Peace Econ.* **20**, 359–372 (2009).
7. Buhaug, H. Climate not to blame for African civil wars. *Proc. Natl Acad. Sci. USA* **107**, 16477–16482 (2010).
8. Ropelewski, C. F. & Halpert, M. S. Global and regional precipitation patterns associated with the El Niño/Southern Oscillation. *Mon. Weath. Rev.* **115**, 1606–1626 (1987).
9. Chiang, J. C. H. & Sobel, A. H. Tropical tropospheric temperature variations caused by ENSO and their influence on the remote tropical climate. *J. Clim.* **15**, 2616–2631 (2002).
10. Sarachik, E. S. & Cane, M. A. *The El Niño–Southern Oscillation Phenomenon* (Cambridge Univ. Press, 2010).
11. Grove, R. H. The great El Niño of 1789–93 and its global consequences: Reconstructing an extreme climate event in world environmental history. *Mediev. Hist. J.* **10**, 75–98 (2007).
12. Davis, M. *Late Victorian Holocausts: El Niño Famines and the Making of the Third World* (Verso, 2002).
13. Fagan, B. *Floods, Famines and Emperors: El Niño and the Fate of Civilizations* (Basic Books, 2009).
14. Salehyan, I. From climate change to conflict? No consensus yet. *J. Peace Res.* **45**, 315–326 (2008).
15. Zhang, D. D. *et al.* Global climate change, war and population decline in recent human history. *Proc. Natl Acad. Sci. USA* **104**, 19214–19219 (2007).
16. Tol, R. S. J. & Wagner, S. Climate change and violent conflict in Europe over the last millennium. *Clim. Change* **99**, 65–79 (2009).
17. Strand, H. *Onset of Armed Conflict: A New List for the Period 1946–2004, with Applications*. Technical report (<http://www.prio.no/CSCW/Datasets/Armed-Conflict>) (Center for the Study of Civil War, 2006).
18. Blattman, C. & Miguel, E. Civil war. *J. Econ. Lit.* **48**, 3–57 (2010).
19. Holland, P. W. Statistics and causal inference. *J. Am. Stat. Assoc.* **81**, 945–960 (1986).
20. Rosenzweig, C. & Hillel, D. *Climate Variability and the Global Harvest: Impacts of El Niño and Other Oscillations on Agro-ecosystems* (Oxford Univ. Press, 2008).
21. Hsiang, S. M. Temperatures and cyclones strongly associated with economic production in the Caribbean and Central America. *Proc. Natl Acad. Sci. USA* **107**, 15367–15372 (2010).
22. Jones, B. & Olken, B. Climate shocks and exports. *Am. Econ. Rev.* **100**, 454–459 (2010).
23. Chen, D., Cane, M., Kaplan, A., Zebiak, S. & Huang, D. Predictability of El Niño over the past 148 years. *Nature* **428**, 733–736 (2004).
24. Schlenker, W. & Roberts, M. Nonlinear temperature effects indicate severe damages to U.S. crop yields under climate change. *Proc. Natl Acad. Sci. USA* **106**, 15594–15598 (2009).
25. Carmargo, S. J. & Sobel, A. H. Western North Pacific tropical cyclone intensity and ENSO. *J. Climate* **18**, 2996–3006 (2005).
26. Kovats, R. S., Bouma, M. J., Hajat, S., Worrall, E. & Haines, A. El Niño and health. *Lancet* **12**, 917–932 (2003).
27. Larrick, R. P., Timmerman, T. A., Carton, A. M. & Abrevaya, J. Temper, temperature, and temptation: heat-related retaliation in baseball. *Psychol. Sci.* **22**, 423–428 (2011).
28. Brunner, A. D. El Niño and world primary commodity prices: warm water or hot air? *Rev. Econ. Stat.* **84**, 176–183 (2002).

**Supplementary Information** is linked to the online version of the paper at [www.nature.com/nature](http://www.nature.com/nature).

**Acknowledgements** S.M.H. was supported by Environmental Protection Agency Science to Achieve Results grant FP-916932 and a postdoctoral fellowship in Applied Econometrics at the National Bureau of Economic Research; K.C.M. was supported by the Paul and Daisy Soros Fellowship for New Americans. We thank W. B. MacLeod, B. Salanié, A. Sobel, J. Sachs, W. Schlenker, E. Miguel, D. Almond, S. Barrett, G. Heal, M. Neidell, J. Mutter, N. Keohane, A. Cassella, J. Currie, W. Kopczuk, C. Pop-Eleches, R. Fisman, S. Naidu, M. Humphreys, D. Lobell, M. Roberts, M. Greenstone, M. Biasutti, G. Wagner, G. McCord, J. Anttila-Hughes, R. Fishman, A. Tompsett, A. Neal, B. R. Chen and seminar participants at Columbia, Massachusetts Institute of Technology, Stanford, University of California Santa Barbara, Environmental Defense Fund, the National Bureau of Economic Research Summer Institute and the American Geophysical Union Fall Meeting for suggestions. We also thank H. Buhaug and M. Burke for sharing replication materials.

**Author Contributions** S.M.H. conceived and designed the study. S.M.H. and K.C.M. conducted the analysis. S.M.H., K.C.M. and M.A.C. wrote the paper.

**Author Information** Reprints and permissions information is available at [www.nature.com/reprints](http://www.nature.com/reprints). The authors declare no competing financial interests. Readers are welcome to comment on the online version of this article at [www.nature.com/nature](http://www.nature.com/nature). Correspondence and requests for materials should be addressed to S.M.H. ([shsiang@princeton.edu](mailto:shsiang@princeton.edu)).

# A Jurassic eutherian mammal and divergence of marsupials and placentals

Zhe-Xi Luo<sup>1</sup>, Chong-Xi Yuan<sup>2</sup>, Qing-Jin Meng<sup>3</sup> & Qiang Ji<sup>2</sup>

Placentals are the most abundant mammals that have diversified into every niche for vertebrates and dominated the world's terrestrial biotas in the Cenozoic. A critical event in mammalian history is the divergence of eutherians, the clade inclusive of all living placentals, from the metatherian–marsupial clade<sup>1–8</sup>. Here we report the discovery of a new eutherian of 160 Myr from the Jurassic of China, which extends the first appearance of the eutherian–placental clade by about 35 Myr from the previous record, reducing and resolving a discrepancy between the previous fossil record and the molecular estimate for the placental–marsupial divergence<sup>9–13</sup>. This mammal has scansorial forelimb features, and provides the ancestral condition for dental and other anatomical features of eutherians.

Class Mammalia  
Clade Boreosphenida<sup>14</sup>  
Infraclass Eutheria  
Order and family incertae sedis  
*Juramaia sinensis* gen. et sp. nov.

**Etymology.** *Jura*, Jurassic; *maia*, mother, in reference to placental affinities; *sinensis*, of China. The binomial refers to 'Jurassic mother from China'.

**Holotype.** Beijing Museum of Natural History (BMNH) PM1143 (Fig. 1) is preserved with full dentition, incomplete skull, anterior part of postcranial skeleton and residual soft tissues, such as hairs.

**Locality and age.** The Daxigou site of Jianchang County of Liaoning Province in the Middle–Late Jurassic Tiaojishan formation. The formation was dated by the SHRIMP U–Pb method on zircon at 164–165 Myr in the neighbouring Ningcheng area<sup>15</sup> and its stratigraphic equivalent dated by the <sup>40</sup>Ar/<sup>39</sup>Ar method on sanidines at 160.7 ± 0.4 Myr in the Beipiao area<sup>16</sup> (Supplementary Information).

**Diagnosis.** I<sup>5</sup>–C<sup>1</sup>–P<sup>5</sup>–M<sup>3</sup>/I<sub>4</sub>–C<sub>1</sub>–P<sub>5</sub>–M<sub>3</sub> (Fig. 2), with identical formula as the eutherian *Eomaia*<sup>3</sup> and typical count of five premolars and three molars for Cretaceous eutherians<sup>1</sup>. Molars tribosphenic, with derived eutherian features of distinctive paraconule, incipient metaconule (M2 only), long preprotocrista past the paracone and long postprotocrista past the metacone. The postmetacrista and the extended postprotocrista of an upper molar form two separate ranks of shearing crests that pass the prevallid crest (paracristid) of the succeeding lower molar (Fig. 3). The preparacrista and the preprotocrista form two ranks of shearing crests that pass the postvallid crest (protocristid) of the preceding lower molar. This kind of stepwise or en-echelon shearing is much better developed in *Juramaia* than in most metatherians<sup>17</sup>. Distinct from metatherians in lacking the vertical keel of the paraconid and the hypoconulid shelf<sup>18,19</sup> and in lacking the close approximation of the hypoconulid and the entoconid as in *Sinodelphys*<sup>7</sup> or the twinning of these cusps in other metatherians<sup>6</sup>. Differs from metatherians (except *Sinodelphys*) in lacking the inflected mandibular angle and flat ventral surface of the angle. *Juramaia sinensis* is similar to many eutherians in having the posterior mental foramen of the mandible below the p4–p5 junction, by contrast to metatherians that have the posterior mental foramen below m1. *Juramaia sinensis* is similar to several Cretaceous eutherians in retaining a deciduous dP3 in

the middle of the right premolar series<sup>1</sup> but differs from metatherians wherein replacement only occurs at the ultimate premolar position<sup>6,20</sup>. *Juramaia sinensis* differs from all australosphenidans in lacking the continuous mesial cingulid and the wrapping cingulid, and from most australosphenidan and pseudotribosphenidan mammals in lacking the postdentary trough on the mandible<sup>14,21–24</sup>. Among the earliest-known eutherians, *Juramaia sinensis* differs from *Eomaia* in having a two-rooted upper canine<sup>3</sup>, and from *Acristatherium* in having different numbers of upper and lower incisors, a larger M3 and absence of

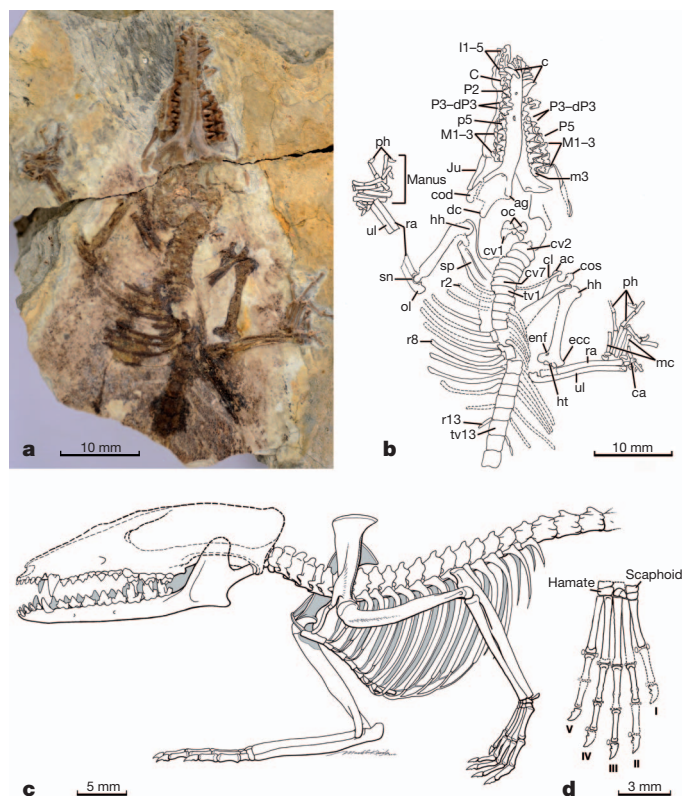


**Figure 1 | Holotype specimen of *Juramaia sinensis*, Beijing Museum of Natural History (BMNH) PM1343B. a, b, Specimen photograph and morphological identification. c, Restoration of the partly preserved skeleton and skull. d, Restoration of hand (ventral view; alignment of incomplete and scattered carpals is conjectural). Abbreviations: ac, acromion (scapula); ag, angular process (dentary); C, c, upper or lower canine; ca, carpals; cl, clavicle; cod, coronoid (dentary); cos, coracoid process (scapula); cv1–7, cervical vertebrae 1–7; dc, dentary condyle; ecc, ectepicondyle; enf, entepicondylar foramen; hh, humeral head; ht, humeral trochlea; I1–5, upper incisors 1–5; Ju, jugal; M, m, upper or lower molar; manus, hand; mc1–5, metacarpals 1–5; oc, occipital condyles; ol, olecranon process; P1–5, upper premolars 1–5; ph, phalanges; r1–13; thoracic ribs 1–13; ra, radius; sn, semilunar notch (ulna); sp., scapular spine; tv1–13, thoracic vertebrae 1–13; ul, ulna.**

<sup>1</sup>Carnegie Museum of Natural History, Pittsburgh, Pennsylvania 15213, USA. <sup>2</sup>Chinese Academy of Geological Sciences, Beijing 100037, China. <sup>3</sup>Beijing Museum of Natural History, Beijing 100050, China.



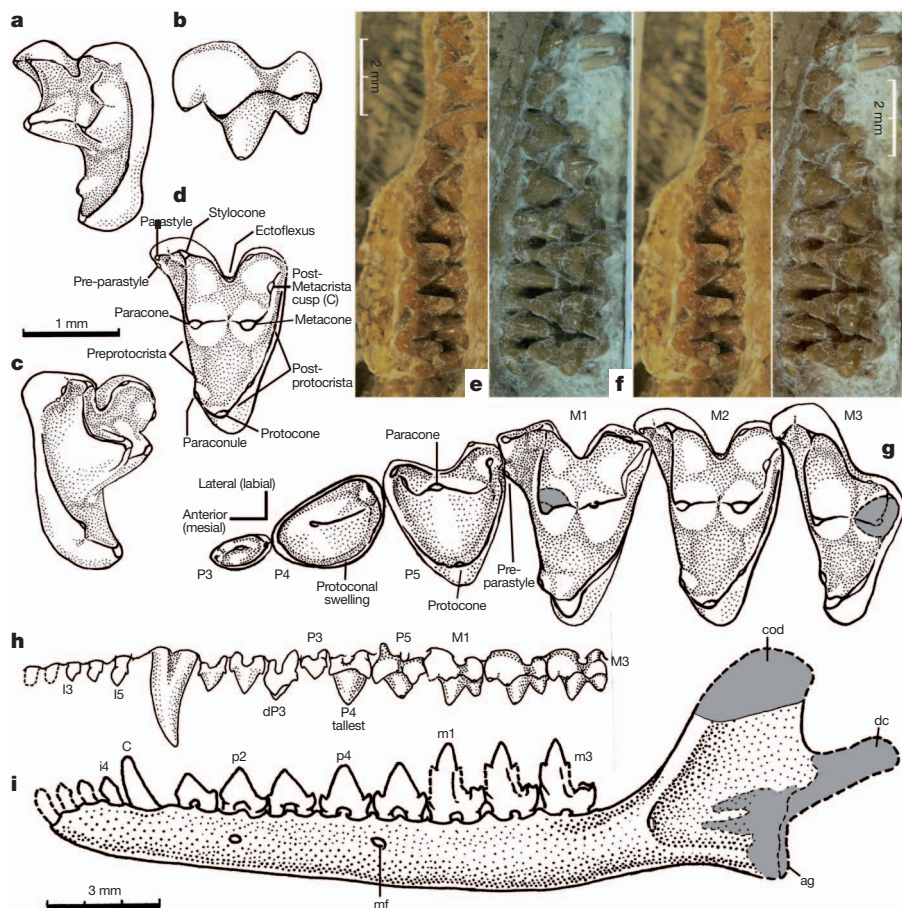


**Figure 2 | Dental and mandibular features of *Juramaia sinensis* (BMNH PM1343B).** **a–d**, Right upper M2 in mesial, occlusal, labial and distal views (composite restoration from both the right and the left sides). **e**, Stereo photographs of right premolars and molars. **f**, Stereo photographs of left premolars and molars. **g**, Right P3–M3 in occlusal view. **h**, Left upper dentition restoration in labial view. **i**, Left lower dentition (restoration) and mandible.

diastemata between the anterior upper premolars<sup>6</sup>. It differs from *Prokennalestes*, *Murtoilestes* and *Acristatherium* in having a much lower protocone and longer postprotocrista<sup>1,25,26</sup>, from all known Early Cretaceous eutherians in a deeper ectoflexus on P5–M2, and from *Montanalestes* in having larger lower premolars 3 and 4. See Supplementary Information for full differential diagnosis and summary of morphological distinction from other Mesozoic mammal groups.

Our study has firmly placed *Juramaia* among the basal-most eutherians, the Mesozoic relatives to the Cenozoic placental mammals (Fig. 3), by phylogenetic analyses of two independent morphological data sets (Supplementary Information). *Juramaia* is more closely related to extant placentals than all metatherians of the Cretaceous including *Sinodelphys* and *Deltatheridium*. In the first parsimony analysis of a comprehensive data set of all Mesozoic mammaliaform clades<sup>24</sup>, *Juramaia* and *Montanalestes* form an unresolved polytomy with the *Eomaia*–*Prokennalestes* clade and other eutherians (Fig. 3, left). Placement of *Juramaia* with eutherians is corroborated by analysis of a second and complementary data set of the largest sampling of Cretaceous eutherians<sup>4,5</sup>; *Juramaia* is placed in a more crown-ward position than the Early Cretaceous eutherian *Acristatherium*<sup>5</sup> (Supplementary Information). Our analysis by the mammaliaform data set reaffirms that the australosphenidan mammals<sup>21</sup> are not eutherians<sup>14</sup>; they represent a separate lineage of Mesozoic mammalian diversity, and are stem taxa to monotremes<sup>1,14</sup>, as corroborated by most of the recent independent studies<sup>4,12,22–24</sup>.

Grey-shaded areas represent reconstruction from incomplete bone or tooth structure or mould outline in matrix. Abbreviations: ag, angular process; cod, coronoid process of dentary; dc, dentary condyle; M, m, upper and lower molars; mf, mental foramen; P, p, upper and lower premolars; dp3, deciduous P3 *in situ*. Terminology of tribosphenic molar follows Fig. 11.1 of ref. 1.

*Juramaia*, at an age of 160 Myr (refs 15, 16), establishes a much older geological time for the split of the metatherian–marsupial and the eutherian–placental lineages than previously shown by the fossil record. The previously earliest eutherian record is *Eomaia* and the metatherian record is *Sinodelphys*, both about 125 Myr (refs 3, 7). The next oldest eutherian with a direct geochronological dating is *Acristatherium* at 123 Myr (ref. 5). *Juramaia* extends the first appearance of eutherians from these previous records by about 35 Myr. Because *Juramaia* is unambiguously placed on the placental side of the marsupial–placental divergence, the marsupial–placental divergence must have occurred before *Juramaia*. Therefore this new fossil serves to re-set the minimal age at 160 Myr for the basal-most diversification of marsupials and placentals, the two clades that collectively make up 99.9% of all living mammals and are very important in terrestrial ecosystems, especially after the Cretaceous/Tertiary extinction of non-avian dinosaurs.

Timing of the divergence of marsupials and placentals is critical for calibrating the rates of evolution in therian mammals, especially for molecular evolutionary studies and comparative genomics<sup>2,10,13</sup>. Previously, some molecular time estimates for marsupial and placental divergence postulated significantly older windows for this divergence than the then-oldest fossil records<sup>3,7</sup>. However, these and other previous molecular estimates differed widely. Several were compatible with relatively young placental intraordinal divergences (for example, ref. 10), and just about all showed wide error margins (reviewed by

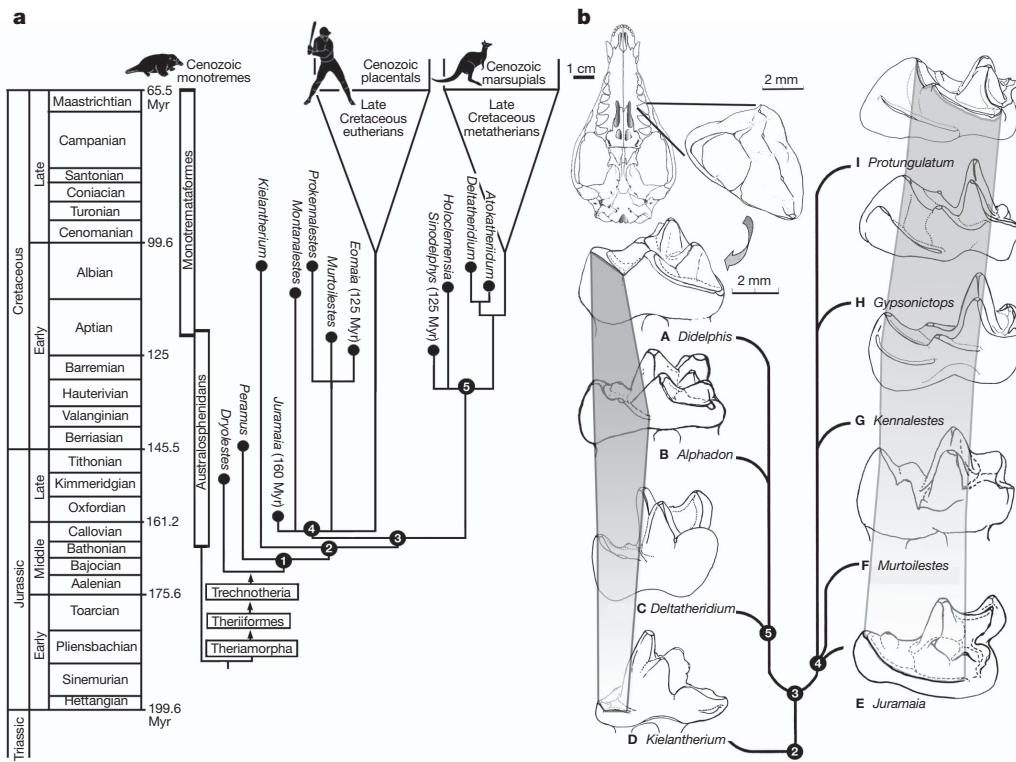


**Figure 3 | Time-calibrated phylogeny of the eutherian *Juramaia* among other boreosphenidan mammals, and comparative morphology of some key molar features. a**, Basal eutherian and metatherian phylogeny from parsimony analysis of data set of ref. 24 (446 characters of 103 cynodont-mammaliaform clades; based on the strict consensus of 172 equally parsimonious trees (each with treelength 2,243; consistency index 0.373, retention index 0.803) from 1,000 PAUP heuristic runs, without any topology constraints and with all multi-state characters unordered, multi-state taxa interpreted as polymorphism). Placement of *Juramaia* in eutherians is significantly different ( $*P < 0.050$ ) from suboptimal hypotheses of *Juramaia* as either a boreosphenidan or a metatherian by Templeton tests. This topology is corroborated by a separate analysis on a different and complementary data set

ref. 13). Regarding the marsupial-placental split, recent molecular rate studies provided estimates of  $147.7 \pm 5.5$  Myr (ref. 11), or 160 Myr (median) with a 95% highest posterior distribution of 143–178 Myr (ref. 12), or a window of 193–186 Myr (ref. 9). This new eutherian fossil age is now similar to the age of placentals at 160 Myr with 95% posterior distribution from 143 to 178 Myr by the latest molecular estimate<sup>12</sup>. The age of *Juramaia* has now set the minimal divergence time by the fossil to coincide with the range of molecular time estimates, serving as a corroboration of the newest fossil record with the molecular clock of evolution. The 160-Myr-old *Juramaia* also has important implications for mammalian evolution as a whole. Eutherian mammals are nested in the more inclusive Mesozoic boreosphenidan clade (Fig. 3, node 1), for which the previously earliest record had been entirely Early Cretaceous<sup>1,27</sup>. The eutherian *Juramaia* requires that the ghost-lineages of boreosphenid and cladotherian mammals would also extend to the Middle Jurassic. Therefore the magnitude of the mammalian faunal turnover from the Early to Middle Jurassic is greater than previously known, and the Early–Middle Jurassic is a critical transition for the appearance of more of the derived mammalian clades<sup>1,2</sup>.

Phylogenetically, *Juramaia sinensis* is one of the basal-most eutherians and it is currently the earliest-known eutherian (Fig. 3); therefore, this fossil provides crucial inferences on the ancestral features of all eutherians. *Juramaia* weighed about 15–17 g, and was an insectivore based on tooth morphology. Its long preprotocrista (Fig. 2c, d) and postprotocrista (Fig. 3e) enhance the en-echelon shearing in which

by refs 4, 5 (389 informative characters of 71 eutherian taxa and outgroups), by the strict consensus of 41 equally parsimonious trees, from 1,000 heuristic runs, without topology constraints and 33 multi-state characters ordered, multi-state taxa as polymorphism. Placement of *Juramaia* among basal eutherians is consistent with topologies from constrained search under molecular scaffolding of extant taxa in the main data set of ref. 24 and the complementary data set of refs 4, 5 (details in Supplementary Information). b, The increased en-echelon postvallum shearing of upper molars in the earliest eutherians<sup>17</sup>, in contrast to metatherians<sup>18</sup> that lack a strongly developed postvallum shearing by metacinculum, except for the Late Cretaceous *Pediomys*<sup>1</sup>. Nodes (1) Cladotheria, (2) Boreosphenida<sup>1,2</sup>, (3) crown Theria, (4) Eutheria (including Placentalia), and (5) Metatheria (including Marsupialia).

more than one crest of the upper molar, arranged in stepwise pattern, shears past the surfaces of the trigonid of the lower molar. This is especially prominent on the posterior face of the upper molar (postvallum) (Fig. 3e–i), an important derived character of eutherians compared with other tribosphenic mammals<sup>17</sup> (Fig. 3).

The forelimb and shoulder girdle of *Juramaia* show several eutherian apomorphies and lack such metatherian features as the supra-scapular notch and the expanded ectepicondylar shelf on the humerus for the supinator muscle<sup>7,28,29</sup>. Its manual phalanges suggest a scansorial adaptation (Fig. 1d). Proximal phalanges of three digits show protuberances of the annular ligament of the digital flexor muscle tendon, suggesting a gripping capability of the hand, common in scansorial extant mammals<sup>3,7</sup>. In the third manual digit, the proximal phalanx is 2.77 mm long, the intermediate phalanx is 2.39 mm and the metacarpal is 4.26 mm. The phalangeal index ((proximal + intermediate phalanges)/metacarpal  $\times 100$ ) (ref. 30) is 121 for *Juramaia*. Most extant mammals with this index value are arboreal. The proximal phalangeal index (proximal/intermediate phalanges  $\times 100$ ) is 65 for *Juramaia*. Extant placental carnivorans, primates and dermopterans with this value also tend to be arborealists, but rodents with this value are all terrestrial<sup>30</sup>. Compared with fossil mammals of the Early Cretaceous Yixian formation, phalangeal indices of *Juramaia* are between *Eomaia scansoria*, a scansorial mammal, and the eutriconodont *Jeholodens jenkinsi*, which is interpreted to be terrestrial<sup>7</sup>. In its habitat preference, *Juramaia* should be similar to the eutherian *Eomaia scansoria*, to the

Cretaceous and Early Cenozoic metatherians<sup>7,28</sup> and to living scansorial or arboreal didelphids<sup>30</sup>. The scansorial habits are also corroborated by the forelimb features, which are indicative of that habitat preference in extant mammals, such as the hypertrophied acromion and the acute posterior angle of the scapula<sup>28</sup>.

The earliest-known eutherians *Juramaia* and *Eomaia* and the earliest metatherian *Sinodelphys* are scansorial mammals, and differ from contemporary Mesozoic mammals, most which are terrestrial<sup>1,2</sup>. This suggests that the phylogenetic split of eutherians and metatherians and their earliest evolution are accompanied by major ecomorphological diversification, notably scansorial adaptation, which made it possible for therians to exploit arboreal niches.

Received 26 December 2010; accepted 10 June 2011.

- Kielan-Jaworowska, Z., Cifelli, R. L. & Luo, Z.-X. *Mammals from the Age of Dinosaurs: Origins, Evolution, and Structure* (Columbia Univ. Press, 2004).
- Luo, Z.-X. Transformation and diversification in the early mammalian evolution. *Nature* **450**, 1011–1019 (2007).
- Ji, Q. *et al.* The earliest known eutherian mammal. *Nature* **416**, 816–822 (2002).
- Wible, J. R., Rougier, G. W., Novacek, M. J. & Asher, R. J. The eutherian mammal *Maelestes gobiensis* from the Late Cretaceous of Mongolia and the phylogeny of Cretaceous Eutheria. *Bull. Am. Mus. Nat. Hist.* **327**, 1–123 (2009).
- Hu, Y. M., Meng, J., Li, C.-K. & Wang, Y.-Q. New basal eutherian mammal from the Early Cretaceous Jehol biota, Liaoning, China. *Proc. R. Soc. B* **277**, 229–236 (2010).
- Rougier, G. W., Wible, J. R. & Novacek, M. J. Implications of *Deltatheridium* specimens for early marsupial history. *Nature* **396**, 459–463 (1998).
- Luo, Z.-X., Ji, Q., Wible, J. R. & Yuan, C.-X. An Early Cretaceous tribosphenic mammal and metatherian evolution. *Science* **302**, 1934–1940 (2003).
- Wilson, G. P. & Riedl, J. A. New specimen reveals deltatheroid affinities of the North American Late Cretaceous mammal *Nanocuris*. *J. Vertebr. Paleontol.* **30**, 872–884 (2010).
- van Rhee, T. *et al.* The platypus is in its place: nuclear genes and Indels confirm the sister group relation of monotremes and therians. *Mol. Biol. Evol.* **23**, 587–597 (2006).
- Kitazoe, Y. *et al.* Robust time estimation reconciles views of the antiquity of placental mammals. *PLoS ONE* **2**, e384 (2007).
- Bininda-Emonds, O. R. P. *et al.* The delayed rise of present-day mammals. *Nature* **446**, 507–512 (2007).
- Phillips, M. J., Bennett, T. H. & Lee, M. S. Y. Molecules, morphology, and ecology indicate a recent, amphibious ancestry for echidnas. *Proc. Natl Acad. Sci. USA* **106**, 17089–17094 (2009).
- Benton, M. J., Donoghue, P. C. J. & Asher, R. J. In *The Timetree of Life* (eds Hedges, S. B. & Kumar S.) 35–86 (Oxford Univ. Press, 2009).
- Luo, Z.-X., Cifelli, R. C. & Kielan-Jaworowska, Z. Dual origin of tribosphenic mammals. *Nature* **409**, 53–57 (2001).
- Liu, Y.-Q., Liu, Y.-X., Ji, S.-A. & Yang, Z.-Q. U-Pb zircon age for the Daohugou Biota at Ningcheng of Inner Mongolia and comments on related issues. *Chin. Sci. Bull.* **51**, 2634–2644 (2006).
- Chang, S.-C., Zhang, H.-C., Renne, P. R. & Fang, F. High-precision <sup>40</sup>Ar/<sup>39</sup>Ar age constraints on the basal Lanqi Formation and its implications for the origin of angiosperm plants. *Earth Planet. Sci. Lett.* **279**, 212–221 (2009).
- Crompton, A. W. & Kielan-Jaworowska, Z. in *Studies in the Development, Function and Evolution of Teeth* (eds Butler, P. M. & Joysey, K. A.) 249–287 (Academic Press, 1978).
- Cifelli, R. L. & de Muizon, C. Dentition and jaw of *Kokopellia juddi*, a primitive marsupial or near marsupial from the medial Cretaceous of Utah. *J. Mamm. Evol.* **4**, 241–258 (1997).
- Averianov, A. O., Archibald, J. D. & Ekdale, E. G. New material of the Late Cretaceous deltatheroidan mammal *Sulestes* from Uzbekistan and phylogenetic reassessment of the metatherian eutherian dichotomy. *J. Syst. Palaeontology* **8**, 301–330 (2010).
- Cifelli, R. L. *et al.* Origin of marsupial pattern of tooth replacement: fossil evidence revealed by high resolution X-ray CT. *Nature* **379**, 715–718 (1996).
- Rich, T. H. *et al.* Early Cretaceous mammals from Flat Rocks, Victoria, Australia. *Rec. Queen Victoria Mus.* **106**, 1–35 (1999).
- Martin, T. & Rauhut, O. W. M. Mandible and dentition of *Asfaltomylos patagonicus* (Australosphenida, Mammalia) and the evolution of tribosphenic teeth. *J. Vertebr. Paleontol.* **25**, 414–425 (2005).
- Rougier, G. W. *et al.* New Jurassic mammals from Patagonia, Argentina: a reappraisal of australosphenidan morphology and interrelationship. *Am. Mus. Novit.* **3566**, 1–54 (2007).
- Luo, Z.-X., Ji, Q. & Yuan, C.-X. Convergent dental evolution in pseudotribosphenic and tribosphenic mammals. *Nature* **450**, 93–97 (2007).
- Kielan-Jaworowska, Z. & Dashzeveg, D. Eutherian mammals from the Early Cretaceous of Mongolia. *Zool. Scr.* **18**, 347–355 (1989).
- Averianov, A. O. & Skutschas, P. P. A new genus of eutherian mammal from the Early Cretaceous of Transbaikalia, Russia. *Acta Palaeontol. Pol.* **46**, 431–436 (2001).
- Sigogneau-Russell, D., Hooker, J. J. & Ensom, P. C. The oldest tribosphenic mammal from Laurasia (Purbeck Limestone Group, Berriasian, Cretaceous, UK) and its bearing on the 'dual origin' of Tribosphenida. *C. R. Acad. Sci. II* **333**, 141–147 (2001).
- Argot, C. Functional-adaptive anatomy of the forelimb in the Didelphidae, and the paleobiology of the Paleocene marsupials *Mayulestes ferox* and *Pucadelphys andinus*. *J. Morphol.* **247**, 51–79 (2001).
- Asher, R. J., Horowitz, I. & Sanchez-Villagra, M. R. First combined cladistic analysis of marsupial mammal interrelationships. *Mol. Phylogenet. Evol.* **33**, 240–250 (2004).
- Kirk, E. C., Lemelin, P., Hamrick, M. W., Boyer, D. M. & Bloch, J. I. Intrinsic hand proportions of euarchontans and other mammals: Implications for the locomotor behavior of plesiadapiforms. *J. Hum. Evol.* **55**, 278–299 (2008).

**Supplementary Information** is linked to the online version of the paper at [www.nature.com/nature](http://www.nature.com/nature).

**Acknowledgements** We thank A. R. Tabrum for his meticulous preparation of the fossil, Y.-Q. Zhang for casting, and M. A. Klingler for assistance with graphics. During this work, we benefited from discussion with Y.-Q. Liu on field geology and dating, and with R. J. Asher, K. C. Beard, R. L. Cifelli, M. R. Dawson, T. Martin and J. R. Wible for discussion on mammal phylogeny. J. Wible and M. Dawson helped to improve the manuscript. Support was given to Z.-X.L. from the National Science Foundation (USA), to C.-X.Y. from the National Natural Science Foundation-China and the Chinese Academy of Geological Sciences, and to Q.J. from the 973 Project of the Ministry of Science and Technology of China and funding from the Chinese Academy of Geological Sciences.

**Author Contributions** Z.-X.L. and Q.J. designed the research plan. All authors participated in morphological studies. Z.-X.L. and C.-X.Y. performed phylogenetic analyses. Z.-X.L. wrote the paper with discussion from all authors.

**Author Information** Reprints and permissions information is available at [www.nature.com/reprints](http://www.nature.com/reprints). The authors declare no competing financial interests. Readers are welcome to comment on the online version of this article at [www.nature.com/nature](http://www.nature.com/nature). Correspondence and requests for materials should be addressed to Z.-X.L. ([luoz@carnegiemnh.org](mailto:luoz@carnegiemnh.org)).



# A chronological framework for the British Quaternary based on *Bithynia* opercula

Kirsty E. H. Penkman<sup>1</sup>, Richard C. Preece<sup>2</sup>, David R. Bridgland<sup>3</sup>, David H. Keen<sup>4</sup>‡, Tom Meijer<sup>5</sup>, Simon A. Parfitt<sup>6,7</sup>, Tom S. White<sup>2</sup> & Matthew J. Collins<sup>1</sup>

Marine and ice-core records show that the Earth has experienced a succession of glacial and interglacials during the Quaternary (last ~2.6 million years), although it is often difficult to correlate fragmentary terrestrial records with specific cycles. Aminostratigraphy is a method potentially able to link terrestrial sequences to the marine isotope stages (MIS) of the deep-sea record<sup>1,2</sup>. We have used new methods of extraction and analysis of amino acids, preserved within the calcitic opercula of the freshwater gastropod *Bithynia*, to provide the most comprehensive data set for the British Pleistocene based on a single dating technique. A total of 470 opercula from 74 sites spanning the entire Quaternary are ranked in order of relative age based on the extent of protein degradation, using aspartic acid/asparagine (Asx), glutamic acid/glutamine (Glx), serine (Ser), alanine (Ala) and valine (Val). This new aminostratigraphy is consistent with the stratigraphical relationships of stratotypes, sites with independent geochronology, biostratigraphy and terrace stratigraphy<sup>3–6</sup>. The method corroborates the existence of four interglacial stages between the Anglian (MIS 12) and the Holocene in the terrestrial succession. It establishes human occupation of Britain in most interglacial stages after MIS 15, but supports the notion of human absence during the Last Interglacial (MIS 5e)<sup>7</sup>. Suspicions that the treeless ‘optimum of the Upton Warren interstadial’ at Isleworth pre-dates MIS 3 are confirmed. This new aminostratigraphy provides a robust framework against which climatic, biostratigraphical and archaeological models can be tested.

Despite the importance of the terrestrial record for climate models, the difficulties of assigning specific sedimentary sequences to individual climate cycles restricts the use of these data in climate modelling. The British Quaternary is exceptional for the number of recorded sites and their biodiversity, which has fluctuated markedly due to the mid-latitude situation of this ephemeral island. A consensus has emerged from attempted differentiation between interglacials in Britain using river terrace stratigraphy<sup>6,8</sup> and biostratigraphy<sup>3–5</sup> (Fig. 1).

This study revisits pioneering research undertaken on bivalves<sup>1</sup> and gastropod shells<sup>2</sup> that used the extent of racemization in the amino acid L-isoleucine (to its diastereomer D-alloisoleucine, yielding a D-alloisoleucine/L-isoleucine (A/I) value) in non-marine mollusc shells to build an aminostratigraphy of terrestrial sequences that could be linked to the marine oxygen isotope stratigraphy. Following debate concerning certain correlations, we developed a revised method of extraction and analysis<sup>9</sup>. Shells of freshwater gastropods (*Bithynia* and *Valvata*) from many of the original sites<sup>10</sup> have been re-analysed, confirming much of the A/I stratigraphy. However, it emerged that within-site and within-stage variability increases in shells from older sites. This variability probably results from diagenetic alteration of the biomineral carbonate from aragonite to the more thermodynamically stable calcite<sup>10,11</sup>.

Our new method has five significant revisions, three of which reduced within-site variability. First, inter-species variation was minimised by analysing only a single genus of freshwater gastropod (*Bithynia*). Second, variability in amino acid concentration and D/L values was significantly lowered when samples were crushed to  $\leq 500\ \mu\text{m}$  and exposed to prolonged wet chemical oxidation (48 h, 12% w/v NaOCl, room temperature), destroying any contamination and leaving a functionally closed-system protein fraction defined as ‘intra-crystalline’<sup>9,12</sup>. Third, the calcitic operculum, which in life closes the aperture of the shell, was analysed instead of the aragonitic shell. Opercula display less within-site variation and greater stability than shells<sup>10,11</sup>, and show subtle but minimal intraspecific differences in racemization (Supplementary Data 1). Further modifications included the analysis of a range of different amino acids<sup>13</sup> (rather than only a single measure of racemization), which allows an estimate of ‘intra-crystalline protein decomposition’ (IcPD). This integrates data from amino acids with differing rates of racemization ( $\text{Asx} \gg \text{Ala} > \text{Val} \approx \text{Glx}$ ) with the extent of dehydration of serine (Ser to Ala concentration ratio) to estimate age (Fig. 2). Finally, comparisons were made between free amino acids (FAA), liberated by diagenesis, and the total extent of racemization (THAA), in order to test closed-system conditions<sup>14</sup>.

The intra-crystalline fraction maintains constant chemical conditions so that the extent of protein degradation can be attributed to the thermal history of the sample. Within the study area differences in thermal history have been minor during the past century and chiefly related to burial depth and the thermal diffusivity of the overburden, mediated by the presence/absence of vegetation and/or snow cover (Supplementary Fig. 1 and Discussion). Opercula with similar levels of protein degradation are therefore thought to be of equivalent age, assuming that similarly small thermal gradients existed during past interglacials, when most of the racemization would have occurred.

The consistency of our method has been tested by measuring opercula from British interglacial stratotypes and/or sites with independent geochronology (Fig. 1, Fig. 2 and Supplementary Data 1). All stratotypes yielding *Bithynia* have been analysed, but stratotypes have not been formally defined for all stages<sup>15</sup>. Sites with independent geochronology can be used to calibrate IcPD results but, as only seven of our pre-Holocene sites have associated dates, we have not done this here. Nevertheless, an age-dependent increase in the level of IcPD is seen from the Holocene to the Early Pleistocene, using a combination of fast (for example, Asx) and slow (for example, Val) racemizing amino acids to span this range.

Increasing protein decomposition within opercula is also consistent with increasing river terrace elevation (and therefore age) in Quaternary fluvial archives (Figs 1 and 3 and Supplementary Data 1 and 2). The formation of river terraces is attributed to climatic forcing and uplift, linking aggradation and incision phases with climatically induced changes in sediment and water supply<sup>6,8,16</sup>. Assemblages of

<sup>1</sup>BioArCh, Departments of Archaeology & Chemistry, University of York, York YO10 5DD, UK. <sup>2</sup>Department of Zoology, University of Cambridge, Downing Street, Cambridge CB2 3EJ, UK. <sup>3</sup>Department of Geography, University of Durham, South Road, Durham DH1 3LE, UK. <sup>4</sup>Institute of Archaeology and Antiquity, University of Birmingham, Birmingham B15 2TT, UK. <sup>5</sup>Cainozoic Mollusca, Netherlands Centre for Biodiversity, Naturalis, P.O. Box 9517, 2300 RA Leiden, The Netherlands. <sup>6</sup>Institute of Archaeology, University College London, 31–34 Gordon Square, London WC1H 0PY, UK. <sup>7</sup>Department of Palaeontology, The Natural History Museum, Cromwell Road, London SW7 5BD, UK.

‡Deceased.

Site number (Supplementary Fig. 1)	Site	Bithynia species	D/L				Independent geochronology	Terrace stratigraphy	Hippopotamus/Corbicula	Arvicola/Mimomys	Archaeology	Consensus MIS
			Ala		Val							
			Number analysed	Mean	Standard deviation	Mean						
1	Acle (modern)	le	3	0.04	0.00	0.02	0.00	•				
2	Acle (modern)	te	2	0.04	0.00	0.02	0.00					
2	Enfield Lock	te	4	0.05	0.01	0.03	0.01					1
3	Quidenham Mere, 250–260 cm	te	4	0.05	0.01	0.03	0.00					1
3	Quidenham Mere, 640–650 cm	te	3	0.05	0.01	0.03	0.00					1
4	Newby Wiske	te	3	0.06	0.01	0.04	0.00	•				1
5	Aston-upon-Trent	te	4	0.06	0.00	0.04	0.00					1
6	Star Carr, 245–250 cm	te	2	0.07	0.01	0.04	0.00	•			♦	1
7	Sproughton	te	4	0.09	0.00	0.05	0.00	•			♦	1
8	Star Carr, 524–528 cm	te	3	0.10	0.02	0.04	0.00	•				2
8	Cassington	te	4	0.12	0.01	0.07	0.00	•	Th			2
9	Isleworth	te	4	0.14	0.01	0.07	0.01	•	Th			5c-4
10	East Mersea (Restaurant)	te	2	0.16	0.02	0.08	0.01		Th			5e
11	Coston	te	3	0.17	0.00	0.08	0.00			•		5e
12	Maxey	te	4	0.17	0.03	0.08	0.02		hW			
13	Woolpack Farm	te	1	0.17	0.00	0.09	0.00					
14	Jaywick Sands	te	4	0.17	0.01	0.09	0.01					
15	Saham Toney, 92	te	4	0.17	0.00	0.10	0.01					
16	Itteringham	te	1	0.18	0.00	0.09	0.01					
17	Tattershall Castle	te	4	0.18	0.01	0.09	0.01	•	TW			5e
18	Bobbittshole	te	3	0.18	0.01	0.10	0.00					5e
19	Shropham	te	4	0.18	0.01	0.09	0.01			•		5e
20	Trafalgar Square	te	6	0.19	0.01	0.10	0.01		Th	•		5e
15	Saham Toney, 94	te	2	0.19	0.00	0.11	0.01					
21	Bardon Quarry, Area 3	te	3	0.19	0.02	0.09	0.01		TW			
15	Saham Toney, 93	te	4	0.19	0.01	0.10	0.01					
16	Itteringham, Bed d	te	4	0.19	0.01	0.10	0.00					
22	Eckington	te	4	0.20	0.01	0.10	0.01					
23	Crophorne New Inn	te	4	0.20	0.01	0.09	0.00		SA	•		5e
23	Crophorne New Inn	te	4	0.20	0.01	0.09	0.00		SA	•		5e
21	Bardon Quarry, Area 2	te	4	0.21	0.03	0.11	0.02					
24	Funtham's Lane East	te	25	0.22	0.01	0.12	0.01		NW	•		
25	Stanton Harcourt	te	4	0.23	0.01	0.11	0.00		Th	•		7
26	Crayford	te	4	0.24	0.00	0.12	0.01		Th		♦	7
27	Barnwell	te	2	0.24	0.01	0.12	0.01			•		
28	Allstone-on-Stour	te	4	0.24	0.01	0.12	0.01		SA	•		
29	Histon Road	te	2	0.24	0.01	0.12	0.01			•		
30	Strensham	te	4	0.25	0.02	0.12	0.02		SA		♦	
31	Stutton	te	4	0.25	0.01	0.14	0.01			•		
32	Coronation Farm	te	1	0.25	0.00	0.13	0.00		TW		♦	7
33	Somersham	te	4	0.25	0.01	0.12	0.00			•		
34	Norton Bottoms	te	15	0.25	0.01	0.13	0.01		TW		♦	7
35	Block Fen	te	4	0.25	0.02	0.13	0.01			•		
33	Somersham	tr	4	0.26	0.01	0.13	0.01				♦	
36	Ebbsfleet, U. loam, U. part	te	1	0.26	0.01	0.14	0.00				♦	
36	Ebbsfleet, U. loam, L. part	te	2	0.26	0.01	0.14	0.01				♦	
37	Brough	te	6	0.27	0.01	0.16	0.01		Th			7
38	Ilford (Uphall Pit)	te	2	0.27	0.01	0.14	0.02		Th	•		7
39	Maidenall	te	2	0.28	0.02	0.15	0.00				♦	
40	West Thurrock (Lion Pit), 4	te	25	0.29	0.01	0.15	0.01		Th	•		7
40	West Thurrock (Lion Pit), 2000	te	3	0.29	0.01	0.16	0.00		Th			7
36	Ebbsfleet, Lmst Brickearth	te	3	0.30	0.01	0.15	0.01				♦	
41	Stoke Tunnel	te	2	0.30	0.01	0.15	0.01				♦	
40	West Thurrock (Lion Pit), 3	te	25	0.30	0.01	0.16	0.02		Th	•		7
40	West Thurrock (Lion Pit), 6	te	5	0.31	0.01	0.16	0.01		Th	•		7
42	Selsey	te	3	0.31	0.01	0.16	0.00				♦	
43	Aveley	te	4	0.32	0.02	0.16	0.01		Th	•		7
44	West Wittering	te	3	0.32	0.00	0.16	0.00				♦	
45	Bushley Green	te	1	0.34	0.00	0.16	0.00		SA			
46	Cudmore Grove	te	4	0.34	0.02	0.19	0.01		Th	•		9
47	Hackney Downs	te	2	0.34	0.01	0.17	0.01		Th	•		9
46	Cudmore Grove, sample PE	te	2	0.36	0.00	0.20	0.00		Th	•		9
48	Belhus Park	te	1	0.36	0.02	0.20	0.02		Th	•		9
49	Purfleet, 1	te	23	0.38	0.01	0.18	0.01	•			▲	9
50	Barling	te	4	0.38	0.01	0.20	0.01		Th			9
49	Purfleet, 6	te	24	0.38	0.01	0.21	0.01	•	Th		▲	9
51	Shoeburyness	te	5	0.39	0.01	0.20	0.01			•		
52	Grays	te	2	0.40	0.01	0.20	0.00		Th	•		9
53	Marks Tey	te	2	0.40	0.01	0.22	0.01				♦	11
48	Belhus Park, BP18	te	4	0.40	0.01	0.21	0.01		Th	•		9
54	Trimingham	te	13	0.40	0.01	0.22	0.01					
55	Hoxne, Stratum B2, 64	te	4	0.40	0.02	0.22	0.01	•				
56	Barnham, BEF92	tr	3	0.40	0.02	0.21	0.01				♦	11
57	Elveden, ELV 96	te	2	0.41	0.01	0.20	0.01				♦	11
57	Elveden, ELV 95	te	5	0.41	0.01	0.21	0.01				♦	11
58	Swanscombe (Barnfield Pit)	te	6	0.42	0.01	0.24	0.03		Th		✕	11
56	Barnham, BEF93	te	6	0.42	0.02	0.20	0.02				♦	11
59	Woodston	te	4	0.42	0.01	0.23	0.01		NW			11
55	Hoxne, Stratum E	te	4	0.42	0.01	0.23	0.01				♦	11
60	West Stow (Beeches Pit)	te	4	0.42	0.01	0.25	0.01	•				11
61	Dierden's Pit (Ingress Vale)	tr	2	0.43	0.01	0.22	0.01		Th	•	✕	11
55	Hoxne, Stratum B2, 50	te	4	0.43	0.01	0.24	0.01	•				11
62	Southfleet Road	te	7	0.43	0.01	0.22	0.01				✕	11
61	Dierden's Pit (Ingress Vale)	te	4	0.45	0.01	0.21	0.01		Th	•		11
63	Clacton-on-Sea	te	4	0.46	0.01	0.25	0.02			•	♦	11
64	Waverley Wood	te	6	0.48	0.03	0.27	0.03					13?
65	Sidestrand, Upper Unio-Bed	te	7	0.54	0.02	0.29	0.01					13?
65	Sidestrand, Lower Unio-Bed	te	5	0.55	0.01	0.29	0.01					13?
66	Sugworth	tr	6	0.56	0.01	0.28	0.01		Th	•		15?
67	Little Oakley	tr	2	0.56	0.00	0.28	0.00			•		15?
68	Pakefield, PaCi	tr	4	0.57	0.03	0.30	0.01					17/15?
68	Pakefield, PaCi	tr	3	0.58	0.01	0.35	0.02					17/15?
69	West Runton	te	11	0.61	0.02	0.33	0.01			•		17/15?
70	Bavel	b/t	4	0.81	0.02	0.54	0.04			•		31?
71	Weybourne (Weybourne Crag)	tr	2	0.89	0.01	0.69	0.03					
72	Tegelen	tr	4	0.90	0.01	0.75	0.03					
71	Weybourne (Weybourne Crag)	te	1	0.92	0.00	0.79	0.01					
73	Thorpe Aldringham (N. Crag)	sp.	1	0.94	0.00	0.84	0.04					
74	Frechen (Pliocene)	te	4	0.93	0.01	0.91	0.02					

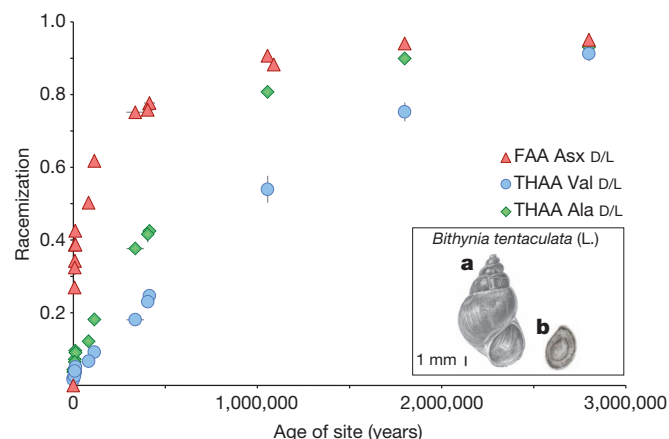


**Figure 2 | Amino acid decomposition at sites of known age.** Comparison of racemization in *Bithynia* opercula for FAA aspartic acid (Asx), THAA alanine (Ala) and valine (Val) for all sites with independent geochronology. Y-axis error bars indicate one standard deviation about the mean for the site. X-axis error bars are not shown for the Early Pleistocene and Pliocene samples, as these estimates of age are not based on numerical methods. Note the rapid racemization in Asx at relatively young sites and the plateau beyond ~0.5 Myr; Asx is therefore most valuable for separating sites younger than MIS 9. In contrast, Val racemizes more slowly and provides poorer resolution for younger sites, but is able to differentiate between sites back to the Pliocene. Using several amino acids with different rates of degradation therefore enables greater age resolution. The increase in racemization is not linear with time, but slows during cold stages. Inset: shell (a) and operculum (b) of *Bithynia tentaculata*.

amino acid values from the Thames sequence, the most complete British fluvial archive<sup>17–19</sup>, clearly correspond with discrete terrace aggradations (Fig. 3 and Supplementary Data 2). Four interglacials after the Anglian (MIS 12) stage are represented in this system, assigned to MIS 11, 9, 7 and 5e on the basis that each aggradation formed during a complete glacial/interglacial cycle<sup>6,16</sup>. Although this relationship might not hold for all rivers<sup>20</sup>, a similar pattern exists between D/L values and terraces in other systems, such as the Severn/Avon<sup>21</sup>, Trent/Witham<sup>22</sup> and Nene/Welland<sup>23</sup>. Support for these interpretations comes from integrating several lines of evidence (for example, biostratigraphy<sup>4,5</sup> and some of the original A/I data<sup>16</sup>), not all of which are wholly independent. However, the ability of the method to differentiate between terrace aggradations (Supplementary Data 2) is not reliant on other

**Figure 1 | Intra-crystalline amino acid data from the opercula of *Bithynia* from sites in southern Britain.** Sites were chosen because they (1) are stratotypes (in bold) of various interglacial stages, (2) have independent geochronology, (3) occur within a fluvial terrace sequence, or (4) have relative ages based on biostratigraphy (Supplementary Data 1). Some additional sites, including three key continental Plio-Pleistocene localities, are listed to show how they fit into this general framework. Sites are listed in rank order based on the THAA Ala D/L value, the most useful single measurement covering the timescales under discussion, but full interpretation requires consideration of the overall IcPD (Supplementary Data 1). Our data are shown alongside terrace stratigraphy (NW: Nene/Welland; SA: Severn/Avon; Th: Thames; TW: Trent/Witham), occurrences of important biostratigraphic indicator species (?), indirect association), *in situ* archaeology and existing consensus views on correlation with the MIS record. Age attributions reliant on amino acid dating alone are excluded. The occurrence of the water vole *Arvicola* (in grey) is only shown for pre-Anglian sites (that is, pre-MIS 12). *Mimomys* is shown in brown. Uptriangles, archaeology found in overlying sediments; downtriangles, archaeology found in underlying sediments; crosses, archaeology from the same horizon as the opercula analysed; diamonds, indirect association (that is, archaeology recorded from the site but not this profile). *Bithynia tentaculata* (L.) does not occur throughout the British Pleistocene, so where necessary we have used other species of *Bithynia* (b/t, *B. bavelensis/tentaculata*; le, *B. leachi*; te, *B. tentaculata*; tr, *B. troschellii*). L., lower; Lmst, lowermost; N., north; U., upper.

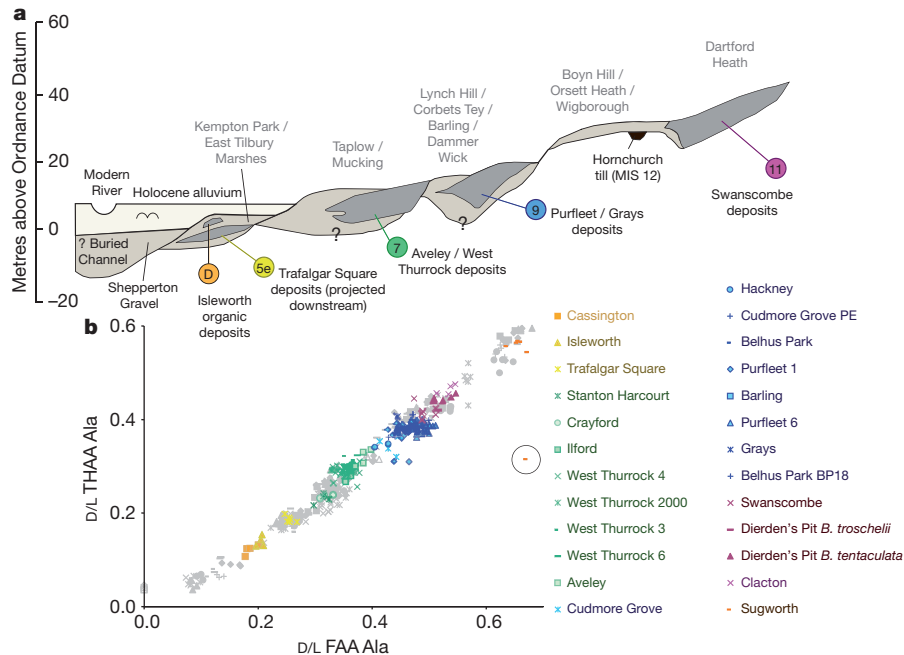
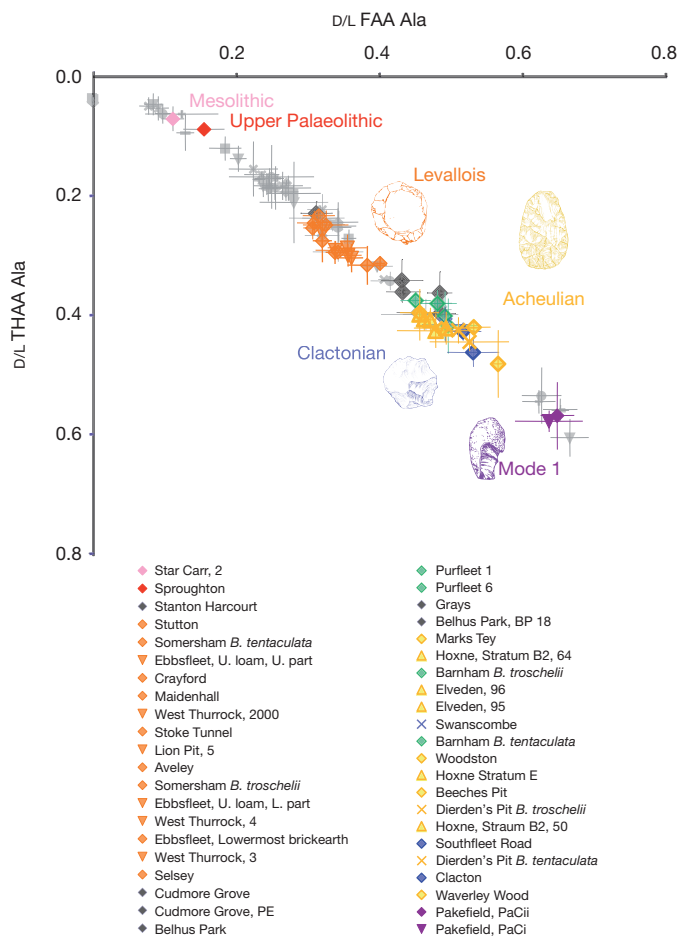


**Figure 3 | THAA versus FAA D/L Ala for individual samples in relation to terrace stratigraphy.** a, b, Idealised transverse sections through the Lower Thames terrace sequence<sup>19</sup> (a) and THAA versus FAA D/L Ala (b). Data from Thames sites (coloured) are superimposed on the full data set. D, Devensian. Note the concordance of terrace aggradations with the extent of protein degradation. This finding is consistent in all four river systems tested (Fig. 1 and Supplementary Data 2). The relation of FAA:THAA is a useful control on the

reliability of the closed system. For example, opercula distorted following deposition showed levels of racemization of THAA far lower than predicted from FAA<sup>14</sup>, indicating that during demineralization and distortion smaller, more mobile, amino acids were lost whereas larger peptides were retained during re-mineralization. Only ~1% of samples analysed here were compromised, such as the outlier from Sugworth (circled).



data and sites where the age attribution is based fundamentally on amino acid data are not assigned 'consensus MIS ages' in Fig. 1.

*Bithynia* is generally rare in cold-stage contexts, although it occurred commonly in the 'Upton Warren interstadial' deposit at Isleworth. This was originally thought to fall within the 'Middle Devensian' (MIS 3) on the basis of a radiocarbon date of ~43 kyr before present<sup>24</sup>. The Isleworth opercula IcPD is consistently higher than that from Cassington, a site tentatively correlated with MIS 5a (ref. 25), but lower than Last Interglacial opercula. Radiocarbon therefore provides only a minimum age for the Isleworth deposits. Our IcPD data indicate an earlier age and suggest that this new method can potentially be used to distinguish marine isotope sub-stages beyond the limits of radiocarbon dating.

Aminostratigraphic data also provide independent support for biostratigraphic age models developed for the Middle Pleistocene<sup>5,26,27</sup>. In the early Middle Pleistocene, the water vole *Arvicola* is thought to have replaced its ancestor *Mimomys savini* within a relatively short time over large regions of Europe<sup>3,27</sup>. This hypothesis gains support from our new data, which show that opercula from sites yielding *Arvicola* show less protein degradation than those containing *M. savini* (Fig. 1).

The occurrence of *Corbicula* (a bivalve) and *Hippopotamus* in the British Pleistocene is mutually exclusive<sup>5,26</sup>. At British sites securely attributable to the Last Interglacial (MIS 5e) *Corbicula* is absent;

**Figure 4 | Mean THAA versus FAA D/L Ala in relation to the occurrence of archaeology.** Data from archaeological sites (coloured) are superimposed on the full data set. Error bars represent two standard deviations about the mean for each site. Symbols as in Fig. 1, with green signifying occurrence of both Clactonian and Acheulian at a site. The earliest Palaeolithic archaeology (Mode 1, that is, flake tools made with hard-hammers) comes from pre-Anglian contexts yielding *Mimomys savini*. Sites with unequivocal Clactonian (core-and-flake) archaeology all fall within MIS 11. Sites yielding Levallois artefacts form a temporally discrete cluster after MIS 9 but before MIS 5e. Archaeology is unknown at British sites attributed to the Last Interglacial (MIS 5e). Opercula have also been analysed from one Upper Palaeolithic and one Mesolithic site.



conversely, after MIS 12, *Hippopotamus* is only known from the Last Interglacial, and is therefore widely regarded as an 'indicator species' for MIS 5e<sup>4</sup>. Our data support these conclusions, as post-Anglian sites with *Hippopotamus* show less protein breakdown than sites yielding *Corbicula*, with levels of protein degradation consistent with attribution to MIS 5e.

The comparisons above demonstrate the remarkable consistency of our new method with independent lines of evidence. This comprehensive dating framework enables us to explore the British archaeological record. Our data show that human occupation occurred within at least two distinct pre-Anglian stages, the older (Pakefield) associated with *Mimomys* and the younger (Waverley Wood) with *Arvicola*. The conclusion that Waverley Wood is younger than the Cromerian stratotype at West Runton supports the biostratigraphic age model<sup>27</sup> and contradicts a conclusion reached in an earlier aminostratigraphical study<sup>2</sup>. Our data can provide age constraints for other archaeological assemblages, enabling attribution to specific marine isotope stages in younger deposits. The development of Levallois technology, characterized by the removal of flakes from specifically prepared cores, is unknown in Britain before MIS 9 (ref. 28). Archaeological evidence from MIS 9 is sparse, but the far better record from sites attributed to MIS 7 shows that Levallois industries had become dominant in southern England; our data support this view (Figs 1 and 4).

In recent years it has become clear that humans were absent from Britain during the Last Interglacial; earlier claims to the contrary have been shown to be based on misinterpretation of archaeological sites previously thought to be of Last Interglacial age (such as Aveley, Crayford, Grays, Purfleet and Stutton), invariably now assigned to earlier stages<sup>29</sup> (Supplementary Data 1). Our results confirm that no British archaeological site can be attributed to the Last Interglacial (Fig. 4), a conclusion consistent with human absence during this stage<sup>7,29</sup>.

This stratigraphical framework provides a secure basis for relating the British terrestrial sequence to global Quaternary climate records. This is fundamental to geological and archaeological research but, as importantly, it enables the rich British record to be used to test the ability of climate models to simulate pre-late Quaternary palaeoclimates. This dating technique offers a means of correlating terrestrial with marine and ice-core records, thereby increasing the confidence of model predictions<sup>30</sup>. Moreover, the calcitic opercula of bithyniid (or similar) gastropods occur commonly in many Quaternary sequences, offering potential for development of regional aminostratigraphies around the world.

Received 21 January; accepted 15 June 2011.

Published online 31 July 2011.

1. Miller, G. H., Hollin, J. T. & Andrews, J. T. Aminostratigraphy of UK Pleistocene deposits. *Nature* **281**, 539–543 (1979).
2. Bowen, D. Q., Hughes, S., Sykes, G. A. & Miller, G. H. Land-sea correlations in the Pleistocene based on isoleucine epimerization in non-marine molluscs. *Nature* **340**, 49–51 (1989).
3. von Koenigswald, W. & van Kolfschoten, T. in *The early Middle Pleistocene in Europe*. (ed. Turner, C.) 211–226 (Balkema, 1996).
4. Schreve, D. C. Differentiation of the British late Middle Pleistocene interglacials: the evidence from mammalian biostratigraphy. *Quat. Sci. Rev.* **20**, 1693–1705 (2001).
5. Keen, D. H. Towards a late Middle Pleistocene non-marine molluscan biostratigraphy for the British Isles. *Quat. Sci. Rev.* **20**, 1657–1665 (2001).
6. Bridgland, D. R. The record from British Quaternary river systems within the context of global fluvial archives. *J. Quaternary Sci.* **25**, 433–446 (2010).
7. Ashton, N. & Lewis, S. G. Deserted Britain: declining populations in the British late Middle Pleistocene. *Antiquity* **76**, 388–396 (2002).
8. Bridgland, D. R., Maddy, D. & Bates, M. River terrace sequences: templates for Quaternary geochronology and marine-terrestrial correlation. *J. Quaternary Sci.* **19**, 203–218 (2004).
9. Penkman, K. E. H., Kaufman, D. S., Maddy, D. & Collins, M. J. Closed-system behaviour of the intra-crystalline fraction of amino acids in mollusc shells. *Quaternary Geochronol.* **3**, 2–25 (2008).

10. Penkman, K. E. H. *et al.* Testing the aminostratigraphy of fluvial archives: the evidence from intra-crystalline proteins within freshwater shells. *Quat. Sci. Rev.* **26**, 2958–2969 (2007).
11. Penkman, K. E. H., Preece, R. C., Keen, D. H. & Collins, M. J. Amino acid geochronology of the type Cromerian of West Runton, Norfolk, UK. *Quaternary Int.* **228**, 25–37 (2010).
12. Sykes, G. A., Collins, M. J. & Walton, D. I. The significance of a geochemically isolated intracrystalline fraction within biominerals. *Org. Geochem.* **23**, 1059–1065 (1995).
13. Kaufman, D. S. & Manley, W. F. A new procedure for determining DL amino acid ratios in fossils using reverse phase liquid chromatography. *Quat. Sci. Rev.* **17**, 987–1000 (1998).
14. Preece, R. C. & Penkman, K. E. H. New faunal analyses and amino acid dating of the Lower Palaeolithic site at East Farm, Barnham, Suffolk. *Proc. Geol. Assoc.* **116**, 363–377 (2005).
15. Bowen, D. Q. *A Revised Correlation of Quaternary Deposits in the British Isles* (Geological Society of London, Special Report) (Geological Society, 1999).
16. Bridgland, D. R. River terrace systems in north-west Europe: an archive of environmental change, uplift and early human occupation. *Quat. Sci. Rev.* **19**, 1293–1303 (2000).
17. Gibbard, P. *The Pleistocene History of the Lower Thames Valley* (Cambridge University Press, 1994).
18. Bridgland, D. R. *Quaternary of the Thames* (Chapman and Hall, 1994).
19. Bridgland, D. R. The Middle and Upper Pleistocene sequence in the Lower Thames: a record of Milankovitch climatic fluctuation and early human occupation of southern Britain: Henry Stopes Memorial Lecture. *Proc. Geol. Assoc.* **117**, 281–305 (2006).
20. Bridgland, D. R. *et al.* The Palaeolithic occupation of Europe as revealed by evidence from the rivers: data from IGCP 449. *J. Quaternary Sci.* **21**, 437–455 (2006).
21. Maddy, D., Keen, D. H., Bridgland, D. R. & Green, C. P. A revised model for the Pleistocene development of the River Avon, Warwickshire. *J. Geol. Soc. Lond.* **148**, 473–484 (1991).
22. White, T. S., Bridgland, D. R. & Howard, A. J. in *The Quaternary of the Trent Valley and Adjoining Regions: Field Guide* (eds White, T. S., Bridgland, D. R., Howard, A. J., & White, M. J.) 10–23 (Quaternary Research Association, 2007).
23. Boreham, S., White, T. S., Bridgland, D. R., Howard, A. J. & White, M. J. The Quaternary history of the Wash fluvial network. *Proc. Geol. Assoc.* **121**, 393–409 (2010).
24. Coope, G. R. & Angus, R. B. An ecological study of a temperate interlude in the middle of the last glaciation, based on fossil Coleoptera from Isleworth, Middlesex. *J. Anim. Ecol.* **44**, 365–391 (1975).
25. Maddy, D. *et al.* The Upper Pleistocene deposits at Cassington, near Oxford, England. *J. Quaternary Sci.* **13**, 205–231 (1998).
26. Meijer, T. & Preece, R. C. A review of the occurrence of *Corbicula* in the Pleistocene of North-west Europe. *Netherlands J. Geosci.* **79**, 241–255 (2000).
27. Preece, R. C. *et al.* Biostratigraphic and aminostratigraphic constraints on the age of the Middle Pleistocene glacial succession in North Norfolk, UK. *J. Quaternary Sci.* **24**, 557–580 (2009).
28. White, M. J. & Ashton, N. Lower Palaeolithic core technology and the origins of the Levallois method in North-Western Europe. *Curr. Anthropol.* **44**, 598–609 (2003).
29. Lewis, S. G., Ashton, N. & Jacobi, R. in *The Ancient Human Occupation of Britain* (eds N. Ashton, S. G. Lewis & C. Stringer) 125–164 (Elsevier, 2010).
30. Jansen, E. *et al.* in *Climate Change 2007: The Physical Science Basis. Contribution of Working Group I to the Fourth Assessment Report of the Intergovernmental Panel on Climate Change* (eds Solomon, S. *et al.*) (Cambridge Univ. Press, 2007).

Supplementary Information is linked to the online version of the paper at [www.nature.com/nature](http://www.nature.com/nature).

**Acknowledgements** We thank D. Maddy, P. Allen, N. Ashton, D. Bain, M. Bates, S. Boreham, D. Bowen, R. Briant, C. Buckingham, J. Clayden, G. R. Coope, A. Cruickshanks, P. Dark, B. Demarchi, M. Greenwood, D. Kaufman, T. van Kolfschoten, H. Langford, S. Lewis, R. Markham, D. Mayhew, H. Roe, J. Rose, D. Schreve, R. Scott, K. Scott, C. Stringer, R. Waggoner, M. Warren and F. Wenban-Smith for providing some of the material analysed and general discussion. C. Helmsley and J. Todd released material from the Natural History Museum, London, for destructive analysis. R. Allen provided technical support. G. Peeters gave permission to reproduce images of *Bithynia*. The analyses were funded by English Heritage, NERC and the Wellcome Trust (grant GR076905MA). This is a contribution to the Ancient Human Occupation of Britain (AHOB) project funded by the Leverhulme Trust.

**Author Contributions** K.E.H.P., M.J.C., R.C.P. and D.H.K. designed the study. R.C.P., D.H.K., T.M., D.R.B., S.A.P., T.S.W. and K.E.H.P. supplied samples. K.E.H.P. undertook the analyses and processed the data. K.E.H.P., M.J.C., R.C.P. and T.S.W. wrote the paper. All authors discussed the results and commented on the manuscript.

**Author Information** Reprints and permissions information is available at [www.nature.com/reprints](http://www.nature.com/reprints). The authors declare no competing financial interests. Readers are welcome to comment on the online version of this article at [www.nature.com/nature](http://www.nature.com/nature). Correspondence and requests for materials should be addressed to K.E.H.P. ([kirsty.penkman@york.ac.uk](mailto:kirsty.penkman@york.ac.uk)).

# The wMel *Wolbachia* strain blocks dengue and invades caged *Aedes aegypti* populations

T. Walker<sup>1\*</sup>, P. H. Johnson<sup>3\*</sup>, L. A. Moreira<sup>1†</sup>, I. Iturbe-Ormaetxe<sup>1</sup>, F. D. Frentiu<sup>1</sup>, C. J. McMeniman<sup>1‡</sup>, Y. S. Leong<sup>1</sup>, Y. Dong<sup>1</sup>, J. Axford<sup>2</sup>, P. Kriesner<sup>2</sup>, A. L. Lloyd<sup>4,5</sup>, S. A. Ritchie<sup>3</sup>, S. L. O'Neill<sup>1,6</sup> & A. A. Hoffmann<sup>2</sup>

Dengue fever is the most important mosquito-borne viral disease of humans with more than 50 million cases estimated annually in more than 100 countries<sup>1,2</sup>. Disturbingly, the geographic range of dengue is currently expanding and the severity of outbreaks is increasing<sup>2–4</sup>. Control options for dengue are very limited and currently focus on reducing population abundance of the major mosquito vector, *Aedes aegypti*<sup>5,6</sup>. These strategies are failing to reduce dengue incidence in tropical communities and there is an urgent need for effective alternatives. It has been proposed that endosymbiotic bacterial *Wolbachia* infections of insects might be used in novel strategies for dengue control<sup>7–9</sup>. For example, the wMelPop-CLA *Wolbachia* strain reduces the lifespan of adult *A. aegypti* mosquitoes in stably transinfected lines<sup>8</sup>. This life-shortening phenotype was predicted to reduce the potential for dengue transmission. The recent discovery that several *Wolbachia* infections, including wMelPop-CLA, can also directly influence the susceptibility of insects to infection with a range of insect and human pathogens<sup>9–11</sup> has markedly changed the potential for *Wolbachia* infections to control human diseases. Here we describe the successful transinfection of *A. aegypti* with the avirulent wMel strain of *Wolbachia*, which induces the reproductive phenotype cytoplasmic incompatibility with minimal apparent fitness costs and high maternal transmission, providing optimal phenotypic effects for invasion. Under semi-field conditions, the wMel strain increased from an initial starting frequency of 0.65 to near fixation within a few generations, invading *A. aegypti* populations at an accelerated rate relative to trials with the wMelPop-CLA strain. We also show that wMel and wMelPop-CLA strains block transmission of dengue serotype 2 (DENV-2) in *A. aegypti*, forming the basis of a practical approach to dengue suppression<sup>12</sup>.

A successful *Wolbachia*-based program for dengue control requires the inherited bacterial infection to efficiently invade wild *A. aegypti* populations. Invasion is based on the induction of a particular reproductive phenotype by *Wolbachia* known as cytoplasmic incompatibility<sup>13,14</sup>, which leads to early embryonic death when *Wolbachia*-infected males mate with uninfected females. In contrast, *Wolbachia*-infected females produce viable embryos when mated with either infected or uninfected males, resulting in a reproductive advantage over uninfected females<sup>13</sup>. Although cytoplasmic incompatibility provides a driving force for *Wolbachia* invasion, successful invasion also depends on both the initial frequency of *Wolbachia* as well as any host fitness costs<sup>15</sup>. As fitness costs increase, higher initial *Wolbachia* frequencies are required for invasion. Mathematical predictions indicate that as the fitness cost of infection approaches 0.5 then spatial spreading of *Wolbachia* slows to zero<sup>15</sup>. Therefore, although the wMelPop-CLA strain induces complete cytoplasmic incompatibility in *A. aegypti*<sup>8</sup>, fitness costs associated with this virulent infection may be sufficient to prevent invasion<sup>15,16</sup>.

In *Drosophila*, interference against insect pathogens is induced by several *Wolbachia* strains closely related to wMelPop-CLA<sup>10</sup>, indicating that strains with more desirable invasion characteristics would also impact human pathogen transmission. The *Wolbachia* strain wMel occurs naturally in *Drosophila melanogaster* flies and has spread globally within the last century<sup>17</sup>. Moreover, it interferes effectively with *Drosophila* RNA viruses in its natural host<sup>10,11</sup>. Considering these properties, we established *A. aegypti* colonies stably infected with this *Wolbachia* strain and determined if wMel might be effective for dengue control programs.

To facilitate transinfection of *A. aegypti*, the wMel strain was first transferred from *Drosophila melanogaster* embryos into the RML-12 mosquito cell line and serially passaged for approximately two years to allow adaptation to the mosquito intracellular environment. A total of 2,541 *A. aegypti* embryos were microinjected with *Wolbachia* purified from this cell line (Supplementary Fig. 1). Three stably infected lines, MGYP1, MGYP2 and MGYP3, were generated independently and PCR screening indicated each line was 100% infected from generations 2–8 (G2–G8) after infection. The MGYP2 line was selected for further characterization and a tetracycline-cured line, MGYP2.tet, was established by G8 after infection. An outbred MGYP2.OUT line was established by backcrossing for three generations to the F1 progeny of wild-caught *A. aegypti* eggs from Cairns, Australia, as outlined elsewhere<sup>16</sup>. The F1 progeny from wild-caught eggs were used as control 'wild-type' mosquitoes for comparison to outbred wMel-infected MGYP2.OUT mosquitoes.

The density of the wMel strain in all three transinfected lines and outcrossed *A. aegypti* female mosquitoes (3 days old) was similar with WSP (*Wolbachia*) to RPS17 (*A. aegypti*) gene ratios of about 10, which was approximately threefold lower than the density of the wMelPop-CLA strain as determined by quantitative PCR (qPCR; Supplementary Fig. 2). The tissue distribution of the wMel infection in adult female mosquitoes was also visualized using fluorescence *in situ* hybridization (FISH). The wMel strain has a wide tissue distribution with infection levels in the ovaries and salivary glands (Fig. 1) similar to those of the wMelPop-CLA strain<sup>9</sup>. The heavy infection of ovaries by both strains supports the high level of maternal transmission and infection frequency observed in infected lines. However, unlike wMelPop-CLA, the wMel strain is not present at high levels in Malpighian tubules and fat bodies (Fig. 1), thoracic ganglia or brain tissues (Supplementary Fig. 3). Therefore, the pathogenic effects of wMelPop-CLA infection previously observed in *A. aegypti*<sup>8,9</sup> may be a direct result of *Wolbachia* colonization of specific mosquito tissues.

Mass reciprocal crossing experiments between MGYP2 and MGYP2.tet mosquitoes (Supplementary Table 1) showed that the wMel strain induces strong cytoplasmic incompatibility (no hatching eggs produced). In contrast, wMel-infected females mated to uninfected and

<sup>1</sup>School of Biological Sciences, The University of Queensland, Brisbane, Queensland 4072, Australia. <sup>2</sup>Bio21 Institute, Department of Genetics, The University of Melbourne, Victoria 3010, Australia. <sup>3</sup>School of Public Health and Tropical Medicine and Rehabilitative Sciences, James Cook University, Cairns, Queensland 4870, Australia. <sup>4</sup>Biomathematics Graduate Program and Department of Mathematics, North Carolina State University, Raleigh, North Carolina 27695, USA. <sup>5</sup>Fogarty International Center, National Institutes of Health, Bethesda, Maryland 20892, USA. <sup>6</sup>School of Biological Sciences, Monash University, Victoria 3800, Australia. <sup>†</sup>Present addresses: Centro de Pesquisas René Rachou-Fiocruz, Belo Horizonte, MG 30190, Brasil (L.A.M.); Laboratory of Neurogenetics and Behavior, The Rockefeller University, 1230 York Avenue, Campus Box 63, New York, New York 10065, USA (C.J.M.).

\*These authors contributed equally to this work.



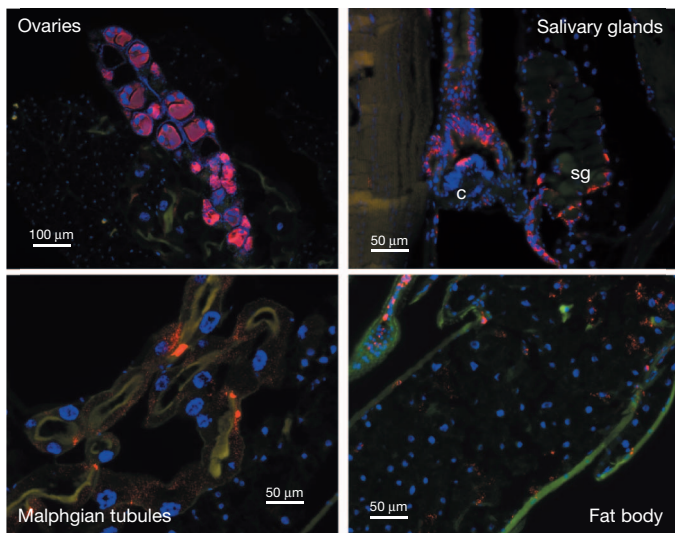


**Figure 1 | Tissue distribution of the *wMel* strain in transinfected *A. aegypti* female mosquitoes.** Fluorescence *in situ* hybridization (FISH) of paraffin sections showing the localization of *Wolbachia* (red) in tissues of 7-day-old female *A. aegypti* mosquitoes. Sections were hybridized with two *Wolbachia*-specific 16S rRNA probes labelled with rhodamine. DNA is stained with DAPI (blue). A green GFP filter was used to enhance contrast. sg, salivary gland; c, cardia.

*wMel*-infected males resulted in embryo hatch rates of approximately 90%. Strong cytoplasmic incompatibility was also observed when *wMel* was introduced into an outbred *A. aegypti* background using backcrossing<sup>16</sup> to produce an outbred MGY2.OUT strain (Supplementary Table 1).

We investigated potential fitness effects by examining fecundity and viability of eggs over time, both strongly influenced by the *wMelPop-CLA* strain of *Wolbachia*<sup>16,18</sup>. As shown in Supplementary Figure 4, under semi-field conditions fecundity in outbred MGY2.OUT mosquitoes was not significantly different to that of uninfected mosquitoes. In contrast to this, a fecundity cost of ~56% was observed for *wMelPop-CLA*-infected females. In addition to fecundity, the viability of eggs is a crucial determinant of *A. aegypti* abundance following a dry season<sup>19</sup> and the *wMelPop-CLA* infection markedly decreased the viability of *A. aegypti* eggs<sup>16,18</sup>. However, the *wMel* infection had no significant effects on viability of eggs at 5–26 days after oviposition (Supplementary Fig. 5), in contrast to a sharp reduction for *wMelPop-CLA*-infected eggs at 12 days. The *wMel* strain is therefore much more likely to persist in wild *A. aegypti* populations in areas with a long dry season such as North Queensland, Australia<sup>19,20</sup>.

The effect of the *wMel* strain on immature mosquito stages was measured through larval development time, a potential correlate of mosquito fitness<sup>21</sup>. The *wMel* strain caused significantly faster larval development for both females and males under high larval nutrition diets (Supplementary Table 2). Under low nutritional levels typically encountered in the field<sup>22</sup>, the *wMel* infection did not affect the development time of either sex. The longevity of adult mosquitoes can influence fitness, and the life-shortening effect of the *wMelPop-CLA* strain was predicted to reduce invasion potential<sup>15</sup>. We tested the effect of the *wMel* strain on lifespan of outbred MGY2.OUT females versus wild-type females and found only approximately 10% reduction in mean longevity (Supplementary Fig. 6), compared to more than 40% for the *wMelPop-CLA* strain<sup>16</sup>. Finally, we found that 100% of offspring from 30 MGY2.OUT females ( $n = 30$  offspring per female) were infected by *wMel*, indicating a high maternal transmission rate of 1.0 (lower 95% confidence interval, 0.89).

We tested the invasion potential of *Wolbachia* in a semi-field facility consisting of two cages (A and B) providing environments that simulate the natural habitat of *A. aegypti* in north Queensland, Australia<sup>23</sup>.

We separately tested the potential of the *wMel* and *wMelPop-CLA* strains to invade uninfected mosquito populations at a starting frequency of 0.65 (likely to be achievable in open releases) and with additional near-weekly supplementary additions of *Wolbachia*-infected mosquitoes<sup>24</sup>. The semi-field cage invasion experiment methodology is summarized in Supplementary Fig. 8. The *wMel* infection increased rapidly and reached fixation in cage B within 30 days and in cage A within 80 days (Fig. 2a). In contrast, *wMelPop-CLA* increased at a slower rate (Fig. 2b) and reached fixation in cage B after 40 days and approximately 80% after 80 days in cage A. The two cages differed in that there were fewer overall mosquitoes present in cage B, most probably because of predation by two geckos found in this cage. This may have increased adult mortality rates and decreased in later life any fitness costs associated with *Wolbachia* infection. *Wolbachia* therefore seemed to be more invasive when overall mortality rates were high (in cage B), which may be a better reflection of field conditions<sup>25</sup>.

To determine if invasion rates could be predicted by model simulations, a deterministic age-structured model was used to describe the population in the cage, tracking daily cohorts of adult mosquitoes, categorized by sex and *Wolbachia* infection status, and their relative fitness (Supplementary Information). Different parameters were used for the two strains of *Wolbachia* because of the lower deleterious fitness effects associated with *wMel* and lack of substantial longevity effects of this strain. The models provided a good fit to the data (Fig. 2), including

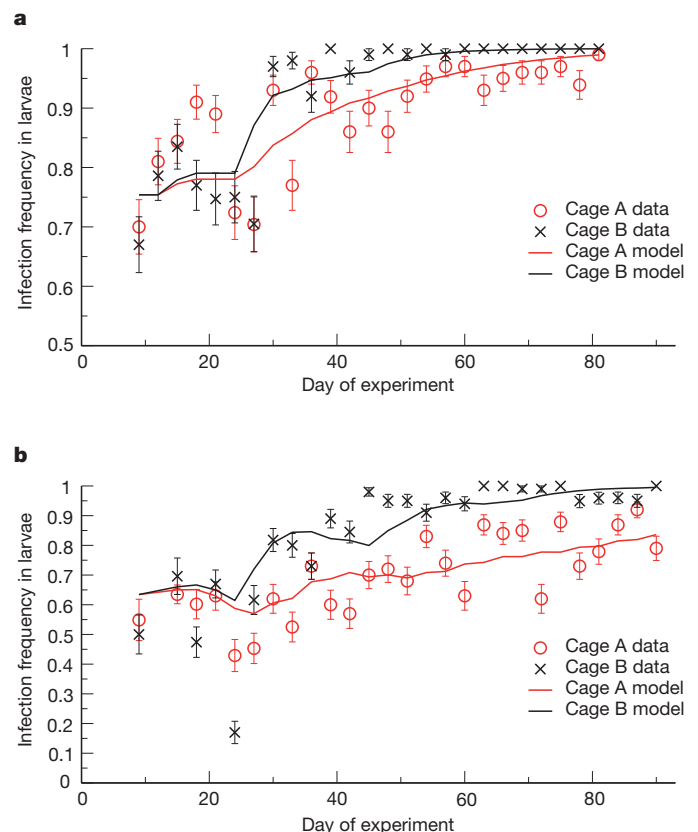


**Figure 2 | Predicted and observed invasion dynamics under semi-field conditions.** a, b, *wMel* strain (a) and *wMelPop-CLA* strain (b) infection frequencies in larvae in cages A (red curves and symbols) and B (black curves and symbols). Curves indicate model-based predictions, as explained in the supplementary information. Symbols denote frequencies observed in the cages with error bars indicating binomial standard errors. Infected pupae initially comprised 65% of the released population in each cage. Eggs were collected from the cage in ovitraps and pupae developing from these eggs were released back into the cage at 3-day intervals. To simulate field releases involving repeated releases of infected mosquitoes, additional infected pupae were released into the cage, comprising a third of the total pupae released.



the difference between cage A and cage B, when additional mortality levels were introduced.

We tested the vector competence of *wMel*-infected females by feeding mosquitoes a dengue serotype 2 (DENV-2)-infected blood meal to determine levels of virus in whole bodies, legs for disseminated virus and saliva for transmission. Virus levels were assessed at 14 days after infection, as the extrinsic incubation period (EIP) for dengue before transmission to a new host is typically 7–14 days<sup>26,27</sup>. Vector competence experiments also included outbred *wMel*-infected MGYP2.OUT mosquitoes to remove any inbreeding effects that might influence dengue vector competence<sup>28,29</sup>. Total DENV-2 levels in *wMel*-infected MGYP2.OUT females (whole bodies) were markedly reduced by *Wolbachia*, with approximately 1,500-fold (3 logs) fewer copies present compared to *Wolbachia*-uninfected controls (Fig. 3a). Levels of DENV-2 in *wMelPop*-CLA-infected PGYP1.OUT females were even lower with 4 logs less virus present compared to controls. Disseminated virus, measured in the legs of individual mosquitoes, was detected in only 12.5% (3/24) of *wMel*-infected MGYP2 females compared to 82.6% (19/23) of *Wolbachia*-uninfected MGYP2.tet mosquitoes. Overall disseminated virus levels in the legs of *wMel*-infected females were approximately 2,600-fold lower than in *Wolbachia*-uninfected females (Fig. 3b), confirming very strong inhibition of dengue virus replication in mosquitoes infected by the *wMel* strain.

In addition to examining levels of dengue nucleic acid in mosquito extracts, we also examined the presence of infectious virus in mosquito saliva. Pooled saliva samples at 14 days after infection were assayed for infectious dengue virus using plaque assays<sup>30</sup>. Infectious virus was present in 29 out of 36 (80.2%) pooled saliva samples from *Wolbachia*-uninfected MGYP2.tet mosquitoes (Table 1). In contrast, infectious virus was only detected in 2 out of 48 pooled saliva samples from the transinfected MGYP2 line with each DENV-2-positive saliva pool containing 2 plaque-forming units (Supplementary Fig. 7). When the individual mosquitoes in these two positive pools were examined, a single individual in each pool was determined to be uninfected with *Wolbachia*. Moreover, these same individuals tested dengue-positive by PCR. Rare *Wolbachia*-uninfected individuals may be occasionally produced through imperfect maternal transmission<sup>8</sup>. No infectious virus was detected in the 36 pooled saliva samples from MGYP2.OUT

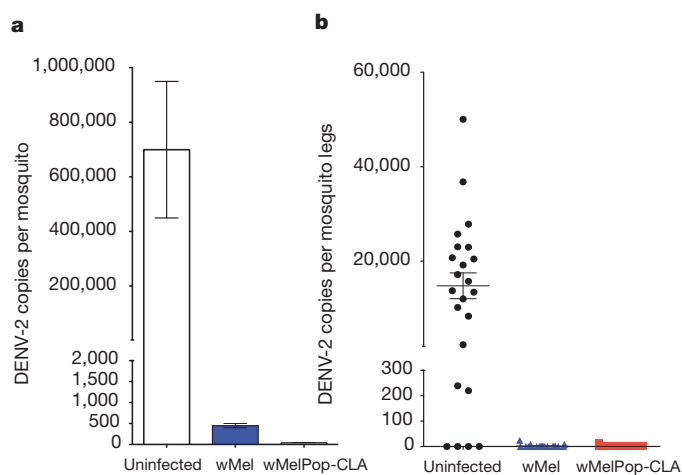


**Figure 3 | Dengue infection levels in mosquitoes.** Mosquitoes were fed DENV-2-infected blood orally (DENV-2 titre  $1.5 \times 10^7$  plaque-forming units per ml) and titre determined at 14 days after infection. **a**, qPCR of total dengue virus in whole female mosquitoes ( $n = 19$ –30). Bars represent overall means  $\pm$  s.e.m. across three independent replicate experiments. White bar, *Wolbachia*-uninfected wild-type control mosquitoes; blue bar, *wMel*-infected MGYP2.OUT; red bar, *wMelPop*-CLA-infected PGYP1.OUT. **b**, qPCR of disseminated dengue virus in the legs of individual *Wolbachia*-uninfected MGYP2.tet (black circles), *wMel*-infected MGYP2 (blue triangles) and *wMelPop*-CLA infected PGYP1 (red squares) mosquitoes ( $n = 23$ –30).

**Table 1 | Prevalence of infectious DENV-2 in pooled saliva extracts.**

Mosquito line	<i>Wolbachia</i> infection	DENV-2-positive pools/total saliva pools	Saliva pools positive for DENV-2 (%)
MGYP2.tet	Uninfected	29/36	80.2
MGYP2	<i>wMel</i>	2/48*	4.2
MGYP2.OUT	<i>wMel</i>	0/36	0.0
PGYP1	<i>wMelPop</i> -CLA	0/14	0.0
PGYP1.OUT	<i>wMelPop</i> -CLA	0/22	0.0

Mosquitoes were orally fed DENV-2 in an artificial blood meal (DENV-2 titer  $1.5 \times 10^7$  plaque-forming units per ml) across three independent replicate experiments. Saliva was collected 14 days after blood feeding by placing the mosquito proboscis into filtered pipette tips and the saliva was pooled into groups of four for plaque assays to determine the presence of infectious virus in the saliva ( $n = 56$ –196 saliva extracts per strain).

\* Both DENV-2-positive saliva pools from the MGYP2 line included saliva contributed from *Wolbachia*-uninfected females.

females. These data indicate complete blockage of DENV-2 transmission under the experimental conditions used. As shown in Table 1, complete absence of DENV-2 in PGYP1 and PGYP1.OUT saliva extracts indicates that the closely related *wMelPop*-CLA strain also blocks DENV-2 transmission.

To our knowledge, this is the first reported case of complete blockage of dengue transmission by *Wolbachia*-infected mosquitoes. No infectious DENV-2 virus was detected in the saliva of any of the 336 *wMel*-infected *A. aegypti* females used in artificial feeding experiments. The *wMel*-infected mosquitoes had detectable DENV-2 virus in their bodies (albeit significantly reduced levels compared to control mosquitoes), but dengue virus did not disseminate into mosquito saliva. This may coincide with the heavy *wMel* infection of salivary gland tissue (Fig. 1). Although the *wAlbB* strain of *Wolbachia* was previously shown to reduce dengue levels in mosquito saliva, infectious virus was still detected in 62.5% of pooled saliva from *wAlbB*-transinfected mosquitoes using similar methodology<sup>30</sup>. The ability of *wMel* to provide protection against dengue virus in *A. aegypti* is unlikely to be transient; *wMel* provides protection against insect viruses in its native *Drosophila melanogaster* host<sup>10</sup> despite a long-term evolutionary association. Recently *wMel* has also been shown to induce strong resistance against West Nile virus in *D. melanogaster*<sup>31</sup>, suggesting potential blocking of other human pathogens.

A major advantage of a *Wolbachia*-based biocontrol approach is that cytoplasmic incompatibility can result in invasion from the release of relatively small numbers of individuals. This invasive potential is demonstrated by the successful global invasion of *D. melanogaster* by *wMel* within the last 80 years<sup>17</sup>. The apparent minimal fitness costs of the *wMel* infection in *A. aegypti* are critical for ensuring a relatively low unstable point (<40%) from which invasions can occur<sup>15,16</sup>, and the semi-field cage experiments demonstrate that rapid invasion is possible.

The direct inhibition of pathogens by *Wolbachia* may also augment cytoplasmic incompatibility as a mechanism for population invasion by providing a positive fitness benefit to insects carrying *Wolbachia*—something that cannot be tested in experimental invasion studies in our semi-field system. This benefit may overlay the traditional ‘Bartonian’ view of cytoplasmic-incompatibility-based invasion dynamics and provide an additional driving force for *Wolbachia*<sup>14,15</sup>. These results pave the way for an open release of *wMel*-infected *A. aegypti* mosquitoes in Cairns, Australia<sup>12</sup>.

## METHODS SUMMARY

The RML-12 cell line was infected with *wMel Wolbachia* from *Drosophila melanogaster* yw<sup>67c23</sup> embryos using the shell vial technique and maintained by continuous serial passage. Embryos of the JCU strain of *A. aegypti* were micro-injected with *Wolbachia* purified from the RML-12 cell line (passages 130–132). Screening for *wMel* infection was done using PCR primers specific for the IS5 repeat element. Routine mosquito maintenance, tetracycline treatment to remove the *wMel* infection and lifespan assays were performed as previously described<sup>8</sup>. An outcrossed line (MGYP2.OUT) was established by backcrossing the MGYP2 line for three generations to the F1 progeny of wild-collected *A. aegypti* eggs<sup>16</sup>. Fitness assessments involved a comparison between the outcrossed line and uninfected line established from the wild-collected eggs of similar genetic background. *Wolbachia*

density was estimated using the single-copy *Wolbachia* surface protein (WSP) and *A. aegypti* RPS17 genes. FISH was carried out on 7-day-old MGY2 and MGY2.OUT adult females using a *Wolbachia*-specific 16S ribosomal RNA probe<sup>9</sup>. Reciprocal mass crosses were conducted between virgin individuals (3 days old) of each sex to determine cytoplasmic incompatibility levels. Fecundity was assessed using multiple human volunteer feeders with 20–25 mosquitoes per feed. Embryo viability and larval development assays were conducted as previously outlined<sup>16</sup>. Two separate cage invasion experiments were performed by releasing wMel-infected MGY2.OUT and wMelPop-CLA-infected PGYP1.OUT mosquitoes at a starting frequency of 0.65 into two independent semi-field cages (A and B) and competing these with uninfected mosquitoes with a similar genetic background. A total of 1,680 mosquitoes were initially introduced into the cages over 6 days. Mosquitoes were provided access to live human blood almost daily. Eggs were collected from the cages every 3 days (starting at day 9), hatched and reared in the laboratory. A sample of the larvae was tested for *Wolbachia* infection and additional larvae were reared to pupae to be released back into the cages following the 3-day egg collection schedule. In addition, from day 7, supplementary cohorts of *Wolbachia*-infected mosquitoes were released in the cages every 6 days to simulate what would be expected in an open field release program<sup>24</sup>. Dengue vector competence was assessed using oral feeding with DENV-2 (92T strain) at 14 days after infection at a titre of  $1.5 \times 10^7$  plaque-forming units per ml as determined using immunoplaque assays. Oral feeding, RNA extraction, cDNA synthesis and qPCR analysis for total DENV-2 levels in females was carried out using protocols previously outlined<sup>9</sup>. Disseminated viral infection rates in mosquito legs were measured after RNA extraction using a QIAamp Viral RNA Mini Kit (Qiagen). Mosquito saliva from four mosquitoes was pooled and used in immunoplaque assays.

**Full Methods** and any associated references are available in the online version of the paper at [www.nature.com/nature](http://www.nature.com/nature).

**Received 14 April; accepted 6 July 2011.**

- Calisher, C. H. Persistent emergence of dengue. *Emerg. Infect. Dis.* **11**, 738–739 (2005).
- Kyle, J. L. & Harris, E. Global spread and persistence of dengue. *Annu. Rev. Microbiol.* **62**, 71–92 (2008).
- Guzman, M. G. *et al.* Dengue: a continuing global threat. *Nature Rev. Microbiol.* **8**, S7–S16 (2010).
- Franco, C., Hynes, N. A., Bouri, N. & Henderson, D. A. The dengue threat to the United States. *Biosecur. Bioterror.* **8**, 273–276 (2010).
- Heintze, C., Garrido, M. V. & Kroeger, A. What do community-based dengue control programmes achieve? A systematic review of published evaluations. *Trans. R. Soc. Trop. Med. Hyg.* **101**, 317–325 (2007).
- Whitehead, S. S., Blaney, J. E., Durbin, A. P. & Murphy, B. R. Prospects for a dengue virus vaccine. *Nature Rev. Microbiol.* **5**, 518–528 (2007).
- Cook, P. E., McMeniman, C. J. & O'Neill, S. L. Modifying insect population age structure to control vector-borne disease. *Adv. Exp. Med. Biol.* **627**, 126–140 (2008).
- McMeniman, C. J. *et al.* Stable introduction of a life-shortening *Wolbachia* infection into the mosquito *Aedes aegypti*. *Science* **323**, 141–144 (2009).
- Moreira, L. A. *et al.* A *Wolbachia* symbiont in *Aedes aegypti* limits infection with dengue, chikungunya, and *Plasmodium*. *Cell* **139**, 1268–1278 (2009).
- Hedges, L. M., Brownlie, J. C., O'Neill, S. L. & Johnson, K. N. *Wolbachia* and virus protection in insects. *Science* **322**, 702 (2008).
- Teixeira, L., Ferreira, A. & Ashburner, M. The bacterial symbiont *Wolbachia* induces resistance to RNA viral infections in *Drosophila melanogaster*. *PLoS Biol.* **6**, e2 (2008).
- Hoffmann, A. A. *et al.* Successful establishment of *Wolbachia* in *Aedes* populations to suppress dengue transmission. *Nature* doi:10.1038/nature10356 (this issue).
- Hoffmann, A. A. & Turelli, M. In *Influent Passengers: Inherited Microorganisms and Arthropod Reproduction* (eds O'Neill, S. L., Hoffmann, A. A. & Werren, J. H.) 42–80 (Oxford Univ. Press, 1997).
- Turelli, M. & Hoffmann, A. A. Rapid spread of an inherited incompatibility factor in California *Drosophila*. *Nature* **353**, 440–442 (1991).
- Turelli, M. Cytoplasmic incompatibility in populations with overlapping generations. *Evolution* **64**, 232–241 (2010).
- Yeap, H. L. *et al.* Dynamics of the “popcorn” *Wolbachia* infection in outbred *Aedes aegypti* informs prospects for mosquito vector control. *Genetics* **187**, 583–595 (2011).
- Riegler, M., Sidhu, M., Miller, W. J. & O'Neill, S. L. Evidence for a global *Wolbachia* replacement in *Drosophila melanogaster*. *Curr. Biol.* **15**, 1428–1433 (2005).
- McMeniman, C. J. & O'Neill, S. L. A virulent *Wolbachia* infection decreases the viability of the dengue vector *Aedes aegypti* during periods of embryonic quiescence. *PLoS Negl. Trop. Dis.* **4**, e748 (2010).
- Kearney, M., Porter, W. P., Williams, C., Ritchie, S. & Hoffmann, A. A. Integrating biophysical models and evolutionary theory to predict climatic impacts on species' ranges: the dengue mosquito *Aedes aegypti* in Australia. *Funct. Ecol.* **23**, 528–538 (2009).
- Montgomery, B. L. & Ritchie, S. A. Roof gutters: a key container for *Aedes aegypti* and *Ochlerotatus notoscriptus* (Diptera: Culicidae) in Australia. *Am. J. Trop. Med. Hyg.* **67**, 244–246 (2002).
- Telang, A. & Wells, M. A. The effect of larval and adult nutrition on successful autogenous egg production by a mosquito. *J. Insect Physiol.* **50**, 677–685 (2004).
- Maciá, A. Differences in performance of *Aedes aegypti* larvae raised at different densities in tires and ovitraps under field conditions in Argentina. *J. Vector Ecol.* **31**, 371–377 (2006).
- Ritchie, S. A. *et al.* A secure semi-field system for the study of *Aedes aegypti*. *PLoS Negl. Trop. Dis.* **5**, e988 (2011).
- Hancock, P. A., Sinkins, S. P. & Godfray, C. J. Population dynamic models of the spread of *Wolbachia*. *Am. Nat.* **177**, 323–333 (2011).
- Harrington, L. C. *et al.* Analysis of survival of young and old *Aedes aegypti* (Diptera: Culicidae) from Puerto Rico and Thailand. *J. Med. Entomol.* **38**, 537–547 (2001).
- Watts, D. M., Burke, D. S., Harrison, B. A., Whitmore, R. E. & Nisalak, A. Effect of temperature on the vector efficiency of *Aedes aegypti* for dengue 2 virus. *Am. J. Trop. Med. Hyg.* **36**, 143–152 (1987).
- Salazar, M. I., Richardson, J. H., Sanchez-Vargas, I., Olson, K. E. & Beaty, B. J. Dengue virus type 2: replication and tropisms in orally infected *Aedes aegypti* mosquitoes. *BMC Microbiol.* **7**, 9 (2007).
- Bennett, K. E. *et al.* Variation in vector competence for dengue 2 virus among 24 collections of *Aedes aegypti* from Mexico and the United States. *Am. J. Trop. Med. Hyg.* **67**, 85–92 (2002).
- Gubler, D. J., Nalim, S., Tan, R., Saipan, H. & Sulianti Saroso, J. Variation in susceptibility to oral infection with dengue viruses among geographic strains of *Aedes aegypti*. *Am. J. Trop. Med. Hyg.* **28**, 1045–1052 (1979).
- Bian, G., Xu, Y., Lu, P., Xie, Y. & Xi, Z. The endosymbiotic bacterium *Wolbachia* induces resistance to dengue virus in *Aedes aegypti*. *PLoS Pathog.* **6**, e1000833 (2010).
- Glaser, R. L. & Meola, M. A. The native *Wolbachia* endosymbionts of *Drosophila melanogaster* and *Culex quinquefasciatus* increase host resistance to West Nile virus infection. *PLoS ONE* **5**, e11977 (2010).

**Supplementary Information** is linked to the online version of the paper at [www.nature.com/nature](http://www.nature.com/nature).

**Acknowledgements** We are grateful to N. Kenny for technical support and to members of the O'Neill laboratory for critical reading of the manuscript. We thank R. Silcock, M. Janes, S. Long, C. Paton and C. Omodei for their assistance in the semi-field cages and laboratory at James Cook University. We are very grateful for all of our volunteers who helped to blood-feed the mosquitoes in the cages and to P. Young for providing the anti-dengue antibodies. This research was supported by a grant from the Foundation for the National Institutes of Health through the Grand Challenges in Global Health Initiative of the Bill and Melinda Gates Foundation, The National Health and Medical Research Council, Australia, the RAPIDD program of the NIH, the Climate and Health Cluster of the CSIRO Flagship collaboration Fund and fellowships from the Australian Research Council.

**Author Contributions** T.W. performed transinfection and initial phenotypic characterization of the infection. P.H.J., Y.S.L., Y.D. and S.A.R. performed cage invasion experiments and fecundity assays on outbred mosquito lines. T.W., L.A.M. and F.D.F. carried out vector competence assays. I.I.-O. performed FISH. C.J.M. established cell lines for transinfection. J.A. and P.K. performed cytoplasmic incompatibility and lifespan assays on outbred mosquito lines. A.L.L. undertook modelling studies. T.W. and A.A.H. performed data analysis. T.W., P.H.J., S.L.O. and A.A.H. wrote the paper. S.L.O., A.A.H. and S.A.R. provided oversight of the design and direction of the work.

**Author Information** Reprints and permissions information is available at [www.nature.com/reprints](http://www.nature.com/reprints). The authors declare no competing financial interests. Readers are welcome to comment on the online version of this article at [www.nature.com/nature](http://www.nature.com/nature). Correspondence and requests for materials should be addressed to S.L.O. ([scottoneill@monash.edu](mailto:scottoneill@monash.edu)).



## METHODS

**Transinfection.** The naturally uninfected JCU strain of *A. aegypti*, established from field-collected eggs from Cairns, Australia, in 2005, was used as the recipient strain for transinfection. Adults were provided with constant access to 10% sucrose solution and 5-day-old females were blood-fed with human blood (UQ Human Ethics Approval 2007001379). *wMel* from *Drosophila melanogaster* yw<sup>67c23</sup> embryos was established in the *Aedes albopictus* cell line RML-12 using the shell vial technique<sup>32</sup> and the infection serially passed as previously described<sup>33</sup>. Preblastoderm embryos were microinjected in the posterior pole with *wMel*, purified from RML-12 cells (*wMel* passage 130–132 in cell lines) as described previously<sup>33</sup>. Microinjection was carried out under  $\times 100$  magnification using a FemtoJet microinjector system (Eppendorf) with type II Femtotip microinjection needles (Eppendorf) using a hydrophilic membrane method. After injection, embryos were incubated at 80% relative humidity and 25 °C for approximately 40 min and transferred to wet filter paper. Embryos were then allowed to develop for 4–5 days before being hatched. Adult females (G0) that survived embryo microinjection were isolated as pupae and mated with JCU males. Following blood feeding and oviposition, DNA was extracted from G0 females using the DNeasy tissue kit (Qiagen). Screening for *wMel* infection was done using PCR primers specific for the IS5 repeat element<sup>17,34</sup>. Females from isofemale lines infected with the *wMel* strain were backcrossed to JCU males until G4 at which time the lines were closed (restricting matings to mosquitoes from within the line) with the population size maintained at several thousand adults. Routine mosquito maintenance and tetracycline treatment to remove the *wMel* infection from the MGYP2 line were carried out as previously described<sup>8</sup>. An outcrossed line (MGYP2.OUT) was established by backcrossing the MGYP2 line for three generations to the F1 progeny of wild-caught *A. aegypti* eggs from the Cairns region<sup>16</sup>. The F1 progeny was also used to generate an outbred wild-type population for comparison to the outbred *wMel*-infected MGYP2.OUT line (that is, with a similar genetic background).

**Wolbachia density and tissue distribution.** Density of the *wMel* strain was assessed by quantitative PCR (qPCR) in 3-day-old females (whole bodies) on MGYP2 and outcrossed MGYP2.OUT females ( $n = 10$ ). *Wolbachia* density was estimated by comparing the abundance of the single-copy *Wolbachia* surface protein gene (WSP) to that of the single-copy *A. aegypti* RPS17 gene. For each sample, qPCR amplification of DNA was performed in triplicate using a Rotor-Gene 6000 system (Corbett Research)<sup>34</sup>. Fluorescence *in situ* hybridization (FISH) was carried out on 7-day-old MGYP2 and MGYP2.OUT adult female mosquitoes using a *Wolbachia*-specific 16S rRNA probe<sup>9,34</sup>.

**Cytoplasmic incompatibility and fitness assays.** Reciprocal mass crosses were conducted between 30 virgin individuals (3 days old) of each sex from the MGYP2 and MGYP2.tet lines to determine cytoplasmic incompatibility levels. This was repeated with 10 virgins from the MGYP2.OUT and wild-type lines. Fecundity, the total number of eggs laid by females, was assessed using 3–5 independent human volunteer blood feeders with 15–25 mosquitoes per feed. This was repeated with MGYP2.OUT and wild-type lines using 21–22 mosquitoes and an additional experiment was carried out to determine the total number of eggs laid over a 6-day period after blood feeding. Diapause egg viability was assessed after MGYP2, MGYP2.tet and PGYP1 females were blood-fed on human volunteers and isolated individually for oviposition. Egg batches were transferred to plastic storage boxes and maintained at a temperature of  $25 \pm 1$  °C and 85% relative humidity using saturated KCl solution as previously described<sup>16</sup>. Larval development time was measured as the time between 1st instar hatching and pupation. A low nutritional level, 0.05 mg of food per larva per day, was previously determined to significantly delay larval development time when compared to the standard rearing nutritional level of 1 mg of food per larva per day<sup>16</sup>. Two-sample *t*-tests were used to compare fecundity, embryo viability and larval development times between mosquito lines as well as mean and median longevity per cage. Mosquito survival was also analysed using Cox regression to determine the equality of the survival distributions between treatments after pooling data across replicates.

**Semi-field cage invasion experiments.** These experiments used the backcrossed lines and controls with a similar genetic background from Cairns. Initial starting frequency of *Wolbachia*-infected mosquitoes for both *wMel* and *wMelPop-CLA* invasion experiments was 0.65, reflecting a release ratio of around 2 infected mosquitoes to 1 uninfected mosquito; this ratio was considered achievable under field conditions in North Queensland given the relatively low number of adult mosquitoes in houses<sup>35</sup>. The *wMelPop-CLA* strain was tested from November 2009 to March 2010 and *wMel* from April to July 2010. The same procedure and schedule were used in both experiments. A total of 1,680 mosquitoes were introduced into the cage over a period of 6 days. Each day 120 female pupae (78 infected and 42 non-infected) and 120 male pupae (78 infected and 42 non-infected) were released into the cage. Mean minimum and maximum

temperature and relative humidity conditions in the cages were: cage A, 20.7–30.1 °C and 64.0–98.0%; cage B, 20.5–29.1 °C and 54.1–97.8% respectively. Mosquitoes were provided access to a blood meal almost daily (at least 6 days per week) using 1–3 human volunteers (James Cook University Human Ethics H2250). The volunteers sat in the cages and allowed mosquitoes to feed uninterrupted for 15 min. For each blood-feeding session, the same volunteers were used for both cages. The first-fed cage was alternated between sessions.

Twelve oviposition sites were distributed throughout each cage. An oviposition site consisted of a 4 l white plastic bucket filled with 2 l of a 10% hay infusion solution. A 10  $\times$  15 cm strip of red flannelette cloth (ovistrip) was attached to the inside of each bucket as an oviposition substrate. All ovistrips were retrieved every 3 days (starting from day 9), moved to the laboratory and kept damp for 3 days so that all eggs could embryonate. Ovistrips were partially dried on the third day and hatched in a dilute solution (1 g in 1 l of water) of activated baker's yeast in the afternoon. Thus, the age of the eggs at hatching was between 3 and 6 days.

Two days after hatching, all larvae were pooled and mixed thoroughly in a 10 l bucket, and a sample of at least 100 larvae was collected to assess *Wolbachia* infection frequency. The sampled larvae were placed in clean water for at least 1 h and then killed and stored in 80% ethanol. Samples were stored at 2–5 °C before being processed to determine infection status. The remaining larvae were reared to pupae and a cohort sample of 60 female and 60 male pupae were returned to each cage. Pupae from the midpoint of the pupation period, usually at days 6–8, were returned. Cohorts of pupae were returned to the cages every 3 days, following the egg-collection schedule. By using this procedure, around 500–700 adults were maintained in each cage. Additional cohorts of *Wolbachia*-infected mosquitoes were regularly released in the cages over the course of the experiment, to simulate an ongoing field release program. Starting on day 7, *Wolbachia*-infected pupae were added to the cage so that they constituted a third of the total pupae released over a 6-day period resulting in 120 *Wolbachia*-infected pupae (60 females and 60 males) included for every 240 cage-cohort pupae. For this purpose, *Wolbachia*-infected mosquitoes were reared in the laboratory and added to the cages to coincide with every second cage-cohort release.

**Wolbachia infection status of *A. aegypti*** was tested with a multiplex PCR assay. Larvae (second instars) hatched from eggs collected in oviposition buckets were preserved in ethanol. Larvae were washed twice individually for at least 10 s in distilled water to remove ethanol residue. Each larva was dried briefly with paper towel and put into a well of a 96-well PCR plate with 20  $\mu$ l of lysis buffer (10 mM Tris pH 8.4, 1 mM EDTA, 50 mM NaCl, 0.25  $\mu$ l DNase Release Additive (Finnzymes Oy)). The samples were then incubated at 56 °C for 5 min and then boiled at 95 °C for 5 min. Multiplex PCR was carried out with primers amplifying a fragment of the WSP gene of *Wolbachia* (185 base pairs) and with primers amplifying a fragment of ribosomal protein S17 (RPS17) from *A. aegypti* (305 bp). The RPS17 primers were designed to act as a control for the presence of amplifiable DNA or any PCR inhibition in the reaction. Reactions (20  $\mu$ l volume) were set up with 1  $\mu$ l extracted DNA as template, 4  $\mu$ l 5 $\times$  Buffer, 2  $\mu$ l of 1 mM dNTPs, 10.6  $\mu$ l water, 0.5  $\mu$ l of 10  $\mu$ M Seq\_rps17F (5'-CTGGAGATTTTCCGTTGTCA-3'), 0.5  $\mu$ l of 10  $\mu$ M Seq\_rps17R (5'-GACACTTCCGGCAGCTAGTT-3'), 0.5  $\mu$ l of 20  $\mu$ M wspFQALL (5'-GCATTGGTTAYAAAATGGACGA-3'), 0.5  $\mu$ l of 20  $\mu$ M wspRQALL (5'-GGAGTGATAGGCATATCTTCAAT-3'), and 0.4  $\mu$ l of PHIRE Hot Start Taq Polymerase (Finnzymes Oy). The temperature profile of the PCR was 98 °C for 3 min, 35 cycles of 98 °C for 5 s, 60 °C for 5 s and 72 °C for 20 s and ended with 72 °C for 1 min. PCR products were analysed by gel electrophoresis in a 2% agarose gel. The larvae were scored as positive for *Wolbachia* infection if *Wolbachia* WSP and RPS17 of the host were positive or if only *Wolbachia* WSP was positive. Larvae were scored as negative for *Wolbachia* infection if *Wolbachia* WSP was negative and RPS17 of the host was positive. If both *Wolbachia* WSP and RPS17 of the host were negative, the sample was excluded.

**Dengue vector competence.** Dengue virus serotype 2 (DENV-2), strain 92T, was passed six times in an *A. albopictus* C6/36 cell line and viral supernatant was collected. Virus titres were determined using immunoplaque assays<sup>36</sup> and kept at –80 °C until use. Oral feeding, RNA extraction, cDNA synthesis and qPCR analysis for total DENV-2 levels in whole female bodies was carried out using protocols previously outlined<sup>37</sup>. Disseminated viral infection rates were measured through quantification of virus copies in mosquito legs after RNA extraction using a QIAamp Viral RNA Mini Kit (Qiagen). Mosquito saliva was collected from orally fed females at 14 days after infection after 24 h of starvation. The legs and wings were removed and the proboscis was inserted into filtered pipette tips containing 20  $\mu$ l of Opti-MEM medium (Invitrogen) supplemented with 20% heat-inactivated FBS (Invitrogen), antibiotics (gentamicin, penicillin/streptomycin) and antimycotics. Mosquitoes were allowed to salivate for 30 min and then the media was transferred to 130  $\mu$ l of Opti-MEM media supplemented with 2% FBS.



Mosquito saliva extracts were immediately placed on dry ice and stored at  $-80^{\circ}\text{C}$  until use in plaque assays.

**Immunoplaque assays.** C6/36 cells were grown to confluence in 24-well plates at  $26^{\circ}\text{C}$  in RPMI 1640 medium (Invitrogen) supplemented with  $1\times$  GlutaMAX (Invitrogen) and 10% FBS and buffered with 25 mM HEPES (pH 8.0). Saliva pools each from four mosquitoes (600  $\mu\text{l}$  total volume) were filtered through a Millex-G 0.22  $\mu\text{m}$  sterile filter and added to the cell monolayers with the growth media removed. Monolayers and saliva samples were incubated with gentle rocking for 10 min, followed by a further incubation for 1.5 h at  $26^{\circ}\text{C}$ . A further 600  $\mu\text{l}$  of a mixture of RPMI media and carboxymethylcellulose (CMC) containing antibiotics and antimycotics was added to the wells, resulting in a final concentration of 2% FBS and 1.5% CMC. Cell monolayers were incubated at  $26^{\circ}\text{C}$  for 6 days after infection, followed by fixation with acetone/PBS and plaques were visualized<sup>36</sup>. Briefly, cell monolayers were incubated with a primary antibody against the DENV-2 NS1 protein, washed three times with PBS and incubated with a secondary anti-rabbit IgG horseradish peroxidase. Plaques were developed using SIGMAFast DAB with Metal Enhancer (Sigma-Aldrich). Data was recorded as negative for virus

transmission if no plaques were detected or recorded as positive if at least one plaque was present in a particular well.

32. Dobson, S. L., Marsland, E. J., Veneti, Z., Bourtzis, K. & O'Neill, S. L. Characterization of *Wolbachia* host cell range via the *in vitro* establishment of infections. *Appl. Environ. Microbiol.* **68**, 656–660 (2002).
33. McMeniman, C. J. *et al.* Host adaptation of a *Wolbachia* strain after long-term serial passage in mosquito cell lines. *Appl. Environ. Microbiol.* **74**, 6963–6969 (2008).
34. Wu, M. *et al.* Phylogenomics of the reproductive parasite *Wolbachia pipiensis* wMel: a streamlined genome overrun by mobile genetic elements. *PLoS Biol.* **2**, e69 (2004).
35. Williams, C. R. *et al.* Rapid estimation of *Aedes aegypti* population size using simulation modeling, with a novel approach to calibration and field validation. *J. Med. Entomol.* **45**, 1173–1179 (2008).
36. Frentiu, F. D., Robinson, J., Young, P. R., McGraw, E. A. & O'Neill, S. L. *Wolbachia*-mediated resistance to dengue virus infection and death at the cellular level. *PLoS ONE* **5**, e13398 (2010).
37. Richardson, J., Molina-Cruz, A., Salazar, M. I. & Black, W. T. Quantitative analysis of dengue-2 virus RNA during the extrinsic incubation period in individual *Aedes aegypti*. *Am. J. Trop. Med. Hyg.* **74**, 132–141 (2006).

# Successful establishment of *Wolbachia* in *Aedes* populations to suppress dengue transmission

A. A. Hoffmann<sup>1</sup>, B. L. Montgomery<sup>2</sup>, J. Popovici<sup>2,3</sup>, I. Iturbe-Ormaetxe<sup>2,3</sup>, P. H. Johnson<sup>4</sup>, F. Muzzi<sup>2</sup>, M. Greenfield<sup>2</sup>, M. Durkan<sup>2</sup>, Y. S. Leong<sup>2</sup>, Y. Dong<sup>2,3</sup>, H. Cook<sup>2</sup>, J. Axford<sup>1</sup>, A. G. Callahan<sup>1</sup>, N. Kenny<sup>2,3</sup>, C. Omodei<sup>4</sup>, E. A. McGraw<sup>2,3</sup>, P. A. Ryan<sup>2,3,5</sup>, S. A. Ritchie<sup>4</sup>, M. Turelli<sup>6</sup> & S. L. O'Neill<sup>2,3</sup>

Genetic manipulations of insect populations for pest control have been advocated for some time, but there are few cases where manipulated individuals have been released in the field and no cases where they have successfully invaded target populations<sup>1</sup>. Population transformation using the intracellular bacterium *Wolbachia* is particularly attractive because this maternally-inherited agent provides a powerful mechanism to invade natural populations through cytoplasmic incompatibility<sup>2</sup>. When *Wolbachia* are introduced into mosquitoes, they interfere with pathogen transmission and influence key life history traits such as lifespan<sup>3–6</sup>. Here we describe how the wMel *Wolbachia* infection, introduced into the dengue vector *Aedes aegypti* from *Drosophila melanogaster*<sup>7</sup>, successfully invaded two natural *A. aegypti* populations in Australia, reaching near-fixation in a few months following releases of wMel-infected *A. aegypti* adults. Models with plausible parameter values indicate that *Wolbachia*-infected mosquitoes suffered relatively small fitness costs, leading to an unstable equilibrium frequency <30% that must be exceeded for invasion. These findings demonstrate that *Wolbachia*-based strategies can be deployed as a practical approach to dengue suppression with potential for area-wide implementation.

Dengue fever is a major health problem throughout the tropics; its geographic distribution and severity of impact are increasing, with more than 50 million people currently estimated to be affected by dengue disease each year<sup>8,9</sup>. Traditional control measures focus on reducing populations of the main transmission vector, the mosquito *A. aegypti*, but these have largely failed to slow the current dengue pandemic. This has led to a search for novel technologies to break dengue transmission cycles.

One promising avenue is provided by the intracellular insect bacterium, *Wolbachia pipientis*, which can spread rapidly into uninfected host populations by inducing cytoplasmic incompatibility. This phenomenon causes embryos from *Wolbachia*-uninfected females to die when they are mated with infected males whereas infected females are not affected in this manner. Because *Wolbachia* are maternally inherited this effect provides a transmission advantage for the symbiont, resulting in rapid invasion of insect host populations<sup>10,11</sup>. Successful invasion depends on the cytoplasmic incompatibility driver overcoming incomplete maternal transmission of the *Wolbachia* infection as well as overcoming a loss of fitness of infected hosts<sup>12,13</sup>. This creates an unstable equilibrium point that must be exceeded for *Wolbachia* to spread rather than be lost from a population<sup>14</sup>.

In addition to being able to effectively invade wild insect populations, *Wolbachia* also influence the ability of insects to transmit pathogens. This can be achieved indirectly by reducing insect lifespan<sup>15</sup> or directly by reducing the ability of viruses and other pathogens to proliferate within the insect. The disruption of dengue transmission

by *Wolbachia* through saliva has been demonstrated to be nearly complete in laboratory assays, with the strength of the effect dependent on the *Wolbachia* strain<sup>3,6,7</sup>. Strain variability is presumably due to variation in the densities and tissue distributions of *Wolbachia*<sup>16</sup>. Of note is the observation that *Wolbachia* strains that provide greater disruption to dengue transmission also confer greater fitness costs to the mosquito host, and successful invasion for dengue control therefore requires a *Wolbachia* strain that balances these two effects<sup>7</sup>.

One such strain has recently been produced; the wMel *Wolbachia* strain from *Drosophila melanogaster* has been stably introduced into *A. aegypti* where it has strong anti-dengue properties and small host fitness costs<sup>7</sup>. Moreover, contained field-cage experiments demonstrated that this strain could successfully invade a small wild-type population and do so more effectively than wMelPop-CLA, the strain of *Wolbachia* originally introduced into *A. aegypti* with the goal of indirectly reducing dengue transmission by reducing mosquito lifespan<sup>4,7</sup>.

Given these results we have now proceeded to a deliberate *Wolbachia* introduction through open releases of mosquitoes with the wMel *Wolbachia* strain into wild Australian *A. aegypti* populations. Field locations chosen for the study were Yorkeys Knob (614 houses) and Gordonvale (668 houses) near Cairns in north-eastern Australia (Supplementary Fig. 1). These open releases were approved by the Australian Pesticides and Veterinary Medicines Authority (APVMA permit 12311) and were preceded by an extensive period of community engagement and subsequent strong community support.

In the month before release, residential properties within the release area were visited and water was removed from visible breeding containers. In early January 2011 during the wet season, adult female and male mosquitoes were released at 184 (Yorkeys Knob) and 190 (Gordonvale) sites spread uniformly throughout each field location. This was followed by an additional 9 releases at each location over the ensuing 9–10 weeks, with a total of 141,600 (Yorkeys Knob) and 157,300 (Gordonvale) adults released. The number of mosquitoes released in a week varied between 10,000 and 22,000 depending on results obtained from monitoring *Wolbachia* infection frequencies (Fig. 1); extra mosquitoes were released where there were perceived weak spots (low infection frequencies) within the release area.

Following the initial release, *Wolbachia* frequencies were monitored every 2 weeks and monitoring was continued after releases were terminated. For monitoring purposes, each suburb was divided into 40–42 blocks. In the first 10 weeks, 320 ovitraps were placed throughout the release area, but this was decreased to around 100 traps later. From each trap, up to 10 larvae were collected and screened for *Wolbachia* using a multiplex PCR assay to both discriminate *A. aegypti* from other *Aedes* species (*Aedes palmarum*, *Aedes notoscriptus*) present as well as determine the wMel infection frequency. A series of experiments was conducted to provide quality control of the *Wolbachia* screening protocol.

<sup>1</sup>Bio21 Institute, Department of Genetics, The University of Melbourne, Victoria 3010, Australia. <sup>2</sup>School of Biological Sciences, The University of Queensland, Brisbane, Queensland 4072, Australia. <sup>3</sup>School of Biological Sciences, Monash University, Victoria 3800, Australia. <sup>4</sup>School of Public Health and Tropical Medicine and Rehabilitative Sciences, James Cook University, Cairns, Queensland 4870, Australia. <sup>5</sup>Queensland Institute of Medical Research, Post Office Royal Brisbane Hospital, Brisbane, Queensland 4029, Australia. <sup>6</sup>Department of Evolution and Ecology, University of California, Davis, California 95616, USA.

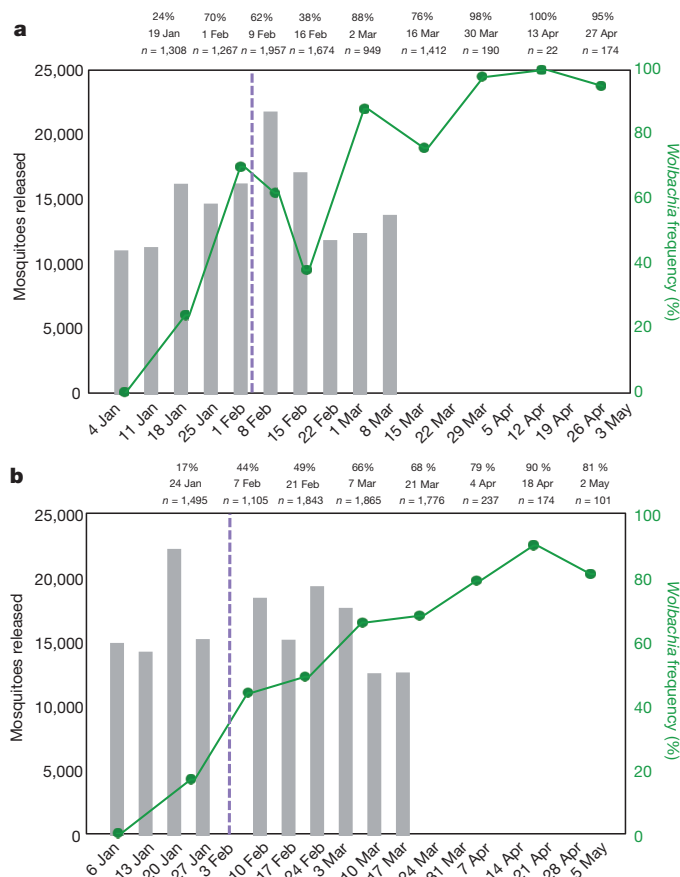


**Figure 1 | Number of mosquitoes released, timing of releases, and changes in infection frequencies over time.** **a, b,** Data based on monitoring with ovitraps at Yorkeys Knob (**a**) and Gordonvale (**b**). Ten releases were carried out at each site. Lower numbers were collected late in the season because of a reduction in trapping intensity and the advent of the dry season. Tropical Cyclone Yasi landed on 3 February (dotted line) and disrupted *Wolbachia* monitoring collections at Yorkeys Knob. A planned release at Gordonvale on 3 February was cancelled.

This included comparisons between samples obtained from the ovitraps with adult samples collected through BioGents Sentinel (BGS) traps and larval samples from natural breeding sites in the same area, as well as experiments to eliminate potential sources of contamination.

The screening procedure indicated that the frequency of *A. aegypti* infected with *Wolbachia* initially increased to more than 15% in both locations 2 weeks after release (Fig. 1). Following further releases, frequencies increased to >60% at Yorkeys Knob. At this stage Cairns was exposed to a Category 5 Tropical Cyclone (Yasi) although the city suffered only minor damage. It is not clear what effects the cyclone had on the resident mosquito population although winds were predominantly offshore during the event. The *Wolbachia* frequency decreased at Yorkeys Knob 6 weeks after the first release, then after the 7th release increased and reached near fixation 5 weeks after releases were terminated. At Gordonvale the *Wolbachia* frequency increased more slowly but steadily to reach 90% at 5 weeks after releases stopped (Fig. 1). In both areas there was a small decrease in *Wolbachia* frequency at the end of the monitoring period as the onset of the dry season caused a sharp decrease in the size of the mosquito population and most probably increased movement of mosquitoes into release areas as reflected by previously detected changes in population genetic structure<sup>17</sup>.

Detailed monitoring of *Wolbachia* frequencies in blocks across the release area pointed to significant spatial heterogeneity in the incidence of *Wolbachia* (Fig. 2 and Supplementary Fig. 2 for block numbering). At Yorkeys Knob in the first monitoring period there were lower

frequencies of *Wolbachia* in some blocks (for example, blocks 15 and 24). These low areas tended to persist in the ensuing 16 February monitoring period; however, following adaptive management involving the release of additional mosquitoes in such blocks, the incidence of *Wolbachia* increased across the entire area. At Gordonvale block-level monitoring also indicated significant spatial structure with some areas having low infection frequencies (for example, blocks 26 and 28) which were identified for adaptive management through additional releases into blocks. Releases in one area of Yorkeys Knob (blocks 17, 19, 20 and 23, Supplementary Fig. 2) ceased on 21 February because of the notification of a single dengue case most likely acquired in Innisfail outside the release area, which led to insecticide intervention by health authorities in a 150-m radius from the case house. This did not adversely influence *Wolbachia* frequencies, which continued to increase despite the absence of further releases within the affected area (Fig. 2 and Supplementary Fig. 2). No local transmission of dengue occurred from the identified case.

Adult surveys in the release area with BioGents Sentinel (BGS) traps (Supplementary Fig. 3) pointed to an increase in numbers at the start of the release period in both locations, followed by a decrease at the end of the release period. By using the average number of adults in the preceding month in each location, we estimated that during the release period the number of adults doubled in Yorkeys Knob and increased 1.5-fold in Gordonvale (there was no equivalent increase in adult numbers in BGS traps placed at Parramatta Park, a suburb in Cairns several kilometres from the release area). Adult numbers in all locations declined in April at the onset of the dry season.

The observed increases in *Wolbachia* frequency, the number of adults released, and estimates of resident population sizes were incorporated into a model of *Wolbachia* population dynamics<sup>12</sup> to infer plausible fitness costs and approximate the resulting unstable equilibrium frequency. This heuristic analysis (Supplementary Information) was consistent with fitness costs on the order of 20% (Supplementary Fig. 4). Estimates are uncertain because population sizes and daily survival rates of *A. aegypti* are poorly known. Fitness costs may be overestimated because our data conflate transient fitness effects associated with laboratory rearing of released *A. aegypti* with inherent costs associated with *Wolbachia* infection, and the model ignores movement into the population of uninfected individuals (for example, from newly submerged eggs). If intrinsic fitness costs are lower than 30%, a spreading wave of infection would be relatively easy to initiate from localized introductions<sup>18</sup>. The data from Gordonvale and Yorkeys Knob were consistent with the same estimated fitness costs; the slower increase of *Wolbachia* frequency in Gordonvale most probably reflects a larger resident *A. aegypti* population (and lower ratio of released to resident mosquitoes).

Monitoring of the *Wolbachia* infection outside the release area during and directly after the release pointed to some spread of infected mosquitoes (Fig. 3). *Wolbachia*-infected larvae were found in Pyramid Estate (Fig. 3b), a part of Gordonvale that is separated by a major highway from the release zone. Highways are often viewed as a physical barrier blocking mosquito movement and gene flow in *A. aegypti*<sup>19</sup>. Around Yorkeys Knob there was movement into a nearby suburb, with *Wolbachia* being detected on two occasions 4 weeks apart within the same region of Holloways Beach (Fig. 3), 1.86 km from the nearest release site. The infection was also detected on one occasion at Trinity Park, 1.03 km from the nearest release site. These results point to occasional long distance movement of *A. aegypti* either through vehicles or adult dispersal, which is inconsistent with the view that *A. aegypti* is a weak disperser but consistent with some experiments and observations<sup>20–22</sup>. Unless fitness costs are essentially zero or unless there are unexpected fitness benefits, we do not expect the infection to spread further in these areas but instead to be swamped by local wild types<sup>18</sup>.

Releases of *Wolbachia*-infected males have previously been used to suppress natural populations of *Culex* mosquitoes through cytoplasmic



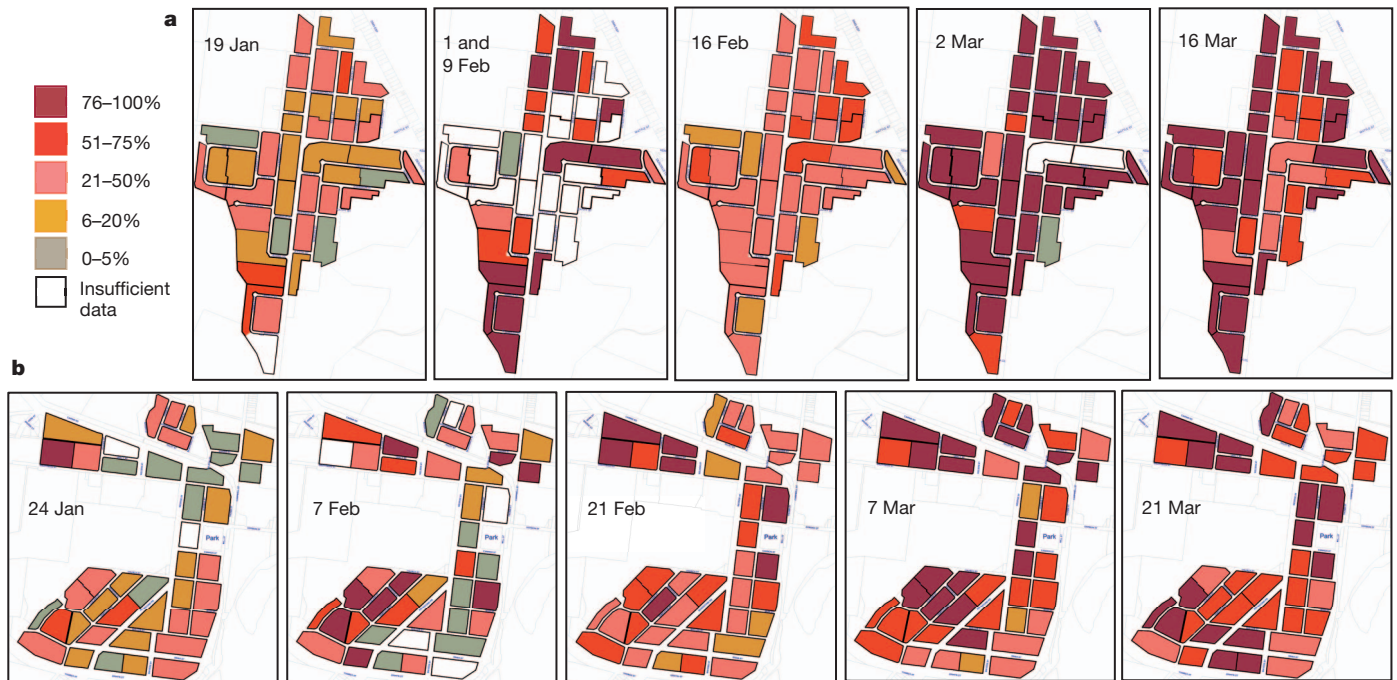


**Figure 2 | Changes in frequencies of *Wolbachia*-infected mosquitoes.**

**a, b,** Data collected in individual blocks within Yorkeys Knob (**a**) and Gordonvale (**b**). Block frequencies are based on samples of 10 or more (usually >30) larvae from 1–8 (usually >3) ovitraps. If fewer than 10 *A. aegypti* were

scored from any given block then the block was scored as having insufficient data. Block data are provided in Supplementary Figure 2. Adaptive management involving additional releases was applied in areas where *Wolbachia* frequencies were relatively low.

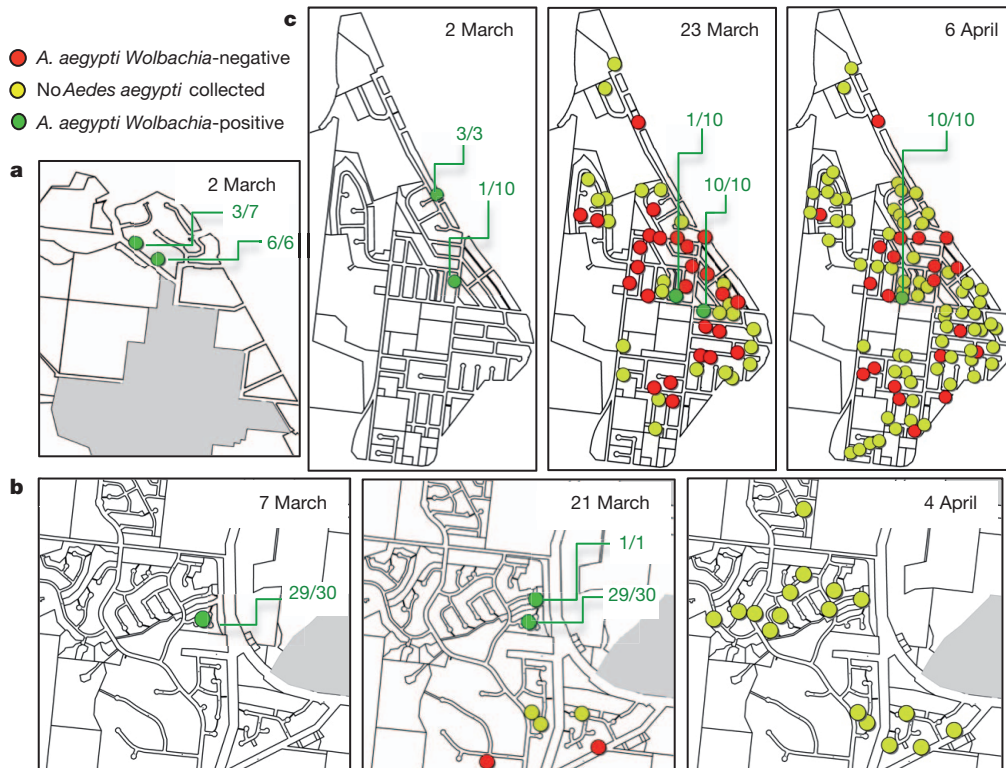


**Figure 3 | Occurrence of *Aedes aegypti* and *Wolbachia* infection in ovitraps outside release areas.** **a–c,** The release areas were adjacent to the Yorkeys Knob release area (**a**), Pyramid Estate, adjacent to the Gordonvale release zone (**b**) and Holloways Beach (**c**; see Supplementary Fig. 1 for locations). Green symbols indicate the presence of *A. aegypti* infected by *Wolbachia*, red symbols

indicate only uninfected *A. aegypti*, whereas yellow symbols indicate no *A. aegypti*. Shaded areas indicate release zones. Numbers on graphs show the number of infected larvae (from total collected). Collections occurred at the onset of the dry season when *A. aegypti* abundance was declining.

incompatibility<sup>23</sup>. However, the present results provide the first case where wild insect populations have been transformed to reduce their ability to act as vectors of human disease agents. This success with the deliberate release of *Wolbachia*-infected insects follows early unsuccessful attempts to manipulate insect populations through other genetic control strategies, including chromosomal manipulations and lethal genes<sup>24,25</sup>. Because *wMel* and other *Wolbachia* strains inhibit dengue virus transmission in the laboratory<sup>3,7</sup>, there is potential to use this technology for area-wide suppression of dengue transmission. We have demonstrated that it is possible to produce *Wolbachia*-infected mosquito populations that can act as 'nursery' areas for future human-assisted collection and further dispersal of *Wolbachia*-infected mosquitoes, without the need to rear additional mosquitoes in an insectary. This should provide a strategy for sustainable dengue control at low cost, with a relatively simple deployment system suitable for implementation in developing countries. The next step is a disease endpoint trial to test efficacy of the method for dengue and dengue haemorrhagic fever control, ongoing monitoring in and around the release area to test for persistence, and releases to test the spatial spread of the infection across a populated area.

## METHODS SUMMARY

The outcrossed *A. aegypti wMel*-infected line described elsewhere<sup>7</sup> was backcrossed to the offspring of Cairns field-collected mosquitoes. Adult mosquitoes from the backcrossed line were maintained in a semi-natural field cage. Offspring were reared to the adult stage in a separate field cage to ensure ambient conditions during development, and then released on 10 occasions at weekly intervals throughout release zones at Yorkeys Knob and Gordonvale starting in early January 2011. Releases and monitoring were interrupted by up to a week when tropical cyclone Yasi made landfall south of Cairns. To monitor *Wolbachia* frequencies, a grid of up to 320 ovitraps was placed at each release area every two weeks. Eggs were hatched and larvae rinsed before being tested for infection status through a multiplexed PCR assay. *Wolbachia* frequencies in release areas were pooled into 40–42 blocks (up to 8 ovitraps per block) and blocks with particularly low infection frequencies were identified for adaptive management consisting of doubling release rates. Releases were terminated after the overall *Wolbachia* frequency exceeded 70%. Traps were also deployed in suburbs adjacent to each release zone to monitor the wider spread of *Wolbachia*. A series of quality control procedures was followed to ensure that frequencies assessed through individual larvae were reliable. This included checking frequencies in independent laboratories and from different trapping methods, and excluding the possibility of cross contamination due to re-use of containers. Community support for the releases was very strong following an extensive period of consultation before commencement of the releases and ongoing communication throughout the release and monitoring periods.

**Full Methods** and any associated references are available in the online version of the paper at [www.nature.com/nature](http://www.nature.com/nature).

**Received 1 June; accepted 6 July 2011.**

- Gould, F. & Schliekelman, P. Population genetics of autocidal control and strain replacement. *Annu. Rev. Entomol.* **49**, 193–217 (2004).
- Turelli, M. & Hoffmann, A. A. Cytoplasmic incompatibility in *Drosophila simulans*: dynamics and parameter estimates from natural populations. *Genetics* **140**, 1319–1338 (1995).
- Moreira, L. A. *et al.* A *Wolbachia* symbiont in *Aedes aegypti* limits infection with dengue, chikungunya, and *Plasmodium*. *Cell* **139**, 1268–1278 (2009).
- McMeniman, C. J. *et al.* Stable introduction of a life-shortening *Wolbachia* infection into the mosquito *Aedes aegypti*. *Science* **323**, 141–144 (2009).
- Kambris, Z., Cook, P. E., Phuc, H. K. & Sinkins, S. P. Immune activation by life-shortening *Wolbachia* and reduced filarial competence in mosquitoes. *Science* **326**, 134–136 (2009).
- Bian, G. W., Xu, Y., Lu, P., Xie, Y. & Xi, Z. Y. The endosymbiotic bacterium *Wolbachia* induces resistance to dengue virus in *Aedes aegypti*. *PLoS Pathog.* **6**, e1000833 (2010).
- Walker, T. *et al.* A non-virulent *Wolbachia* infection blocks dengue transmission and rapidly invades *Aedes aegypti* populations. *Nature* doi:10.1038/nature10355 (this issue).

- Kyle, J. L. & Harris, E. Global spread and persistence of dengue. *Annu. Rev. Microbiol.* **62**, 71–92 (2008).
- Guzman, M. G. *et al.* Dengue: a continuing global threat. *Nature Rev. Microbiol.* **8**, S7–S16 (2010).
- Turelli, M. & Hoffmann, A. A. Rapid spread of an inherited incompatibility factor in California *Drosophila*. *Nature* **353**, 440–442 (1991).
- Riegler, M., Sidhu, M., Miller, W. J. & O'Neill, S. L. Evidence for a global *Wolbachia* replacement in *Drosophila melanogaster*. *Curr. Biol.* **15**, 1428–1433 (2005).
- Turelli, M. Cytoplasmic incompatibility in population with overlapping generations. *Evolution* **64**, 232–241 (2010).
- Yeap, H. L. *et al.* Dynamics of the 'popcorn' *Wolbachia* infection in *Aedes aegypti* in an outbred background. *Genetics* **187**, 583–595 (2011).
- Caspari, E. & Watson, G. S. On the evolutionary importance of cytoplasmic sterility in mosquitoes. *Evolution* **13**, 568–570 (1959).
- McMeniman, C. J. & O'Neill, S. L. A virulent *Wolbachia* infection decreases the viability of the dengue vector *Aedes aegypti* during periods of embryonic quiescence. *PLoS Neglect. Trop. Dis.* **4**, e748 (2010).
- Osborne, S. E., Leong, Y. S., O'Neill, S. L. & Johnson, K. N. Variation in antiviral protection mediated by different *Wolbachia* strains in *Drosophila simulans*. *PLoS Pathog.* **5**, e1000656 (2009).
- Endersby, N. M. *et al.* Changes in the genetic structure of *Aedes aegypti* (Diptera: Culicidae) populations in Queensland, Australia, across two seasons: implications for potential mosquito releases. *J. Med. Entomol.* (in the press).
- Barton, N. H. & Turelli, M. Spatial waves of advance with bistable dynamics: cytoplasmic and genetic analogs of Allee effects. *Am. Nat.* doi:10.1086/661246 (2011).
- Hemme, R., Thomas, C., Chadee, D. & Severson, D. Influence of urban landscapes on population dynamics in a short-distance migrant mosquito: evidence for the dengue vector *Aedes aegypti*. *PLoS Negl. Trop. Dis.* **4**, e634 (2010).
- Reiter, P., Amador, M. A., Anderson, R. A. & Clark, G. G. Dispersal of *Aedes aegypti* in an urban area after blood feeding as demonstrated by rubidium-marked eggs. *Am. J. Trop. Med. Hyg.* **52**, 177–179 (1995).
- Harrington, L. C. *et al.* Dispersal of the dengue vector *Aedes aegypti* within and between rural communities. *Am. J. Trop. Med. Hyg.* **72**, 209–220 (2005).
- David, M. R., Lourenco-de-Oliveira, R. & de Freitas, R. M. Container productivity, daily survival rates and dispersal of *Aedes aegypti* mosquitoes in a high income dengue epidemic neighbourhood of Rio de Janeiro: presumed influence of differential urban structure on mosquito biology. *Mem. Inst. Oswaldo Cruz* **104**, 927–932 (2009).
- Laven, H. Eradication of *Culex pipiens fatigans* through cytoplasmic incompatibility. *Nature* **216**, 383–384 (1967).
- Curtis, C. F. Genetic control of insect pests: growth industry or lead balloon? *Biol. J. Linn. Soc.* **26**, 359–374 (1985).
- Foster, G. G. Genetic control of sheep blowfly (*Lucilia cuprina*) and the logistics of the CSIRO control program. *Wool Technol. Sheep Breed.* **28**, 5–10 (1980).

**Supplementary Information** is linked to the online version of the paper at [www.nature.com/nature](http://www.nature.com/nature).

**Acknowledgements** We are grateful to J. Sutton, C. Paton, G. Ormodei, S. Long, A. Gofton, V. White, A. Weeks, A. James, J. Dick, R. Bagita, P. Gibson, J. Jeffery, E. Rances, D. Rossi and J. Gough for technical and mapping support. We thank B. Kay for ongoing advice. We acknowledge and thank both D. McNaughton and D. Eastop for the early community engagement work preceding the trial. We thank all of our volunteers who helped blood-feed the mosquito colonies and we are particularly grateful to the residents of Gordonvale and Yorkeys Knob for their strong support and participation. This research was supported by a grant from the Foundation for the National Institutes of Health through the Grand Challenges in Global Health Initiative of the Bill and Melinda Gates Foundation, The National Health and Medical Research Council, Australia, the National and International Research Alliances Program of the Queensland Government, the RAPIDD program of the NIH, the Climate Health Cluster of the CSIRO Flagship Collaboration Fund, the National Science Foundation and Fellowships from the Australian Research Council.

**Author Contributions** A.A.H. and S.L.O. provided oversight of the releases and drafted most of the paper. S.A.R. and B.L.M. provided knowledge of local mosquito populations and liaison with authorities. J.P., I.I.-O., Y.D. and Y.S.L. carried out the *Wolbachia* screening. P.H.J., C.O., J.A., N.K., E.A.M. and A.G.C. were responsible for mosquito culture and backcrossing. Field releases and monitoring collections were undertaken by F.M., M.G., M.D. and B.L.M. and coordinated by B.L.M. and P.A.R. M.T. developed models to interpret the results and A.A.H. interpreted data during the release. H.C., S.L.O., S.A.R., M.D. and P.A.R. were involved in community engagement and mapping. S.L.O. and I.I.-O. were responsible for gaining regulatory approvals for the releases.

**Author Information** Reprints and permissions information is available at [www.nature.com/reprints](http://www.nature.com/reprints). The authors declare no competing financial interests. Readers are welcome to comment on the online version of this article at [www.nature.com/nature](http://www.nature.com/nature). Correspondence and requests for materials should be addressed to S.L.O. ([scott.oneill@monash.edu](mailto:scott.oneill@monash.edu)).



## METHODS

**Regulatory approval.** Approval for the release of *Aedes aegypti* containing *Wolbachia* was provided by the Australian Pesticides and Veterinary Medicines Authority. Considering the novelty of the proposed experiment it was not initially clear how the open release of *Wolbachia* infected mosquitoes should be regulated in Australia<sup>26</sup>. Finally after considerable consultation the Australian Government chose to regulate the release under existing legislation as a Veterinary Chemical product<sup>26</sup>. This is the approach taken to regulate microbial pesticides within Australia.

**Community engagement.** An extensive community engagement program ran for 2 years before the open release experiments reported here<sup>27,28</sup>, with consultation taking place through public meetings, one-on-one meetings, and through engagement with existing community groups. Resident concerns were canvassed and addressed through communication materials and in some cases additional experimental studies<sup>27</sup>. In general community support was extremely high (>85%) as measured through random telephone surveys on two occasions ( $n = 300$ ). Prior to the field trials residents were asked to provide written permission for three separate activities to take place on their properties. These included pre-release suppression of mosquitoes by removing water from potential breeding sites, release of mosquitoes containing *Wolbachia* and the placement of monitoring traps in resident yards. It is notable that recruitment of resident participation at one location, Yorkeys Knob, was led by a local community group, the State Emergency Service, indicating considerable local ownership of the research program. Approximately 66% of 599 households were able to be contacted at Yorkeys Knob and 54% of 652 households at Gordonvale. Of these households 97% agreed and 3% elected not to participate at both locations ( $n = 17$  and 11 declining households for Yorkeys Knob and Gordonvale, respectively, on 4 January). Mosquitoes were only released at properties where residents had given permission. No mosquitoes were released at properties of households that chose not to participate (or at properties adjacent to these households). In addition, mosquito control at the household level was offered to a concerned household. During the release period a small number of households became concerned about mosquito releases and their properties were excluded from subsequent releases and monitoring. We also encountered residents that wished to take part during the study and these households were recruited.

During the release period we continued to undertake close engagement with the local community to ensure that residents were informed about the study and were comfortable with continuation of the program. This included monthly random household surveys and monthly meetings with a reference group of residents and community leaders, and ongoing promotion of a free phone number and accessible city project office. Finally, periodic result updates were provided to the community through letterbox leaflet drops, paid advertisements in a local newspaper and engagement with local newspaper and radio media outlets.

**Mass rearing and backcrossing.** We initiated crosses with a wMel infected population that had already been backcrossed to a population originating from collections around the Cairns area for three generations<sup>7</sup>. This population was backcrossed again to F1 offspring of females collected from Cairns field females for another three generations (that is, nuclear background was expected to be 99.9% from the Cairns region, which forms a genetically homogeneous group<sup>29</sup>). For the backcrosses, eggs from field females were collected and stored at approximately 80% relative humidity in diapause and then hatched as required to be used in successive backcross generations<sup>13</sup>. Populations were then expanded for a generation and used to establish a release population at James Cook University as well as backup colonies at The University of Queensland and The University of Melbourne.

Mosquitoes for release were reared at James Cook University, Cairns campus, in the Mosquito Research Facility which comprises a laboratory and two large ( $8.0 \times 9.0 \times 4.1$  m) semi-field cages<sup>30</sup>. The adult colony was allowed to fly freely in one cage, and larvae and adults prepared for release were maintained in the other cage under ambient conditions. Mean daily minimum and maximum temperature and relative humidity conditions in the adult cage were  $23.5\text{--}29.4^\circ\text{C}$  and  $78.1\text{--}95.5\%$ , whereas in the rearing cage it was  $23.9\text{--}30.1^\circ\text{C}$  and  $76.6\text{--}95.7\%$ .

A population of 800–1,600 female *A. aegypti* (and a similar number of males) was maintained in the adult cage. This cage was initially populated with 900 mosquitoes from the backcrossed colony replenished weekly by 240–720 additional female and male pupae from the larval rearing cage. To minimise laboratory adaptation, male *A. aegypti* pupae from field-collected *A. aegypti* (F1–F2 eggs) were introduced to the cage each week so that they constituted around 20% of the new male population. Mosquitoes were provided access to human volunteer blood-feeders almost daily in this colony (JCU Human Ethics Approval H2250). Volunteer blood feeders were initially bled and tested for dengue infection by IgM ELISA and PCR, then aural temperature was taken before each feeding to exclude individuals with fever (temperature  $> 38^\circ\text{C}$ ). Eggs were collected on red

flannel cloth in twelve 4.2 l plastic ovibuckets spread throughout the cage, incubated for 3 days and stored in the laboratory for further use.

Three cohorts of approximately 10,000 adults (15,000 larvae) were reared each week. Eggs were hatched in a fresh baker's yeast solution ( $0.8\text{--}1.0$  g in 2 l tap water). The following day, larvae were transferred to buckets (4 l) in the rearing cage at a density of approximately 150–200 larvae per 2 l water. Larvae were fed TetraMin Tropical Tablets (total  $0.90\text{--}1.20$  g per rearing bucket over 6 days plus  $0.08$  g at hatching). Seven days after hatching, when approximately 75% of larvae had pupated, larvae and pupae were concentrated by decanting excess water from the buckets. Pupae/larvae were transferred with a large pipette to adult release cups. These consisted of 750 ml clear plastic cups with the inside surface scratched and roughened with sandpaper, covered with mesh cloth and secured with plastic lids with holes (Supplementary Fig. 5). Approximately 50–70 pupae/larvae were normally added to each release cup with 300 ml clean water and no food. Adults were allowed to emerge and mature in the release cups over 6 days and were provided with a 50% honey solution on a sponge resting on top of each cup. On the day before a release, water was poured off and the honey-soaked sponge was replaced. Adults were 2–6 days old at the time of release, and the sex ratio in the cups was close to 1:1 (51% females). Mortality was minimal ( $<5\%$ ) in the release cups.

Two backup colonies each capable of producing around 10,000 adults per week were maintained in insectaries at The University of Queensland (UQ) and The University of Melbourne (UM). These colonies were maintained with human blood feeding (UQ Human Ethics Approval 2007001379, UM Human Ethics Approval 0723847.2) of adults in cages (around 200 adults per cage, eight cages per colony) and rearing larvae in trays (around 50 trays per colony). These colonies were maintained as a contingency in the event that the main rearing was compromised, but they were not needed for the releases.

**Releases.** Field teams visited all residential properties within both study locations (Yorkeys Knob, 614 properties; Gordonvale, 668 properties) 1–4 weeks before the commencement of the adult release schedule and were provided access to around half of them. Water bearing containers were emptied, and larger containers were siphoned out whenever possible. Chemicals were not applied, to minimize disruption to potential mosquito breeding sites following adult releases. Where possible, *Aedes* eggs were removed by scrubbing the inside of these containers with a brush.

Weekly releases of adults were undertaken for 10 consecutive weeks, starting 4 January 2011. Adult release cups were transported from the Mosquito Research Facility in vehicles with dampened black cloth covering crates to maximise humidity. A minimum number of 184 (Yorkeys Knob) or 190 (Gordonvale) release points were evenly distributed throughout the release area. Each week release points were rotated between adjacent properties to minimize any discomfort to residents due to mosquito biting activity. Adults were released at the property fence line or front yard by removing the container lids and gently shaking out any mosquitoes that did not immediately fly out. Releases commenced at 08:00 a.m. and were usually completed within 2 h. We removed mosquitoes in the delivery vehicles at the conclusion of each release event with a sweep net. Five unopened cups were immediately returned to James Cook University to assess the impact of transportation on mortality.

**Release management and monitoring.** Adult *A. aegypti* populations were monitored in the release area by BioGents Sentinel mosquito traps (BGS) which are an effective surveillance tool for adult *A. aegypti*<sup>31</sup>. A network of these traps was established in residential properties ( $n = 16$  and 13 for Yorkeys Knob and Gordonvale, respectively) and serviced each week since October 2009. In Yorkeys Knob, 16 BGS traps collected a mean of 0.48 (confidence interval =  $0.25\text{--}0.70$ ) female *A. aegypti* over a 4-week period (2–30 December 2010), while in Gordonvale the 14 BGS traps collected a mean of 0.92 (confidence interval =  $0.38\text{--}1.46$ ) females. Mark-release-recapture trials conducted in houses in Cairns indicated that BGS traps captured 25% (confidence interval 21–29%) of released female *A. aegypti* within 24 h (P. H. Johnson, unpublished data). Thus the BGS mean daily trap collection needs to be multiplied by at least four to estimate the population of female *A. aegypti* per premise. However, these are underestimates because both teneral (recently emerged adults) and engorged, blood-fed female *A. aegypti* are poor fliers and undersampled by BGS traps<sup>32</sup>. Furthermore, *A. aegypti* in upper level rooms, other buildings and cryptic sites are not included in the mark-release study; the number of female *A. aegypti* per premise is therefore likely to have been substantially higher, most likely five or more per premise for Yorkeys Knob and double this figure for Gordonvale.

A confirmed case of dengue fever was reported by Queensland Health at a Yorkeys Knob address on 21 February 2011. The case originated in Innisfail where dengue transmission occurred in 2011. All properties within the dengue response zone (approximately 150 m radius from case house) were subjected to the emergency response protocols activated by Queensland Health. Control activities included yard inspections to treat all water-bearing containers with *s*-methoprene (an insect growth regulator) and the application of residual insecticide (deltamethrin) to mosquito harbourage areas (for example, underside of furniture) within houses



with permission. No further releases were conducted in the affected area after 15 February 2011 (week 7) following this health advice. No cases of dengue were subsequently reported.

Tropical Cyclone Yasi made landfall south of Cairns on 3 February 2011 and resulted in the suspension of a scheduled release at Gordonvale for a week. Releases at Yorkeys Knob were not affected but only half the ovitraps used for monitoring (below) could be collected before the cyclone, and the other half were collected a week later.

**Monitoring in release areas.** *Wolbachia* infections were monitored fortnightly for 9–10 collection events at each area (January to May, Fig. 1). The ovitraps consisted of 1.2 l black plastic golf-divot buckets (Clayton Plastics) fitted with a red flannel (Spotlight) strip (15 × 12 cm)<sup>33</sup>. The cloth strip provided a vertical oviposition substrate within the bucket and was secured with a clip (Supplementary Fig. 5). Ovitrap were filled with tap water on site and an infusion created by adding half an alfalfa pellet (approximately 0.5 mg).

Ovitrap were deployed at fixed addresses after release zones were subdivided into blocks (40 and 42 in Yorkeys Knob and Gordonvale, respectively, area 0.0085 to 0.0328 km<sup>2</sup>). Initially two ovitraps were deployed per property with four properties per block to provide an array of 320 ovitraps per zone, but as *Wolbachia* infection rates increased a single ovitrap was placed at each property and this was further reduced to 100 ovitraps per release zone. This reduction was due to a redeployment of the trapping grid outside of the release area into adjacent suburbs when *Wolbachia*-infected mosquitoes were first detected there (see below). Each ovitrap was bar-coded to enable each trap to be re-deployed to the same address.

Ovitrap were collected 7 days after deployment, and strips were detached from the ovitrap wall before buckets were flooded with water and a 5% yeast extract to induce hatching. Approximately 40 h later each ovitrap was inspected for larvae. The larvae were transferred through a sieve and placed into a 50 ml container holding approximately 200 ml of water and left for 1 h to purge their gut content and minimize contamination due to ingestion of *Wolbachia*-infected exuvia. All larvae were transferred into 80% ethanol vials (5 ml) with barcodes before shipping overnight to University of Queensland for PCR analyses.

We used Spatial Analysis by Distance IndicEs (SADIE) (<http://www.rothamsted.bbsrc.ac.uk/pie/sadie>) to test for non-randomness of *Wolbachia* frequencies at the property level across the release areas in the January (both locations) and 7 February (Gordonvale) monitoring events. Significant structure (randomization test,  $P < 0.01$ ) was detected in both release zones on these occasions, pointing to areas with consistently low or high *Wolbachia* frequencies, and providing impetus for adaptive management.

**Adaptive management.** In the first two monitoring periods, blocks with a low frequency of *Wolbachia* were identified and release rates doubled within these blocks in the ensuing release. Individual properties with particularly low frequencies of *Wolbachia* were subject to property inspections (when permitted by the resident) to identify and remove any containers where mosquitoes were breeding.

Because *Wolbachia* frequencies increased rapidly in Yorkeys Knob, additional traps were deployed in adjacent communities (Supplementary Fig. 1) at Holloway's Beach (92 traps), Trinity Park (96 traps), and Pyramid Estate (25 traps).

**Wolbachia screening.** *Wolbachia* infection status of *A. aegypti* larvae collected in ovitraps was tested with a multiplex PCR assay. DNA was extracted from larvae as described previously<sup>7</sup>. Multiplex PCR was carried out with primers amplifying a fragment of the IS5 repeat element of *Wolbachia* (820 bp) and with primers amplifying the ribosomal DNA internal transcribed spacer 2 (ITS2) from *A. aegypti* (approximately 320 bp). The ITS2 primers were designed to act as a control for the presence of amplifiable DNA or any PCR inhibition in the reaction and to discriminate between the different *Aedes* species present in North Queensland: *Aedes aegypti* (approximately 320 bp), *Aedes palmarum* (approximately 380 bp) and *Aedes notoscriptus* (approximately 400 bp). Volume reactions (10 µl) were set up with 1 µl of extracted DNA as template, 2 µl of 5× buffer, 2 µl of 1 mM dNTPs, 3.55 µl water, 0.125 µl of 20 µM ITS2A (5'-TGTGAAGTCAGGACACAT-3'), 0.125 µl of 20 µM ITS2B (5'-TATGCTTAATTCAGGGGT-3')<sup>34</sup>, 0.5 µl of 20 µM ISSF (5'-GTATCCAACAGATCTAAGC-3'), 0.5 µl of 20 µM ISSR

(5'-ATAACCCTACTCATAGCTAG-3'), and 0.2 µl of PHIRE Hot Start Taq Polymerase (Finnzymes Oy). The temperature profile of the PCR was 98 °C for 3 min, 35 cycles of 98 °C for 5 s, 55 °C for 5 s and 72 °C for 20 s and ended with 72 °C for 1 min. PCR products were analysed by gel electrophoresis in a 2% agarose gel. The larvae were scored as positive for *Wolbachia* infection if *Wolbachia* IS5 and ITS2 of *A. aegypti* were present. Larvae were scored as negative for *Wolbachia* infection if *Wolbachia* IS5 was absent and ITS2 of *A. aegypti* was present. If both *Wolbachia* IS5 and ITS2 of the host were absent, the sample was excluded. If the ITS2 product had a size ≥ approximately 380 bp, the larvae were designated as 'other species' and not *A. aegypti*.

**Quality control.** We validated the PCR method across laboratories by transferring larval samples from the same eight containers to screening laboratories in both The University of Queensland and The University of Melbourne. Screening indicated that four of the containers were completely infected based on samples of 10 or 20 individuals ( $n = 60$  in total). The same containers also produced only infected individuals in the assay run at The University of Melbourne using samples of 12–20 individuals ( $n = 70$  in total). The other containers were polymorphic in the The University of Queensland assay, with a total of 57 infected larvae and 18 uninfected larvae. At The University of Melbourne there were 39 infected larvae and 21 uninfected larvae. The proportion of uninfected and infected larvae did not differ between laboratories by a contingency test ( $G = 1.96$ ,  $df = 1$ ,  $P = 0.161$ ).

To confirm that *Wolbachia*-infected larvae were breeding in natural resources and not just in ovitraps, larvae were collected from pot plant bases, buckets and other containers, and tested for infection status by PCR. For Yorkeys Knob, larvae were collected from 14 containers between 7 March and 1 April. There were 237 *A. aegypti* larvae, of which 208 (87.8%) were infected. For Gordonvale, larvae were retrieved from 8 containers in late February/early March, and yielded 126 infected larvae out of a total of 146 (*Wolbachia* frequency of 86.3%).

Ovitrap were cleaned in different ways before being used in separate collections. This raises the possibility of cross contamination due to residues from a high abundance of infected larvae in the previous trapping period. To test this, 12 ovitraps from Yorkeys Knob where infection frequencies were high (>90%) were retested. The ovitraps were left dry for one week from the last time they were collected, subjected to different treatments and placed inside cages with uninfected adult *A. aegypti* mosquitoes. In all cases, there was no contamination from previously infected larvae which had developed in the same container: all 470 uninfected larvae were scored as negative in the PCR assays.

26. De Barro, P., Murphy, B., Jansen, C. & Murray, J. The proposed release of the yellow fever mosquito, *Aedes aegypti* containing a naturally occurring strain of *Wolbachia pipiensis*, a question of regulatory responsibility. *J. Cons. Protect. Food Safety* **6** (suppl. 1), 33–40 (2011).
27. Popovici, J. et al. Assessing key safety concerns of a *Wolbachia*-based strategy to control dengue transmission by *Aedes* mosquitoes. *Mem. Inst. Oswaldo Cruz* **105**, 957–964 (2010).
28. McNaughton, D., Clough, A., Johnson, P. H., Ritchie, S. A. & O'Neill, S. L. Beyond the 'back yard': lay knowledge about *Aedes aegypti* in northern Australia and its implications for policy and practice. *Acta Trop.* **116**, 74–80 (2010).
29. Endersby, N. M. et al. Genetic structure of *Aedes aegypti* in Australia and Vietnam revealed by microsatellite and exon primed intron crossing markers suggests feasibility of local control options. *J. Med. Entomol.* **46**, 1074–1083 (2009).
30. Ritchie, S. A. et al. A secure semi-field cage for the study of *Aedes aegypti*. *PLoS Negl. Trop. Dis.* **5**, e988 (2011).
31. Williams, C. R. et al. Field efficacy of the BG-Sentinel compared with CDC backpack aspirators and CO<sub>2</sub>-baited EVS traps for collection of adult *Aedes aegypti* in Cairns, Queensland, Australia. *J. Am. Mosq. Control Assoc.* **22**, 296–300 (2006).
32. Ball, T. S. & Ritchie, S. A. Sampling biases of the BG-sentinel trap with respect to physiology, age, and body size of adult *Aedes aegypti* (Diptera: Culicidae). *J. Med. Entomol.* **47**, 649–656 (2010).
33. Ritchie, S. A. Effect of some animal feeds and oviposition substrates on *Aedes* oviposition in ovitraps in Cairns, Australia. *J. Am. Mosq. Control Assoc.* **17**, 206–208 (2001).
34. Beebe, N. W. & Saul, A. Discrimination of all members of the *Anopheles punctulatus* complex by polymerase chain reaction restriction-fragment-polymorphism analysis. *Am. J. Trop. Med. Hyg.* **53**, 478–481 (1995).

# Adult hippocampal neurogenesis buffers stress responses and depressive behaviour

Jason S. Snyder<sup>1</sup>, Amélie Soumier<sup>1</sup>, Michelle Brewer<sup>1</sup>, James Pickel<sup>1</sup> & Heather A. Cameron<sup>1</sup>

Glucocorticoids are released in response to stressful experiences and serve many beneficial homeostatic functions. However, dysregulation of glucocorticoids is associated with cognitive impairments and depressive illness<sup>1,2</sup>. In the hippocampus, a brain region densely populated with receptors for stress hormones, stress and glucocorticoids strongly inhibit adult neurogenesis<sup>3</sup>. Decreased neurogenesis has been implicated in the pathogenesis of anxiety and depression, but direct evidence for this role is lacking<sup>4,5</sup>. Here we show that adult-born hippocampal neurons are required for normal expression of the endocrine and behavioural components of the stress response. Using either transgenic or radiation methods to inhibit adult neurogenesis specifically, we find that glucocorticoid levels are slower to recover after moderate stress and are less suppressed by dexamethasone in neurogenesis-deficient mice than intact mice, consistent with a role for the hippocampus in regulation of the hypothalamic–pituitary–adrenal (HPA) axis<sup>6,7</sup>. Relative to controls, neurogenesis-deficient mice also showed increased food avoidance in a novel environment after acute stress, increased behavioural despair in the forced swim test, and decreased sucrose preference, a measure of anhedonia. These findings identify a small subset of neurons within the dentate gyrus that are critical for hippocampal negative control of the HPA axis and support a direct role for adult neurogenesis in depressive illness.

Functional granule neurons are generated in the hippocampus throughout life by a multistep process that begins with glial fibrillary acidic protein (GFAP)-expressing radial cell precursors<sup>8,9</sup>. To investigate the role of adult neurogenesis in hippocampal function, we created mice that express herpes simplex virus thymidine kinase (TK) under control of the GFAP promoter (TK mice; Fig. 1a). Thymidine kinase renders mitotic cells sensitive to the antiviral drug valganciclovir but spares post-mitotic cells<sup>10</sup>. Stellate astrocytes and radial neuronal precursor cells both express GFAP, and both cell types express thymidine kinase in the transgenic mice. However, the number of astrocytes is unaltered by treatment with valganciclovir in TK mice (Fig. 1b, c), consistent with a lack of cell proliferation in astrocytes in the adult brain<sup>11</sup>. In contrast, immature neurons expressing doublecortin (DCX) were virtually eliminated in the dentate gyrus of valganciclovir-treated TK (v-TK) mice (Fig. 1d and Supplementary Fig. 1). One-day-old neuronal progenitors, identified with DCX and the cell-cycle marker bromodeoxyuridine (BrdU), were reduced in v-TK mice by 99% relative to control conditions (Fig. 1e). Transgene expression alone and valganciclovir treatment of wild-type (WT) mice had no effect (Fig. 1e). v-TK mice showed weight gain comparable to v-WT mice (Supplementary Fig. 2), and histopathological examination found no abnormalities in the small intestine or submucosal or myenteric plexuses (not shown), indicating that the gastrointestinal effects described in another strain expressing thymidine kinase under the

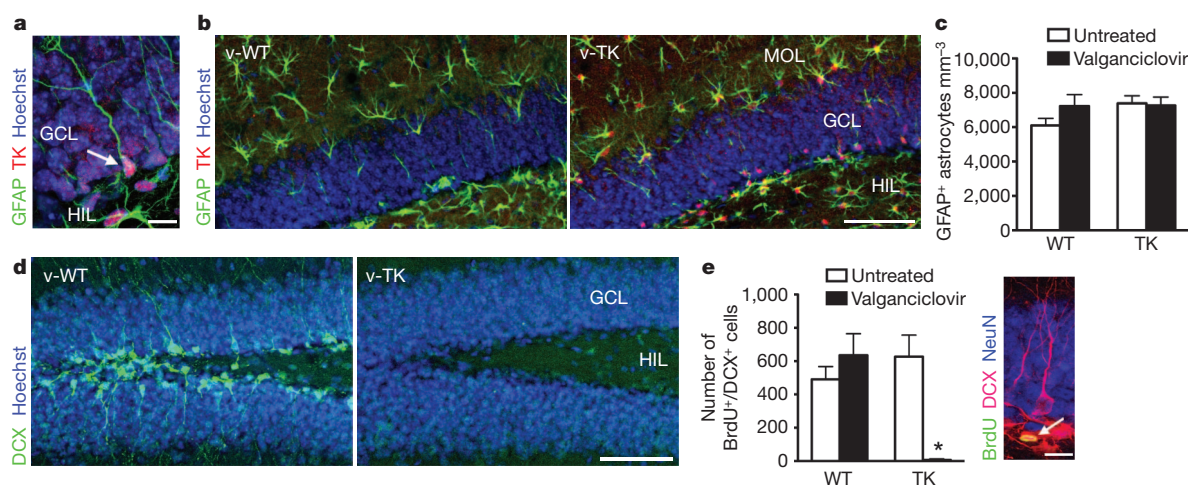


**Figure 1 | GFAP-TK mice show specific inhibition of adult neurogenesis.** **a**, Confocal image of endogenous GFAP and transgenic thymidine kinase expression in a radial precursor cell in the dentate gyrus (arrow). **b**, Confocal photographs of valganciclovir-treated mice show GFAP<sup>+</sup> astrocytes in the hilus and molecular layer in both genotypes, despite strong thymidine kinase expression in all GFAP-expressing cells in TK mice. **c**, Valganciclovir treatment did not affect numbers of GFAP<sup>+</sup> astrocytes (genotype effect  $F_{1,20} = 1.7$ ,  $P = 0.2$ ; valganciclovir effect  $F_{1,20} = 1.0$ ,  $P = 0.3$ ; interaction  $F_{1,20} = 1.5$ ,  $P = 0.2$ ;  $n = 6$  per group), confirming the expectation that valganciclovir does not kill astrocytes, which are post-mitotic in the adult. **d**, Confocal photographs

of dentate gyrus doublecortin (DCX) immunostaining in mice treated with valganciclovir (v-WT and v-TK) for 4 weeks. DCX<sup>+</sup> young neurons are abundant in v-WT mice but absent in v-TK mice. **e**, The number of BrdU<sup>+</sup>/DCX<sup>+</sup> young neurons was unaltered in v-WT mice but reduced by 99% in v-TK mice (genotype effect  $F_{1,20} = 20$ ,  $P = 0.0002$ ; valganciclovir effect  $F_{1,20} = 19$ ,  $P = 0.0003$ ; interaction  $F_{1,20} = 40$ ,  $P < 0.0001$ ;  $*P < 0.001$  versus untreated TK and v-WT;  $n = 6$  per group). Inset shows example of 1-day-old BrdU<sup>+</sup>/DCX<sup>+</sup> neuron (arrow). Error bars, s.e.m.; scale bars, 10  $\mu$ m in **a**, **e**, 100  $\mu$ m in **b**, **d**. MOL, molecular layer; GCL, granule cell layer; HIL, hilus.

<sup>1</sup>National Institute of Mental Health, National Institutes of Health, Bethesda, Maryland 20892, USA.

GFAP promoter<sup>8</sup> are absent in this line of mice. Taken together, these data indicate that v-TK mice have a specific loss of adult neurogenesis without detectable effects on astrocytes or general health.

The hippocampus provides negative control of the HPA axis<sup>6,7</sup>, but the circuitry involved is not well understood. Because adult hippocampal neurogenesis is highly sensitive to stress and glucocorticoids<sup>3</sup>, we hypothesized that adult neurogenesis may be important for hippocampal regulation of the HPA axis. We therefore examined serum levels of corticosterone, the predominant rodent glucocorticoid, in several conditions that activate the HPA axis. Neurogenesis-deficient v-TK and control v-WT mice had equivalent levels of corticosterone at the onset of both the light and the dark phase (Supplementary Fig. 3), indicating that adult-born neurons are not required for normal circadian fluctuation of glucocorticoids. v-WT and v-TK mice also had similar corticosterone levels after exposure to a novel environment (Supplementary Fig. 3), a mild stressor, consistent with previous findings<sup>12</sup>.

To test the response to, and recovery from, a moderate psychological stressor, we subjected mice to 30 min of restraint and measured corticosterone 0, 30 or 60 min later (Fig. 2a). v-TK mice and v-WT mice had similar levels of corticosterone immediately after termination of the stressor. However, v-TK mice had elevated corticosterone relative to v-WT mice 30 min after stress, suggesting impaired negative feedback control of glucocorticoid release similar to that observed in mice with complete loss of glucocorticoid receptors in the forebrain<sup>13</sup>. To investigate whether the hypersecretion of glucocorticoids habituates, mice were subjected to daily restraint for 16 additional days, and corticosterone was measured on the final day. As on the first day of restraint, v-TK mice had elevated corticosterone relative to v-WT mice (Fig. 2b). Control TK mice, which were never treated with valganciclovir and therefore had normal levels of neurogenesis, had levels of corticosterone identical to untreated WT mice 30 min after restraint (Fig. 2c). Therefore, corticosterone

hypersecretion in neurogenesis-deficient mice is not caused by non-specific or insertion site effects of the thymidine kinase transgene.

The experiments above indicate that adult neurogenesis regulates the endocrine stress response, but they do not pinpoint the brain region involved. Hippocampal damage primarily alters the response to psychological stressors such as restraint, which produce fear without causing a direct threat to well-being, but does not typically affect responses to physical stressors, such as hypoxia, haemorrhage, inflammation or anaesthesia<sup>7</sup>. Consistent with HPA regulation at the level of the hippocampus, v-WT and v-TK mice showed comparable elevations in corticosterone after exposure to isoflurane anaesthesia (Supplementary Fig. 4). Additionally, in agreement with the lack of global HPA dysregulation, we found no evidence for reduced cell birth in the hypothalamic paraventricular nucleus of v-TK mice (Supplementary Fig. 5).

To test the contribution of adult neurogenesis in other regions directly, we exploited the spatial specificity of X-irradiation to reduce hippocampal neurogenesis while sparing neurogenesis in the subventricular zone<sup>12,14</sup>, a source of GFAP<sup>+</sup> neuronal precursors added to the olfactory bulb throughout adulthood<sup>8,15</sup>. Irradiated mice had elevated corticosterone during recovery from restraint stress (Fig. 3), replicating the initial finding with an independent ablation method. In addition, there was no relationship between the extent of subventricular zone neurogenesis inhibition and the corticosterone response in irradiated mice (Fig. 3). Therefore, the most parsimonious interpretation of our results is that inhibition of adult neurogenesis in the dentate gyrus leads to hypersecretion of glucocorticoids in response to stress.

A functional link between new neurons and anxiety/depression has been suggested by the demonstration that some antidepressant effects on behaviour are blocked by irradiation<sup>12,16–18</sup>. However, normal anxiety- and depressive-like behaviour in animals lacking neurogenesis has led

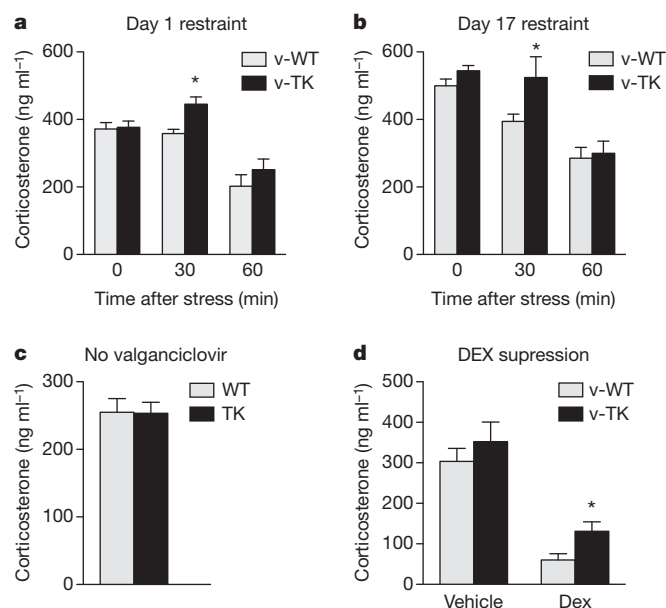


**Figure 2 | The glucocorticoid response to stress is increased in neurogenesis-deficient mice.** **a**, Restraint, a moderate psychogenic stressor, resulted in higher corticosterone in neurogenesis-deficient v-TK mice than in v-WT mice 30 min after the end of stress. **b**, The effect of restraint was still observed after repeated exposure to stress (for both days: genotype effect  $F_{1,65} > 5$ ,  $P < 0.05$ ; time effect  $F_{2,65} > 24$ ,  $P < 0.001$ ;  $*P < 0.05$  post hoc versus v-WT;  $n = 6–17$  per group per time point). **c**, In untreated control mice, corticosterone levels 30 min after restraint stress were not different between WT and TK mice, indicating that altered glucocorticoid response to stress is not a non-specific effect of transgene expression ( $t_{30} = 0.1$ ,  $P = 0.95$ ;  $n = 16$  per group). **d**, Valganciclovir-treated v-TK mice show impaired dexamethasone suppression of corticosterone in response to restraint ( $*t_{13} = 2.5$ ,  $P = 0.03$ ;  $n = 7–8$  per group). Error bars, s.e.m.

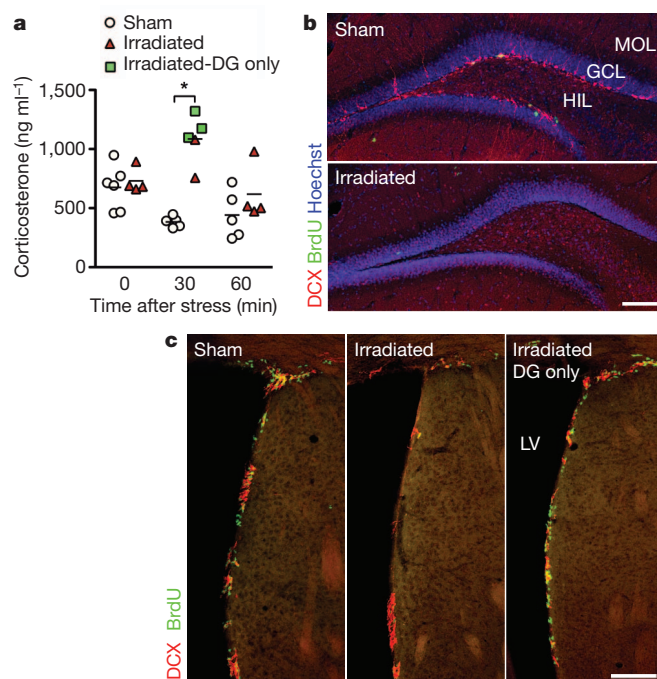


**Figure 3 | Increased stress response is not due to reduced neurogenesis in the subventricular zone.** **a**, Increased corticosterone response 30 min after restraint was confirmed in mice in which neurogenesis was reduced by irradiation (irradiation effect  $F_{1,50} = 2.0$ ,  $P = 0.16$ ; time effect  $F_{2,50} = 5.1$ ,  $P = 0.01$ ; irradiation  $\times$  time interaction  $F_{2,50} = 5.7$ ,  $P = 0.006$ ;  $*P < 0.01$  post hoc;  $n = 4–6$  per group per time point). Green squares at the 30 min time point indicate corticosterone levels in irradiated mice that showed unaffected neurogenesis in the subventricular zone. **b**, Confocal images of BrdU<sup>+</sup> and DCX<sup>+</sup> cells in the dentate gyrus; neurogenesis was reduced in all irradiated mice. **c**, Confocal images of BrdU<sup>+</sup> and DCX<sup>+</sup> cells illustrating sparing of neurogenesis in the subventricular zone. Scale bars, 100  $\mu$ m. LV, lateral ventricle.



to speculation that impaired neurogenesis does not directly contribute to the aetiology of depression in adulthood<sup>4,5</sup>. Our findings above suggest that stress may be a key unexplored factor linking adult-born neurons to anxiety- and depressive-like behaviours.

To probe a potential interaction between stress, neurogenesis and depression, we first used the dexamethasone suppression test, which is commonly used to test HPA axis feedback in depressed patients. A subgroup of depressed patients, and mice that display depressive behaviours, show impaired inhibition of endogenous glucocorticoids by the synthetic glucocorticoid dexamethasone<sup>19,20</sup>. We found that dexamethasone effectively suppressed the restraint-induced rise in corticosterone to near basal levels in v-WT mice (Fig. 2d). However, the level of corticosterone in dexamethasone-injected v-TK mice was significantly higher than that in v-WT mice, consistent with a depressive-like phenotype.

We next examined whether adult neurogenesis regulates the behavioural response to stress in the novelty-suppressed feeding (NSF) test, which shows robust effects of antidepressants that are blocked by irradiation<sup>12,18</sup>. In this test, food-deprived mice are introduced to a novel open field containing a food pellet at its centre and the latency to begin feeding is recorded<sup>12</sup>. When assessed in the NSF test under normal conditions, v-WT and v-TK mice showed similar feeding latencies (Fig. 4a), indicating similar levels of approach-avoidance behaviour. Restraint stress just before testing, however, significantly increased the feeding latency in v-TK mice while having no effect on v-WT mice. Moreover, by the end of the 10 min test only 53% of stressed v-TK mice had fed compared with 92% of stressed v-WT mice (Fig. 4b). Mice from all groups consumed food upon returning to their home cage, indicating that decreased motivation to eat was not responsible for change in behaviour (Supplementary Fig. 6). Thus, adult neurogenesis does not alter behaviour under baseline conditions in this test, consistent with previous observations<sup>12,18</sup>, but buffers the effects of stress on feeding behaviour.

Because the NSF test is associated with both anxiety- and depressive-like behaviour, we investigated the interaction of neurogenesis and stress in additional behavioural tests. In the elevated plus maze, a test of anxiety-like behaviour, there was an anxiogenic effect of stress but no significant difference between v-WT and v-TK mice (Supplementary Fig. 7). We next tested depressive-like behaviour, using the forced swim test, in which rodents are placed in an inescapable cylinder of water and immobility is used as a measure of behavioural despair<sup>21</sup>. Under control conditions neurogenesis-deficient v-TK mice became immobile more rapidly and for a greater duration than v-WT mice (Fig. 4c, d), consistent with a depressive phenotype. In v-WT mice, restraint stress reduced the latency to become immobile and increased total immobility to the level of v-TK mice. Thus, neurogenesis-deficient mice displayed a depressive phenotype at baseline, which could be induced in intact mice by acute stress. Consistent with previous reports<sup>16,18,22</sup>, v-WT and v-TK mice showed similar levels of immobility during later stages of the test, when high (potentially ceiling) levels of behavioural despair are observed<sup>21</sup> (Supplementary Fig. 8).

Anhedonia is a hallmark symptom of depression and, in rodents, presents as a decrease in preference for a sucrose solution compared with water<sup>23</sup>. To assess whether adult neurogenesis is required for hedonic behaviours, we habituated v-WT and v-TK mice to freely available water and 1% sucrose for 3 days. Both groups similarly preferred sucrose (Supplementary Fig. 9a). Then, after water and sucrose deprivation, the bottles were reintroduced and preference was measured during a 10 min test. To introduce an aspect of reward-based decision making<sup>23</sup>, bottle locations were switched for the test. Although v-WT mice showed a preference for sucrose as before, neurogenesis-deficient v-TK mice showed no sucrose preference during the test (Fig. 4e). The decreased sucrose preference in v-TK mice was observed not only in the 10-min test but also during the next night (Fig. 4f). Overall consumption levels were not different, indicating that preference differences did not result from altered thirst or motivation to drink (Supplementary Fig. 9a–d). No differences were

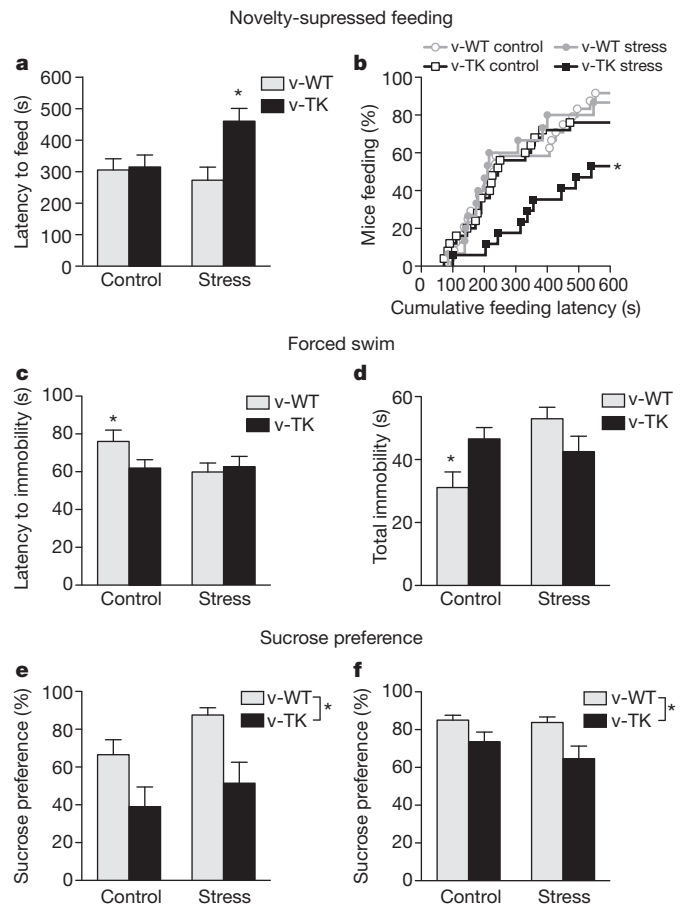


**Figure 4 | Mice lacking neurogenesis show increased anxiety/depression-like behaviours.** **a**, In the NSF test, v-TK mice showed increased latency to feed in a novel environment after restraint stress but not under control conditions (genotype effect  $F_{1,75} = 5.9$ ,  $P = 0.02$ ; stress effect  $F_{1,75} = 1.9$ ,  $P = 0.17$ ; genotype  $\times$  stress interaction  $F_{1,75} = 4.8$ ,  $P = 0.03$ ;  $*P < 0.05$  versus v-TK control and  $*P < 0.01$  versus v-WT stressed;  $n = 13$ –25 per group). **b**, Cumulative distribution of feeding latencies for the NSF test (log-rank test;  $*P < 0.05$  versus all other groups). **c**, Neurogenesis-deficient v-TK mice became immobile faster in the forced swim test. Restraint stress reduced the latency to immobility in v-WT mice but did not affect v-TK mice (genotype effect  $F_{1,88} = 1.1$ ,  $P = 0.3$ ; stress effect  $F_{1,88} = 2.2$ ,  $P = 0.14$ ; genotype  $\times$  stress interaction  $F_{1,88} = 2.6$ ,  $P = 0.11$ ;  $*T_{46} = 2.1$ ,  $P < 0.05$  versus v-WT stressed; v-TK control versus v-TK stressed  $T_{42} = 0.1$ ,  $P = 0.9$ ;  $n = 22$ –26 per group). **d**, Under control conditions, the total time spent immobile was greater in v-TK mice than in v-WT mice. Restraint stress significantly increased total immobility in v-WT mice but had no effect on v-TK mice (genotype effect  $F_{1,88} = 0.3$ ,  $P = 0.6$ ; stress effect  $F_{1,88} = 4.2$ ,  $P = 0.04$ ; genotype  $\times$  stress interaction  $F_{1,88} = 9.1$ ,  $P = 0.003$ ;  $*P < 0.05$  versus control v-TK,  $*P < 0.001$  versus stressed v-WT, stressed v-WT versus stressed v-TK  $P > 0.05$ ;  $n = 22$ –26 per group). **e**, Neurogenesis-deficient v-TK mice showed reduced preference for sucrose in an acute test, compared with v-WT mice, under both control and restraint conditions (genotype effect  $F_{1,20} = 11.2$ ,  $P < 0.01$ ; stress effect  $F_{1,20} = 3.1$ ,  $P = 0.09$ ; genotype  $\times$  stress interaction  $F_{1,20} = 0.2$ ,  $P = 0.7$ ;  $n = 4$ –8 per group). **f**, Sucrose preference remained lower in v-TK mice than v-WT mice during the subsequent dark cycle (genotype effect  $F_{1,25} = 6.8$ ,  $P = 0.01$ ; stress effect  $F_{1,25} = 0.8$ ,  $P = 0.4$ ; genotype  $\times$  stress interaction  $F_{1,25} = 0.5$ ,  $P = 0.5$ ;  $n = 4$ –10 per group). Error bars, s.e.m.

observed in WT and control TK mice that were not treated with valganciclovir, indicating that anhedonic behaviour does not result from thymidine kinase expression alone (Supplementary Fig. 9e–g). The loss of sucrose preference in v-TK mice was observed whether or not the mice were restrained before testing, perhaps reflecting a basic difference between reward-related behaviours tested in this paradigm and the stress response behaviours tested in despair and avoidance situations. Taken together, our behavioural results suggest that adult

neurogenesis buffers the effect of previous stress in the NSF test, buffers the effect of inescapable stress in the forced swim test and enhances reward-seeking behaviour independent of stress in the sucrose preference test.

Elucidating the strong but poorly understood association between stress and depression is critical for development of more effective treatments<sup>1,2</sup>. The hippocampus has long been known to regulate the HPA axis<sup>6,7</sup>, and the importance of the hippocampus for emotional behaviour is emerging<sup>24</sup>. Our data show that adult-born hippocampal granule neurons dynamically regulate stress reactivity at both the endocrine and behavioural levels. A direct role for adult neurogenesis in depression-like behaviour was observed in three behavioural situations that are commonly used to assess antidepressant efficacy and characterize the development of a depressive phenotype in response to chronic stress<sup>12,18,25</sup>. In addition to its effects on emotional behaviour, stress is an important modulator of learning and memory<sup>26</sup>. Our results therefore also suggest that buffering of stress responses by new neurons may play a role in learning and memory under novel or aversive conditions, in addition to any more direct function of young neurons in encoding of information. Because the production of new granule neurons is itself strongly regulated by stress and glucocorticoids<sup>3</sup>, this system forms a loop through which stress, by inhibiting adult neurogenesis, could lead to enhanced responsiveness to future stress. This type of programming could be adaptive, predisposing animals to behave in ways best suited to the severity of their particular environments<sup>27</sup>. However, maladaptive progression of such a feed-forward loop could potentially lead to increased stress responsiveness and depressive behaviours that persist even in the absence of stressful events.

## METHODS SUMMARY

All procedures followed the Institute of Laboratory Animal Research guidelines and were approved by the Animal Care and Use Committee of the National Institute of Mental Health. Transgenic mice expressing HSV-TK under the GFAP promoter were generated from a previously generated plasmid<sup>28</sup> using standard techniques and bred on a mixed C57Bl/6:CD-1 background. Male v-WT and v-TK mice were treated with valganciclovir for 8 weeks (dexamethasone experiment), 10–19 weeks (endocrine), 12 weeks (behaviour) or 4 weeks (histology; histology after 12 weeks in Supplementary Fig. 1), beginning at 8 weeks of age. Male C57Bl/6 mice were irradiated under pentobarbital anaesthesia, as described previously<sup>29</sup>, and tested 9 weeks later. For immunohistochemical analyses, mice were given BrdU 6 weeks (for analysis of the paraventricular nucleus) or 24 h before being killed, brain sections were immunostained as previously described<sup>29</sup> and labelled cells were counted stereologically.

Serum corticosterone was measured by radioimmunoassay (MP Biomedicals) from submandibular blood samples obtained directly from the home cage condition or after exploration of a novel box, restraint or isoflurane exposure. For the dexamethasone suppression test, dexamethasone (Sigma; 50 µg kg<sup>-1</sup> in propylene glycol) or vehicle were injected 90 min before restraint, and blood was sampled immediately after 10 min restraint.

Behavioural tests were performed after 30 min of restraint or directly from the home cage. Different cohorts of mice were tested in the NSF test, elevated plus maze, forced swim test and sucrose preference test as previously described<sup>12,18,21,30</sup>. Statistical analyses were performed by *t*-test, log-rank test or ANOVA with Fisher's least significant difference test for post-hoc comparisons. Significance was set at *P* < 0.05.

**Full Methods** and any associated references are available in the online version of the paper at [www.nature.com/nature](http://www.nature.com/nature).

**Received 7 April; accepted 13 June 2011.**

**Published online 3 August 2011.**

- Holsboer, F. & Ising, M. Stress hormone regulation: biological role and translation into therapy. *Annu Rev. Psychol.* **61**, 81–109 (2010).
- McEwen, B. S. Physiology and neurobiology of stress and adaptation: central role of the brain. *Physiol. Rev.* **87**, 873–904 (2007).
- Mirescu, C. & Gould, E. Stress and adult neurogenesis. *Hippocampus* **16**, 233–238 (2006).

- Sapolsky, R. M. Is impaired neurogenesis relevant to the affective symptoms of depression? *Biol. Psychiatry* **56**, 137–139 (2004).
- Drew, M. R. & Hen, R. Adult hippocampal neurogenesis as target for the treatment of depression. *CNS Neurol. Disord. Drug Targets* **6**, 205–218 (2007).
- Roosendaal, B. et al. Memory retrieval impairment induced by hippocampal CA3 lesions is blocked by adrenocortical suppression. *Nature Neurosci.* **4**, 1169–1171 (2001).
- Jankord, R. & Herman, J. P. Limbic regulation of hypothalamo-pituitary-adrenocortical function during acute and chronic stress. *Ann. NY Acad. Sci.* **1148**, 64–73 (2008).
- Garcia, A. D., Doan, N. B., Imura, T., Bush, T. G. & Sofroniew, M. V. GFAP-expressing progenitors are the principal source of constitutive neurogenesis in adult mouse forebrain. *Nature Neurosci.* **7**, 1233–1241 (2004).
- Seri, B., Garcia-Verdugo, J. M., McEwen, B. S. & Alvarez-Buylla, A. Astrocytes give rise to new neurons in the adult mammalian hippocampus. *J. Neurosci.* **21**, 7153–7160 (2001).
- Borrelli, E., Heyman, R. A., Arias, C., Sawchenko, P. E. & Evans, R. M. Transgenic mice with inducible dwarfism. *Nature* **339**, 538–541 (1989).
- Burns, K. A., Murphy, B., Danzer, S. C. & Kuan, C.-Y. Developmental and post-injury cortical gliogenesis: a genetic fate-mapping study with Nestin-CreER mice. *Glia* **57**, 1115–1129 (2009).
- Santarelli, L. et al. Requirement of hippocampal neurogenesis for the behavioral effects of antidepressants. *Science* **301**, 805–809 (2003).
- Furay, A. R., Bruestle, A. E. & Herman, J. P. The role of the forebrain glucocorticoid receptor in acute and chronic stress. *Endocrinology* **149**, 5482–5490 (2008).
- Wojtowicz, J. M. Irradiation as an experimental tool in studies of adult neurogenesis. *Hippocampus* **16**, 261–266 (2006).
- Doetsch, F., Caille, I., Lim, D. A., Garcia-Verdugo, J. M. & Alvarez-Buylla, A. Subventricular zone astrocytes are neural stem cells in the adult mammalian brain. *Cell* **97**, 703–716 (1999).
- Airan, R. D. et al. High-speed imaging reveals neurophysiological links to behavior in an animal model of depression. *Science* **317**, 819–823 (2007).
- Surget, A. et al. Antidepressants recruit new neurons to improve stress response regulation. *Mol. Psychiatry* doi:10.1038/mp.2011.48 (2011).
- David, D. J. et al. Neurogenesis-dependent and -independent effects of fluoxetine in an animal model of anxiety/depression. *Neuron* **62**, 479–493 (2009).
- Anacker, C., Zunszain, P. A., Carvalho, L. A. & Pariante, C. M. The glucocorticoid receptor: pivot of depression and of antidepressant treatment? *Psychoneuroendocrinology* **36**, 415–425 (2011).
- Ridder, S. et al. Mice with genetically altered glucocorticoid receptor expression show altered sensitivity for stress-induced depressive reactions. *J. Neurosci.* **25**, 6243–6250 (2005).
- Castagné, V., Moser, P. & Porsolt, R. D. in *Methods of Behavior Analysis in Neuroscience* 2nd edn (ed. Buccafusco, J. J.) Ch. 6 (CRC Press, 2009).
- Revest, J.-M. et al. Adult hippocampal neurogenesis is involved in anxiety-related behaviors. *Mol. Psychiatry* **14**, 959–967 (2009).
- Treadway, M. T. & Zald, D. H. Reconsidering anhedonia in depression: lessons from translational neuroscience. *Neurosci. Biobehav. Rev.* **35**, 537–555 (2011).
- Barkus, C. et al. Hippocampal NMDA receptors and anxiety: at the interface between cognition and emotion. *Eur. J. Pharmacol.* **626**, 49–56 (2010).
- Duman, C. H. Models of depression. *Vitam. Horm.* **82**, 1–21 (2010).
- Sandi, C. & Pinelo-Nava, M. T. Stress and memory: behavioral effects and neurobiological mechanisms. *Neural Plast.* **2007**, 78970 (2007).
- Oomen, C. A. et al. Severe early life stress hampers spatial learning and neurogenesis, but improves hippocampal synaptic plasticity and emotional learning under high-stress conditions in adulthood. *J. Neurosci.* **30**, 6635–6645 (2010).
- Delaney, C. L., Brenner, M. & Messing, A. Conditional ablation of cerebellar astrocytes in postnatal transgenic mice. *J. Neurosci.* **16**, 6908–6918 (1996).
- Snyder, J. et al. Adult-born hippocampal neurons are more numerous, faster maturing, and more involved in behavior in rats than in mice. *J. Neurosci.* **29**, 14484–14495 (2009).
- Brown, T. S. & Murphy, H. M. Factors affecting sucrose preference behavior in rats with hippocampal lesions. *Physiol. Behav.* **11**, 833–844 (1973).

**Supplementary Information** is linked to the online version of the paper at [www.nature.com/nature](http://www.nature.com/nature).

**Acknowledgements** We thank A. Sowers and J. Mitchell for help with irradiation, M. Brenner for providing the plasmid construct, GlaxoSmithKline for providing the antibody against HSV-TK, and K. Sanzone, F. Kamhi, L. Glover, S. Ferrante and L. Grigereit for assisting with mouse breeding and treatment. This research was supported by the Intramural Program of the National Institute of Mental Health, National Institutes of Health, USA, ZIA MH002784 (to H.A.C.).

**Author Contributions** J.S.S. performed histological, endocrine and behavioural experiments, analysed data and wrote the paper; A.S. performed behavioural experiments and analysed behavioural data; H.A.C. performed endocrine experiments, analysed data and wrote the paper; J.P. and M.B. generated the transgenic mice.

**Author Information** Reprints and permissions information is available at [www.nature.com/reprints](http://www.nature.com/reprints). The authors declare no competing financial interests. Readers are welcome to comment on the online version of this article at [www.nature.com/nature](http://www.nature.com/nature). Correspondence and requests for materials should be addressed to H.A.C. ([heathercameron@mail.nih.gov](mailto:heathercameron@mail.nih.gov)).

## METHODS

All procedures followed the Institute of Laboratory Animal Research guidelines and were approved by the Animal Care and Use Committee of the National Institute of Mental Health.

**Transgenic animals.** Transgenic mice expressing HSV-TK under the GFAP promoter (GFAP-TK) were generated on a C57Bl/6 background using the pGfa2-TK1 plasmid<sup>28</sup> applying standard techniques and were outcrossed onto a mixed C57Bl/6:CD-1 background. For all GFAP-thymidine kinase experiments, male mice were weaned at 3 weeks of age, genotyped by PCR, and housed four per cage with mixed genotype siblings. Mice were housed on a 12 h light/dark cycle with lights on at 6.00 a.m. All experiments were performed on different, naive cohorts of mice except the home cage, exploration and 17 day restraint corticosterone experiments, which were performed on the same cohort. Beginning at 8 weeks of age, valganciclovir was mixed into powdered chow (0.3%, approximately  $35 \text{ mg kg}^{-1} \text{ day}^{-1}$ ) for 4 days, alternating with standard pelleted chow for 3 days. Mice were treated for 8 weeks before dexamethasone testing, 10–19 weeks before other endocrine testing and 12 weeks before behavioural testing. Histology was performed after 4 weeks, to assess effectiveness when animals were younger and neurogenesis was higher but was also routinely confirmed after longer treatments in tested mice (Supplementary Fig. 1). All mice within each experiment were tested at the same time point after the start of treatment.

**Irradiation.** Male C57Bl/6 mice were irradiated under pentobarbital anaesthesia, as described previously<sup>29</sup>, and tested 9 weeks later.

**Immunohistochemical analyses.** Immunohistochemistry was performed on 40- $\mu\text{m}$  sections as previously described<sup>29</sup>, using the following primary antibodies: goat anti-GFAP (Santa Cruz Biotechnology), rabbit anti-HSV-thymidine kinase (gift from GlaxoSmithKline), goat anti-doublecortin (Santa Cruz Biotechnology), rat anti-BrdU (Accurate) and mouse anti-BrdU (BD Biosciences). Alexa-conjugated secondary antibodies made in donkey (Invitrogen) and the nuclear counterstain Hoechst 33258 (Sigma) were used for all fluorescent labelling. The ABC method (Vector Labs) and DAB were used for enzymatic staining with cresyl violet nuclear counterstaining.

For dentate gyrus analyses, valganciclovir-treated and untreated WT and TK mice were injected once with BrdU ( $200 \text{ mg kg}^{-1}$ ), after 4 weeks of treatment, and perfused 24 h later. Stereological counts of BrdU<sup>+</sup> cells were performed on a 1 in 12 series of sections in the dentate gyrus. Counts of BrdU<sup>+</sup>/DCX<sup>+</sup> neurons were obtained by multiplying total BrdU<sup>+</sup> cell counts by the proportion that expressed DCX. To quantify GFAP<sup>+</sup> astrocytes, the most medial 500  $\mu\text{m}$  of the molecular layer of the suprapyramidal blade was imaged with a confocal microscope (Olympus FV300) and a  $\times 60$  oil-immersion lens. The total number of GFAP<sup>+</sup> cells was divided by the volume examined for each animal to obtain a measure of astrocyte density.

For analyses of the paraventricular nucleus, mice were given BrdU water ( $1 \text{ mg ml}^{-1}$ ) for 1 week, beginning in the fifth week of valganciclovir treatment, and perfused 6 weeks later. Stereological counts were performed in a one in two series of sections through the paraventricular nucleus.

For irradiation experiments, mice received a single BrdU injection and were perfused 24 h later. Immunostaining for BrdU and DCX was used to confirm a reduction in dentate gyrus neurogenesis, and BrdU and DCX labelling was examined in the subventricular zone of mice from the 30 min post-restraint group to assess the spatial specificity of irradiation-induced reduction of adult neurogenesis.

**Stress and corticosterone measurement.** To measure circadian fluctuations in baseline corticosterone, submandibular blood samples were obtained directly from the home cage condition, using animal lancets (Medipoint) at 7.00–8.00 a.m. or 7.00–8.00 p.m. Blood samples were centrifuged, and serum was collected and stored at  $-80^\circ\text{C}$  until use. Serum corticosterone was measured by radioimmunoassay (MP Biomedicals).

For exploration stress, mice were placed in an open field (white plastic box,  $50 \text{ cm} \times 50 \text{ cm} \times 50 \text{ cm}$ ) for 5 min and allowed to explore. Blood samples were

obtained 30 min later. During the interval between exploration and blood sampling, mice were placed individually in clean, empty cages to prevent social interactions that could influence HPA activity. Morning and evening exploration occurred between 8.00 and 11.00 a.m. and 6.00 and 8.00 p.m., respectively. Locomotor behaviour was analysed using Ethovision software (Noldus).

For all restraint stress experiments, mice were restrained for 30 min in decapicones (Bainbridge Scientific). For isoflurane experiments, mice were exposed to 4% isoflurane in oxygen for 30 min. Blood samples were obtained 0, 30 or 60 min after stress on different subsets of mice; all mice were stressed at the same time and each mouse was used for only one of the three time points. For the 30- and 60-min groups, mice were individually placed in empty cages between stress and blood sampling. Restraint and isoflurane experiments were performed between 12.00 and 4.00 p.m.

For the dexamethasone suppression test, mice were injected with dexamethasone (Sigma;  $50 \mu\text{g kg}^{-1}$  in propylene glycol) or vehicle 90 min before restraint. Blood samples were taken immediately after 10 min restraint.

**Novelty-suppressed feeding.** Mice were handled for 2 min  $\text{day}^{-1}$  for 3 days before testing to familiarize them with experimenter handling. Food was removed from the cage 24 h before testing. Mice were weighed just before food deprivation and again before testing to assess body weight loss. For testing, mice were placed for 10 min in a brightly lit open field ( $50 \text{ cm} \times 50 \text{ cm} \times 50 \text{ cm}$  white plastic boxes containing bedding) with a food pellet at the centre on a slightly (1 cm) elevated platform. Mice were either placed in the arena directly from their home cage or after 30 min of restraint stress and 2 min back in their home cage. Behaviour was videotaped, and the latency for each mouse to begin feeding was scored, offline, by an experimenter blind to the genotype and condition for each mouse. Upon returning to their home cage, the total amount of food consumed during a 5-min period was analysed to test whether feeding differences in the novel environment were due to differences in hunger/motivation.

**Elevated plus maze.** Mice were handled for 3 days and were placed in an elevated plus maze for 5 min either directly from their home cage or after 30 min restraint and 2 min back in their home cage. Behaviour was tracked using Ethovision software and the amount of time spent in the open arms was measured.

**Forced swim test.** Mice were individually placed in a Plexiglas cylinder (19 cm diameter, 30 cm height) containing 19 cm water ( $23 \pm 1^\circ\text{C}$ ) and were videotaped for 6 min. Active (swimming, climbing, struggling) or passive (immobility) behaviours were scored using a time sampling technique to rate the predominant behaviour in each 5-s interval. In contrast to protocols designed to detect reductions in immobility<sup>21</sup> (for example, scoring minutes 2–6 of testing, when immobility is very high in controls, to detect antidepressant effects), the first 2 min of the test were scored separately to better detect potential increases in immobility. The latency to become immobile for the first time was also measured. After the swim session, mice were dried and placed in a cage surrounded by a heating pad. The water was changed between each animal.

**Sucrose preference.** Mice were not handled but were individually housed and given a water bottle containing water and a second with 1% sucrose with the left/right location balanced across animals. After 3 days of habituation, both bottles were removed at 12.00 p.m.<sup>30</sup>. Beginning at 6.30 p.m., mice were subjected to either 30-min restraint or brief experimenter handling, returned to their home cage, and given access to water and sucrose with bottles in the reversed left/right location. Bottles were weighed before testing and again after 10 min, and sucrose preference was expressed as  $(\Delta\text{weight}_{\text{sucrose}})/(\Delta\text{weight}_{\text{sucrose}} + \Delta\text{weight}_{\text{water}}) \times 100$ . The bottles were weighed again at 1 h and on the subsequent morning, and sucrose preference over this interval was used as a long-term, overnight measure.

**Statistical analyses.** Statistical analyses were performed by *t*-test, log-rank test or ANOVA with Fisher's LSD test for post-hoc comparisons. Significance was set at  $P < 0.05$ .



# Polar actomyosin contractility destabilizes the position of the cytokinetic furrow

Jakub Sedzinski<sup>1,2\*</sup>, Maté Biro<sup>1,2\*</sup>, Annelie Oswald<sup>1</sup>, Jean-Yves Tinevez<sup>1,2†</sup>, Guillaume Salbreux<sup>3</sup> & Ewa Paluch<sup>1,2</sup>

**Cytokinesis, the physical separation of daughter cells at the end of mitosis, requires precise regulation of the mechanical properties of the cell periphery<sup>1,2</sup>. Although studies of cytokinetic mechanics mostly focus on the equatorial constriction ring<sup>3</sup>, a contractile actomyosin cortex is also present at the poles of dividing cells<sup>2,4</sup>. Whether polar forces influence cytokinetic cell shape and furrow positioning remains an open question. Here we demonstrate that the polar cortex makes cytokinesis inherently unstable. We show that limited asymmetric polar contractions occur during cytokinesis, and that perturbing the polar cortex leads to cell shape oscillations, resulting in furrow displacement and aneuploidy. A theoretical model based on a competition between cortex turnover and contraction dynamics accurately accounts for the oscillations. We further propose that membrane blebs, which commonly form at the poles of dividing cells<sup>5</sup> and whose role in cytokinesis has long been enigmatic, stabilize cell shape by acting as valves releasing cortical contractility. Our findings reveal an inherent instability in the shape of the dividing cell and unveil a novel, spindle-independent mechanism ensuring the stability of cleavage furrow positioning.**

Cell division is driven by the constriction of an actomyosin ring at the cell equator. However, throughout cytokinesis, a substantial actomyosin cortex remains in regions outside of the equatorial ring (the cell poles), both in cultured cells<sup>6</sup>, and *in vivo*<sup>7,8</sup> (Supplementary Fig. 1 and Supplementary Movie 1). Mechanical studies indicate that the polar cortex regulates cleavage dynamics by generating resistive forces that slow furrow ingression<sup>6,9</sup> (Supplementary Model section 1). The polar cortex is also able to exert stresses, for example to correct for shape perturbations<sup>10</sup>. Moreover, the formation of membrane blebs, known to be caused by cortical contractions, is commonly observed at the poles of dividing cells<sup>5</sup> (Supplementary Movie 1). However, how polar contractile forces contribute to the overall cytokinetic cell shape is poorly understood.

During asymmetric division, unbalanced contraction of one of the poles has been shown to directly generate different-sized daughters in *Caenorhabditis elegans* QR.a neuroblasts<sup>11</sup>. In symmetrically dividing cells, depletion of the actin-binding proteins anillin<sup>12–14</sup>, supervillin<sup>15</sup>, profilin or diaphanous<sup>16</sup>, as well as astral microtubule stabilization<sup>17</sup>, result in improper polar contractions, leading to oscillations of the furrow position and division failure. It is, however, not known whether the poles influence furrow positioning in untreated cells. Reasoning that if substantial contractile forces are exerted at the poles, shape instabilities might arise (Fig. 1a), we asked whether a precise balance of polar forces is necessary for accurate symmetric division and, if so, how the cell achieves such a balance.

We first investigated whether asymmetries in polar forces could be observed during cytokinesis. To this aim, we quantified cytoplasm movements in dividing HeLa and L929 fibroblasts, as an imbalance in polar contractions would result in cytoplasm transfer between the poles. We detected cytoplasmic flows of amplitude at least two times higher than noise level (estimated using metaphase cells as a reference)

in 20% of HeLa ( $n = 20$ ) and 25% of L929 cells ( $n = 40$ ) (Fig. 1b, c, Supplementary Fig. 2 and Supplementary Movie 2). In most cases, the direction of the flows alternated, resulting in small oscillations. Strikingly, observations of a large number of dividing cells revealed that in about 2% of HeLa ( $n = 282$ ) and L929 ( $n = 526$ ) cells (Supplementary Table 1), dramatic shape oscillations occurred, where each pole fully contracted before reversal of the flow direction, destabilizing the equatorial position of the furrow and leading to division failure (Supplementary Movie 3). To test whether the shape instabilities were driven by cortex contractions, we used Y27632, a Rho-kinase inhibitor that, at low doses, decreases myosin activity, and thus cortical tension<sup>18</sup>, without preventing cytokinesis<sup>19</sup>. No cytoplasmic flows could be detected during cytokinesis in Y27632-treated cells (Fig. 1b, c and Supplementary Fig. 2,  $n = 10$ ), supporting the view that cortical contractions drive the observed flows. We then tested the involvement of spindle microtubules, which influence polar contractility<sup>20,21</sup>. Spindle disassembly with nocodazole increased the occurrence of shape instabilities (Supplementary Fig. 3, Supplementary Movie 4 and Supplementary Table 1), suggesting that the spindle is unlikely to drive cytokinetic oscillations. Taken together, our observations suggest that actomyosin contractions cause shape instabilities during cytokinesis, which can lead to division failure if their amplitude is not limited.

To assess which factors may trigger shape instabilities, we developed a minimal physical model of a cytokinetic cell. The dividing cell with a cortex under contractile tension is reminiscent of two connected soap bubbles, where Laplace pressure resulting from surface tension is known to lead to instabilities<sup>22</sup> (Fig. 1d). Similarly, in a dividing cell, cortical tension generates hydrostatic pressure at each pole<sup>9</sup>. However, the cell interior is a poro-elastic material<sup>23</sup> that resists deformations and could stabilize cell shape against cortex-driven instabilities (Fig. 1d). In a first approximation, we assumed that each pole has a constant tension  $T$  and a linear bulk elasticity  $K$  (Supplementary Fig. 4a and Supplementary Model section 2), which accounts for the effects of cellular elastic components and of substrate adhesions (Supplementary Fig. 5, Supplementary Movie 5 and Supplementary Model section 5). Previous mechanical models of the polar cortex in cytokinesis have focused on symmetric cells<sup>6,9</sup>, while we allowed variations in pole sizes. A stability analysis reveals that above a critical value of a stability parameter  $T/R_0K$  (with  $R_0$  the radius of one daughter cell), any fluctuation in volume or tension destabilizes the symmetric cell shape and leads to cytosol flows between the poles (Supplementary Fig. 4b). Moreover, if a large enough difference in tension is introduced between the two poles, no bipolar solution for the shape of the cell can be found (Supplementary Fig. 4c).

To test whether an imbalance in contractile forces between the poles indeed destabilizes cell shape, we artificially introduced such a tension imbalance. Using a double-pipette local delivery setup (Fig. 2a), we disrupted the cortex at one pole of dividing HeLa cells by short application of the actin-depolymerizing drug cytochalasin D. Local polar cortex disruption resulted in the formation of a large bleb and destabilized the

<sup>1</sup>Max Planck Institute of Molecular Cell Biology and Genetics, 01307 Dresden, Germany. <sup>2</sup>International Institute of Molecular and Cell Biology, 02109 Warsaw, Poland. <sup>3</sup>Max Planck Institute for the Physics of Complex Systems, 01187 Dresden, Germany. <sup>†</sup>Present address: Pasteur Institute, 75724 Paris, France.

\*These authors contributed equally to this work.

shape of the cell, triggering extensive shape oscillations (Fig. 2b and Supplementary Movie 6; see Supplementary Table 1). As an alternative method for cortex disruption, we used laser ablation<sup>18</sup> (Fig. 2c). Polar cortex ablation also triggered bleb formation, followed by shape oscillations and division failure in a large portion of cytokinetic HeLa (Fig. 2d and Supplementary Movie 7, 35% of 20 cells) and L929 cells (50% of 20 cells). These experiments indicate that introducing a tension imbalance between the poles of a cleaving cell can trigger shape instabilities.

Our physical description also predicts that a global polar tension increase favours shape instabilities (Supplementary Fig. 4b). Cytokinetic shape oscillations had previously been observed upon depletion of the actin-binding scaffold protein anillin<sup>12–14</sup>. Anillin depletion affects the

cortex globally; it is thus unlikely to lead to a strong inhomogeneity in tension between the poles. We analysed cortex distribution along the cell contour in HeLa and L929 cells expressing myosin regulatory light chain (MRLC)–tandem-dimer red fluorescent protein (tdRFP) and Lifeact–green fluorescent protein (GFP) to mark F-actin<sup>24</sup>. We found that in anillin-depleted cells, the cortex was less enriched at the equator than in control cells, suggesting an enhanced polar contractility before shape oscillations (Fig. 2e–g, Supplementary Fig. 6 and Supplementary Movie 8). Another example of global cortex reinforcement was observed after cortex ablation in L929 cells, where oscillations could be triggered by ablation in any region of the cortex (Supplementary Fig. 7a and Supplementary Movie 9, 55% of 60 cells). Laser ablation in these cells led to cycles of cortex disassembly and reassembly, and resulted in an enhancement of the polar cortex at the expense of the equator (Supplementary Fig. 7). Taken together, these observations support the hypothesis that a global polar cortex reinforcement favours shape instabilities.

Our initial theoretical description predicted that the dividing cell shape should be unstable; however, it did not predict shape oscillations, which we systematically observe upon polar cortex perturbation. To gain insight into the oscillation mechanism, we analysed cortex and pole size dynamics during oscillations in anillin-depleted and laser-ablated cells. The mean fluorescence intensities of cortical Lifeact and

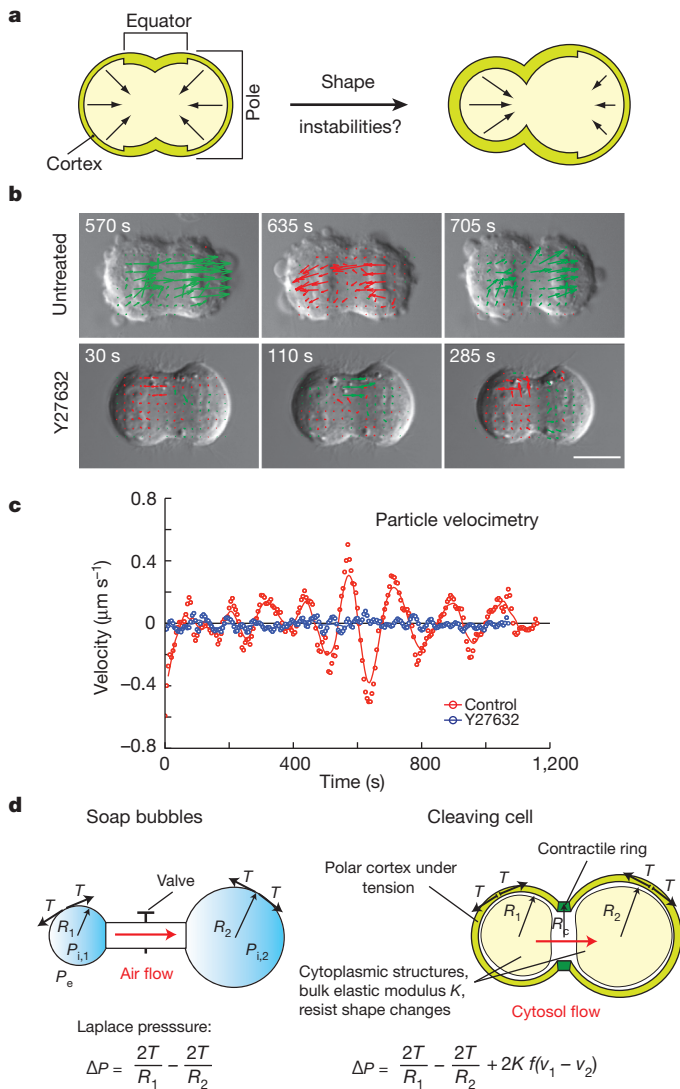


**Figure 1 | The shape of the cleaving cell displays inherent shape instabilities.** **a**, Polar cortex contraction could destabilize the cleavage furrow position. **b**, Stills from differential interference contrast (DIC) time-lapses of cytokinesis in control and Y27632-treated cells. Green and red arrows, rightward and leftward particle image velocimetry flow fields respectively; scale bar, 10  $\mu\text{m}$ . **c**, Mean velocity of the flow field projected on the long cell axis as a function of time in the control (red circles) and the Y27632-treated (blue circles) cells pictured in **b**. Solid lines, data smoothed by factor 5. **d**, Left, schematic of the experiment demonstrating the instability of two soap bubbles of interfacial tension  $T$  connected by a pipe.  $P_e$ , outside pressure;  $P_{i,1}$ ,  $P_{i,2}$ , pressures inside the bubbles;  $R_1$ ,  $R_2$ , bubble radii. Right, schematic of a cytokinetic cell.  $R_1$ ,  $R_2$ , radii of the future daughter cells;  $R_c$ , cleavage furrow radius;  $T$ , polar cortex tension;  $Kf(v_1 - v_2)$ , cell elastic response;  $\Delta P$  is the pressure difference between the poles.

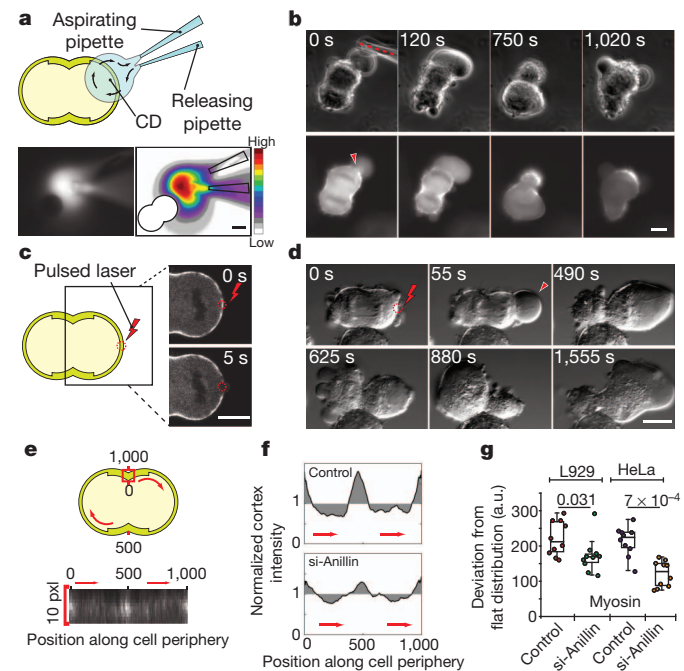


**Figure 2 | Perturbation of the polar cortex enhances cytokinetic shape instabilities.** **a**, Top, the local drug delivery experiment; bottom, fluorescent image of the released solution (visualized with Alexa Fluor 568; left, greyscale; right, pseudo-colour). **b**, Montage of a cleaving HeLa cell expressing actin-GFP, treated with cytochalasin D (CD) at a pole. 0 s, onset of cytochalasin D application. Red dotted line, position of the releasing pipette; the red arrowhead points to the rupture in the actin cortex. **c**, Left, the laser ablation experiment; right, example of polar cortex ablation in a HeLa cell expressing MRLC–tdRFP (red circle, ablation spot). **d**, Time-lapse of shape oscillations in a cleaving HeLa cell ablated at the polar cortex (red circle). 0 s, onset of ablation. Arrowhead points to the bleb induced by cortex ablation. Scale bars, 10  $\mu\text{m}$ . **e**, Left, description of the measurement of cortex distribution along the cell periphery. **f**, Representative plots of the cortical distribution of MRLC–tdRFP in a control and an anillin-depleted cell (see Supplementary Fig. 1 and Methods). **g**, Integrals of cortical myosin distributions (shaded regions in **f**), in control and anillin-depleted cells shortly before the onset of oscillations. Boxes extend from the 25th to 75th percentiles, with a line at the median.  $P$  values, Mann–Whitney  $U$  test ( $n = 10$ ). a.u., arbitrary units.

MRLC oscillated in phase opposition with the size of the poles, indicating that cortex density increases as a pole contracts (Fig. 3a, b, Supplementary Fig. 8 and Supplementary Movies 8 and 9). We thus refined our model to include the effect of cortex turnover. With  $\tau$  the turnover time, cortex dynamics are described by  $d(Sc)/dt = S(c_0 - c)/\tau$ , where  $c$  is the cortex density,  $c_0$  the steady-state density and  $S$  the surface area of a pole. This equation implies that when perturbed, cortex density and the resulting tension relax to their reference levels on a timescale  $\tau$  (Supplementary Model section 3). Cytoplasm movements are described by  $2\alpha dv_i/dt = -\Delta P$  where  $\alpha$  is a friction coefficient limiting the variation of the normalized volume  $v_i$  of a pole in response to a pressure difference  $\Delta P$  between the poles (Fig. 1d). For intermediate values of the stability parameter  $T_0/R_0K$  and for slow enough actin turnover, the system described by these two equations exhibits spontaneous shape oscillations (Fig. 3c, d and Supplementary Model). The underlying mechanism is as follows: if polar contraction is faster than cortex turnover, the cortex accumulates during contraction. As elasticity slows down contraction, cortex turnover leads to tension decrease at the contracting pole and increase at the opposing pole, and reversal of the oscillation direction. Cortex and pole size dynamics during oscillations could be very accurately fitted to the driving equations of the model (Fig. 3e, Supplementary Fig. 9 and Model Section 4). These fits allowed us to extract mechanical parameters, including the stability parameter  $T_0/R_0K$  from the data. We could thus position the oscillating cells in the state diagram and found that they were located in the linearly unstable oscillatory region (Fig. 3d and Supplementary Fig. 9). The period of the simulated oscillations was in good agreement with the period measured experimentally (Fig. 3c and Supplementary Fig. 8). Finally, the model predicts that the cell has a characteristic response time to pressure changes given by the ratio of friction to elasticity  $\tau_c = \alpha/2K$ . Consistently, we observed that cortex intensities reached a maximum and started decreasing before the reversal of the oscillation direction (Fig. 3b and Supplementary Fig. 8c, e). These observations show that the model (summarized in Fig. 4a) is in very good agreement with the experimental data.

Our findings indicate that polar tension must be tightly controlled during cytokinesis, raising the question of how this control is achieved. One striking difference between oscillating and control cells is that while control cells display blebs at both poles throughout division (Supplementary Movie 1), in oscillating cells, blebbing seems to alternate between the poles (Supplementary Movies 8 and 9). As bleb growth releases cortical tension and the resulting intracellular pressure<sup>18,25</sup>, it is likely that blebbing effectively lowers polar tension and thus limits polar contractions (Fig. 4a). We tested the effect of inducing blebbing by laser ablation in oscillating anillin-depleted HeLa cells. Bleb induction in a contracting pole stopped the expansion of the opposite pole, while cytoplasm flowed into the bleb (Fig. 4b and Supplementary Movie 10), indicating that bleb formation can interfere with polar contraction. We then globally inhibited blebbing during cell division by treating cells with wheat germ agglutinin (WGA) and concavalin A, tetraivalent lectins that crosslink and stabilize the cortex from the outside<sup>26</sup>. These treatments strongly decreased bleb formation during cytokinesis and triggered shape oscillations and division failure in 35% (WGA,  $n = 102$ ) to 45% (conavalin A,  $n = 130$ ) of L929 cells (Fig. 4c and Supplementary Movie 11), suggesting that hindering bleb formation favours shape instabilities. On the basis of these experiments, we propose that during cytokinesis, blebs act as pressure sinks that reduce contractile tension and the resulting intracellular pressure at the cell poles (Fig. 4a). Importantly, bleb size must be tightly controlled, as the formation of very large blebs can destabilize cell shape by introducing, rather than buffering, a tension imbalance between the poles (Fig. 2b, d and Supplementary Discussion).

Notably, shape instabilities arise only for high polar tensions (Fig. 3d), and high tension also favours bleb formation. Cortical tension and bleb formation could thus constitute a self-regulating mechanical feedback loop. Bleb nucleation results either from local detachment of

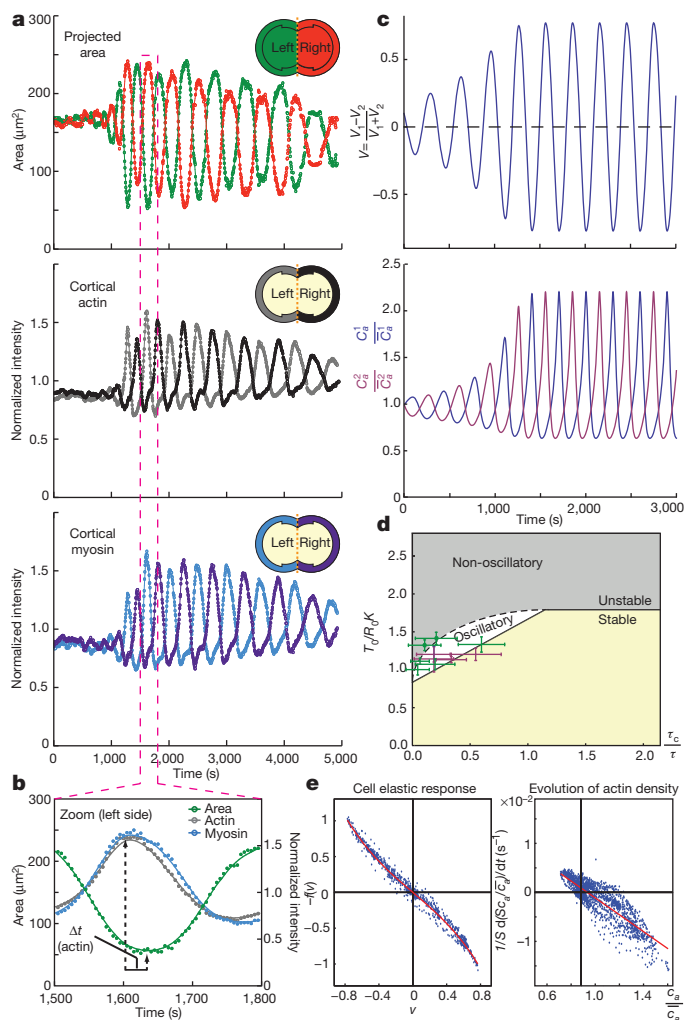


**Figure 3 | Dynamic characterization and model of shape oscillations.**

**a**, Cross-sectional areas of the two poles of an oscillating anillin-depleted L929 cell and mean intensities of cortical actin and myosin, left and right of the cleavage furrow, as a function of time. **b**, Zoom on the regions highlighted in **a** for the left pole. **a**, **b**, Intensities are normalized to their average. Circles, data points; solid lines, data smoothed by factor 5. **c**, Simulation of the evolution of the difference of volumes  $v$  of the two poles (top) and of the polar actin densities (bottom:  $c_a$ , cortex density;  $\bar{c}_a$ , mean cortex density) using parameters extracted from the cell in **a** (see Supplementary Model). **d**, Phase diagram of the linear stability analysis of a symmetric cell with respect to volume perturbation in the model coupling actin turnover and cell mechanics, in the parameter space ( $\tau_c/\tau$ ,  $T_0/R_0K$ ), with  $R_0/R_0 = 0.8$ ;  $T_0$  is the polar tension before oscillations. Cells are positioned on the diagram according to parameters extracted from fits as in **e** (magenta, anillin depleted cells; green, laser-ablated cells). Error bars, standard deviation of the fit parameters. **e**, Fit of the experimental parameters of the cell in **a** (blue points) to the driving equations of the model (red curves). Left, fit to the dynamic equation of  $v$ , yielding the elastic response of the cell  $f(v)$ ; right, fit to the equation for cortex density (see Supplementary Model).

the membrane from the cortex or from local cortex tearing (Supplementary Fig. 10). Both mechanisms are favoured by high cortical tension<sup>5</sup>. It is thus possible that the cytokinetic cortex is tuned to form blebs, and thus release tension, as soon as polar tension exceeds the threshold for shape instabilities. Alternatively, cytokinetic bleb formation could result from a mechanosensing signalling cascade. However, we found that calcium ions, common mediators of mechanosensory responses, which have been shown to be implicated in blebbing<sup>27</sup>, were not involved in cytokinetic bleb formation and shape oscillations (Supplementary Fig. 11). Other elements such as the spindle also contribute to maintaining the cleavage furrow at the equator<sup>20,21</sup>, and mechanical properties, such as cell elasticity, can also prevent shape



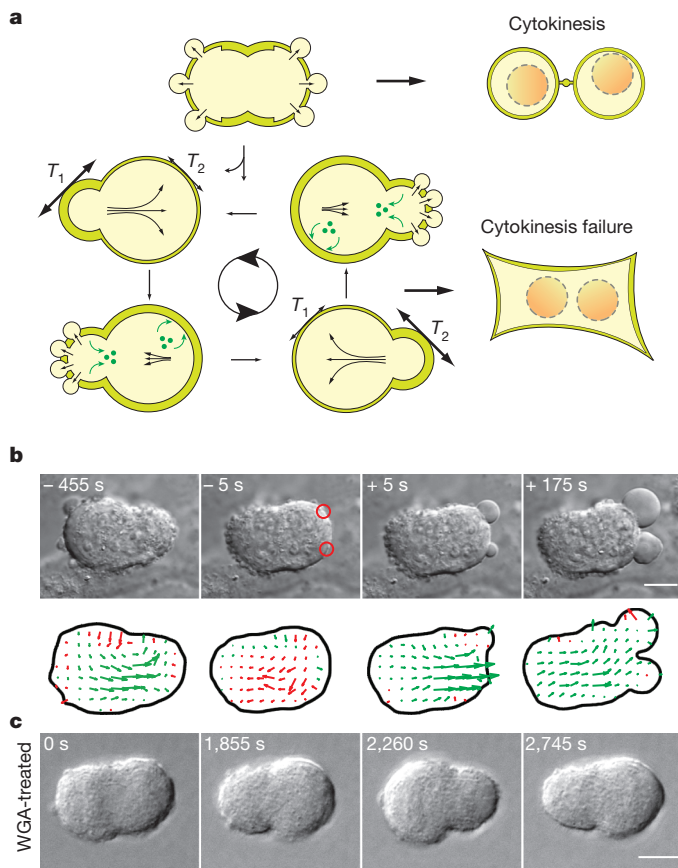


**Figure 4 | Cell shape stability during cytokinesis.** **a**, Top, in control cells, bleb formation constantly releases polar pressure and helps ensure the success of cytokinesis. Bottom, high polar tension or a large pressure imbalance between the poles can trigger shape oscillations. Model of the oscillations: if cortex contraction (resulting from tension  $T$ ) is faster than cortex turnover (green arrows), cortex contractility, dynamics and cell elasticity result in cycles of cortex contraction, disassembly and subsequent reassembly. **b**, Laser ablation at the contracting pole of an oscillating anillin-depleted HeLa cell arrests the flow of cytoplasm between the poles and causes a premature reversal of the flow direction (15 cells out of 16). Top, DIC time-lapse; bottom, corresponding particle image velocimetry vectors and cell outline. Two consecutive ablations were performed (red circles); 0 s, first frame after ablation. **c**, DIC image series of a cytokinetic L929 cell oscillating after WGA treatment. Scale bars, 10  $\mu$ m.

instabilities. Therefore, polar bleb formation may act as a partly redundant safety mechanism. Such redundancy is common in cytokinesis and is thought to provide robustness to the process<sup>28</sup>. Future studies will have to elucidate how exactly cellular mechanical properties, molecular pathways and bleb formation are integrated into a fine-tuned mechanical system ensuring the success of cytokinesis.

Our findings may have important implications for asymmetric cell division. A recent study in *C. elegans* QR.a neuroblasts<sup>11</sup> shows that asymmetric divisions can be the direct result of myosin-driven cortex contraction of one of the poles at the expense of the other, a mechanism that could also be relevant for asymmetric division of *Drosophila* neuroblasts<sup>8</sup> (see Supplementary Discussion). An important open question is how such an asymmetric shape, with more cortical myosin and thus a higher tension in the smaller pole, can be stable. It will be interesting to investigate the mechanics of contractility-driven asymmetric divisions.

Finally, the oscillation mechanism proposed here could be relevant for other systems where cortex oscillations are observed, such as during epithelial contractions in *Drosophila* development<sup>29,30</sup> (Supplementary Discussion). A common feature of all these oscillations is that they display cycles of cortex contraction, disassembly and reassembly,

suggesting they might be driven by a common mechanism coupling contractility, cortex turnover and cell elasticity.

## METHODS SUMMARY

**Culture conditions and cell treatments.** Cell culture, drug treatments, gene silencing by RNA interference, knockdown quantification by quantitative PCR and cell transfections are detailed in the Supplementary Methods.

**Local cytochalasin D delivery.** We conducted local delivery of cytochalasin D using two micropipettes mounted on a motorized micromanipulator (Eppendorf) connected to pressure regulators. Imaging was performed on a Carl Zeiss Axiovert 200M inverted microscope.

**Local laser ablation.** Laser ablation experiments were performed as described in ref. 18 on a scanning confocal microscope (Olympus FV1000) equipped with two scanning heads. For ablation, we used a 405-nm picosecond-pulsed laser with a nominal power of 3 mW for 2.5 s.

**Particle image velocimetry and image processing.** Cytoplasmic flows in dividing cells were determined with a custom-made particle image velocimetry algorithm in MATLAB (MathWorks). Images were processed, automatically analysed and visualized using custom code in MATLAB (MathWorks) (detailed in the Supplementary Methods).

**Full Methods** and any associated references are available in the online version of the paper at [www.nature.com/nature](http://www.nature.com/nature).

Received 17 December 2010; accepted 13 June 2011.

Published online 7 August 2011; corrected 25 August 2011 (see full-text HTML version for details).

- Eggert, U. S., Mitchison, T. J. & Field, C. M. Animal cytokinesis: from parts list to mechanisms. *Annu. Rev. Biochem.* **75**, 543–566 (2006).
- Robinson, D. N. & Spudich, J. A. Mechanics and regulation of cytokinesis. *Curr. Opin. Cell Biol.* **16**, 182–188 (2004).
- Pollard, T. D. Mechanics of cytokinesis in eukaryotes. *Curr. Opin. Cell Biol.* **22**, 50–56 (2010).
- Wang, Y. L. The mechanism of cortical ingression during early cytokinesis: thinking beyond the contractile ring hypothesis. *Trends Cell Biol.* **15**, 581–588 (2005).
- Charras, G. & Paluch, E. Blebs lead the way: how to migrate without lamellipodia. *Nature Rev. Mol. Cell Biol.* **9**, 730–736 (2008).
- Zhang, W. & Robinson, D. N. Balance of actively generated contractile and resistive forces controls cytokinesis dynamics. *Proc. Natl Acad. Sci. USA* **102**, 7186–7191 (2005).
- Werner, M., Munro, E. & Glotzer, M. Astral signals spatially bias cortical myosin recruitment to break symmetry and promote cytokinesis. *Curr. Biol.* **17**, 1286–1297 (2007).
- Cabernard, C., Prehoda, K. E. & Doe, C. Q. A spindle-independent cleavage furrow positioning pathway. *Nature* **467**, 91–94 (2010).
- Yoneda, M. & Dan, K. Tension at the surface of the dividing sea-urchin egg. *J. Exp. Biol.* **57**, 575–587 (1972).
- Effler, J. C., Iglesias, P. A. & Robinson, D. N. A mechanosensory system controls cell shape changes during mitosis. *Cell Cycle* **6**, 30–35 (2007).
- Ou, G., Stuurman, N., D'Ambrosio, M. & Vale, R. D. Polarized myosin produces unequal-size daughters during asymmetric cell division. *Science* **330**, 677–680 (2010).
- Straight, A. F., Field, C. M. & Mitchison, T. J. Anillin binds nonmuscle myosin II and regulates the contractile ring. *Mol. Biol. Cell* **16**, 193–201 (2005).
- Hickson, G. R. & O'Farrell, P. H. Rho-dependent control of anillin behavior during cytokinesis. *J. Cell Biol.* **180**, 285–294 (2008).
- Piekny, A. J. & Glotzer, M. Anillin is a scaffold protein that links RhoA, actin, and myosin during cytokinesis. *Curr. Biol.* **18**, 30–36 (2008).
- Smith, T. C., Fang, Z. & Luna, E. J. Novel interactors and a role for supervillin in early cytokinesis. *Cytoskeleton* **67**, 346–364 (2010).
- Dean, S. O., Rogers, S. L., Stuurman, N., Vale, R. D. & Spudich, J. A. Distinct pathways control recruitment and maintenance of myosin II at the cleavage furrow during cytokinesis. *Proc. Natl Acad. Sci. USA* **102**, 13473–13478 (2005).
- Rankin, K. E. & Wordeman, L. Long astral microtubules uncouple mitotic spindles from the cytokinetic furrow. *J. Cell Biol.* **190**, 35–43 (2010).
- Tinevez, J. Y. et al. Role of cortical tension in bleb growth. *Proc. Natl Acad. Sci. USA* **106**, 18581–18586 (2009).
- Kosako, H. et al. Rho-kinase/ROCK is involved in cytokinesis through the phosphorylation of myosin light chain and not ezrin/radixin/moesin proteins at the cleavage furrow. *Oncogene* **19**, 6059–6064 (2000).
- Bringmann, H. & Hyman, A. A. A cytokinesis furrow is positioned by two consecutive signals. *Nature* **436**, 731–734 (2005).
- Werner, M. & Glotzer, M. Control of cortical contractility during cytokinesis. *Biochem. Soc. Trans.* **36**, 371–377 (2008).
- Plateau, J. A. F. *Statique Expérimentale et Théorique des Liquides Soumis aux Seules Forces Moléculaires*, Vol. 2, Ch. 7 (Gauthier-Villars, 1873).
- Mitchison, T. J., Charras, G. T. & Mahadevan, L. Implications of a poroelastic cytoplasm for the dynamics of animal cell shape. *Semin. Cell Dev. Biol.* **19**, 215–223 (2008).
- Riedl, J. et al. Lifeact: a versatile marker to visualize F-actin. *Nature Methods* **5**, 605–607 (2008).

25. Charras, G. T., Yarrow, J. C., Horton, M. A., Mahadevan, L. & Mitchison, T. J. Non-equilibration of hydrostatic pressure in blebbing cells. *Nature* **435**, 365–369 (2005).
26. Rosenblatt, J., Cramer, L. P., Baum, B. & McGee, K. M. Myosin II-dependent cortical movement is required for centrosome separation and positioning during mitotic spindle assembly. *Cell* **117**, 361–372 (2004).
27. Blaser, H. *et al.* Migration of zebrafish primordial germ cells: a role for myosin contraction and cytoplasmic flow. *Dev. Cell* **11**, 613–627 (2006).
28. Burgess, D. R. & Chang, F. Site selection for the cleavage furrow at cytokinesis. *Trends Cell Biol.* **15**, 156–162 (2005).
29. Blanchard, G. B., Murugesu, S., Adams, R. J., Martinez-Arias, A. & Gorfinkiel, N. Cytoskeletal dynamics and supracellular organisation of cell shape fluctuations during dorsal closure. *Development* **137**, 2743–2752 (2010).
30. Martin, A. C., Kaschube, M. & Wieschaus, E. F. Pulsed contractions of an actin-myosin network drive apical constriction. *Nature* **457**, 495–499 (2009).

**Supplementary Information** is linked to the online version of the paper at [www.nature.com/nature](http://www.nature.com/nature).

**Acknowledgements** We thank J. S. Bois, A. G. Clark, S. W. Grill, C. P. Heisenberg, J. Howard, A. A. Hyman, J. F. Joanny, D. K. Lubensky, A. Oates, M. Piel, I. M. Tolic-Norrelykke, W. Zachariae and M. Zerial for discussions and comments on the manuscript, and J. Roensch and the Max Planck Institute of Molecular Cell Biology and Genetics Light Microscopy Facility for technical assistance. This work was supported by the Polish Ministry of Science and Higher Education and by the Max Planck Society.

**Author Contributions** J.S., M.B., G.S. and E.P. designed the research and wrote the paper; J.S. performed the experiments except the local drug delivery; M.B. developed the image analysis tools; J.S., M.B. and G.S. analysed the data; A.O. and J.-Y.T. designed and performed the local drug-delivery experiments; G.S. developed the theoretical model.

**Author Information** Reprints and permissions information is available at [www.nature.com/reprints](http://www.nature.com/reprints). The authors declare no competing financial interests. Readers are welcome to comment on the online version of this article at [www.nature.com/nature](http://www.nature.com/nature). Correspondence and requests for materials should be addressed to E.P. ([paluch@mpi-cbg.de](mailto:paluch@mpi-cbg.de)).

## METHODS

**Cell lines and culture.** L929 and HeLa fibroblasts were grown in DMEM (GIBCO, Invitrogen) supplemented with 10% foetal bovine serum, 1% glutamine and 1% penicillin-streptomycin in polystyrene culture flasks (Nunc). For all the time-lapse experiments, the cells were plated on glass-bottom dishes (Mattek), maintained at 37 °C and supplied with 5% CO<sub>2</sub> on the microscope stage. All cell lines are adherent and maintain attachments to the substrate throughout division (Supplementary Fig. 5 and Supplementary Movie 5). The stable HeLa-GFP-actin line was a gift from F. Buchholz. The stable HeLa-EB3-GFP-Lifeact-mCherry line was a gift from the laboratory of M. Piel.

**Cell treatments, plasmids, RNAi and cell transfection.** Rho-kinase was inhibited with Y27632 (Merck Bioscience, at least 30 min treatment at 10 µM). To stabilize the cortex and limit bleb formation, we used wheat germ agglutinin (Invitrogen) and concavalin A (Sigma Aldrich-Chemie) at 25 µg ml<sup>-1</sup> for up to 2 h as described in refs 26 and 31. Lifeact-GFP<sup>24</sup> was a gift from R. Wedlich-Söldner. MRLC-tDRFP was a gift from G. Charras. mCherry-CAAX was generated by replacing the GFP cassette with an mCherry cassette in a CAAX-GFP plasmid (gift from G. Charras), by cutting with BamHI and EcoRI (performed by M. Bergert). For experiments requiring increased substrate adhesiveness, glass-bottom dishes were coated with 15 µg ml<sup>-1</sup> collagen type I from rat tail (Sigma) and fibronectin 0.1% solution (diluted 1:1,000 in H<sub>2</sub>O) from bovine plasma (Sigma). Mouse stealth anillin short interfering RNA (siRNA) (5'-CCGUUGGAAGGUCACAUCUGUUUAA), stealth Gelsolin (5'-ACGGGUGAUGCCUUAU GUCAUCCUAA) and scrambled control were obtained from Invitrogen. Mouse cofilin siRNA (5'-GAAUCAAGCAUGAAUUACATT) was obtained from Ambion. Human anillin siRNA (5'-GAUGCUUGCUACAAACCUATT) was obtained from Qiagen. For L929 cells, transfection of 2 µg per well plasmid DNA or 4 pmol per well siRNA was achieved by electroporation using the Cell Line 96-well Nucleofector Kit SE (Lonza) according to the instructions supplied (program code EH-100). For siRNA transfection in HeLa cells, Lipofectamine RNAiMax (Invitrogen) was used. The final concentration of siRNA was 10 nM. For co-transfection of plasmid and siRNA in HeLa cells, Lipofectamine 2000 (Invitrogen) was used. Final concentrations were 10 nM for siRNA and 0.2 µg ml<sup>-1</sup> for plasmid. Cells were used 30 h after transfection in laser ablation and anillin depletion experiments. Intracellular Ca<sup>2+</sup> was chelated by an incubation of no less than 15 min in 40 µM BAPTA-AM (Invitrogen). Extracellular Ca<sup>2+</sup> was removed by performing the experiments in Ca<sup>2+</sup>-free normal Tyrode's solution. Additional chelation with 500 µM EGTA (Sigma) was tested but had no further effect. Microtubules were depolymerized with 5 µM nocodazole (Sigma).

**RNA isolation and quantitative PCR.** The extent of anillin depletion in L929 and HeLa cells (Supplementary Fig. 14) was estimated by performing qPCR with reverse transcription and comparing the levels of messenger RNA (mRNA) to endogenous levels of mBeta-2- microglobulin (L929) or GAPDH (HeLa) mRNA. Total RNA was isolated using the RNeasy kit (Qiagen) according to the manufacturer's instructions. RNA was cleaned of genomic DNA by DNase digestion with RNase-Free DNase Set digest kit (Qiagen). Complementary DNA was subsequently synthesized from 0.5 µg of RNA using SuperScript III RNase H-Reverse Transcriptase kit (Invitrogen). Comparative qPCR was performed using the Absolute qPCR SYBR Green mix (Thermo Fisher Scientific) and an Mx3000P cyclor (Stratagene). Primers were as follows: L929 Anillin, forward 5'-AAATCGAATGCAAAGGCTTG, reverse 5'-AATGGGTGGCTTAGAAGGTG; L929 mBeta-2-microglobulin, forward 5'-ATTACCCCTGAGACTG, reverse 5'-TGCTATTCTTTCTGCGTGC; HeLa Anillin, forward 5'-GACAAATCTACGACACCAGGAG, reverse 5'-CTTGGATGGCCTTTGTATTGTG; HeLa GAPDH, forward 5'-GAGTCAACGGATTGTGTCGT, reverse 5'-TGGAAGATGGTGATGGGATT.

**Local cytochalasin D delivery.** Local delivery of cytochalasin D<sup>32</sup> was performed on a Carl Zeiss Axiovert 200M inverted microscope equipped with motorized micromanipulator arms (Eppendorf TransferMan NK2) and imaged through a Carl Zeiss Neofluar ×63 (numerical aperture = 0.75) objective. Micropipettes were pulled with a flaming pipette-puller (P-97, Sutter Instruments), and forged with a home-built forge. The releasing micropipette was loaded with 20 µl of 5 µg ml<sup>-1</sup> cytochalasin D (Sigma) diluted in culture medium added with Alexa Fluor 568 Succinimidyl Ester diluted to a final concentration of 600 nM (Invitrogen), and mounted together with the aspiration micropipette on a double pipette holder (Eppendorf TwinTip-Holder). The aspiration pipette was positioned slightly behind the releasing pipette (Fig. 2a). Both micropipettes were connected to pressure regulators: a FemtoJet Microinjector (Eppendorf) for the releasing pipette and a pump for the aspiration pipette (Eppendorf CellTram Air). The flowfield was monitored by tracking fluorescent Alexa Fluor 568. The pipettes were positioned so that only one pole of a dividing cell was exposed to the released drug. The release of cytochalasin D was maintained only until local bleb formation

was observed (about 30 s). For the dimethylsulphoxide control, cytochalasin D was replaced by dimethylsulphoxide at 1:1,000 dilution in the releasing pipette.

**Laser ablation and cell imaging.** Laser ablation experiments were performed as described in ref. 18 on a scanning confocal microscope (Olympus FV1000) equipped with two scanning heads. The first was used for standard imaging; the second was coupled to a laser head (LDH-P-C-405B, PicoQuant), driven by a power source (PDL 800-B, PicoQuant) delivering 405-nm picosecond pulses with a nominal power of 3 mW. For ablation, the pulsed laser underwent spiralling movements within a circle of 800-nm nominal diameter for 2.5 s. Unless otherwise specified, cells were imaged transversally through a single central confocal Z plane, midway between the substrate and the top of the cell, through an Olympus UPlanApo ×60 oil immersion objective (numerical aperture = 1.35). Imaging for volume measurements was performed on an Andor IQ spinning disc confocal microscope by acquiring Z stacks through the entire volume of cells, through an Olympus UPlanApo ×60 water immersion objective (numerical aperture = 1.2) and ×1.6 Optovar. Long-term time-lapse microscopy was performed on an Olympus-IX81 widefield microscope through an Olympus UPlanApo ×20 air objective (numerical aperture = 0.5).

**Image processing and automated image analysis.** Images were processed, automatically analysed and visualized using custom code in MATLAB (MathWorks). Particle image velocimetry<sup>33</sup> was performed on DIC images yielding local measures of the cytoplasmic flows. Particle image velocimetry is an image-processing-based technique for measuring fluid displacement by cross-correlation between images from consecutive time points. For illustration purposes, the flow vectors were colour-coded according to their angles with respect to the cleavage furrow. Vectors with rightward direction were coloured green, and vectors with leftward direction were coloured red. The mean vector component along the pole-pole axis was calculated for each time-point then smoothed with a moving average of window size 5. The angular distribution and amplitudes of the mean vectors per time-point formed the basis of the classification of cells as either displaying cytoplasmic flows or not (Supplementary Fig. 2). Flows in cytokinetic cells were considered significant when their amplitude was more than two times higher than the amplitude of flows typically observed in metaphase cells.

Cell contour detection and definition of cellular regions: segmentation and tracking of cells was based on a combination of image filtering, ellipse fitting, adaptive thresholding and edge detection operations on raw fluorescent intensities from one of the fluorescent channels. The cortex was defined as a region of fixed depth underlying the segmented cell contour. The cytoplasmic region was taken as the difference between the segmented cell area and the cortical region. The cleavage furrow was defined by a straight line between two points, the positions of which were determined automatically along the cell contour. The end points were repositioned manually when the algorithm failed to position the furrow line correctly. The furrow line delimited the left side of the cell from the right side. The definition of the cell contour, cortical, cytoplasmic and left/right delimitations allowed for the extraction of region-specific morphological parameters, intensity values and oscillation periods (Supplementary Fig. 12).

Cortex intensity measurements: mean fluorescence intensities  $I_{\text{mean}}$  of F-actin (Lifeact) and myosin (MRLC) in the cortex were determined in the defined cortical region (described above). As the depth of this region was kept constant while the apparent thickness of the cortex varied both along the cell contour and within a time-lapse, the cortical region was chosen so as to overestimate the actual cortex. The region therefore included pixels belonging both to a varying depth of cortex and to the cytoplasm. The mean intensities measured in this region thus constitute a combined measure of both the average cortical intensity per unit area and the actual thickness of the cortex. Cortical intensity profiles (Fig. 2f and Supplementary Figs 1, 6 and 7) depict the mean cortical intensity along the cell contour  $I_{\text{mean}}(s)$ , where  $s$  is the position along the cell contour. The profiles start at one intersection of the furrow line with the cell contour and then follow the cell contour in the cortex region in a clockwise direction. To allow for comparison of cells with different contour lengths, the path length was set to a constant length of 1,000 points and intensity values were interpolated by a factor of 1,000 per actual path length. The intensity values were then normalized to the global cortex mean intensity ( $I_{\text{mean}}(s)/\langle I_{\text{mean}} \rangle$ ), so that values greater (respectively smaller) than 1 indicate that the local cortex intensity is larger (respectively smaller) than the global cortex mean. To measure the deviation from a perfectly flat intensity profile, which would indicate a perfectly uniform distribution of intensities in the cortex, we integrated the deviations of the intensity profiles of cortical proteins, normalized as described above, from 1 ( $|I_{\text{mean}}(s)/\langle I_{\text{mean}} \rangle - 1|ds$ ).

**Volume measurements.** Volume measurements during cytokinesis were performed on dividing L929 cells (Supplementary Fig. 13). Oscillations were induced by anillin depletion, as described above. Cells were loaded with an intracellular fluorescent dye (2.5 µM CMFDA (5-chloromethylfluorescein diacetate), Invitrogen) excitable at 488 nm and emitting at approximately 520 nm for 30 min at 37 °C and 5% CO<sub>2</sub>



and then changed into conditioned medium for 1 h before imaging. 5  $\mu$ M Alexa Fluor 568 Succinimidyl Ester (Invitrogen) was then added to the medium as an extracellular dye excitable at 561 nm and emitting at approximately 590 nm. Imaging and data acquisition were performed on an Andor IQ spinning disc confocal microscope. Time-lapses were bleach corrected using a custom plugin, the Alexa Fluor 568 channel inverted and multiplied with the CMFDA channel using Fiji Is Just ImageJ. Surface rendering and volume calculations were then performed in Imaris  $\times 64$  (Bitplane). We estimate an error in volume measurements no greater than 10.65%, based on an allowed error of 1 voxel diagonal in

determining the cell boundary at every point of a spherical cell of 3,000  $\mu\text{m}^3$  (imaging voxels were on average 181 nm  $\times$  181 nm  $\times$  580 nm).

31. Kunda, P., Pelling, A. E., Liu, T. & Baum, B. Moesin controls cortical rigidity, cell rounding, and spindle morphogenesis during mitosis. *Curr. Biol.* **18**, 91–101 (2008).
32. O'Connell, C. B., Warner, A. K. & Wang, Y.-I. Distinct roles of the equatorial and polar cortices in the cleavage of adherent cells. *Curr. Biol.* **11**, 702–707 (2001).
33. Raffel, M., Willert, C. E., Wereley, S. T. & Kompenhans, J. *Particle Image Velocimetry – A Practical Guide* (Springer, 2007).

# A role for cohesin in T-cell-receptor rearrangement and thymocyte differentiation

Vlad C. Seitan<sup>1,2,3\*</sup>, Bingtao Hao<sup>4\*</sup>, Kikue Tachibana-Konwalski<sup>5\*</sup>, Thais Lavagnoli<sup>1,3</sup>, Hegias Mira-Bontenbal<sup>1,3</sup>, Karen E. Brown<sup>1,3</sup>, Grace Teng<sup>6</sup>, Tom Carroll<sup>3</sup>, Anna Terry<sup>1,3</sup>, Katie Horan<sup>7</sup>, Hendrik Marks<sup>8</sup>, David J. Adams<sup>9</sup>, David G. Schatz<sup>6,10</sup>, Luis Aragon<sup>2,3</sup>, Amanda G. Fisher<sup>1,3</sup>, Michael S. Krangel<sup>4</sup>, Kim Nasmyth<sup>5</sup> & Matthias Merkenschlager<sup>1,3</sup>

Cohesin enables post-replicative DNA repair and chromosome segregation by holding sister chromatids together from the time of DNA replication in S phase until mitosis<sup>1</sup>. There is growing evidence that cohesin also forms long-range chromosomal cis-interactions<sup>2–4</sup> and may regulate gene expression<sup>2–10</sup> in association with CTCF<sup>8,9</sup>, mediator<sup>4</sup> or tissue-specific transcription factors<sup>10</sup>. Human cohesinopathies such as Cornelia de Lange syndrome are thought to result from impaired non-canonical cohesin functions<sup>7</sup>, but a clear distinction between the cell-division-related and cell-division-independent functions of cohesin—as exemplified in *Drosophila*<sup>11–13</sup>—has not been demonstrated in vertebrate systems. To address this, here we deleted the cohesin locus *Rad21* in mouse thymocytes at a time in development when these cells stop cycling and rearrange their T-cell receptor (TCR)  $\alpha$  locus (*Tcra*). *Rad21*-deficient thymocytes had a normal lifespan and retained the ability to differentiate, albeit with reduced efficiency. Loss of *Rad21* led to defective chromatin architecture at the *Tcra* locus, where cohesin-binding sites flank the TEA promoter and the Ea enhancer, and demarcate *Tcra* from interspersed *Tcrd* elements and neighbouring housekeeping genes. Cohesin was required for long-range promoter–enhancer interactions, *Tcra* transcription, H3K4me3 histone modifications that recruit the recombination machinery<sup>14,15</sup> and *Tcra* rearrangement. Provision of pre-rearranged TCR transgenes largely rescued thymocyte differentiation, demonstrating that among thousands of potential target genes across the genome<sup>4,8–10</sup>, defective *Tcra* rearrangement was limiting for the differentiation of cohesin-deficient thymocytes. These findings firmly establish a cell-division-independent role for cohesin in *Tcra* locus rearrangement and provide a comprehensive account of the mechanisms by which cohesin enables cellular differentiation in a well-characterized mammalian system.

The somatic rearrangement of lymphocyte receptor loci is central to adaptive immunity<sup>16</sup>. Gene segments distributed over millions of base pairs of genomic DNA are transcribed, brought into proximity with each other, and recombined in a cell-lineage- and developmental-stage-specific fashion<sup>17–19</sup>. In developing thymocytes, proliferation and differentiation are tightly linked and the activity of Rag (recombination activating gene) proteins is restricted to the G1 phase of the cell cycle<sup>20</sup>. Early thymocytes at CD4<sup>–</sup> CD8<sup>–</sup> double-negative (DN) stages 1 and 2 proliferate in response to cytokines and briefly arrest at the DN3 stage, where they rearrange the TCR  $\beta$  locus (Fig. 1a). Pre-TCR signals drive a phase of proliferation that extends to the early CD4<sup>+</sup> CD8<sup>+</sup> double-positive (DP) stage. Shortly after the acquisition of CD4 and CD8, DP thymocytes lose the expression of the transferrin receptor CD71 (ref. 21) and become small, non-proliferating CD71<sup>–</sup>

DP cells (Fig. 1a), which represent the great majority of thymocytes. During their life span of 3 to 4 days, DP thymocytes undergo several rounds of *Tcra* rearrangement<sup>16,18,19</sup>. Successful TCR expression and engagement selects a minority (3–5%) of DP thymocytes for differentiation via a CD4<sup>+</sup> CD8<sup>lo</sup> intermediate stage towards long-lived CD4 or CD8 single-positive (SP) cells, again with minimal proliferation<sup>16,22</sup> (Fig. 1a).

To address the role of cohesin in *Tcra* rearrangement and thymocyte differentiation, we combined a conditional allele encoding the cohesin subunit Rad21 (*Rad21*<sup>lox</sup>; Fig. 1b and Supplementary Fig. 1a) with a Cre transgene under the control of *Cd4* regulatory elements (CD4-Cre), which becomes active at the transition from the CD4<sup>–</sup> CD8<sup>–</sup> DN to the DP stage<sup>23</sup>. Pilot experiments with yellow fluorescent protein (YFP) reporters showed CD4-Cre-dependent accumulation of YFP after the CD71<sup>+</sup> proliferative stage in non-dividing DP thymocytes (Supplementary Fig. 1b). Proliferating CD4-Cre *Rad21*<sup>lox/lox</sup> CD71<sup>+</sup> DP cells showed partial locus deletion but retained >50% *Rad21* messenger RNA and protein (Fig. 1c). *Rad21* genomic deletion was essentially complete (>97%) and *Rad21* RNA and protein levels were substantially reduced in non-dividing DP thymocytes (Fig. 1c). Hence, cohesin was selectively depleted from non-dividing thymocytes. Importantly, CD4-Cre *Rad21*<sup>lox/lox</sup> DP thymocyte numbers were normal (Fig. 1d). Intermediate CD4<sup>+</sup> CD8<sup>lo</sup> and mature CD4 SP and CD8 SP thymocytes accumulated slowly in CD4-Cre *Rad21*<sup>lox/lox</sup> mice (Supplementary Fig. 2a) but were present in normal numbers by 6 weeks of age (Fig. 1d).

Bromodeoxyuridine (BrdU) incorporation into replicating DNA can identify proliferating thymocyte populations and track their differentiation<sup>22</sup>. Pulse-chase experiments labelled proliferating (CD71<sup>+</sup>) DP but not non-proliferating CD4<sup>+</sup> CD8<sup>lo</sup>, CD4 SP or CD8 SP thymocytes<sup>22</sup> (Fig. 1e, 2 h time point). During the subsequent chase period, BrdU-labelled DP cells differentiated to become CD4<sup>+</sup> CD8<sup>lo</sup> and eventually CD4 or CD8 SP cells (Fig. 1e, left). This sequence of differentiation was preserved in CD4-Cre *Rad21*<sup>lox/lox</sup> thymocytes, but the proportion of DP thymocytes that became CD4 SP or CD8 SP was reduced (Fig. 1e, right, and Supplementary Fig. 2b).

In continuous BrdU labelling experiments, the percentage of BrdU<sup>+</sup> cells indicates population turnover<sup>22</sup>. Importantly, cohesin-deficient and control DP thymocytes labelled with similar kinetics (Fig. 1f). Consistent with the pulse-labelling data (Fig. 1e), the accumulation of CD4<sup>+</sup> CD8<sup>lo</sup> and CD4 SP subsets was reduced in CD4-Cre *Rad21*<sup>lox/lox</sup> mice (Supplementary Fig. 2c). Hence, cohesin depletion impaired the differentiation of DP thymocytes, but not their survival.

Unlike many other differentiated cell types, mature thymocytes can be induced to re-enter the cell cycle. *In vitro* activated CD4-Cre

<sup>1</sup>Lymphocyte Development Group, MRC Clinical Sciences Centre, Imperial College London, Du Cane Road, London W12 0NN, UK. <sup>2</sup>Cell Cycle Group, MRC Clinical Sciences Centre, Imperial College London, Du Cane Road, London W12 0NN, UK. <sup>3</sup>Epigenetics Section, MRC Clinical Sciences Centre, Imperial College London, Du Cane Road, London W12 0NN, UK. <sup>4</sup>Department of Immunology, Duke University Medical Center, Durham, North Carolina 27710, USA. <sup>5</sup>Department of Biochemistry, University of Oxford, South Parks Road, Oxford OX1 3QU, UK. <sup>6</sup>Department of Immunobiology, Yale University School of Medicine, 300 Cedar Street, New Haven, Connecticut 06520-8011, USA. <sup>7</sup>Central Biological Services, Imperial College London, Du Cane Road, London W12 0NN, UK. <sup>8</sup>Department of Molecular Biology, Nijmegen Center for Molecular Life Sciences, Radboud University, 6500 HB Nijmegen, The Netherlands. <sup>9</sup>Wellcome Trust Sanger Institute, Wellcome Trust Genome Campus, Cambridge CB10 1SA, UK. <sup>10</sup>Howard Hughes Medical Institute, Yale University School of Medicine, 300 Cedar Street, New Haven, Connecticut 06520-8011, USA.

\*These authors contributed equally to this work.

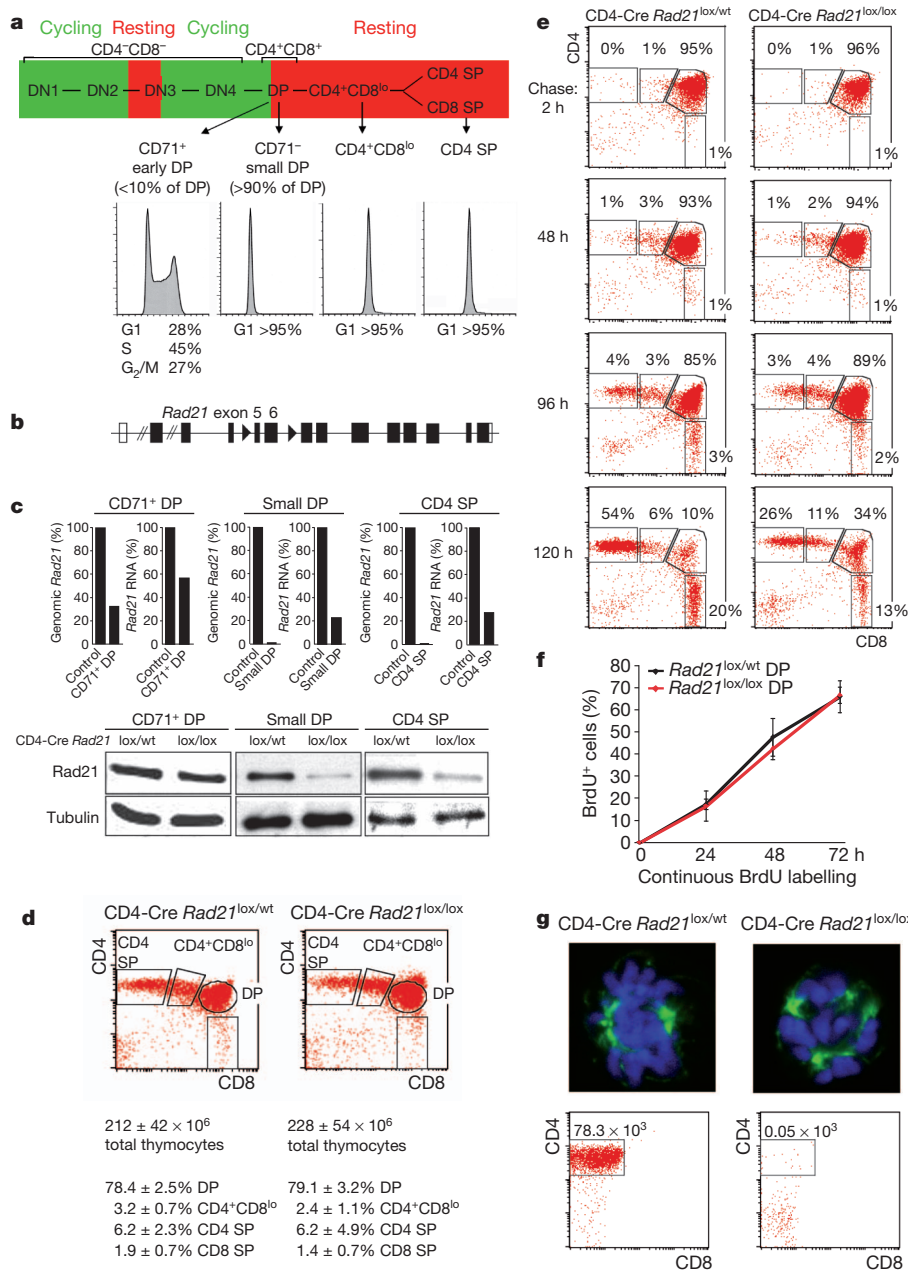


**Figure 1 | Genetic cohesin depletion in non-dividing thymocytes.**

a, Thymocyte differentiation from left to right: CD4<sup>+</sup> CD8<sup>-</sup> DN stages 1 to 4; CD4<sup>+</sup> CD8<sup>+</sup> DP, CD4<sup>+</sup> CD8<sup>lo</sup>; CD4 or CD8 SP cells. Proliferation is in green, cell cycle arrest in red. Histograms show DNA content. b, Conditional *Rad21* allele (see Supplementary Fig. 1a). c, Real-time genomic PCR of *Rad21* locus deletion, RT-PCR of *Rad21* RNA and western blotting of Rad21 protein. d, Cell numbers and flow cytometric analysis of thymocyte subsets in 6-week-old CD4-Cre *Rad21*<sup>lox/lox</sup> and CD4-Cre *Rad21*<sup>lox/wt</sup> mice (mean ± standard

*Rad21*<sup>lox/lox</sup> CD4 SP thymocytes showed abnormal mitotic figures with multiple spindles, chromosome segregation defects (Fig. 1g and Supplementary Fig. 3) and poor survival (Fig. 1g). CD4-Cre-mediated deletion of *Rad21* therefore generates thymocytes that die when forced to divide, yet have a normal lifespan as non-dividing cells *in vivo*. This allows the interrogation of cohesin functions in interphase, independent of essential cohesin functions during cell division.

Rad21 chromatin immunoprecipitation and sequencing (ChIP-seq) mapped cohesin to key positions within the *Tcra* locus in DP thymocytes (Fig. 2a). Cohesin was abundant at the locus control region<sup>24</sup>, which separates the *Tcra* enhancer E $\alpha$  from the neighbouring *Dad1* housekeeping gene<sup>25,26</sup>. Other prominent cohesin sites separated

deviation (s.d.),  $n = 12$ ). **e**, Pulse chase analysis of CD4-Cre *Rad21*<sup>lox/wt</sup> and CD4-Cre *Rad21*<sup>lox/lox</sup> thymocytes. Dot blots are gated on BrdU<sup>+</sup> cells (see Supplementary Fig. 2b). **f**, Continuous BrdU labelling for DP thymocyte turnover. See Supplementary Fig. 2c for CD4<sup>+</sup> CD8<sup>lo</sup> and CD4 SP subsets (mean  $\pm$  s.d.,  $n = 3-5$  per data point). **g**, Top, metaphase spreads of 2 day activated thymocytes stained for  $\alpha$ -tubulin (green) and DNA (DAPI, blue; see Supplementary Fig. 3). Magnification,  $\times 2,500$ . Bottom, cells recovered after 5 days.

the *Tcra* TEA promoter from the *Tcrd* enhancer E $\delta$ , which controls *Tcrd* gene segments that are interspersed within the *Tcra* locus but follow a distinct developmental stage-specific program<sup>18</sup>. Cohesin colocalization with the insulator protein CTCF<sup>8,9</sup> is found at the *Dad1* site 10 kb downstream of E $\alpha$ , whereas at the J $\alpha$ 49 promoter cohesin associates with its loading protein Nipbl and mediator subunits<sup>4</sup> more than with CTCF (Supplementary Fig. 4). Interestingly, the major *Tcra* regulatory elements E $\alpha$  and TEA bound copious amounts of cohesin, Nipbl and mediator as well as CTCF (Supplementary Fig. 4).

RNA sequencing (RNA-seq) indicated that *Tcra* constant region (C $\alpha$ ) transcripts were considerably more abundant than transcripts from the neighbouring *Dad1* gene and the *Tcrd* constant region (C $\delta$ ) in



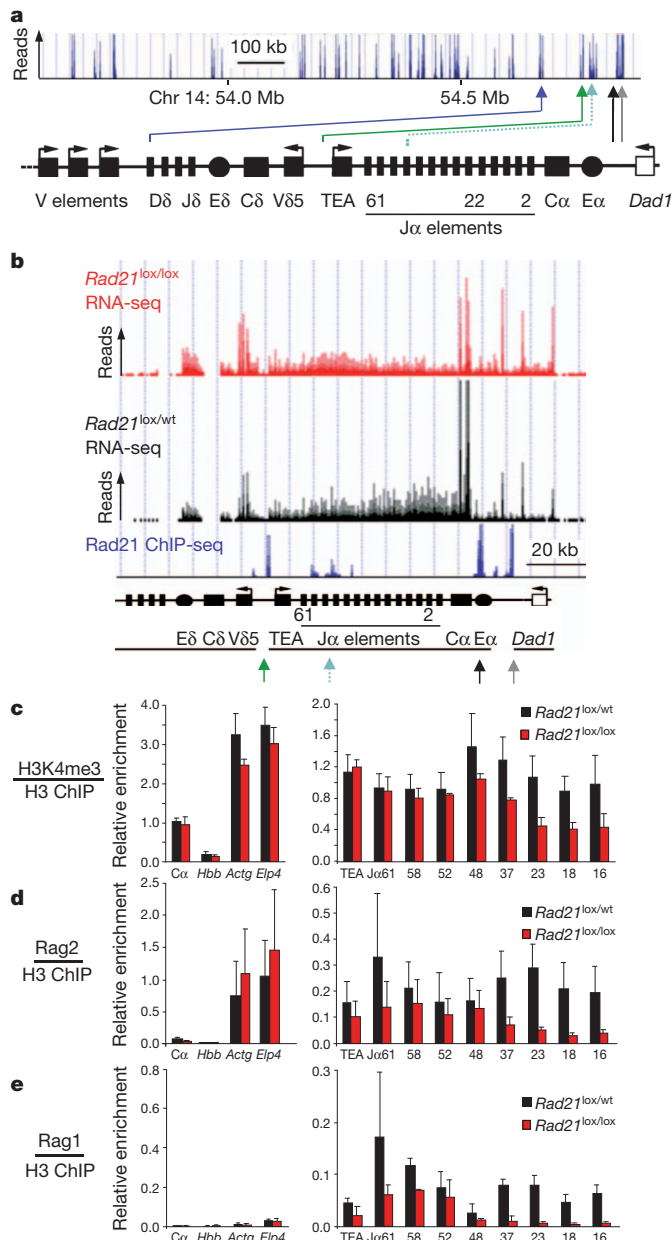


**Figure 2 | Cohesin affects *Tcra* transcription and Rag recombinase recruitment.** **a**, *Rad21* ChIP-seq of the 3' part of the *Tcra* locus in DP thymocytes. Arrowheads highlight cohesin sites at the *Eα* enhancer (black), the *Tcra* locus control region (grey), *Jα* promoters (turquoise), the TEA promoter (green) and between *Tcrd* elements and V gene segments (blue). **b**, RNA-seq of *Tcra* in CD4-Cre *Rad21*<sup>lox/lox</sup> (red) and control *Rad21*<sup>lox/wt</sup> (black) DP thymocytes. *Rad21* ChIP-seq is in blue. **c**, ChIP of H3K4me3 relative to total H3 in CD4-Cre *Rad21*<sup>lox/lox</sup> and control DP thymocytes. *Hbb* is a negative and *Actg* and *Elp4* are positive control loci (mean  $\pm$  s.e. of two independent experiments).  $P = 0.016$  for all *Jα* elements;  $P = 0.38$  (not significant) for proximal (*Jα*61–48) and  $P = 0.004$  for distal (*Jα*37–16) *Jα* elements. **d**, ChIP of Rag2 relative to total H3 as in **c** (mean  $\pm$  s.e. of three independent experiments).  $P = 0.0001$  for all *Jα* elements;  $P = 0.054$  (not significant) for proximal (*Jα*61–48) and  $P = 0.0001$  for distal (*Jα*37–16) *Jα* elements. **e**, ChIP of Rag1 relative to total H3 as in **c** (mean  $\pm$  s.e. of two independent experiments).  $P = 0.005$  for all *Jα* elements;  $P = 0.17$  (not significant) for proximal (*Jα*61–48) and  $P = 0.003$  for distal (*Jα*37–16) *Jα* elements.

control DP thymocytes. In cohesin-depleted small DP thymocytes, *Cδ* and *Dad1* transcripts were elevated at the expense of *Cα* transcripts (Fig. 2b) as confirmed by real-time polymerase chain reaction with reverse transcription (RT-PCR) (Supplementary Fig. 5a). Moreover, transcription across the *Tcra* joining elements, *Jα*, was skewed: control DP thymocytes preferentially transcribed distal (3') *Jα* elements, whereas cohesin-depleted DP thymocytes preferentially transcribed proximal (5') *Jα* elements (Fig. 2b).

Transcription of lymphocyte receptor loci facilitates rearrangement<sup>27</sup> in part via the trimethylation of histone H3 at lysine 4 (H3K4me3). H3K4me3 recruits Rag2 protein<sup>14,15,28</sup>, which together with Rag1 forms the recombinase complex<sup>18</sup>. ChIP showed reduced H3K4me3 deposition (Fig. 2c) and Rag binding (Fig. 2d, e) at distal *Jα* elements in CD4-Cre *Rad21*<sup>lox/lox</sup> DP thymocytes. Hence, cohesin deficiency affected *Tcra* transcription, H3K4me3 histone modifications and the recruitment of Rag recombinases.

Primary *Tcra* rearrangements involve proximal (5') *Jα* elements and occur in early CD71<sup>+</sup> DP thymocytes, whereas secondary rearrangements involve progressively more distal (3') *Jα* elements in non-dividing DP thymocytes<sup>18</sup> (Supplementary Fig. 1b). CD71<sup>+</sup> DP CD4-Cre *Rad21*<sup>lox/lox</sup> thymocytes had near-normal *Rad21* protein levels (Fig. 1c) and *Cδ*, *Cα* and *Dad1* transcription (Supplementary Fig. 5b), and primary rearrangements of proximal *Jα* elements were present at normal levels (Fig. 3a, b). In contrast, secondary *Tcra* rearrangements were substantially impaired in non-dividing CD4-Cre *Rad21*<sup>lox/lox</sup> DP thymocytes (Fig. 3a, b), which were depleted of cohesin (Fig. 1c). The usage of the distal *Jα*22 element, for example,

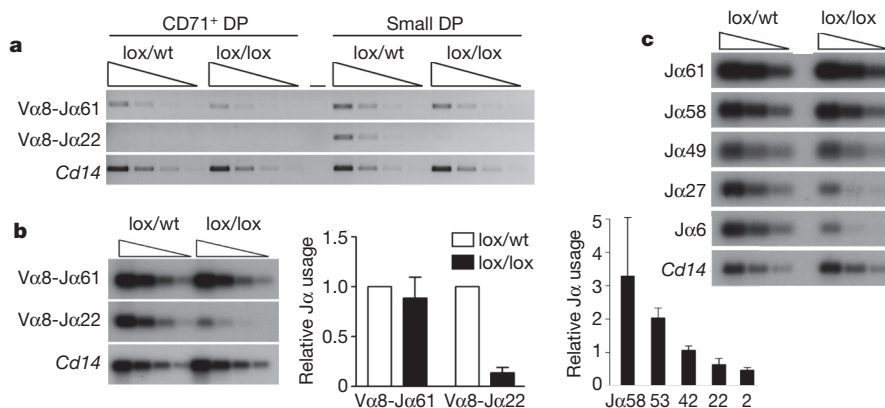


**Figure 3 | Cohesin affects *Tcra* rearrangement.** **a**, Threefold dilutions of genomic *Vα8-Jα* PCR products from CD71<sup>+</sup> or CD71<sup>−</sup> DP thymocytes visualized with ethidium bromide. *Cd14* is a genomic control. **b**, Genomic PCR products from small DP thymocytes visualized by Southern blotting with *Jα*-specific probes (left). Usage of the distal *Jα*22 element was reduced by 86%

(middle; mean  $\pm$  s.e.,  $n = 3$ ). Southern blotting of *Vα8-Jα* RT-PCR products from CD4-Cre *Rad21*<sup>lox/lox</sup> normalized to control DP thymocytes (right; mean  $\pm$  s.e.,  $n = 3$ ). **c**, Double-strand breaks in threefold serially diluted genomic DNA from CD4-Cre *Rad21*<sup>lox/lox</sup> and control DP thymocytes detected by ligation-mediated PCR.

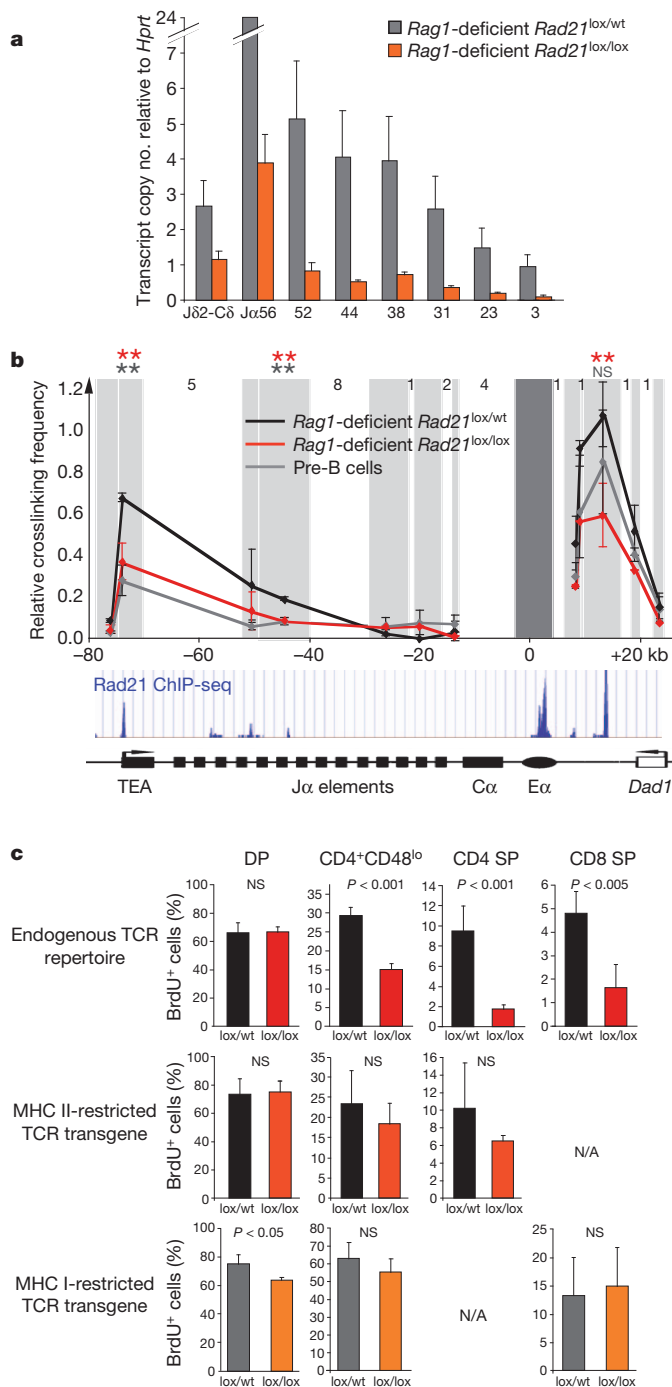


**Figure 4 | Cohesin mediates long-range interactions between regulatory elements that control *Tcrα* transcription.** **a**, Transcript copy number of the unrearranged *Tcrα* J region in *Rag1*-deficient CD4-Cre *Rad21*<sup>lox/lox</sup> and *Rad21*<sup>lox/wt</sup> DP thymocytes (mean ± s.e., *n* = 3). **b**, 3C analysis of long-range interactions between *Eα* and *Tcrα* restriction fragments (shaded) in *Rag1*-deficient CD4-Cre *Rad21*<sup>lox/wt</sup> (black; mean ± s.d., *n* = 3), CD4-Cre *Rad21*<sup>lox/lox</sup> (red; mean ± s.d., *n* = 3) DP thymocytes and pre-B cells (grey; mean ± s.d., *n* = 3). Intervening HindIII fragment numbers and genomic distances are indicated. Asterisks indicate *P* < 0.05 (grey, control thymocytes versus pre-B cells; red, control versus cohesin-depleted thymocytes). NS, not significant. **c**, TCR transgenes rescue the differentiation of cohesin-depleted thymocytes. Top, percentages of BrdU<sup>+</sup> cells in CD4<sup>+</sup> CD8<sup>lo</sup>, CD4 SP and CD8 SP thymocytes. The differentiation of cohesin-depleted thymocytes is rescued by MHC class II-restricted (middle) and MHC class I-restricted TCR transgenes (bottom). N/A, not applicable. *n* = 3–5 per data point ± s.d.

was reduced on average by 86% (Fig. 3b, middle), reflecting a progressive underrepresentation of 3' Jα segments (Fig. 3b, right). This was confirmed by analysis of additional Vα gene families (Supplementary Fig. 6a) and by RT-PCR-based copy number analysis of mature *Tcrα* transcripts (Supplementary Fig. 6b). Therefore, primary rearrangements occurred before the depletion of cohesin, whereas reduced cohesin expression impaired secondary rearrangements in non-dividing DP thymocytes. Normal BrdU labelling kinetics (Fig. 1f) exclude decreased lifespan as an explanation for aberrant *Tcrα* rearrangement<sup>29</sup>. Consistent with the defective recruitment of Rag proteins to the *Tcrα* locus (Fig. 2d, e), double-strand breaks were reduced in cohesin-deficient thymocytes (Fig. 3c). This identifies Rag cleavage rather than double-strand break repair as the limiting step for *Tcrα* rearrangements in cohesin-deficient thymocytes.

Because *Tcrα* rearrangement changes the positioning of regulatory elements<sup>18</sup>, altered *Tcrα* transcription (Fig. 2b) could either be a direct consequence of cohesin depletion, or result indirectly from defective rearrangement. To distinguish between these possibilities we compared intronic *Tcrα* transcript copy numbers in the absence of rearrangement in *Rag1*-deficient control and CD4-Cre *Rad21*<sup>lox/lox</sup> DP thymocytes. Cohesin depletion reduced the transcription (Fig. 4a) and H3K4me3 methylation (Supplementary Fig. 7) at Jα independently of *Tcrα* rearrangement.

To explore how cohesin affects *Tcrα* transcription, we analysed long-range interactions between the TEA promoter and Eα, which are separated by approximately 80 kb of genomic DNA and together regulate the transcription of *Tcrα*. In chromosome conformation capture (3C) assays<sup>30</sup>, Eα interacted strongly with TEA in DP thymocytes (Fig. 4b) but cohesin depletion reduced these interactions to the level found in pre-B cells, where *Tcrα* is not detectably transcribed (Fig. 4b). Hence, the extent of *Tcrα* enhancer–promoter interactions was cell-type specific, correlated with *Tcrα* transcription and was cohesin dependent. A role for cohesin in additional enhancer–promoter interactions during sequential *Tcrα* rearrangements is suggested by Eα contacts with promoters between Jα49 and Jα37 (Fig. 4b), which can drive Jα transcription in the absence of TEA<sup>18</sup>, and by cohesin binding to numerous Vα promoters (Fig. 2a). Cohesin depletion also affected Eα interactions with the neighbouring *Dad1* cohesin site, and therefore the topology of the *Tcrα* locus control region<sup>24</sup>, which has CTCF-dependent transcriptional insulator function<sup>25,26</sup> (Fig. 4b). As cohesin mediates CTCF-dependent transcriptional insulation<sup>8,9</sup>, increased *Dad1* expression at the expense of Cα (Fig. 2b) may indicate impaired insulator function.

To test whether aberrant *Tcrα* rearrangement caused inefficient differentiation, we equipped cohesin-deficient thymocytes with transgenes encoding rearranged TCRs. Compared to endogenously rearranged TCRs (Fig. 4c, top), the expression of MHC class II- (Fig. 4c, middle) or MHC class I-restricted TCRs (Fig. 4c, bottom) markedly improved the generation of CD4-Cre *Rad21*<sup>lox/lox</sup> CD4<sup>+</sup> CD8<sup>lo</sup> and SP thymocytes.

In summary, cohesin shapes the chromatin architecture of the *Tcrα* locus by mediating cell-type-specific long-range interactions between enhancer and promoter elements that control transcription, H3K4me3 deposition, Rag recombinase recruitment, and ultimately *Tcrα* rearrangement. These defects compromise thymocyte differentiation by limiting the number and diversity of sequential *Tcrα* rearrangements. Hence, cohesin contributes to cellular differentiation in a well-characterized mammalian system.

## METHODS SUMMARY

The conditional *Rad21* allele was generated by inserting *loxP* sites into introns 4 and 6 (Supplementary Fig. 1a). Methods used for RT-PCR and genomic PCR<sup>2</sup>, flow cytometry<sup>2</sup>, 3C analysis<sup>2</sup>, ChIP for cohesin<sup>2</sup>, histone modifications<sup>30</sup> and Rag proteins<sup>30</sup> have been described. See Methods for other mouse strains, BrdU labelling and detection, ChIP-seq and RNA-seq protocols, ligation-mediated PCR, confocal microscopy, *Tcrα* rearrangement assays and copy number measurements.

**Full Methods** and any associated references are available in the online version of the paper at [www.nature.com/nature](http://www.nature.com/nature).

**Received 30 November 2010; accepted 20 June 2011.**

**Published online 10 August 2011.**

1. Nasmyth, K. & Haering, C. H. Cohesin: its roles and mechanisms. *Annu. Rev. Genet.* **43**, 525–558 (2009).
2. Hadjur, S. *et al.* Cohesins form chromosomal *cis*-interactions at the developmentally regulated *IFNG* locus. *Nature* **460**, 410–413 (2009).
3. Degner, S. C. *et al.* CCCTC-binding factor (CTCF) and cohesin influence the genomic architecture of the *Igh* locus and antisense transcription in pro-B cells. *Proc. Natl Acad. Sci. USA*. doi:10.1073/pnas.1019391108 (23 May 2011).
4. Kagey, M. H. *et al.* Mediator and cohesin connect gene expression and chromatin architecture. *Nature* **467**, 430–435 (2010).
5. Hagstrom, K. A. & Meyer, B. J. Condensin and cohesin: more than chromosome compactor and glue. *Nature Rev. Genet.* **4**, 520–534 (2003).
6. Rollins, R. A., Morcillo, P. & Dorsett, D. Nipped-B, a *Drosophila* homologue of chromosomal adherins participates in activation by remote enhancers in the cut and Ultrabithorax genes. *Genetics* **152**, 577–593 (1999).
7. Strachan, T. Cornelia de Lange syndrome and the link between chromosomal function, DNA repair and developmental gene regulation. *Curr. Opin. Genet. Dev.* **15**, 258–264 (2005).
8. Parelho, V. *et al.* Cohesins functionally associate with CTCF on mammalian chromosome arms. *Cell* **132**, 422–433 (2008).
9. Wendt, K. S. *et al.* Cohesin mediates transcriptional insulation by CCCTC-binding factor. *Nature* **451**, 796–801 (2008).
10. Schmidt, D. *et al.* A CTCF-independent role for cohesin in tissue-specific transcription. *Genome Res.* **20**, 578–588 (2010).
11. Schuldiner, O. *et al.* piggyBac-based mosaic screen identifies a postmitotic function for cohesin in regulating developmental axon pruning. *Dev. Cell* **14**, 227–238 (2008).
12. Pauli, A. *et al.* Cell-type-specific TEV protease cleavage reveals cohesin functions in *Drosophila* neurons. *Dev. Cell* **14**, 239–251 (2008).
13. Pauli, A. *et al.* A direct role for cohesin in gene regulation and ecdysone response in *Drosophila* salivary glands. *Curr. Biol.* **20**, 1787–1798 (2010).
14. Matthews, A. G. *et al.* RAG2 PHD finger couples histone H3 lysine 4 trimethylation with V(D)J recombination. *Nature* **450**, 1106–1110 (2007).
15. Liu, Y., Subrahmanyam, R., Chakraborty, T., Sen, R. & Desiderio, S. A plant homeodomain in Rag-2 that binds hypermethylated lysine 4 of histone H3 is necessary for efficient antigen-receptor-gene rearrangement. *Immunity* **27**, 561–571 (2007).
16. Kiehl, P. & von Boehmer, H. Development and selection of T cells: facts and puzzles. *Adv. Immunol.* **58**, 87–209 (1995).
17. Stanhope-Baker, P., Hudson, K. M., Shaffer, A. L., Constantinescu, A. & Schlissel, M. S. Cell type-specific chromatin structure determines the targeting of V(D)J recombinase activity *in vitro*. *Cell* **85**, 887–897 (1996).
18. Krangel, M. S. Mechanics of T cell receptor gene rearrangement. *Curr. Opin. Immunol.* **21**, 133–139 (2009).
19. Jhunjhunwala, S., van Zelm, M. C., Peak, M. M. & Murre, C. Chromatin architecture and the generation of antigen receptor diversity. *Cell* **138**, 435–448 (2009).
20. Desiderio, S., Lin, W. C. & Li, Z. The cell cycle and V(D)J recombination. *Curr. Top. Microbiol. Immunol.* **217**, 45–59 (1996).
21. Brekelmans, P. *et al.* Transferrin receptor expression as a marker of immature cycling thymocytes in the mouse. *Cell. Immunol.* **159**, 331–339 (1994).
22. Huesmann, M., Scott, B., Kiehl, P. & von Boehmer, H. Kinetics and efficacy of positive selection in the thymus of normal and T cell receptor transgenic mice. *Cell* **66**, 533–540 (1991).
23. Lee, P. P. *et al.* A critical role for Dnmt1 and DNA methylation in T cell development, function, and survival. *Immunity* **15**, 763–774 (2001).
24. Diaz, P., Cado, D. & Winoto, A. A locus control region in the T cell receptor  $\alpha$  locus. *Immunity* **1**, 207–217 (1994).
25. Magdinier, F., Yusufzai, T. M. & Felsenfeld, G. Both CTCF-dependent and -independent insulators are found between the mouse T cell receptor  $\alpha$  and *Dad1* genes. *J. Biol. Chem.* **279**, 25381–25389 (2004).
26. Zhong, X. P. & Krangel, M. S. Enhancer-blocking activity within the DNase I hypersensitivity site 2 to 6 region between the T cell receptor  $\alpha$  and *Dad1* genes. *J. Immunol.* **163**, 295–300 (1999).
27. Abarrategui, I. & Krangel, M. S. Germine transcription: a key regulator of accessibility and recombination. *Adv. Exp. Med. Biol.* **650**, 93–102 (2009).
28. Ji, Y. *et al.* The *in vivo* pattern of binding of RAG1 and RAG2 to antigen receptor loci. *Cell* **141**, 419–431 (2010).
29. Guo, J. *et al.* Regulation of the TCR $\alpha$  repertoire by the survival window of CD4<sup>+</sup>CD8<sup>+</sup> thymocytes. *Nature Immunol.* **3**, 469–476 (2002).
30. Dekker, J. The three 'C' s of chromosome conformation capture: controls, controls, controls. *Nature Methods* **3**, 17–21 (2006).

**Supplementary Information** is linked to the online version of the paper at [www.nature.com/nature](http://www.nature.com/nature).

**Acknowledgements** We thank S. Hadjur, D. Tough, L. Williams, Z. Webster, J. Godwin and H.-Y. Shih for help and advice, L. Game and M. Jones for high-throughput sequencing, A. Giess for sequence alignment, and J. Elliott and P. Hexley for cell sorting. Supported by the Medical Research Council, UK (V.S., T.L., H.M.-B., K.E.B., T.C., A.T., L.A., A.G.F., K.N., M.M.), the European Union FP6 integrated project HEROIC (H.M.), EU and the Marie Curie Research Training Network Chromatin Plasticity (H.M.-B.), the Boehringer Ingelheim Fonds (T.L.), the Wellcome Trust (D.J.A., K.N.) and the National Institutes of Health (B.H., M.S.K., G.T., D.G.S.). D.G.S. is an investigator of the Howard Hughes Medical Institute.

**Author Contributions** V.S. and M.M. conceived the study with critical input from D.G.S., L.A., A.G.F., M.S.K. and K.N., V.S., B.H., K.T.-K., T.L., H.M.-B., K.E.B., G.T., K.H. and M.M. conducted experiments, K.T.-K., D.J.A., K.N., G.T. and D.G.S. designed and generated novel materials, T.C., A.T. and H.M. analysed data, V.S. and M.M. wrote the paper and all authors discussed the results and commented on the manuscript.

**Author Information** Reprints and permissions information is available at [www.nature.com/reprints](http://www.nature.com/reprints). The authors declare no competing financial interests. Readers are welcome to comment on the online version of this article at [www.nature.com/nature](http://www.nature.com/nature). Correspondence and requests for materials should be addressed to M.M. ([matthias.merkenschlager@csc.mrc.ac.uk](mailto:matthias.merkenschlager@csc.mrc.ac.uk)), K.M. ([kim.nasmyth@bioch.ox.ac.uk](mailto:kim.nasmyth@bioch.ox.ac.uk)) or M.S.K. ([krang001@mc.duke.edu](mailto:krang001@mc.duke.edu)).



## METHODS

**Mice.** *Rag1*-deficient mice<sup>31</sup>, OT-I as well as AND TCR transgenic mice<sup>32,33</sup> have been described. To generate a conditional *Rad21* allele, *loxP* sites were inserted into introns 4 and 6 to allow Cre-mediated excision of exons 5 and 6. Correctly targeted clones were detected by Southern blotting of BmtI and PacI digested genomic DNA to confirm the presence of 5' and 3' *loxP* sites, respectively. A *puroAtk* cassette flanked by *FRT* sites was excised to generate the conditional allele (Supplementary Fig. 1a). For genomic deletion analysis DNA was extracted and 50 ng were used per real-time PCR reaction. Primers were designed to detect the intact and not the deleted *Rad21*<sup>lox</sup> allele. Data were normalized to the geometric mean of two genomic DNA (gDNA) sites on chromosome 2 and 3, respectively.

*Rad21*<sup>lox</sup>, forward, CATGGTTGGCAGATGAGCAAC; *Rad21*<sup>lox</sup>, reverse, CTACTTTCCCGTAGCAACTG; gDNA chr 2, forward, CCCGGGCTAAT TCTCTATGTC; gDNA chr 2, reverse, GCTGTAAAGTCAGTCGCTCGTG; gDNA chr 3, forward, TGTGCCAGCATCTTTGCC; gDNA chr 3, reverse, GCGTGTGGAATTAAGGCC.

Mice were on a mixed C57BL/6 and 129 background and were matched for age and *Tcra* haplotypes in all experiments involving *Tcra* expression or rearrangement. *Tcra* haplotypes were determined by genomic PCR.

Primer 1, GAGGAAAAATGGCCCGTAG; primer R, TTCAGTAGTCCCT CTCCACG. PCR amplification 94 °C for 5 min, 5 cycles of 94 °C for 30 s, 68 °C for 30 s, 72 °C for 1 min, 5 cycles of 94 °C for 30 s, 65 °C for 30 s, 72 °C for 1 min, 5 cycles of 94 °C for 30 s, 60 °C for 30 s, 72 °C for 1 min, 20 cycles of 94 °C for 30 s, 58 °C for 30 s, 72 °C for 1 min, 10 min extension at 72 °C, HindIII digestion yields a 300 bp band for 129 and a 150 bp band for C57BL/6.

*Rag1*-deficient thymocytes were induced to progress to the CD4<sup>+</sup> CD8<sup>+</sup> DP stage by injecting 4–6 week-old *Rag1*-deficient mice once with 100 µg anti-CD3 (145-2C11) intraperitoneally. Thymocytes were harvested 10 days later. For BrdU labelling experiments, mice were given a single intraperitoneal injection of 2 mg BrdU (pulse-chase) or 0.6 mg BrdU every 12 h (continuous labelling). Mouse work was done under project licence PPL70/6845 issued by the Home Office, UK.

J $\alpha$  segment usage was assessed by RT-PCR using V $\alpha$ 8 and C $\alpha$  primers, following which Southern blots of PCR products were hybridized with radiolabelled J $\alpha$ -specific and C $\alpha$ -specific probes<sup>34</sup>.

**Ligation-mediated PCR.** This was done as described<sup>35</sup> using J $\alpha$ -specific primers and probes (5' to 3'). J $\alpha$ 61, primer (internal), AGTCCCTTCTCAGGCAAGAT GG; probe, TGAGGAACACGGAGTATCTC. J $\alpha$ 58, primer, ATGGCTTTGGAC CATGGATG; probe, TCTGAAACTCGCACAGTGGA. J $\alpha$ 49, primer, AGGGAA AGTGACACCAGGG; probe, AGGTGTAGATTCTAGCTCTG; J $\alpha$ 27, primer, ATGGCAGATAGAATGGAGCGG; probe, TACCTCCACCTGTCTTCTCA. J $\alpha$ 6, primer, ATCAGACCAGACTGTCTGCC; probe, GACCAATGGCAAAG GGAGGT.

**Confocal analysis.** Mitotic figures were stained for  $\alpha$ -tubulin (DM1A, Sigma) and DAPI as described<sup>36</sup>.

**Real-time PCR.** Real-time PCR was carried out in a 20 µl reaction volume using iQ SYBR Green Supermix (Bio-Rad) and 0.5 µM primers. Amplification was 95 °C for 3 min, then 40 cycles of 94 °C for 15 s, 60 °C for 30 s and 72 °C for 30 s followed by plate read.

**RT-PCR and transcript copy number analysis.** Total RNA was extracted using RNeasy (Tel-Test) and 1 µg was treated with 1 µl Turbo DNase (Ambion). Following DNase inactivation the RNA was reverse transcribed using 200 U Superscript III (Invitrogen) and 0.5 µg oligo(dT) or 3 µg random primers in a 20 µl reaction volume. 1/80 was used per real-time PCR reaction.

To estimate the number of transcripts, standard curves were generated for each pair of primers. The PCR amplicons generated by individual primer pairs were separated by agarose gel electrophoresis, gel purified and their concentration was determined using Quant-iT PicoGreen (Invitrogen). The molar weight of the amplicons was calculated based on their sequence using OligoCalc<sup>37</sup>, which allowed the enumeration of copies in each sample. Twofold serial dilutions from 2,500,000 to 1,220 copies (spliced transcripts) and 2,000,000 to 976 copies (intronic transcripts) were analysed by real-time PCR. The standard curves were compiled by plotting the real-time PCR  $C_t$  values against seeded copy numbers and subsequently fitting a logarithmic function. Only primers that generated a log fit  $R^2 > 0.99$  were used. These standard curves were subsequently used to extrapolate the number of transcripts in the biological samples based on the  $C_t$  values obtained after real-time RT-PCR. For the analysis of spliced transcripts the forward primer was specific to the respective J $\alpha$  segment and the reverse primer to C $\alpha$ .

eJ $\alpha$ 56, forward, CTGGAGGCAATAATAAGCTGACT; eJ $\alpha$ 52, forward, AACACTGGA AAGCTCACGTTTGG; eJ $\alpha$ 44, forward, GGCAGTGGTGGAAA ACTCACT; eJ $\alpha$ 38, forward, AGCTGATTTGGGGCTGGGGA; eJ $\alpha$ 31, forward, GGACGCAGCTGGTGGTGAAGC; eJ $\alpha$ 23, forward, GCTTATCTTTGGACAG GGAACCA; eJ $\alpha$ 18, forward, AACTTTTGAATCGGAACCAGGG; eJ $\alpha$ 9, forward,

ACAAACTTACCTTCGGGACAGG; TCra-C, reverse, TCCATAGCTTTTCATGT CCAGC.

Germline transcripts were analysed using primer pairs specific to introns adjacent to the J $\alpha$  segments included in the spliced transcripts analysis. No amplification was detected without reverse transcriptase.

iJ $\alpha$ 56, forward, CCCTTGAACCCGTGATATGC; iJ $\alpha$ 56, reverse, CAGCCATT GTTTGGATTGGA; iJ $\alpha$ 52, forward, CTGTGGGCTGTGCTTTCTG; iJ $\alpha$ 52, reverse, AGGGAATGGTGGGTACACG; iJ $\alpha$ 44, forward, GAAGAGGCCTC ATGGAGGAA; iJ $\alpha$ 44, reverse, TCTCACAGACCGAAGGGACA; iJ $\alpha$ 38, forward, AGGACTTGGGGTCATCTCCA; iJ38, reverse, GGCTCCTCAGGACAGAC CAG; iJ $\alpha$ 31, forward, GCAGCCTGCCAGCTATCTTT; iJ $\alpha$ 31, reverse, CAAA GCGACCAACCAACAA; iJ $\alpha$ 23, forward, AGAGGAGGCCGAAAGTCTCC; iJ $\alpha$ 23, reverse, TGCACAAATCCAGGCCTATG; iJ $\alpha$ 3, forward, TCTGGACCC TTGGCAATCAT; iJ $\alpha$ 3, reverse, CCCTGCCCTGGTCTACTGTG; iJ $\delta$ 2-C $\delta$ , forward, GGGTTTGTAGTTGGCTTTGG; iJ $\delta$ 2-C $\delta$ , reverse, GGCATGTATTTT GCGGTTGA.

**ChIP-seq.** Single-read high-throughput sequencing libraries were prepared from 10 ng of ChIP DNA and sequenced according to the manufacturer's protocols (Illumina Genome Analyser II). Reads of 38 bases were aligned to the *Mus musculus* mm9 genome assembly using ELAND (Illumina) and wig files generated with FindPeaks<sup>38</sup> were visualized with the UCSC Genome Browser (<http://www.genome.ucsc.edu/>).

**RNA sequencing.** 10 µg total RNA were depleted of ribosomal RNA using RiboMinus (Invitrogen). Depletion was verified using an Agilent 2100 Bioanalyser and the retention of mRNA by real-time RT-PCR. The samples were treated with DNaseI, and the RNA was fragmented for 2 min at 94 °C in RNA fragmentation buffer (final concentration: 40 mM Tris acetate, pH 8.2, 100 mM potassium acetate and 30 mM magnesium acetate). The reaction was stopped by placing the samples on ice and the fragmented RNA was column purified (RNAeasy Minelute Kit, Qiagen), eluted in 10 µl, and used as template for cDNA synthesis using 5 µg random hexamers in a total volume of 20 µl. Second-strand synthesis was performed by adding 91.8 µl water, 30 µl 5\* Second strand buffer (Invitrogen), 3 µl 10 mM dNTPs, 4 µl *E. coli* polymerase I (10 U µl<sup>-1</sup>), 1 µl *E. coli* DNA ligase (10 U µl<sup>-1</sup>) and 0.2 µl RNase H (10 U µl<sup>-1</sup>), followed by 2 h at 16 °C. 1 µl T4 DNA Polymerase (10 U µl<sup>-1</sup>) was added followed by an additional 10 min at 16 °C. The double-stranded cDNA was purified using the Minelute Reaction Cleanup Kit (Qiagen), eluting twice in 10 µl. Following quantification, 20 ng double-stranded cDNA was used for the preparation of a single-read high-throughput sequencing library according to Illumina protocols.

**Rearrangement frequency analysis by semi-quantitative PCR.** Threefold serial dilutions of 100 ng genomic DNA were used for PCR amplification with forward primers specific to V $\alpha$ 5 or V $\alpha$ 7 and reverse primers specific to J $\alpha$ 56, J $\alpha$ 38 or J $\alpha$ 27, respectively<sup>39</sup> (this reference refers to V $\alpha$ 5 as TRAV3-4 and V $\alpha$ 7 as TRADV15-1). Primers for the Calreticulin locus were used as a loading control. PCR products were separated by agarose gel electrophoresis and stained with ethidium bromide.

V $\alpha$ 7, forward, GCAGGATCTAATGTGGCCAGAAAGTGATTCA; V $\alpha$ 5, forward, AGGTGATCACAGAGGCATCCT; J $\alpha$ 56, reverse, ACGTACCTGGTA TAACACTCAGAAC; J $\alpha$ 38, reverse, CAAAGACGACTTTGTTGG; J $\alpha$ 27, reverse, TTAAGAGCCCAAGCAGATGCATAAG; calreticulin, forward, TCAT GAGTTCCCCACATCTTTG; calreticulin, reverse, CTGCCCTATCCTGAGTC TGACA.

**3C.** Cells were fixed in 10% FCS, 1% formaldehyde for 10 min at room temperature (22 °C) and fixation was stopped with glycine (0.125 M). 10<sup>7</sup> cells per sample were lysed in 10 mM Tris, pH 8, 10 mM NaCl, 5 mM MgCl<sub>2</sub>, 0.2% NP-40 for 30 min on ice. The nuclei were pelleted and re-suspended in 0.5 ml 1.2 $\times$  digestion buffer (NEB2, New England Biolabs) and permeabilized with SDS (0.5% final concentration) for 1 h at 37 °C, shaking at 800 r.p.m. and 3.3% Triton X-100 were added for an additional 1 h at 37 °C. 2,000 U HindIII (New England Biolabs) were added before incubation over night at (37 °C, 800 r.p.m.) and inactivated with SDS (1.5%, 65 °C, 30 min). The reaction was diluted in 6.2 ml 1.1 $\times$  T4 ligase buffer (New England Biolabs) and incubated at 37 °C for 1 h after addition of 1% Triton X-100. 800 U T4 DNA ligase (New England Biolabs) was added for 4 h at 16 °C, crosslinking was reversed by 300 µg proteinase K (65 °C, 16 h). 300 µg RNase A was added for 1 h at 37 °C. DNA was isolated by phenol/chloroform extraction and ethanol precipitation, quantified using Quant-iT PicoGreen (Invitrogen) and 200 ng DNA were used per TaqMan PCR reaction (QuantiFast, Qiagen). Data were normalized to the cross-linking frequency between the anchor and the neighbouring HindIII fragment. HindIII digestion efficiency was calculated as described<sup>2</sup> (Supplementary Fig. 8a). The efficiency and linearity of 3C primers was tested on templates obtained by HindIII digestion and religation of genomic PCR products spanning the HindIII restriction sites. The products of each primer pair were gel purified and quantified to calculate copy numbers. Standard curves were constructed by tenfold serial dilution (2  $\times$  10<sup>6</sup> to 20 copies). 3C primers were

selected for >90% efficiency and efficiency and a logarithmic coefficient of determination ( $R^2$ ) >0.99 (Supplementary Fig. 8b, c).

Distance from anchor, -75 kb; 3C primer, CTGCCCCAAAAGAGAGCTTGG; reverse primer, GCATGTGAATGAGAGAGGATGG. Distance from anchor, -73 kb (TEA); 3C primer, GCGGATTTGGGCAAGAATAA; reverse primer, CACAGGCTGCTCCAGAGATG. Distance from anchor, -50 kb; 3C primer, TCTCGAAGGTCCACAAAGCA; reverse primer, GGACACGCTTCCTTGGCTAC. Distance from anchor, -44 kb; 3C primer, AGTCGTGTGGCTGAACCTTTC; reverse primer, TGGTGTCTTTATGGGGTTAGGA. Distance from anchor, -26 kb; 3C primer, TTGGCCAGGGGACCATATTA; reverse primer, CTTGCTTC CCGTGATGTCTG. Distance from anchor, -19 kb; 3C primer, CACAGGAGAAATGAGGCTCAGA; reverse primer, CTGACCAGGCCTTCAGATAA. Distance from anchor, -13 kb; 3C primer, TGTCTCTGCCACAAGTGCT; reverse primer, TAGGAGGACGAGAGGCTGGA. Distance from anchor, 0 kb (anchor); 3C primer, AGCATGGGAGACAGACGTAATG; reverse primer, ATTCCGGTCTCCGTGTGAAT. Normalization fragment, 3C primer, ACCTAGTGACGCCCTG GTGA; reverse primer, TTGGCAGGAGTCGGTTCTTT. Distance from anchor, 8 kb; 3C primer, AATGCGGGCATCTCAGACTT; reverse primer, GAGACTCCCAGGCCTTACCC. Distance from anchor, 9 kb; 3C primer, GCACTTGTCTTA TACTGCCCAAGA; reverse primer, ATTGTCTGGAACGGCACCA. Distance from anchor, 13 kb; 3C primer, ATTGTCTGGAACGGCACCA; reverse primer, GCACTTGTCTTATACTGCCCCAAGA. Distance from anchor, 19 kb; 3C primer, GGGGAAAACAACACATCAGA; reverse primer, GGGTCATCATTCATCCC

AGTC. Distance from anchor, 23 kb; 3C primer, TTTAAAAGGCCAGACTGCAACA; reverse primer, CTCCCACATCCATTTCACCA. TaqMan probe, 3C primer, [FAM]-CCTGCCTGCCTGAG GACTGC-[BHQ1].

31. Spanopoulou, E. *et al.* Functional immunoglobulin transgenes guide ordered B-cell differentiation in Rag-1-deficient mice. *Genes Dev.* **8**, 1030–1042 (1994).
32. Hogquist, K. A. *et al.* T cell receptor antagonist peptides induce positive selection. *Cell* **76**, 17–27 (1994).
33. Kaye, J. *et al.* Selective development of CD4<sup>+</sup> T cells in transgenic mice expressing a class II MHC-restricted antigen receptor. *Nature* **341**, 746–749 (1989).
34. Abarrategui, I. & Krangel, M. S. Regulation of T cell receptor- $\alpha$  gene recombination by transcription. *Nature Immunol.* **7**, 1109–1115 (2006).
35. Jackson, A., Kondilis, H. D., Khor, B., Sleckman, B. P. & Krangel, M. S. Regulation of T cell receptor  $\beta$  allelic exclusion at a level beyond accessibility. *Nature Immunol.* **6**, 189–197 (2005).
36. Toyoda, Y. & Yanagida, M. Coordinated requirements of human topo II and cohesin for metaphase centromere alignment under Mad2-dependent spindle checkpoint surveillance. *Mol. Biol. Cell* **17**, 2287–2302 (2006).
37. Kibbe, W. A. OligoCalc: an online oligonucleotide properties calculator. *Nucleic Acids Res.* **35**, W43–W46 (2007).
38. Fejes, A. P. *et al.* FindPeaks 3.1: a tool for identifying areas of enrichment from massively parallel short-read sequencing technology. *Bioinformatics* **24**, 1729–1730 (2008).
39. Lee, Y. N. *et al.* Differential utilization of T cell receptor TCR $\alpha$ /TCR $\delta$  locus variable region gene segments is mediated by accessibility. *Proc. Natl Acad. Sci. USA* **106**, 17487–17492 (2009).

# A plastidial sodium-dependent pyruvate transporter

Tsuyoshi Furumoto<sup>1,2</sup>, Teppei Yamaguchi<sup>2†</sup>, Yumiko Ohshima-Ichie<sup>2</sup>, Masayoshi Nakamura<sup>2†</sup>, Yoshiko Tsuchida-Iwata<sup>2</sup>, Masaki Shimamura<sup>1</sup>, Junichi Ohnishi<sup>3</sup>, Shingo Hata<sup>2,4</sup>, Udo Gowik<sup>5</sup>, Peter Westhoff<sup>5</sup>, Andrea Bräutigam<sup>6</sup>, Andreas P. M. Weber<sup>6</sup> & Katsura Izui<sup>2,7</sup>

Pyruvate serves as a metabolic precursor for many plastid-localized biosynthetic pathways, such as those for fatty acids<sup>1</sup>, terpenoids<sup>2</sup> and branched-chain amino acids<sup>3</sup>. In spite of the importance of pyruvate uptake into plastids (organelles within cells of plants and algae), the molecular mechanisms of this uptake have not yet been explored. This is mainly because pyruvate is a relatively small compound that is able to passively permeate lipid bilayers<sup>4</sup>, which precludes accurate measurement of pyruvate transport activity in reconstituted liposomes. Using differential transcriptome analyses of C<sub>3</sub> and C<sub>4</sub> plants of the genera *Flaveria* and *Cleome*, here we have identified a novel gene that is abundant in C<sub>4</sub> species, named BASS2 (*BILE ACID:SODIUM SYMPORTER FAMILY PROTEIN 2*). The BASS2 protein is localized at the chloroplast envelope membrane, and is highly abundant in C<sub>4</sub> plants that have the sodium-dependent pyruvate transporter. Recombinant BASS2 shows sodium-dependent pyruvate uptake activity. Sodium influx is balanced by a sodium:proton antiporter (NHD1), which was mimicked in recombinant *Escherichia coli* cells expressing both BASS2 and NHD1. *Arabidopsis thaliana* *bass2* mutants lack pyruvate uptake into chloroplasts, which affects plastid-localized isopentenyl diphosphate synthesis, as evidenced by increased sensitivity of such mutants to mevastatin, an inhibitor of cytosolic isopentenyl diphosphate biosynthesis. We thus provide molecular evidence for a sodium-coupled metabolite transporter in plastid envelopes. Orthologues of BASS2 can be detected in all the genomes of land plants that have been characterized so far, thus indicating the widespread importance of sodium-coupled pyruvate import into plastids.

Pyruvate is an essential metabolite for many plastid-localized metabolic pathways of plants, including the C<sub>4</sub> photosynthetic CO<sub>2</sub>-concentrating mechanism<sup>1–3</sup>. Despite the crucial role of pyruvate import into plastids, the molecule mediating pyruvate transport is still unknown. Because of its essential role in regenerating the CO<sub>2</sub> acceptor of the C<sub>4</sub> photosynthetic carbon-concentrating mechanism, the rate of pyruvate transport into mesophyll cell chloroplasts of C<sub>4</sub> plants exceeds the rates observed in C<sub>3</sub> plants by at least one order of magnitude<sup>4,5</sup> (Supplementary Information). Since the first report of pyruvate transport activity in C<sub>4</sub> plant mesophyll cell chloroplasts<sup>6</sup>, the stimulation of its activity by light<sup>7</sup> and two distinct mechanisms of pyruvate uptake—one proton-dependent<sup>8</sup> and one sodium-dependent<sup>9</sup>—have been characterized in a wide range of C<sub>4</sub> plants<sup>10</sup> (Supplementary Information). Therefore, we proposed (1) that the gene encoding the sodium-dependent plastidial pyruvate transporter should be expressed at substantially higher levels in C<sub>4</sub> than in C<sub>3</sub> plants, (2) that its expression should be low in plants of the proton-dependent C<sub>4</sub> type, and (3) that it should be expressed commonly in plants of the sodium-dependent C<sub>4</sub> type<sup>11</sup>. To isolate genes potentially encoding the pyruvate transporter, we conducted comparative transcriptome analyses between a C<sub>3</sub> plant species, *Flaveria pringlei*, and the closely related sodium-dependent type

C<sub>4</sub> plant species, *Flaveria trinervia* and *Flaveria bidentis*<sup>12</sup>; we used two independent strategies, namely, differential complementary DNA screening and next-generation messenger RNA sequencing.

By using these transcriptome analyses, we identified three novel C<sub>4</sub> species-abundant genes, which are predicted to encode putative chloroplast-targeted membrane proteins (Fig. 1a). In the *Arabidopsis* information resources, related proteins are annotated as ‘bile acid: sodium symporter family proteins’ (BASS2 (ref. 13)/BAT1 (ref. 14) for At2g26900 and BASS4 (ref. 13) for At3g56160) and ‘sodium:hydrogen antiporter 1’ (NHD1 (ref. 15) for At3g19490). Therefore we named

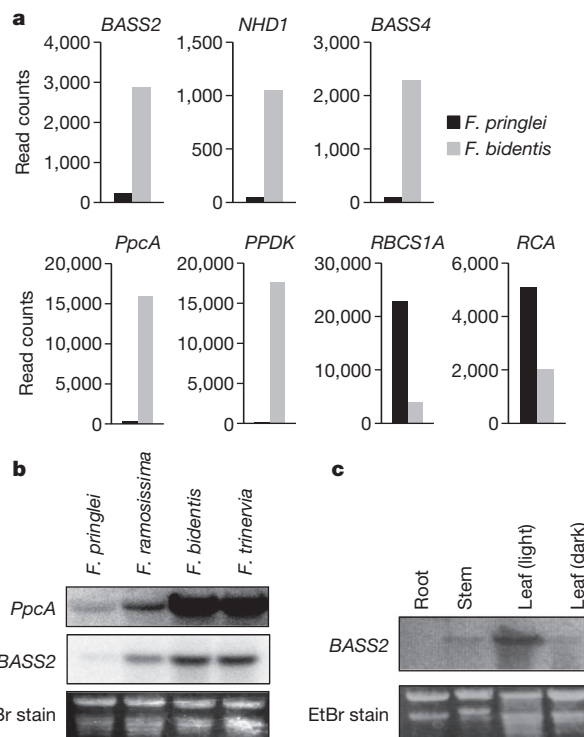


**Figure 1 | The novel C<sub>4</sub>-associated transcripts encoding plastid-targeted membrane proteins.** **a**, From the RNA-seq data set of *Flaveria* species, BASS2, BASS4 and NHD1 expressions (top row) were compared (bottom row) with those of C<sub>4</sub> genes encoding PEPC (*PpcA*) and PPDK (*PPDK*) and C<sub>3</sub> genes encoding RubisCO small subunit (*RBCS1A*) and RubisCO activase (*RCA*). Each read count is indicated. **b**, **c**, BASS2 and *PpcA* transcript levels in the indicated four *Flaveria* species (**b**) and in the indicated tissues of *F. trinervia* (**c**). Leaf (light), leaves taken during light exposure; leaf (dark), leaves taken during the dark period. Ten micrograms of total RNA were loaded in each lane for RNA gel-blot analyses. Radiolabelled *PpcA* and BASS2 of *F. trinervia* were used as probes. The ethidium bromide (EtBr)-stained RNA gels are shown as loading controls in the lower panels.

<sup>1</sup>Graduate School of Science, Hiroshima University, 1-3-1, Kagamiyama, Higashi-Hiroshima, 739-8526, Japan. <sup>2</sup>Graduate School of Biostudies, Kyoto University, Kitashirakawa-Oiwake-cho, Sakyo-ku, Kyoto, 606-8502, Japan. <sup>3</sup>Graduate School of Science and Engineering, Saitama University, 255, Shimo-ohkubo, Sakura-ku, Saitama, 338-8570, Japan. <sup>4</sup>Graduate School of Bioagricultural Sciences, Nagoya University, Furo-cho, Chikusa-ku, Nagoya, 464-8601, Japan. <sup>5</sup>Institut für Entwicklungs- und Molekularbiologie der Pflanzen, Heinrich-Heine Universität Düsseldorf, D-40225 Düsseldorf, Germany. <sup>6</sup>Institut für Biochemie der Pflanzen, Heinrich-Heine Universität Düsseldorf, D-40225 Düsseldorf, Germany. <sup>7</sup>Faculty of Biology-Oriented Science and Technology, Kinki University, 930 Nishimitani, Kinokawa, Wakayama, 649-6493, Japan. <sup>†</sup>Present addresses: Department of Molecular and Cell Biology, University of California Berkeley, 16 Barker Hall, M/C 3204, Berkeley, California 94720-3204, USA (T.Y.); Department of Plant Biology, Carnegie Institution for Science, 260 Panama Street, Stanford, California 94305, USA (M.N.).



them *F. trinervia* BASS2, *F. trinervia* BASS4 and *F. bidentis* NHD1. Because BASS2 and NHD1, but not BASS4, were commonly upregulated in another sodium-dependent type  $C_4$  species, *Cleome gynandra* (Supplementary Information), compared to a  $C_3$  species *Cleome spinosa*<sup>16</sup> (Supplementary Fig. 1 and Supplementary Information), we focused on BASS2 and NHD1.

Except for the putative chloroplast-targeting peptide region, the remainder of the primary structure is highly conserved in all known plant BASS2 proteins (Supplementary Fig. 2a and Supplementary Information). The *F. trinervia* BASS2 gene encodes a protein that features a predicted amino-terminal chloroplast-targeting peptide, 7–9 predicted transmembrane regions, and a cluster of charged amino acids at its carboxy-terminal end (Supplementary Fig. 2b). Although six related genes are found in the genome of *A. thaliana*, the proteins most closely related to BASS2 form a distinct clade (Supplementary Fig. 3), suggesting that these proteins might share a common biochemical function. Transcripts encoding BASS2 are extremely abundant in the  $C_4$  species *F. trinervia* and *F. bidentis*, highly abundant in the  $C_3/C_4$  intermediate species *Flaveria ramosissima*, and not very abundant in the  $C_3$  species *F. pringlei* (Fig. 1b). In *F. trinervia*, BASS2 transcripts accumulated specifically in leaves, in particular during the light period (Fig. 1c).

We assessed BASS2 protein levels using a polyclonal antiserum directed against the C-terminal charged amino acid cluster, PIPVDDKDDDFKE, which is identical among the BASS2 proteins of three *Flaveria* species (Supplementary Fig. 2a). Only one protein band,

with an apparent molecular mass of 28 kDa, was detected (Fig. 2a). The signal was highly abundant in the  $C_4$  species *F. trinervia* and *F. bidentis*, whereas it was faint in the  $C_3$  species *F. pringlei*. Among various species, the BASS2 level gradually increased in accordance with the evolutionary sequence from  $C_3$  to  $C_4$  in the genus *Flaveria*<sup>12</sup> (Supplementary Fig. 4 and Supplementary Information). BASS2 was clearly detectable in the mesophyll cell chloroplast fraction (Supplementary Fig. 5), which was confirmed by immunohistochemical analyses (Fig. 2b). In addition to the signal from the mesophyll cell chloroplasts, a significant signal was also observed in bundle sheath cell chloroplasts, indicating a function of the BASS2 protein in both cells. The localization of BASS2 in plastids was also evidenced by the green fluorescent protein (GFP) fluorescent image of a BASS2–GFP fusion protein, which was stably introduced into transgenic tobacco plants (Supplementary Fig. 6). A cross-reacting protein band was clearly detectable in both monocotyledonous and dicotyledonous  $C_4$  plant species for which a sodium-dependent mode of pyruvate transport was previously established<sup>10</sup> (Fig. 2c). There was no immuno-detectable protein in proton-dependent type  $C_4$  plants, including maize, which is consistent with previous analyses of the maize chloroplast envelope proteome, in which BASS2 and NHD1 were not detected<sup>5,17</sup> (Supplementary Information).

We sought to confirm the biochemical function of BASS2 in a heterologous expression system. Recombinant BASS2 protein was expressed in *E. coli*, and was found to be predominantly localized to

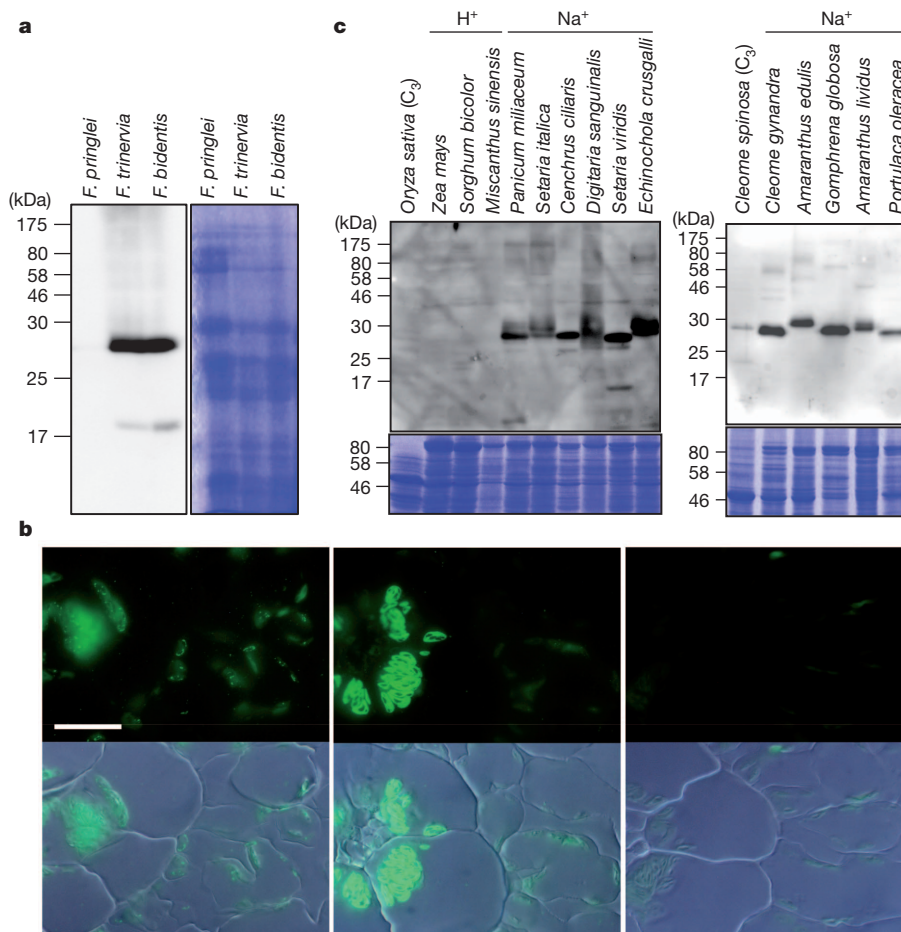


**Figure 2 | BASS2 protein levels.** **a**, BASS2 protein levels in three *Flaveria* species. Left, immunoblot analysis; right, Coomassie brilliant blue (CBB)-stained gel used as a loading control. **b**, Top, fluorescent immunohistochemistry on transverse sections of the leaves of *F. trinervia* using anti-BASS2 antiserum (left), anti-RubisCO antiserum (centre) or without the anti-serum (right). Bottom, merged figures with fluorescence view and

differential interference view. Scale bar, 50  $\mu$ m. **c**, Generality of BASS2 protein in arbitrarily selected monocotyledonous (left panel) and dicotyledonous (right panel)  $C_3$  and  $C_4$  plants. The biochemical classifications of pyruvate uptake are indicated at the top ( $H^+$ ,  $Na^+$ ). Top, western blotting data; bottom, CBB staining used as a loading control.

the plasma membrane (Supplementary Fig. 7a, b). In comparison to the empty-vector control, *E. coli* cells expressing BASS2 showed significantly higher rates of pyruvate uptake (Fig. 3a, b). Even without the addition of sodium chloride, some pyruvate uptake was observed after extended incubation, which is possibly due to the presence of trace amounts of sodium ions introduced by the *E. coli* culture. Notably, another monovalent cation, lithium, could not substitute for sodium as reported previously<sup>9</sup> (Fig. 3b).

Next, we simultaneously expressed BASS2 and NHD1 in *E. coli* (Supplementary Fig. 7a, b) and performed uptake experiments (Fig. 3c). Although significant sodium-dependent uptake was always observed, pyruvate uptake in the absence of externally added sodium chloride was observed in some experiments. As to this experimental variation, we noticed that the NHD1 protein levels were quite variable among independent experiments, whereas the BASS2 protein levels were highly reproducible (Fig. 3d). In the presence of sodium chloride, the uptake activity was always correlated with the BASS2 protein level. On the other hand, in the absence of applied sodium chloride a correlation with NHD1 protein levels was observed. These results indicate that NHD1 could establish a sodium gradient across the *E. coli* membrane, thereby promoting BASS2-dependent pyruvate uptake.

Whereas the physiological function of sodium-dependent pyruvate uptake is well established for *C<sub>4</sub>* plants (Supplementary Information), the role of plastidial pyruvate uptake in *C<sub>3</sub>* plants is not well characterized. Publicly available microarray data indicate that the *A. thaliana* BASS2 orthologue, *At2g26900*, is highly expressed in developing leaves, whereas expression in mature leaves is low<sup>13,18</sup> (Supplementary Fig. 8), which was also confirmed by promoter::reporter analyses and by immunoblot analysis (Supplementary Fig. 9). In two independent mutant lines, named *bass2-1* and *bass2-2* (Supplementary Fig. 10a), no BASS2 expression was detected (Supplementary Fig. 10b, c). These mutant plants did not show an apparent phenotype under normal growth

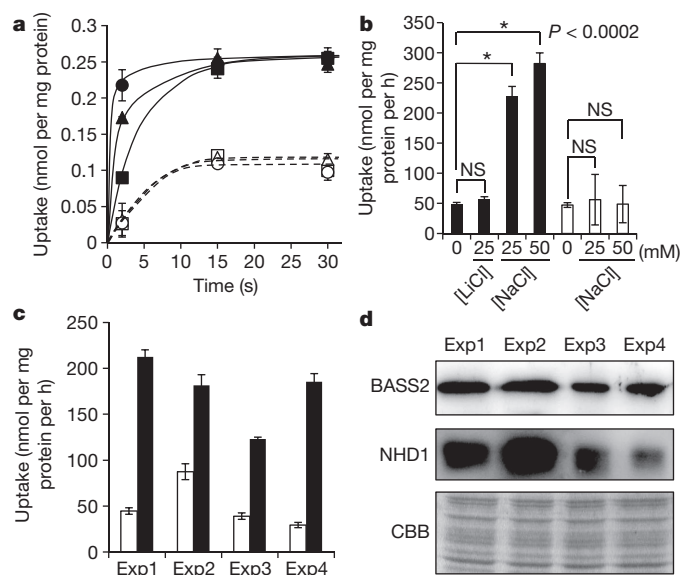


**Figure 3 | Pyruvate uptake activity.** **a**, Whole *E. coli* cells with (filled symbols) or without (open symbols) BASS2 recombinant protein were incubated with 0 mM (squares), 25 mM (triangles) or 50 mM (circles) NaCl. Data are mean  $\pm$  s.d.,  $n = 4$ . **b**, Uptake activities of BASS2-expressing *E. coli* (black columns) and empty vector control (white columns) at the initial time point under indicated concentrations of LiCl or NaCl. Data are mean  $\pm$  s.d., from four independent experiments.  $P$  values were produced by Student's  $t$ -test. NS, not significant. **c**, Uptake activities of the dual-expressing *E. coli* in the absence (white columns) and the presence (black columns) of NaCl. Mean values of four experimental repeats of four independent experiments are indicated, with s.d. **d**, The recombinant proteins detected by BASS2-peptide-antibody (upper panel) or by the fused artificial tag (middle panel). The lower panel indicates CBB staining used as a loading control.

conditions (Fig. 4c). Isolated chloroplasts from 5-day-old wild-type plants displayed sodium-dependent pyruvate uptake activity in the dark, whereas pyruvate was taken up without simultaneous addition of sodium in the light, as reported in sodium-dependent *C<sub>4</sub>* plants<sup>9,10</sup> (Fig. 4a). Its specific activity was calculated at 4.53  $\mu$ mol per mg chlorophyll per hour, which is approximately one-fifth of the average activity (23.6) observed in sodium-dependent *C<sub>4</sub>* plants<sup>10</sup> (Fig. 4b). On the other hand, chloroplasts isolated from the *bass2* mutants entirely lacked sodium-dependent pyruvate uptake activity (Fig. 4a, b).

Pyruvate is one of the two crucial substrates of the methyl erythritol phosphate (MEP) pathway<sup>2</sup>. If BASS2 is required for fuelling the MEP pathway, *bass2* mutants should be more sensitive to mevastatin, an inhibitor of hydroxymethylglutaryl-CoA reductase (the rate-limiting enzyme of the cytosolic mevalonic acid pathway), than the wild type (Supplementary Fig. 11). Indeed, in the presence of 50 nM mevastatin, a slight growth retardation was observed in the wild type, as reported previously<sup>19</sup>. This growth retardation was more severe and a yellow-leaf phenotype was observed in both *bass2* mutants (Fig. 4c). This mevastatin-sensitive phenotype of *bass2* mutants strongly indicates that BASS2 functions to supply pyruvate to the MEP pathway.

For the efficient import of pyruvate, a mechanism to export sodium cations from the chloroplasts would be needed. On the basis of our data, we propose that sodium-dependent pyruvate transport into mesophyll cells of certain *C<sub>4</sub>* plant species is facilitated by a two-translocator system, consisting of a sodium:pyruvate cotransporter (BASS2) and a sodium:proton antiporter (NHD1) (Supplementary Fig. 12a). In addition, the molecular mechanism of the light-driven uptake of pyruvate into isolated chloroplasts in *C<sub>4</sub>* plants<sup>9,10</sup> and in the *C<sub>3</sub>* plant *A. thaliana* without exogenous sodium ions (Fig. 4a) can be explained by this coupling reaction, as follows. Under light conditions, proton uptake

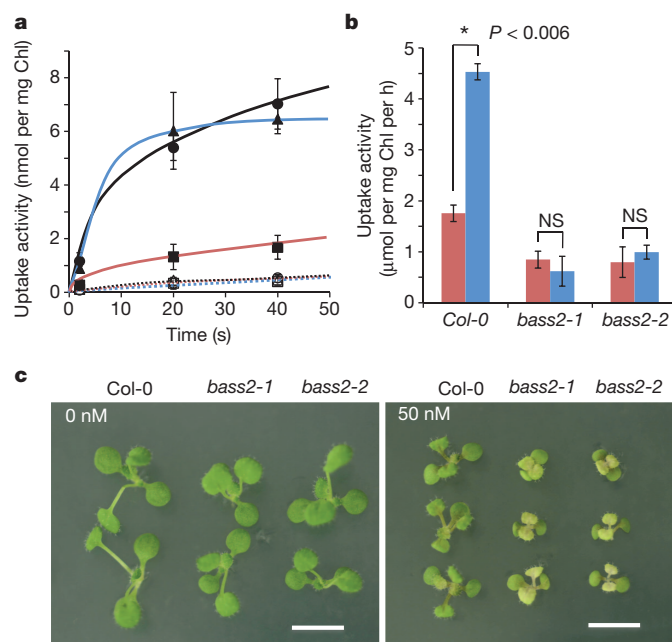


**Figure 4 | BASS2 function in *A. thaliana*.** **a**, Time-dependent pyruvate uptake activities of wild-type Col-0 (solid lines) and *bass2-1* (dotted lines). Isolated plastids were incubated with (triangles with blue lines) or without (squares with orange lines) 12.5 mM NaCl under dark conditions, or without NaCl under light conditions (circles with black lines). Data show mean  $\pm$  s.d.,  $n = 3-4$ . **b**, Uptake activities of wild-type Col-0 and *bass2* mutants at the initial time point (2 s). These activities were measured under near-saturating conditions with (blue bar) or without (red bar) NaCl, and mean values with s.d. were determined by three experiments performed on separate chloroplast preparations.  $P$  values were produced by Student's  $t$ -test. NS, not significant. **c**, Mevastatin-sensitive phenotype of *bass2* mutants. Plants were grown without (left) or with (50 nM) mevastatin for 10 days. Scale bar, 5 mm.

into thylakoid alkalizes the stroma<sup>20</sup>, NHD1 exchanges sodium with protons, thereby establishing a sodium gradient across the envelope, and then BASS2 takes up pyruvate. We propose that in *C<sub>4</sub>* plants this proton gradient is maintained by stoichiometrically coupling pyruvate import to the export of phosphoenolpyruvate (PEP) (Supplementary Information and Supplementary Fig. 12a).

Extensive efforts have been made to identify organelle-localized pyruvate carriers, both in mitochondria and in plastids<sup>21</sup>; however, the mitochondrial pyruvate importer has remained elusive (Supplementary Information). As shown in Supplementary Fig. 12b, we demonstrate, using evidence from both gain-of-function and loss-of-function experiments, that BASS2 is a plastid-localized sodium-dependent pyruvate transporter functioning in *C<sub>4</sub>* photosynthesis and in the MEP pathway in *C<sub>3</sub>* plants.

## METHODS SUMMARY

**Differential screening and RNA-seq of the genus *Flaveria*.** Both mRNA populations were prepared from well-expanded leaves of *F. trinervia* and *F. pringlei* sampled in the middle of the light period. Poly-A<sup>+</sup> mRNA was isolated and used to prepare single-strand radiolabelled cDNA as described<sup>22</sup>. Each radiolabelled probe was hybridized to duplicate nylon membranes containing approximately 9,000 phage clones of a *F. trinervia* leaf cDNA library<sup>23</sup>. Except for the major *C<sub>4</sub>* marker genes encoding phosphoenolpyruvate carboxylase (PEPC), pyruvate, orthophosphate dikinase (PPDK) and NADP-ME, we isolated 56 clones as novel *C<sub>4</sub>*-abundant signals, which were classified into 19 genes by determining their cDNA sequences. By comparing the cDNA fragments to the known genome of *A. thaliana*, we found the BASS2 and BASS4 partial cDNA sequences. The cDNA library was rescreened using these partial cDNA fragments as probes, and the full-length cDNAs were isolated. The sequences of these cDNAs were deposited in DDBJ (accession numbers: *F. trinervia* BASS2, AB522102; *F. trinervia* BASS4, AB522103).

The transcriptomes of *F. bidentis*, *F. pringlei*, *C. gynandra* and *C. spinosa* leaves were analysed by RNA sequencing (RNA-seq) as described previously<sup>16,24</sup>. The *F. bidentis* BASS2, and *F. pringlei* BASS2 full-length cDNA sequences were obtained from the RNA-seq contig data.

**Pyruvate uptake measurement.** Isolated plastids from wild-type Col-0 or *bass2* mutants were incubated with 0.2 mM or 0.5 mM pyruvate (0.5  $\mu$ Ci [<sup>2-<sup>14</sup>C]</sup>pyruvate, American Radiolabelled Chemicals, Inc.) and with indicated concentrations of NaCl in accordance with the silicone-oil bilayer method<sup>20</sup>.

**Full Methods** and any associated references are available in the online version of the paper at [www.nature.com/nature](http://www.nature.com/nature).

Received 19 December 2010; accepted 1 June 2011.

- Schwender, J., Ohlrogge, J. & Shachar-Hill, Y. Understanding flux in plant metabolic networks. *Curr. Opin. Plant Biol.* **7**, 309–317 (2004).
- Hemmerlin, A. *et al.* Cross-talk between the cytosolic mevalonate and the plastidial methylerythritol phosphate pathways in tobacco Bright Yellow-2 cells. *J. Biol. Chem.* **278**, 26666–26676 (2003).
- Schulze-Siebert, D., Heineke, D., Scharf, H. & Schultz, G. Pyruvate-derived amino acids in spinach chloroplasts: synthesis and regulation during photosynthetic carbon metabolism. *Plant Physiol.* **76**, 465–471 (1984).
- Proudlove, M. O. & Thurman, D. A. The uptake of 2-oxoglutarate and pyruvate by isolated pea chloroplasts. *New Phytol.* **88**, 255–264 (1981).
- Bräutigam, A., Hoffmann-Benning, S. & Weber, A. P. M. Comparative proteomics of chloroplast envelopes from *C<sub>3</sub>* and *C<sub>4</sub>* plants reveals specific adaptations of the plastid envelope to *C<sub>4</sub>* photosynthesis and candidate proteins required for maintaining *C<sub>4</sub>* metabolite fluxes. *Plant Physiol.* **148**, 568–579 (2008).
- Huber, S. C. & Edwards, G. E. Transport in *C<sub>4</sub>* mesophyll chloroplasts. Characterization of the pyruvate carrier. *Biochim. Biophys. Acta* **462**, 583–602 (1977).
- Flügge, U. I., Stitt, M. & Heldt, H. W. Light-driven uptake of pyruvate into mesophyll chloroplasts from maize. *FEBS Lett.* **183**, 335–339 (1985).
- Ohnishi, J. & Kanai, R. Pyruvate uptake induced by a pH jump in mesophyll chloroplasts of maize and sorghum, NADP-malic enzyme type *C<sub>4</sub>* species. *FEBS Lett.* **269**, 122–124 (1990).
- Ohnishi, J. & Kanai, R. Na<sup>+</sup>-induced uptake of pyruvate into mesophyll chloroplasts of a *C<sub>4</sub>* plant, *Panicum miliaceum*. *FEBS Lett.* **219**, 347–350 (1987).

- Aoki, N., Ohnishi, J. & Kanai, R. Two different mechanisms for transport of pyruvate into mesophyll chloroplasts of *C<sub>4</sub>* plants — a comparative study. *Plant Cell Physiol.* **33**, 805–809 (1992).
- Weber, A. P. M. & von Caemmerer, S. Plastid transport and metabolism of *C<sub>3</sub>* and *C<sub>4</sub>* plants — comparative analysis and possible biotechnological exploitation. *Curr. Opin. Plant Biol.* **13**, 1–9 (2010).
- McKown, A. D., Moncalvo, J.-M. & Dengler, N. G. Phylogeny of *Flaveria* (Asteraceae) and inference of *C<sub>4</sub>* photosynthesis evolution. *Am. J. Bot.* **92**, 1911–1928 (2005).
- Sawada, Y. *et al.* Arabidopsis bile acid:sodium symporter family protein 5 is involved in methionine-derived glucosinolate biosynthesis. *Plant Cell Physiol.* **50**, 1579–1586 (2009).
- Gigolashvili, T. *et al.* The plastidic bile acid transporter 5 is required for the biosynthesis of methionine-derived glucosinolates in *Arabidopsis thaliana*. *Plant Cell* **21**, 1813–1829 (2009).
- Cellier, F. *et al.* Characterization of AtCHX17, a member of the cation/H<sup>+</sup> exchangers, CHX family, from *Arabidopsis thaliana* suggests a role in K<sup>+</sup> homeostasis. *Plant J.* **39**, 834–846 (2004).
- Bräutigam, A. *et al.* An mRNA blueprint for *C<sub>4</sub>* photosynthesis derived from comparative transcriptomics of closely related *C<sub>3</sub>* and *C<sub>4</sub>* species. *Plant Physiol.* **155**, 142–156 (2011).
- Majeran, W. *et al.* Consequences of *C<sub>4</sub>* differentiation for chloroplast membrane proteomes in maize mesophyll and bundle sheath cells. *Mol. Cell. Proteomics* **7**, 1609–1638 (2008).
- Weber, A. P. M., Schwacke, R. & Flügge, U. I. Solute transporters of the plastid envelope membrane. *Annu. Rev. Plant Biol.* **56**, 133–164 (2005).
- Suzuki, M. *et al.* Loss of function of 3-hydroxy-3-methylglutaryl coenzyme A reductase 1 (*HMG1*) in *Arabidopsis* leads to dwarfing, early senescence and male sterility, and reduced sterol levels. *Plant J.* **37**, 750–761 (2004).
- Aoki, N. & Kanai, R. Reappraisal of the role of sodium in the light-dependent active transport of pyruvate into mesophyll chloroplasts of *C<sub>4</sub>* plants. *Plant Cell Physiol.* **38**, 1217–1225 (1997).
- Sugden, M. C. & Holness, M. J. Trials, tribulations and finally, a transporter: the identification of the mitochondrial pyruvate transporter. *Biochem. J.* **374**, e1–e2 (2003).
- Furumoto, T., Hata, S. & Izui, K. cDNA cloning and characterization of maize phosphoenolpyruvate carboxykinase, a bundle sheath cell-specific enzyme. *Plant Mol. Biol.* **41**, 301–311 (1999).
- Furumoto, T. *et al.* Vascular-tissue abundant expression of plant *TAF10*, an orthologous gene for TATA box-binding protein-associated factor 10, in *Flaveria trinervia* and abnormal morphology of *Arabidopsis thaliana* transformants on its over-expression. *Plant Cell Physiol.* **46**, 108–117 (2005).
- Weber, A. P. M., Weber, K. L., Carr, K., Wilkerson, C. & Ohlrogge, J. B. Sampling the *Arabidopsis* transcriptome with massively parallel pyrosequencing. *Plant Physiol.* **144**, 32–42 (2007).

**Supplementary Information** is linked to the online version of the paper at [www.nature.com/nature](http://www.nature.com/nature).

**Acknowledgements** We thank G. Schönknecht, S. Yamaguchi and Y. Kamiya for discussions; N. Das, S. von Caemmerer and R. T. Furbank for critical reading of the manuscript; R. F. Sage, T. Endo, M. Munekage, J. Hibberd and M. Ku for gifts of seeds; T. Kinoshita for technical advice on the BASS2 immunoblot analysis; N. Aoki and S. Koreeda for technical advice on the pyruvate-uptake measurements; A. Izumida for preparation of the *F. trinervia* cDNA library; and Y. Takahashi for suggesting the dual expression system. This work was supported in part by the Ministry of Education, Science and Culture of Japan (Grants-in-Aid for Scientific Research to T.F. and K.I.), by a Sasakawa Scientific Research Grant from the Japan Science Society to T.F., and by the German Research Foundation (CRC-TR1 and IRTG 1525/1 to A.P.M.W., and CRC 590 to P.W.).

**Author Contributions** T.Y. performed the differential screening and isolated the BASS2 gene. M.N. and Y.O.-I. analysed *C<sub>4</sub>*-abundant genes. Y.O.-I. prepared the *bass2* mutants and revealed BASS2 expression. M.S. performed the confocal laser micro-scanning and the analyses of immunohistochemistry. J.O. and T.F. performed the pyruvate-uptake measurements on isolated chloroplasts, and A.B., A.P.M.W. and T.F. performed the *E. coli* whole-cell uptake measurements. U.G., P.W., A.B. and A.P.M.W. performed *Flaveria* and *Cleome* transcriptome analyses and the phylogenetic analysis. S.H. was involved in designing the study, T.F. and K.I. designed the study, and T.F. and A.P.M.W. wrote the paper.

**Author Information** cDNA sequences for *F. trinervia* BASS2, *F. trinervia* BASS4 and *F. bidentis* NHD1 have been deposited in the DNA Data Bank of Japan, with respective accession numbers AB522102, AB511103 and AB642169. Reprints and permissions information is available at [www.nature.com/reprints](http://www.nature.com/reprints). The authors declare no competing financial interests. Readers are welcome to comment on the online version of this article at [www.nature.com/nature](http://www.nature.com/nature). Correspondence and requests for materials should be addressed to T.F. (tfurumoto@hiroshima-u.ac.jp).



## METHODS

**Plant growth and crude protein extraction.** All plants except for *A. thaliana* and transgenic tobacco plants were grown under natural light in a greenhouse from September to October 2008 in Hiroshima, Japan. *A. thaliana* and tobacco were grown in a growth chamber under constant light at 21 °C and at 28 °C, respectively. In promoter::reporter analyses, *A. thaliana* was grown on soil for 19 days, and in the pyruvate uptake measurements plants were grown on half-strength MS agar plates for 5 days. Leaf samples were frozen in liquid nitrogen and ground with a mortar and pestle into fine powder. Crude protein was extracted with 3 volumes (w/v) of extraction buffer (50 mM Tris-HCl (pH 8.0), 0.5% Triton X-100, 0.1% Nonidet P-40, protein inhibitor cocktail (Complete-mini, Sigma), 1 mM phenylmethylsulphonyl fluoride, 1 mM dithiothreitol). The homogenates were centrifuged at 12,000g for 15 min, and the supernatants were used for immunoblot analysis. Immunoblot analyses were performed as previously described<sup>25</sup>, except that the anti-BASS2-peptide polyclonal antiserum, diluted 1:5,000, was used as the first antibody.

**Immunohistochemical analysis.** *F. trinervia* leaves were dissected into small pieces, and transferred into vials containing the fixative solution (4% formaldehyde in 0.05 M phosphate buffer (pH 7.0)); the vials were evacuated by a water aspirator until the specimens sank to the bottom of the vials. After fixation for 8 h at 4 °C, the samples were rinsed in 0.05 M phosphate buffer. Then, the samples were dehydrated in a graded acetone series and embedded in plastic resin (Technovit 8100, Kulzer) using a graded series of acetone and resin. Semi-thin sections for light microscopy were obtained with an ultramicrotome using glass knives. The tissue sections were transferred onto glass slides and dried for 20 min at 37 °C. After rinsing in PBS, the sections were incubated with 1% bovine serum albumin in PBS for 5 min. Then, sections were incubated for 1 h with the anti-BASS2-peptide antiserum diluted 1:1,000, or anti-RubisCO antiserum diluted 1:5,000, in PBS at 37 °C in a moist chamber. For the control sections, this incubation step was omitted. After three washes in PBS, the sections were incubated for 1 h with the secondary antibody conjugated with Alexa 488 fluorochrome (Molecular Probes) diluted 1:200 in PBS at 37 °C in a moist chamber. Signals were visualized by epifluorescence microscopy (E600, Nikon) and images were captured with a CCD camera (DXM 1200, Nikon).

**BASS2/NHD1 expression in *E. coli* and uptake measurements.** The recombinant BASS2 was expressed in *E. coli* (BL21 DE3) using the pETduet-1 expression vector (Novagen), similarly to a previously reported method<sup>22</sup>. For preparation of the expression vector, an internal NcoI site was mutated without amino acid substitution and an artificial EcoRI site was introduced at the end of the putative chloroplast-targeting site. To introduce these mutations, two primer sets were used for PCR: 5'-AAGAATTCTGCCAAGCAGCAACAAATGTAC-3', 5'-GTTTAAGGAATCCGTGGACTGTAGGTGTAG-3' and 5'-GTTTAAGGAATCCGTGGACTGTAGGTGTAG-3', 5'-CAAGTCGACTTACTCCTTGAAATCATC-3'. The amplified DNA fragment was subcloned into the EcoRI and SalI sites of pBluescript KS(-); after the sequence was confirmed to be correct, this fragment was amplified with two primers, 5'-AACCATGGGCTGCCAAGCAGCAACAAATGTA-3' and 5'-AGGTCGACTTACTCCTTGAAATCATCTT-3'. The former includes an artificial NcoI site, and the latter includes a SalI site. After confirming its sequence, this fragment was introduced into the NcoI and SalI sites of the pETduet-1 vector. The N-terminal putative plastid-targeting peptide was removed, and the resulting mature protein was expressed without tags. The NHD1 cDNA fragment was amplified with two primers (5'-TGCATATGGCAGAAGATAAGGCACGTGG-3', 5'-TGCTCGAGCGAGCCGAGATGAATGGAA-3') from reverse-transcribed cDNA sources. The former and the latter contained an artificial NdeI site and an artificial XhoI site, respectively. After PCR, amplified cDNA fragments were subcloned into pGEM-T vector before the correct sequence

was confirmed. The NHD1 fragment was introduced into the NdeI and XhoI site of pETduet-1, resulting in a translational S-tag fusion at the C-terminus. The transgenic *E. coli* was grown in LB medium (pH 7.0), where NaCl was replaced by KCl (87 mM)<sup>26</sup>. When the  $D_{600}$  was approximately 0.5, 0.1 mM IPTG was added to the *E. coli* culture which was further incubated for 4 h at 25 °C (ref. 27). An artificial pH gradient was formed across the *E. coli* membrane as described previously<sup>28</sup>. *E. coli* was washed with inside buffer (50 mM KHPO<sub>4</sub> (pH 8.2), 0.1 mM MgSO<sub>4</sub>, 0.1 mM CaCl<sub>2</sub>) once, and then incubated in the same buffer containing 50 µM of carbonyl cyanide *m*-chlorophenylhydrazide and 1 mM As<sub>2</sub>O<sub>3</sub> for 15 min at room temperature. After centrifugation, the *E. coli* was resuspended with reaction buffer (50 mM KHPO<sub>4</sub> (pH 7.8), 0.1 mM MgSO<sub>4</sub>, 0.1 mM CaCl<sub>2</sub>, 0.1 mM [2-<sup>14</sup>C]pyruvate) with the indicated concentration of NaCl. Two pyruvate concentrations, 0.5 mM or 0.1 mM, were adopted for the uptake reactions. The former was in accordance with the previous assay conditions using isolated plastids<sup>8,9</sup>, and the latter was adjusted for *E. coli* whole-cell assay to avoid the rapid saturation of uptake. After incubation for the indicated amount of time, the *E. coli* suspension was used in the silicone-oil filtration-centrifugation method to stop the uptake reaction<sup>20</sup>. Mean values of the uptake activities and standard deviations were determined from three to four independent *E. coli* preparations.

**BASS2 expression in *A. thaliana* and *bass2* mutants.** Seeds of two independent *bass2* mutants (*bass2-1* and *bass2-2*) were obtained from the ABRC seed stock centre (SALK\_101808 and SALK\_098962, respectively). Each homozygote was isolated as described previously<sup>29</sup>. Ten-day-old, 7-day-old and 5-day-old plants were used for an RNA gel-blot (northern blot) analysis, a protein gel-blot (western blot) analysis, and for pyruvate uptake measurements, respectively. For the measurement of short periods of uptake (predicted 2 s), the silicone-oil double layer method was used, and for longer periods of uptake, the silicone-oil single layer method was used in accordance with a previous report<sup>20</sup>. To measure pyruvate uptake activity, two conditions were adopted: (1) as a near non-saturating condition, isolated plastids were incubated for the indicated number of seconds in reaction mixture (50 mM HEPES (KOH) (pH 7.8), 5 mM EDTA, 0.35 M sorbitol), which includes 0.2 mM pyruvate (0.5 µCi [2-<sup>14</sup>C]pyruvate) with or without 12.5 mM NaCl; and (2) as a near-saturating condition, isolated plastids were incubated in the same buffer, including 0.5 mM pyruvate (0.5 µCi [2-<sup>14</sup>C]pyruvate) with or without 50 mM NaCl. Sodium-dependence was measured under dark conditions. Under light conditions, approximately 50 µmol m<sup>-2</sup> s<sup>-1</sup> of white light was applied for 10 min before measurement on ice and during centrifugation steps. The cytoplasmic concentration of sodium in 5-day-old *A. thaliana* is not known. Thus, 12.5 mM sodium was adopted, based on the previous biochemical characterization of the pyruvate uptake activity on the plastids isolated from *C<sub>4</sub>* plants, which was about twice the  $K_m$  value for sodium (4.8 mM)<sup>9</sup>.

25. Furumoto, T., Izui, K., Quinn, V., Furbank, R. T. & von Caemmerer, S. Phosphorylation of phosphoenolpyruvate carboxylase is not essential for high photosynthetic rates in the *C<sub>4</sub>* species *Flaveria bidentis*. *Plant Physiol.* **144**, 1936–1945 (2007).
26. Padan, E., Maisler, N., Taglicht, D., Karpel, R. & Schuldiner, S. Deletion of *ant* in *Escherichia coli* reveals its function in adaptation to high salinity and an alternative Na<sup>+</sup>/H<sup>+</sup> antiporter system(s). *J. Biol. Chem.* **264**, 20297–20302 (1989).
27. Pavón, L. R. et al. *Arabidopsis* ANTR1 is a thylakoid Na-dependent phosphate transporter. *J. Biol. Chem.* **283**, 13520–13527 (2008).
28. Tsuchiya, T., Hasan, S. M. & Raven, J. Glutamate transport driven by an electrochemical gradient of sodium ions in *Escherichia coli*. *J. Bacteriol.* **131**, 848–853 (1977).
29. Tamada, Y. et al. Temporary expression of the *TAF10* gene and its requirement for normal development of *Arabidopsis thaliana*. *Plant Cell Physiol.* **48**, 134–146 (2007).

## ADDENDUM

doi:10.1038/nature10395

## The thermodynamic meaning of negative entropy

Lídia del Rio, Johan Åberg, Renato Renner, Oscar Dahlsten  
& Vlatko Vedral

*Nature* **474**, 61–63 (2011)

To clarify the implications of our result, we note that, although the erasure processes we considered in our Letter can have negative work cost (that is, they can yield work), they do not violate the second law of thermodynamics, because they are not cyclic processes. A negative work cost is associated with the consumption of entanglement, which can only be restored by doing work. Our results are also consistent with the original unconditional form of Landauer's principle, which says that if there is no information available about the data being erased, the cost of erasure is always positive. Similarly, because in a computation with deterministic classical output the joint entropy of all registers conditioned on the output cannot be negative, the overall work cost of such a computation is always positive or zero (even though temporary quantum correlations may be created and exploited during the course of the computation). In fact, standard techniques of reversible information processing allow any deterministic classical algorithm to be performed, on a classical or quantum computer, in a thermodynamically reversible fashion, with work cost arbitrarily close to zero<sup>1,2</sup>. These clarifications are developed in more detail in the Supplementary Information to this Addendum. We thank Charles H. Bennett for remarks on reversible computation.

**Supplementary Information** is linked to the online version of the Addendum at [www.nature.com/nature](http://www.nature.com/nature).

1. Bennett, C. H. The thermodynamics of computation—a review. *Int. J. Theor. Phys.* **21**, 905–940 (1982).
2. Watrous, J. Quantum computational complexity. In *Encyclopaedia of Complexity and Systems Science* (ed. Meyers, R. A.) Part 17, 7174–7201 (Springer, 2009).

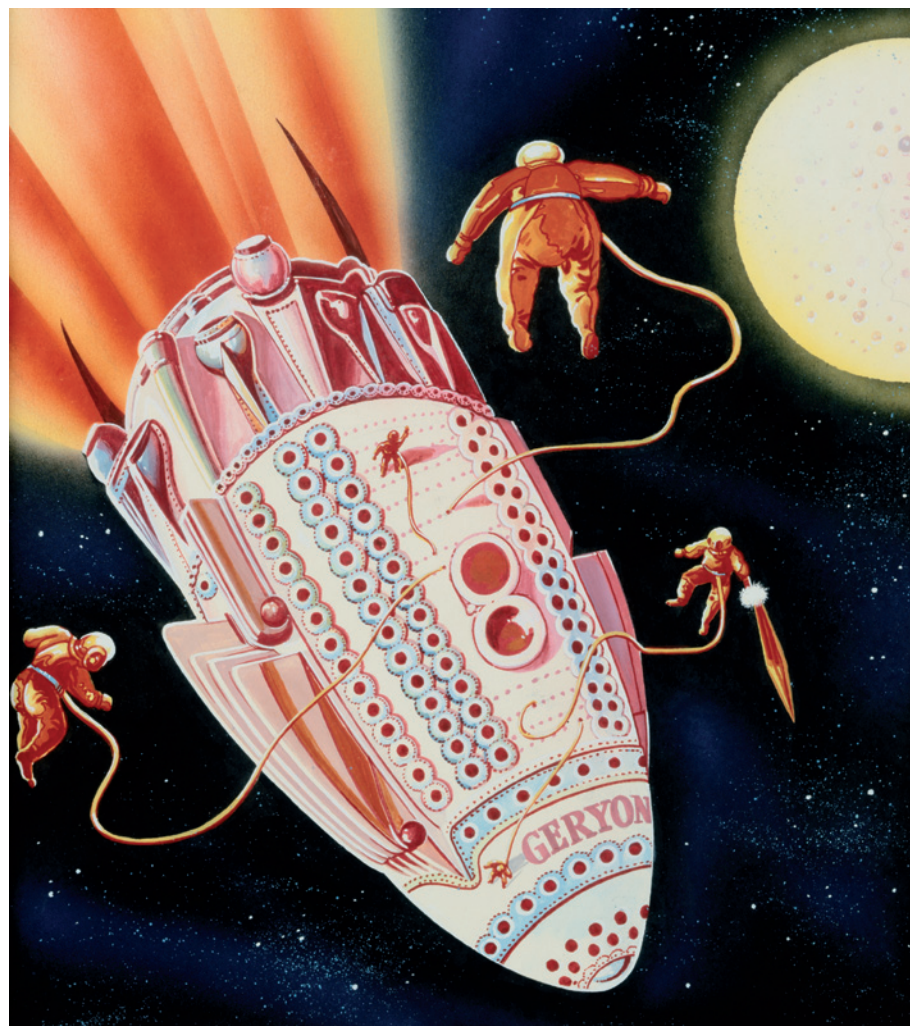
# CAREERS

**COLLABORATIONS** US industry-academia partnerships on the rise **p.478**

**COLUMN** How to build up your own 'old boy' network **p.479**

**NATUREJOBS** For the latest career listings and advice **www.naturejobs.com**

FORREST J. ACKERMAN COLLECTION/CORBIS



## COMMERCIAL SPACE FLIGHT

# Scientists in space

*Adventure-seeking researchers could benefit from NASA's exit from manned space flight.*

BY KATHARINE SANDERSON

Jason Reimuller has always dreamed of being an astronaut for NASA. "I grew up with an aviator — my grandfather was an air-force general who flew B-25 aircraft in the Second World War," he says.

Reimuller, a climate researcher at the

University of Colorado at Boulder, never gave up on that dream. He studies high-altitude clouds from a plane in desolate polar regions, which feeds his love of science and adventure. He also applied for NASA's astronaut programme and made it to the last round, but was unsuccessful. So in 2010, Reimuller applied to train with Astronauts4Hire (A4H). The

non-profit group, registered in Tampa, Florida, aims to train scientists to do research in space, and link them with groups that need such skills.

"The prospects of becoming an astronaut through the traditional route, through space agencies, are slim," says Brian Shiro, chief executive of A4H and a geophysicist at the US National Oceanic and Atmospheric Administration's Pacific Tsunami Warning Center in Ewa Beach, Hawaii. "The opportunities are probably better in the commercial sector."

In 2010, NASA cancelled its Constellation programme, which would have developed rockets to take people to the Moon; in July, the agency flew its last space-shuttle mission. Commercial companies are hoping to fill the void by developing rockets to carry humans into orbit, and firms and organizations such as A4H hope to supply the astronauts. Researchers, most with full-time jobs, train in their spare time — for now. Eventually, A4H hopes to be a fully fledged, professional training body for commercial astronauts, with full-time staff.

A4H has grown quickly since it launched last year. The team now includes 22 flight members (trainee astronauts) from around the world, and a growing number of associate members, who support and get involved in its activities. At the basic level, trainees take a three-day course on which they learn to cope with low oxygen levels, go through centrifuge training to simulate the high and low G-forces experienced on suborbital parabolic flights, and learn some relevant human physiology. The next level requires experience in scuba diving, piloting a plane and running experiments in microgravity. Training costs start at US\$10,000.

Once flight members have completed their training, academic principal investigators or companies interested in microgravity research will be able to hire them to fly research payloads on suborbital aircraft flights or — eventually — into orbit. Members will be paid directly by clients and might spend months with them, developing and learning about an instrument. A4H already has its first paying customer: a collaboration between Saber Astronautics Australia in Sydney and the 4 Pines Brewing Company in Manly, Australia, which in February tested the effects of microgravity on a beer developed for consumption in space.

A4H is not the only group teaching scientists to work in space. The Southwest Research Institute (SwRI) in Boulder, Colorado, offers microgravity training without the more rigorous wilderness training or pilot experience demanded by NASA and A4H. A4H's ►



## NETWORKING

## Contacts help men most

Fewer women than men secure jobs informally through workplace social contacts, a study says. Author Steve McDonald, a sociologist at North Carolina State University in Raleigh, analysed results from a US Bureau of Labor Statistics study of 3,200 people between 1979 and 1998, in which respondents specified how they made job transitions. He found that as men accumulate time in a field, they become more likely to be recruited for new jobs by their workplace contacts. Women are not recruited in the same way, possibly because their social workplace interactions focus less on work, and because their contacts don't have recruiting and hiring authority, McDonald suggests. The study will be published in *Social Science Research* in November.

## NOBEL LAUREATES

## Top status doesn't linger

Nobel laureates' celebrated status within the scientific community wanes sooner than one might expect, says a study led by Christine Charyton, a visiting neurologist at Ohio State University in Columbus. The analysis, based on citations and other metrics, shows that after a peak, most laureates' later work involving the Nobel-winning idea is no more accepted than their earliest articles. The study measured the impact of articles by 187 researchers who won Nobel Prizes in physics, chemistry or medicine between 1980 and 2009. Charyton, who presented the paper on 6 August at the American Psychological Association Convention in Washington DC, suggests that later papers expand on and diverge from the Nobel-winning idea.

## ACADEMIC-INDUSTRIAL PARTNERSHIPS

## Cooperation increases

Industrial sponsors invested US\$4.3 billion in research at US universities in 2010, up 5.6% from 2009, according to a survey of university technology-transfer activities by the Association of University Technology Managers in Deerfield, Illinois. Robin Rasor, president of the group, says that there has been an increase in partnerships because firms have cut back on in-house early-stage research to reduce costs, and are focusing on development. "Companies are looking more to universities for cutting-edge innovations," she adds. Collaborations could lead to industry jobs for PhD students and postdocs working on those innovations, says Rasor.



John Pojman of Louisiana State University works on an experiment on a low-gravity suborbital flight.

► model, admits Dan Durda, a space scientist at the SwRI, does decrease the likelihood that the rigours of flight will scare away trainees when it's time to go up, something that he has seen happen. But only time will tell whether there will be a large academic demand for astronauts, and Durda is not worried about the competition. If A4H offers another way for people to get off the planet, all the better, he says, adding, "we're all in this business because we want to fly in space".

## A SHIFT IN SPACE SCIENCE

A4H's scientists will still need to find a ship, and several companies provide options. Virgin Galactic, based in Las Cruces, New Mexico, offers tourists and scientists seats on its suborbital craft *SpaceShipTwo* for \$200,000 each and claims its first flight could be as early as 2013. This year, it contracted to fly SwRI scientists into space — Durda has secured a place. Zero-G in Vienna, Virginia, also offers suborbital flights; A4H uses the company's facilities in its training programme. SpaceX in Hawthorne, California, is making a reusable vehicle to transport people and supplies into orbit, and Bigelow Aerospace in North Las Vegas, Nevada, is developing a modular space station that it hopes to launch in 2014. On 9 August, NASA awarded two-year contracts to seven companies to take technology and people on suborbital flights.

The costs of getting into orbit promise to fall to less than \$100,000 for a spot on a flight, some claim, and the number of seats and amount of lab space available will increase as more companies get their hardware working. Eventually, scientists might be able to charter a space flight for a course of experiments, much like booking a slot at a synchrotron light-source facility.

Research might include atmospheric science, exploring the effects of microgravity on human physiology or studying changes in gene expression induced by microgravity,

which could offer clues to potential drug targets. But experiments will have to be carefully crafted and expectations limited, warns Walter Peeters, dean of the International Space University in Strasbourg, France. Scientists "only have a few minutes of microgravity time", he says. Even so, he sees opportunities for pharmaceutical companies, among others.

John Pojman, a materials chemist at Louisiana State University in Baton Rouge, who researches how polymers behave in microgravity, foresees a demand for technicians to run experiments on suborbital or orbital flights. But he cautions that it isn't yet clear how such research will be financed, particularly in terms of hardware and instrument development. No major US funding agency has yet announced a programme.

Despite that, prospects for aspiring commercial astronauts are better in the United States than in Europe or elsewhere, says Jack van Loon, a gravitational biologist at the Free University in Amsterdam. "The commercial space flight that is developing is very much an American activity," he laments, noting that it is likely to generate jobs and business.

In July, A4H's first class of trainees graduated with qualifications in doing science on suborbital flights. Reimuller was among them. "I hope I will get the opportunity and I hope that I will provide returns, in terms of the data and science I bring back, that will justify the expense involved," he says.

Shiro does not claim that these astronauts for hire will be as highly qualified as NASA astronauts, but points out that it is still early days. "If our training programme gets respected enough and gets mature enough and we get enough experienced people on board," he says, "over time it could certainly become just as effective as what NASA has." ■

**Katharine Sanderson** is a freelance journalist in Toulouse, France.

## NETWORKING

## Contacts help men most

Fewer women than men secure jobs informally through workplace social contacts, a study says. Author Steve McDonald, a sociologist at North Carolina State University in Raleigh, analysed results from a US Bureau of Labor Statistics study of 3,200 people between 1979 and 1998, in which respondents specified how they made job transitions. He found that as men accumulate time in a field, they become more likely to be recruited for new jobs by their workplace contacts. Women are not recruited in the same way, possibly because their social workplace interactions focus less on work, and because their contacts don't have recruiting and hiring authority, McDonald suggests. The study will be published in *Social Science Research* in November.

## NOBEL LAUREATES

## Top status doesn't linger

Nobel laureates' celebrated status within the scientific community wanes sooner than one might expect, says a study led by Christine Charyton, a visiting neurologist at Ohio State University in Columbus. The analysis, based on citations and other metrics, shows that after a peak, most laureates' later work involving the Nobel-winning idea is no more accepted than their earliest articles. The study measured the impact of articles by 187 researchers who won Nobel Prizes in physics, chemistry or medicine between 1980 and 2009. Charyton, who presented the paper on 6 August at the American Psychological Association Convention in Washington DC, suggests that later papers expand on and diverge from the Nobel-winning idea.

## ACADEMIC-INDUSTRIAL PARTNERSHIPS

## Cooperation increases

Industrial sponsors invested US\$4.3 billion in research at US universities in 2010, up 5.6% from 2009, according to a survey of university technology-transfer activities by the Association of University Technology Managers in Deerfield, Illinois. Robin Rasor, president of the group, says that there has been an increase in partnerships because firms have cut back on in-house early-stage research to reduce costs, and are focusing on development. "Companies are looking more to universities for cutting-edge innovations," she adds. Collaborations could lead to industry jobs for PhD students and postdocs working on those innovations, says Rasor.



John Pojman of Louisiana State University works on an experiment on a low-gravity suborbital flight.

► model, admits Dan Durda, a space scientist at the SwRI, does decrease the likelihood that the rigours of flight will scare away trainees when it's time to go up, something that he has seen happen. But only time will tell whether there will be a large academic demand for astronauts, and Durda is not worried about the competition. If A4H offers another way for people to get off the planet, all the better, he says, adding, "we're all in this business because we want to fly in space".

## A SHIFT IN SPACE SCIENCE

A4H's scientists will still need to find a ship, and several companies provide options. Virgin Galactic, based in Las Cruces, New Mexico, offers tourists and scientists seats on its suborbital craft *SpaceShipTwo* for \$200,000 each and claims its first flight could be as early as 2013. This year, it contracted to fly SwRI scientists into space — Durda has secured a place. Zero-G in Vienna, Virginia, also offers suborbital flights; A4H uses the company's facilities in its training programme. SpaceX in Hawthorne, California, is making a reusable vehicle to transport people and supplies into orbit, and Bigelow Aerospace in North Las Vegas, Nevada, is developing a modular space station that it hopes to launch in 2014. On 9 August, NASA awarded two-year contracts to seven companies to take technology and people on suborbital flights.

The costs of getting into orbit promise to fall to less than \$100,000 for a spot on a flight, some claim, and the number of seats and amount of lab space available will increase as more companies get their hardware working. Eventually, scientists might be able to charter a space flight for a course of experiments, much like booking a slot at a synchrotron light-source facility.

Research might include atmospheric science, exploring the effects of microgravity on human physiology or studying changes in gene expression induced by microgravity,

which could offer clues to potential drug targets. But experiments will have to be carefully crafted and expectations limited, warns Walter Peeters, dean of the International Space University in Strasbourg, France. Scientists "only have a few minutes of microgravity time", he says. Even so, he sees opportunities for pharmaceutical companies, among others.

John Pojman, a materials chemist at Louisiana State University in Baton Rouge, who researches how polymers behave in microgravity, foresees a demand for technicians to run experiments on suborbital or orbital flights. But he cautions that it isn't yet clear how such research will be financed, particularly in terms of hardware and instrument development. No major US funding agency has yet announced a programme.

Despite that, prospects for aspiring commercial astronauts are better in the United States than in Europe or elsewhere, says Jack van Loon, a gravitational biologist at the Free University in Amsterdam. "The commercial space flight that is developing is very much an American activity," he laments, noting that it is likely to generate jobs and business.

In July, A4H's first class of trainees graduated with qualifications in doing science on suborbital flights. Reimuller was among them. "I hope I will get the opportunity and I hope that I will provide returns, in terms of the data and science I bring back, that will justify the expense involved," he says.

Shiro does not claim that these astronauts for hire will be as highly qualified as NASA astronauts, but points out that it is still early days. "If our training programme gets respected enough and gets mature enough and we get enough experienced people on board," he says, "over time it could certainly become just as effective as what NASA has." ■

**Katharine Sanderson** is a freelance journalist in Toulouse, France.



## COLUMN

# Courting connections

In the search for a job, contacts matter. **Peter J. Feibelman** explains how to assemble a personal ‘old boy’ network while still a PhD student or postdoc.

When job openings are scarce, an advertisement for a research position is likely to attract dozens, even hundreds, of applications. Will they all be read? It's unlikely. And this raises questions: how can you expect to be invited for an interview if your painstakingly written application letter is not seriously reviewed? How can you ensure that your CV will get to the top of the pile and be read — and that you will have at least a chance to vie for the job?

A good way to start is to determine how others have succeeded — and to reflect on whether you can follow their approach. You might be tempted to dismiss that idea, attributing your predecessors' good fortune to the legendary ‘old boy’ network, to which you do not belong. This is not an unreasonable thought; connections to established scientists are often helpful. Whether spontaneous or requested, a timely, enthusiastic call from your successful colleague's prominent supervisor or mentor to a prospective employer may well have led to an interview invitation.

Still, wallowing in envy will not improve your job prospects. A more effective approach, if you can muster the psychological resources, is to throw off passivity, self-doubt and self-pity, and adopt the active mode. Ask yourself how you can establish a network of your own. You can do it by drawing attention to your abilities and accomplishments, and by starting early enough that people will get to know you as a scientific colleague, not just another job seeker.

You can begin at your desk. Have you read a stimulating paper related to your work? Has it raised compelling questions? Could interacting with the author help you to make progress? If the answer to any of these is yes, try initiating an e-mail exchange with him or her. Not only could you learn something that has a bearing on your current research, but when you start looking for a job, your correspondent might recall your inquiry or critique, and be willing to work on your behalf.

On the home front, you could lead a journal-club session on a paper that you have found exciting. Run the topic past someone more experienced — perhaps a researcher working in a related area — and, if his or her response is encouraging, ask for time to make

a departmental presentation. That will be good practice in any case; it never hurts to polish your speaking skills. More importantly, your scientific leadership will be perceived as valuable. You can win respect and support by alerting colleagues to significant results, or by persuasively arguing for a new research direction.

In a university or lab, communication tends to happen within groups rather than between them, so you and your organization stand to

conference, scan the abstracts — they are probably available on the Internet. Pick out those most relevant to your interests, then download recent papers by their authors. Go to the gathering with questions, and meet selected speakers after their sessions end. Tell them what you have been doing — what issues your research has already resolved, what still baffles you — and ask them if they would have time for a chat.

Will you be travelling? Is there a lab near your destination at which you might like to work one day? Perhaps you can arrange to visit. Or, if you are staying at home, you could send a note asking to spend a week or a month there during the summer. Depending on the host lab's policy, they might let you visit informally for a few days or weeks, or ask you to apply for an internship. If you do arrange a stay, and make a positive impression, your chances of landing a job later are likely to improve. It is easier for an employer to hire someone whom he or she has met and sized up, than someone who has come for a brief interview, and whose recommendations might be inflated. Aim to be the person that your potential employer already knows.

The theme connecting these ideas is that the way to gain recognition as a scientist is to act like one. Although being in the lab or at your computer is necessary for your research project, budgeting time week-to-week to engage with the scientific community at home and on the outside is not a diversion but an essential activity, part of the life of every working scientist. It is also how you establish your own old boy network.

Do not imagine that you can lock yourself in a lab or office until your research project is almost complete, then burst successfully onto the job market in the few months before your pay cheque stops coming. That is a recipe for stress, not for landing an interview. It is better to court invitations to apply for the research job you would like — and a successful courtship is not an overnight project. ■

*Theoretical physicist **Peter J. Feibelman** works and resides in Albuquerque, New Mexico. This column is adapted from the revised edition of his book *A PhD Is Not Enough!* (Basic Books, 2011).*



profit if you can encourage interaction across group or departmental divisions. Set aside time to learn what people outside your group are working on — they will be pleased by your interest. Attend their seminars and talks. If your expertise might be of use to them, engage them in dialogue. When you solicit recommendation letters, they will know who you are and what you have to offer.

Scientific meetings are opportunities to publicize your research results, to learn what others are doing and to broaden your perspective. They are also a prime venue for meeting potential employers. Before you attend a



# OUT OF THE BLUE

Reality check.

BY MOHAMAD ATIF SLIM

“Yargh-thr! You Chinese?” The ten-eyed Gorgon stared at me, drunk.

“No, I’m Malay.”

“Wussat?” His spittle flew like rockets.

“Human subclass.”

“Human? You sure you’re not Chinese?”

Goo oozed from one corner of his mouth.

I gave him a sympathetic look. This is why I don’t drink. “You should go home. Wife might be worried.”

“Wife? What wife?” All ten eyes went blank, then bulged in recognition. “Oh. Yargh!”

I left the bar by the back door. On a crowded night like this, usually, if one alien picks on you, the rest will too. Lone human in the bar, let’s ask him if he speaks Chinese and eats carrots, if he can get us bootleg ethanol. But I guess I can’t blame them — the Chinese were the first humans to venture out to space since First Contact, after all. Still, you’d think the rest of the Universe would grow out of stereotyping minorities — I don’t think I’ve ever met a carrot-eating Chinese in my whole life.

Outside the bar, it was quieter. The Chicken Nebula — named after an extinct legendary beast from Old Earth, I was told — shone like a parade of angel starships in the blue interstellar sky.

I pulled out my banjo, leaned against the dingy wall of the building, and started plucking a few chords.

That was when Shankarlatti appeared.

“Hello, stranger.”

I looked up and saw her standing.

“Why, hello there,” I said, taking my hat off.

She smiled. “You’re quite the gentleman.”

“My auntie brought me up after my parents died in a drowning skyscraper, taught me all I need to know. Brush your teeth, eat your legumes, and most of all respect women ... particularly ...”

“Particularly ...?”

“Say, are you ...?”

“Part-human?” Each blue tooth stood out like the ridge of a knuckle in her grin. “I am.” She twirled around, as if to prove she wasn’t hiding a tail or an extra head somewhere. “I saw you there, lone cowboy, thought I’d say hello. Rare to see another human — full human, especially — in this sector, you know.

“But you must know, of course.”

Well I did, and I also knew why she was *really* here. I’ve been approached by girls like Shankarlatti too many times not to know immediately what the deal is before they even breathe the ‘h’ in their ‘hello’. The



hair pulled tight into a neat bun. Old-fashioned aluminium tweed coat. Horn-rimmed glasses. The pile of books under her left arm. Crafty lips, like she had debated her way out of her mama’s womb. The pens in her skirt pocket. Oldest profession in the Universe.

“Like what you see?” She twirled again, then took out a pen, as if to make a point.

I clicked my tongue. “Sorry, ma’am. I mean no offence — you’re a very pretty lady, you are — but, unfortunately for you, I’m Muslim.”

Shankarlatti seemed momentarily stunned. Then she burst out laughing. “Are you really?” she asked, disbelieving. “A Muslim cowboy? Well I’ll be damned. Did your auntie bring you up to be the generic human poster boy?”

“Afraid she did, butt of everyone’s jokes back in school.” The way I said it, it was as though she had just given me a compliment.

She paused, eyeing my features. “Don’t tell me you’re Chinese, too?”

“No, I’m not, but —” I twanged my banjo almost guiltily — “I am a country singer.”

That seemed to make some fireworks inside her sputter and explode. She laughed so hard, she dropped all her books: *Astro-physiology of the Pleiadean 298th Century*, *Martian Art History through the Lightyears*, *Cosmo Sutra* ...

“As one does, I sing about religion and sex after marriage, too,” I added, gratefully soaking in every inflection in her laughter, every crease of reaction in her face. I’ve always known I was a walking stereotype — just

short of the right subclass to meet the alien encyclopaedic definition of humanness. Trying to hide who I was

from my friends (who were all aliens) was pretty difficult, especially having to pray five times a day, so I’ve got used to being everyone’s favourite punchline.

But to meet someone who can laugh at me — not *mockingly*, but *appreciatively*, and not in expectant surprise, but with an utterly pleasant manner of shock — was new.

Wonderful.

Exciting.

Incredible, even.

Shankarlatti was clutching her stomach, laughter now fading into hiccupy sobs. Finally, she straightened up. “I didn’t mean to laugh at you. I’m sorry.”

“You don’t have to be, I laugh at myself too sometimes. Heck, when I told my auntie I was going to be a country singer, she almost passed out — there isn’t a human who’d want to do country music these days if he weren’t a parody of himself.”

Shankarlatti had picked up all her books. “I guess you haven’t made it anywhere yet?”

“Tried all seven sectors, ma’am. Am still trying,” I said, striking a chord on my banjo, as if to prove that I was.

“Well, you keep trying, aspiring human country singer. If I hear you on the space-waves, I’ll buy your album.”

“I’d appreciate that.” There was a momentary silence between us, more filled with a comfortable timidity than awkwardness.

“Hey, I know a place just two lightstops from here,” she said, finally. “You want to get coffee or something?”

“I’d be happy to,” I responded, almost too quickly, then made up for it, as quickly. “I’m sorry, ma’am, I forgot to introduce myself — name’s Yismaël.”

Her azure dentals flashed again. “Yismaël, I’m Shankarlatti.”

*Shan-kar-la-ti*, I pronounced in my head, letting each viscous syllable ring full. My heart gave a whoop.

“Shankarlatti,” I repeated. “Like the butterfly?”

“Like the butterfly.” She extended her hand. “Come.” I hesitated. “Anything wrong?” she asked.

“No. It’s just that I think I want to write a song about you. And I think I’ve got a tune already.”

“What’re you going to call it?”

“*Out of the blue*.” ■

**Mohamad Atif Slim** is originally from Malaysia. He lives in New Zealand, where he is a fourth-year medical student.

JACEY

# Continued clearance of apoptotic cells critically depends on the phagocyte Ucp2 protein

Daeho Park<sup>1,2</sup>, Claudia Z. Han<sup>1,2,3</sup>, Michael R. Elliott<sup>1,2</sup>, Jason M. Kinchen<sup>1,2,3</sup>, Paul C. Trampont<sup>1,2</sup>, Soumita Das<sup>4</sup>, Sheila Collins<sup>5</sup>, Jeffrey J. Lysiak<sup>6</sup>, Kyle L. Hoehn<sup>7</sup> & Kodi S. Ravichandran<sup>1,2,3</sup>

**Rapid and efficient removal of apoptotic cells by phagocytes is important during development, tissue homeostasis and in immune responses<sup>1–5</sup>. Efficient clearance depends on the capacity of a single phagocyte to ingest multiple apoptotic cells successively, and to process the corpse-derived cellular material<sup>6</sup>. However, the factors that influence continued clearance by phagocytes are not known. Here we show that the mitochondrial membrane potential of the phagocyte critically controls engulfment capacity, with lower potential enhancing engulfment and vice versa. The mitochondrial membrane protein Ucp2, which acts to lower the mitochondrial membrane potential<sup>7–9</sup>, was upregulated in phagocytes engulfing apoptotic cells. Loss of Ucp2 reduced phagocytic capacity, whereas Ucp2 overexpression enhanced engulfment. Mutational and pharmacological studies indicated a direct role for Ucp2-mediated mitochondrial function in phagocytosis. Macrophages from Ucp2-deficient mice<sup>10,11</sup> were impaired in phagocytosis *in vitro*, and Ucp2-deficient mice showed profound *in vivo* defects in clearing dying cells in the thymus and testes. Collectively, these data indicate that mitochondrial membrane potential and Ucp2 are key molecular determinants of apoptotic cell clearance. As Ucp2 is linked to metabolic diseases and atherosclerosis<sup>11,12</sup>, this newly discovered role for Ucp2 in apoptotic cell clearance has implications for the complex aetiology and pathogenesis of these diseases.**

When a phagocyte engulfs a dying cell it essentially doubles its cellular contents. Yet phagocytes often ingest multiple apoptotic cells sequentially, and the factors regulating the ‘engulfment capacity’ of a given phagocyte are not understood. Because metabolites derived from the ingested apoptotic cells could influence phagocyte mitochondrial function, we asked whether the phagocyte mitochondrial membrane potential is altered. Phagocytes labelled with the dyes JC-1 (the red-to-green fluorescence ratio of which depends on mitochondrial membrane potential<sup>13</sup>; Supplementary Fig. 1a) or TMRE were incubated with apoptotic thymocytes for different periods of time. To focus on phagocytes with ingested targets, the thymocytes were labelled with cypHer5E, a pH-dependent dye for which the fluorescence increases after the apoptotic corpse enters the acidic phagolysosome. There was a significant increase in the relative mitochondrial membrane potential in phagocytes with engulfed targets (1.99-fold  $\pm$  0.11,  $P < 0.001$ ,  $n = 6$ ) compared to non-engulfing phagocytes within the same population (Fig. 1a and Supplementary Fig. 1b). The enhanced mitochondrial membrane potential was not derived from the apoptotic thymocytes (Supplementary Fig. 1c). Remarkably, phagocytes ingesting synthetic targets showed no increase in mitochondrial membrane potential (Fig. 1a and Supplementary Fig. 1b), even though the synthetic targets use components of the apoptotic cell engulfment machinery<sup>14</sup>. As the synthetic targets do not have a metabolic load, the higher mitochondrial membrane potential could not be attributed to a general effect of engulfment. The mitochondrial membrane potential returned

to baseline over the next few hours (Fig. 1b). In general, cellular ATP levels are maintained within a fairly narrow range and the engulfing phagocytes had a modest 10% increase in cellular ATP at the 2-h point (Supplementary Fig. 1d). Therefore, the return to baseline of the mitochondrial membrane potential within phagocytes suggested a mechanism for uncoupling nutrient oxidation from ATP generation<sup>8</sup>.

A well-known mechanism for uncoupling the proton gradient and ATP generation is mediated by uncoupling proteins (UCPs)<sup>8</sup>. UCPs regulate the mitochondrial membrane potential through dissipation of the proton gradient across the inner mitochondrial membrane, without ATP generation. Compared to Ucp1 (restricted to brown adipose tissue)<sup>15</sup>, Ucp2 is more ubiquitously expressed<sup>8</sup>, with expression also occurring in several phagocytic cell types (Supplementary Fig. 2a). Whereas messenger RNA levels of *Ucp2* were not detectably altered within engulfing phagocytes, mitochondrial Ucp2 protein levels increased after incubation with apoptotic cells (Fig. 1c, left, and Supplementary Fig. 2b, c). The higher Ucp2 protein levels were not derived from ingested targets, as Ucp2 levels in thymocytes were below detection, and *Ucp2*-deficient apoptotic thymocytes used as targets also enhanced Ucp2 protein levels in phagocytes (Fig. 1c and Supplementary Fig. 2d). The synthetic targets did not induce higher levels of Ucp2, consistent with their lack of effect on mitochondrial membrane potential (Fig. 1c, right).

To test directly the role of Ucp2 in engulfment, we knocked down endogenous *Ucp2* expression in phagocytes via short interfering RNA (siRNA) (Supplementary Fig. 1e). *Ucp2* knockdown in NIH/3T3 cells led to increased mitochondrial membrane potential basally and during engulfment (Fig. 1d and Supplementary Fig. 2f). We observed two key phenotypes in Ucp2-depleted cells. First, *Ucp2* knockdown phagocytes were less efficient engulferers, with a lower percentage of phagocytes ingesting apoptotic cells over a 6-h time course (Fig. 1e, left). Second, *Ucp2* knockdown reduced the phagocytic ‘capacity’ with a lower amount of apoptotic material being ingested per phagocyte (mean fluorescence intensity derived from the labelled apoptotic cells) (Fig. 1e, right). Again, the uptake of synthetic targets was unaffected by *Ucp2* knockdown (Fig. 1f). These data indicated that phagocytes engulfing apoptotic cells upregulate Ucp2 and that Ucp2 expression influences phagocytic capacity.

To test whether overexpressing Ucp2 might provide a ‘gain of function’ for engulfing apoptotic cells, we transiently overexpressed Flag-tagged Ucp2 in LR73 phagocytes. Ucp2-Flag was properly targeted to the mitochondria (Supplementary Fig. 3a, b), and Ucp2-Flag cells showed three striking phenotypes. First, a greater percentage of Ucp2-Flag cells ingested apoptotic cells, and this enhanced uptake depended on the known engulfment machinery components (Fig. 2a and Supplementary Fig. 4a, b). Second, in a time course, Ucp2-Flag cells continued to ingest apoptotic targets for up to 6 h whereas control-transfected LR73 cells reached a plateau by 2 h (Fig. 2b). Ucp2-overexpressing cells had

<sup>1</sup>Center for Cell Clearance, University of Virginia, Charlottesville, Virginia 22908, USA. <sup>2</sup>Beirne B. Cater Center for Immunology Research, University of Virginia, Charlottesville, Virginia 22908, USA.

<sup>3</sup>Department of Microbiology, University of Virginia, Charlottesville, Virginia 22908, USA. <sup>4</sup>Department of Medicine, University of Virginia, Charlottesville, Virginia 22908, USA. <sup>5</sup>Diabetes and Obesity Research Center, Sanford-Burnham Medical Research Institute, Orlando, Florida 32827, USA. <sup>6</sup>Department of Urology, University of Virginia, Charlottesville, Virginia 22908, USA. <sup>7</sup>Department of Pharmacology and CVRC, University of Virginia, Charlottesville, Virginia 22908, USA.

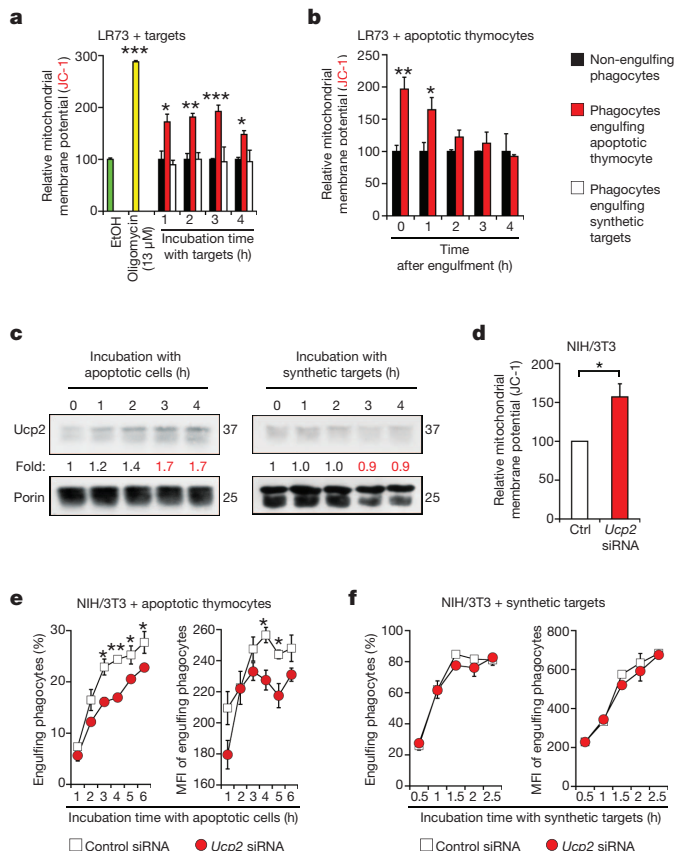


**Figure 1 | Modulation of mitochondrial membrane potential and Ucp2 during engulfment.** **a**, Increase in mitochondrial membrane potential in engulfing phagocytes. LR73 phagocytes were stained with JC-1 and incubated with cypHer5E-labelled apoptotic thymocytes or synthetic targets. Mitochondrial membrane potentials in engulfing and non-engulfing phagocytes within the same population (based on cypHer5E and Pacific blue signal) were compared. Oligomycin-treated phagocytes served as a positive control for increased mitochondrial membrane potential. **b**, LR73 cells were incubated with cypHer5E-stained apoptotic thymocytes (3 h), washed to remove unengulfed targets, and further incubated for the indicated times, stained with JC-1 dye and analysed as above. **c**, LR73 cells were incubated with targets (apoptotic thymocytes from *Ucp2* knockout mice or synthetic targets), and the mitochondrial fractions were immunoblotted for endogenous Ucp2. The mitochondrial membrane protein porin served as loading control. **d**, Mitochondrial membrane potential in control (Ctrl) or *Ucp2* siRNA transfected NIH/3T3 (2 days post-transfection) was determined via JC-1 dye and flow cytometry. **e**, **f**, NIH/3T3 cells transfected with control or *Ucp2*-specific siRNA were incubated with apoptotic thymocytes stained with the dye TAMRA (**e**) or synthetic targets (**f**) and the percentage of cells engulfing targets (left) and phagocytic capacity (using the apoptotic-cell-derived fluorescence per phagocyte) were determined. Data are shown as mean  $\pm$  standard deviation (s.d.) and are representative of at least two independent experiments. \* $P < 0.05$ , \*\* $P < 0.01$ , \*\*\* $P < 0.001$ .

more ingested apoptotic cells per phagocyte (Fig. 2c, d). Third, the rate of uptake of synthetic targets was unaffected in *Ucp2*-Flag cells (Supplementary Fig. 4c), suggesting a role for Ucp2 in sensing the metabolic load derived from apoptotic cells. Overexpression of Ucp2 homologues (Ucp1 or Ucp3; Supplementary Fig. 4d) also promoted engulfment. Thus, higher levels of Ucp2 provide a gain-of-function phenotype, conferring a capacity for phagocytes to 'continue to eat' apoptotic cells.

*Ucp2*-Flag cells showed decreased mitochondrial membrane potential compared to controls (Fig. 2e). The signal for MitoTracker, a dye that accumulates as the mitochondrial membrane potential increases<sup>16</sup>, was distinctly weaker in *Ucp2*-Flag-expressing cells compared to neighbouring non-transfected cells (Fig. 2f). The drug genipin, which inhibits mitochondrial uncoupling by Ucp2 (ref. 17), blunted the

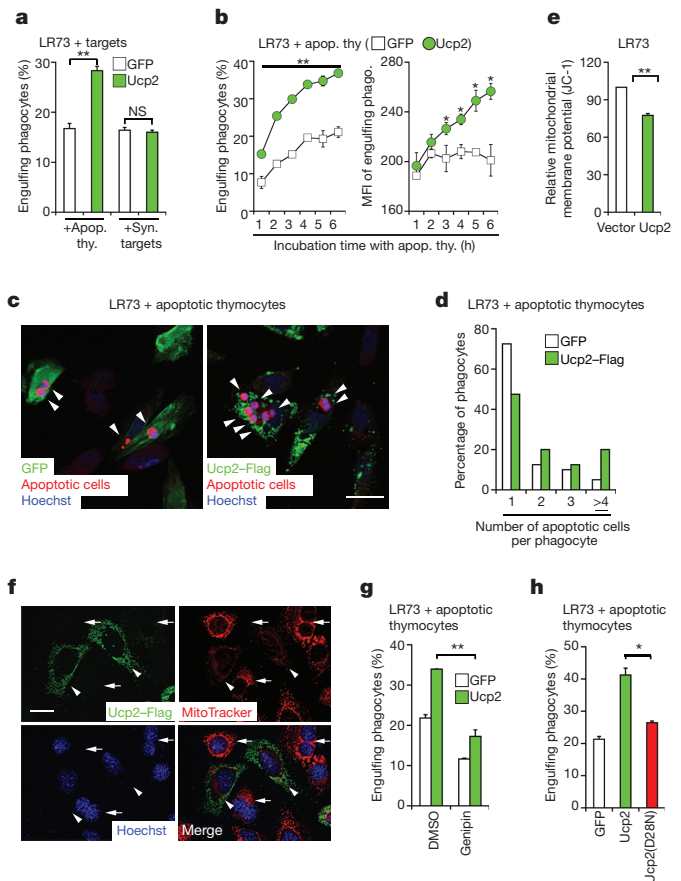


**Figure 2 | Ucp2 overexpression promotes continued uptake of apoptotic cells.** **a**, LR73 cells transfected with Ucp2 show enhanced uptake of apoptotic thymocytes (Apop. thy.) but not synthetic targets (Syn. targets). NS, not significant. **b**, LR73 cells expressing GFP or Ucp2 were incubated with TAMRA-stained apoptotic thymocytes for the indicated times, and the percentage (left) and mean fluorescence intensity of engulfing phagocytes, which reflects the ability to continue to ingest apoptotic cells (right), are shown. **c**, Comparison of LR73 cells transfected with GFP alone or Ucp2-Flag engulfing TAMRA-stained apoptotic thymocytes (4 h) assessed by confocal microscopy. Arrowheads indicate engulfed apoptotic thymocytes. Scale bar, 20  $\mu$ m. **d**, Forty randomly chosen fields from **c** were counted, and the percentage of phagocytes with the indicated number of internalized apoptotic cells is shown. **e**, Mitochondrial membrane potential of LR73 cells transfected with Ucp2 or control vector. **f**, Fluorescence microscopy of NIH/3T3 cells transfected with Ucp2-Flag and stained with MitoTracker and anti-Flag antibody. Arrowheads indicate NIH/3T3 cells expressing Ucp2-Flag and arrows indicate non-transfected cells. Scale bar, 20  $\mu$ m. **g**, LR73 phagocytes expressing GFP or Ucp2 were pre-treated with vehicle control or genipin (100  $\mu$ M) for 1 h and assessed for engulfment. **h**, Ucp2(D28N) mutant fails to enhance engulfment of apoptotic thymocytes. Data are shown as mean  $\pm$  s.d. and are representative of at least three independent experiments. \* $P < 0.05$ , \*\* $P < 0.01$ .

enhanced engulfment by Ucp2 (Fig. 2g and Supplementary Fig. 4e). As a parallel approach, we generated a *Ucp2*(D28N) mutant with decreased uncoupling activity<sup>18,19</sup>. The *Ucp2*(D28N) mutant was expressed and localized to the mitochondria (as did wild type), yet *Ucp2*(D28N) failed to enhance engulfment of apoptotic cells (Fig. 2h and Supplementary Fig. 4f). Collectively, the decrease in mitochondrial membrane potential by Ucp2 correlates with enhanced and continued uptake of apoptotic cells.

We then asked whether the effect of Ucp2 could be mimicked by synthetic uncouplers that lower the mitochondrial membrane potential<sup>20,21</sup>. We tested 2,4-dinitrophenol (2,4-DNP) and carbonyl cyanide 4-(trifluoromethoxy)phenylhydrazone (FCCP) over a range of concentrations at which the total cellular ATP levels were unaltered and



the phagocytes appeared morphologically similar to controls (Supplementary Fig. 5a, b). Both 2,4-DNP and FCCP significantly enhanced the uptake of apoptotic thymocytes by LR73 phagocytes (Fig. 3a); this increased uptake correlated with decreased mitochondrial membrane potential induced by these drugs (Supplementary Fig. 5c, d). Synthetic uncoupling also promoted phagocytes to continue to ingest multiple apoptotic cells over a time course (similar to Ucp2 overexpression) (Fig. 3b, c and Supplementary Fig. 5g). To test whether mitochondrial membrane potential itself was the signal for enhanced engulfment capacity—that is, independent of increased proton leak and electron transport chain flux—we tested sodium azide, an inhibitor of complex IV of the electron transport chain that slows electron transport flux and lowers mitochondrial membrane potential.

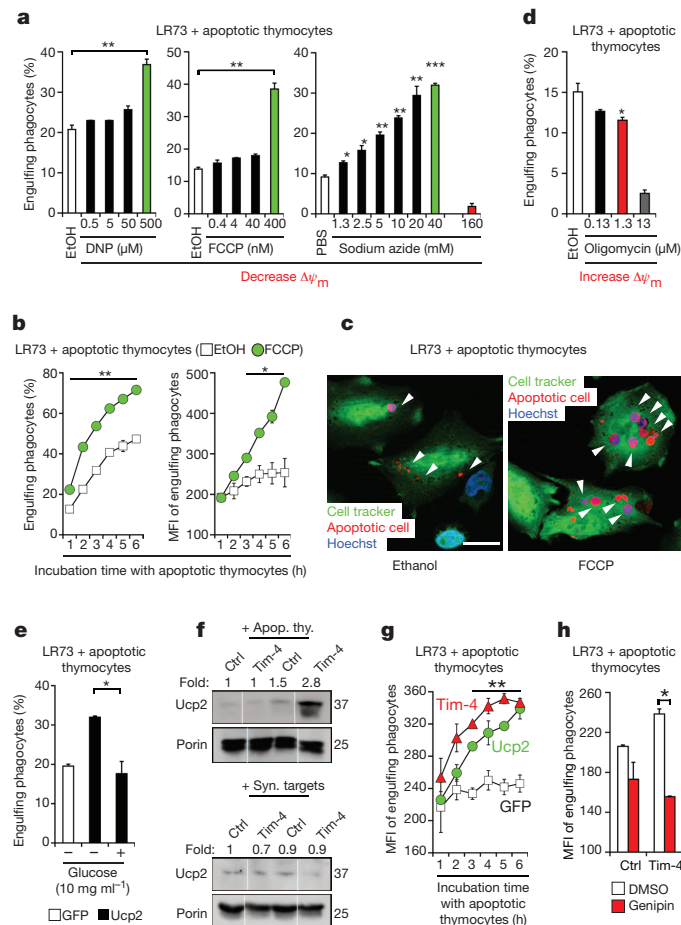


**Figure 3 | Ucp2 links mitochondrial membrane potential to engulfment of apoptotic cells.** **a**, LR73 cells pre-treated with synthetic uncouplers DNP (left), FCCP (middle), or the electron transport chain inhibitor  $\text{Na}_3\text{N}$  (right) or vehicle control were assessed for engulfment. **b**, LR73 cells pre-treated with FCCP were incubated with apoptotic thymocytes and the percentage of phagocytes engulfing targets (left) and the MFI of engulfing phagocytes (right) are shown. **c**, Engulfment by FCCP-treated LR73 cells determined by confocal microscopy. Arrowheads indicate engulfed apoptotic thymocytes. Scale bar, 20  $\mu\text{m}$ . **d**, Apoptotic cell engulfment by LR73 cells pre-treated with oligomycin to increase mitochondrial membrane potential. **e**, LR73 cells transfected with GFP or Ucp2 were assessed for engulfment in the presence or absence of  $10 \text{ mg ml}^{-1}$  glucose. **f**, LR73 cells stably overexpressing vector control or Tim-4 were incubated with apoptotic thymocytes (top) or synthetic targets (bottom) for 3 h and the levels of endogenous Ucp2 in mitochondrial fractions are shown. **g**, Continued uptake of apoptotic thymocytes by Tim-4- and Ucp2-overexpressing cells (compared to GFP-transfected cells that reach a plateau) was determined by the MFI of phagocytes over a time course of engulfment. **h**, The increased uptake of apoptotic thymocytes by Tim-4-overexpressing cells was inhibited by genipin. Data are shown as mean  $\pm$  s.d. and are representative of at least two independent experiments. \* $P < 0.05$ , \*\* $P < 0.01$ , \*\*\* $P < 0.001$ .

At sodium azide concentrations that did not affect cellular ATP levels, it enhanced engulfment with a progressive decrease in the mitochondrial membrane potential (Fig. 3a and Supplementary Fig. 5e, f). Higher sodium azide concentrations that lower cellular ATP levels did block engulfment (an ATP-dependent process) (Fig. 3a and Supplementary Fig. 5f).

We next asked whether raising the mitochondrial membrane potential would dampen engulfment. Oligomycin, an inhibitor of ATP synthase, increased the mitochondrial membrane potential within phagocytes and strongly inhibited engulfment (Fig. 3d). The concentration of oligomycin used here affected the mitochondrial membrane potential but did not alter cellular ATP levels (Supplementary Fig. 5h, i). To test whether modulating the metabolic state of the phagocytes would affect apoptotic cell engulfment, we cultured phagocytes in glucose-free medium that decreased mitochondrial membrane potential, and in turn enhanced apoptotic cell engulfment (Supplementary Fig. 6a, b). Conversely, excess glucose (leading to higher mitochondrial membrane potential) reversed the effect of Ucp2 overexpression or FCCP (Fig. 3e and Supplementary Fig. 6c–e). Thus, the mitochondrial membrane potential within phagocytes is a critical determinant in regulating phagocytic capacity and continued uptake by phagocytes.

Increased metabolic load in phagocytes during engulfment may affect many aspects of metabolism. As Ucp2 is known to increase  $\beta$ -oxidation and decrease reactive oxygen species (ROS) production<sup>8</sup>, perhaps excess cellular lipids or ROS feedback could slow down the engulfment pathway. Incubating phagocytes with apoptotic thymocytes (but not synthetic targets) increased the rate of fatty acid oxidation (Supplementary Fig. 7a, b); however, both Ucp2-overexpressing cells and Ucp2-deficient phagocytes showed higher fatty acid oxidation rates (Supplementary Fig. 7c, d), yet they have opposite phenotypes in apoptotic cell engulfment. This suggested that the possible effect of Ucp2 on lipid oxidation alone is not a major regulator of apoptotic cell clearance.

Ucp2 has also been shown to decrease ROS levels, which could be a potential mechanism by which Ucp2 promotes continued engulfment. However, increasing phagocyte mitochondrial ROS levels via the drugs rotenone or antimycin A (blocking complexes I or III within the electron transport chain, respectively) did not decrease apoptotic cell engulfment (Supplementary Fig. 8a, b). Rather, these drugs modestly increased phagocytosis, probably owing to the decreased mitochondrial membrane potential. Furthermore, ameliorating ROS with FCCP, overexpression of the mitochondrial antioxidant enzyme superoxide dismutase 2 (SOD2), or scavenging ROS with well-known scavengers (Tiron or MitoTEMPO) did not increase engulfment (Supplementary Fig. 8a–g). PGC1 $\alpha$ , the master transcription factor for mitochondrial biogenesis, was not altered during engulfment and overexpressing PGC1 $\alpha$  did not promote engulfment of apoptotic cells (data not shown and Supplementary Fig. 8h). Moreover, neither the AMPK nor the mTOR signalling pathways were activated during engulfment (Supplementary Fig. 8i, j). While these data cannot rule out a contribution of  $\beta$ -oxidation and ROS, they could not provide a mechanistic reason for Ucp2 function during apoptotic cell engulfment. Ucp2-mediated regulation of the phagocyte mitochondrial membrane potential seemed to correlate best with continued phagocytosis of apoptotic cells.

To determine whether signalling via specific engulfment receptors may link to Ucp2/mitochondrial signalling, we generated LR73 cells overexpressing the phosphatidylserine receptor Tim-4 (LR73<sup>Tim-4</sup> cells). Tim-4 overexpression led to increased apoptotic cell engulfment<sup>6,22,23</sup>. Three lines of data indicated a link between Tim-4-mediated apoptotic cell recognition and Ucp2. First, although there was no difference in the basal Ucp2 level between control and LR73<sup>Tim-4</sup> cells, the latter upregulated Ucp2 to a higher level (Fig. 3f, top). Importantly, synthetic targets did not increase Ucp2 expression, even though Tim-4 overexpression promotes uptake of synthetic targets (Fig. 3f, bottom). Second, LR73<sup>Tim-4</sup> cells continued to take up multiple apoptotic cells (as indicated by mean fluorescence intensity (MFI)), consistent with

the increased upregulation of Ucp2 and the phenocopying of LR73 cells transfected with Ucp2 (Fig. 3g). Third, the Ucp2 inhibitor genipin blocked Tim-4-mediated enhanced uptake (Fig. 3h). We also tested whether synthetic uncoupling or Ucp2 overexpression affected Tim-4 levels. However, surface expression of endogenous Tim-4 or haemagglutinin-tagged (HA)-Tim-4 was unaffected by Ucp2 overexpression, Ucp2 deficiency, synthetic uncoupling or by scavenging ROS (Supplementary Fig. 9a–e). These data indicate a link between apoptotic cell recognition at the membrane and the mitochondrial membrane potential of phagocytes, with Ucp2 serving as a molecular intermediate.

We next addressed the relative importance of Ucp2 in apoptotic cell clearance *in vivo* using Ucp2-deficient mice<sup>10,12</sup>. Bone-marrow-derived macrophages (BMDMs) from Ucp2<sup>-/-</sup> mice had a higher mitochondrial membrane potential compared to controls (Fig. 4a). *In vitro*, BMDMs from Ucp2<sup>-/-</sup> mice consistently showed lower phagocytic capacity for apoptotic cells (Fig. 4b), but no defect in uptake of synthetic targets, live or dead bacteria, or zymosan particles (Fig. 4c and Supplementary Fig. 10a–f). This suggested that use of Ucp2 for apoptotic cell clearance is dependent both on the metabolic load (absent in synthetic targets) and on the nature of phagocytosis (for example,

bacteria and yeast that do carry a metabolic load are taken up via other types of phagocytic receptors). There was residual engulfment in Ucp2-null phagocytes, which may in part be due to the upregulation of Ucp3 seen in 6-day cultures of cells from Ucp2<sup>-/-</sup> mice (Supplementary Fig. 11a–c).

We next asked how Ucp2<sup>-/-</sup> phagocytes clear apoptotic cells when a significant population of cells within a tissue are undergoing apoptosis. Injection of dexamethasone induces rapid and synchronous death of thymocytes, and the subsequent clearance of apoptotic thymocytes by resident phagocytes can provide a quantitative *in vivo* model of apoptotic cell clearance<sup>24</sup>. Whereas control mice show a decrease in overall thymic size at 6 h after dexamethasone injection, Ucp2<sup>-/-</sup> mice showed only a limited reduction in thymic size after dexamethasone injection (Fig. 4d). The absolute number of cells confirmed that dexamethasone-injected Ucp2<sup>-/-</sup> mice had much higher total thymic cell numbers compared to controls (Fig. 4e). Ucp2<sup>-/-</sup> thymocytes underwent apoptosis comparable to control littermates (Supplementary Fig. 12a, b); moreover, the migration of monocytes or macrophages towards find-me signals from apoptotic cells was unaffected by Ucp2 levels or mitochondrial uncoupling (Supplementary Fig. 13a–e).

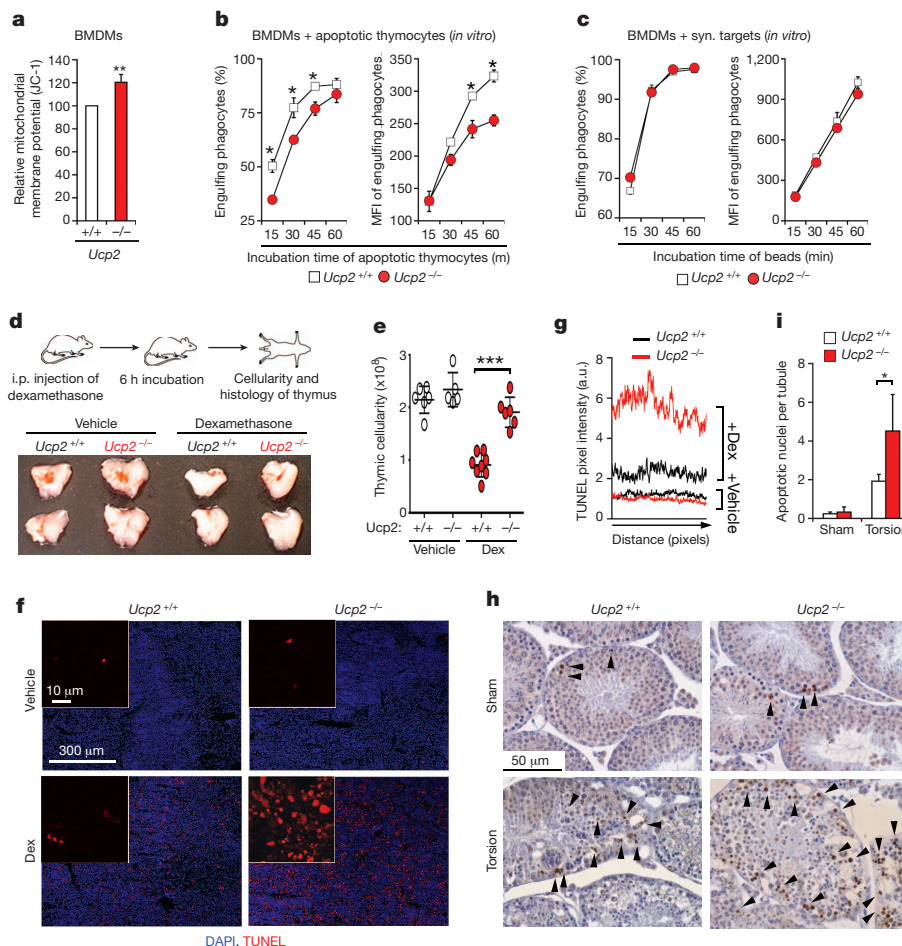


**Figure 4 | Impaired clearance of apoptotic cells in Ucp2-deficient mice.**

**a**, Mitochondrial membrane potential of BMDMs from Ucp2<sup>+/+</sup> and Ucp2<sup>-/-</sup> mice assessed by JC-1 staining. **b**, Engulfment of TAMRA-labelled apoptotic thymocytes by BMDMs from Ucp2<sup>+/+</sup> and Ucp2<sup>-/-</sup> mice was assessed over a time course. The less pronounced effect of BMDM cultures could be due to compensatory Ucp3 upregulation (see Supplementary Fig. 11). **c**, Comparable engulfment of synthetic targets by BMDMs from Ucp2<sup>+/+</sup> and Ucp2<sup>-/-</sup> mice. **d**, Top, schematic of the assay for assessing clearance of apoptotic thymocytes *in vivo*. i.p., intraperitoneal. Bottom, photographs of representative thymuses from Ucp2<sup>+/+</sup> and Ucp2<sup>-/-</sup> mice treated with vehicle or dexamethasone. **e**, Total thymic cellularity of thymuses from Ucp2<sup>+/+</sup> and Ucp2<sup>-/-</sup> mice

treated with dexamethasone (Dex) for 6 h. *n* = 5 to ~8 mice per group. **f**, Cryosections of thymuses from Ucp2<sup>+/+</sup> and Ucp2<sup>-/-</sup> mice treated with dexamethasone stained with TUNEL (red) and 4',6-diamidino-2-phenylindole (DAPI; blue). **g**, Histogram of TUNEL staining from thymic sections in **f**. Data were averaged from 9 slices of thymus and 3 mice per group. **h**, **i**, Staining of apoptotic nuclei in testes sections (specifically the seminiferous tubules), showing increased numbers of apoptotic germ cells in Ucp2<sup>-/-</sup> mice after testicular torsion. The average number of apoptotic cells per tubule was quantified from 4 slices of each testis and from 2 to ~3 mice per group. Data are shown as mean ± s.d. and are representative of at least two independent experiments. \*P < 0.05, \*\*P < 0.01, \*\*\*P < 0.001.

Thus, the increased thymic cellularity in dexamethasone-treated *Ucp2*<sup>-/-</sup> mice resulted from defective clearance. The thymuses of dexamethasone-treated *Ucp2*<sup>-/-</sup> mice consistently had higher levels of unengulfed corpses by TdT-mediated dUTP nick end labelling (TUNEL) and a threefold increase in TUNEL fluorescence, without altered density of F4/80-positive cells (Fig. 4f, g and Supplementary Fig. 13f–h). We also tested the ability of *Ucp2*<sup>-/-</sup> mice to clear apoptotic cells in other tissues. By initiating acute apoptosis of germ cells in the testes via testicular torsion, we assessed the clearance of dying germ cells by Sertoli cells. The testes of *Ucp2*<sup>-/-</sup> mice contained increased numbers of uncleared apoptotic cells per seminiferous tubule compared to *Ucp2*<sup>+/+</sup> mice (Fig. 4h, i). These data demonstrate an essential role for *Ucp2* in apoptotic cell clearance *in vivo*.

Although significant recent progress has been made in understanding how phagocytes recognize and engulf apoptotic cells<sup>25</sup>, this work provides additional insights on this process. First, mitochondrial membrane potential critically controls how well a phagocyte can engulf apoptotic cells, with an inverse correlation between mitochondrial membrane potential and engulfment capacity. Second, the *Ucp2* protein acts as a regulator of mitochondrial membrane potential within phagocytes during apoptotic cell engulfment, with a requirement for *Ucp2* in efficient apoptotic cell clearance *in vivo*. Third, a previously unappreciated crosstalk exists between the mitochondria and the engulfment machinery within phagocytes, with the ‘sensing’ of the total mitochondrial membrane potential critically influencing phagocytic capacity. This has broad implications for apoptotic cell clearance *in vivo*, because failed clearance has been linked to inflammation and autoimmune diseases. Moreover, *Ucp2* deficiency was linked to impaired pancreatic  $\beta$ -cell function and glucose-induced insulin secretion<sup>26,27</sup>, and *Ucp2*<sup>-/-</sup> mice show increased atherosclerosis<sup>11,12,28</sup>. The data presented here provide a new and unexpected link between mitochondrial function, *Ucp2* and apoptotic cell clearance and may help to provide a better understanding of the complex aetiology of metabolic diseases.

## METHODS SUMMARY

To detect mitochondrial membrane potential, phagocytes (LR73, NIH/3T3 or BMDMs)<sup>14,24</sup> were stained with Mitotracker Deep Red FM, TMRE or JC-1, incubated with apoptotic cells and analysed by flow cytometry. Cell clearance in the thymus was analysed as detailed previously<sup>24</sup>. Testicular torsion was performed as per the guidelines of the Society for the Study of Reproduction.

**Full Methods** and any associated references are available in the online version of the paper at [www.nature.com/nature](http://www.nature.com/nature).

Received 21 December 2010; accepted 28 June 2011.

Published online 21 August 2011.

1. Elliott, M. R. & Ravichandran, K. S. Clearance of apoptotic cells: implications in health and disease. *J. Cell Biol.* **189**, 1059–1070 (2010).
2. Henson, P. M. & Hume, D. A. Apoptotic cell removal in development and tissue homeostasis. *Trends Immunol.* **27**, 244–250 (2006).
3. Gregory, C. D. & Pound, J. D. Cell death in the neighbourhood: direct microenvironmental effects of apoptosis in normal and neoplastic tissues. *J. Pathol.* **223**, 178–195 (2011).
4. Muñoz, L. E., Lauber, K., Schiller, M., Manfredi, A. A. & Herrmann, M. The role of defective clearance of apoptotic cells in systemic autoimmunity. *Nature Rev. Rheumatol.* **6**, 280–289 (2010).
5. Tabas, I. Macrophage death and defective inflammation resolution in atherosclerosis. *Nature Rev. Immunol.* **10**, 36–46 (2010).
6. Miyashita, M. et al. Identification of Tim4 as a phosphatidylserine receptor. *Nature* **450**, 435–439 (2007).

7. Krauss, S., Zhang, C. Y. & Lowell, B. B. A significant portion of mitochondrial proton leak in intact thymocytes depends on expression of UCP2. *Proc. Natl Acad. Sci. USA* **99**, 118–122 (2002).
8. Krauss, S., Zhang, C. Y. & Lowell, B. B. The mitochondrial uncoupling-protein homologues. *Nature Rev. Mol. Cell Biol.* **6**, 248–261 (2005).
9. Fleury, C. et al. Uncoupling protein-2: a novel gene linked to obesity and hyperinsulinemia. *Nature Genet.* **15**, 269–272 (1997).
10. Arsenijevic, D. et al. Disruption of the uncoupling protein-2 gene in mice reveals a role in immunity and reactive oxygen species production. *Nature Genet.* **26**, 435–439 (2000).
11. Blanc, J. et al. Protective role of uncoupling protein 2 in atherosclerosis. *Circulation* **107**, 388–390 (2003).
12. Moukdar, F. et al. Reduced antioxidant capacity and diet-induced atherosclerosis in uncoupling protein-2-deficient mice. *J. Lipid Res.* **50**, 59–70 (2009).
13. Reers, M., Smith, T. W. & Chen, L. B. J-aggregate formation of a carbocyanine as a quantitative fluorescent indicator of membrane potential. *Biochemistry* **30**, 4480–4486 (1991).
14. Park, D. et al. BAI1 is an engulfment receptor for apoptotic cells upstream of the ELMO/Dock180/Rac module. *Nature* **450**, 430–434 (2007).
15. Enerbäck, S. et al. Mice lacking mitochondrial uncoupling protein are cold-sensitive but not obese. *Nature* **387**, 90–94 (1997).
16. Lugli, E. et al. Characterization of cells with different mitochondrial membrane potential during apoptosis. *Cytometry A* **68**, 28–35 (2005).
17. Zhang, C. Y. et al. Genipin inhibits UCP2-mediated proton leak and acutely reverses obesity- and high glucose-induced beta cell dysfunction in isolated pancreatic islets. *Cell Metab.* **3**, 417–427 (2006).
18. Echay, K. S., Winkler, E., Bienengraeber, M. & Klingenberg, M. Site-directed mutagenesis identifies residues in uncoupling protein (UCP1) involved in three different functions. *Biochemistry* **39**, 3311–3317 (2000).
19. Urbánková, E., Hanak, P., Skobisova, E., Ruzicka, M. & Jezek, P. Substitutional mutations in the uncoupling protein-specific sequences of mitochondrial uncoupling protein UCP1 lead to the reduction of fatty acid-induced H<sup>+</sup> uniport. *Int. J. Biochem. Cell Biol.* **35**, 212–220 (2003).
20. Buckler, K. J. & Vaughan-Jones, R. D. Effects of mitochondrial uncouplers on intracellular calcium, pH and membrane potential in rat carotid body type I cells. *J. Physiol. (Lond.)* **513**, 819–833 (1998).
21. Sokal, A. & Bartosz, G. Uncouplers of mitochondrial oxidative phosphorylation are not substrates of the erythrocyte glutathione-S-conjugate pump. *Arch. Biochem. Biophys.* **349**, 113–121 (1998).
22. Park, D., Hochreiter-Hufford, A. & Ravichandran, K. S. The phosphatidylserine receptor TIM-4 does not mediate direct signaling. *Curr. Biol.* **19**, 346–351 (2009).
23. Kobayashi, N. et al. TIM-1 and TIM-4 glycoproteins bind phosphatidylserine and mediate uptake of apoptotic cells. *Immunity* **27**, 927–940 (2007).
24. Elliott, M. R. et al. Nucleotides released by apoptotic cells act as a find-me signal to promote phagocytic clearance. *Nature* **461**, 282–286 (2009).
25. Ravichandran, K. S. & Lorenz, U. Engulfment of apoptotic cells: signals for a good meal. *Nature Rev. Immunol.* **7**, 964–974 (2007).
26. Azzu, V. & Brand, M. D. The on-off switches of the mitochondrial uncoupling proteins. *Trends Biochem. Sci.* **35**, 298–307 (2010).
27. Andrews, Z. B. et al. UCP2 mediates ghrelin's action on NPY/AgRP neurons by lowering free radicals. *Nature* **454**, 846–851 (2008).
28. Pi, J. & Collins, S. Reactive oxygen species and uncoupling protein 2 in pancreatic  $\beta$ -cell function. *Diabetes Obes. Metab.* **12** (Suppl. 2), 141–148 (2010).

**Supplementary Information** is linked to the online version of the paper at [www.nature.com/nature](http://www.nature.com/nature).

**Acknowledgements** We thank M. Schwartz and members of the K.S.R. laboratory for discussions. This work was supported by grants from the National Institute of General Medical Sciences (to K.S.R.), and ARRA funding from National Institute of Child Health and Development (to J.J.L. and K.S.R.). K.S.R. is a Bill Benter Senior Fellow of the American Asthma Foundation. J.M.K. is supported by an American Heart Association Award.

**Author Contributions** D.P., C.Z.H., M.R.E., P.C.T., J.M.K., S.D., J.J.L. and K.L.H. designed and performed all of the experiments. S.C. provided advice and the *Ucp2* knockout mice. K.S.R. helped in the design of many of the experiments and provided overall coordination. D.P., K.L.H. and K.S.R. wrote and edited the manuscript with input from other authors.

**Author Information** Reprints and permissions information is available at [www.nature.com/reprints](http://www.nature.com/reprints). The authors declare no competing financial interests. Readers are welcome to comment on the online version of this article at [www.nature.com/nature](http://www.nature.com/nature). Correspondence and requests for materials should be addressed to K.S.R. ([ravi@virginia.edu](mailto:ravi@virginia.edu)).



## METHODS

**Cell culture and transfections.** LR73 cells were cultured in  $\alpha$ -MEM, whereas NIH/3T3 cells and J774 macrophage cells were maintained in DMEM and Jurkat cells were cultured with RPMI, along with 10% FBS and 1% penicillin-streptomycin-glutamine. SCI cells were cultured in  $\alpha$ -MEM and 1 mM of sodium pyruvate. LR73 cells were transfected using Lipofectamine 2000 (Invitrogen) according to the manufacturer's instructions. NIH/3T3 cells were nucleofected using amaxa nucleofector (kit R, program U-030) or transfected with Lipofectamine 2000 according to the manufacturer's instructions.

**Primary cell culture.** Bone marrow cells from 6-week-old mice were cultured in RPMI medium with 10% FBS, 1% penicillin-streptomycin-glutamine, and 10% L929 cell conditioned medium. Two or six days later, more than 85% of the adherent cells were F4/80 positive and 95% of the cells were CD11b positive. Resident peritoneal cells were collected from 6-week-old mice and plated with RPMI supplemented with 10% FBS and 1% penicillin-streptomycin-glutamine. Four hours later, floating cells were washed with warm PBS twice and adherent cells were regarded as resident peritoneal macrophages and used in further assays.

**Plasmids and mutagenesis.** All constructs generated were sequenced to confirm fidelity and the presence of the appropriate mutations. The pEBB-Ucp2 and pEBB-Ucp2-Flag constructs were generated from the *Ucp2* cDNA templates by a PCR-based strategy in the pEBB-Flag vector. pEBB-Ucp2(D28N) was generated by site-directed mutagenesis. ELMO, Dock180, Rac, BAI1 and Tim-4 constructs used in this study have been described previously<sup>19</sup>.

**Immunoblotting and antibodies.** The antibodies used were anti-Ucp2 (Santa Cruz Biotechnology, C-20), anti-Flag (Sigma, M-2), anti-porin (Abcam, ab15895), anti-Erk2 (Santa Cruz, C-14) and anti-AIF (Cell Signaling, D39D2). Phospho-AMPK $\alpha$  (Thr 172), AMPK $\alpha$  antibody, phospho-p70 S6 kinase (Thr 389) and p70 S6 kinase were purchased from Cell Signaling Technology. To detect endogenous Ucp2, it is necessary to isolate mitochondria. For the isolation of mitochondria, cells were resuspended in 500  $\mu$ l of TS buffer (10 mM Tris, pH 7.5, 250 mM sucrose, 2  $\mu$ g ml<sup>-1</sup> DNase and protease inhibitor cocktail), and then subjected to three cycles of 5-min freezing in liquid nitrogen followed by 10-min thawing at 37 °C. Unbroken cells and nuclei were removed by centrifugation at 800g for 10 min and mitochondria were collected from the supernatant by centrifugation at 10,000g for 20 min. The isolated mitochondria were lysed in RIPA buffer and subjected to immunoblotting. To measure induction of Ucp2 during apoptotic cell engulfment,  $2.0 \times 10^6$  LR73 cells were plated on a 100-mm culture dish 2 days before  $1.0 \times 10^8$  apoptotic thymocytes in 10 ml of  $\alpha$ -MEM were added. After incubation for 3 h, the mitochondria were isolated and the Ucp2 levels were analysed. For BMDMs,  $5.0 \times 10^6$  BMDMs were plated on a 100-mm Petri dish 1 day before the assay. The next day,  $1.0 \times 10^8$  apoptotic thymocytes in 10 ml of RPMI were added to the BMDMs and incubated for 1 h. The cells were extensively washed with cold PBS and trypsinized and analysed for Ucp2 levels. To detect overexpressed Ucp2, LR73 cells were transiently transfected with Flag-tagged Ucp2 using Lipofectamine 2000 (Invitrogen). One day after transfection, the cells were lysed and subjected to immunoblotting against the respective tags or endogenous proteins.

**Immunofluorescence microscopy.** NIH/3T3 fibroblasts were plated on glass chamber slides and transfected with Flag-Ucp2 either alone or in combination with YFP-Rab5 or YFP-Rab7. To stain lysosomes or mitochondria, cells were incubated with Lysotracker Red (1:10,000 dilution) or Mitotracker Deep Red (100 nM) in DMEM/10% FBS for 20 min. Cells were then fixed with 3% paraformaldehyde (Sigma) in PBS for 30 min, permeabilized with 0.1% Triton X-100 (Sigma) and blocked with 5% milk that had been clarified by high-speed centrifugation. Antibody staining was then performed using antibodies to Flag (clone M5, Sigma) and/or AIF (D39D2, Cell Signaling) detected with either Alexa 488 or Alexa-555 goat anti-mouse and/or Alexa-555 goat anti-rabbit antibodies (highly cross-absorbed, Invitrogen), respectively. YFP was detected using an Alexa-488 anti-GFP antibody (Invitrogen). The stained cells were analysed by Axio imager 2 with Apotome (Zeiss).

**Quantitative RT-PCR.** Total RNA was isolated using the RNeasy Mini Kit (Qiagen) and cDNA was generated from total RNA with Superscript III (Invitrogen) according to the manufacturers' protocol. *Ucp1*, *Ucp2* and *Ucp3* mRNA were detected by PCR using cDNA as template. For siRNA transfected NIH/3T3 cells and *Ucp2* knockout mice, relative *Ucp2* or *Ucp3* mRNA levels were determined by normalizing to *Hprt* using the StepOnePlus qPCR system (Applied Biosystems).

**Phagocytosis assay.** Phagocytosis assays were performed as described previously<sup>14</sup>.  $1.0 \times 10^5$  LR73 cells were transiently transfected in triplicates with the indicated plasmids either with GFP or GFP fusion proteins in a 24-well plate. The cells were incubated with apoptotic thymocytes or 2  $\mu$ m carboxylate-modified red fluorescent beads (Invitrogen), which mimic the negative charge on apoptotic cells and can serve as simplified targets. For the induction of apoptosis, thymocytes were incubated with 50  $\mu$ M dexamethasone (Calbiochem) at 37 °C for 4 h. The

thymocytes were resuspended to a final concentration of  $1.0 \times 10^7$  cells per 300  $\mu$ l with  $\alpha$ -MEM (or cell culture medium for specific cell types) supplemented with 2% FBS and 0.2% penicillin-streptomycin-glutamine for the phagocytosis assay of LR73. The transfected cells were incubated with 300  $\mu$ l of the apoptotic thymocyte resuspension in a 5% CO<sub>2</sub> incubator at 37 °C for the desired time. After incubation of the phagocytes with targets, the phagocytes were extensively washed with cold PBS, trypsinized, resuspended in cold medium (with 1% NaN<sub>3</sub>), and analysed by two-colour flow cytometry (FACSCalibur from BD). The transfected cells were recognized by their GFP fluorescence and targets were recognized by red fluorescence (carboxylate-modified red fluorescent beads or apoptotic thymocytes). Forward and side-scatter parameters were used to distinguish free unbound targets from phagocytes. The majority of 'double-positive' cells scored in the FACS assay represented targets engulfed by phagocytes, or targets in the process of being engulfed. The MFI in the red channel of the cells taking up targets provided an indication of the capacity of uptake (proportional to the number of particles taken up). For measuring phagocytosis by BMDMs,  $2.0 \times 10^4$  BMDMs were plated in the 24-well plate one day before the phagocytosis assay. Next day, the cells were incubated with  $2.0 \times 10^6$  TAMRA-stained apoptotic thymocytes for the desired time and analysed for engulfment as above.

**Internalization assay.** Thymocytes were double stained with TAMRA (25  $\mu$ M) and cypHer5E (1  $\mu$ M; GE Healthcare) and the phagocytosis assay was performed as described above. TAMRA and cypHer5E high-double-positive cells were considered to be phagocytes internalizing apoptotic cells, and TAMRA-positive but cypHer5E-low cells were regarded as bound but uninternalized targets on phagocytes.

**Phagocytosis of dead *Escherichia coli*, *Staphylococcus aureus* and zymosan.**  $2.0 \times 10^4$  BMDMs from wild-type or *Ucp2*-deficient mice were plated on a well of a 24-well plate. Next day, BMDMs were incubated with alexa-488 conjugated  $5 \times 10^6$  *E. coli* and *S. aureus* or  $5 \times 10^5$  zymosan particles (Invitrogen) for the desired time. Unbound targets were extensively washed with cold PBS five times and BMDMs were trypsinized and subjected to FACS analysis. Alexa-488-positive BMDMs were considered to be phagocytes engulfing targets.

**Gentamicin protection assay for bacterial internalization.** Quantification of intracellular bacteria was done using the gentamicin protection assay.  $2 \times 10^5$  BMDMs per well were seeded into a 24-well culture dish 18 h before infection at a multiplicity of infection of 10 for 1 h in antibiotic-free media in a 37 °C CO<sub>2</sub> incubator. Cells were then washed and incubated with gentamicin for 90 min to kill extracellular bacteria. Subsequently, cells were lysed in 1% Triton-X 100, lysates were serially diluted, and plated directly onto Luria-Bertani agar plates. Total colony-forming units (c.f.u.) were enumerated the next day after overnight incubation at 37 °C. Values were standardized to levels of colonization in control cell preparations.

**Ucp2 knockdown.** NIH/3T3 cells were nucleofected according to the manufacturer's manual (Kit R, U-030, amaxa) with minor modifications.  $1.0 \times 10^6$  cells were nucleofected with 6 picomoles per sample control or *Ucp2* siRNA (Dharmacon *Ucp2* smart pool) and plated onto 3 wells of a 6-well plate. Twenty-four hours after nucleofection, the cells were trypsinized and  $2.0 \times 10^4$  cells were replated in the 12-well plate. Two days after nucleofection, the cells were incubated with  $1.0 \times 10^6$  TAMRA-stained apoptotic SCI or Jurkat cells in DMEM supplemented with 10% FBS and 1% penicillin-streptomycin-glutamine at 37 °C for the desired time.

**Measurement of mitochondrial membrane potential.** To detect the mitochondrial membrane potential, cells treated with the indicated experimental conditions were stained with Mitotracker Deep Red FM (Invitrogen), the accumulation of which in mitochondria is dependent on mitochondrial membrane potential. Mitochondrial membrane potential was also measured using TMRE (Invitrogen) or a dual emission potential-sensitive probe, JC-1 dye (SIGMA-Aldrich), according to the manufacturer's protocol. For TMRE staining, cells were incubated with 50 nM of TMRE in culture medium in a 5% CO<sub>2</sub> incubator at 37 °C for 30 min and fluorescence coming from cells was measured by flow cytometry. For JC-1 staining, cells in a 24-well plate were incubated with 1 ml of mitochondrial staining solution containing the 50% medium used for cell growth and 2.5  $\mu$ g ml<sup>-1</sup> of JC-1 dye in a 5% CO<sub>2</sub> incubator at 37 °C for 20 min. The cells were then washed twice with warm PBS and trypsinized. Overflow of green fluorescent signal to red fluorescence was compensated and the intensity of red fluorescence coming from JC-1 aggregates was detected by flow cytometry using the FACSCalibur instrument (Becton Dickinson).

**Measurement of intracellular ATP.** Intracellular ATP levels were measured using CellTiter-Glo Luminescent Cell Viability Assay kit (Promega) according to the manufacturer's manual. Cells were treated with experimental conditions and trypsinized.  $2.5 \times 10^4$  cells per 50  $\mu$ l were added into a well of a 96-well plate. Then, 50  $\mu$ l of CellTiter-Glo Reagent was added to the well containing the cells. The cells were incubated on an orbital shaker for 2 min and followed by incubation

at room temperature (25 °C) for 10 min. Luminescence was measured using MicroBeta TriLux (EG&G WALLAC).

**Analysis of cell clearance in the thymus.** Five-to-six-week-old wild-type and *Ucp2*-deficient mice were intraperitoneally injected with 300 µl of PBS containing 250 µg dexamethasone dissolved in ethanol (10 mg ml<sup>-1</sup>). Six hours after injection, the mice were killed and thymuses were extracted. For quantification of thymic cellularity, thymocytes were resuspended with HBSS supplemented with 5% FBS. The cells were diluted and mixed with 50 µl of quantification beads (Spherotech). The mixture was subjected to flow cytometric analysis to allow for the quantification of thymocytes. To monitor the presence of TUNEL-positive uncleared apoptotic cells, 6 h after injection thymuses from the mice were extracted and embedded in O.C.T. compound. The O.C.T.-compound-embedded thymuses then were frozen in liquid nitrogen. After that, thymic cryosections on glass slides were stained using the *In situ* Cell Death Red kit according to manufacturer's instructions (Roche). Sections were mounted with Prolong Antifade plus DAPI medium and analysed by Axio Imager 2 with Apotome (ZEISS). To monitor *ex vivo* apoptosis of thymocytes,  $1.0 \times 10^7$  thymocytes from 5 to ~6-week-old *Ucp2* wild-type and deficient littermate mice were incubated with 50 µM dexamethasone at 37 °C for 4 or 6 h. The cells were washed with PBS once and then stained with annexin V and propidium iodide (Annexin V: FITC apoptosis detection kit II, BD).

**Cell migration assay.**  $2 \times 10^6$  cells ml<sup>-1</sup> THP-1 cells were resuspended with RPMI containing 5% FBS, 1% penicillin, streptomycin and glutamine and 10 mM HEPES and were pre-incubated with the desired concentration of FCCP for 1 h. Five-hundred microlitres of apoptotic supernatant or MCP-1 (25 ng ml<sup>-1</sup>) was added to the lower chamber of a 24-well plate with a 5-µm pore size transwell (5-µm pore size, Corning) and 100 µl of cells ( $2 \times 10^6$  cells ml<sup>-1</sup>) were loaded on the upper chamber of the plate and then incubated at 37 °C for 1 h. The percentage of migrated cells was determined by FACS with 5.1-µm AccuCount beads and compared to input cells. For BMDM migration,  $4.0 \times 10^5$  cells ml<sup>-1</sup> were resuspended in RPMI containing 1% BSA, 1% penicillin, streptomycin and glutamine and 10 mM HEPES. Five-hundred microlitres of apoptotic supernatant or Sdf-1 (50 ng ml<sup>-1</sup>) was added to the lower chamber of a 24-well transwell plate and 100 µl of BMDMs was added on the upper chamber and incubated at 37 °C for 3 h. The number of BMDMs that migrated on the underside of the membrane was determined by Diff-Quick staining and counted using microscopy.

**Thymus staining.** Tissue sections were blocked for 15 min with 2% normal goat serum and then were stained for 60 min at 25 °C with PE-conjugated F4/80 (eBioscience) and FITC-conjugated anti pan-cytokeratin (Sigma). After incubation, slides were washed three times in PBS and then mounted with GelMount (Molecular Probes, Invitrogen).

**Fatty acid oxidation assay.** Phagocytes were seeded in a 12-well plate at a density of  $2 \times 10^5$  cells per well on the day before the fatty acid oxidation

(FAO) assay. Next day, the phagocytes were incubated with  $2 \times 10^7$  apoptotic thymocytes or 2-µm carboxylate-modified beads for the desired times. After incubation, each well was washed five times with PBS. Rates of FAO were determined over the next 2 h as follows: a 0.2 ml PCR tube with 50 µl 1 M NaOH was leaned diagonally in each well before addition of 300 µl FAO buffer (Krebs Ringer phosphate buffer pH 7.4 containing 1% fatty-acid-free BSA (Sigma Aldrich), 5 mM glucose (Sigma Aldrich), 125 µM palmitate (Sigma Aldrich), 1 mM carnitine (Sigma Aldrich), and 6 µCi 1-<sup>14</sup>C-palmitate (Perkin Elmer)). The wells were immediately sealed with masking tape and incubated at 37 °C for 2 h before 100 µl of 2 M perchloric acid was injected through the tape to stop the reaction and release <sup>14</sup>CO<sub>2</sub> trapped as bicarbonate. The plate was incubated for 2 h at room temperature to trap the released <sup>14</sup>CO<sub>2</sub> as bicarbonate in NaOH. The tape was removed and NaOH from each tube was diluted with 5 ml scintillant and counted with a Beckman LS6500 scintillation counter. Partially oxidized metabolites of <sup>14</sup>C-palmitate were recovered from the FAO buffer precipitate by extraction in chloroform:methanol (2:1). Acid-soluble <sup>14</sup>C-metabolites were recovered from the aqueous phase, diluted in scintillant and counted. Rates of total FAO were determined by summing <sup>14</sup>CO<sub>2</sub>- and <sup>14</sup>C-labelled acid-soluble metabolite disintegration rates and normalizing to the specific activity of the FAO buffer, cell number and the duration of incubation.

**Measurement of superoxide.** LR73 cells were plated at a density of  $1.0 \times 10^5$  cells per well in a 12-well plate in  $\alpha$ -MEM supplemented with 10% FBS and 1% penicillin, streptomycin and glutamine. The cells were treated with the indicated drugs for 4 h and incubated with 2 µM MitoSox (Invitrogen) for 30 min. The cells were trypsinized and analysed by flow cytometry.

**Testicular torsion.** This work was conducted in accordance with the Guiding Principles of the Care and Use of Research Animals promulgated by the Society for the Study of Reproduction. Adult male C57BL/6 mice were anaesthetized with an intraperitoneal injection of 0.01 mg g<sup>-1</sup> sodium pentobarbital and the testis was exteriorized through a low midline laparotomy, the gubernaculum was divided, and the testis was freed from the epididymo-testicular membrane. The testis was rotated 720° for 2 h, during which time it remained in the abdomen with a closed incision. Following the 2 h torsion, the incision was reopened, the testis was counter-rotated to the natural position, the gubernaculum was rejoined, and the testis was reinserted into the scrotum via the inguinal canal. Testes were examined at the time of repair for the degree of ischaemia and reperfusion. Sham-operated animals were treated identically except that upon completion of the torsion manoeuvre the testis was immediately counter-rotated.

**Statistical analysis.** Data are shown as mean  $\pm$  standard deviation. For analysis of statistical difference between experiments involving two groups, a Student's two-tailed *t*-test was applied. A one-way ANOVA was applied for statistical analysis of three or more groups. Significance was defined when *P* values were <0.05.

# Ebola virus entry requires the cholesterol transporter Niemann–Pick C1

Jan E. Carette<sup>1†\*</sup>, Matthijs Raaben<sup>2\*</sup>, Anthony C. Wong<sup>3\*</sup>, Andrew S. Herbert<sup>4</sup>, Gregor Obernosterer<sup>1†</sup>, Nirupama Mulherkar<sup>3</sup>, Ana I. Kuehne<sup>4</sup>, Philip J. Kranzusch<sup>2</sup>, April M. Griffin<sup>2</sup>, Gordon Ruthel<sup>4</sup>, Paola Dal Cin<sup>5</sup>, John M. Dye<sup>4</sup>, Sean P. Whelan<sup>2</sup>, Kartik Chandran<sup>3</sup> & Thijn R. Brummelkamp<sup>1†</sup>

Infections by the Ebola and Marburg filoviruses cause a rapidly fatal haemorrhagic fever in humans for which no approved antivirals are available<sup>1</sup>. Filovirus entry is mediated by the viral spike glycoprotein (GP), which attaches viral particles to the cell surface, delivers them to endosomes and catalyses fusion between viral and endosomal membranes<sup>2</sup>. Additional host factors in the endosomal compartment are probably required for viral membrane fusion; however, despite considerable efforts, these critical host factors have defied molecular identification<sup>3–5</sup>. Here we describe a genome-wide haploid genetic screen in human cells to identify host factors required for Ebola virus entry. Our screen uncovered 67 mutations disrupting all six members of the homotypic fusion and vacuole protein-sorting (HOPS) multisubunit tethering complex, which is involved in the fusion of endosomes to lysosomes<sup>6</sup>, and 39 independent mutations that disrupt the endo/lysosomal cholesterol transporter protein Niemann–Pick C1 (NPC1)<sup>7</sup>. Cells defective for the HOPS complex or NPC1 function, including primary fibroblasts derived from human Niemann–Pick type C1 disease patients, are resistant to infection by Ebola virus and Marburg virus, but remain fully susceptible to a suite of unrelated viruses. We show that membrane fusion mediated by filovirus glycoproteins and viral escape from the vesicular compartment require the NPC1 protein, independent of its known function in cholesterol transport. Our findings uncover unique features of the entry pathway used by filoviruses and indicate potential antiviral strategies to combat these deadly agents.

We have developed haploid genetic screens to gain insight into the biological processes relevant to human disease<sup>8,9</sup>. Here we use this approach to explore the filovirus entry pathway at an unprecedented level of detail. To interrogate millions of gene disruption events for defects in Ebola virus entry, we used a replication-competent vesicular stomatitis virus bearing the Ebola virus glycoprotein (rVSV-GP-EboV)<sup>10</sup>. Although this virus replicates in most cell lines, it inefficiently killed near-haploid KBM7 cells (Supplementary Fig. 1c). In an unsuccessful attempt to induce pluripotency in KBM7 cells by expression of OCT4 (also called POU5F1), SOX2, MYC and KLF4 (ref. 11), we obtained HAP1 cells (Supplementary Fig. 1a). HAP1 cells grew adherently and no longer expressed haematopoietic markers (Supplementary Fig. 1b). Most of these cells in early passage cultures were haploid for all chromosomes, including chromosome 8 (which is diploid in KBM7 cells). Unlike KBM7 cells, HAP1 cells were susceptible to rVSV-GP-EboV (Supplementary Fig. 1c), allowing screens for filovirus host factors.

We used a retroviral gene-trap vector<sup>9</sup> to mutagenize early-passage HAP1 cells. To generate a control data set, we mapped ~800,000 insertions using deep sequencing (Supplementary Table 1). Next, we selected rVSV-GP-EboV-resistant cells, expanded them as a pool, and mapped insertion sites. Enrichment for mutations in genes was calculated by

comparing a gene's mutation frequency in resistant cells to that in the control data set (Supplementary Fig. 2). We identified a set of genes enriched for mutations in the rVSV-GP-EboV-resistant cell population (Fig. 1a, Supplementary Fig. 3 and Supplementary Table 2). Nearly all of these candidate host factors are involved in the architecture and trafficking of endo/lysosomal compartments. Our screen identified cathepsin B (CTSB), the only known host factor for which deletion inhibits Ebola virus entry<sup>5</sup>. Further inspection showed that mutations were highly enriched in genes encoding all six subunits of the HOPS complex (*VPS11*, *VPS16*, *VPS18*, *VPS33A*, *VPS39* and *VPS41*), for which we identified 67 independent mutations. The HOPS complex mediates fusion of endosomes and lysosomes<sup>6</sup> and affects endosome maturation<sup>12,13</sup>. The identification of all members of the HOPS complex demonstrates high, and possibly saturating, coverage of our screen. We also identified factors involved in the biogenesis of endosomes (PIKFYVE, FIG4)<sup>14</sup>, lysosomes (BLOC1S1, BLOC1S2)<sup>15</sup>, and in targeting of luminal cargo to the endocytic pathway (GNPTAB)<sup>16</sup>. The strongest hit was the Niemann–Pick disease locus *NPC1*, encoding an endo/lysosomal cholesterol transporter<sup>7</sup>. NPC1 also affects endosome/lysosome fusion and fission<sup>17</sup>, calcium homeostasis<sup>18</sup> and HIV-1 release<sup>19</sup>.

We subcloned the resistant cell population to obtain clones deficient for *VPS11*, *VPS33A* and *NPC1* (Supplementary Fig. 4a, b and Fig. 1b). These mutants displayed marked resistance to infection by rVSV-GP-EboV and VSV pseudotyped with Ebola virus or Marburg virus GP (Fig. 1c and Supplementary Fig. 4c). Cells lacking a functional HOPS complex or NPC1 were nonetheless fully susceptible to infection by a large panel of other enveloped and non-enveloped viruses, including VSV and recombinant VSV bearing different viral glycoproteins (Fig. 1d and Supplementary Fig. 5). The susceptibility of HAP1 clones to rVSV-GP-EboV infection was restored by expression of the corresponding cDNAs (Supplementary Fig. 6a–c).

Loss of NPC1 causes Niemann–Pick disease, a neurovisceral disorder characterized by cholesterol and sphingolipid accumulation in lysosomes<sup>7</sup>. We tested the susceptibility of patient primary fibroblasts to filovirus-GP-dependent infection. *NPC1*-mutant cells were infected poorly or not at all by rVSV-GP-EboV and VSV pseudotyped with filovirus GP proteins (Fig. 2a, b), and infection was restored by expression of wild-type NPC1 (Fig. 2c).

Mutations in *NPC2* cause identical clinical symptoms and phenotype defects in lipid transport<sup>20</sup>. Surprisingly, *NPC2*-mutant fibroblasts derived from different patients were susceptible to filovirus-GP-dependent infection (Fig. 2a, b and Supplementary Fig. 7), despite a similar accumulation of cholesterol in *NPC2*- and *NPC1*-mutant cells (Fig. 2a). Moreover, cholesterol clearance from *NPC1*-null cells by cultivation in lipoprotein-depleted growth medium did not confer susceptibility (Supplementary Fig. 8). Therefore, resistance of NPC1-deficient

<sup>1</sup>Whitehead Institute for Biomedical Research, Nine Cambridge Center, Cambridge, Massachusetts 02142, USA. <sup>2</sup>Department of Microbiology and Molecular Genetics, Harvard Medical School, Boston, Massachusetts 02115, USA. <sup>3</sup>Department of Microbiology and Immunology, Albert Einstein College of Medicine, Bronx, New York 10461, USA. <sup>4</sup>US Army Medical Research Institute of Infectious Diseases, 1425 Porter St, Fort Detrick, Maryland 21702-5011, USA. <sup>5</sup>Center for Advanced Molecular Diagnostics, Shapiro 5-058, 70 Francis Street, Boston, Massachusetts 02115, USA. <sup>†</sup>Present addresses: Department of Microbiology and Immunology, Stanford University School of Medicine, Stanford, California 94304, USA (J.E.C.); Netherlands Cancer Institute, Plesmanlaan 121, 1066 CX Amsterdam, The Netherlands (G.O., T.R.B.).

\*These authors contributed equally to this work.



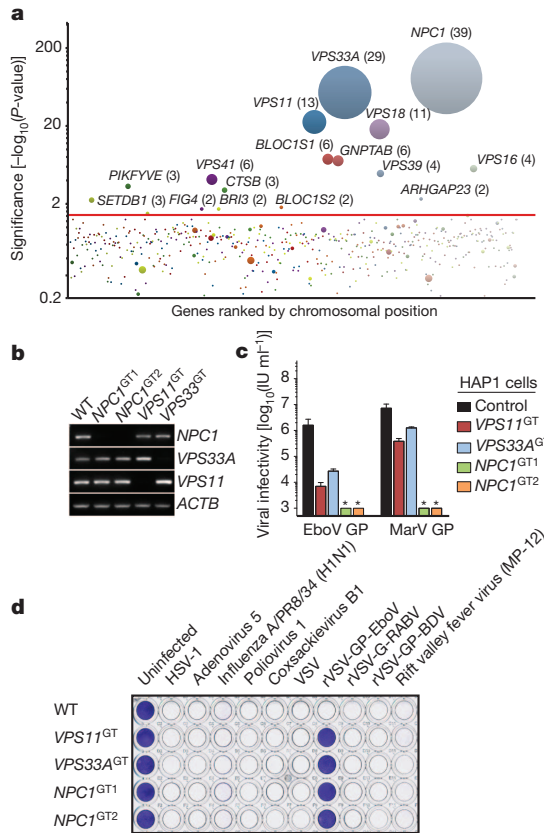


**Figure 1 | A haploid genetic screen identifies the HOPS complex and NPC1 as host factors for filovirus entry.** **a**, Genes enriched for gene-trap insertions in the rVSV-GP-EboV-selected cell population compared to unselected control cells. Circles represent genes and their size corresponds to the number of independent insertions identified in the rVSV-GP-EboV-selected population. Genes are ranked on the x-axis based on chromosomal position. **b**, RT-PCR analysis of the expression levels of NPC1, VPS33A and VPS11 in mutant clones. **c**, Infectivity of VSV pseudotyped with the indicated filovirus glycoproteins. IU, infectious units. Means  $\pm$  standard deviation (s.d.) ( $n = 3$ ) are shown. EboV, Ebola virus (Zaire); MarV, Marburg virus. Asterisk indicates below detection limit. **d**, HAP1 clones were infected with viruses including recombinant VSV viruses carrying rabies or Borna disease virus glycoproteins (rVSV-G-RABV and rVSV-GP-BDV) and stained with crystal violet.

cells to rVSV-GP-EboV is not caused by defects in cholesterol transport per se.

Filoviruses display broad mammalian host and tissue tropism<sup>21,22</sup>. To determine if NPC1 is generally required for filovirus-GP-mediated infection, we used *Npc1*-null Chinese hamster ovary (CHO) cells. Loss of NPC1 conferred complete resistance to viral infection (Supplementary Fig. 6d) that was reversed by expression of human NPC1 (Supplementary Fig. 6e). Certain small molecules such as U18666A (ref. 23) and the antidepressant imipramine<sup>24</sup> cause a cellular phenotype similar to NPC1 deficiency possibly by targeting NPC1 (ref. 23). Prolonged U18666A treatment has been reported to modestly inhibit VSV<sup>25</sup>. However, we found that brief exposure of Vero cells and HAP1 cells to U18666A or imipramine potentially inhibited viral infection mediated by Ebola virus GP but not VSV or rabies virus G (Fig. 2d and Supplementary Figs 9 and 10). Because U18666A inhibits rVSV-GP-EboV infection only when added at early time points, it probably affects entry rather than replication (Supplementary Fig. 10). Thus, NPC1 has a critical role in infection mediated by filovirus glycoproteins that is conserved in mammals and probably independent of NPC1's role in cholesterol transport.

Filoviruses bind to one or more cell-surface molecules<sup>2,26,27</sup> and are internalized by macropinocytosis<sup>28,29</sup>. In VPS33A- and NPC1-mutant cells, we observed no significant differences in binding or internalization

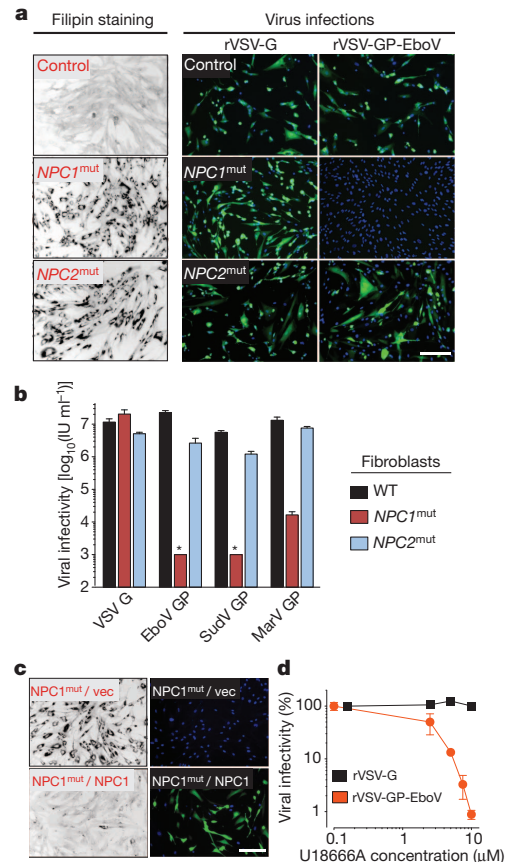


**Figure 2 | Viral infection mediated by filovirus glycoproteins requires NPC1 but not NPC2.** **a**, Primary skin fibroblasts from a healthy individual and patients carrying homozygous mutations in NPC1 or NPC2 were stained with Filipin, or challenged with rVSV-G or rVSV-GP-EboV. Filipin-stained (black) and infected cells (green) were visualized by fluorescence microscopy. Filipin-stained images were inverted for clarity. Blue indicates Hoechst nuclear counterstain. **b**, Infectivity of VSV pseudotyped with the indicated viral glycoproteins in control and Niemann-Pick fibroblasts. Asterisk indicates below detection limit. SudV, Sudan virus. **c**, NPC1 patient fibroblasts expressing empty vector or human NPC1 were stained with Filipin or challenged with rVSV-GP-EboV. **d**, Infectivity of rVSV-G and rVSV-GP-EboV in Vero cells pre-incubated for 30 min with the indicated concentrations of U18666A. Scale bars, 200  $\mu\text{m}$  (a, c). Means  $\pm$  s.d. ( $n = 3-6$ ) are shown (b, d).

of Alexa-647-labelled rVSV-GP-EboV (Fig. 3a and Supplementary Figs 11 and 12a). Similar results were obtained by flow cytometry using fluorescent Ebola-virus-like particles (Supplementary Fig. 12b). Moreover, bullet-shaped VSV particles were readily observed by electron microscopy at the cell periphery and within plasma membrane invaginations resembling nascent macropinosomes (Fig. 3b). Finally, VPS33A- and NPC1-null cells were fully susceptible to vaccinia virus entry by macropinocytosis (Supplementary Fig. 13). Thus, GP-mediated entry is not inhibited at viral attachment or early internalization steps in NPC1- or HOPS-defective cells, indicating a downstream defect.

Cathepsin L (CATL; also called CTSL1)-assisted cleavage of Ebola virus GP by CTSSB is required for viral membrane fusion<sup>3,5</sup>. Mutant HAP1 cells possess normal CTSSB/CATL activity (Supplementary Fig. 14b, c) and were fully susceptible to mammalian reoviruses, which use CTSSB or CATL for entry (Supplementary Fig. 14d). Moreover, these cells remained refractory to *in vitro*-cleaved rVSV-GP-EboV particles (Fig. 3c) that no longer required CTSSB/CATL activity within Vero cells (Supplementary Fig. 14a). Therefore the HOPS complex and NPC1 are probably required downstream of the initial GP proteolytic processing steps that generate a primed entry intermediate.

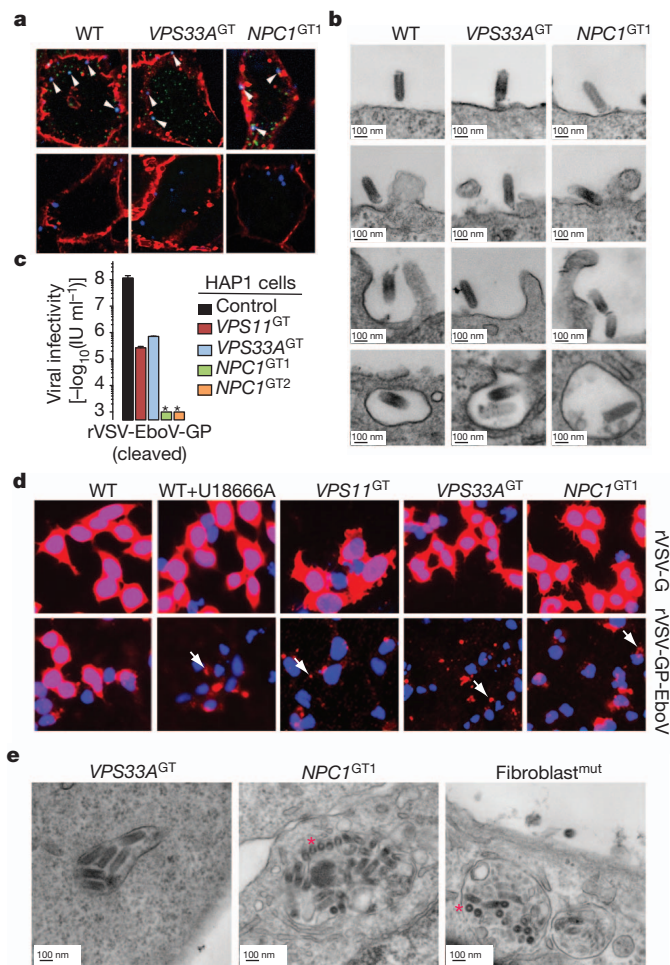


**Figure 3 | Virus entry is arrested at a late step in cells deficient for the HOPS complex and NPC1.** **a**, Viral particles attach and internalize into HOPS- and NPC1-deficient cells. Indicated HAP1 clones were infected with Alexa-647-labelled rVSV-GP-EboV (blue) at 4 °C. Non-internalized, bound viral particles (arrowheads, blue) were also stained with a GP-specific antibody (green) and the plasma membrane with Alexa-594-wheat germ agglutinin (red) (top panels). To assess viral internalization, cells were heated to 37 °C (bottom panels). Internalized viral particles (blue puncta) are resistant to acid-stripping and inaccessible to a GP antibody. Original magnification,  $\times 63$ . **b**, Cells were inoculated with rVSV-GP-EboV and examined by transmission electron microscopy. Representative images of early entry steps are shown. **c**, *In vitro*-cleaved rVSV-GP-EboV cannot bypass the infection block observed in *VPS11*<sup>GT</sup>, *VPS33A*<sup>GT</sup> and *NPC1*<sup>GT1</sup> cells. GT, gene trap. Infectivity of thermolysin-cleaved rVSV-GP-EboV in the indicated HAP1 clones is shown. Asterisk indicates below the limit of detection. **d**, Viral escape into the cytoplasm is blocked in HOPS-complex- and NPC1-deficient cells. Wild-type HAP1 cells treated with U18666A (10  $\mu\text{g ml}^{-1}$ ) and the indicated mutant clones were infected with rVSV-G or rVSV-GP-EboV virus for 3 h and processed for VSV M staining (red). Punctate staining is indicated by arrows. Original magnification,  $\times 20$ . **e**, Electron micrographs of rVSV-GP-EboV-infected *VPS33A*<sup>GT</sup> and *NPC1*<sup>GT1</sup> HAP1 cells and NPC1-deficient fibroblasts showing agglomerations of bullet-shaped VSV particles in vesicular compartments. All images were taken at 3 h after inoculation. Asterisks highlight rVSV-GP-EboV particles in cross-section.

Finally, we used the intracellular distribution of the internal VSV M (matrix) protein as a marker for membrane fusion (Fig. 3d). Cells were infected with native VSV or rVSV-GP-EboV and immunostained to visualize the incoming M protein. Endosomal acid-pH-dependent entry of either virus into wild-type HAP1 cells caused redistribution of the incoming viral M throughout the cytoplasm (Fig. 3d and Supplementary Fig. 15a). By contrast, only punctate, perinuclear M staining was obtained in drug-treated and mutant cells infected with

rVSV-GP-EboV or rVSV-GP-MarV (Fig. 3d and Supplementary Fig. 15b). Electron micrographs of mutant cells infected with rVSV-GP-EboV revealed agglomerations of viral particles within vesicular compartments (Fig. 3e and Supplementary Fig. 16a) containing LAMP1 (Supplementary Fig. 16b), indicating that fusion and uncoating of incoming virus is arrested. Similarly, U18666A treatment increased the number of viral particles in NPC1- and LAMP1-positive endosomes (Supplementary Fig. 17). Therefore, NPC1 and the HOPS complex are required for late step(s) in filovirus entry leading to viral membrane fusion and escape from the lysosomal compartment.

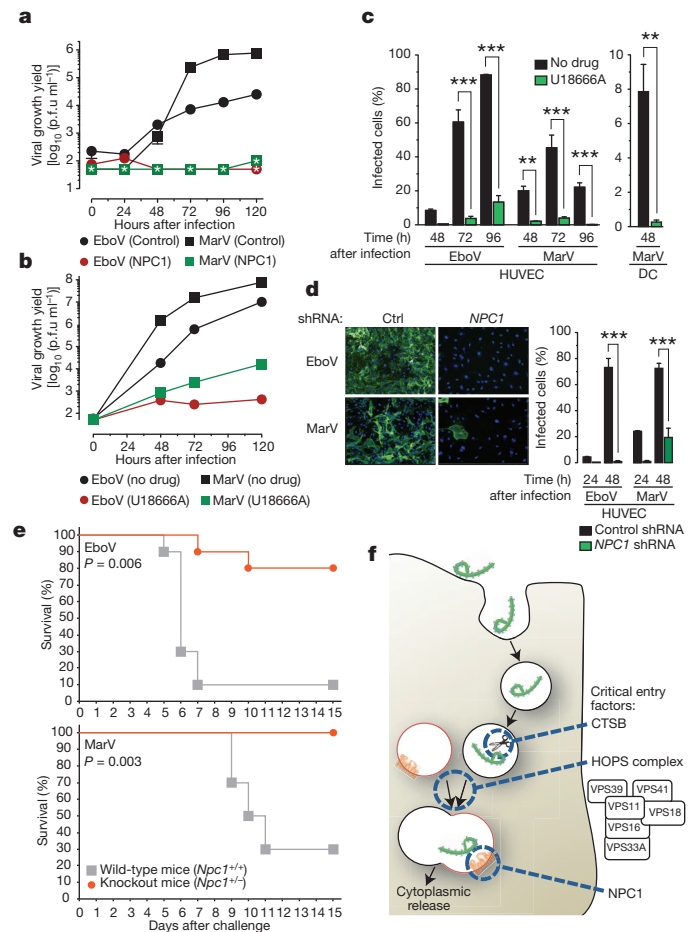


**Figure 4 | NPC1 function is required for infection by authentic Ebola and Marburg viruses.** **a**, NPC1 patient fibroblasts were exposed to Ebola virus (EboV) or Marburg virus (MarV) at a multiplicity of infection (MOI) of 0.1. Supernatants were harvested and yields of infectious virus were measured. Asterisk indicates below detection limit. p.f.u., plaque-forming units. **b**, Vero cells treated with DMSO or U18666A (20  $\mu\text{M}$ ) were infected with Ebola virus or Marburg virus at a MOI of 0.1 and yields of infectious virus were measured. **c**, Human peripheral blood monocyte-derived dendritic cells (DC) and umbilical-vein endothelial cells (HUVEC) were infected in the presence or absence of U18666A at a MOI of 3 and the percentage of infected cells was determined by immunostaining. **d**, HUVECs were transfected with lentiviral vectors expressing a non-targeting short hairpin (sh)RNA (Ctrl) or an shRNA targeting *NPC1*, infected with Ebola virus or Marburg virus at a MOI of 3 and the percentage of infected cells was determined. Representative images of cells 48 h after infection are also shown: green, viral antigen; blue, nuclear counterstain. For panels **a–d**, Means  $\pm$  s.d. are shown ( $n = 2–3$ ). In panels **a**, **b**, error bars are not visible because they are within the symbols. For panels **c**, **d**,  $**P < 0.01$ ;  $***P < 0.001$ . **e**, Survival of *Npc1*<sup>+/+</sup> and *Npc1*<sup>+/−</sup> mice ( $n = 10$  for each group) inoculated intraperitoneally with  $\sim 1,000$  p.f.u. of mouse-adapted Ebola virus or Marburg virus. **f**, A proposed hypothetical model for the roles of CTSB, the HOPS complex and NPC1 in Ebola virus entry.



We next tested if infection by authentic Ebola virus and Marburg virus is affected in *NPC1*-mutant primary patient fibroblasts. Yields of viral progeny were profoundly reduced for both viruses in mutant cells (Fig. 4a). Marked reductions in viral yield were also obtained in Vero cells treated with U18666A (Fig. 4b). Moreover U18666A greatly reduced infection of human peripheral blood monocyte-derived dendritic cells and umbilical-vein endothelial cells (HUVECs) (Fig. 4c), without affecting cell number or morphology (Supplementary Fig. 19). Finally, knock-down of *NPC1* in HUVECs diminished infection by filoviruses (Fig. 4d and Supplementary Fig. 18). These findings indicate that *NPC1* is critical for authentic filovirus infection.

We assessed the effect of *NPC1* mutation in lethal mouse models of Ebola virus and Marburg virus infection. Heterozygous *Npc1* (*Npc1*<sup>+/-</sup>) knockout mice and their wild-type littermates were challenged with mouse-adapted Ebola virus or Marburg virus and monitored for 28 days. Whereas *Npc1*<sup>+/+</sup> mice rapidly succumbed to infection with either filovirus, *Npc1*<sup>+/-</sup> mice were largely protected (Fig. 4e).

We have used global gene disruption in human cells to discover components of the unusual entry pathway used by filoviruses. Most of the identified genes affect aspects of lysosome function, indicating that filoviruses exploit this organelle differently from all other viruses that we have tested (Fig. 4f). The unanticipated role for the hereditary disease gene *NPC1* in viral entry, infection and pathogenesis may facilitate the development of antifilovirus therapeutics.

## METHODS SUMMARY

Adherent HAP1 cells were generated by the introduction of OCT4/SOX2/Myc and KLF4 transcription factors. 100 million cells were mutagenized using a retroviral gene-trap vector. Insertion sites were mapped for approximately 1% of the unselected population using parallel sequencing. Cells were infected with rVSV-GP-EboV and the resistant cell population was expanded. Genes that were statistically enriched for mutation events in the selected population were identified, and the roles of selected genes in filovirus entry were characterized.

**Full Methods** and any associated references are available in the online version of the paper at [www.nature.com/nature](http://www.nature.com/nature).

Received 9 December 2010; accepted 30 June 2011.

Published online 24 August 2011.

- Feldmann, H. & Geisbert, T. W. Ebola haemorrhagic fever. *Lancet* **377**, 849–862 (2010).
- Lee, J. E. & Saphire, E. O. Ebolavirus glycoprotein structure and mechanism of entry. *Future Virol.* **4**, 621–635 (2009).
- Schornberg, K. *et al.* Role of endosomal cathepsins in entry mediated by the Ebola virus glycoprotein. *J. Virol.* **80**, 4174–4178 (2006).
- Kuhn, J. H. *et al.* Conserved receptor-binding domains of Lake Victoria marburgvirus and Zaire ebolavirus bind a common receptor. *J. Biol. Chem.* **281**, 15951–15958 (2006).
- Chandran, K., Sullivan, N. J., Felbor, U., Whelan, S. P. & Cunningham, J. M. Endosomal proteolysis of the Ebola virus glycoprotein is necessary for infection. *Science* **308**, 1643–1645 (2005).
- Nickerson, D. P., Brett, C. L. & Merz, A. J. Vps-C complexes: gatekeepers of endolysosomal traffic. *Curr. Opin. Cell Biol.* **21**, 543–551 (2009).
- Carstea, E. D. *et al.* Niemann-Pick C1 disease gene: homology to mediators of cholesterol homeostasis. *Science* **277**, 228–231 (1997).
- Carette, J. E. *et al.* Global gene disruption in human cells to assign genes to phenotypes by deep sequencing. *Nature Biotechnol.* **29**, 542–546 (2011).
- Carette, J. E. *et al.* Haploid genetic screens in human cells identify host factors used by pathogens. *Science* **326**, 1231–1235 (2009).
- Wong, A. C., Sandesara, R. G., Mulherkar, N., Whelan, S. P. & Chandran, K. A forward genetic strategy reveals destabilizing mutations in the Ebolavirus glycoprotein that alter its protease dependence during cell entry. *J. Virol.* **84**, 163–175 (2010).
- Takahashi, K. *et al.* Induction of pluripotent stem cells from adult human fibroblasts by defined factors. *Cell* **131**, 861–872 (2007).
- Poteryaev, D., Datta, S., Ackema, K., Zerial, M. & Spang, A. Identification of the switch in early-to-late endosome transition. *Cell* **141**, 497–508 (2010).
- Rink, J., Ghigo, E., Kalaidzidis, Y. & Zerial, M. Rab conversion as a mechanism of progression from early to late endosomes. *Cell* **122**, 735–749 (2005).
- Sbrissa, D. *et al.* Core protein machinery for mammalian phosphatidylinositol 3,5-bisphosphate synthesis and turnover that regulates the progression of endosomal transport. Novel Sac phosphatase joins the ArPIKfyve-PIKfyve complex. *J. Biol. Chem.* **282**, 23878–23891 (2007).
- Dell'Angelica, E. C. The building BLOC(k)s of lysosomes and related organelles. *Curr. Opin. Cell Biol.* **16**, 458–464 (2004).
- Tiede, S. *et al.* Mucopolidiosis II is caused by mutations in GNPTA encoding the alpha/beta GlcNAc-1-phosphotransferase. *Nature Med.* **11**, 1109–1112 (2005).
- Goldman, S. D. & Krise, J. P. Niemann-Pick C1 functions independently of Niemann-Pick C2 in the initial stage of retrograde transport of membrane-impermeable lysosomal cargo. *J. Biol. Chem.* **285**, 4983–4994 (2010).
- Lloyd-Evans, E. *et al.* Niemann-Pick disease type C1 is a sphingosine storage disease that causes deregulation of lysosomal calcium. *Nature Med.* **14**, 1247–1255 (2008).
- Tang, Y. Y., Leao, I. C., Coleman, E. M., Broughton, R. S. & Hildreth, J. E. K. Deficiency of Niemann-Pick type C-1 protein impairs release of human immunodeficiency virus type 1 and results in Gag accumulation in late endosomal/lysosomal compartments. *J. Virol.* **83**, 7982–7995 (2009).
- Naureckiene, S. *et al.* Identification of HE1 as the second gene of Niemann-Pick C disease. *Science* **290**, 2298–2301 (2000).
- Takada, A. *et al.* A system for functional analysis of Ebola virus glycoprotein. *Proc. Natl Acad. Sci. USA* **94**, 14764–14769 (1997).
- Wool-Lewis, R. J. & Bates, P. Characterization of Ebola virus entry by using pseudotyped viruses: identification of receptor-deficient cell lines. *J. Virol.* **72**, 3155–3160 (1998).
- Cenedella, R. J. Cholesterol synthesis inhibitor U18666A and the role of sterol metabolism and trafficking in numerous pathophysiological processes. *Lipids* **44**, 477–487 (2009).
- Rodriguez-Lafrasse, C. *et al.* Abnormal cholesterol metabolism in imipramine-treated fibroblast cultures. Similarities with Niemann-Pick type C disease. *Biochim Biophys Acta* **1043**, 123–128 (1990).
- Sobo, K. *et al.* Late endosomal cholesterol accumulation leads to impaired intra-endosomal trafficking. *Plos One* **2**, e851 (2007).
- Kondratowicz, A. S. *et al.* T-cell immunoglobulin and mucin domain 1 (TIM-1) is a receptor for Zaire Ebolavirus and Lake Victoria Marburgvirus. *Proc. Natl Acad. Sci. USA* **108**, 8426–8431 (2011).
- Alvarez, C. P. *et al.* C-type lectins DC-SIGN and L-SIGN mediate cellular entry by Ebola virus *in cis* and *in trans*. *J. Virol.* **76**, 6841–6844 (2002).
- Saeed, M. F., Kolokoltsov, A. A., Albrecht, T. & Davey, R. A. Cellular entry of ebola virus involves uptake by a macropinocytosis-like mechanism and subsequent trafficking through early and late endosomes. *PLoS Pathog.* **6**, <http://dx.doi.org/10.1371/journal.ppat.1001110> (2010).
- Nambo, A. *et al.* Ebolavirus is internalized into host cells via macropinocytosis in a viral glycoprotein-dependent manner. *PLoS Pathog.* **6**, <http://dx.doi.org/10.1371/journal.ppat.1001121> (2010).

**Supplementary Information** is linked to the online version of the paper at [www.nature.com/nature](http://www.nature.com/nature).

**Acknowledgements** We would like to thank M. Kielian, H. Ploegh, V. Prasad and D. Sabatini for critical reading of the manuscript and valuable advice; C. Guimaraes, V. Blomen and T. Peterson for suggestions; M. Bogoy for providing the CTSS/CATL activity probe (GB111); T.-Y. Chang for the gift of NPC1-null CHO cells; D. Lyles for the antibody to VSV M; M. Nibert for providing reovirus; J. de la Torre for providing rVSV-GP-BDV; J. Wojcechowskyj for providing RVF; E. Muhlberger for providing Ebola cDNA; and M. Ericsson for support with electron microscopy. This research was supported by NIH grants R01 AI088027 (K.C.), AI081842 and U54 AI057159 (NERCE-BEID) (S.P.W.), and R21 HG004938 (T.R.B.), and by the DTRA Project, CBM.VAXPLAT.05.10.RD.005 (J.M.D.). T.R.B. was additionally supported by the Whitehead Fellows Program. S.P.W. is a recipient of a Burroughs Wellcome Investigators in the Pathogenesis of Infectious Disease Award. A.C.W. was additionally supported by NIH-funded training programs T32 GM007288 and T32 AI070117 at the Albert Einstein College of Medicine. Opinions, interpretations, conclusions and recommendations are those of the authors and are not necessarily endorsed by the US Army.

**Author Contributions** K.C., S.P.W., T.R.B. and J.M.D. were the senior authors of this study and made equivalent contributions. The study was conceived by K.C., S.P.W. and T.R.B. J.E.C. and T.R.B. devised and implemented the haploid genetic screen, generated the HAP1 cells and identified hits by deep sequencing and cell cloning. P.D.C. carried out karyotype analysis on the HAP1 line. K.C. created and characterized the rVSV-GP-EboV virus used in the screen. A.M.G. created the rVSV-G-RABV. J.E.C., G.O. and K.C. performed entry and infection experiments with the HAP1 cells. A.C.W. and K.C. carried out entry and infection experiments with rVSVs in human fibroblasts, CHO and Vero cells. N.M. and K.C. carried out RNAi experiments with primary cells. M.R. was involved in experimental strategy and design and performed entry and infection experiments by high-resolution fluorescence and electron microscopy. N.M. carried out VLP entry experiments and P.J.K., the replicon assay. A.C.W. performed the cysteine cathepsin enzyme assays. A.S.H., A.I.K. and J.M.D. performed the infection and animal challenge experiments with the authentic viral agents. G.R. performed fluorescence microscopy and image analysis with filovirus-infected cell cultures. J.E.C., K.C., S.P.W. and T.R.B. wrote the paper.

**Author Information** Reprints and permissions information is available at [www.nature.com/reprints](http://www.nature.com/reprints). The authors declare competing financial interests: details accompany the full-text HTML version of the paper at [www.nature.com/nature](http://www.nature.com/nature). Readers are welcome to comment on the online version of this article at [www.nature.com/nature](http://www.nature.com/nature). Correspondence and requests for materials should be addressed to T.R.B. ([tbrummelkamp@nki.nl](mailto:tbrummelkamp@nki.nl)), K.C. ([kartik.chandran@einstein.yu.edu](mailto:kartik.chandran@einstein.yu.edu)), S.P.W. ([sean\\_whelan@hms.harvard.edu](mailto:sean_whelan@hms.harvard.edu)) or J.M.D. ([John.M.Dye1@us.army.mil](mailto:John.M.Dye1@us.army.mil)).



## METHODS

**Cells.** KBM7 cells and derivatives were maintained in IMDM supplemented with 10% FCS, L-glutamine, and penicillin–streptomycin. Vero cells and primary human dermal fibroblasts (Coriell Institute for Medical Research) were maintained in DMEM supplemented with 10% FCS, L-glutamine and penicillin–streptomycin. Wild-type and NPC1-null (CT43) Chinese hamster ovary (CHO) fibroblasts were maintained in DMEM–Ham's F-12 medium (50–50 mix) supplemented with 10% FCS, L-glutamine and penicillin–streptomycin<sup>30</sup>.

To generate dendritic cells, primary human monocytes were cultured at 37 °C, 5% CO<sub>2</sub>, and 80% humidity in RPMI supplemented with 10% human serum, L-glutamine, sodium pyruvate, HEPES, penicillin–streptomycin, recombinant human granulocyte monocyte-colony stimulating factor (50 ng ml<sup>−1</sup>) and recombinant human interleukin-4 (50 ng ml<sup>−1</sup>) for 6 days. Cytokines were added every 2 days by replacing half of the culture volume with fresh culture media. Dendritic cells were collected on day 6, characterized by flow cytometry (see below) and used immediately. Human umbilical vein endothelial cells (HUVECs) were obtained from Lonza and maintained in endothelial grown medium (EGM; Lonza).

HAP1 cells were used for the haploid screen and fibroblasts or CHO cells were used for hit validation and functional studies. Vero cells are commonly used in studies of filovirus replication, because they are highly susceptible to infection. Dendritic cell and HUVECs resemble cell types that are early and late targets of filovirus infection *in vivo*, respectively<sup>31,32</sup>.

**Flow cytometry of dendritic cells.** Human dendritic cells were treated with Fc-block (BD Pharmingen) before incubation with mouse anti-human CD11c-APC (BioLegend) and mouse anti-human CD209-PE or isotype controls. Dendritic cells were washed and re-suspended in PBS for flow cytometric analysis using a BD FACSCanto II flow cytometer (BD Biosciences). Data analysis was completed using FlowJo software. >95% of cells were routinely observed to be CD11c<sup>+</sup>, DC-SIGN<sup>+</sup>.

**Viruses.** Recombinant VSV expressing eGFP and Ebola virus GP (rVSV-GP-EboV) was recovered and amplified as described<sup>10</sup>. Recombinant rVSV-GP-BDV was provided by J. C. de la Torre. rVSV-G-RABV was generated by replacement of the VSV G ORF in VSV-eGFP<sup>33</sup> with that of the SAD-B19 strain of rabies virus, and recombinant virus was recovered and amplified<sup>34</sup>. VSV pseudotypes bearing glycoproteins derived from Ebola virus, Sudan virus and Marburg virus were generated as described<sup>35</sup>.

The following non-recombinant viruses were used: adenovirus type 5 (ATCC), coxsackievirus B1 (ATCC), poliovirus 1 Mahoney (provided by C. Schlieker), HSV-1 KOS (provided by H. Ploegh), influenza A/PR8/34 (H1N1) (Charles Rivers), Rift valley fever virus MP-12 (provided by J. Wojcechowskyj), and mammalian reovirus serotype 1 (provided by M. Nibert).

**Generation of HAP1 cells.** Retroviruses encoding SOX2, MYC, OCT4 and KLF4 were produced<sup>36</sup>. Concentrated virus was used to infect near-haploid KBM7 cells in three consecutive rounds of spin-infection with an interval of 12 h. Colonies were picked and tested for ploidy. One clonally derived cell line (referred to as HAP1) was further grown and characterized. Karyotyping analysis demonstrated that most cells (27 of 39) were fully haploid, a smaller population (9 of 39) was haploid for all chromosomes except chromosome 8, like the parental KBM7 cells. Less than 10% (3 of 39) was diploid for all chromosomes except for chromosome 8, which was tetraploid.

**Haploid genetic screen.** Gene-trap virus was produced in 293T cells by transfection of pGT-GFP, pGT-GFP+1 and pGT-GFP+2 combined with pAdvantage, CMV-VSVG and Gag-pol. The virus was concentrated using ultracentrifugation for 1.5 h at 25,000 r.p.m. in a Beckman SW28 rotor. 100 million HAP1 cells were infected. A proportion of the cells was harvested for genomic DNA isolation to create a control data set. For the screen, 100 million mutagenized cells were exposed to rVSV-GP-EboV at a MOI ~100. The resistant colonies were expanded and ~30 million cells were used for genomic DNA isolation.

**Sequence analysis of gene-trap insertion sites.** Insertion sites were identified by sequencing the genomic DNA flanking gene-trap proviral DNA as described before<sup>8</sup>. In short, a control data set was generated containing insertion sites in mutagenized HAP1 cells before selection with rVSV-GP-EboV. Genomic DNA was isolated from ~40 million cells and subjected to a linear PCR followed by linker ligation, PCR and sequencing using the Genome Analyser platform (Illumina). Insertion sites were mapped to the human genome and insertion sites were identified that were located in Refseq genes. Insertions in this control data set comprise ~400,000 independent insertions that meet this criteria (Supplementary Table 1). To generate the experimental data set, insertions in the mutagenized HAP1 cells after selection with rVSV-GP-EboV were identified using an inverse PCR protocol followed by sequencing using the Genome Analyser. The number of inactivating mutations (that is, sense orientation or present in exon) per individual gene was counted as well as the total number of inactivating insertions for all genes. Enrichment of a gene in the screen was calculated by comparing how often that

gene was mutated in the screen compared to how often the gene carries an insertion in the control data set. For each gene a *P*-value (corrected for false discovery rate) was calculated using the one-sided Fisher exact test (Supplementary Table 2).

**Characterization of the HAP1 mutant lines.** Genomic DNA was isolated using Qiamp DNA mini kit (Qiagen). To confirm that the cells were truly clonal and to confirm the absence of the wild-type DNA locus, a PCR was performed with primers flanking the insertion site using the following primers: (NPC-F1, 5'-GAAGTTGGTCTGGCGATGGAG-3'; NPC1-R2, 5'-AAGGTCCTGATCTAAACTCTAG-3'; VPS33A-F1, 5'-TGTCCTACGCCGAGTGAACC-3'; VPS33A-R1, 5'-CTGTACACTTTGCTCAGTTTCC-3'; VPS11-F1, 5'-GAAGGAGCCGCTGAGCAATGATG-3'; VPS11-R1, 5'-GGCCAGAATTTAGTAGCAGCAAC-3'). To confirm the correct insertion of the gene trap at the different loci a PCR was performed using the reverse (R1) primers of NPC1, VPS11 and VPS33A combined with a primer specific for the gene trap vector: PGT-F1; 5'-TCTCCAAATCTCGGTGGAAC-3'. To determine RNA expression levels of NPC1, VPS11 and VPS33A, total RNA was reverse transcribed using Superscript III (Invitrogen) and amplified using gene-specific primers: VPS11, 5'-CTGCTTCAAGTTCCTTTGC-3' and 5'-AAGATTTCAGTGCAGAGTGG-3'; NPC1, 5'-CCACAGCATGACCGTC-3' and 5'-CAGCTCACAAAACAGGTTTCAG-3'; VPS33A, 5'-TTAACACCTCTTGCCACTCAG-3' and 5'-TGTGTCTTTCTCTGAATGCTG-3'.

**Generation of stable cell populations expressing an NPC1-Flag fusion protein.** A human cDNA encoding NPC1 (Origene) was ligated in-frame to a triple Flag sequence and the resulting gene encoding a C-terminally Flag-tagged NPC1 protein was subcloned into the pBABE-puro retroviral vector<sup>37</sup>. Retroviral particles packaging the NPC1-Flag gene or no insert were generated by triple transfection in 293T cells, and used to infect control and NPC1-deficient human fibroblasts and CHO lines. Puromycin-resistant stable cell populations were generated.

**Cell viability assays for virus treatments.** KBM7 and HAP1 cells were seeded at 10,000 cells per well in 96-well tissue culture plates and treated with the indicated concentrations of rVSV-GP-EboV. After 3 days cell viability was measured using an XTT colorimetric assay (Roche). Viability is plotted as percentage viability compared to untreated control. To compare susceptibility of the HAP1 mutants to different viruses, they were seeded at 10,000 cells per well and treated with different cytolitic viruses at a concentration that in pilot experiments was the lowest concentration to produce extensive cytopathic effects. Three days after treatment, viable, adherent cells were fixed with 4% formaldehyde in phosphate-buffered saline (PBS) and stained with crystal violet.

**VSV infectivity measurements.** Infectivities of VSV pseudotypes were measured by manual counting of eGFP-positive cells using fluorescence microscopy at 16–26 h after infection, as described previously<sup>7</sup>. rVSV-GP-EboV infectivity was measured by fluorescent-focus assay (FFA), as described previously<sup>10</sup>.

**Filipin staining.** Filipin staining to visualize intracellular cholesterol was done as described<sup>38</sup>. Cells were fixed with paraformaldehyde (3%) for 15 min at 25 °C. After three PBS washes, cells were incubated with filipin complex from *Streptomyces filipinensis* (Sigma-Aldrich) (50 µg ml<sup>−1</sup>) in the dark for 1 h at room temperature. After three PBS washes, cells were visualized by fluorescence microscopy in the DAPI channel.

**Measurements of cysteine cathepsin activity.** Enzymatic activities of CTSB and CATL in acidified post-nuclear extracts of Vero cells, human fibroblasts and CHO lines were assayed with fluorogenic peptide substrates Z-Arg-Arg-AMC (Bachem Inc.) and (Z-Phe-Arg)2-R110 (Invitrogen) as described<sup>39</sup>. As a control for assay specificity, enzyme activities were also assessed in extracts pre-treated with E-64 (10 µM), a broad-spectrum cysteine protease inhibitor, as previously described<sup>10</sup>. Active CTSB and CATL within intact cells were labelled with the fluorescently labelled activity-based probe GB111 (1 µM) and visualized by gel electrophoresis and fluorimaging, as described previously<sup>40</sup>.

**Purification and dye conjugation of rVSV-GP-EboV.** rVSV-GP-EboV was purified and labelled with Alexa Fluor 647 (Molecular Probes, Invitrogen Corporation) as described<sup>41</sup> with minor modifications. Briefly, Alexa Fluor 647 (Molecular Probes, Invitrogen Corporation) was solubilized in DMSO at 10 mg ml<sup>−1</sup> and incubated at a concentration of 31.25 µg ml<sup>−1</sup> with purified rVSV-GP-EboV (0.5 mg ml<sup>−1</sup>) in 0.1 M NaHCO<sub>3</sub> (pH 8.3) for 90 min at room temperature. Virus was separated from free dye by ultracentrifugation. Labelled viruses were re-suspended in NTE (10 mM Tris pH 7.4, 100 mM NaCl, 1 mM EDTA) and stored at −80 °C.

**Virus binding/internalization assay.** Cells were inoculated with a MOI of 200–500 of Alexa-647-labelled rVSV-GP-EboV at 4 °C for 30 min to allow binding of virus to the cell surface. Cells were subsequently fixed in 2% paraformaldehyde (to examine virus binding) or after a 2-h incubation at 37 °C and an acid wash to remove surface-bound virus. The cellular plasma membrane was labelled by incubation of

cells with  $1 \mu\text{g ml}^{-1}$  Alexa Fluor 594 wheat germ agglutinin (Molecular Probes, Invitrogen) in PBS for 15 min at room temperature. External virus particles were detected using a 1:2,000 dilution of antibody 265.1, a mouse monoclonal antibody specific for Ebola GP. The GP antibodies were detected by Alexa-488-conjugated goat anti-mouse secondary antibody (Molecular Probes, Invitrogen). After washing with PBS, cells were mounted onto glass slides using Prolong Antifade Reagent (Invitrogen, Molecular Probes). Fluorescence was monitored with an epifluorescence microscope (Axiovert 200M; Carl Zeiss) equipped with a  $\times 63$  objective and representative images were acquired using Slidebook 4.2 software (Intelligent Imaging Innovations)<sup>41,42</sup>.

**VSV M protein-release assay.** Cells grown on 12-mm coverslips coated with poly-D-lysine (Sigma-Aldrich) were pre-treated with  $5 \mu\text{g ml}^{-1}$  puromycin for 30 min and inoculated with rVSV at a MOI of 200–500 in the presence of puromycin. After 3 h, cells were washed once with PBS and fixed with 2% paraformaldehyde in PBS for 15 min at room temperature. To detect VSV M protein, fixed cells were incubated with a 1:7,500 dilution of monoclonal antibody 23H12 (gift of D. Lyles<sup>43</sup>) in PBS containing 1% BSA and 0.1% Triton X-100 for 30 min at room temperature. Cells were washed three times with PBS, and the anti-M antibodies were detected using a 1:750 dilution of Alexa 594-conjugated goat anti-mouse secondary antibodies. Cells were counter-stained with DAPI to visualize nuclei. Cells were washed three times and mounted onto glass slides after which M localization images were acquired using a Nikon TE2000-U inverted epifluorescence microscope (Nikon Instruments) equipped with a  $\times 20$  objective. Representative images were acquired with Metamorph software (Molecular Devices).

**Electron microscopy.** Confluent cell monolayers in 6-well plates were inoculated with rVSV-GP-EboV at a MOI of 200–500 for 3 h. Cells were fixed for at least 1 h at room temperature in a mixture of 2.5% glutaraldehyde, 1.25% paraformaldehyde and 0.03% picric acid in 0.1 M sodium cacodylate buffer (pH 7.4). Samples were washed extensively in 0.1 M sodium cacodylate buffer (pH 7.4) and treated with 1% osmium tetroxide and 1.5% potassiumferrocyanide in water for 30 min at room temperature. Treated samples were washed in water, stained in 1% aqueous uranyl acetate for 30 min, and dehydrated in grades of alcohol (70%, 90%,  $2\times 100\%$ ) for 5 min each. Cells were removed from the dish with propyleneoxide and pelleted at 3,000 r.p.m. for 3 min. Samples were infiltrated with Epon mixed with propyleneoxide (1:1) for 2 h at room temperature. Samples were embedded in fresh Epon and left to polymerize for 24–48 h at  $65^\circ\text{C}$ . Ultrathin sections (about 60–80 nm) were cut on a Reichert Ultracut-S microtome and placed onto copper grids. For preparation of cryosections the virus-inoculated cells were rinsed once with PBS and removed from the dish with 0.5 mM EDTA in PBS. The cell suspension was layered on top of an 8% paraformaldehyde cushion in an Eppendorf tube and pelleted for 3 min at 3,000 r.p.m. The supernatant was removed and fresh 4% paraformaldehyde was added. After 2 h incubation, the fixative was replaced with PBS. Before freezing in liquid nitrogen the cell pellets were infiltrated with 2.3 M sucrose in PBS for 15 min. Frozen samples were sectioned at  $-120^\circ\text{C}$  and transferred to formvar-carbon-coated copper grids. Grids were stained for lysosomes with a mouse monoclonal antibody raised against LAMP1 (H4A3; Santa Cruz Biotechnology). The LAMP1 antibodies were visualized with Protein-A gold secondary antibodies. Contrasting/embedding of the labelled grids was carried out on ice in 0.3% uranyl acetate in 2% methyl cellulose. All grids were examined in a TecnaiG<sup>2</sup> Spirit BioTWIN mission electron microscope and images were recorded with an AMT 2k CCD camera.

**Authentic filoviruses and infections.** Vero cells were pre-treated with culture medium lacking or containing U18666A ( $20 \mu\text{M}$ ) for 1 h at  $37^\circ\text{C}$ . VERO cells and primary human dermal fibroblasts were exposed to Ebola virus Zaire 1995 or Marburg virus Ci67 at a MOI of 0.1 for 1 h. Viral inoculum was removed and fresh culture media with or without drug was added. Samples of culture supernatants were collected and stored at  $-80^\circ\text{C}$  until plaque assays were completed.

Dendritic cells were collected and seeded in 96-well poly-D-lysine-coated black plates (Greiner Bio-One) at  $5 \times 10^4$  cells per well or in 6-well plates at  $10^6$  cells per well in culture media and incubated overnight at  $37^\circ\text{C}$ . They were pre-treated with medium lacking or containing U18666A as described above. Dendritic cells were exposed to Ebola virus Zaire 1995 or Marburg virus Ci67 at a MOI of 3 for 1 h. Virus inoculum was removed and fresh culture media with or without drug was added. Uninfected cells with or without drug served as negative controls. Cells were incubated at  $37^\circ\text{C}$  and fixed with 10% formalin at designated times. HUVECs were seeded in 96-well poly-D-lysine-coated black plates at  $5 \times 10^4$  cells per well in culture media, treated with U18666A, infected, and processed as described above for dendritic cells.

**Cytotoxicity analysis.** Dendritic cells and HUVECs were seeded in 96-well plates. After overnight incubation at  $37^\circ\text{C}$ , U18666A was added at the same concentrations used for the viral infection studies. Cells in culture media without drug served as the untreated control. At indicated times after treatment, an equal volume of

CellTiter-Glo Reagent (Promega) was added to wells containing cells in culture media. Luminescence was measured using a plate reader.

**Plaque assays for titration of filoviruses.** Tenfold serial dilutions of culture supernatants or serum were prepared in modified Eagle's medium with Earle's balanced salts and nonessential amino acids (EMEM/NEAA) plus 5% heat-inactivated fetal bovine serum. Each dilution was inoculated into a well of a 6-well plate containing confluent monolayers of Vero 76 cells. After adsorption for 1 h at  $37^\circ\text{C}$ , monolayers were overlaid with a mixture of 1 part of 1% agarose (Seakem) and 1 part of  $2\times$  Eagle basal medium (EBME), 30 mM HEPES buffer and 5% heat-inactivated fetal bovine serum. After incubation at  $37^\circ\text{C}$ , 5%  $\text{CO}_2$ , 80% humidity for 6 days, a second overlay with 5% Neutral red was added. Plaques were counted the following day, and titres were expressed as p.f.u.  $\text{ml}^{-1}$ .

**Analysis of filovirus-infected cultures by immunofluorescence.** Formalin-fixed cells were blocked with 1% bovine serum albumin solution before incubation with primary antibodies. Ebola-virus-infected cells and uninfected controls were incubated with Ebola virus GP-specific monoclonal antibodies 13F6 (ref. 44) or KZ52 (ref. 45). Marburg-virus-infected cells and uninfected controls were incubated with Marburg virus GP-specific monoclonal antibody 9G4. Cells were washed with PBS before incubation with either goat anti-mouse IgG or goat anti-human IgG conjugated to Alexa 488. Cells were counterstained with Hoechst stain (Molecular Probes), washed with PBS and stored at  $4^\circ\text{C}$ .

**Image analysis.** Images were acquired at 9 fields per well with a  $\times 10$  objective lens on a Discovery-1 high content imager (Molecular Devices) or at 6 fields per well with a  $\times 20$  objective lens on an Operetta (Perkin Elmer) high content device. Discovery-1 images were analysed with the 'live/dead' module in MetaXpress software. Operetta images were analysed with a customized scheme built from image analysis functions present in Harmony software.

**Animals and filovirus challenge experiments.** Mouse-adapted Ebola virus has been described<sup>46</sup>. Mouse-adapted Marburg virus Ci67 was provided by S. Bavari<sup>47</sup>. Female and male BALB/c *Npc1*<sup>+/-</sup> mice and BALB/c *Npc1*<sup>+/+</sup> mice (5–8-week-old) were obtained from Jackson Laboratory. Mice were housed under specific pathogen-free conditions. Research was conducted in compliance with the Animal Welfare Act and other federal statutes and regulations relating to animals and experiments involving animals and adhered to principles stated in the Guide for the Care and Use of Laboratory Animals (National Research Council, 1996). The facility where this research was conducted is fully accredited by the Association for the Assessment and Accreditation of Laboratory Animal Care International. For infection, mice were inoculated intraperitoneally with a target dose of 1,000 p.f.u. ( $30,000\times$  the 50% lethal dose) of mouse-adapted Ebola virus or mouse-adapted Marburg Ci67 virus in a biosafety level 4 laboratory. Mice were observed for 28 days after challenge by study personnel and by an impartial third party. Daily observations included evaluation of mice for clinical symptoms such as reduced grooming, ruffled fur, hunched posture, subdued response to stimulation, nasal discharge and bleeding. Serum was collected from surviving mice to confirm virus clearance. Back titration of the challenge dose by plaque assay determined that Ebola-virus-infected mice received 900 p.f.u. per mouse and Marburg-virus-infected mice received 700 p.f.u. per mouse.

**RNA interference.** Lentiviral vectors expressing an shRNA specific for NPC1 (Sigma-Aldrich; clone# TRCN0000005428; sequence CCACAAGTCTATAC CATATT) or a non-targeting control shRNA (Sigma-Aldrich; SHC002; sequence CAACAAGATGAAGAGCACCAA) were packaged into HIV-1 pseudotype virus by transfection in HEK 293T cells and lentivirus-containing supernatants were harvested at 36 h and 48 h after transfection and centrifuged onto HUVECs in 12-well plates in the presence of  $6 \mu\text{g ml}^{-1}$  polybrene at 2,500 r.p.m.,  $25^\circ\text{C}$  for 90 min. HepG2 cells were transduced as above but without the centrifugation step. Cells were subjected to puromycin selection 24 h after the last lentiviral transduction (HepG2,  $1 \mu\text{g ml}^{-1}$ ; HUVECs,  $1.5 \mu\text{g ml}^{-1}$ ) for 48–72 h before harvest for experiments. The level of NPC1 knockdown was assessed by SDS-polyacrylamide gel electrophoresis of cell extracts and immunoblotting with an anti-NPC1 polyclonal antibody (Abcam).

**Ebola virus replicon assay.** Ebola virus support plasmids were created by cloning the NP, VP35, VP30 and L genes from cDNA (provided by E. Mühlberger<sup>48</sup>) into pGEM3 (Promega) and the mutant pL-D742A plasmid was generated by QuikChange site-directed mutagenesis (Stratagene). Truncated versions of the Ebola virus non-coding sequence were generated by overlap-extension PCR and appended to the eGFP ORF. The replicon pZEm was prepared as described previously<sup>49</sup>. The replicon RNA sequence is flanked on the 5' end by a truncated T7 promoter with a single guanosine nucleotide and on the 3' end by the HDV ribozyme sequence and T7 terminator. The transcribed replicon RNA consists of the following EboV Zaire sequences (GenBank accession AF086833): [5']-single guanosine nucleotide–176-nucleotide genomic 5' terminus–55-nucleotide L mRNA 3' UTR–eGFP ORF (antisense orientation)–100-nucleotide NP mRNA 5' UTR–155-nucleotide genomic 3' terminus–[3']. The viral replicon

assay was performed as described previously<sup>49</sup> except that U18666A (20  $\mu\text{g ml}^{-1}$ ) was included in the supplemented DMEM where indicated. Images were collected directly from 6-cm dishes with a Zeiss Axioplan inverted fluorescent microscope.

30. Cruz, J. C., Sugii, S., Yu, C. & Chang, T. Y. Role of Niemann-Pick type C1 protein in intracellular trafficking of low density lipoprotein-derived cholesterol. *J. Biol. Chem.* **275**, 4013–4021 (2000).
31. Geisbert, T. W. *et al.* Pathogenesis of Ebola hemorrhagic fever in cynomolgus macaques: evidence that dendritic cells are early and sustained targets of infection. *Am. J. Pathol.* **163**, 2347–2370 (2003).
32. Geisbert, T. W. *et al.* Pathogenesis of Ebola hemorrhagic fever in primate models: evidence that hemorrhage is not a direct effect of virus-induced cytolysis of endothelial cells. *Am. J. Pathol.* **163**, 2371–2382 (2003).
33. Whelan, S. P., Barr, J. N. & Wertz, G. W. Identification of a minimal size requirement for termination of vesicular stomatitis virus mRNA: implications for the mechanism of transcription. *J. Virol.* **74**, 8268–8276 (2000).
34. Whelan, S. P., Ball, L. A., Barr, J. N. & Wertz, G. T. Efficient recovery of infectious vesicular stomatitis virus entirely from cDNA clones. *Proc. Natl Acad. Sci. USA* **92**, 8388–8392 (1995).
35. Takada, A., Watanabe, S., Okazaki, K., Kida, H. & Kawaoka, Y. Infectivity-enhancing antibodies to Ebola virus glycoprotein. *J. Virol.* **75**, 2324–2330 (2001).
36. Carette, J. E. *et al.* Generation of iPSCs from cultured human malignant cells. *Blood* **115**, 4039–4042 (2010).
37. Morgenstern, J. P. & Land, H. Advanced mammalian gene transfer: high titre retroviral vectors with multiple drug selection markers and a complementary helper-free packaging cell line. *Nucleic Acids Res.* **18**, 3587–3596 (1990).
38. Pentchev, P. G. *et al.* The cholesterol storage disorder of the mutant BALB/c mouse. A primary genetic lesion closely linked to defective esterification of exogenously derived cholesterol and its relationship to human type C Niemann-Pick disease. *J. Biol. Chem.* **261**, 2772–2777 (1986).
39. Ebert, D. H., Deussing, J., Peters, C. & Dermody, T. S. Cathepsin L and cathepsin B mediate reovirus disassembly in murine fibroblast cells. *J. Biol. Chem.* **277**, 24609–24617 (2002).
40. Blum, G. *et al.* Dynamic imaging of protease activity with fluorescently quenched activity-based probes. *Nature Chem. Biol.* **1**, 203–209 (2005).
41. Cureton, D. K., Massol, R. H., Saffarian, S., Kirchhausen, T. L. & Whelan, S. P. Vesicular stomatitis virus enters cells through vesicles incompletely coated with clathrin that depend upon actin for internalization. *PLoS Pathog.* **5**, e1000394 (2009).
42. Ehrlich, M. *et al.* Endocytosis by random initiation and stabilization of clathrin-coated pits. *Cell* **118**, 591–605 (2004).
43. Lefrançois, L. & Lyles, D. S. The interaction of antibody with the major surface glycoprotein of vesicular stomatitis virus. I. Analysis of neutralizing epitopes with monoclonal antibodies. *Virology* **121**, 157–167 (1982).
44. Wilson, J. A. *et al.* Epitopes involved in antibody-mediated protection from Ebola virus. *Science* **287**, 1664–1666 (2000).
45. Maruyama, T. *et al.* Ebola virus can be effectively neutralized by antibody produced in natural human infection. *J. Virol.* **73**, 6024–6030 (1999).
46. Bray, M., Davis, K., Geisbert, T., Schmaljohn, C. & Huggins, J. A mouse model for evaluation of prophylaxis and therapy of Ebola hemorrhagic fever. *J. Infect. Dis.* **178**, 651–661 (1998).
47. Warfield, K. L. *et al.* Development of a model for marburgvirus based on severe-combined immunodeficiency mice. *Viol. J.* **4**, 108 (2007).
48. Muhlberger, E., Weik, M., Volchkov, V. E., Klenk, H. D. & Becker, S. Comparison of the transcription and replication strategies of Marburg virus and Ebola virus by using artificial replication systems. *J. Virol.* **73**, 2333–2342 (1999).
49. Kranzusch, P. J. *et al.* Assembly of a functional Machupo virus polymerase complex. *Proc. Natl Acad. Sci. USA* **107**, 20069–20074 (2010).



# Solution structure of a minor and transiently formed state of a T4 lysozyme mutant

Guillaume Bouvignies<sup>1,2,3\*</sup>, Pramodh Vallurupalli<sup>1,2,3\*</sup>, D. Flemming Hansen<sup>1,2,3</sup>, Bruno E. Correia<sup>4,5</sup>, Oliver Lange<sup>4</sup>, Alaji Bah<sup>6</sup>, Robert M. Vernon<sup>4,6</sup>, Frederick W. Dahlquist<sup>7</sup>, David Baker<sup>4</sup> & Lewis E. Kay<sup>1,2,3,6</sup>

Proteins are inherently plastic molecules, whose function often critically depends on excursions between different molecular conformations (conformers)<sup>1–3</sup>. However, a rigorous understanding of the relation between a protein's structure, dynamics and function remains elusive. This is because many of the conformers on its energy landscape are only transiently formed and marginally populated (less than a few per cent of the total number of molecules), so that they cannot be individually characterized by most biophysical tools. Here we study a lysozyme mutant from phage T4 that binds hydrophobic molecules<sup>4</sup> and populates an excited state transiently (about 1 ms) to about 3% at 25 °C (ref. 5). We show that such binding occurs only via the ground state, and present the atomic-level model of the 'invisible', excited state obtained using a combined strategy of relaxation-dispersion NMR (ref. 6) and CS-Rosetta<sup>7</sup> model building that rationalizes this observation. The model was tested using structure-based design calculations identifying point mutants predicted to stabilize the excited state relative to the ground state. In this way a pair of mutations were introduced, inverting the relative populations of the ground and excited states and altering function. Our results suggest a mechanism for the evolution of a protein's function by changing the delicate balance between the states on its energy landscape. More generally, they show that our approach can generate and validate models of excited protein states.

A detailed characterization of the conformers along a protein's energy landscape is important for understanding the structure–function relationship and also because such an analysis provides insight into fundamental aspects of protein structure and dynamics. In this vein, numerous detailed studies of mutant lysozymes and lysozyme complexes from phage T4 have greatly increased our understanding of the inter-relation between structure, stability, folding and motion in proteins<sup>8</sup>. Among the approximately 700 mutant lysozymes and lysozyme complexes that have been characterized is a family where each member contains an engineered cavity in its hydrophobic core, generated by replacing larger amino acids with alanine (ref. 9). The point mutant causing the most pronounced stability change involved the replacement of a leucine at position 99 (referred to in what follows as L99A T4L), creating a cavity of ~150 Å<sup>3</sup> in the carboxy terminus of the enzyme that is able to bind hydrophobic ligands<sup>4</sup>. Interestingly, X-ray studies showed that the L99A mutant undergoes the least rearrangement at the site of mutation, with the structure essentially unchanged<sup>9</sup>.

Despite the fact that the wild-type and L99A T4L structures are virtually identical in the crystalline state, solution NMR studies of the L99A mutant indicated that many of the peaks were significantly broadened relative to the corresponding resonances in data sets recorded of the wild-type protein<sup>5</sup>. Spectral broadening is indicative of dynamics on the microsecond–millisecond timescale<sup>6</sup>, and in this

case provides a clear indication that cavity creation introduces one or more dynamic processes that are not observed in the wild-type enzyme. Such dynamics can be studied by NMR transverse spin-relaxation experiments, in which the relaxation rates of probe nuclei are measured as a function of the strength of applied radio-frequency fields<sup>6,10</sup>. These experiments provide a powerful approach to quantify structural transitions in proteins because they are sensitive to microsecond–millisecond exchange processes in which a highly populated ground state (G) interconverts with conformers that can have much lower populations (>0.5%), referred to in what follows as excited states (E).

Initial <sup>15</sup>N Carr–Purcell–Meiboom–Gill (CPMG) relaxation dispersion NMR experiments indicated that L99A T4L undergoes a dynamic process involving residues that are proximal to the cavity. The relaxation data were well fitted to a model in which a highly populated ground state (97%, 25 °C) interconverts with a second state that because of its low population (3%) and short lifetime (~1 ms) is 'invisible' in NMR spectra<sup>5</sup>. Using recently developed CPMG dispersion experiments<sup>11</sup>, we have obtained nearly all of the backbone <sup>1</sup>H, <sup>15</sup>N and <sup>13</sup>C chemical shifts—as well as side-chain methyl <sup>13</sup>C chemical shifts—of the invisible excited state with a high level of accuracy (Supplementary Fig. 1, Supplementary Tables 1–5). Such chemical shifts are powerful constraints in structure calculations; when combined with computational protocols<sup>7,12</sup> they can be used to calculate accurate folds of small proteins, even in the absence of additional information, such as inter-nuclear distances<sup>13,14</sup>.

A comparison of the chemical shifts of the ground and excited states shows that conformational rearrangements occur in the vicinity of the cavity involving the C-terminal region of helix E and helices F, G, H and I (Fig. 1a, b). These regions do not become disordered in the excited state, as calculated squared order parameters reporting on the amplitudes of backbone motion from chemical shifts<sup>15</sup>,  $S^2_{\text{RCD}}$ , change little between states (Fig. 1c). However, a decrease in helix propensity is noted for the C-terminal region of helix E, with a very significant concomitant increase in the helix content for the loop connecting helices F and G (Fig. 1d).

The <sup>15</sup>N, <sup>1</sup>H<sup>N</sup>, <sup>1</sup>H<sup>α</sup>, <sup>13</sup>C<sup>α</sup> and <sup>13</sup>C<sup>γ</sup> chemical shifts of the excited state were used to guide Rosetta 'loop' building and refinement<sup>16</sup> to generate structural models of the excited state (described in Supplementary Information, Supplementary Fig. 2). Only regions with significant chemical shift changes (residues 100–120, 132–146; Fig. 1a) were allowed to deviate from the X-ray structure of the L99A cavity mutant. The CS-Rosetta-based excited state conformers so produced are well converged, with pair-wise backbone root-mean-squared deviations (r.m.s.d.) for ten representative, low energy structures of  $0.7 \pm 0.2$  Å over the region that was allowed to vary in the calculations (Supplementary Table 6). As a control, an identical protocol was used to generate the structure of the ground state in the vicinity of the cavity mutant, based on the same number of chemical shifts as for the excited

<sup>1</sup>Department of Molecular Genetics, The University of Toronto, Toronto, Ontario M5S 1A8, Canada. <sup>2</sup>Department of Biochemistry, The University of Toronto, Toronto, Ontario M5S 1A8, Canada. <sup>3</sup>Department of Chemistry, The University of Toronto, Toronto, Ontario M5S 1A8, Canada. <sup>4</sup>Department of Biochemistry, University of Washington, Seattle, Washington 98195, USA. <sup>5</sup>Program in Computational Biology, Instituto Gulbenkian de Ciência, P-2780-156 Oeiras, Portugal. <sup>6</sup>Hospital for Sick Children, Program in Molecular Structure and Function, 555 University Avenue, Toronto, Ontario M5G 1X8, Canada.

<sup>7</sup>Department of Chemistry and Biochemistry, University of California Santa Barbara, Santa Barbara, California 93106, USA.

\*These authors contributed equally to this work.

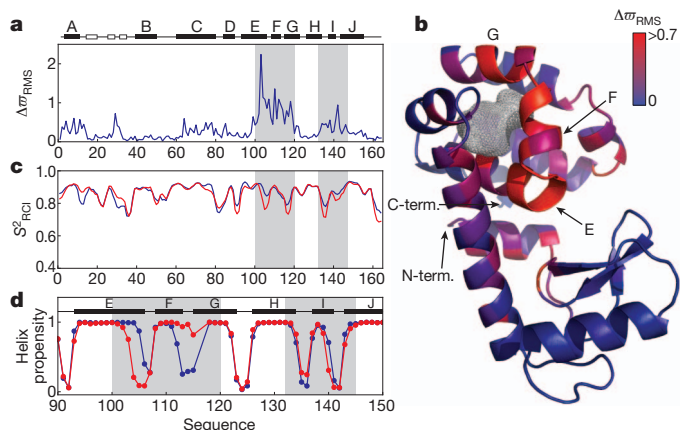


**Figure 1** | L99A T4L exchanges between ground (visible) and excited (invisible) states, each with distinct conformations. **a**, Plot of

$\Delta\sigma_{\text{RMS}} = \sqrt{\frac{1}{N} \sum_i \left( \frac{\Delta\sigma_i}{\Delta\sigma_{i,\text{STD}}} \right)^2}$  as a function of residue, where  $\Delta\sigma_i$  is the shift difference in p.p.m. between states,  $\Delta\sigma_{i,\text{STD}}$  is a nucleus specific value that corresponds to the range of shift values (1 s.d.) that are observed in a database of protein chemical shifts (<http://www.bmrb.wisc.edu>) for the nucleus in question ( $^1\text{H}^{\text{N}}$ ,  $^{15}\text{N}$ ,  $^{13}\text{C}^{\alpha}$ ,  $^1\text{H}^{\alpha}$  and  $^{13}\text{C}'$ ) and  $N$  is the number of nuclei  $\leq 5$  that are included in the average. Significant  $\Delta\sigma_{\text{RMS}}$  differences are localized to a pair of regions (100–120, 132–146) that are highlighted in grey. The secondary structure of the ground state of L99A T4L is illustrated. **b**, Values of  $\Delta\sigma_{\text{RMS}}$  colour-coded onto the X-ray structure of L99A T4L (PDB: 3DMV<sup>28</sup>), ranging from blue ( $\Delta\sigma_{\text{RMS}} = 0$ ) to red ( $\Delta\sigma_{\text{RMS}} > 0.7$ ). The mesh surface indicates the position of the cavity formed by the Leu to Ala substitution at position 99. **c**,  $S^2_{\text{RCI}}$  values for the backbone amide groups in the ground (blue) and excited (red) states of L99A T4L as predicted by the RCI approach<sup>15</sup>. **d**, Helix propensity values, predicted using TALOS+ (ref. 29), highlighting important changes in secondary structure between ground (blue) and excited (red) L99A T4L conformers.

state conformer. The lowest energy structures so obtained are in excellent agreement with the L99A crystal structure (r.m.s.d. of  $0.6 \pm 0.2$  Å, Supplementary Table 6). Figure 2 shows an overlay of ten low energy representative excited state structures (Fig. 2a), along with the X-ray structure of the ground state (Fig. 2b) for comparison. As predicted on the basis of the input chemical shift data (Fig. 1a), there are clear structural differences between ground and excited states. These occur in a region immediately surrounding the cavity, involving rearrangement of the pair of short helices F and G that are orthogonal in the wild-type structure and that form a single, continuous and nearly straight helix in the excited state. This conformational rearrangement also includes a significant change in the backbone dihedral angle ( $\Psi$ ) of Phe 114 to a helical value in the excited state ( $+49^\circ$  to  $-36^\circ$ ) and a reorientation of its side chain caused by a change in the torsion angle ( $\chi_1$ ) from a *gauche*– to a *trans* conformation (see below). The change in  $\chi_1$  projects the Phe 114 benzyl moiety into the cavity of L99A T4L, significantly decreasing its volume (Fig. 2c).

To cross-validate the excited state structures, we used Rosetta structure based design calculations to identify substitutions predicted to stabilize the excited state relative to the ground state (Supplementary Table 7). One such substitution is G113A, which replaces one of the most helix destabilizing residues (Gly) with the most favourable (Ala)<sup>17</sup> in a region of the structure that is predicted to become more helical in the excited state.  $^1\text{H}$ - $^{15}\text{N}$  and  $^1\text{H}$ - $^{13}\text{C}$  spectra of L99A,G113A T4L (recorded at low temperature (1 °C) to slow down the exchange and hence improve spectral quality) show two sets of cross-peaks that can be connected by magnetization exchange<sup>18,19</sup> (Fig. 3a, Supplementary Fig. 3). The first set corresponds to those observed for the L99A ground state, with a second set occurring at the positions predicted for the excited state on the basis of the chemical shifts obtained from CPMG relaxation dispersion experiments recorded on L99A T4L (Fig. 3b). Intensities of peaks from magnetization exchange experiments can be

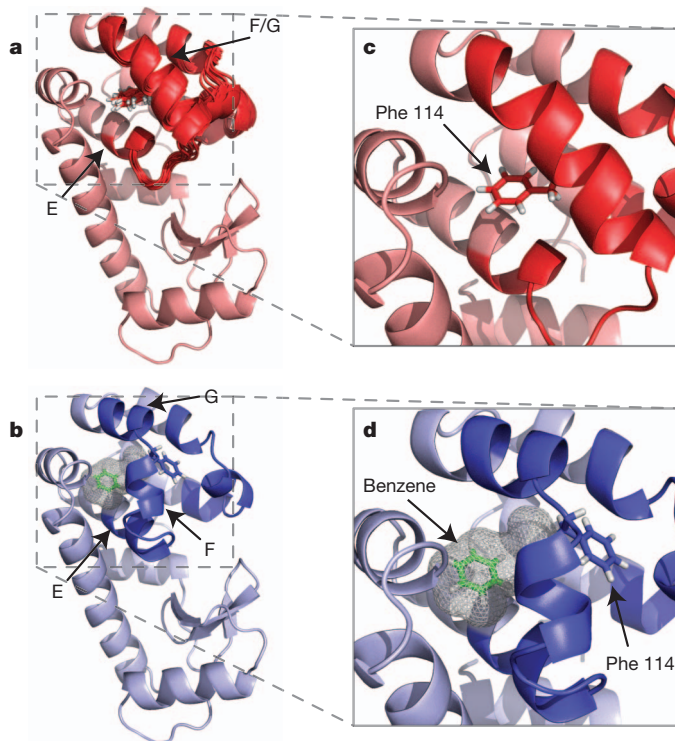


**Figure 2** | The structure of the invisible, excited state of L99A T4L.

**a**, Superposition of the 10 lowest energy structures of the L99A T4L excited state. The locations of helices E, F and G are indicated, along with the side chain of Phe 114 (see c). Only residues 100–120 and 132–146 were allowed to deviate from the L99A T4L ground state X-ray structure in calculations of the excited conformer (Methods). **b**, Ground state structure of L99A T4L, showing helices E, F and G and the position of Phe 114 (PDB: 3DMV<sup>28</sup>) or of benzene (green; PDB: 3DMX<sup>28</sup>) when it is bound inside the cavity (see d). **c**, **d**, Expanded regions of the excited state (c) and ground state (d) structures, focusing on the differences between helices F and G and the position of Phe 114.

fitted to extract the population of the excited state,  $p_E$ , and an exchange rate,  $k_{\text{ex}} = k_{\text{GE}} + k_{\text{EG}}$  ( $k_{ij}$  is the exchange rate from state  $i$  to  $j$ ); values of  $p_E = 34 \pm 2\%$  and  $k_{\text{ex}} = 48 \pm 1 \text{ s}^{-1}$ , at 1 °C, are obtained (Supplementary Fig. 4, Supplementary Table 8). Thus, the G113A mutation shifts the  $\text{G} \rightleftharpoons \text{E}$  equilibrium, as expected from the excited state structure, from  $p_E < 0.5\%$  to 34% at 1 °C.

In a previous set of studies based on analysis of  $^{15}\text{N}$  and methyl  $^{13}\text{C}$  CPMG relaxation dispersion profiles, we speculated that the excited state of L99A T4L is an open conformation where ligands can access the cavity<sup>5</sup>. The solution structure of the low populated L99A T4L conformer, however, predicts that hydrophobic ligands would not bind the excited state because the cavity is occupied by the side chain of Phe 114 (Fig. 2c). As a second cross-validation of the structure, we measured the binding of benzene to the ground and excited conformers independently using a sample of L99A,G113A T4L, where separate peaks can be observed for each state (Fig. 3a). A previous study has established that benzene binds to L99A T4L with a millimolar  $K_D$  and a dissociation rate of close to  $1,000 \text{ s}^{-1}$  at 20 °C (ref. 20). Lowering the temperature to 1 °C decreases both the rate of benzene binding and the rate of exchange between ground and excited states; these rates are reduced to the point where separate peaks are observed for the methyl group of Met 102 in  $^1\text{H}$ - $^{13}\text{C}$  HSQC spectra of the ground, excited and benzene-bound states of L99A, G113A T4L to which one molar equivalent of benzene was added (Fig. 3c). Rates of exchange between the three states can be quantified by analysis of magnetization exchange experiments<sup>18,19,21</sup>. From fits of the time-dependencies of the auto-peaks (labelled ‘G’, ‘E’, ‘B’ in Fig. 3c, diagonal panels of Fig. 3d) and cross-peaks (cross panels) to a model of three-site exchange (Fig. 3e and Supplementary

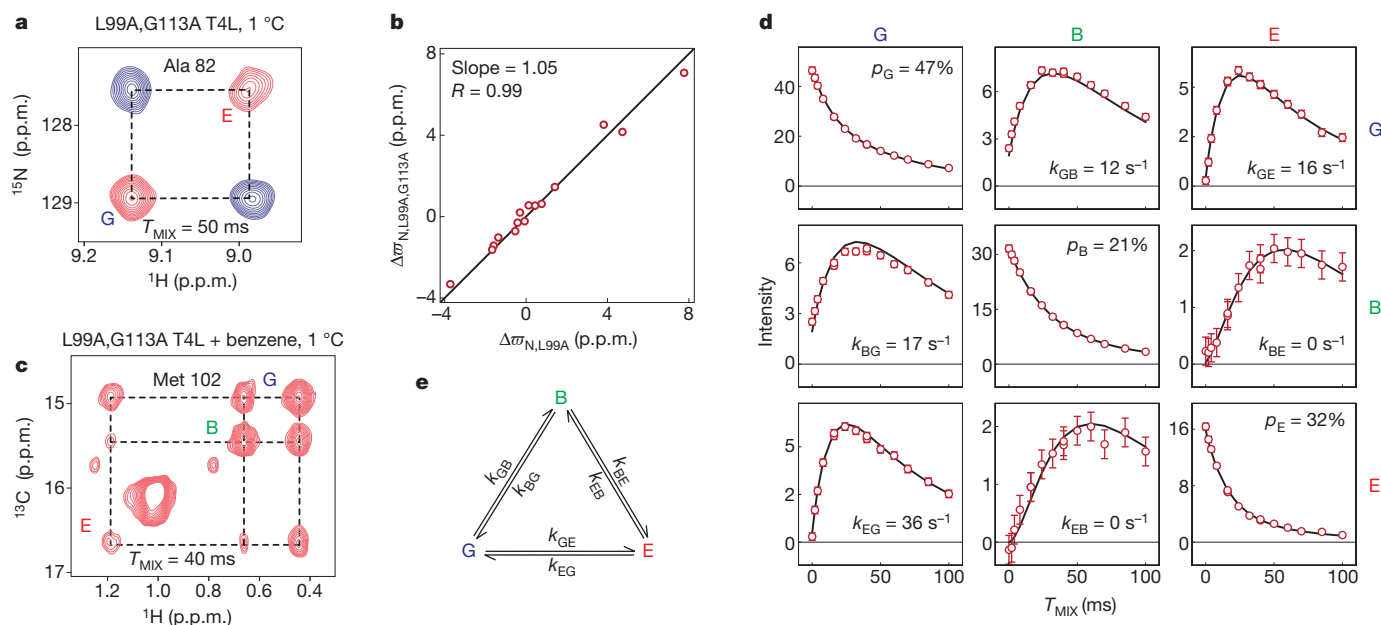


**Figure 3 | Hydrophobic ligands do not bind the excited state of L99A T4L.** **a**, Selected region of the  $^1\text{H}$ - $^{15}\text{N}$  correlation map from a magnetization exchange experiment recorded on L99A,G113A T4L at  $1^\circ\text{C}$ , showing separate peaks for the ground (G) and excited (E) states. A pair of data sets are obtained, with the mixing time ( $T_{\text{MIX}} = 50$  ms) recorded before or after the  $^{15}\text{N}$  chemical shift evolution period, and the data sets subtracted so that diagonal- (cross-) peaks are positive (negative)<sup>30</sup>. **b**, Correlation between  $\Delta\omega_{\text{N}}$  values measured directly from the spectrum in **a** (y axis) and corresponding values from CPMG

relaxation dispersion measurements of L99A T4L ( $25^\circ\text{C}$ ; x axis). **c**, Magnetization exchange spectrum ( $T_{\text{MIX}} = 40$  ms) recorded on an L99A,G113A T4L sample with a 1:1 molar equivalent of benzene, focusing on Met 102 that shows well resolved correlations from ground, excited and benzene-bound (B) states. **d**, Intensity of auto- and cross-peaks for residue Met 102 from magnetization exchange experiments recorded as a function of  $T_{\text{MIX}}$  (red circles), along with the best fit of the data (solid lines) to the exchange model of **e**. Values of rates of exchange,  $k_{ij}$ , are indicated.

Table 8), the six relevant rates,  $k_{ij}$ , are extracted. Best fit values for  $k_{\text{EB}}$ ,  $k_{\text{BE}}$  are  $<0.1 \text{ s}^{-1}$  (Supplementary Fig. 5), and F-test analyses establish that there is no difference in the quality of the fits when these rates are set to zero, indicating that binding to the excited state does not occur. By contrast,  $k_{\text{GB}} = 11.6 \pm 0.3 \text{ s}^{-1}$  and  $k_{\text{BG}} = 17.4 \pm 0.4 \text{ s}^{-1}$ , so that ligand binding proceeds via the ground state. The mechanism by which this occurs is not at present known, but it must involve excursions of the ground state to additional conformations, presumably on a timescale faster than those that are accessible to the dispersion experiments described here.

Whereas the G113A mutation shifts the fractional population of the excited state from approximately 3% to 34%, we were interested in perturbing the equilibrium still further. The R119P substitution is predicted by Rosetta to further favour the excited state because the X-ray structure of the L99A ground state<sup>9</sup> is incompatible with a Pro at position 119 due to steric clashes involving an  $\text{H}^\delta$  proton and the C' of Thr 115. Consistent with this prediction, the  $^1\text{H}$ - $^{15}\text{N}$  HSQC spectrum of G113A,R119P,L99A T4L contains a single set of peaks (Supplementary Fig. 6) at resonance positions identical to those of the invisible, excited state of L99A that were determined by relaxation dispersion measurements (Supplementary Fig. 7). Further relaxation dispersion experiments recorded on the triple mutant established that the dominant conformer in solution, corresponding to the ligand inaccessible state (Supplementary Table 6), interconverts with a minor state conformer whose structure is that of the L99A ground state (Supplementary Fig. 8) (population of  $3.8 \pm 0.1\%$ ,  $k_{\text{ex}} = 806 \pm 28 \text{ s}^{-1}$ ,  $1^\circ\text{C}$ ). Thus, the pair of mutations G113A,R119P inverts the populations of ground and excited states relative to L99A T4L.

This population inversion, rendering the ligand-inaccessible state the major conformer, allows an additional test of the structure of the invisible L99A T4L excited state. Quantitative  $J$ -based scalar coupling experiments<sup>22</sup> recorded on L99A,G113A,R119P T4L confirm that the  $\chi_1$  rotamer state for Phe 114 is *trans*, as observed in the CS-Rosetta based structure of the excited state (Supplementary Fig. 9, Supplementary Table 9, see above). By contrast, similar experiments

recorded on the ground state of L99A T4L are consistent only with a *gauche*- conformation, as expected from the X-ray structure<sup>9</sup>. The *trans*  $\chi_1$  rotameric state for Phe 114 is a novel feature of the L99A T4L excited state and L99A,G113A,R119P T4L. In a G113A variant T4L, as examined here but where Leu is retained at position 99, a *gauche*- conformation is observed<sup>23</sup> for Phe 114; a *trans*  $\chi_1$  angle would lead to steric clashes with Leu 99 (Supplementary Fig. 10).

The L99A mutation in T4L creates an energy landscape in which a low-lying excited state is transiently populated. We have shown that this invisible, excited state has different functional properties from the

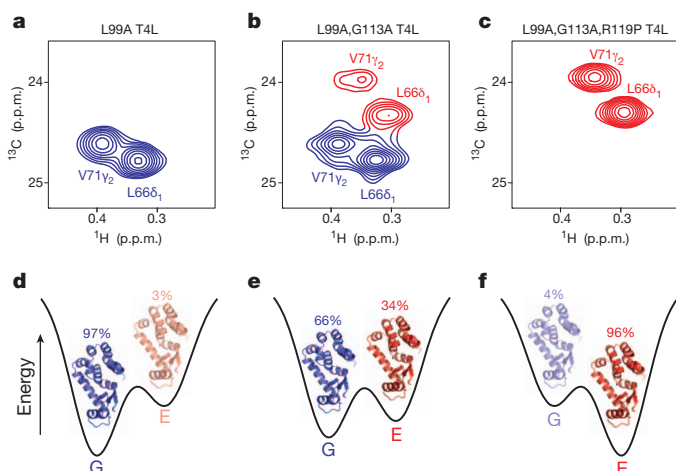


**Figure 4 | The delicate balance between states on the energy landscape can be readily manipulated through mutation, providing a path for protein evolvability.** **a–c**, Selected regions from  $^1\text{H}$ - $^{13}\text{C}$  HSQC spectra (recorded at  $1^\circ\text{C}$ ) of L99A T4L (**a**), L99A,G113A T4L (**b**) and L99A,G113A,R119P T4L (**c**), with the peaks from the ground and excited states coloured in blue and red, respectively. **d–f**, Corresponding energy landscapes, showing the structures of the ground and excited states and their fractional populations.



ground state—it does not bind hydrophobic ligands. This divergence in function can be controlled through mutation, with the G113A single mutation and the G113A,R119P double mutation changing the ratio of binding-competent to binding-incompetent states from 97% to 66% (G113A) and to less than 5% (G113A,R119P) (Fig. 4). The picture of evolving protein function suggested by our studies of L99A T4L is consistent with an emerging view of protein plasticity<sup>24,25</sup>, with each molecule sampling a range of structures. Each unique conformer can, in turn, potentially carry out a different function<sup>24,26,27</sup>. A small number of mutations can then shift the relative populations of the conformers, thereby changing the activity of the protein, as has been observed in directed evolution experiments involving the introduction of mutations into flexible loop regions of enzymes<sup>24</sup>. Insight into the relation between protein dynamics, structure and evolvability is greatly facilitated through the powerful combination of relaxation dispersion NMR and Rosetta enabling individual protein states that populate the energy landscape to be investigated, even in cases where these conformers are invisible to other biophysical techniques. As applications of this methodology continue to grow, so too will our understanding of how protein dynamics control function, increasing the scope for the rational design of proteins with specific properties.

## METHODS SUMMARY

**Protein expression and purification.** All NMR samples were prepared following previously published protocols, as described in detail in Methods.

**NMR experiments and structure calculations.** NMR experiments were recorded and analysed as described in Methods. Structure calculations of the L99A T4L excited state were based on experimental backbone <sup>15</sup>N, <sup>13</sup>C and <sup>1</sup>H chemical shifts obtained from CPMG dispersion experiments. The structures of regions in the excited state with significant variations in chemical shift values relative to those in the ground state were computed using the loop modelling application of Rosetta<sup>16</sup>.

**Full Methods** and any associated references are available in the online version of the paper at [www.nature.com/nature](http://www.nature.com/nature).

Received 11 March; accepted 30 June 2011.

Published online 21 August 2011.

- Karplus, M. & Kuriyan, J. Molecular dynamics and protein function. *Proc. Natl Acad. Sci. USA* **102**, 6679–6685 (2005).
- Boehr, D. D., McElheny, D., Dyson, H. J. & Wright, P. E. The dynamic energy landscape of dihydrofolate reductase catalysis. *Science* **313**, 1638–1642 (2006).
- Henzler-Wildman, K. A. *et al.* Intrinsic motions along an enzymatic reaction trajectory. *Nature* **450**, 838–844 (2007).
- Eriksson, A. E., Baase, W. A., Wozniak, J. A. & Matthews, B. W. A cavity-containing mutant of T4 lysozyme is stabilized by buried benzene. *Nature* **355**, 371–373 (1992).
- Mulder, F. A. A., Mittermaier, A., Hon, B., Dahlquist, F. W. & Kay, L. E. Studying excited states of protein by NMR spectroscopy. *Nature Struct. Biol.* **8**, 932–935 (2001).
- Palmer, A. G., Kroenke, C. D. & Loria, J. P. NMR methods for quantifying microsecond-to-millisecond motions in biological macromolecules. *Methods Enzymol.* **339**, 204–238 (2001).
- Shen, Y. *et al.* Consistent blind protein structure generation from NMR chemical shift data. *Proc. Natl Acad. Sci. USA* **105**, 4685–4690 (2008).
- Baase, W. A., Liu, L., Tronrud, D. E. & Matthews, B. W. Lessons from the lysozyme of phage T4. *Protein Sci.* **19**, 631–641 (2010).
- Eriksson, A. E. *et al.* Response of a protein structure to cavity-creating mutations and its relation to the hydrophobic effect. *Science* **255**, 178–183 (1992).
- Korzhnev, D. M. & Kay, L. E. Probing invisible, low-populated states of protein molecules by relaxation dispersion NMR spectroscopy: an application to protein folding. *Acc. Chem. Res.* **41**, 442–451 (2008).
- Hansen, D. F., Vallurupalli, P. & Kay, L. E. Using relaxation dispersion NMR spectroscopy to determine structures of excited, invisible protein states. *J. Biomol. NMR* **41**, 113–120 (2008).
- Cavalli, A., Salvatella, X., Dobson, C. M. & Vendruscolo, M. Protein structure determination from NMR chemical shifts. *Proc. Natl Acad. Sci. USA* **104**, 9615–9620 (2007).
- Vallurupalli, P., Hansen, D. F. & Kay, L. E. Structures of invisible, excited protein states by relaxation dispersion NMR spectroscopy. *Proc. Natl Acad. Sci. USA* **105**, 11766–11771 (2008).
- Korzhnev, D. M., Religa, T. L., Banachewicz, W., Fersht, A. R. & Kay, L. E. A transient and low-populated protein-folding intermediate at atomic resolution. *Science* **329**, 1312–1316 (2010).
- Berjanskii, M. V. & Wishart, D. S. A simple method to predict protein flexibility using secondary chemical shifts. *J. Am. Chem. Soc.* **127**, 14970–14971 (2005).
- Wang, C., Bradley, P. & Baker, D. Protein-protein docking with backbone flexibility. *J. Mol. Biol.* **373**, 503–519 (2007).
- Fersht, A. *Structure and Mechanism in Protein Science* (Freeman and Company, 1999).
- Montelione, G. T. & Wagner, G. 2D chemical-exchange NMR-spectroscopy by proton detected heteronuclear correlation. *J. Am. Chem. Soc.* **111**, 3096–3098 (1989).
- Farrow, N. A., Zhang, O., Forman-Kay, J. D. & Kay, L. E. A heteronuclear correlation experiment for simultaneous determination of <sup>15</sup>N longitudinal decay and chemical exchange rates of systems in slow equilibrium. *J. Biomol. NMR* **4**, 727–734 (1994).
- Feher, V. A., Baldwin, E. P. & Dahlquist, F. W. Access of ligands to cavities within the core of a protein is rapid. *Nature Struct. Biol.* **3**, 516–521 (1996).
- Religa, T. L., Sprangers, R. & Kay, L. E. Dynamic regulation of archaeal proteasome gate opening as studied by TROSY NMR. *Science* **328**, 98–102 (2010).
- Hu, J. S., Grzesiek, S. & Bax, A. Two-dimensional NMR methods for determining  $\chi_1$  angles of aromatic residues in proteins from three-bond  $J_{\text{CC}'}'$  and  $J_{\text{NC}'}'$  couplings. *J. Am. Chem. Soc.* **119**, 1803–1804 (1997).
- Nicholson, H., Tronrud, D. E., Becktel, W. J. & Matthews, B. W. Analysis of the effectiveness of proline substitutions and glycine replacements in increasing the stability of phage T4 lysozyme. *Biopolymers* **32**, 1431–1441 (1992).
- Tokuriki, N. & Tawfik, D. S. Protein dynamism and evolvability. *Science* **324**, 203–207 (2009).
- Jensen, R. A. Enzyme recruitment in evolution of new function. *Annu. Rev. Microbiol.* **30**, 409–425 (1976).
- Walden, W. E. *et al.* Structure of dual function iron regulatory protein 1 complexed with ferritin IRE-RNA. *Science* **314**, 1903–1908 (2006).
- Tang, C., Schwieters, C. D. & Clore, G. M. Open-to-closed transition in apo maltose-binding protein observed by paramagnetic NMR. *Nature* **449**, 1078–1082 (2007).
- Liu, L. J., Baase, W. A. & Matthews, B. W. Halogenated benzenes bound within a non-polar cavity in T4 lysozyme provide examples of I...S and I...Se halogen-bonding. *J. Mol. Biol.* **385**, 595–605 (2009).
- Shen, Y., Delaglio, F., Cornilescu, G. & Bax, A. TALOS+: a hybrid method for predicting protein backbone torsion angles from NMR chemical shifts. *J. Biomol. NMR* **44**, 213–223 (2009).
- Rodriguez, J. C., Jennings, P. A. & Melacini, G. Using chemical exchange to assign non-covalent protein complexes in slow exchange with the free state: enhanced resolution and efficient signal editing. *J. Biomol. NMR* **30**, 155–161 (2004).

**Supplementary Information** is linked to the online version of the paper at [www.nature.com/nature](http://www.nature.com/nature).

**Acknowledgements** We thank J. Forman-Kay for providing laboratory space, and J. Forman-Kay and T. Alber for discussions. G.B. acknowledges The European Molecular Biology Organization and The Canadian Institutes of Health Research (CIHR) for postdoctoral fellowships. L.E.K. holds a Canada Research Chair in Biochemistry. This work was supported by the CIHR and the Natural Sciences and Engineering Research Council of Canada, with computations performed on the GPC supercomputer at the SciNet HPC Consortium.

**Author Contributions** G.B., P.V. and D.F.H. made samples. G.B., P.V., D.F.H. and L.E.K. designed and performed all NMR experiments. G.B., P.V., B.E.C., O.L. and R.M.V. performed structure calculations. G.B., P.V. and A.B. carried out initial crystallization trials. F.W.D., D.B., G.B., P.V. and L.E.K. designed experiments and wrote the paper.

**Author Information** The structural ensembles of the L99A excited state and L99A,G113A,R119P T4L have been deposited with PDB (accession codes 2LCB, 2LC9). Reprints and permissions information is available at [www.nature.com/reprints](http://www.nature.com/reprints). The authors declare no competing financial interests. Readers are welcome to comment on the online version of this article at [www.nature.com/nature](http://www.nature.com/nature). Correspondence and requests for materials should be addressed to L.E.K. ([kay@pound.med.utoronto.ca](mailto:kay@pound.med.utoronto.ca)).

## METHODS

**Protein expression and purification.** The gene for expression of L99A T4L was optimized for protein production (Genscript) and placed in a pET-29b plasmid. Additional plasmids for the expression of the mutants used in this study (L99A,G113A T4L; L99A,G113A,R119P T4L) were constructed from the L99A T4L plasmid. T4L proteins were expressed in *Escherichia coli* BL21(DE3) cells grown in M9 minimal media with glucose ( $3\text{--}4\text{ g l}^{-1}$ , typically) and ammonium chloride ( $\text{NH}_4\text{Cl}$ ,  $1\text{ g l}^{-1}$ ) as the sole carbon and nitrogen sources, respectively. Proteins with specific labelling patterns (see below) were obtained by expression in M9 media containing the appropriately labelled glucose,  $^{15}\text{NH}_4\text{Cl}$  and solvent ( $\text{H}_2\text{O}$  or  $\text{D}_2\text{O}$ )<sup>31</sup>. The labelling patterns (carbon source/solvent) used in this study are: uniform (U)  $^{15}\text{N}$  (glucose/ $\text{H}_2\text{O}$ ), U- $^{13}\text{C}/^{15}\text{N}$  ( $^{13}\text{C}_6$ -glucose/ $\text{H}_2\text{O}$ ), U- $^2\text{H}/^{13}\text{C}/^{15}\text{N}$  ( $^{13}\text{C}_6$ ,  $^2\text{H}_7$ -glucose/100%  $\text{D}_2\text{O}$ ), U- $^2\text{H}/^{15}\text{N}$  ( $^2\text{H}_7$ -glucose/100%  $\text{D}_2\text{O}$ ),  $^{13}\text{C}/^{15}\text{N}$  ( $^{13}\text{C}_6$ -glucose/100%  $\text{H}_2\text{O}$ ), U- $^{13}\text{C}/^{15}\text{N}/50\% ^2\text{H}$  ( $^{13}\text{C}_6$ ,  $^2\text{H}_7$ -glucose/50%  $\text{D}_2\text{O}$ ),  $^{13}\text{CH}_3$ -Met/ $^{15}\text{N}$  (glucose/ $\text{H}_2\text{O}$ , supplemented with  $100\text{ mg l}^{-1}$  of  $^{13}\text{CH}_3$ -Met added to the media 30 min before induction of protein overexpression). *E. coli* BL21(DE3) cells transformed with the appropriate plasmid were grown in one or two litres of media at  $37^\circ\text{C}$  until an  $\text{OD}_{600}$  of  $\sim 1$ . The temperature was then reduced to  $16^\circ\text{C}$  and protein expression was induced with  $1\text{ mM IPTG}$  for 14–18 h. The cells were harvested by centrifugation and frozen. The protein was purified from the cells as described<sup>32</sup>.

**Samples.** NMR samples ( $\sim 1.5\text{ mM}$  in protein) were prepared in a buffer consisting of  $50\text{ mM}$  sodium phosphate,  $25\text{ mM}$  NaCl,  $2\text{ mM}$  EDTA,  $2\text{ mM}$   $\text{NaN}_3$ , pH 5.5 in either 10% or 100%  $\text{D}_2\text{O}$ . The experiments were performed on Varian Inova spectrometers operating at frequencies ( $^1\text{H}$ ) of 500, 600 and 800 MHz, at a temperature of  $25^\circ\text{C}$ , unless stated otherwise.

**Assignments.** Complete assignments for L99A T4L have been reported previously<sup>5</sup>. The major (ground) state peaks in the L99A,G113A T4L mutant were assigned by comparison with assigned spectra of L99A T4L. Minor (excited-) state  $^1\text{H}$ - $^{15}\text{N}$  resonance assignments were obtained using an  $^{15}\text{N}$  magnetization exchange experiment<sup>19</sup> recorded at 800 MHz,  $1^\circ\text{C}$ , with a mixing time ( $T_{\text{MIX}}$ ) of 50 ms. At  $1^\circ\text{C}$  the excited state is populated to  $\sim 34\%$ ,  $k_{\text{ex}} \approx 50\text{ s}^{-1}$ , so that very clear exchange peaks correlate ground and excited state resonances. Backbone  $^1\text{H}/^{13}\text{C}/^{15}\text{N}$  and  $^{13}\text{C}^{\beta}$  assignments for the L99A,G113A,R119P T4L mutant were obtained using standard triple resonance experiments<sup>33</sup> recorded at  $34^\circ\text{C}$  either at 500 or 800 MHz. Assignments were very close to complete. The elevated temperature ( $34^\circ\text{C}$ ) and lower field (500 MHz) were used to minimize signal loss due to chemical exchange.

**CPMG experiments.**  $^1\text{H}/^{15}\text{N}/^{13}\text{C}$  constant-time (CT) CPMG relaxation dispersion experiments were (usually) performed at two static magnetic fields. Typically, dispersion curves were composed of a large number ( $\sim 15$ ) of  $\nu_{\text{CPMG}}$  values with errors estimated based on two or three repeat values<sup>34</sup>. Here  $\nu_{\text{CPMG}} = 1/(4\tau_{\text{CPMG}})$ , where  $2\tau_{\text{CPMG}}$  is the spacing between the refocusing  $\pi$  pulses applied during the CT delay of length  $T_{\text{Relax}}$ . Details of the experiments<sup>6,35,36</sup> used to characterize the excited state of L99A T4L are summarized in Supplementary Table 1.

**Sign experiments.** Single-quantum CPMG relaxation dispersion experiments provide only the magnitude of the change in chemical shift  $|\Delta\omega_{\text{GE}}| = |\omega_{\text{E}} - \omega_{\text{G}}|$  between the two exchanging states. Signs were obtained by comparing the positions of the ground state peaks in HSQC spectra recorded at different static magnetic fields and/or between peak positions in HSQC/HMQC spectra recorded at the same field<sup>37,38</sup>. Once the signs of amide nitrogen  $\Delta\omega$  values were obtained, the corresponding signs of the amide protons were generated from zero-quantum (ZQ) and double-quantum (DQ) CPMG experiments<sup>39</sup>. Experiments used to obtain this information are listed in Supplementary Table 2.

**Quantitative J-modulated experiments.**  $\chi_1$  angles of aromatic residues in both L99A T4L (ground state) and L99A,G113A,R119P T4L (ground state that is a mimic of the L99A T4L excited state structure, see Supplementary Fig. 7 and text) were determined by measurement of three-bond  $J_{\text{CC}'}^{\text{C}'}_Y$  and  $J_{\text{NC}'}^{\text{C}'}_Y$  scalar couplings using quantitative J-based experiments<sup>22,40</sup> recorded with dephasing delays of 100 ms ( $J_{\text{CC}'}^{\text{C}'}_Y$ ) and 120 ms ( $J_{\text{NC}'}^{\text{C}'}_Y$ ), respectively. All experiments were obtained at  $35^\circ\text{C}$  on a 600 MHz spectrometer, using uniformly  $^{15}\text{N}$ ,  $^{13}\text{C}$  enriched samples. Difference spectra for both experiments and both proteins are shown in Supplementary Fig. 9. Measured scalar coupling values are summarized in Supplementary Table 9 along with the  $\chi_1$  angles for the aromatic residues of the ground and excited state structures.

**Magnetization-exchange experiments.**  $^{15}\text{N}$  magnetization exchange experiments, recorded at  $1^\circ\text{C}$ , 800 MHz, were used for assignment of excited state correlations of L99A,G113A T4L, as described above. A pair of experiments were recorded in which the exchange mixing period,  $T_{\text{MIX}}$  (50 ms), was placed (1) before and (2) after indirect detection of  $^{15}\text{N}$  magnetization. Subtraction of the two data sets so obtained generates a two-dimensional spectrum where correlations from ground and excited states (positive) are connected by cross-peaks (negative), forming a 'rectangular' structure<sup>30</sup> (Fig. 3a). Quantitative methyl  $^{13}\text{C}$

magnetization exchange experiments to quantify exchange,  $\text{G} \xrightleftharpoons[k_{\text{EG}}]{k_{\text{GE}}} \text{E}$  (see below or text), in L99A,G113A T4L were performed at 600 MHz,  $1^\circ\text{C}$ , using a sample in which only Met-C $^{\beta}$  was  $^{13}\text{C}$  enriched. A second similarly labelled sample to which a small amount of benzene was added (approximately 1:1 molar equivalents of benzene and protein) was used to study exchange between the ground, excited and benzene-bound states of L99A,G113A T4L. Experiments were recorded with  $T_{\text{MIX}}$  values ranging between 0 and 85 ms (100 ms in the presence of benzene) with errors estimated based on repeat measurements.

**Data processing.** The NMRpipe software package<sup>41</sup> was used to process all of the NMR data. Subsequent visualization and peak picking was achieved using the program Sparky<sup>42</sup>. The intensities of peaks ( $I$ ) were obtained using the program FuDA (<http://pound.med.utoronto.ca/software.html>), while the CcpNmr set of programs<sup>43</sup> was used to analyse some of the triple resonance assignment experiments.

**Analysis of CPMG data.** Relaxation dispersion (RD) profiles,  $R_{2,\text{eff}}(\nu_{\text{CPMG}})$ , were generated from peak intensities,  $I(\nu_{\text{CPMG}})$ , measured in a series of 2D correlation maps recorded at various CPMG frequencies,  $\nu_{\text{CPMG}}$ . The effective relaxation rates,  $R_{2,\text{eff}}(\nu_{\text{CPMG}})$ , were computed via the relation:

$$R_{2,\text{eff}}(\nu_{\text{CPMG}}) = -\frac{1}{T_{\text{Relax}}} \ln \left( \frac{I(\nu_{\text{CPMG}})}{I_0} \right)$$

where  $I_0$  is the peak intensity extracted from a reference spectrum recorded without the CPMG block. RD profiles were analysed assuming a two-state exchanging system,  $\text{G} \rightleftharpoons \text{E}$ , where the major state, G, interconverts with the minor state, E, as described previously in the context of the L99A system<sup>5,44</sup>. The model parameters defining the chemical exchange process, that is the exchange rate,  $k_{\text{ex}}$ , the population of the minor state,  $p_{\text{E}}$ , and the absolute difference in chemical shifts between the two states,  $|\Delta\omega_{\text{GE}}| = |\omega_{\text{E}} - \omega_{\text{G}}|$ , were determined by minimizing the target function:

$$\chi^2(\zeta) = \sum_{i=1}^N \left( \frac{R_{2,\text{eff}}^{\text{Exp}} - R_{2,\text{eff}}^{\text{Calc}}(\zeta)}{\Delta R_{2,\text{eff}}^{\text{Exp}}} \right)^2$$

where  $R_{2,\text{eff}}^{\text{Exp}}$  and  $\Delta R_{2,\text{eff}}^{\text{Exp}}$  are the experimental effective transverse relaxation rates and their associated uncertainties,  $R_{2,\text{eff}}^{\text{Calc}}(\zeta)$  are back-calculated relaxation rates obtained by numerical integration of the Bloch-McConnell equations<sup>45</sup> using the program CATIA (<http://pound.med.utoronto.ca/software.html>),  $\zeta$  represents the set of adjustable model parameters and the sum is over all the experimental data points.

**Analysis of quantitative magnetization exchange data.** As described above and in the text, methyl  $^{13}\text{C}$  magnetization exchange experiments were recorded on L99A,G113A T4L ( $1^\circ\text{C}$ ) without and with added benzene using a pulse scheme described previously<sup>21,46</sup>. Data from Met 102 were analysed because separate, well-resolved correlations are obtained for the ground, excited and benzene-bound states that could be accurately quantified. At the low temperature used ( $1^\circ\text{C}$ ), the interconversion between ground and excited states as well as benzene binding are in the slow exchange regime, a requirement for the magnetization exchange experiment. The intensity  $I$  of auto- (cross-) peaks corresponding to magnetization that is not (is) transferred between states during a mixing time,  $T_{\text{MIX}}$ , has been analysed by numerically solving the Bloch-McConnell equations for the evolution of magnetization in the presence of chemical exchange<sup>45</sup>. The time dependence of magnetization during the entire pulse sequence was simulated (details are available from the authors on request). The resonance frequencies of the peaks and their transverse relaxation rates were obtained from the positions and linewidths of the peaks in spectra, respectively. The fitted parameters include the total magnetization, longitudinal relaxation rates ( $R_1$ ) for each state, the fractional populations of each state,  $p_i$  (subject to the constraint that  $\sum_i p_i = 1$ ), and the rates of exchange between states  $i$  and  $j$ ,  $k_{\text{ex}ij} = k_{ji} + k_{ij}$ . The fitting parameters were optimized using a simplex procedure to minimize the function:

$$\chi^2 = \sum_{i=1}^N \left( \frac{I_i^{\text{Exp}} - I_i^{\text{Calc}}}{\sigma_i^{\text{Exp}}} \right)^2$$

Here the summation is over all the experimental data points,  $I_i^{\text{Exp}}$  is the experimental intensity,  $I_i^{\text{Calc}}$  is the calculated intensity and  $\sigma_i^{\text{Exp}}$  is the error in the intensity. In the case of two-state exchange (no benzene), 48 data points from four peaks associated with Met 102 (two auto- and two cross-peaks  $\times 12 T_{\text{MIX}}$  values) were fitted using five fitting parameters. For the three-state exchange (approximately 1:1 molar equivalent protein:benzene), 117 data points from nine Met 102 peaks (three auto- and six cross-peaks  $\times 13 T_{\text{MIX}}$ ; Fig. 3d) were fitted using nine fitting parameters. The minimum error in the intensities was assumed to be 3%. Errors in the fitted parameters were estimated using a Monte Carlo



procedure<sup>47</sup>. Here 50 synthetic data sets were generated using the best-fit parameters in which random error was added to magnetization intensities and  $^{13}\text{C}/^1\text{H}$   $R_2$  values (based on the experimental errors) and each of the data sets fitted as per the experimental data. Errors are calculated as 1 s.d. in the extracted values.

These experiments clearly indicate that only the ground state binds benzene. As shown in Fig. 3d, fits of the time dependencies of diagonal- and cross-peaks from magnetization exchange spectra establish that  $k_{\text{BE}}$ ,  $k_{\text{EB}} < 0.1 \text{ s}^{-1}$ . To further support the result that benzene does not bind the excited state, Supplementary Fig. 5 plots the reduced  $\chi^2$  obtained from the fit of the magnetization exchange data as a function of  $k_{\text{exBE}} = k_{\text{BE}} + k_{\text{EB}}$ . A clear minimum occurs for  $k_{\text{exBE}} \approx 0$  ( $\chi^2_{\text{red}} = 1.1$ ). Of note, when  $k_{\text{exBE}}$  is fixed to the relatively small value of  $0.5 \text{ s}^{-1}$ ,  $\chi^2_{\text{red}}$  increases by fivefold (to 5.4), clearly indicating that  $k_{\text{exBE}}$  is very small. From the principle of detailed balance for the equilibrium denoted in Fig. 3e, it is predicted that the ratios  $\frac{p_{\text{E}}}{p_{\text{E}} + p_{\text{G}}}$ ,  $\frac{k_{\text{GE}}}{k_{\text{EG}}}$  will be independent of ligand (benzene) concentration, as observed to within experimental error (Supplementary Table 8). As expected, binding of benzene shifts the equilibrium from the excited (binding incompetent) to the ground/bound states. These results are in complete agreement with the structure of the excited state of L99A T4L, showing clearly that Phe 114 is inserted into the cavity, hence obstructing the binding of hydrophobic ligands.

**L99A excited state chemical shifts.** Excited state amide nitrogen, amide proton and carbonyl chemical shifts are available for nearly all the (164) L99A T4L residues (Supplementary Tables 3–5). In cases where the sign of  $\Delta\omega_{\text{GE}}$  is obtained, the chemical shift of the excited state is readily calculated,  $\omega_{\text{E}} = \omega_{\text{G}} + \Delta\omega_{\text{GE}}$ . In cases where the sign is not available, the excited state chemical shift is ambiguous but restricted to two values,  $\omega_{\text{E}} = \omega_{\text{G}} + \Delta\omega_{\text{GE}}$  or  $\omega_{\text{E}} = \omega_{\text{G}} - \Delta\omega_{\text{GE}}$ . The magnitude of the change in chemical shift,  $|\Delta\omega_{\text{GE}}|$ , also provides useful information (see section on Rosetta calculations below).

**Calculation of L99A T4L excited state structures.** The structure of the excited state of L99A T4L was obtained by using the CS-Rosetta approach developed for the determination of ground state protein structures<sup>7</sup>, with a number of important differences relative to the standard protocol. Based on the  $\Delta\omega_{\text{RMS}}$  values (see text), we assumed that only the regions encompassing residues 100–120 and 132–146 adopt different conformations in the ground and excited states. The structure of the rest of the molecule was fixed to the ground state crystal structure of L99A T4L (3DMV<sup>28</sup>). The structures of these two regions in the excited state were computed using the loop modelling application of Rosetta<sup>16</sup>. As a control, identical CS-Rosetta computations of the ground state structure were also performed using the same limited set of ground state shifts (that is, that are available for the excited state). To avoid any bias, T4 lysozyme structures were removed from the fragment databases in all the computations described here. Two hundred starting 3mer and 9mer fragments were selected for each position using the CS-Rosetta approach<sup>7</sup>, modified to include ambiguous excited state shifts in cases where the sign of  $\Delta\omega_{\text{GE}}$  could not be determined. Fragments were scored against ambiguous shifts by selecting the shift which agreed best with the one predicted for the fragment. Ambiguous chemical shifts were similarly taken into account during the scoring of the final structures. The selected fragments were then used in a standard Rosetta loop modelling protocol<sup>16</sup> to generate 9,600 structures (the target secondary structure propensities input into Rosetta are those predicted by TALOS<sup>+29</sup>). Supplementary Fig. 2a and b plots the energies of the resultant ground state structures, generated with ground state chemical shifts (Supplementary Fig. 2a, CS-Rosetta energy; Supplementary Fig. 2b, chemical shift component of the CS-Rosetta energy term) versus r.m.s.d. to the L99A ground state X-ray structure. The characteristic funnel shape energy profile so obtained is an excellent indicator of convergence and indeed the lowest energy 10 (50) structures have pair-wise backbone r.m.s.d. values of  $0.6 \pm 0.15$  ( $0.55 \pm 0.15$ ) Å relative to the ground state crystal structure, including only those residues that were allowed to move in the calculations. The corresponding plots for the excited state structures are shown in Supplementary Fig. 2c and d.

Some of the low energy CS-Rosetta structures produced with the excited state chemical shifts are very similar to the ground state structure (Supplementary Fig. 2c). This is not surprising, given the experimental finding that the ground state is more stable than the excited state by  $\sim 2 \text{ kcal mol}^{-1}$ . However, the chemical shift score by itself clearly indicates that the ground state structure is not a 'good' solution (Supplementary Fig. 2d). Hence a two-step selection procedure was used. Out of the 9,600 structures that were generated initially, 960 structures with the best CS-Rosetta score were selected for further analysis. As a second selection step, 96 of these structures with the best chemical shift score were retained. In this way, structures with both low energy CS-Rosetta and low energy chemical shift scores are selected. It is noteworthy that the structures so generated were essentially identical irrespective of whether selection was first performed on the basis of the Rosetta score followed by selection according to chemical shifts (as described here) or whether the opposite order of scoring was used. We find that there is a major cluster of structures with an r.m.s.d. of  $\sim 1.4$  Å to the ground state crystal

structure and a much smaller cluster with an r.m.s.d. of  $\sim 1$  Å to the ground state conformer; the final 96 structures selected are indicated in green in Supplementary Fig. 2c and d. Only one out of the forty lowest energy structures after the second round of filtering is part of the second cluster (10% of the 96 structures). A major difference between the two sets of structures is the  $\chi_1$  angle of Phe 114, with this dihedral angle assuming a *trans* (*gauche*–) conformation in the major (minor) cluster. Quantitative- $J$  experiments<sup>22,40</sup> recorded on the L99A,G113A,R119P T4L mutant that is an excellent mimic of the excited state (Supplementary Fig. 7, Supplementary Table 6, see text) clearly show that the *trans* conformation is the only one populated (Supplementary Fig. 9, Supplementary Table 9). Notably, CS-Rosetta computations performed with the full set of chemical shifts for this mutant (L99A,G113A,R119P T4L) produced structures that have a conformation that is essentially identical to that obtained for the excited state of L99A T4L (Supplementary Table 6). All structure calculations were performed on the University of Toronto SciNet super-computer cluster<sup>48</sup>. Each set of 9,600 structures required 10 h of computational time using 256 processor cores. Pymol<sup>49</sup> and Chimera<sup>50</sup> were used to visualize and analyse the resultant structures.

**Mutations shifting ground and excited state populations.** Predictions of free energy differences ( $\Delta\Delta G$ ) were performed as described<sup>51</sup>. Briefly, single point mutants of the 19 amino acids (except cysteine) were made *in silico* in the region corresponding to residues 105–120 and  $\Delta\Delta G$  values were computed for representative structures of both ground and excited states. The crystal structure of L99A T4L (3DMV<sup>28</sup>) was used as the ground state, with a representative low energy structure obtained from CS-Rosetta simulations performed with excited state chemical shifts used for the excited state. The free energy difference between corresponding point mutants in the excited and ground states was computed ( $\Delta\Delta G_{\text{E}} - \Delta\Delta G_{\text{G}}$ ; negative values indicate relative stabilization of the excited state). We screened for single point mutants that energetically favoured the excited state conformation and simultaneously disfavoured the ground state conformation (Supplementary Table 7). Mutations for experimental characterization were selected according to two criteria: secondary structure propensity of the excited state and Rosetta  $\Delta\Delta G$  predictions.

- Lundström, P., Vallurupalli, P., Hansen, D. F. & Kay, L. E. Isotope labeling methods for studies of excited protein states by relaxation dispersion NMR spectroscopy. *Nature Protocols* **4**, 1641–1648 (2009).
- Vallurupalli, P., Hansen, D. F., Lundström, P. & Kay, L. E. CPMG relaxation dispersion NMR experiments measuring glycine  $^1\text{H}\alpha$  and  $^{13}\text{C}\alpha$  chemical shifts in the 'invisible' excited states of proteins. *J. Biomol. NMR* **45**, 45–55 (2009).
- Sattler, M., Schleucher, J. & Griesinger, C. Heteronuclear multidimensional NMR experiments for the structure determination of proteins in solution employing pulsed field gradients. *Prog. Nucl. Magn. Reson. Spectrosc.* **34**, 93–158 (1999).
- Korzhnev, D. M. *et al.* Low-populated folding intermediates of Fyn SH3 characterized by relaxation dispersion NMR. *Nature* **430**, 586–590 (2004).
- Vallurupalli, P., Hansen, D. F., Stollar, E., Meirovitch, E. & Kay, L. E. Measurement of bond vector orientations in invisible excited states of proteins. *Proc. Natl Acad. Sci. USA* **104**, 18473–18477 (2007).
- Hansen, D. F., Vallurupalli, P., Lundström, P., Neudecker, P. & Kay, L. E. Probing chemical shifts of invisible states of proteins with relaxation dispersion NMR spectroscopy: how well can we do? *J. Am. Chem. Soc.* **130**, 2667–2675 (2008).
- Skrynnikov, N. R., Dahlquist, F. W. & Kay, L. E. Reconstructing NMR spectra of "invisible" excited protein states using HSQC and HMQC experiments. *J. Am. Chem. Soc.* **124**, 12352–12360 (2002).
- Bouvignies, G. *et al.* A simple method for measuring signs of  $^1\text{H}^{\text{N}}$  chemical shift differences between ground and excited protein states. *J. Biomol. NMR* **47**, 135–141 (2010).
- Orekhov, V. Y., Korzhnev, D. M. & Kay, L. E. Double- and zero-quantum NMR relaxation dispersion experiments sampling millisecond time scale dynamics in proteins. *J. Am. Chem. Soc.* **126**, 1886–1891 (2004).
- Hu, J. S. & Bax, A. Determination of  $\phi$  and  $\chi_1$  angles in proteins from  $^{13}\text{C}$ - $^{13}\text{C}$  three-bond J couplings measured by three-dimensional heteronuclear NMR. How planar is the peptide bond? *J. Am. Chem. Soc.* **119**, 6360–6368 (1997).
- Delaglio, F. *et al.* NMRpipe – a multidimensional spectral processing system based on Unix pipes. *J. Biomol. NMR* **6**, 277–293 (1995).
- Goddard, T. D. & Kneller, D. G. SPARKY 3 (University of California, San Francisco, 2006).
- Vranken, W. F. *et al.* The CCPN data model for NMR spectroscopy: development of a software pipeline. *Proteins Struct. Funct. Bioinform.* **59**, 687–696 (2005).
- Mulder, F. A., Hon, B., Muhandiram, D. R., Dahlquist, F. W. & Kay, L. E. Flexibility and ligand exchange in a buried cavity mutant of T4 lysozyme studied by multinuclear NMR. *Biochemistry* **39**, 12614–12622 (2000).
- McConnell, H. M. Reaction rates by nuclear magnetic resonance. *J. Chem. Phys.* **28**, 430–431 (1958).
- Sprangers, R., Gribun, A., Hwang, P. M., Houry, W. A. & Kay, L. E. Quantitative NMR spectroscopy of supramolecular complexes: dynamic side pores in ClpP are important for product release. *Proc. Natl Acad. Sci. USA* **102**, 16678–16683 (2005).
- Press, W. H., Flannery, B. P., Teukolsky, S. A. & Vetterling, W. T. *Numerical Recipes in C. The Art of Scientific Computing* 2nd edn (Cambridge Univ. Press, 1992).
- Loken, C. *et al.* SciNet: Lessons learned from building a power-efficient top-20 system and data centre. *J. Phys. Conf. Ser.* **256**, 012026 (2010).



49. The PyMOL Molecular Graphics System, Version 1.3 (Schrödinger, LLC, 2010).
50. Pettersen, E. F. *et al.* UCSF Chimera – a visualization system for exploratory research and analysis. *J. Comput. Chem.* **25**, 1605–1612 (2004).
51. Kellogg, E. H., Leaver-Fay, A. & Baker, D. Role of conformational sampling in computing mutation-induced changes in protein structure and stability. *Proteins* **79**, 830–838 (2011).

# Mutations in *UBQLN2* cause dominant X-linked juvenile and adult-onset ALS and ALS/dementia

Han-Xiang Deng<sup>1\*</sup>, Wenjie Chen<sup>1\*</sup>, Seong-Tshool Hong<sup>1†</sup>, Kym M. Boycott<sup>2</sup>, George H. Gorrie<sup>1†</sup>, Nailah Siddique<sup>1</sup>, Yi Yang<sup>1</sup>, Faisal Fecto<sup>1,3</sup>, Yong Shi<sup>1</sup>, Hong Zhai<sup>1</sup>, Hujun Jiang<sup>1†</sup>, Makito Hirano<sup>1†</sup>, Evadnie Rampersaud<sup>4</sup>, Gerard H. Jansen<sup>5</sup>, Sandra Donkervoort<sup>1</sup>, Eileen H. Bigio<sup>6</sup>, Benjamin R. Brooks<sup>7</sup>, Kaouther Ajroud<sup>1</sup>, Robert L. Sufit<sup>1</sup>, Jonathan L. Haines<sup>8</sup>, Enrico Mugnaini<sup>3,9</sup>, Margaret A. Pericak-Vance<sup>4</sup> & Teepu Siddique<sup>1,3,9</sup>

**Amyotrophic lateral sclerosis (ALS) is a paralytic and usually fatal disorder caused by motor-neuron degeneration in the brain and spinal cord. Most cases of ALS are sporadic but about 5–10% are familial. Mutations in superoxide dismutase 1 (*SOD1*)<sup>1,2</sup>, TAR DNA-binding protein (*TARDBP*, also known as *TDP43*)<sup>3,4</sup> and fused in sarcoma (*FUS*, also known as translocated in liposarcoma (*TLS*))<sup>5,6</sup> account for approximately 30% of classic familial ALS. Mutations in several other genes have also been reported as rare causes of ALS or ALS-like syndromes<sup>7–15</sup>. The causes of the remaining cases of familial ALS and of the vast majority of sporadic ALS are unknown. Despite extensive studies of previously identified ALS-causing genes, the pathogenic mechanism underlying motor-neuron degeneration in ALS remains largely obscure. Dementia, usually of the frontotemporal lobar type, may occur in some ALS cases. It is unclear whether ALS and dementia share common aetiology and pathogenesis in ALS/dementia. Here we show that mutations in *UBQLN2*, which encodes the ubiquitin-like protein ubiquilin 2, cause dominantly inherited, chromosome-X-linked ALS and ALS/dementia. We describe novel ubiquilin 2 pathology in the spinal cords of ALS cases and in the brains of ALS/dementia cases with or without *UBQLN2* mutations. Ubiquilin 2 is a member of the ubiquilin family, which regulates the degradation of ubiquitinated proteins. Functional analysis showed that mutations in *UBQLN2* lead to an impairment of protein degradation. Therefore, our findings link abnormalities in ubiquilin 2 to defects in the protein degradation pathway, abnormal protein aggregation and neurodegeneration, indicating a common pathogenic mechanism that can be exploited for therapeutic intervention.**

We identified a five-generation family (family 186) with ALS, including 19 affected individuals (Supplementary Information). The disease is transmitted in a dominant fashion with reduced penetrance in females. Mutations in the known ALS-linked genes were excluded. No evidence of genetic linkage was found with a genome-wide set of autosomal microsatellite markers. There was no evidence for male-to-male transmission of the disease, so we screened the family with markers from the X chromosome. Linkage was established with several microsatellite markers on the X chromosome, with the highest two-point lod score of 5.0 occurring with marker DXS9736 at  $\Theta = 0$  (Supplementary Table 1). Detailed mapping with dense microsatellite markers and Illumina's Sentrix HumanHap300 Genotyping BeadChip defined the disease-causing gene in a 21.3-megabase (Mb) minimum candidate

region (MCR) between markers rs6417786 and DXS1275, located in the pericentric region from Xp11.23 to Xq13.1.

No other large ALS families without male-to-male transmission were available to us to narrow down the MCR. We therefore focused on finding the causative gene in family 186. Of the 206 genes in this MCR, 191 were protein-coding. Genes in the MCR were analysed on the basis of their expression profile, function, structure and the potential relevance of their encoded proteins to disease. Forty-one genes were sequenced and a unique mutation in *UBQLN2* was identified. This mutation, a C to A substitution at position 1,490 at the level of coding DNA (c.1490C>A), is predicted to result in an amino-acid substitution of proline with histidine at codon 497 at the protein level (p.P497H) (Fig. 1a). The c.1490 C>A mutation co-segregated with the disease in this large X-linked-ALS pedigree (Fig. 1a). This mutation was not present in the SNP database, nor was it present in 928 ethnically matched control samples (representing 1,332 X chromosomes).

*UBQLN2* is an intronless gene. To test whether mutations of *UBQLN2* are causative for other ALS patients, we analysed 188 probands from families with ALS or ALS/dementia, but without male-to-male transmission. Mutations in *SOD1*, *TDP43* and *FUS* were excluded in this cohort. The sequenced region covered the entire coding sequence (see Methods). We found four other *UBQLN2* mutations in four unrelated families, including c.1489 C>T (p.P497S), c.1516 C>A (p.P506T), c.1525 C>T (p.P509S) and c.1573 C>T (p.P525S) (Fig. 1 and Supplementary Fig. 1). All the amino-acid residues at the mutated sites are conserved (Fig. 1c). None of these mutations was present in the SNP database or in 928 control samples. Notably, all five ALS-linked *UBQLN2* mutations identified in this study involved proline residues in a unique PXX repeat region (Fig. 1c, d).

Clinical data were obtained from 40 individuals in the five families with *UBQLN2* mutations, including 35 patients and five obligate carriers. We estimated a penetrance of approximately 90% by the age of 70 years. The age of onset of the disease ranged from 16 to 71 years. A significant difference in age at onset was noted between male and female patients, with male patients having an earlier age of onset ( $33.9 \pm 14.0$  versus  $47.3 \pm 10.8$  years,  $P = 0.003$ , two-tailed Student's *t*-test) (Supplementary Table 2). However, differences in the duration of the disease were not statistically significant ( $43.1 \pm 42.1$  versus  $48.5 \pm 19.9$  months,  $P = 0.61$ ). Eight patients with both ALS and dementia were identified. Dementia in these patients was similar to the frontotemporal lobar

<sup>1</sup>Division of Neuromuscular Medicine, Davee Department of Neurology and Clinical Neurosciences, Northwestern University Feinberg School of Medicine, Chicago, Illinois 60611, USA. <sup>2</sup>Department of Pediatrics, University of Ottawa and Children's Hospital of Eastern Ontario Research Institute, Ottawa, Ontario K1H 8L1, Canada. <sup>3</sup>Interdepartmental Neuroscience Program, Northwestern University Feinberg School of Medicine, Chicago, Illinois 60611, USA. <sup>4</sup>John P. Hussman Institute for Human Genomics, University of Miami, Miller School of Medicine, Miami, Florida 33136, USA. <sup>5</sup>Division of Anatomic Pathology, The Ottawa Hospital, Ottawa, Ontario K1Y 4E9, Canada. <sup>6</sup>Division of Neuropathology, Department of Pathology, Northwestern University Feinberg School of Medicine, Chicago, Illinois 60611, USA. <sup>7</sup>Department of Neurology, Neuroscience and Spine Institute, Carolinas Medical Center, Charlotte, North Carolina 28207, USA. <sup>8</sup>Center for Human Genetics Research, Vanderbilt University, Nashville, Tennessee 37232, USA. <sup>9</sup>Department of Cell and Molecular Biology, Northwestern University Feinberg School of Medicine, Chicago, Illinois 60611, USA. <sup>†</sup>Present addresses: Laboratory of Genetics and Department of Microbiology, Chonbuk National University Medical School, Chonbuk 561-712, South Korea (S.-T.H.); Institute of Neurological Sciences, Southern General Hospital, Glasgow G51 4TF, UK (G.H.G.); Department of Health Sciences, National Natural Science Foundation of China, Beijing 100085, China (H.J.); Department of Neurology, Sakai Hospital Kinki University Faculty of Medicine, Osaka 590-0132, Japan (M.H.).

\*These authors contributed equally to this work.

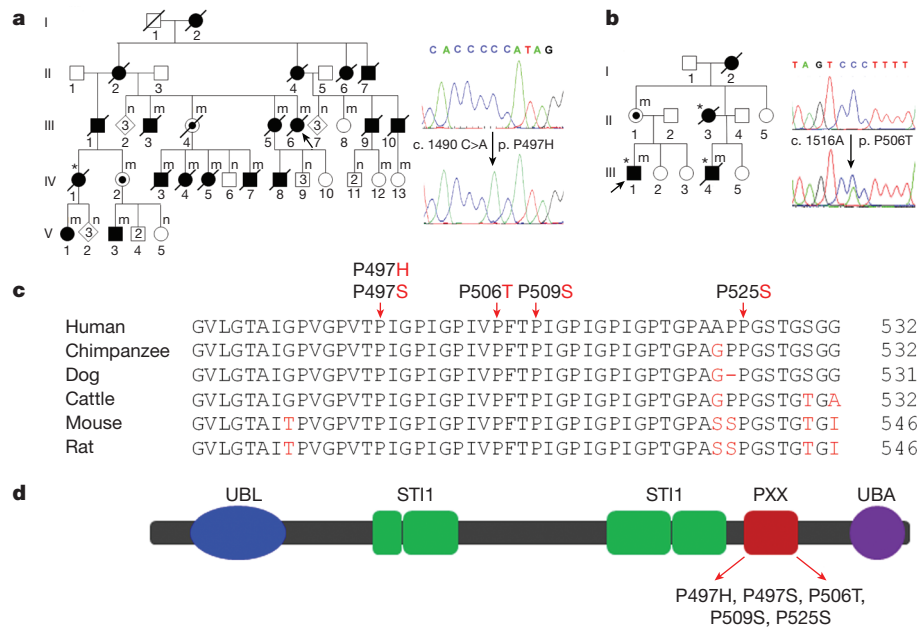


**Figure 1 | Mutations of *UBQLN2* in patients with ALS and ALS/dementia.** **a**, The mutation c.1490 C>A, resulting in p.P497H, was identified in a large family with ALS (family 186). This family was used to map X-linked ALS. The pedigree is shown on the left and DNA sequences are shown on the right: wild-type sequence (upper panel) and a representative hemizygous mutation in a male patient, V3 (lower panel). All affected members whose DNA samples were available for sequencing had the mutation. Two obligate carriers (III 4 and IV 2) were identified as having the same mutation. For simplicity and clarity, more than one unaffected individuals of both genders are represented by a single diamond and more than one unaffected male individual is represented by a single square. Filled symbols, affected individuals; open symbols, unaffected individuals; m, individuals with a mutation in *UBQLN2*; n, individuals without a mutation in *UBQLN2*. **b**, The mutation c.1516 C>A (p.P506T) was identified in family 6316: the pedigree is shown in the left panel and sequences in the right panel (showing a heterozygous mutation from a female obligate carrier, II 1). In

**a** and **b**, probands are indicated with arrows and patients with dementia are indicated with asterisks. **c**, Evolutionary conservation of amino acids in the mutated region of ubiquitin 2 in various species. Comparison of human (*Homo sapiens*) ubiquitin 2 and its orthologues in chimpanzee (*Pan troglodytes*), dog (*Canis lupus familiaris*), cattle (*Bos taurus*), mouse (*Mus musculus*) and rat (*Rattus norvegicus*). Amino acids identical to those in the human protein are shown in black and non-identical ones are in red. The positions of the C-terminal amino acids are shown on the right. Mutated amino acids are indicated by arrows. **d**, Predicted structural and functional domains of ubiquitin 2, a protein of 624 amino acids. Predicted structural and functional domains include a ubiquitin-like domain (UBL, 33–103), four heat-shock-chaperonin-binding motifs (ST11), twelve PXX repeats (491–526) and a ubiquitin-associated domain (UBA). ALS- and ALS/dementia-linked mutations are clustered in the 12 PXX repeats.

type (FTD), including abnormalities in both behaviour and executive function. The dementia was progressive, and eventually global in most ALS/dementia patients. In some cases, the dementia preceded motor symptoms, but all patients eventually developed motor disability. Pathological analysis of spinal-cord autopsy samples from two patients with either the P497H or P506T mutation revealed axonal loss in the corticospinal tract, loss of anterior horn cells and astrogliosis in the anterior horn of the spinal cord (Supplementary Fig. 2).

Protein aggregates or inclusions have been recognized as a pathological hallmark of several neurodegenerative disorders, such as extracellular amyloid- $\beta$  plaques and intracellular tau neurofibrillary tangles in Alzheimer's disease, and  $\alpha$ -synuclein-containing Lewy bodies in Parkinson's disease<sup>16</sup>. In ALS, protein aggregates or inclusions are most common in spinal motor neurons, and are typically skein-like in morphology. These ubiquitin-positive inclusions, among others, are considered to be a hallmark of ALS pathology. Notably, several proteins that are mutated in a small subset of ALS, such as SOD1, TDP43, FUS and optineurin (OPTN) are prominent components of these inclusions<sup>6,12,17–20</sup>. To test whether ubiquitin 2 is present in the characteristic skein-like inclusions, we performed immunohistochemical analysis of post-mortem spinal-cord sections from two patients with a P497H or P506T mutation. Two different ubiquitin 2 antibodies were used. One was a commercially available mouse monoclonal antibody raised with a polypeptide of 71 amino acids from the carboxy terminus (amino acids 554–624, ubiquitin 2-C). The other was a rabbit polyclonal antibody that we generated using a polypeptide of 17 amino acids from the amino terminus (amino acids 8–24, ubiquitin 2-N). This polypeptide is unique to ubiquitin 2 and is not

present in other members of the ubiquitin family or in any other known protein. The ubiquitin 2-N antibody immunoreacted with human and mouse ubiquitin 2 (Supplementary Fig. 3). We also detected a single band of the expected size in western blots using ubiquitin 2-N and ubiquitin 2-C antibodies with human spinal-cord autopsy tissues (Supplementary Fig. 3). Using immunohistochemistry, we saw skein-like inclusions that were immunoreactive with both the ubiquitin 2-C and ubiquitin 2-N antibodies (Supplementary Fig. 4), indicating that ubiquitin 2 is involved in inclusion formation in X-linked ALS. We then examined whether the inclusions in cases of X-linked ALS were also immunoreactive with antibodies against other proteins that are known to be involved in the formation of inclusions in other types of ALS. We found that the skein-like inclusions in the X-linked ALS patients were also immunoreactive with antibodies to ubiquitin, p62, TDP43, FUS and optineurin (Fig. 2a–c and Supplementary Figs 4 and 5), but not SOD1.

Mutations in TDP43, FUS or optineurin occur in a small fraction of familial ALS, but these proteins have been found in the inclusions of a wide spectrum of ALS<sup>6,12,17,18,20</sup>. To test whether ubiquitin 2 is involved in inclusion formation in other types of ALS, we examined 47 post-mortem spinal-cord samples, including cases of sporadic ALS ( $n = 23$ ), familial ALS without mutations in *SOD1*, *TDP43* and *FUS* ( $n = 5$ ), ALS with dementia ( $n = 5$ ), familial ALS with *SOD1* mutations ( $n = 7$  (A4V,  $n = 4$ ; G85R,  $n = 2$ ; E100G,  $n = 1$ )), familial ALS with a G298S mutation in *TDP43* ( $n = 1$ ), and controls without ALS ( $n = 6$ ). We observed ubiquitin-2-positive skein-like inclusions in all ALS cases (Supplementary Figs 6 and 7), indicating that ubiquitin 2 is a common component in the skein-like inclusions of a wide variety of ALS.



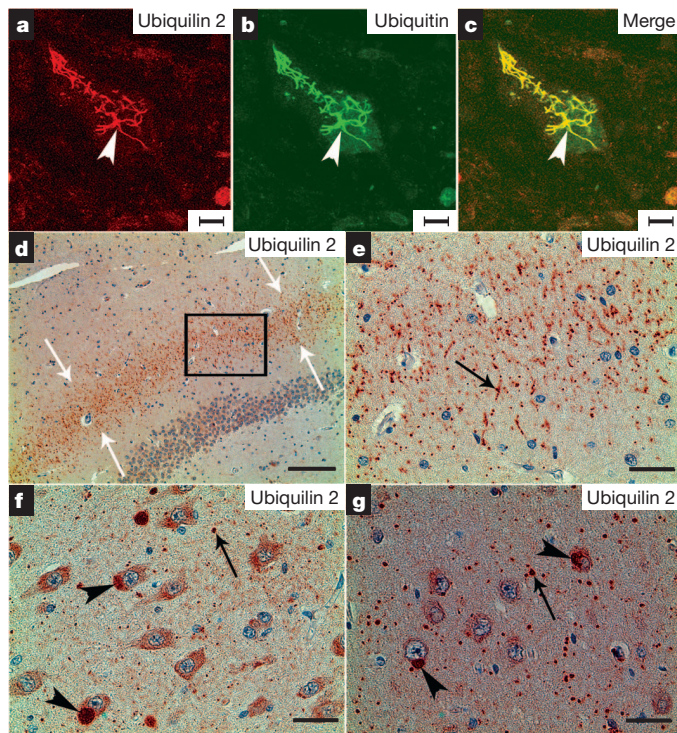


**Figure 2 | Ubiquitin-2-immunoreactive inclusions in the spinal cord and hippocampus.** **a–g.** Spinal cord (**a–c**) and hippocampal (**d–g**) sections from a patient with a  $UBQLN2^{P506T}$  mutation were analysed with confocal microscopy (**a–c**) and immunohistochemistry (**d–g**), using a monoclonal antibody against ubiquitin 2 (ubiquitin 2-C). The ubiquitin-2-positive and skein-like inclusions (arrowhead) are shown in a spinal motor neuron (**a**). These inclusions are also ubiquitin-positive (**b, c**). In the hippocampus, the ubiquitin-2-positive inclusions are shown in the molecular layer of the fascia dentata (**d, e**), CA3 (**f**) and CA1 (**g**). White arrows in **d** indicate the middle region of the molecular layer with ubiquitin-2-positive inclusions. A higher-magnification image of the boxed area in **d** is shown in **e**. Black arrows indicate representative inclusions in neurites (**e–g**), and arrowheads indicate cytoplasmic inclusions in the cell bodies (**f** and **g**). Scale bars: **a–c**, 10  $\mu\text{m}$ ; **d**, 200  $\mu\text{m}$ ; **e**, 50  $\mu\text{m}$ ; **f** and **g**, 25  $\mu\text{m}$ .

Dementia was a prominent feature in eight  $UBQLN2$ -linked cases. To examine whether ubiquitin-2-immunoreactive inclusions are present in the brain, and to explore the potential link between ubiquitin 2 inclusions and dementia, we analysed brain autopsy samples from two patients with the P506T mutation. We saw ubiquitin 2 pathology, which was most prominent in the hippocampus (Fig. 2d–g and Supplementary Fig. 8). Small ubiquitin 2 inclusions (1–5  $\mu\text{m}$  in diameter) were predominantly situated in the neuropil. The fascia dentata presented with a band of radially oriented dendritic and neuropil inclusions in the intermediate region of the molecular layer (Supplementary Fig. 8). In addition to the small neuropil inclusions, large inclusions (up to 20  $\mu\text{m}$  in diameter) were observed in some pyramidal neurons, especially those in the CA3 and CA1 regions (Fig. 2f, g and Supplementary Fig. 8). Co-localization of ubiquitin 2 and ubiquitin in these inclusions was confirmed with confocal microscopy (Supplementary Fig. 8). This type of hippocampal pathology has not previously been observed in any other neurodegenerative disorder. The ubiquitin-2-positive and ubiquitin-positive inclusions did not seem to be co-localized with major glial markers (Supplementary Fig. 9). In addition, we observed a novel, membrane-bound perikaryal structure, which contained eosinophilic granules of varying sizes, in some hippocampal pyramidal neurons. These structures were strongly immunoreactive for ubiquitin 2 (Supplementary Fig. 10).

To test whether ubiquitin 2 pathology is present in the hippocampus of ALS/dementia cases without  $UBQLN2$  mutations, and to explore the correlation of ubiquitin 2 pathology with dementia in ALS, we

examined hippocampal sections of 15 pathologically characterized ALS cases without  $UBQLN2$  mutations, including five cases of ALS/dementia with pathological signatures corresponding to frontotemporal lobar degeneration of motor-neuron-disease type (FTLD-MND/FTLD-U). We found prominent ubiquitin 2 pathology in the hippocampus of all five cases with ALS/dementia (Supplementary Fig. 11). Similar to the ubiquitin 2 inclusions in  $UBQLN2$ -linked ALS/dementia cases, the ubiquitin 2 inclusions in these non- $UBQLN2$ -linked cases were also positive for ubiquitin and p62 (Supplementary Fig. 11), but negative for FUS. Although there was no apparent TDP43 neuritic pathology in the dentate molecular layer, we saw variable numbers of cytoplasmic TDP43 inclusions in dentate granule cells. These have previously been shown in ALS/dementia<sup>18</sup> (Supplementary Fig. 11). However, a notable number of the inclusions containing ubiquitin 2, ubiquitin and p62 were negative for TDP43 (Supplementary Figs 11 and 12). The absence of TDP43 in ubiquitin-2-positive inclusions was further confirmed with an antibody that specifically detects phosphorylated TDP43 in cytoplasmic TDP43 inclusions<sup>18</sup> (Supplementary Fig. 13). We also observed that the inclusions containing ubiquitin 2, ubiquitin and p62 were mostly negative for TDP43 in the CA regions in the non- $UBQLN2$ -linked ALS/dementia cases (Supplementary Fig. 12). We did not observe ubiquitin 2 pathology in the hippocampus of the ten ALS cases without dementia. The correlation of hippocampal ubiquitin 2 pathology to dementia in ALS cases with or without  $UBQLN2$  mutations indicates that ubiquitin 2 is widely involved in ALS-related dementia, even without  $UBQLN2$  mutations.

TDP43 inclusions have been observed in dentate granule cells of the hippocampus in most cases with FTLD-U<sup>18</sup>, and FUS inclusions have been shown in most TDP43-negative FTLD-U cases<sup>21,22</sup>. To test whether ubiquitin 2 co-aggregates with these two known ALS- and dementia-linked proteins *in vitro*, we generated ten expression constructs (Supplementary Information) and co-transfected Neuro-2a cells with different combinations of them. Both wild-type and mutant ubiquitin 2 were mostly distributed in the cytosol. We did not observe obvious differences in the distributions of wild-type and mutant ubiquitin 2. Wild-type FUS and wild-type TDP43 were located almost exclusively in the nuclei (Fig. 3 and Supplementary Fig. 14), whereas mutant FUS showed prominent cytoplasmic distribution (Supplementary Fig. 14) and the C-terminal fragment (218–414, C-TDP43) of TDP43 that has been linked to ALS and FTLD<sup>18,23</sup> was almost exclusively located in the cytosol (Fig. 3). We did not observe cytoplasmic inclusions in cells transfected with wild-type FUS and mutant FUS (Supplementary Fig. 14), nor with wild-type TDP43 (Fig. 3). However, cytoplasmic inclusions were seen in cells expressing either wild-type or mutant ubiquitin 2. Notably, C-TDP43 was co-localized with either wild-type or mutant ubiquitin 2 in the cytoplasmic inclusions (Fig. 3). We obtained consistent data using two expression systems: either tagged ubiquitin 2 or tag-free ubiquitin 2 (Fig. 3 and Supplementary Figs 14 and 15). These data indicate that both ALS- and dementia-linked ubiquitin 2 and TDP43 are prone to co-aggregation. We also noted that inclusion formation was apparently dose-dependent, because the cells with the lowest expression of wild-type or mutant ubiquitin 2, or C-TDP43, did not show cytoplasmic inclusions. However, ubiquitin-2-positive but C-TDP43-negative inclusions were frequently seen in cells with relatively lower levels of ubiquitin 2 and C-TDP43 expression (Fig. 3). This phenomenon indicates that ubiquitin 2 may be more prone to aggregation than TDP43. This is consistent with the pathology observed in ALS/dementia cases, in which the ubiquitin-2-containing inclusions in the molecular layer and in some dentate granule cells were TDP43-negative.

Ubiquitin 2 is a member of the ubiquitin-like protein family (ubiquitins). Humans have four ubiquitin genes, each encoding a separate protein. Ubiquitins are characterized by the presence of an N-terminal ubiquitin-like domain and a C-terminal ubiquitin-associated domain (Fig. 1d). The middle part of ubiquitins is highly variable. This structural organization is characteristic of proteins that deliver ubiquitinated

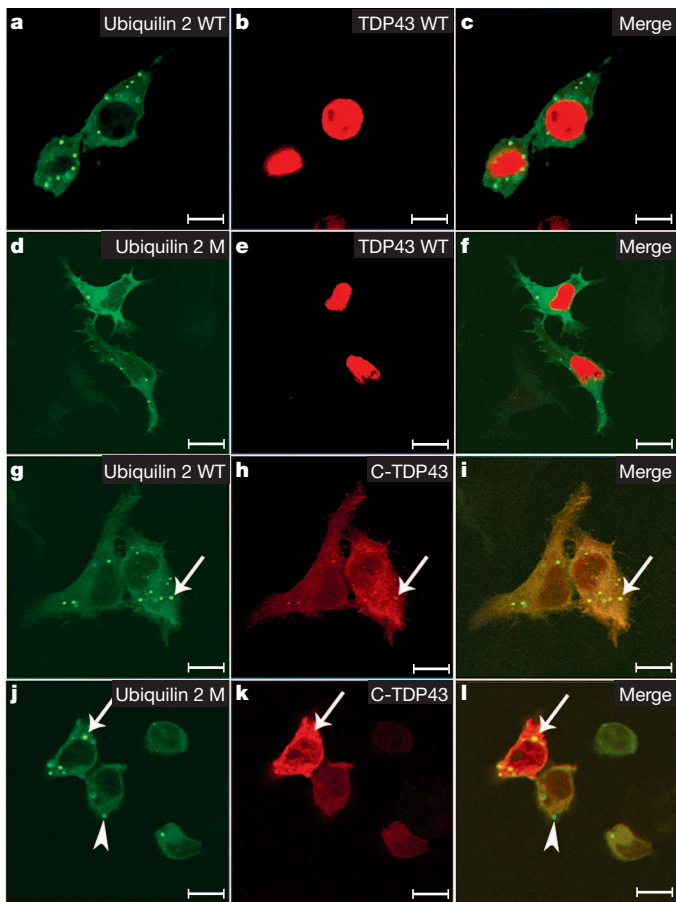


**Figure 3 | Co-localization of ubiquitin 2 with ALS- and dementia-linked TDP43.** **a–l**, Neuro-2a cells were transfected with various combinations of wild-type (WT) ubiquitin 2, mutant (M) ubiquitin 2 (P497H), wild-type TDP43 and a C-terminal fragment of TDP43 (amino acids 218–414) that is linked to ALS and FTL. Ubiquitin 2 is GFP-tagged and TDP43 is mCherry-tagged. Wild-type and mutant ubiquitin 2 are mostly cytoplasmic. Wild-type TDP43 is located almost exclusively in the nuclei and C-TDP43 is almost exclusively cytoplasmic. TDP43 inclusions are co-localized with wild-type (**g–i**) and mutant (P497H) (**j–l**) ubiquitin 2 (arrows). Some ubiquitin-2-positive inclusions are TDP43-negative (arrowhead). Scale bars, 10  $\mu$ m.

proteins to the proteasome for degradation. In accordance with this function, the ubiquitin-like domain of the ubiquilins binds to subunits of the proteasome, and the ubiquitin-associated domain binds to poly-ubiquitin chains that are typically conjugated onto proteins marked for degradation by the proteasome<sup>24</sup>. In addition to the ubiquitin-like and ubiquitin-associated domains that are shared by all ubiquilins, ubiquitin 2 has a unique repeat region containing 12 PXX tandem repeats (Fig. 1d). Notably, all five ALS-linked mutations identified in this study involve proline residues in this short PXX repeat region (Fig. 1c, d), indicating that these mutations may confer on ubiquitin 2 a common property that may be related to the pathogenic mechanism of the disease.

On the basis of the involvement of ubiquitin 2 in the protein degradation pathway, we then investigated the functional consequences of mutant ubiquitin 2 in protein degradation through the ubiquitin–proteasome system (UPS). We used a UPS reporter substrate, ubiquitin<sup>G76V</sup> fused with green fluorescent protein (Ub<sup>G76V</sup>–GFP)<sup>25</sup> to test the effects of mutant ubiquitin 2 on ubiquitin-mediated protein degradation. Two mutations at two different sites were tested (P497H and P506T) using the Ub<sup>G76V</sup>–GFP reporter system. The G76V substitution prevents removal of N-terminally fused ubiquitin by cellular de-ubiquitinating enzymes, leading to efficient proteasomal degradation of the Ub<sup>G76V</sup>–GFP reporter<sup>25</sup>. First, we tested the transfection

efficiency of wild-type and mutant ubiquitin 2 constructs, and saw similar levels of exogenous ubiquitin 2 expression (Supplementary Fig. 16). We also tested the functionality of the Ub<sup>G76V</sup>–GFP reporter system using the proteasome inhibitor MG-132 in transiently transfected cells. As expected, incubation with MG-132 resulted in marked accumulation of the Ub<sup>G76V</sup>–GFP signal (Supplementary Fig. 17). We then examined the accumulation of Ub<sup>G76V</sup>–GFP in Neuro-2a cells transiently transfected with either wild-type or mutant ubiquitin 2 constructs. Expression of mutant ubiquitin 2 resulted in significantly higher accumulation of Ub<sup>G76V</sup>–GFP than expression of wild-type ubiquitin 2 (Fig. 4a). Similar data were obtained using SH-SY5Y cells (Supplementary Fig. 18).

We further analysed the dynamics of Ub<sup>G76V</sup>–GFP degradation after new protein synthesis was blocked with cycloheximide for 0, 2, 4 and 6 h in Neuro-2a cells. We found that the rates of reporter degradation were significantly slower in cells expressing both the P497H and P506T ubiquitin 2 mutants, when compared to wild-type ubiquitin 2, at 4 h ( $P < 0.05$ ) and 6 h ( $P < 0.001$ ) (Fig. 4b), further supporting the notion that the ubiquitin 2 mutants impair the protein degradation pathway.

It is notable that all five ALS-linked *UBQLN2* mutations identified here involve four proline residues in the PXX region. Proline is a unique amino acid in that it has a side chain cyclized onto the backbone nitrogen atom, leading to steric restriction of its rotation, and thus hindering the formation of major known secondary structures. Moreover, among the primary structures of many ligands for protein–protein interactions, a proline residue is often critical<sup>26</sup>. Some protein–protein interaction domains, such as SH3, prefer ligand sequences containing tandem PXX motifs, as noted in the PXX domain of ubiquitin 2, for high affinity and selectivity of such interactions<sup>27</sup>. Further studies of the consequences of the proline mutations may reveal interacting molecular partners that are relevant to the functions of ubiquitin 2.

The exact function of ubiquitin 2 is not well understood. However, there is increasing evidence that ubiquilins, together with their interactions with other proteins, may be involved in neurodegenerative disorders. Ubiquitin 1, another member of the ubiquilin family, is associated with Alzheimer's disease and interacts with presenilins 1 and 2 (ref. 28) and TDP43 (ref. 29). We observed that ubiquitin 2 formed cytoplasmic inclusions with ALS- and FTL-linked TDP43, indicating that an interaction between TDP43 and ubiquitin 2 may underlie the pathogenesis of ALS and ALS/dementia, and possibly other neurodegenerative disorders as well.

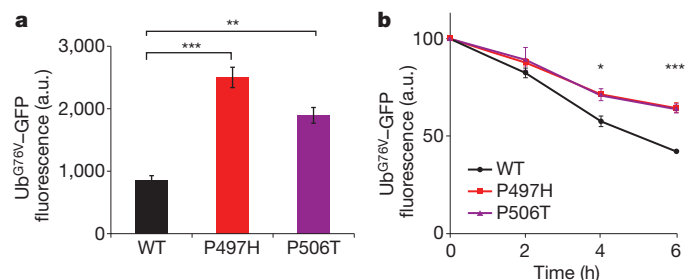


**Figure 4 | Mutations in ubiquitin 2 lead to ubiquitin-mediated impairment of proteasomal degradation.** **a, b**, Ub<sup>G76V</sup>–GFP fluorescence intensity (arbitrary units, a.u.) was quantified by flow cytometry 48 h after transient transfection of Neuro-2a cells with either wild-type (WT) or mutant (P497H or P506T) *UBQLN2* (**a**). The dynamics of Ub<sup>G76V</sup>–GFP reporter degradation after blockage of protein synthesis with cycloheximide for 0, 2, 4, and 6 h are shown in **b**. Rates of UPS-reporter degradation were significantly slower for both the P497H and P506T mutants when compared to the wild-type at 4 h and 6 h. Mean fluorescence before cycloheximide administration was standardized as 100%. Data are averaged from at least three independent experiments. \*,  $P < 0.05$ ; \*\*,  $P < 0.01$ ; \*\*\*,  $P < 0.001$  (indicating significant differences when compared to wild-type by two-tailed Student's *t*-test). Error bars, means  $\pm$  s.e.m.



The removal of misfolded or damaged proteins is critical for optimal cell functioning. In the cytosol and the nucleus, a major proteolytic pathway to recycle misfolded or damaged proteins is the UPS. Although an impaired UPS is thought to be associated with the formation of proteinaceous inclusions in many neurodegenerative disorders, direct evidence of mutations in the UPS pathway has been limited<sup>30</sup>. In this study, we show mutations of ubiquilin 2, a ubiquitin-like protein, in five families with ALS and ALS/dementia. We also show that inclusions containing ubiquilin 2 are a common pathological feature in a wide spectrum of ALS and ALS/dementia. Functional studies indicate an impairment of ubiquitin-mediated proteasomal degradation in cells expressing mutant ubiquilin 2. These data provide robust evidence for an impairment of protein turnover in the pathogenesis of ALS and ALS/dementia, and possibly in other neurodegenerative disorders as well. Further elucidation of these processes may be central to the understanding of pathogenic pathways. These pathways should provide novel molecular targets for the design of rational therapies for these disorders.

## METHODS SUMMARY

Genomic DNA was PCR-amplified and Sanger-sequenced using a CEQ 8000 genetic analysis system (Beckman Coulter). Western blotting, immunohistochemistry and confocal microscopy were performed using previously established methods<sup>17</sup>. Construction of expression vectors, cell culture and flow cytometry were performed according to standard protocols. For statistical analysis, all graphs show mean  $\pm$  s.e.m. and significance was calculated using Student's *t*-test.

**Full Methods** and any associated references are available in the online version of the paper at [www.nature.com/nature](http://www.nature.com/nature).

Received 20 November 2010; accepted 5 July 2011.

Published online 21 August 2011.

- Deng, H. X. *et al.* Amyotrophic lateral sclerosis and structural defects in Cu,Zn superoxide dismutase. *Science* **261**, 1047–1051 (1993).
- Rosen, D. R. *et al.* Mutations in Cu/Zn superoxide dismutase gene are associated with familial amyotrophic lateral sclerosis. *Nature* **362**, 59–62 (1993).
- Kabashi, E. *et al.* TARDBP mutations in individuals with sporadic and familial amyotrophic lateral sclerosis. *Nature Genet.* **40**, 572–574 (2008).
- Sreedharan, J. *et al.* TDP-43 mutations in familial and sporadic amyotrophic lateral sclerosis. *Science* **319**, 1668–1672 (2008).
- Kwiatkowski, T. J. Jr *et al.* Mutations in the FUS/TLS gene on chromosome 16 cause familial amyotrophic lateral sclerosis. *Science* **323**, 1205–1208 (2009).
- Vance, C. *et al.* Mutations in FUS, an RNA processing protein, cause familial amyotrophic lateral sclerosis type 6. *Science* **323**, 1208–1211 (2009).
- Chen, Y. Z. *et al.* DNA/RNA helicase gene mutations in a form of juvenile amyotrophic lateral sclerosis (ALS4). *Am. J. Hum. Genet.* **74**, 1128–1135 (2004).
- Greenway, M. J. *et al.* ANG mutations segregate with familial and 'sporadic' amyotrophic lateral sclerosis. *Nature Genet.* **38**, 411–413 (2006).
- Nishimura, A. L. *et al.* A mutation in the vesicle-trafficking protein VAPB causes late-onset spinal muscular atrophy and amyotrophic lateral sclerosis. *Am. J. Hum. Genet.* **75**, 822–831 (2004).
- Yang, Y. *et al.* The gene encoding alsin, a protein with three guanine-nucleotide exchange factor domains, is mutated in a form of recessive amyotrophic lateral sclerosis. *Nature Genet.* **29**, 160–165 (2001).
- Chow, C. Y. *et al.* Deleterious variants of FIG4, a phosphoinositide phosphatase, in patients with ALS. *Am. J. Hum. Genet.* **84**, 85–88 (2009).
- Maruyama, H. *et al.* Mutations of optineurin in amyotrophic lateral sclerosis. *Nature* **465**, 223–226 (2010).
- Ticozzi, N. *et al.* Paraoxonase gene mutations in amyotrophic lateral sclerosis. *Ann. Neurol.* **68**, 102–107 (2010).
- Mitchell, J. *et al.* Familial amyotrophic lateral sclerosis is associated with a mutation in D-amino acid oxidase. *Proc. Natl Acad. Sci. USA* **107**, 7556–7561 (2010).
- Johnson, J. O. *et al.* Exome sequencing reveals VCP mutations as a cause of familial ALS. *Neuron* **68**, 857–864 (2010).
- Lansbury, P. T. & Lashuel, H. A. A century-old debate on protein aggregation and neurodegeneration enters the clinic. *Nature* **443**, 774–779 (2006).
- Deng, H. X. *et al.* FUS-immunoreactive inclusions are a common feature in sporadic and non-SOD1 familial amyotrophic lateral sclerosis. *Ann. Neurol.* **67**, 739–748 (2010).
- Neumann, M. *et al.* Ubiquitinated TDP-43 in frontotemporal lobar degeneration and amyotrophic lateral sclerosis. *Science* **314**, 130–133 (2006).
- Shibata, N. *et al.* Intense superoxide dismutase-1 immunoreactivity in intracytoplasmic hyaline inclusions of familial amyotrophic lateral sclerosis with posterior column involvement. *J. Neuropathol. Exp. Neurol.* **55**, 481–490 (1996).
- Mackenzie, I. R. *et al.* Pathological TDP-43 distinguishes sporadic amyotrophic lateral sclerosis from amyotrophic lateral sclerosis with SOD1 mutations. *Ann. Neurol.* **61**, 427–434 (2007).
- Neumann, M. *et al.* Frontotemporal lobar degeneration with FUS pathology. *Brain* **132**, 2922–2931 (2009).
- Urwin, H. *et al.* FUS pathology defines the majority of tau- and TDP-43-negative frontotemporal lobar degeneration. *Acta Neuropathol.* **120**, 33–41 (2010).
- Nonaka, T., Kametani, F., Arai, T., Akiyama, H. & Hasegawa, M. Truncation and pathogenic mutations facilitate the formation of intracellular aggregates of TDP-43. *Hum. Mol. Genet.* **18**, 3353–3364 (2009).
- Ko, H. S., Uehara, T., Tsuruma, K. & Nomura, Y. Ubiquilin interacts with ubiquitylated proteins and proteasome through its ubiquitin-associated and ubiquitin-like domains. *FEBS Lett.* **566**, 110–114 (2004).
- Dantuma, N. P., Lindsten, K., Glas, R., Jellne, M. & Masucci, M. G. Short-lived green fluorescent proteins for quantifying ubiquitin/proteasome-dependent proteolysis in living cells. *Nature Biotechnol.* **18**, 538–543 (2000).
- Kay, B. K., Williamson, M. P. & Sudol, M. The importance of being proline: the interaction of proline-rich motifs in signaling proteins with their cognate domains. *FASEB J.* **14**, 231–241 (2000).
- Aitio, O. *et al.* Recognition of tandem PxxP motifs as a unique Src homology 3-binding mode triggers pathogen-driven actin assembly. *Proc. Natl Acad. Sci. USA* **107**, 21743–21748 (2010).
- Haapasalo, A. *et al.* Emerging role of Alzheimer's disease-associated ubiquilin-1 in protein aggregation. *Biochem. Soc. Trans.* **38**, 150–155 (2010).
- Kim, S. H. *et al.* Potentiation of amyotrophic lateral sclerosis (ALS)-associated TDP-43 aggregation by the proteasome-targeting factor, ubiquilin 1. *J. Biol. Chem.* **284**, 8083–8092 (2009).
- Aguzzi, A. & O'Connor, T. Protein aggregation diseases: pathogenicity and therapeutic perspectives. *Nature Rev. Drug Discov.* **9**, 237–248 (2010).

**Supplementary Information** is linked to the online version of the paper at [www.nature.com/nature](http://www.nature.com/nature).

**Acknowledgements** This study was supported by the National Institute of Neurological Disorders and Stroke (NS050641), the Les Turner ALS Foundation, the Vena E. Schaff ALS Research Fund, the Harold Post Research Professorship, the Herbert and Florence C. Wenske Foundation, the David C. Asselin MD Memorial Fund, the Help America Foundation and the Les Turner ALS Foundation/Herbert C. Wenske Foundation Professorship. F.F. has support from NIH (T32 AG20506). K.A. is a postdoctoral fellow of the Blazeman Foundation for ALS. G.H.G. received travel funds from MND Scotland. We thank N. Dantuma for the UPS reporter plasmid (through Addgene) and the staff of the Northwestern University Robert H. Lurie Comprehensive Cancer Center flow cytometry core facility for technical assistance. Imaging work was performed at the Northwestern University Cell Imaging Facility, supported by NCI CCSG P30 CA060553 awarded to the Robert H. Lurie Comprehensive Cancer Center.

**Author Contributions** T.S. conceived and supervised this project. W.C., S.-T.H., Y.Y., H.J., M.H., H.-X.D. and T.S. did the sequencing analysis. S.T.H., E.R., J.L.H., M.P.-V. and T.S. performed linkage analysis. K.M.B., G.H.G., F.F., G.H.J., H.Z., E.H.B., K.A., E.M., H.-X.D. and T.S. performed immunohistochemical, confocal and pathological analysis. F.F., Y.S. and H.-X.D. performed functional analysis. N.S., S.D. and T.S. collected family information and coordinated this study. K.M.B., G.H.J., B.R.B., R.L.S. and T.S. did clinical studies. H.-X.D. and T.S. analysed the data and wrote the paper.

**Author Information** Reprints and permissions information is available at [www.nature.com/reprints](http://www.nature.com/reprints). The authors declare no competing financial interests. Readers are welcome to comment on the online version of this article at [www.nature.com/nature](http://www.nature.com/nature). Correspondence and requests for materials should be addressed to T.S. (t-siddique@northwestern.edu).



## METHODS

**Patients and samples.** This study was approved by the local institutional review boards. ALS patients met the diagnosis of probable or definite ALS as defined in the revised EL-Scorial<sup>31</sup>. Patients with dementia met the criteria for FTD or FTLD proposed in refs 32 and 33. The dementia was similar to frontal variant FTD on inception and was progressive, and eventually global in most patients. One patient had mild mental retardation before the onset of dementia. There were eight patients with both ALS and dementia. Dementia preceded motor symptoms in some patients, but no patient remained free of motor involvement. The FTLD symptoms included abnormalities in both behaviour and executive function, although the degree of severity varied between individuals in different stages of the disease. Pedigrees and clinical data were collected by specialists in neuromuscular medicine and were verified by medical records or recent examination to establish diagnosis (Supplementary Table 2). DNA and other samples were taken after obtaining written informed consent. Overall, DNA from more than 200 ALS cases and 928 controls was used for genetic analysis. Spinal-cord autopsy samples from two X-linked ALS cases (P497H or P506T), 41 cases with ALS or ALS/dementia and six non-ALS controls were studied. In addition, available autopsy samples from the motor-cortex region of a patient with the P497H mutation (family 186, IV 7), brain regions (including hippocampus, cerebellum, optic nerve, visual cortex, pons and midbrain) of two patients with the P506T mutation (family 6316, II 3 and III 4), and the hippocampal regions of ten ALS and five ALS/dementia cases were also used for pathological and immunohistological studies. These five ALS/dementia cases were classified as having FTLD-MND/FTLD-U, including four cases with pathological type 3 and one case with pathological type 2 according to the classification system proposed in ref. 34. These cases were evaluated by a neuropathologist (E.H.B.).

**Genetic analysis.** Genomic DNA was extracted by standard methods (Qiagen) from whole peripheral blood, transformed lymphoblastoid cell lines or tissues. Intronic primers flanking exons were designed at least 50 nucleotides away from the intron/exon boundary. When a PCR product was larger than 500 base pairs (bp), several overlapping primers were designed with an average of 50-bp overlap. Genomic DNA (40 ng) was used for PCR amplification. The amplification protocol consisted of the following steps: incubation at 95 °C for 1 min, 32 cycles of 95 °C (30 s), 55 °C (30 s) and 72 °C (1 min), and a final 5-min extension at 72 °C, with modifications when necessary. Excess dNTPs and primers were digested with exonuclease I and shrimp alkaline phosphatase (ExoSAP-IT, USB). When non-specific PCR amplification occurred, the PCR products were separated on a 1.5% agarose gel and the specific PCR product was cut out from the gel and purified using QIAquick gel extraction kit (Qiagen). For sequencing of a PCR product, fluorescent-dye-labelled single-stranded DNA was amplified using Beckman Coulter sequencing reagents (GenomeLab DTCS quick start kit), followed by single-pass bidirectional sequencing with a CEQ 8000 genetic analysis system (Beckman Coulter). We sequenced the entire protein-coding exons and intronic sequences of 30–50 bp flanking the exons. *UBQLN2* is an intronless gene. We divided the *UBQLN2* gene into five overlapping PCR fragments for sequencing analysis. These fragments cover the entire coding sequence (1,872 bp), 125 bp of the 5' UTR and 293 bp of the 3' UTR. Primers were as follows: Ubqln2-1F, 5'-cttcacacagaggtacgtg-3'; Ubqln2-1R, 5'-gtgtggagttactctgggag-3'; Ubqln2-2F, 5'-catgatggctgactgttcac-3'; Ubqln2-2R, 5'-ctctgtgctgagcattcagcatc-3'; Ubqln2-3F, 5'-gactgtgctcttagcaatctag-3'; Ubqln2-3R, 5'-gtgtctgctgattctgcatctgc-3'; Ubqln2-4F, 5'-cacagatgatgctgaatagcc-3'; Ubqln2-4R, 5'-gctgaatgaactgctggttg-3'; Ubqln2-5F, 5'-ctgcacttagtgaaccacag-3'; Ubqln2-5R, 5'-aacagcattgtaccacac-3'. For fragments 4 and 5, the PCR protocol consisted of the following steps: incubation at 96 °C for 2 min, 32 cycles of 96 °C (30 s), 56 °C (30 s) and 72 °C (1 min), and a final 5-min extension at 72 °C. The PCR products were separated on a 1.5% agarose gel and purified with QIAquick gel extraction kit (Qiagen) before sequencing.

**Antibodies.** Two anti-ubiquitin 2 antibodies were used. One was a mouse monoclonal antibody (5F5, H00029978-M03, Novus Biologicals Inc.). We made the other antibody, which was raised in rabbit using a polypeptide of human ubiquitin 2 (amino acids 8–24, SGPPRPSRGPAQAQGS). The antiserum was affinity-purified. Other polyclonal and monoclonal antibodies used in this study included: anti-ubiquitin (PRB-268C, Covance; 10R-U101B, Fitzgerald Industries International; Ub(N-19):sc-6085, Santa Cruz Biotechnology), anti-p62 (H00008878-M01, Abnova; NB110-74805, Novus Biologicals Inc.), anti-TDP43 (TIP-PTD-P01, Cosmo Bio Co; 10782-2-AP, ProteinTech Group; 60019-2-Ig, ProteinTech Group; WH0023435M1-100UG, Sigma-Aldrich), anti-FUS (11570-1-AP, ProteinTech Group), anti-optineurin (100000, Cayman), anti-SOD1 (ref. 35), anti-Myc (MMS-150P, Covance), anti-GFAP (Z0334, Dako North America; G3893, Sigma-Aldrich), anti-Iba1 (019-19741, Wako Pure Chemical Industries) and anti-CNPase (MAB326R, Millipore).

**Immunohistochemistry and confocal microscopy.** The basic protocols for immunohistochemistry and confocal microscopy have been described in detail in a previous study<sup>17</sup>. In brief, 6-µm sections were cut from formalin-fixed,

paraffin-embedded spinal cord and brain regions containing the frontal lobe or the hippocampus. The sections were deparaffinized with xylene and rehydrated with a descending series of diluted ethanol and water. Antigens in the sections were retrieved using a high-pressure decloaking chamber. For immunohistochemistry, endogenous peroxidase activity was blocked with 2% hydrogen peroxide. Non-specific background was blocked with 1% bovine serum albumin. The titres of the antibodies were determined on the basis of preliminary studies using serial dilution of the antibodies. Various antibodies against ubiquitin 2 or other proteins were used as primary antibodies. These included rabbit polyclonal anti-ubiquitin 2 (ubiquitin 2-N; 0.5 µg ml<sup>-1</sup>; generated by us), mouse monoclonal anti-ubiquitin 2 (ubiquitin 2-C; 0.2 µg ml<sup>-1</sup>; H00029978-M03, Novus Biologicals), rabbit polyclonal anti-FUS (3 µg ml<sup>-1</sup>; 11570-1-AP, ProteinTech Group), mouse monoclonal anti-TDP43 (1 µg ml<sup>-1</sup>; 60019-2-Ig, ProteinTech Group), rabbit polyclonal anti-TDP43 (0.1 µg ml<sup>-1</sup>; 10782-2-AP, ProteinTech Group), mouse monoclonal anti-ubiquitin (0.5 µg ml<sup>-1</sup>; 10R-U101B, Fitzgerald Industries International), rabbit polyclonal anti-ubiquitin (0.5 µg ml<sup>-1</sup>; PRB-268C, Covance), goat polyclonal anti-ubiquitin (0.5 µg ml<sup>-1</sup>; Ub(N-19):sc-6085, Santa Cruz Biotechnology), mouse monoclonal anti-p62 (1 µg ml<sup>-1</sup>; H00008878-M01, Abnova Corporation) and rabbit polyclonal anti-optineurin (C-term; 0.2 µg ml<sup>-1</sup>; 100000, Cayman). Biotinylated goat anti-rabbit and anti-mouse IgG, biotinylated mouse anti-goat IgG, or biotinylated rabbit anti-mouse IgG were used as the secondary antibodies. Immunoreactive signals were detected with peroxidase-conjugated streptavidin (BioGenex) using 3-amino-9-ethylcarbazole as a chromogen. The slides were counterstained with haematoxylin and sealed with Aqua PolyMount (Polyscience).

For confocal microscopy, antibodies generated in different species were used in various combinations. These antibodies included those against ubiquitin 2, FUS, TDP43, p62, optineurin, ubiquitin, Myc, GFAP, Iba1 and CNPase. Fluorescence signals were detected with appropriate secondary anti-rabbit, anti-mouse or anti-goat IgG, conjugated with Alexa Fluor 488 or Alexa Fluor 555 (Invitrogen), using an LSM 510 META laser-scanning confocal microscope with the multi-tracking setting<sup>17</sup>. The same pinhole diameter was used to acquire each channel.

**Western blotting.** Western blotting was performed using the protocol previously described<sup>17</sup>. Briefly, cells or spinal-cord tissues from lumbar segments were processed and homogenized. Cell lysates or the supernatants of tissue homogenates were subjected to total protein quantification, gel electrophoresis and blotting on PVDF membranes. Ubiquitin 2 was detected using the ubiquitin 2-N or ubiquitin 2-C antibodies. The membranes were then stripped and blotted with an antibody against β-actin (A5441, Sigma-Aldrich).

**Expression constructs.** A full-length human cDNA clone (*Homo sapiens* ubiquitin 2, IMAGE:4543266) was used as a template for construction of the expression constructs. Two primers anchored with a XhoI site (ubiquitin 2-TP1, 5'-ttctcaggcccgccatgctgagaat-3') and a BamHI site (ubiquitin 2-TP2, 5'-catgatcctgtatgtctgtattacc-3') were used to amplify the full-length coding sequence. The amplified fragment was cloned into plasmid vector pBluescript M13. The ubiquitin 2 sequence was verified by direct sequencing. The P497H and P506T mutations were introduced into the plasmid vector by site-directed mutagenesis using a primer containing each respective mutation. The XhoI/BamHI fragment containing wild-type *UBQLN2*, *UBQLN2*<sup>P497H</sup> or *UBQLN2*<sup>P506T</sup> was released from the pBluescript M13 vector and cloned into the XhoI and BamHI sites of dual expression vectors pIRES2-DsRed2 or pIRES2-ZsGreen1 (Clontech), to create such constructs as wtUBQLN2-ZsGreen1 and mUBQLN2-ZsGreen1 (mutant ubiquitin 2 (P497H or P506T)).

We generated seven additional expression constructs, including wild-type ubiquitin 2 tagged with GFP (wtUBQLN2-GFP), mutant ubiquitin 2 (P497H or P506T) tagged with GFP (mUBQLN2-GFP), wild-type TDP43 tagged with mCherry (wtTDP43-mCherry), an ALS- and dementia-linked C-terminal fragment of TDP43 (amino acids 218–414, C-TDP43)<sup>18,23</sup> tagged with mCherry (C-TDP43-mCherry), wild-type FUS tagged with Myc (Myc-wtFUS) and mutant FUS (R495X) tagged with Myc (Myc-mFUS).

**Cell culture, transfection and immunocytochemistry.** SH-SY5Y, Neuro-2a and HEK293 cell lines were grown on collagen-coated plates in Dulbecco's modified Eagle's medium containing 10% (v/v) human serum, 2 mM L-glutamine, 2 U ml<sup>-1</sup> penicillin and 2 mg ml<sup>-1</sup> streptomycin, at 37 °C in a humidity-controlled incubator with 5% CO<sub>2</sub>. The cells were transiently transfected with different combinations of expression vectors using Lipofectamine 2000 (Invitrogen) according to manufacturer's instructions. Immunocytochemistry was performed as previously described<sup>16</sup>.

**UPS reporter assay.** SH-SY5Y and Neuro-2a cells were grown in 24-well plates and double-transfected with a UPS-reporter vector encoding Ub<sup>G76V</sup>-GFP (ref. 25) (Addgene plasmid 11941), and a dual expression vector encoding DsRed2 with either wild-type or mutant ubiquitin 2. Cells were harvested 48 h after transfection and resuspended in PBS. Cells transfected with the Ub<sup>G76V</sup>-GFP vector were used for control experiments to test the functionality of the UPS reporter. In these control experiments, the medium was changed 24 h after

transfection to medium containing 5  $\mu$ M proteasomal inhibitor MG-132 (A.G. Scientific Inc.). Cells were incubated in this medium for 24 h and then harvested and resuspended in PBS. For cycloheximide chase of Ub<sup>G76V</sup>-GFP, transiently transfected Neuro-2a cells were used. The cells were transferred 24 h after transfection to medium containing 5  $\mu$ M MG-132. After incubation with MG-132 for 16 h to accumulate the Ub<sup>G76V</sup>-GFP reporter, cells were washed in sterile PBS and incubated with medium containing 100  $\mu$ g ml<sup>-1</sup> cycloheximide (Sigma) for 0, 2, 4, and 6 h. At each time point, cells were washed, harvested and resuspended in ice-cold PBS supplemented with 100  $\mu$ g ml<sup>-1</sup> cycloheximide. The fluorescence intensities at each time point were measured by flow cytometry. The fluorescence intensity at 0 h was taken to be maximal fluorescence (100%). All flow-cytometric data were collected and analysed using a MoFlo cell sorter and Summit software (DakoCytomation). Argon-ion (488 nm) and yellow (565 nm) lasers were used for excitation. The GFP and DsRed2 signals were collected using 530/540-nm and 600/630-nm bandpass filters, respectively. In all experiments, data were gated on GFP/DsRed2 dual-labelled cells. At least 500–1,000 such events were recorded in each experiment. The DsRed2 expression levels and profiles were similar across

experiments. Data were collected from three independent experiments. Two-tailed unpaired Student's *t*-test ( $P < 0.05$ ) was used for statistical analysis.

31. Brooks, B. R., Miller, R. G., Swash, M. & Munsat, T. L. El Escorial revisited: revised criteria for the diagnosis of amyotrophic lateral sclerosis. *Amyotroph. Lateral Scler. Other Motor Neuron Disord.* **1**, 293–299 (2000).
32. Neary, D. *et al.* Frontotemporal lobar degeneration: a consensus on clinical diagnostic criteria. *Neurology* **51**, 1546–1554 (1998).
33. Cairns, N. J. *et al.* Neuropathologic diagnostic and nosologic criteria for frontotemporal lobar degeneration: consensus of the consortium for frontotemporal lobar degeneration. *Acta Neuropathol.* **114**, 5–22 (2007).
34. Mackenzie, I. R. *et al.* Heterogeneity of ubiquitin pathology in frontotemporal lobar degeneration: classification and relation to clinical phenotype. *Acta Neuropathol.* **112**, 539–549 (2006).
35. Deng, H. X. *et al.* Conversion to the amyotrophic lateral sclerosis phenotype is associated with intermolecular linked insoluble aggregates of SOD1 in mitochondria. *Proc. Natl Acad. Sci. USA* **103**, 7142–7147 (2006).
36. Fecto, F. *et al.* Mutant TRPV4-mediated toxicity is linked to increased constitutive function in axonal neuropathies. *J. Biol. Chem.* **286**, 17281–17291 (2011).

# Three classical Cepheid variable stars in the nuclear bulge of the Milky Way

Noriyuki Matsunaga<sup>1</sup>, Takahiro Kawadu<sup>2</sup>, Shogo Nishiyama<sup>3</sup>, Takahiro Nagayama<sup>4</sup>, Naoto Kobayashi<sup>1,5</sup>, Motohide Tamura<sup>3</sup>, Giuseppe Bono<sup>6,7</sup>, Michael W. Feast<sup>8,9</sup> & Tetsuya Nagata<sup>2</sup>

The nuclear bulge is a region with a radius of about 200 parsecs around the centre of the Milky Way<sup>1</sup>. It contains stars with ages<sup>2–4</sup> ranging from a few million years to over a billion years, yet its star-formation history and the triggering process for star formation remain to be resolved. Recently, episodic star formation, powered by changes in the gas content, has been suggested<sup>5</sup>. Classical Cepheid variable stars have pulsation periods that decrease with increasing age<sup>6</sup>, so it is possible to probe the star-formation history on the basis of the distribution of their periods<sup>7,8</sup>. Here we report the presence of three classical Cepheids in the nuclear bulge with pulsation periods of approximately 20 days, within 40 parsecs (projected distance) of the central black hole. No Cepheids with longer or shorter periods were found. We infer that there was a period about 25 million years ago, and possibly lasting until recently, in which star formation increased relative to the period of 30–70 million years ago.

We conducted a near-infrared survey for the  $0.33^\circ$  by  $0.5^\circ$  area around the Galactic Centre<sup>9</sup>, where no classical Cepheids were known before<sup>10,11</sup>. Approximately 90 time-series images were collected in each of the  $J$  ( $1.25\ \mu\text{m}$ ),  $H$  ( $1.63\ \mu\text{m}$ ) and  $K_s$  ( $2.14\ \mu\text{m}$ ) wave-passbands during eight years between 2001 and 2008. We discovered 45 variable stars with pulsation periods shorter than 60 days, among which we determined three to be classical Cepheids (Table 1, Fig. 1 and Supplementary Fig. 1) on the basis of their light curves and other observed properties (Supplementary Information). Both their extinctions and distances can be determined<sup>9</sup> using the period–luminosity relations in the three passbands<sup>12</sup>. Their derived distances (Table 1) agree closely with each other. The mean distance is 7.9 kiloparsecs (kpc), with standard error of the mean  $\pm 0.2$  kpc, although there remains a systematic error of  $\pm 0.3$  kpc, of which the dominant source is an error in the total-to-selective extinction ratio (that is, the coefficient used to convert a colour excess into an extinction). This result from a fundamental distance indicator agrees with the distance to the Galactic Centre derived from orbits round the central black hole<sup>13</sup> ( $8.28 \pm 0.33$  kpc) amongst other estimates<sup>9,14–16</sup>. We also note that the Cepheids are located close to the plane containing the central black hole ( $b = -0.05^\circ$ ), well within 10 parsec (pc) in projected distance, which is consistent with their being within the thin disk-like structure of the nuclear bulge<sup>1,5</sup>. These results clearly locate the three objects inside the nuclear bulge.

All of our classical Cepheids have periods close to 20 days. Figure 2 compares their period distribution with that of known Cepheids in a wide region around the Sun<sup>17</sup>. Despite the small number of the objects found, the histogram contrasts our targets with the absence of shorter-period Cepheids in the nuclear bulge. Although the older, shorter-period Cepheids are expected to be the fainter ones<sup>6</sup>, our survey would have detected those with periods longer than 5 days if they existed (Supplementary Fig. 2). Our sample shows a concentration in the period range where the proportion of Cepheids is generally small; such a period distribution has not been seen in nearby galaxies<sup>18</sup>. The period distribution can be affected by metallicity<sup>18</sup>, but the metallicities of young objects in the nuclear bulge have been reported to be approximately solar<sup>19</sup>. The 20-day Cepheids have an age of  $25 \pm 5$  million years (Myr), where the error is derived from the standard deviation of the period–age relation<sup>6</sup>. The uncertainty in the metallicity has a smaller effect on the age estimate than the above error<sup>6</sup>. All three Cepheids found in the nuclear bulge are approximately the same age. We discuss the possibility that the two stars projected close to each other might have formed within a cluster, although this is not probable, in the Supplementary Information.

We can estimate the star-formation rate at about 25 Myr ago by assuming an initial mass function<sup>20</sup> and the lifetime spent by the Cepheid inside the instability strip<sup>21</sup>. To allow comparison with previous work, we take into account the survey area and the region hidden by extreme interstellar extinction. We find that the star-formation rate was  $0.075^{+0.15}_{-0.05}$  solar masses per year in the entire nuclear bulge 20–30 Myr ago. The uncertainty comes from Poisson noise, the uncertainty in the Cepheid lifetime, and the uncertainty in the ratio of the effective survey area to the entire nuclear bulge (Supplementary Information). On the other hand, the absence of shorter-period Cepheids leads to 0.02 solar masses per year as a  $1\sigma$  upper limit on the star-formation rate for 30–70 Myr ago. The Poisson noise remains the dominant uncertainty in our discussions. We can ignore the uncertainty in the effective area of our survey, a factor of two, when we compare the two star-formation rates. If the star-formation rate remained as high as the value obtained with the 20–30-Myr-old Cepheids, the probability of finding no 30–70-Myr-old Cepheid is low. Thus we conclude that the change in the star-formation rate between 20 and 70 Myr ago is significant at the level of  $\sim 2\sigma$ , assuming the Poisson statistics.

**Table 1 | Catalogue of the classical Cepheids in the nuclear bulge**

Star	RA	Dec.	$l$ (deg)	$b$ (deg)	$\Delta_l$ (pc)	$\Delta_b$ (pc)	$J$ (mag)	$H$ (mag)	$K_s$ (mag)	$P$ (days)	$\mu_0$ (mag)	$A_{K_s}$ (mag)
a	17:46:06.01	–28:46:55.1	+0.1864	–0.0095	+33.9	+6.5	15.63	12.04	10.18	23.54	14.55	2.46
b	17:45:32.27	–29:02:55.2	–0.1054	–0.0433	–6.9	+0.4	15.42	12.00	10.17	19.96	14.49	2.35
c	17:45:30.89	–29:03:10.5	–0.1116	–0.0412	–7.8	+0.7	16.36	12.44	10.35	22.76	14.42	2.74

RA, right ascension; Dec., declination (J2000.0);  $l$  and  $b$  are the galactic coordinates;  $\Delta_l$  and  $\Delta_b$  are the projected distances of the Cepheids from the central black hole at 8 kpc;  $J$ ,  $H$  and  $K_s$  are the mean intensity magnitudes in those wave-passbands. The standard errors for the estimates of the true distance modulus  $\mu_0$  and the  $K_s$ -band foreground extinction  $A_{K_s}$  are  $\pm 0.13$  mag and  $\pm 0.08$  mag, respectively (see Supplementary Information).

<sup>1</sup>Kiso Observatory, Institute of Astronomy, University of Tokyo, 10762-30 Mitake, Kiso-machi, Kiso-gun, Nagano 397-0101, Japan. <sup>2</sup>Department of Astronomy, Kyoto University, Kitashirakawa-Oiwake-cho, Sakyo-ku, Kyoto 606-8502, Japan. <sup>3</sup>National Astronomical Observatory of Japan, 2-21-1 Osawa, Mitaka, Tokyo 181-8588, Japan. <sup>4</sup>Department of Astrophysics, Nagoya University, Furo-cho, Chikusa-ku, Nagoya, Aichi 464-8602, Japan. <sup>5</sup>Institute of Astronomy, University of Tokyo, 2-21-1 Osawa, Mitaka, Tokyo 181-0015, Japan. <sup>6</sup>Dipartimento di Fisica, Università di Roma Tor Vergata, Via della Ricerca Scientifica 1, 00133 Rome, Italy. <sup>7</sup>INAF—Osservatorio Astronomico di Roma, Via Frascati 33, 00040 Monte Porzio Catone, Italy. <sup>8</sup>Astrophysics, Cosmology and Gravity Centre, Astronomy Department, University of Cape Town, 7701 Rondebosch, South Africa. <sup>9</sup>South African Astronomical Observatory, PO Box 9, 7935 Observatory, South Africa.



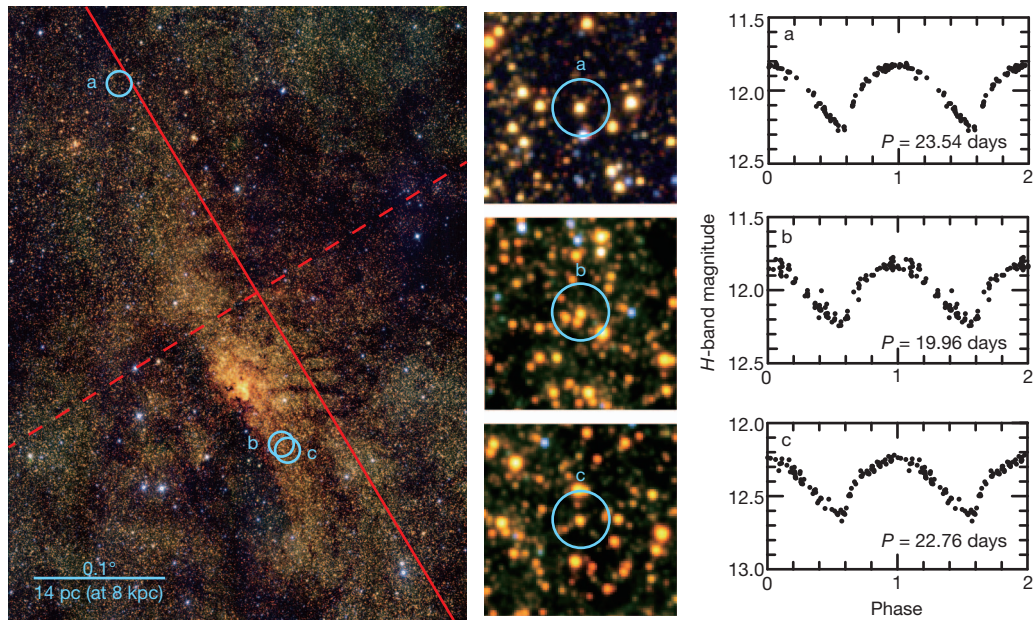


**Figure 1 | The classical Cepheids discovered in the Nuclear Bulge.** The left panel shows the observed field of  $0.33^\circ$  by  $0.5^\circ$ . This false-colour image is composed of images, a subset of the data we used in analysis, in three passbands:  $J$  ( $1.25\ \mu\text{m}$ ),  $H$  ( $1.63\ \mu\text{m}$ ) and  $K_s$  ( $2.14\ \mu\text{m}$ ). The data were taken with the Infrared Survey Facility (IRSF) 1.4-m telescope and the SIRIUS near-infrared camera located at the South African Astronomical Observatory. North is up and east is left. The Galactic plane (that is,  $b = 0^\circ$ ) is indicated by the solid red line running from the top-left to the bottom-right, while the dashed red line shows the axis of  $l = 0^\circ$ . An angle of  $0.1^\circ$  corresponds to a scale of 14 pc at the distance of the Galactic nuclear bulge (about 8 kpc), as indicated in the image.

A recent investigation suggested that the star-formation rate was low a few tens of millions of years ago and then increased to a peak at about 0.1 Myr ago, followed by a decline in very recent times<sup>5</sup>. However, the tracers used give only a rough timescale for the range 1–100 Myr ago. Our estimates have much higher time resolution for the 20–70-Myr range and indicate an increase in star-formation rate within this period. These results are illustrated in Fig. 3, which also shows a scenario of continuous star formation<sup>4</sup> (the value of ref. 4 has also been corrected to our scale by taking into account the mass of the entire nuclear bulge, which is  $(1.4 \pm 0.6) \times 10^9$  solar masses<sup>1</sup>).

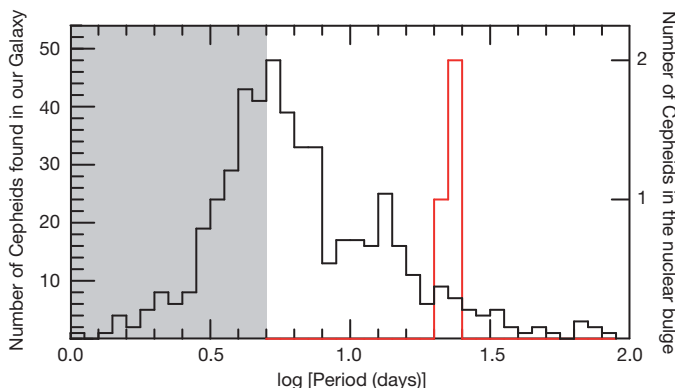


**Figure 2 | Period distribution of the nuclear bulge Cepheids and those previously found in the Milky Way.** The period distribution of the three Cepheids in the nuclear bulge (red) is compared with that of the previously known Cepheids in the Milky Way<sup>17</sup> (black). The grey region indicates the period range for which our survey could not reach classical Cepheids in the nuclear bulge with typical extinction of  $A_K \approx 3$  mag, even if they were there (see Supplementary Information).

The central black hole is located at the heart of the most crowded region in the chart ( $l = -0.056^\circ$ ,  $b = -0.046^\circ$ ). Our survey field includes two famous clusters: Quintuplet ( $l = +0.16^\circ$ ,  $b = -0.06^\circ$ ) and Arches ( $l = +0.12^\circ$ ,  $b = +0.02^\circ$ ). The three panels in the middle column are close-ups, around the circles labelled a, b and c in the left panel, covering a 40-arcsecond square around each object in Table 1. Again, north is up and east is left. The right panels show the light curves in the  $H$  band for the stars labelled a, b and c. The variations of the  $H$ -band magnitude are folded according to the periods  $P$  indicated, and plotted against the phase. The three light curves, showing a clear resemblance to each other, have the typical variations of classical Cepheids.

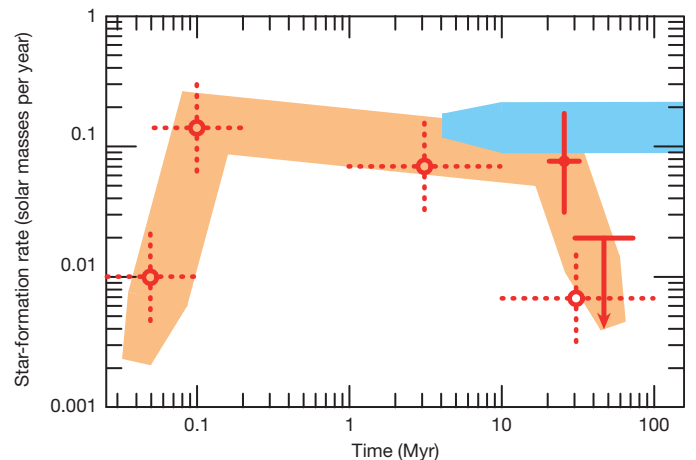


**Figure 3 | Star-formation history in the nuclear bulge during the last hundred million years.** The star-formation rates we derived are indicated by the point at 25 Myr and the arrow at about 50 Myr. The vertical error bar for the point at 25 Myr corresponds to a factor of 2.5, taking errors like the Poisson noise of the Cepheid number into account. The vertical error bar for the arrow at about 50 Myr indicates the  $1\sigma$  upper limit. The uncertainty in the correction for our effective survey coverage (a factor of 2) is not included here, in order to illustrate the difference between these estimates, but it should be considered when the star-formation rates are compared with other data below. The horizontal error bars indicate the durations for the corresponding estimates. More details on these error bars are given in the Supplementary Information. The star-formation rates given in ref. 5 are indicated by open circles, and the dashed horizontal bars show the approximate uncertainty in the age for each tracer. The errors of the star-formation rates in ref. 5 were not given, but they cannot be smaller than a factor of two, considering the uncertainty in the age estimate of young stellar objects. The orange stripe indicates our scenario of the episodic star formation, combining our results and those of ref. 5, while the blue stripe indicates the continuous star-formation scenario suggested in ref. 4.

It is of interest to consider, in the context of galactic structure and evolution, how and why such time variations in star formation occurred. Episodic star formation has been suggested in some of the so-called pseudobulges<sup>22,23</sup>, the central regions of a few barred spiral galaxies, possibly growing with bar-driven gas inflow<sup>24</sup>. Likewise, our result suggests that episodic star formation on a short timescale of about 25 Myr occurred in the nuclear bulge, which some authors claim to be a pseudobulge<sup>25</sup>. The timescale is comparable with that of the cyclic gas accumulation predicted for the central part of the Milky Way<sup>26</sup>.

Received 13 March; accepted 6 July 2011.

Published online 24 August 2011.

- Launhardt, R., Zylka, R. & Mezger, P. G. The nuclear bulge of the Galaxy. III. Large-scale physical characteristics of stars and interstellar matter. *Astron. Astrophys.* **384**, 112–139 (2002).
- Serabyn, E. & Morris, M. Sustained star formation in the central stellar cluster of the Milky Way. *Nature* **382**, 602–604 (1996).
- van Loon, J. Th. *et al.* Infrared stellar populations in the central parts of the Milky Way galaxy. *Mon. Not. R. Astron. Soc.* **338**, 857–879 (2003).
- Figer, D. F., Rich, R. M., Kim, S. S., Morris, M. & Serabyn, E. An extended star formation history for the Galactic Center from Hubble Space Telescope NICMOS observations. *Astrophys. J.* **601**, 319–339 (2004).
- Yusef-Zadeh, F. *et al.* Star formation in the central 400 pc of the Milky Way: Evidence for a population of massive young stellar objects. *Astrophys. J.* **702**, 178–225 (2009).
- Bono, G. *et al.* Classical Cepheid pulsation models. X. The period-age relation. *Astrophys. J.* **621**, 966–977 (2005).
- Alcock, C. *et al.* The MACHO project LMC variable star inventory. VIII. The recent star formation history of the Large Magellanic Cloud from the Cepheid period distribution. *Astron. J.* **117**, 920–926 (1999).
- Meschin, I., Gallart, C., Aparicio, A., Cassisi, S. & Rosenberg, A. Cepheid variable stars in the Pegasus dwarf irregular galaxy: constraints on the star formation history. *Astron. J.* **137**, 3619–3631 (2009).
- Matsunaga, N. *et al.* A near-infrared survey of Miras and the distance to the Galactic Centre. *Mon. Not. R. Astron. Soc.* **399**, 1709–1729 (2009).
- Peeples, M. S., Stanek, K. Z. & DePoy, D. L. A study of stellar photometric variability within the central 4 pc of the Galactic Center with infrared image subtraction. *Acta Astron.* **57**, 173–199 (2007).
- Rafelski, M., Ghez, A. M., Hornstein, S. D., Lu, J. R. & Morris, M. Photometric stellar variability in the Galactic Center. *Astrophys. J.* **659**, 1241–1256 (2007).
- van Leeuwen, F., Feast, M. W., Whitelock, P. A. & Laney, C. D. Cepheid parallaxes and the Hubble constant. *Mon. Not. R. Astron. Soc.* **379**, 723–737 (2007).
- Gillessen, S. *et al.* Monitoring stellar orbits around the massive black hole in the Galactic Center. *Astrophys. J.* **692**, 1075–1109 (2009).
- Nishiyama, S. *et al.* The distance to the Galactic Center derived from infrared photometry of bulge red clump stars. *Astrophys. J.* **647**, 1093–1098 (2006).
- Groenewegen, M. A. T., Udalski, A. & Bono, G. The distance to the Galactic centre based on population II Cepheids and RR Lyrae stars. *Astron. Astrophys.* **481**, 441–448 (2008).
- Tripp, S. *et al.* Kinematics of the old stellar population at the Galactic centre. *Astron. Astrophys.* **492**, 419–439 (2008).
- Fernie, J. D., Evans, N. R., Beattie, B. & Seager, S. A database of Galactic classical Cepheids. *Inform. Bull. Variable Stars* **4148**, 1 (1995).
- Antonello, E., Fugazza, D. & Mantegazza, L. Variable stars in nearby galaxies. VI. Frequency-period distribution of Cepheids in IC 1613 and other galaxies of the Local Group. *Astron. Astrophys.* **388**, 477–482 (2002).
- Davies, B. *et al.* The chemical abundances in the Galactic Center from the atmospheres of red supergiants. *Astrophys. J.* **694**, 46–55 (2009).
- Kroupa, P. On the variation of the initial mass function. *Mon. Not. R. Astron. Soc.* **322**, 231–246 (2001).
- Bono, G. *et al.* Intermediate-mass star models with different helium and metal contents. *Astrophys. J.* **543**, 955–971 (2000).
- Kormendy, J., Cornell, M. E., Block, D. L., Knapen, J. H. & Allard, E. L. Pseudobulges in the disk galaxies NGC 7690 and NGC 4593. *Astrophys. J.* **642**, 765–774 (2006).
- Schinnerer, E., Böker, T., Emsellem, E. & Downes, D. Bar-driven mass build-up within the central 50 pc of NGC 6946. *Astron. Astrophys.* **462**, L27–L30 (2007).
- Kormendy, J. & Kennicutt, R. C. Secular evolution and the formation of pseudobulges in disk galaxies. *Annu. Rev. Astron. Astrophys.* **42**, 603–683 (2004).
- Binney, J. in *The Galaxy Disk in Cosmological Context* (eds Andersen, J., Bland-Hawthorn, J. & Nordström, B.) 145–152 (Proc. IAU Symp. 254, Cambridge Univ. Press, 2009).
- Stark, A. A. *et al.* Gas density, stability, and starbursts near the inner Lindblad resonance of the Milky Way. *Astrophys. J.* **614**, L41–L44 (2004).

**Supplementary Information** is linked to the online version of the paper at [www.nature.com/nature](http://www.nature.com/nature).

**Acknowledgements** We thank the IRSF/SIRIUS team in Nagoya University, the National Astronomical Observatory of Japan, Kyoto University and the University of Tokyo, and the staff of the South African Astronomical Observatory (SAAO) for their support during our near-IR observations. This work was supported by Grants-in-Aid for Scientific Research from the Japan Society for the Promotion of Science (JSPS). M.W.F. acknowledges the support from National Research Foundation (NRF) of South Africa.

**Author Contributions** N.M. led the programme, carried out the analysis and wrote most of the text. T.K., S.N. and T. Nagayama as well as N.M. carried out the monitoring observations at the IRSF. S.N., N.K., M.T., G.B., M.W.F. and T. Nagata took part in discussions, especially those on their own research fields such as evolution of galaxies, star formation and stellar pulsation. All authors contributed to the writing of the paper. The figures, including those in the Supplementary Information, were generated by the authors.

**Author Information** Reprints and permissions information is available at [www.nature.com/reprints](http://www.nature.com/reprints). The authors declare no competing financial interests. Readers are welcome to comment on the online version of this article at [www.nature.com/nature](http://www.nature.com/nature). Correspondence and requests for materials should be addressed to N.M. ([matsunaga@ioa.s.u.-tokyo.ac.jp](mailto:matsunaga@ioa.s.u.-tokyo.ac.jp)).

# The mechanism of membrane-associated steps in tail-anchored protein insertion

Malaiyalam Mariappan<sup>1\*</sup>, Agnieszka Mateja<sup>2\*</sup>, Malgorzata Dobosz<sup>2</sup>, Elia Bove<sup>2</sup>, Ramanujan S. Hegde<sup>1†</sup> & Robert J. Keenan<sup>2</sup>

**Tail-anchored (TA) membrane proteins destined for the endoplasmic reticulum are chaperoned by cytosolic targeting factors that deliver them to a membrane receptor for insertion. Although a basic framework for TA protein recognition is now emerging, the decisive targeting and membrane insertion steps are not understood. Here we reconstitute the TA protein insertion cycle with purified components, present crystal structures of key complexes between these components and perform mutational analyses based on the structures. We show that a committed targeting complex, formed by a TA protein bound to the chaperone ATPase Get3, is initially recruited to the membrane through an interaction with Get2. Once the targeting complex has been recruited, Get1 interacts with Get3 to drive TA protein release in an ATPase-dependent reaction. After releasing its TA protein cargo, the now-vacant Get3 recycles back to the cytosol concomitant with ATP binding. This work provides a detailed structural and mechanistic framework for the minimal TA protein insertion cycle.**

Approximately 5% of eukaryotic membrane proteins are anchored to the lipid bilayer by a single carboxy-terminal transmembrane domain<sup>1–4</sup> (TMD). These ‘tail-anchored’ proteins are found in virtually all cellular membranes and perform essential functions in processes including protein trafficking, degradation, cell death and membrane biogenesis. TA proteins in compartments of the secretory and endocytic pathways are first targeted to and inserted into the ER membrane by a post-translational targeting pathway conserved across eukaryotes<sup>5–9</sup> and archaea<sup>10,11</sup>.

This pathway begins with a ‘pre-targeting’ factor that captures newly synthesized TA proteins through their TMDs near the ribosome<sup>12,13</sup>. In yeast, the pre-targeting factor is Sgt2, which assembles with Get3, Get4 and Get5 (also known as Mdy2) to form a TMD recognition complex<sup>12,14,15</sup>. Assembly of TMD recognition complexes permits substrates to be transferred from Sgt2 to Get3 in an ATP-dependent manner<sup>12</sup>. Get3 (TRC40, or ASNA1, in mammals) is a homodimeric ATPase whose conformation is regulated by its nucleotide state<sup>16–20</sup>. Both crystallographic and functional analyses support a model in which an ATP-bound, ‘closed’ dimer of Get3 binds substrates in a large hydrophobic groove that spans both subunits<sup>16–18,20</sup>. This substrate–Get3–nucleotide complex is therefore the committed targeting complex (Supplementary Discussion).

In yeast, genetic and physical interaction studies have identified the ER-localized membrane proteins Get1 and Get2 as potential receptors for Get3 (refs 7, 21). It is not known whether Get1, Get2 and Get3 constitute the minimal targeting and insertion machinery, how they function or what their essential roles are during TA protein insertion. In this Article, we combine functional reconstitution of TA protein insertion with structural analysis of key intermediate complexes to provide a mechanistic framework for the TA protein insertion cycle in *Saccharomyces cerevisiae*.

## The minimal insertion machinery

We first reconstituted the TA protein insertion cycle with purified recombinant factors. A functional TA protein targeting complex was

assembled and purified from *in vitro* translation reactions (Supplementary Fig. 1). The complex contained radio-labelled and epitope-tagged Sec61 $\beta$  (an ER-localized TA protein) bound to recombinant yeast Get3 in roughly the 2:1 ratio expected from structural studies. This recombinant targeting complex was functional as judged by membrane insertion of Sec61 $\beta$  into ER-derived yeast rough microsomes (yRMs) but not into protein-free liposomes (Fig. 1a). Microsomes from  $\Delta$ Get1 and  $\Delta$ Get2 yeast strains showed little insertion activity, whereas  $\Delta$ Get3 microsomes were similar to wild-type yRMs. Sec61 $\beta$  insertion efficiency with the purified targeting complex was approximately two-fold higher than for Sec61 $\beta$  in crude translation reactions (data not shown), consistent with the observation that the latter contains a heterogeneous mixture of Sec61 $\beta$  complexes with other factors<sup>8,13,22</sup>. Thus, purified Get3–Sec61 $\beta$  is a committed targeting complex for Get1- and Get2-dependent membrane insertion.

The TA insertion defect of  $\Delta$ Get1 and  $\Delta$ Get2 microsomes is due solely to loss of Get1 and/or Get2. To show this, purified recombinant Get1 and Get2 (rGet1 and rGet2; Supplementary Fig. 2) produced from *Escherichia coli* were added to detergent extracts prepared from  $\Delta$ Get1 or  $\Delta$ Get2 yRMs, reconstituted into proteoliposomes and tested for function (Supplementary Fig. 3). Proteoliposomes from  $\Delta$ Get1 yRMs were inactive for TA protein insertion, but were restored by replenishment with physiologic levels of rGet1 but not rGet2.  $\Delta$ Get2 proteoliposomes required both rGet1 and rGet2 to restore insertion to near wild-type levels (Supplementary Fig. 3), as expected because Get1 is absent from  $\Delta$ Get2 yRMs (Fig. 1a). We also biochemically depleted Get1 and Get2 from wild-type yRM and showed that the resulting insertion defect could be corrected by replenishment with rGet1 and rGet2 but with neither individually (Supplementary Fig. 4). Thus, rGet1 and rGet2 are fully functional in replacing their native counterparts during Get3-dependent TA protein insertion.

The lack of membrane proteins co-purifying with Get1 and Get2 (Supplementary Fig. 5), and the absence of other membrane proteins found in genetic studies<sup>15,23,24</sup>, suggested that Get1 and Get2 are

<sup>1</sup>Cell Biology and Metabolism Program, National Institute of Child Health and Human Development, National Institutes of Health, Room 101, Building 18T, 18 Library Drive, Bethesda, Maryland 20892, USA.

<sup>2</sup>Department of Biochemistry & Molecular Biology, The University of Chicago, Gordon Center for Integrative Science, Room W238, 929 East 57th Street, Chicago, Illinois 60637, USA. †Present address: MRC Laboratory of Molecular Biology, Hills Road, Cambridge CB2 0QH, UK.

\*These authors contributed equally to this work.



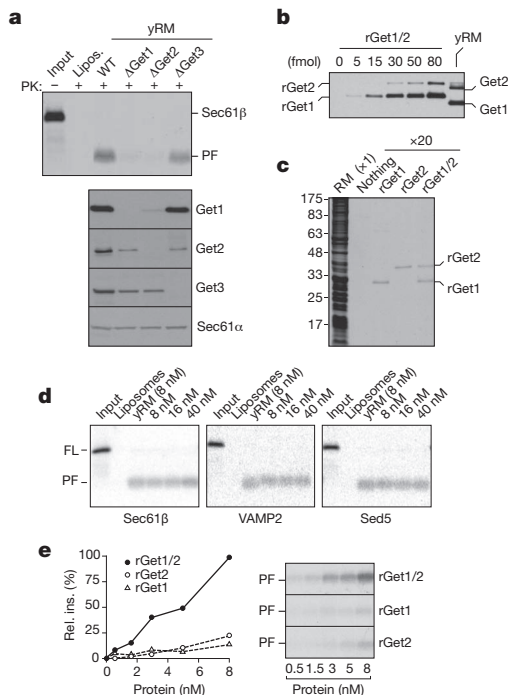


**Figure 1 | Reconstitution of TA protein insertion with purified components.** **a**, Yeast rough microsomes (yRMs) from the indicated strains were tested for insertion of purified Get3–Sec61 $\beta$  targeting complex (top) or by immunoblotting (bottom). The protease-protected fragment (PF) is diagnostic of successful insertion. Liposomes are a negative control. PK, proteinase K; WT, wild type. **b**, Quantification of Get1 and Get2 concentrations in yRMs by immunoblotting. **c**, Protein composition of yRMs and proteoliposomes containing recombinant proteins. Proteoliposomes in 20-fold relative excess were analysed. **d**, Insertion of purified targeting complexes into liposomes, yRMs, or rGet1/2 proteoliposomes. VAMP2 and Sed5, TMDs from rat VAMP2 or yeast Sed5. Concentrations of the Get1/2 complex are indicated FL, full length. **e**, Relative efficiency of insertion of purified Get3–Sec61 $\beta$  targeting complex into rGet1, rGet2 or rGet1/2 proteoliposomes. Autoradiographs and quantified data are shown.

sufficient for Get3-mediated TA protein insertion. Indeed, proteoliposomes containing physiologic concentrations of only rGet1 and rGet2 (Fig. 1b, c) were indistinguishable from yRM in mediating insertion of three different purified TA protein targeting complexes (Fig. 1d). Incorporating super-physiologic levels of rGet1 and rGet2 did not further improve insertion (Fig. 1d), and lower levels reduced overall insertion efficiency (Fig. 1e).

The recombinant system required both rGet1 and rGet2 (Fig. 1e), precisely mirroring the results *in vivo*<sup>7</sup> and in crude proteoliposomes (Supplementary Figs 3 and 4). Interaction analysis confirmed that rGet1 and rGet2 form a complex through their membrane domains in detergent solution (Supplementary Fig. 6), suggesting that during reconstitution they are incorporated as a complex. Taken together, the dependence on rGet1 and rGet2, their interaction with each other, their functionality in replacing the endogenous proteins and the high-efficiency insertion at native concentrations argue strongly that we have reconstituted physiologically relevant TA protein insertion with a defined targeting complex and only two membrane proteins.

### The Get2c–Get3–ADP•AlF<sub>4</sub><sup>−</sup> complex

Membrane targeting presumably involves an interaction between Get3 and the conserved cytosolic domains of Get1 and/or Get2 (Figs 2a and 3a and Supplementary Fig. 10). These fragments ('Get1c' and 'Get2c') did not interact with each other (Supplementary Figs 6 and 7), but both bound tightly to Get3 (Supplementary Figs 7 and 8) and inhibited the insertion of Sec61 $\beta$  into yRMs (Supplementary Fig. 8). The ability of Get3 to interact with either subunit of the Get1/2 complex suggested that each interaction might serve a different purpose in the insertion cycle.

The closed-dimer form of ADP•AlF<sub>4</sub><sup>−</sup>-bound Get3 probably mimics the TA substrate-bound conformation that targets to the membrane<sup>16–18,20</sup>. This Get3–ADP•AlF<sub>4</sub><sup>−</sup> complex crystallized with Get2c, and we determined the structure to a resolution of 2.1 Å (Supplementary Table 1 and Supplementary Fig. 9). The structure reveals Get3 in a 'closed'-dimer conformation with ADP•AlF<sub>4</sub><sup>−</sup> bound at each active site (Fig. 2b). Two Get2 fragments, each comprising two helices connected by a short linker, bind to equivalent sites on opposite faces of the symmetric Get3 homodimer. Each interface buries ~960 Å<sup>2</sup> of surface area, largely restricted to a single Get3 monomer (Fig. 2c, green, and

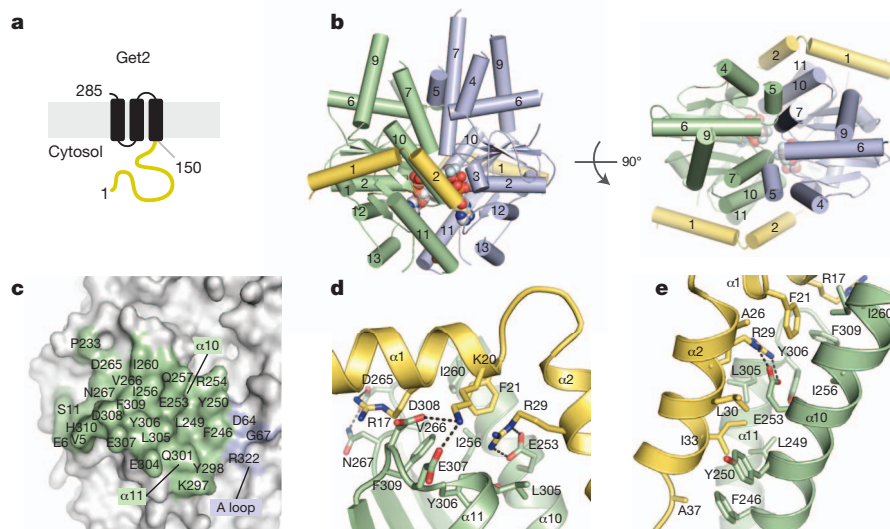


**Figure 2 | Get2 fragment complex with ADP•AlF<sub>4</sub><sup>−</sup>-bound Get3.** **a**, Predicted topology of *S. cerevisiae* Get2 with its large cytosolic-facing region (yellow). **b**, Structure of two Get2 fragments (yellow) bound to the closed Get3 dimer (green, blue). Two Mg<sup>2+</sup>–ADP•AlF<sub>4</sub><sup>−</sup> complexes and a zinc atom are indicated (spheres). An orthogonal view into the substrate-binding composite hydrophobic groove is shown on the right. **c**, Get3 residues in the Get2 interface

are indicated. Most contacts are to one Get3 monomer (green); poorly ordered contacts are to the conserved A-loop ATPase motif. **d**, Close-up of interactions along helix  $\alpha$ 1 of Get2, including Arg 17, Lys 20 and Phe 21. **e**, Close-up of interactions along helix  $\alpha$ 2 of Get2, including the conserved salt bridge between Arg 29 and Glu 253.

Supplementary Fig. 10). Get3 residues within the interface undergo little conformational change on binding to Get2c (Supplementary Fig. 11). The amino-terminal helix of Get2 lies in a cleft defined at one end by short loops following helices  $\alpha 10$  and  $\alpha 11$  of Get3, and at the other end by the loop following helix  $\alpha 9$  and the extreme N terminus of Get3 (Fig. 2d). Three conserved, negatively charged residues in Get3, namely Asp 265, Glu 307 and Asp 308, make direct contact with Get2c. The second helix of Get2 lies in a cleft defined by Get3 helices  $\alpha 10$  and  $\alpha 11$  (Fig. 2e). This surface is largely hydrophobic except for a conserved salt bridge between Glu 253 (Get3) and Arg 29 (Get2c). The C-terminal end of the Get2 fragment, which is not conserved, makes poorly ordered contacts with the adjacent Get3 monomer (Fig. 2c, blue).

The TA substrate-binding site in Get3 comprises a large hydrophobic groove spanning the  $\alpha$ -helical subdomains of both monomers<sup>16</sup>. In the Get2c–Get3 complex, this groove is intact (Fig. 2b and Supplementary Fig. 20), suggesting that Get2 captures the closed Get3 targeting complex without disrupting the TA binding site. The long, flexible linker that tethers the helical N terminus of Get2 to its first TMD would facilitate this process. Thus, we propose that the Get2c–Get3–ADP•AlF<sub>4</sub><sup>−</sup> structure represents a snapshot of the initial encounter between the closed-dimer targeting complex and the receptor.

### The Get1c–Get3 complex

Get3 was also crystallized in the presence of Get1c. Whether or not ADP•AlF<sub>4</sub><sup>−</sup> was present during crystallization, the Get3–Get1c crystals lacked nucleotide. We determined the structure of this nucleotide-free complex to a resolution of 3.0 Å (Supplementary Table 1 and Supplementary Fig. 9) and revealed Get3 in an ‘open’ conformation, with two Get1 fragments bound to equivalent sites on opposite faces of the symmetric Get3 homodimer (Fig. 3b). Each Get1 fragment adopts an antiparallel coiled-coil structure and buries ~1,030 Å<sup>2</sup> of surface area in a bipartite interface split evenly between the two Get3 subunits (Fig. 3c and Supplementary Fig. 10). As observed in the Get2c complex, Get3 residues on the interface undergo little conformational change on binding to Get1c (Supplementary Fig. 11). Binding to one Get3 monomer is primarily mediated by hydrophobic

contacts between helix  $\alpha 2$  of Get1c and the cleft defined by helices  $\alpha 10$  and  $\alpha 11$  of Get3 (Fig. 3c, d, green). Binding to the other monomer is mediated by helix  $\alpha 1$  of Get1c, which interacts with Get3 helices  $\alpha 4$  and  $\alpha 5$ , and by a six-residue loop in Get1c that directly contacts the ATP-binding site (Fig. 3c, e, blue; see below).

Importantly, many of the Get3 residues that contact Get1c also mediate interactions with Get2c (Supplementary Figs 10 and 11). For example, the conserved Arg 73 (Get1c)/Glu 253 (Get3) salt bridge almost perfectly mimics the Arg 29 (Get2c)/Glu 253 (Get3) interaction (Figs 2e and 3d). The presence of overlapping binding sites suggests that Get1 and Get2 cannot simultaneously occupy the same site on Get3, as illustrated by dissociation of the Get3–Get2c complex by Get1c (Supplementary Fig. 11). Previous work underscores the functional significance of this region of Get3: alanine substitutions within the shared interface, including F246A, Y250A, E253A and Y298A, have a strong loss-of-function phenotype in yeast<sup>18</sup>. Moreover, two of these positions, Tyr 250 and Glu 253, have been implicated in the ATP-dependent binding of Get4<sup>25</sup>. Thus, the  $\alpha 10$ – $\alpha 11$  region of Get3 is a binding hotspot that probably plays an important regulatory role at different stages of the targeting cycle.

The most striking aspect of the Get3–Get1c structure is how the Get1 coiled coil wedges between the Get3 subunits, completely disrupting the hydrophobic TA substrate-binding site (Fig. 3b). Such an interaction could effect substrate release from the Get3 targeting complex. However, parts of the bipartite Get1-binding site on Get3—including the ATPase motifs and portions of helices  $\alpha 4$  and  $\alpha 5$  (Fig. 3c, blue)—are buried in the ATP-bound, fully closed-dimer conformation. By contrast, the bipartite Get1-binding site is largely exposed to solvent in the Mg<sup>2+</sup>-ADP-bound state<sup>17,20</sup> (Supplementary Fig. 12). This implies that ATP hydrolysis by the targeting complex is needed to expose the Get1-binding site on Get3 (Fig. 3c and Supplementary Fig. 12, green and blue). Once exposed, Get1 would complete the Get3 transition from closed to open, disrupting the hydrophobic groove to promote release of the TA substrate and ADP (which binds weakly to substrate-free Get3; Supplementary Fig. 18). Importantly, the rigid Get1 coiled coil is perpendicular to

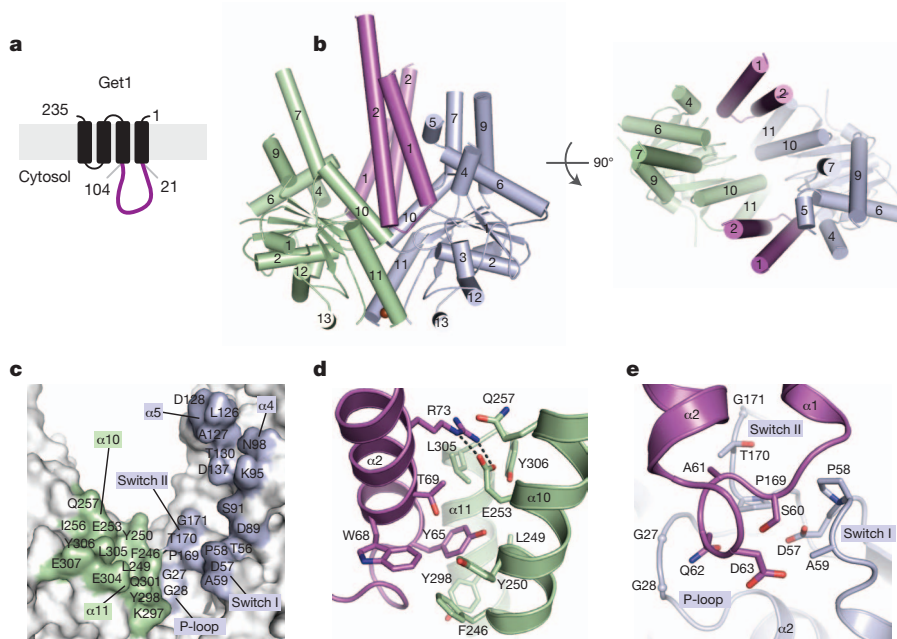


**Figure 3 | Get1 fragment complex with Get3.** **a**, Predicted topology of *S. cerevisiae* Get1 with a large cytosolic-facing region (magenta). **b**, Structure of two Get1 fragments (magenta) bound to the open dimer state of Get3 (green, blue). The composite hydrophobic groove is completely disrupted. **c**, Get3 residues in the Get1 interface are indicated; significant contacts are made to both monomers (green, blue), including the P-loop, switch I and switch II

ATPase motifs. **d**, Close-up of interactions between Get1 helix  $\alpha 2$  (magenta) and one Get3 monomer (green), including the conserved salt bridge between Arg 73 and Glu 253. This interface overlaps extensively with the Get2c binding surface (Fig. 2e and Supplementary Fig. 11). **e**, Close-up of interactions between the Get1 hairpin loop and the active site of the adjacent Get3 monomer (blue).

the plane of the membrane, thereby positioning the hydrophobic groove of Get3 parallel to the membrane. This implies that the TMD of a TA protein is precisely released along the membrane surface, presumably facilitating its subsequent insertion.

### Targeting and substrate release

Conserved contacts between Get3–Get2 and Get3–Get1 were disrupted with point mutations (R17E and R73E, respectively), verified to prevent binding (Supplementary Fig. 13) and shown to reduce insertion in the reconstituted system sharply (Fig. 4a). When the substrate–Get3 interaction was monitored by crosslinking (Supplementary Fig. 14), Get1c, but not Get2c, was found to release TA substrate from Get3 (>50% at 500 nM; Fig. 4b). This activity was abolished by the R73E mutation that disrupts Get3–Get1c interactions (Fig. 4c). Thus, Get1c and Get2c both inhibit insertion (Supplementary Fig. 8), but for different reasons: Get1c causes premature substrate release whereas Get2c competitively precludes targeting.

When reconstituted into proteoliposomes at more-physiologic concentrations, neither rGet1 nor rGet2 was able to effect substrate release, whereas the complete rGet1/2 complex was active (Fig. 4d). Importantly, disrupting the Get3–Get1 interaction (with R73E) or the Get3–Get2 interaction (with R17E) abolished the ability of the rGet1/2 complex to stimulate substrate release (Fig. 4e). Thus, whereas Get1c at super-physiologic concentrations can drive substrate release on its own, full-length Get1 in the membrane is unable to do so at physiologic levels. In this context, Get1 requires Get2 (specifically its ability to bind Get3) to release substrate from Get3.

On the basis of the Get3–Get1c structure, ATP hydrolysis by the Get3 targeting complex is likely to be necessary for its interaction with Get1. Indeed, targeting complexes containing an ATPase-deficient Get3 mutant (D57N) were poorly inserted into proteoliposomes containing the rGet1/2 complex (Fig. 4f) despite no impairment of the interaction of Get3 (D57N) with substrate or the rGet1/2 complex (Supplementary Fig. 15 and data not shown). Analysis of the interaction between TA substrate and Get3 (D57N) revealed that the rGet1/2 complex was unable to induce release (Fig. 4d, e). Taken together, the results of the functional analysis indicate that the Get3–Get2 interaction is important for targeting, and that this step

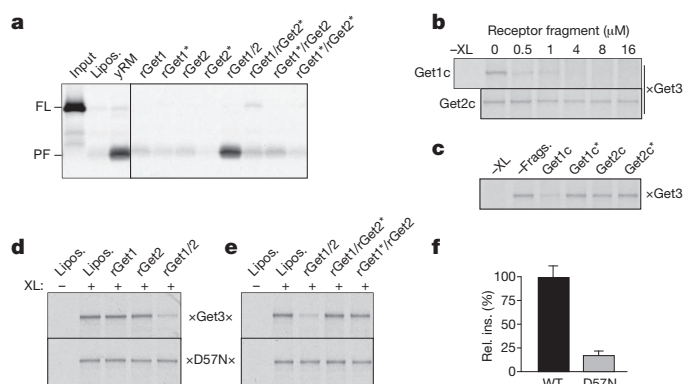


**Figure 4 | Mutational analysis of the function of Get1, Get2 and Get3.**

**a**, Insertion assay with purified Get3–Sec61β targeting complex and proteoliposomes containing the indicated purified proteins. Liposomes and yRM are controls. Get1\* and Get2\* indicate mutants inactive in Get3 interaction (R73E and R17E, respectively). **b**, Substrate release from targeting complexes incubated with Get1c or Get2c; release was monitored by loss of the crosslink (XL) between radio-labelled substrate and Get3. Square brackets indicate concentration. **c**, As in **b**, with wild-type and mutant fragments at a concentration of 0.5 μM. **d**, Substrate interaction with Get3 or the ATPase-deficient Get3 (D57N) was assessed by crosslinking after incubation with liposomes or proteoliposomes containing the indicated recombinant proteins. **e**, As in **d**, but comparing wild-type and mutant complexes of Get1 and Get2. **f**, Relative efficiency of insertion (mean ± s.e.m.; *n* = 6) into rGet1/2 proteoliposomes with targeting complexes prepared from wild-type Get3 or Get3 (D57N).

is a prerequisite for substrate release. Substrate release, in turn, depends on both ATP hydrolysis by Get3 and the ability of Get3 to interact with Get1.

### ATP-dependent recycling

The ATP that Get3 hydrolyses before substrate release is apparently acquired from the *in vitro* translation reaction (and maintained during purification) because insertion proceeds efficiently without additional ATP in the purified system (Fig. 5a). This is consistent with structural analysis suggesting that nucleotide is shielded from bulk solvent in the fully closed Get3–ATP–substrate ternary complex (Supplementary Discussion). However, we (Supplementary Fig. 16) and others<sup>6,17</sup> have found that insertion reactions into crude yRMs, but not rGet1/2 proteoliposomes, are stimulated by ATP, non-hydrolysable ATP analogues or ADP. The explanation for this discrepancy proved to be the near-stoichiometric presence of Get3 on the Get1/2 complex in yRMs (Supplementary Fig. 5), but not on rGet1/2 proteoliposomes. Accordingly, binding Get3 to rGet1/2 proteoliposomes restored ATP dependence (Fig. 5b), whereas removing Get3 from yRM (by using ΔGet3 yeast) eliminated the ATP requirement for maximal insertion (Fig. 5c).

These results indicate that after TA substrate release, Get3 remains bound to microsomal membranes. In the nucleotide-free Get3–Get1c structure, which mimics this ‘post-insertion’ complex, residues within the conserved loop of Get1 (<sup>59</sup>ISAQDN<sup>64</sup>) insert into the Get3 active site (Fig. 3e) and deform it relative to the ADP•AlF<sub>4</sub><sup>−</sup>-bound conformation (Fig. 5d). Modelling ATP into the active site reveals steric and electrostatic clashes between Get1 and ATP, suggesting that free ATP should displace Get3 from Get1. Indeed, the Get3–Get1c interaction was quantitatively disrupted by micromolar concentrations of ATP (Fig. 5e). ADP was far less effective, and AMP failed to disrupt the Get3–Get1c complex. This ATP-dependent Get3 dissociation was also verified with full-length Get1 using pull-down assays (Supplementary Fig. 19). By contrast, none of the tested nucleotides

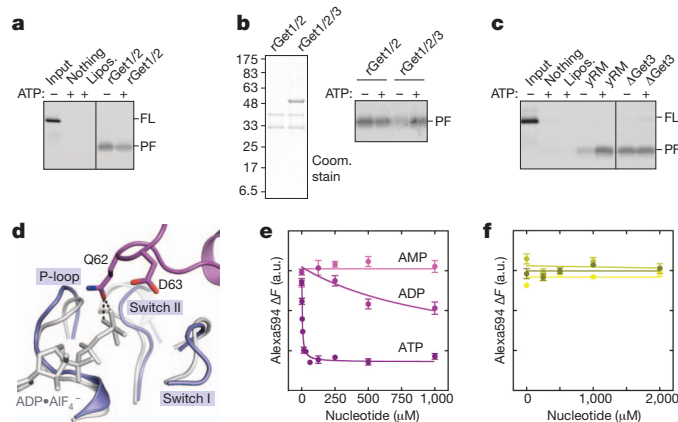


**Figure 5 | ATP-dependent recycling of empty Get3 from Get1.** **a**, Insertion activity of purified Get3–Sec61β targeting complex using the indicated vesicles with or without an ATP regenerating system. **b**, Proteoliposomes containing the rGet1/2 complex, or the rGet1/2 complex bound to Get3 (left panel), were tested for insertion activity of purified targeting complex in the presence or absence of ATP (right panel). Coom., Coomassie blue. **c**, Purified targeting complex was tested for insertion into wild-type yRMs or those from a ΔGet3 strain, with or without ATP. **d**, Close-up of the Get1c–Get3 complex (magenta and blue) modelled onto the active site of the closed, ADP•AlF<sub>4</sub><sup>−</sup>-bound Get3 dimer (grey). Steric (dashed lines) and electrostatic clashes between conserved residues in Get1 and the nucleotide γ-phosphate are apparent. **e**, Dissociation of Get3–Get1c, monitored by the change in fluorescence resonance energy transfer (ΔF), on titration with the indicated nucleotides. Curve fits of triplicate measurements (mean ± s.e.m.) are shown. a.u., arbitrary units. The reaction contained 10 nM Get3 (D57N) and 100 nM Get1c. **f**, As in **e**, but with 10 nM Get3 (D57N) and 200 nM Get2c.



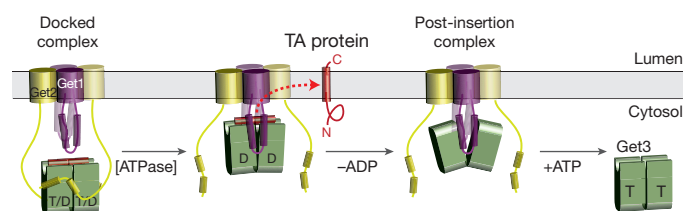


**Figure 6 | Model for TA protein insertion.** Nucleotide- and tail-anchored substrate-bound Get3 in a closed-dimer conformation forms the ‘docked complex’ by association with Get2. D, ADP; T, ATP. Following ATP hydrolysis, Get1 interacts with and orients Get3 along the membrane surface. This stabilizes the open-dimer conformation of Get3, disrupts the composite hydrophobic groove and promotes TA substrate release for membrane insertion. The Get3–Get1 post-insertion complex is dissociated by ATP binding, recycling Get3 back to the cytosol. See Supplementary Discussion for more details.

disrupted Get2c binding to Get3 (Fig. 5f). Thus, free ATP binding dissociates the Get1–Get3 complex to recycle Get3 from the membrane after TA substrate release.

### A model for the insertion cycle

Figure 6 illustrates our working framework for the insertion cycle. Substrate-bound Get3 in the closed conformation and loaded with nucleotide (either ATP or ADP; see Supplementary Discussion) is captured at the membrane by the cytosolic domain of Get2. The apparently long and flexible Get2 tether may facilitate this initial encounter and bring the intact targeting complex near to the site of insertion. After this targeting step, Get1 mediates the post-targeting reactions of substrate release and insertion. Get1 binding to the targeting complex would be facilitated by partial destabilization of the closed dimer after ATP hydrolysis, and by the high local concentration of Get3 achieved by its recruitment through Get2. Binding to the rigid Get1 coiled coil would orient Get3 such that the substrate is in close proximity to the membrane. Moreover, by stabilizing the open conformation, Get1 binding would disrupt the Get3 hydrophobic groove and promote release of substrate and ADP. At present, we do not know whether the Get1/2 complex functions as a heterodimer or heterotetramer, although we favour the latter given the symmetric structure of the Get3 dimer. The released substrate would insert unassisted into the lipid bilayer directly<sup>26,27</sup> or would be chaperoned by the TMDs of the Get1/2 complex. Finally, the empty Get3 would be released from Get1 concomitant with ATP binding, and would be primed to accept the next substrate from the cytosolic pre-targeting complex for another round of targeting.

### METHODS SUMMARY

**Reagents and assays.** Constructs, proteins and antibodies derived from earlier studies<sup>8,13,16</sup> are described in Methods. Antibodies against Get1 and Get2 were produced in rabbits. *In vitro* translation, insertion, crosslinking and immunoprecipitation were as described previously<sup>8,13,28</sup>. Get1 and Get2 (full length and fragments) were expressed in *E. coli* and purified by Ni-NTA chromatography; fragments were further purified by size exclusion chromatography. <sup>35</sup>S-labelled targeting complexes were affinity-purified from *in vitro* translation reactions containing recombinant Get3.

**Liposomes, microsomes and proteoliposomes.** Liposomes containing a 4:1 ratio of egg phosphatidylcholine and dipalmitoylphosphatidylethanolamine were prepared by extrusion<sup>27,29</sup>. Yeast rough microsomes were prepared as before<sup>30–33</sup>. Proteoliposome reconstitutions from solubilized yRMs or purified Get1 and/or Get2 were done by optimizing (Supplementary Fig. 17) earlier methods<sup>30,33,34</sup>.

**Interaction analysis.** Binding assays were performed by gel filtration and multi-angle light scattering, pull-down assays or fluorescence resonance energy transfer. Substrate release was monitored by amine-reactive crosslinking<sup>8</sup>.

**Structure determination.** Complexes of Get3 with Get1c or Get2c were co-expressed in *E. coli* and purified by Ni-NTA and size exclusion chromatography. Diffraction data were collected at Advanced Photon Source beamline 21-IDG, Argonne National Laboratory. Structures were determined by molecular replacement in PHASER<sup>35</sup>. Refinement and model building was done using PHENIX<sup>36</sup> and COOT<sup>37</sup>.

**Full Methods** and any associated references are available in the online version of the paper at [www.nature.com/nature](http://www.nature.com/nature).

**Received 7 April; accepted 13 July 2011.**

**Published online 24 August 2011.**

- Kutay, U., Hartmann, E. & Rapoport, T. A. A class of membrane proteins with a C-terminal anchor. *Trends Cell Biol.* **3**, 72–75 (1993).
- Beilharz, T., Egan, B., Silver, P. A., Hofmann, K. & Lithgow, T. Bipartite signals mediate subcellular targeting of tail-anchored membrane proteins in *Saccharomyces cerevisiae*. *J. Biol. Chem.* **278**, 8219–8223 (2003).
- Kalbfleisch, T., Cambon, A. & Wattenberg, B. W. A bioinformatics approach to identifying tail-anchored proteins in the human genome. *Traffic* **8**, 1687–1694 (2007).
- Kriechbaumer, V. *et al.* Subcellular distribution of tail-anchored proteins in *Arabidopsis*. *Traffic* **10**, 1753–1764 (2009).
- Favaloro, V., Spasic, M., Schwappach, B. & Dobberstein, B. Distinct targeting pathways for the membrane insertion of tail-anchored (TA) proteins. *J. Cell Sci.* **121**, 1832–1840 (2008).
- Favaloro, V., Vilardi, F., Schlecht, R., Mayer, M. P. & Dobberstein, B. Asna1/TRC40-mediated membrane insertion of tail-anchored proteins. *J. Cell Sci.* **123**, 1522–1530 (2010).
- Schuldiner, M. *et al.* The GET complex mediates insertion of tail-anchored proteins into the ER membrane. *Cell* **134**, 634–645 (2008).
- Stefanovic, S. & Hegde, R. S. Identification of a targeting factor for posttranslational membrane protein insertion into the ER. *Cell* **128**, 1147–1159 (2007).
- Borgese, N. & Fasana, E. Targeting pathways of C-tail-anchored proteins. *Biochim. Biophys. Acta* **1808**, 937–946 (2011).
- Sherrill, J., Mariappan, M., Dominik, P., Hegde, R. S. & Keenan, R. J. A conserved archaeal pathway for tail-anchored membrane protein insertion. *Traffic* doi:10.1111/j.1600-0854.2011.01229.x (3 July 2011).
- Borgese, N. & Rigbi, M. Remote origins of tail-anchored proteins. *Traffic* **11**, 877–885 (2010).
- Wang, F., Brown, E. C., Mak, G., Zhuang, J. & Denic, V. A chaperone cascade sorts proteins for posttranslational membrane insertion into the endoplasmic reticulum. *Mol. Cell* **40**, 159–171 (2010).
- Mariappan, M. *et al.* A ribosome-associating factor chaperones tail-anchored membrane proteins. *Nature* **466**, 1120–1124 (2010).
- Chang, Y.-W. *et al.* Crystal structure of Get4-Get5 complex and its interactions with Sgt2, Get3, and Ydj1. *J. Biol. Chem.* **285**, 9962–9970 (2010).
- Jonikas, M. C. *et al.* Comprehensive characterization of genes required for protein folding in the endoplasmic reticulum. *Science* **323**, 1693–1697 (2009).
- Mateja, A. *et al.* The structural basis of tail-anchored membrane protein recognition by Get3. *Nature* **461**, 361–366 (2009).
- Bozkurt, G. *et al.* Structural insights into tail-anchored protein binding and membrane insertion by Get3. *Proc. Natl Acad. Sci. USA* **106**, 21131–21136 (2009).
- Suloway, C. J., Chartron, J. W., Zaslaver, M. & Clemons, W. M. Jr. Model for eukaryotic tail-anchored protein binding based on the structure of Get3. *Proc. Natl Acad. Sci. USA* **106**, 14849–14854 (2009).
- Yamagata, A. *et al.* Structural insight into the membrane insertion of tail-anchored proteins by Get3. *Genes Cells* **15**, 29–41 (2010).
- Hu, J., Li, J., Qian, X., Denic, V. & Sha, B. The crystal structures of yeast Get3 suggest a mechanism for tail-anchored protein membrane insertion. *PLoS ONE* **4**, e8061 (2009).
- Auld, K. L. *et al.* The conserved ATPase Get3/Arr4 modulates the activity of membrane-associated proteins in *Saccharomyces cerevisiae*. *Genetics* **174**, 215–227 (2006).
- Leznicki, P., Clancy, A., Schwappach, B. & High, S. Bat3 promotes the membrane integration of tail-anchored proteins. *J. Cell Sci.* **123**, 2170–2178 (2010).
- Schuldiner, M. *et al.* Exploration of the function and organization of the yeast early secretory pathway through an epistatic miniarray profile. *Cell* **123**, 507–519 (2005).
- Costanzo, M. *et al.* The genetic landscape of a cell. *Science* **327**, 425–431 (2010).
- Chartron, J. W., Suloway, C. J. M., Zaslaver, M., a. & Clemons, W. M. Structural characterization of the Get4/Get5 complex and its interaction with Get3. *Proc. Natl Acad. Sci. USA* **107**, 12127–12132 (2010).
- Renthal, R. Helix insertion into bilayers and the evolution of membrane proteins. *Cell. Mol. Life Sci.* **67**, 1077–1088 (2010).
- Brambilla, S. *et al.* Transmembrane topogenesis of a tail-anchored protein is modulated by membrane lipid composition. *EMBO J.* **24**, 2533–2542 (2005).
- Sharma, A., Mariappan, M., Appathurai, S. & Hegde, R. S. *In vitro* dissection of protein translocation into the mammalian endoplasmic reticulum. *Methods Mol. Biol.* **619**, 339–363 (2010).
- Brambilla, S., Yabal, M., Makarow, M. & Borgese, N. Unassisted translocation of large polypeptide domains across phospholipid bilayers. *J. Cell Biol.* **175**, 767–777 (2006).
- Panzner, S., Dreier, L., Hartmann, E., Kostka, S. & Rapoport, T. A. Posttranslational protein transport in yeast reconstituted with a purified complex of Sec proteins and Kar2p. *Cell* **81**, 561–570 (1995).
- Rothblatt, J. A. & Meyer, D. I. Secretion in yeast: reconstitution of the translocation and glycosylation of alpha-factor and invertase in a homologous cell-free system. *Cell* **44**, 619–628 (1986).
- Hansen, W., Garcia, P. D. & Walter, P. *In vitro* protein translocation across the yeast endoplasmic reticulum: ATP-dependent posttranslational translocation of the prepro-alpha-factor. *Cell* **45**, 397–406 (1986).

33. Gorlich, D. & Rapoport, T. A. Protein translocation into proteoliposomes reconstituted from purified components of the endoplasmic reticulum membrane. *Cell* **75**, 615–630 (1993).
34. Fons, R. D., Bogert, B. A. & Hegde, R. S. Substrate-specific function of the translocon-associated protein complex during translocation across the ER membrane. *J. Cell Biol.* **160**, 529–539 (2003).
35. McCoy, A. J. *et al.* Phaser crystallographic software. *J. Appl. Crystallogr.* **40**, 658–674 (2007).
36. Adams, P. D. *et al.* PHENIX: a comprehensive Python-based system for macromolecular structure solution. *Acta Crystallogr. D* **66**, 213–221 (2010).
37. Emsley, P. & Cowtan, K. Coot: model-building tools for molecular graphics. *Acta Crystallogr. D* **60**, 2126–2132 (2004).

**Supplementary Information** is linked to the online version of the paper at [www.nature.com/nature](http://www.nature.com/nature).

**Acknowledgements** Data were collected at beamline 21-IDG at the Advanced Photon Source (APS), Argonne National Laboratory, and we thank the beamline staff for support. We thank T. Dever for yeast strains, T. Rapoport for the Sec61 $\alpha$  antibody, M. Downing for technical assistance, members of the Hegde, Keenan and E. Perozo labs and D. Freymann for advice, and A. Shiau and S. Shao for discussions and comments on the manuscript. Use of the APS, an Office of Science User Facility operated for the US Department of Energy (DOE) Office of Science by Argonne National Laboratory, was

supported by the US DOE under contract no. DE-AC02-06CH11357. This work was supported by the Intramural Research Program of the NIH (to R.S.H.), the Camille and Henry Dreyfus Postdoctoral Program in Environmental Chemistry (to R.J.K. and E.B.), an Edward Mallinckrodt, Jr. Foundation Grant (to R.J.K.) and NIH Grant R01 GM086487 (to R.J.K.).

**Author Contributions** A.M., M.D. and E.B. produced, purified and characterized recombinant Get1, Get2 (full length and fragments) and Get3. M.M. and R.S.H. performed the reconstitution experiments, including the substrate release and membrane insertion assays. A.M., M.D. and R.J.K. carried out crystallization and structure determination as well as the interaction analyses. R.S.H. and R.J.K. designed the project. M.M., R.S.H. and R.J.K. wrote the paper. All authors discussed the results and commented on the manuscript.

**Author Information** Atomic coordinates and structure factors for *S. cerevisiae* Get3 in complex with Get1(21–104) and for Mg<sup>2+</sup>-ADP•AlF<sub>4</sub><sup>−</sup>-bound *S. cerevisiae* Get3 in complex with Get2(1–38) have been deposited in the Protein Data Bank under accession codes 3ZS8 and 3ZS9, respectively. Reprints and permissions information is available at [www.nature.com/reprints](http://www.nature.com/reprints). The authors declare no competing financial interests. Readers are welcome to comment on the online version of this article at [www.nature.com/nature](http://www.nature.com/nature). Correspondence and requests for materials should be addressed to R.J.K. ([bkeenana@uchicago.edu](mailto:bkeenana@uchicago.edu)) or R.S.H. ([hegde.science@gmail.com](mailto:hegde.science@gmail.com)).

## METHODS

**Reagents and basic procedures.** Antibodies against Get1 (residues 61–74) and Get2 (residues 2–12) were generated against synthetic peptides conjugated to KLH via terminal cysteines. Antibody against yeast Get3 was against the whole recombinant protein. Antibody production was by LAMPIRE Biological Laboratories. The antibodies against the 3F4 tag and Sec61 $\beta$  have been described previously<sup>8</sup>. The Sec61 $\alpha$  antibody was a gift from Tom Rapoport (Harvard University). DeoxyBigCHAP (DBC) was obtained from Calbiochem. Yeast strains were from Open Biosystems collections and were provided by Tom Dever. The following lipids were obtained from Avanti Polar Lipids: egg phosphatidylcholine (PC), 1-palmitoyl-2-oleoyl-*sn*-glycero-3-phosphoethanolamine (PE) and 1,2-dipalmitoyl-*sn*-glycero-3-phosphoethanolamine-*N*-lissamine rhodamine B (rhodamine-PE). Each lipid was dissolved and stored in chloroform at  $-20^{\circ}\text{C}$  or  $-80^{\circ}\text{C}$ . Protease inhibitor cocktail was from Roche (EDTA-free Complete tablets) and dissolved as a  $\times 25$  stock in aqueous buffer just before use. *In vitro* translation, chemical crosslinking and immunoprecipitations were as described previously<sup>8,13,28</sup>.

**Preparation of proteins for functional analysis.** The genes encoding full-length or cytosolic fragments of *S. cerevisiae* Get1, Get2 and Get3 were amplified by PCR from genomic DNA. Site-directed mutants were obtained by QuikChange mutagenesis (Stratagene). Unless otherwise noted, all constructs were subcloned into a pET28 derivative (Novagen) modified to incorporate a tobacco etch virus (TEV) protease cleavage site between an N-terminal 6 $\times$ His tag and the polylinker. All constructs were verified by DNA sequencing.

Expression and purification of full-length Get3 (wild type and D57N) was carried out as described previously<sup>16</sup>. Full-length Get1 and Get2 (wild type and mutants) were expressed in *E. coli* Rosetta2/pLysS (Novagen) using the Overnight Express Autoinduction System 1 (Novagen). Cells were disrupted in buffer A (50 mM HEPES, pH 8.0, 500 mM NaCl, 10 mM imidazole, 5% glycerol) with 1 mM PMSF using a high-pressure microfluidizer (Avestin), and the insoluble pellet was isolated by centrifugation. This pellet was washed in buffer A, recentrifuged and solubilized for 1 h at  $4^{\circ}\text{C}$  in buffer A containing 0.5% *n*-dodecyl-*N,N*-dimethylamine-*N*-oxide (LDAO). The detergent-soluble fraction was then subjected to nickel-affinity chromatography (Ni-NTA agarose, Qiagen) in buffer A containing 30 mM imidazole and 0.1% LDAO. Protein was eluted at  $\sim 1\text{ mg ml}^{-1}$  in buffer A containing 200 mM imidazole and 0.1% LDAO, and stored in aliquots at  $-80^{\circ}\text{C}$ . Protein concentrations were determined using calculated  $A_{280}$  extinction coefficients.

The cytosolic Get1 fragment (residues 21–104) was expressed for 3 h at  $37^{\circ}\text{C}$  (wild type) or overnight at  $25^{\circ}\text{C}$  (R73E mutant) in *E. coli* BL21(DE3)/pRIL (Novagen), following induction with 0.1 mM IPTG. Cells were disrupted in buffer B (50 mM Tris, pH 7.5, 500 mM NaCl, 10 mM imidazole, 5% glycerol, 5 mM  $\beta$ -mercaptoethanol) with 1 mM PMSF using a microfluidizer. After clearing by centrifugation, the supernatant was batch-purified by nickel-affinity chromatography. Protein was eluted in buffer B containing 200 mM imidazole, dialyzed into 10 mM Tris, pH 7.5, 250 mM NaCl and 40% glycerol, and then stored at  $-80^{\circ}\text{C}$ . This was typically followed by gel filtration (Superdex 200 10/300 GL, GE Healthcare) in 10 mM Tris, pH 7.5, and 200 mM NaCl. Fractions were pooled and stored in aliquots at  $-80^{\circ}\text{C}$ . Protein concentrations were determined using calculated  $A_{280}$  extinction coefficients.

The cytosolic Get2 fragment (residues 1–38 or 1–106; wild type and R17E) was expressed with an N- or C-terminal 6 $\times$ His tag overnight at  $25^{\circ}\text{C}$  and purified by nickel-affinity chromatography as described above for the Get1 fragment. After dialysis against 10 mM Tris, pH 7.5, and 200 mM NaCl, proteins were further purified by gel filtration in 10 mM Tris, pH 7.5, and 150 mM NaCl. Fractions were pooled, concentrated and stored in aliquots at  $-80^{\circ}\text{C}$ . Protein concentration was determined by BCA (Pierce).

**Preparation of liposomes.** The standard liposome mixture typically contained PC:PE:rhodamine-PE at a mass ratio of 8:1.9:0.1. Rhodamine-PE serves as a tracer to follow the lipid recovery. Lipid solutions were mixed in the above ratios as chloroform stocks, adjusted to 10 mM DTT and dried in a glass tube by centrifugation under vacuum (SpeedVac, Eppendorf) for 12 h. Lipid films were hydrated to a final concentration of  $20\text{ mg ml}^{-1}$  in lipid buffer (50 mM HEPES-KOH, pH 7.4, 15% glycerol) and mixed end to end for 6 h at  $25^{\circ}\text{C}$  with intermittent vortexing. The milky and uniform suspension was subjected to three freeze-thaw cycles (freeze in liquid nitrogen; thaw at  $37^{\circ}\text{C}$ ) and extruded at  $65^{\circ}\text{C}$  11 times through 100-nm polycarbonate membranes using an Avanti mini-extruder<sup>27,29</sup>. Single-use aliquots (100  $\mu\text{l}$ ) of the final clear liposome solution were flash-frozen in liquid nitrogen and stored at  $-80^{\circ}\text{C}$ .

**Purification of recombinant targeting complex.** The DNA template for the double-Strep-tagged human Sec61 $\beta$  was generated by PCR using a 5' oligonucleotide that encodes the T7 promoter, start codon and tag. This template was transcribed and translated in RRL as described previously<sup>28</sup>, but with  $0.15\text{ mg ml}^{-1}$

His-Get3 (added from a  $20\text{ mg ml}^{-1}$  stock in 10 mM Tris-HCl, pH 7.5, 100 mM NaCl and 40% glycerol). A 2-ml translation reaction was diluted twofold with ice-cold column buffer (20 mM HEPES-KOH, pH 7.4, 100 mM potassium acetate, 2 mM magnesium acetate, 1 mM DTT) and centrifuged for 30 min at 540,960g in a TLA100.3 rotor at  $4^{\circ}\text{C}$ . The post-ribosomal supernatant was bound to a 400- $\mu\text{l}$  DEAE-Sepharose fast-flow column at  $4^{\circ}\text{C}$ , washed with column buffer and eluted with a buffer containing 50 mM HEPES-KOH, pH 7.4, 320 mM potassium acetate, 7 mM magnesium acetate and 1 mM DTT. The elution was passed over 200  $\mu\text{l}$  Strep-Tactin agarose (IBA, Germany) one to three times. After washing with four column volumes of Strep-Tactin buffer (50 mM HEPES-KOH, pH 7.4, 10% glycerol, 150 mM potassium acetate, 7 mM magnesium acetate, 1 mM DTT) at  $4^{\circ}\text{C}$ , bound proteins were eluted with  $5 \times 50\text{ }\mu\text{l}$  Strep-Tactin buffer containing 10 mM Desthiobiotin (Novagen). The peak fractions, measured by counting radioactivity, were pooled. The final sample contained  $\sim 10,000\text{ c.p.m. }\mu\text{l}^{-1}$ . The concentration of Get3 in the final sample was estimated to be  $\sim 80\text{ nM}$ . Thus, the targeting complex in our typical preparation has a concentration of  $\sim 40\text{ nM}$ , assuming a 2:1 ratio of Get3 to Sec61 $\beta$ . This was either used immediately or frozen in aliquots in liquid nitrogen and stored at  $-80^{\circ}\text{C}$ . Targeting complexes containing the TMDs of rat VAMP2 and *S. cerevisiae* Sed5 in place of the Sec61 $\beta$  TMD were made similarly.

**Insertion assay.** Post-translational insertion assay was performed as described before<sup>8</sup>, with the following minor modifications. For a standard reaction, 8  $\mu\text{l}$  of purified targeting complex was mixed with 1  $\mu\text{l}$  of ATP regenerating system (2 mM ATP, 10 mM creatine phosphate and  $40\text{ }\mu\text{g ml}^{-1}$  creatine kinase) and 1  $\mu\text{l}$  of yRMs, liposomes, reconstituted proteoliposomes or a matched buffer. ATP regenerating system was omitted in some reactions as indicated in the figure legends. After incubation at  $32^{\circ}\text{C}$  for 30 min, the samples were treated with proteinase K ( $0.5\text{ mg ml}^{-1}$ ) for 60 min on ice, and the protease digestion was terminated with 5 mM PMSF and transferred to 100  $\mu\text{l}$  of boiling 1% SDS as described previously<sup>8</sup>. The protease-protected fragment was then immunoprecipitated using the 3F4 antibody directed against the C terminus of the Sec61 $\beta$  construct. Immunoprecipitated products were analysed by SDS-polyacrylamide gel electrophoresis (SDS-PAGE) and quantified by phosphor imaging.

**Preparation of rough microsomes from yeast.** Yeast microsomes were prepared by modifications of the methods previously described<sup>30–32,38</sup>. TAP-tagged Get1 (Open Biosystems) or Get deletion strains (gift from T. Dever) were grown at  $30^{\circ}\text{C}$  to a density of  $2A_{600}\text{ U}$  in 1 l of YPD medium containing 2% glucose. Cells were collected by centrifugation at 3,000g for 5 min and washed twice with ice-cold distilled water. All subsequent steps were on ice or at  $4^{\circ}\text{C}$ . The cell pellet was resuspended in 50 ml of homogenization buffer (20 mM HEPES-KOH, pH 7.4, 100 mM potassium acetate, 2 mM magnesium acetate) and centrifuged for 5 min at 3,000g. The resulting cell pellet was resuspended in homogenization buffer containing 2 mM DTT and protease inhibitor cocktail (Roche) at a concentration of 1 ml per gram of cell pellet. Pre-chilled glass beads were added ( $3\text{ g ml}^{-1}$  of suspension), and cell lysis was induced as follows: the tube was vigorously shaken up and down over a 50-cm path at  $\sim 1\text{--}2\text{ cycles s}^{-1}$  for three 1-min periods separated by 1 min chilling on ice. Approximately 50% of the cells were broken by this method as visualized by microscopy. The fluid phase was drained off through a fine nylon mesh into a JA17 tube and spun at 10,000g for 10 min. The post-mitochondrial supernatant was briefly centrifuged in a MLA80 rotor at 339,707g for 8 min. Each 2 ml of the clear supernatant was layered on 1 ml of 0.67 M sucrose cushion in homogenization buffer and centrifuged for 30 min in a TLA100.3 rotor at 265,070g. The resulting membrane pellet was resuspended in homogenization buffer containing 250 mM sucrose and 2 mM DTT to a final standard concentration of  $100A_{280}$  (measured after solubilization in 1% SDS). At this concentration, 1  $\mu\text{l}$  yRM is defined as two equivalents (equiv.). One litre of culture yielded about 2,400 equiv. Aliquots were frozen in liquid nitrogen and stored at  $-80^{\circ}\text{C}$ .

**Depletion of Get1 and Get2 from microsomal extract.** TAP-Get1 yRMs (1.5 ml, or 1,500 equiv.) were adjusted to 1% DBC in solubilization buffer (50 mM HEPES-KOH, pH 7.4, 500 mM potassium acetate, 5 mM magnesium acetate, 250 mM sucrose, 1 mM DTT and protease inhibitor cocktail). After 10 min incubation on ice, the detergent extract was centrifuged at 540,960g for 30 min in a TLA100.3 rotor at  $4^{\circ}\text{C}$ . The supernatant (yRM extract) was incubated with 0.1 ml of IgG Sepharose (GE Healthcare) for 1 h at  $25^{\circ}\text{C}$ . The unbound fraction was incubated with 0.1 ml of anti-Get2 antibodies coupled to protein-A agarose for 1 h at  $25^{\circ}\text{C}$ . The flow-through was finally incubated with a mixture of 0.1 ml each of anti-Get1 and anti-Get2-antibodies coupled to protein-A agarose for 1 h at  $25^{\circ}\text{C}$ . The flow-through from this column was used for reconstitution studies. It should be noted that a residual amount of the Get1/2 complex is sufficient to achieve the maximal insertion under *in vitro* conditions. Therefore, multiple rounds of depletion of the Get1/2 complex (with at least  $\sim 95\%$  depletion) were necessary to fully deplete insertion activity. For purification of TAP-Get1 (and



associated proteins), the IgG Sepharose resin from above was washed with low-salt buffer (10 mM Tris, pH 7.4, 150 mM NaCl, 10% glycerol, 0.25% DBC and 1 mM DTT) and eluted with 70 U TEV-protease (Invitrogen) overnight at 4 °C. The TEV elution was adjusted to 2.5 mM CaCl<sub>2</sub> and incubated with calmodulin Sepharose (GE Healthcare) for 90 min at 4 °C. The beads were washed with low-salt buffer containing CaCl<sub>2</sub> and eluted with low-salt buffer containing 5 mM EGTA. The eluted proteins were precipitated with TCA and analysed by SDS-PAGE.

**Reconstitution of proteoliposomes from microsome extracts.** Following earlier methods<sup>30,33,34</sup>, yRMs were adjusted to a concentration of 1 equiv.  $\mu\text{l}^{-1}$  in the following conditions: 50 mM HEPES-KOH, pH 7.4, 500 mM potassium acetate, 5 mM magnesium acetate, 250 mM sucrose, 1 mM DTT, 1% DBC and protease inhibitor cocktail. After 10 min on ice, the ribosomes were removed by centrifugation at 540,960g for 30 min in a TLA100.3 rotor at 4 °C. Typically, 100  $\mu\text{l}$  of this clarified yRM extract was mixed with 10  $\mu\text{l}$  of liposomes (200  $\mu\text{g}$ ) and 50 mg of Biobeads SM2 (Bio-Rad). The Biobeads were prewashed extensively ahead of time with methanol and water. The mixture was incubated for 12–16 h with gentle overhead mixing at 4 °C. The fluid phase was separated from the beads, diluted with five volumes of ice-cold distilled water and sedimented in a TLA100.3 rotor in micro-test tubes at 304,290g for 30 min at 4 °C. The proteoliposomes were resuspended in 25  $\mu\text{l}$  of membrane buffer (50 mM HEPES-KOH, pH 7.4, 100 mM potassium acetate, 5 mM magnesium acetate, 250 mM sucrose, and 1 mM DTT).

**Reconstitution of proteoliposomes with purified proteins.** The optimum method for reconstitution of purified Get1 or Get2 was empirically determined after testing various detergents and reconstitution methods (Supplementary Fig. 17). The precise method of reconstitution proved to be important for obtaining maximally functional proteoliposomes. The incorporation and activity of Get1 and Get2 varied with different detergents. Of those tested, DBC worked the best to achieve the maximal activity of Get1 and Get2. Every batch of DBC requires some degree of optimization with respect to the amount of Biobeads used for detergent removal. For a standard reconstitution reaction, 100  $\mu\text{l}$  of reconstitution buffer (50 mM HEPES-KOH, pH 7.4, 500 mM potassium acetate, 5 mM magnesium acetate, 250 mM sucrose, 1 mM DTT, 0.25% DBC) was mixed with 10  $\mu\text{l}$  of liposome (200  $\mu\text{g}$ ) and purified Get1 or Get2 at the desired concentration. For preparation of liposomes used as controls in the assays, purified proteins were omitted. This mixture was added to between 25 and 30 mg of Biobeads (optimized for each batch of DBC), and incubated with overhead mixing for 12 h at 4 °C. The fluid phase was separated and diluted with five volumes of ice-cold water. In some instances, the proteoliposomes were mixed with Get3 and incubated for 15 min at 25 °C, followed by 30 min at 4 °C with shaking, to allow binding. After dilution, the liposomes were sedimented in a TLA100.3 rotor in micro-test tubes at 304,290g for 30 min at 4 °C. The proteoliposomes were resuspended in 25  $\mu\text{l}$  of membrane buffer as above. SDS-PAGE Coomassie staining and immunoblots were performed to assess the efficiency of protein incorporation; the rhodamine-PE served as a marker for lipid recovery. Typical recovery for Get1 and Get2 reconstitution was ~50%.

**Multi-angle light scattering.** The absolute molecular masses of individual proteins and complexes were measured by static multi-angle light scattering. Purified samples were injected onto a Superdex 200 HR 10/30 gel filtration column (GE Healthcare) equilibrated with 10 mM Tris, pH 7.5, 150 mM NaCl and 2 mM DTT. The purification system was coupled to an online, static, light-scattering detector (Dawn HELEOS II, Wyatt Technology), a refractive-index detector (Optilab rEX, Wyatt Technology) and a ultraviolet-light detector (UPC-900, GE Healthcare). Absolute weight-averaged molar masses were calculated using the ASTRA software (Wyatt Technology).

**Receptor fragment binding assays.** Gel-filtration-purified, 6 $\times$ His-tagged Get1(21–104), Get2(1–106) and Get3 (wild type and D57N) proteins were labelled with amine-reactive succinimidyl esters of Alexa488 or Alexa594 (Invitrogen). Labelling reactions were carried out by incubating ~150  $\mu\text{M}$  protein and ~600  $\mu\text{M}$  dye for 1 h at room temperature (23 °C) in 100 mM NaHCO<sub>3</sub>, pH 8.3, and 200 mM NaCl. After labelling, proteins were desalted and concentrated in Amicon Ultra filtration units (Millipore) to ~100  $\mu\text{M}$  in 20 mM HEPES, pH 7.5, and 200 mM NaCl (receptor fragments) or 20 mM HEPES, pH 7.5, 200 mM NaCl and 2 mM DTT (Get3), and stored in aliquots at –80 °C. Protein concentration was determined using calculated A<sub>280</sub> extinction coefficients after correcting for dye absorbance. Under these labelling conditions, we typically observed ~0.5–1.5 mol of dye per mole of protein.

Dissociation constants ( $K_d$ ) were determined by titrating a fixed amount of labelled, nucleotide-free Get3 with labelled Get1c or Get2c. Fluorescence measurements were made in 96-well format using a Safire2 (Tecan) plate reader. Alexa594-labelled fragments were excited by fluorescence resonance energy transfer from Alexa488-labelled Get3 (wild type or D57N), using excitation and emission wavelengths of 495 and 615 nm, respectively. All experiments were

carried out in 150  $\mu\text{l}$  of 50 mM HEPES, pH 7.5, 100 mM NaCl, 5 mM MgCl<sub>2</sub>, 5% glycerol, 0.02% Tween20 and 2 mM DTT. Blank titrations were carried out in the absence of labelled Get3 and were subtracted from the respective titration curves obtained in the presence of labelled Get3. The difference curves were evaluated by nonlinear regression using the following quadratic binding equation:  $\Delta Y = 0.5B_{\text{max}}/P(K_d + P + X - \sqrt{((K_d + P + X)^2 - 4PX)})$ , where  $B_{\text{max}}$  is the amplitude,  $P$  is the total concentration of labelled Get3, and  $X$  is the total concentration of labelled Get1c or Get2c.

Chase titrations were carried out by measuring fluorescence resonance energy transfer between Alexa488-labelled Get3 (wild type or D57N) and Alexa594-labelled fragments in the presence of increasing concentrations of an unlabelled fragment or nucleotide. Blank titrations were performed in the absence of labelled Get3 and were subtracted from the respective titration curves obtained in the presence of labelled Get3. The difference curves were evaluated by nonlinear regression using the following equation:  $\Delta Y = F_{\text{end}} + B_{\text{max}}P/(P + K_{d,\text{labelled}}(1 + X/K_d))$ , where  $F_{\text{end}}$  is the signal at saturation,  $B_{\text{max}}$  is the amplitude of the signal change,  $P$  is the total concentration of labelled fragment,  $K_{d,\text{labelled}}$  is the dissociation constant of the Get3 fragment complex,  $X$  is the total concentration of the unlabelled component and  $K_d$  is the dissociation constant of the unlabelled component.

**Nucleotide binding assays.** Fluorescence measurements were made in 96-well format using a Safire2 plate reader with excitation and emission wavelengths of 285 and 446 nm, respectively (Supplementary Fig. 18). All experiments were carried out with gel-filtration-purified, 6 $\times$ His-tagged Get3 (D57N) in 150  $\mu\text{l}$  of 50 mM HEPES, pH 7.5, 100 mM NaCl, 5 mM MgCl<sub>2</sub>, 5% glycerol, 0.02% Tween20 and 2 mM DTT. The dissociation constant of mant-ATP was measured by incubating 1  $\mu\text{M}$  of Get3 (D57N) with increasing concentrations of mant-ATP (Molecular Probes). Dissociation constants of unlabelled nucleotides were determined by incubating 1  $\mu\text{M}$  Get3 (D57N) with 1  $\mu\text{M}$  mant-ATP and chasing with increasing concentrations of the corresponding unlabelled nucleotide. In each case, blank titrations were performed in the absence of Get3 and were subtracted from titration curves obtained in the presence of labelled Get3. ATP and ADP concentrations were determined by absorbance ( $\epsilon^{259} = 15,400 \text{ M}^{-1} \text{ cm}^{-1}$ ). Dissociation constants were determined by curve fitting as described above.

**Tail-anchored substrate release assay.** Get3–substrate complexes were assembled by *in vitro* translation in a phenyl- and DEAE-Sepharose-depleted RRL<sup>10</sup> supplemented with 6 $\times$ His-Get3 at ~2  $\mu\text{g ml}^{-1}$ . This translation extract lacks endogenous TA binding proteins (particularly TRC40 and Bag6). Translation of the TA substrate in this system was verified to result in Get3–substrate complexes by crosslinking, and was functional as judged by Get1/2-dependent insertion (data not shown). Complexes generated by this method were mixed with the fragments or proteoliposomes as indicated in the figure legends, incubated for 30 min at 32 °C and subjected to crosslinking with disuccinimidyl suberate as described previously<sup>8</sup>. The samples were denatured in 1% SDS, diluted tenfold in 1% Triton X-100 buffer and subjected to pull-downs of 6 $\times$ His-Get3 with immobilized Co<sup>2+</sup> bound to chelating Sepharose (GE). The Get3–substrate crosslink was visualized by autoradiography.

**Preparation of Get3 receptor fragment complexes for crystallization.** The gene encoding native, full-length *S. cerevisiae* Get3 was subcloned into pET19b (Novagen). For co-expression with N-terminal 6 $\times$ His-tagged Get1(21–104), plasmids were co-transformed into *E. coli* BL21(DE3)/pRIL (Novagen). Proteins were expressed at 37 °C for 3 h by induction with 0.1 mM IPTG after the cells reached an A<sub>600</sub> of ~0.6. Cells were disrupted and purified by nickel-affinity chromatography as described above for the Get1 and Get2 fragments. Protein was eluted in buffer B containing 200 mM imidazole, and then dialysed into 10 mM Tris, pH 7.5, 100 mM NaCl, 2 mM DTT and 40% glycerol. This was followed by cleavage with 6 $\times$ His-tagged TEV protease and removal of residual uncleaved Get1 fragments and the 6 $\times$ His-tagged TEV protease by subtractive Ni-NTA purification. Finally, the complex was separated from excess Get1 fragments by gel filtration. Fractions were pooled, concentrated to ~10 mg ml<sup>–1</sup> in 10 mM Tris, pH 7.5, 100 mM NaCl and 2 mM DTT, and stored in aliquots at –80 °C.

Co-expression of native Get3 and N-terminal 6 $\times$ His-tagged Get2(1–106) or Get2(1–38) was performed as above, except that proteins were expressed at 25 °C for 6–8 h after induction. Following cell lysis and purification by nickel-affinity chromatography, the protein was dialysed into 10 mM Tris, pH 7.5, 200 mM NaCl and 2 mM DTT. This was followed by cleavage with 6 $\times$ His-tagged TEV protease and subtractive Ni-NTA purification. Finally, the complex was separated from excess Get2 fragments by gel filtration. Fractions were pooled, concentrated to ~15–20 mg ml<sup>–1</sup> in 10 mM Tris, pH 7.5, 150 mM NaCl and 2 mM DTT, and stored in aliquots at –80 °C.

**Crystallization.** Crystals of *S. cerevisiae* Get1(21–104) in complex with *S. cerevisiae* Get3 were grown at room temperature using hanging-drop vapour diffusion by mixing equal volumes of a protein solution with a reservoir solution containing 0.2 M K/Na tartrate, 16% PEG 3350, 0.1 M HEPES, pH 7.2, and 6% polypropylene

glycol P400. Crystals were cryoprotected in mother liquor supplemented with 20% ethylene glycol, and flash-frozen in liquid nitrogen.

Crystals of *S. cerevisiae* Get2(1–38) in complex with *S. cerevisiae* Get3 and ADP•AlF<sub>4</sub><sup>−</sup> were grown at room temperature using hanging-drop vapour diffusion by mixing equal volumes of a protein solution containing 2 mM ADP, 2 mM MgCl<sub>2</sub>, 2 mM AlCl<sub>3</sub> and 8 mM NaF with a reservoir solution containing 30% PEG 3350, 0.3 M ammonium acetate and 0.1 M Bis-Tris, pH 6.0. Crystals were briefly soaked in mother liquor supplemented with 20% ethylene glycol and flash-frozen in liquid nitrogen.

**Structure determination and refinement.** All data were collected at 100 K at APS beamline 21-IDG ( $\lambda = 0.97856$  Å) and processed using HKL2000 (HKL Research). Data collection and refinement statistics are listed in Supplementary Table 1.

The structure of the Get1(21–104) complex with Get3 was determined to a resolution of 3.0 Å by molecular replacement with PHASER<sup>35</sup>, using the open-dimer (nucleotide-free) form of *S. cerevisiae* Get3 (PDB ID, 3H84<sup>20</sup>; with the  $\alpha$ -helical subdomain removed) as the search model. No solution could be obtained using the closed-dimer form of *S. cerevisiae* Get3 as the search model. Clear density was observed for the helical Get1 fragment and portions of the Get3  $\alpha$ -helical subdomain in the initial electron density maps. Model building and refinement were carried out in PHENIX<sup>36</sup> and COOT<sup>37</sup>. The final model contains one Get3 homodimer (chains A and B), two Get1 fragments (chains C and D) and one zinc atom, and was refined to an *R*-factor of 22.4% (*R*<sub>free</sub> = 28.2%). Most (94.3%) of the residues are in favoured regions of the Ramachandran plot, and 0.9% are outliers. Side-chain density is generally weakest in the  $\alpha$ -helical subdomains, and no interpretable density was observed for residues 1–4, 97–134, 155–157, 198–219, 280–284 and 352–354 in chain A; 1–4, 99–125, 191–210,

280–284 and 352–354 in chain B; 21–35 and 103–104 in chain C; and 21–36 and 99–104 in chain D.

The structure of the Get2(1–38) complex with Get3 was determined to a resolution of 2.1 Å by molecular replacement with PHASER using a monomer of *S. cerevisiae* Get3 (PDB ID, 2WOJ<sup>16</sup>; with the  $\alpha$ -helical subdomain and ligands removed) as the search model. Density for the two helices of Get2(1–38) and portions of the Get3  $\alpha$ -helical subdomain was clearly visible in the initial electron density maps. Model building and refinement were carried out in PHENIX and COOT. The final model contains one Get3 homodimer (chains A and B), two Get2 fragments (chains C and D), two Mg<sup>2+</sup>-ADP•AlF<sub>4</sub><sup>−</sup> complexes, one zinc atom and 231 water molecules, and was refined to an *R*-factor of 18.8% (*R*<sub>free</sub> = 23.3%). Again, most (98.0%) of the residues are in favoured regions of the Ramachandran plot, and 0.8% are outliers. No interpretable electron density was observed for residues 1–4, 101–126, 188–211, 280–284 and 353–354 in chain A; 1–3, 102–125, 154–158, 199–211, 280–282 and 351–354 in chain B; 1–3 and 35–38 in chain C; and 1–3 in chain D.

**Miscellaneous.** SDS–PAGE was done with 15% Tris–glycine or 12% Tris–tricine gels. Quantification was by phosphor imaging using a Typhoon system with accompanying software. Most images for the figures were generated by exposure to Kodak MR X-ray film. Films were digitized by scanning. Structure figures were generated with Pymol<sup>39</sup> and all figures were assembled using Adobe Photoshop and Illustrator.

38. Deshaies, R. J. & Schekman, R. SEC62 encodes a putative membrane protein required for protein translocation into the yeast endoplasmic reticulum. *J. Cell Biol.* **109**, 2653–2664 (1989).

39. DeLano, W. L. PyMOL Molecular Viewer (<http://www.pymol.org>) (2002).

# A stress response pathway regulates DNA damage through $\beta_2$ -adrenoreceptors and $\beta$ -arrestin-1

Makoto R. Hara<sup>1</sup>, Jeffrey J. Kovacs<sup>1</sup>, Erin J. Whalen<sup>1</sup>, Sudarshan Rajagopal<sup>1</sup>, Ryan T. Strachan<sup>1</sup>, Wayne Grant<sup>2</sup>, Aaron J. Towers<sup>1,3</sup>, Barbara Williams<sup>1</sup>, Christopher M. Lam<sup>1</sup>, Kunhong Xiao<sup>1</sup>, Sudha K. Shenoy<sup>1</sup>, Simon G. Gregory<sup>1,3</sup>, Seungkirl Ahn<sup>1</sup>, Derek R. Duckett<sup>2</sup> & Robert J. Lefkowitz<sup>1,4</sup>

The human mind and body respond to stress<sup>1</sup>, a state of perceived threat to homeostasis, by activating the sympathetic nervous system and secreting the catecholamines adrenaline and noradrenaline in the 'fight-or-flight' response. The stress response is generally transient because its accompanying effects (for example, immunosuppression, growth inhibition and enhanced catabolism) can be harmful in the long term<sup>2</sup>. When chronic, the stress response can be associated with disease symptoms such as peptic ulcers or cardiovascular disorders<sup>3</sup>, and epidemiological studies strongly indicate that chronic stress leads to DNA damage<sup>4,5</sup>. This stress-induced DNA damage may promote ageing<sup>6</sup>, tumorigenesis<sup>4,7</sup>, neuropsychiatric conditions<sup>8,9</sup> and miscarriages<sup>10</sup>. However, the mechanisms by which these DNA-damage events occur in response to stress are unknown. The stress hormone adrenaline stimulates  $\beta_2$ -adrenoreceptors that are expressed throughout the body, including in germline cells and zygotic embryos<sup>11</sup>. Activated  $\beta_2$ -adrenoreceptors promote Gs-protein-dependent activation of protein kinase A (PKA), followed by the recruitment of  $\beta$ -arrestins, which desensitize G-protein signalling and function as signal transducers in their own right<sup>12</sup>. Here we elucidate a molecular mechanism by which  $\beta$ -adrenergic catecholamines, acting through both Gs-PKA and  $\beta$ -arrestin-mediated signalling pathways, trigger DNA damage and suppress p53 levels respectively, thus synergistically leading to the accumulation of DNA damage. In mice and in human cell lines,  $\beta$ -arrestin-1 (ARRB1), activated via  $\beta_2$ -adrenoreceptors, facilitates AKT-mediated activation of MDM2 and also promotes MDM2 binding to, and degradation of, p53, by acting as a molecular scaffold. Catecholamine-induced DNA damage is abrogated in *Arrb1*-knockout (*Arrb1*<sup>-/-</sup>) mice, which show preserved p53 levels in both the thymus, an organ that responds prominently to acute or chronic stress<sup>13</sup>, and in the testes, in which paternal stress may affect the offspring's genome. Our results highlight the emerging role of ARRB1 as an E3-ligase adaptor in the nucleus, and reveal how DNA damage may accumulate in response to chronic stress.

As a model of chronic stress and prolonged stimulation of  $\beta_2$ -adrenoreceptors<sup>7,13</sup>, wild-type mice were infused for four weeks with either saline or the  $\beta_2$ -adrenoreceptor-agonist isoproterenol, a synthetic analogue of adrenaline. First, we tested whether this regimen affects DNA damage by examining phosphorylation of histone H2AX ( $\gamma$ -H2AX), one of the earliest indicators of DNA damage<sup>14</sup>. Isoproterenol infusion leads to DNA damage in the thymus (Fig. 1a, left panel). Accumulation of DNA damage indicates compromised genome maintenance. To investigate the potential mechanism, we examined p53 levels in the thymus and found that isoproterenol infusion leads to decreased levels of p53 (Fig. 1a, right panel). Consistent with the effects of isoproterenol *in vivo*, chronic stimulation of  $\beta_2$ -adrenoreceptors with  $\beta$ -adrenergic catecholamines (isoproterenol, adrenaline or noradrenaline) leads to accumulation of DNA damage and a decrease in p53 levels in cultured U2OS cells (Supplementary

Fig. 1a–c), which endogenously express wild-type p53 and only the  $\beta_2$ -subtype of  $\beta$ -adrenoreceptors (Supplementary Fig. 2a–c). Moreover, the p53 in these cells, as well as in all other cell lines used in these studies (fibroblasts and HEK-293 cells), was demonstrated to be functional by a variety of techniques (Supplementary Fig. 3a–k), and all cell lines endogenously expressed only the  $\beta_2$ -subtype of  $\beta$ -adrenoreceptors (Supplementary Fig. 2a–c).

The isoproterenol-induced reduction in p53 levels results from p53 degradation, and is abolished by proteasome inhibition (Supplementary

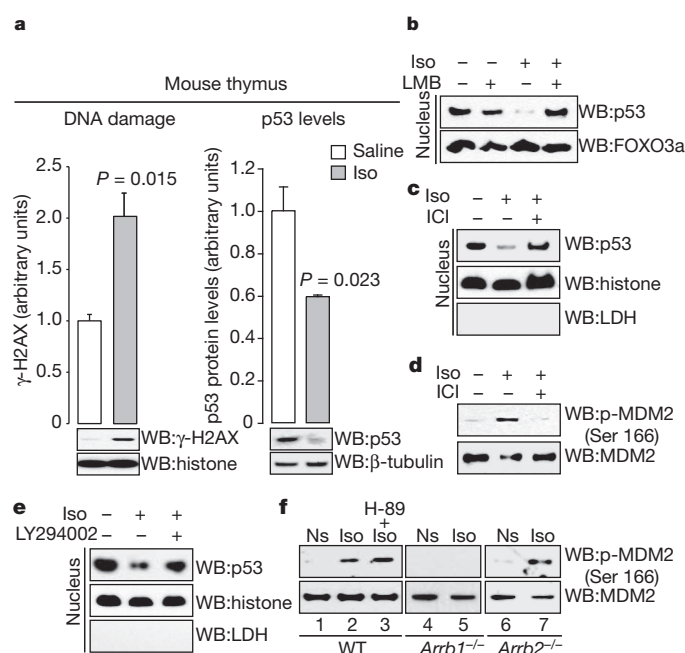


**Figure 1 | Chronic catecholamine stimulation leads to p53 degradation and accumulation of DNA damage via ARRB1/AKT-mediated activation of MDM2.** **a**, Isoproterenol infusion leads to accumulation of DNA damage and decreased p53 levels. Mice ( $n = 3$ –5 for each condition) were infused with saline or isoproterenol ( $30 \text{ mg kg}^{-1} \text{ d}^{-1}$ ) for 4 weeks. All bars represent mean  $\pm$  s.e.m. Histone, histone H2B; Iso, isoproterenol; WB, western blot. **b**, Isoproterenol-induced p53 reduction is dependent on nuclear export. This effect is specific to p53, in that another nuclear–cytosol shuttling molecule, FOXO3a, is not affected. LMB, leptomycin B. **c**, Preincubation with the  $\beta_2$ -adrenoreceptor-selective antagonist ICI 118,551 (ICI) blocks isoproterenol-induced nuclear export of p53. Lactate dehydrogenase (LDH) is a cytosolic marker and histone is a nuclear marker. **d**, Isoproterenol stimulation leads to MDM2 phosphorylation at Ser 166, and is blocked by preincubation with ICI 118,551. **e**, Inhibition of the PI3K/AKT cascade abolishes isoproterenol-stimulated decreases in p53 levels in U2OS cells. LY294002 is a PI3K inhibitor. **f**, Isoproterenol stimulation leads to Gs-independent, ARRB1-dependent MDM2 phosphorylation at Ser 166. Ns, not stimulated.

<sup>1</sup>Department of Medicine, Duke University Medical Center, Durham, North Carolina 27710, USA. <sup>2</sup>Translational Research Institute, The Scripps Research Institute, Jupiter, Florida 33458, USA. <sup>3</sup>Center for Human Genetics, Duke University Medical Center, Durham, North Carolina 27710, USA. <sup>4</sup>Howard Hughes Medical Institute, Duke University Medical Center, Durham, North Carolina 27710, USA.



Fig. 1d). Because nuclear export of p53 has been shown to be involved in its degradation<sup>15</sup>, we examined p53 localization. Subcellular fractionation shows that isoproterenol stimulation leads to a decrease in nuclear p53 and an increase in cytosolic p53 (Supplementary Fig. 1e, lower panels), thus, isoproterenol stimulation leads to p53 nuclear export. Immunocytochemical examination also shows increased levels of cytosolic p53 after isoproterenol stimulation (Supplementary Fig. 1e, upper panels). Isoproterenol concentrations as low as 1 nM lead to p53 nuclear export, resulting in a decrease in total p53 levels (Supplementary Fig. 1f). The importance of nuclear export in modulating p53 levels was investigated by treating cells with leptomycin B, an inhibitor of nuclear export. Leptomycin B pretreatment reverses isoproterenol-induced nuclear export of p53 (Fig. 1b).

To examine whether isoproterenol-induced effects were specifically mediated by  $\beta_2$ -adrenoreceptors, U2OS cells were stimulated with isoproterenol in the presence or absence of the subtype-selective  $\beta_2$ -adrenoreceptor antagonist ICI 118,551. Preincubation with ICI 118,551 abrogates the isoproterenol-induced decrease in p53 levels (Fig. 1c). During *in vivo* experiments, isoproterenol infusion leads to accumulation of DNA damage in the cerebellum, where  $\beta_2$ -adrenoreceptors are the major subtype of  $\beta$ -adrenoreceptor<sup>16</sup> (Supplementary Fig. 1g). Furthermore, targeted disruption of the *Adrb2* gene in mice markedly reduces accumulation of DNA damage upon isoproterenol infusion (Supplementary Fig. 1h). Taken together, these data indicate that stimulation of the  $\beta_2$ -adrenoreceptor results in the nuclear export and degradation of p53 in a specific manner.

The E3 ligase MDM2 has been shown to have an important role in the regulation of p53 nuclear export and degradation<sup>15</sup>. Consistent with this, leptomycin B abrogates the ability of MDM2 to degrade p53 (ref. 15). Before MDM2-mediated ubiquitination of p53, the phosphoinositide 3-kinase (PI3K)/AKT cascade phosphorylates MDM2, activating its E3 ligase function<sup>17</sup>. To examine whether stimulation of  $\beta_2$ -adrenoreceptors leads to MDM2 phosphorylation via the PI3K/AKT cascade, wild-type mouse embryonic fibroblasts (MEFs) were stimulated with isoproterenol in the presence or absence of ICI 118,551. Isoproterenol stimulation leads to MDM2 phosphorylation at Ser166, an AKT phosphorylation site, and the effect is

antagonized by ICI 118,551 (Fig. 1d and Supplementary Fig. 1i). To confirm that MDM2 is phosphorylated by the PI3K/AKT cascade upon isoproterenol stimulation, U2OS cells were stimulated with isoproterenol in the presence of either the PI3K inhibitor wortmannin or the AKT inhibitor AKTi. MDM2 phosphorylation is abolished by either wortmannin or AKTi (Supplementary Fig. 1j). Furthermore, a PI3K inhibitor also abolishes catecholamine-induced lowering of p53 levels in the nucleus (Fig. 1e and Supplementary Fig. 1k). The importance of MDM2 phosphorylation at Ser166 was demonstrated by the overexpression of a phosphomimetic mutant at Ser166 (MDM2-S166D)<sup>17</sup>, which facilitates the degradation of p53 when compared to wild-type MDM2 (Supplementary Fig. 1l). These data implicate the PI3K/AKT cascade downstream of the  $\beta_2$ -adrenoreceptor as a mediator of p53 stability through the phosphorylation of MDM2.

Upon activation of  $\beta_2$ -adrenoreceptors, the PI3K/AKT cascade can be stimulated by both the Gs-PKA<sup>18</sup> and  $\beta$ -arrestin-mediated signalling pathways<sup>19,20</sup>. To elucidate which pathway was involved, we examined the effect of  $\beta_2$ -adrenoreceptor stimulation in wild-type MEFs in the presence of H-89, a PKA inhibitor, or in *Arrb1*<sup>-/-</sup> or *Arrb2*-knockout (*Arrb2*<sup>-/-</sup>) MEFs. In wild-type MEFs, H-89 does not inhibit isoproterenol-stimulated MDM2 phosphorylation (Fig. 1f, lane 3). In contrast, the isoproterenol effect is abrogated in *Arrb1*<sup>-/-</sup> (Fig. 1f, lane 5), but not in *Arrb2*<sup>-/-</sup> MEFs (Fig. 1f, lane 7). Furthermore, rescuing *Arrb1* expression in *Arrb1*<sup>-/-</sup> MEFs restores the effects of isoproterenol stimulation (Supplementary Fig. 1m), and the effects of isoproterenol on MDM2 phosphorylation are abrogated in *Arrb1*<sup>-/-</sup> mice (Supplementary Fig. 1n). These data elucidate a Gs-independent, ARRB1-dependent signalling pathway that regulates the activation state of MDM2 through the PI3K/AKT cascade.

$\beta$ -Arrestins can serve as adaptors for E3 ligases and their substrates<sup>21</sup>. Because we found that MDM2 activation by the PI3K/AKT cascade is an ARRB1-dependent event, we examined the binding between  $\beta$ -arrestins and p53, a known MDM2 substrate. In HEK-293 cells stably overexpressing ARRB1 or ARRB2, p53 binds preferentially to ARRB1, an isoform localized to both the cytosol and nucleus<sup>22</sup>, but not to ARRB2, which predominantly localizes to the cytosol<sup>22-25</sup> (Supplementary Fig. 4a). Binding between these two molecules at

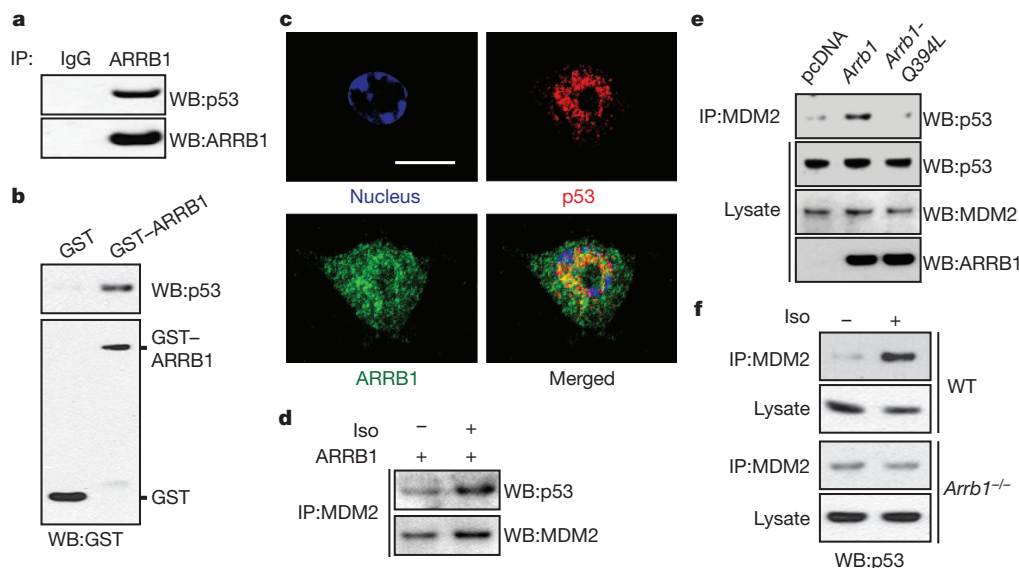


**Figure 2 | ARRB1 functions as an E3 ligase adaptor for MDM2 and p53 upon catecholamine stimulation.** **a**, Endogenous binding of p53 and ARRB1. Cell lysates from HEK-293 cells were used for immunoprecipitation (IP) with an anti-ARRB1 (K-16) antibody or normal IgG, and analysed by immunoblotting with anti-p53 (DO-1) antibody. **b**, *In vitro* binding of p53 and ARRB1. Purified p53 was incubated with either GST or GST-ARRB1 and precipitated with glutathione beads. Precipitates were analysed by immunoblotting with an anti-p53 (DO-1) antibody. **c**, Confocal analysis of

co-localization of p53 and ARRB1 in non-treated RAW264.7 macrophages, which endogenously express high levels of both p53 and ARRB1. Scale bar, 10  $\mu$ m. **d**, Isoproterenol stimulation facilitates the binding of MDM2 to p53 in ARRB1 overexpressed cells. **e**, Nuclear ARRB1 facilitates MDM2 binding to p53. U2OS cells were transfected with either empty vector (pcDNA), *Arrb1* or *Arrb1*-Q394L. **f**, ARRB1 facilitates isoproterenol-induced MDM2 binding to p53. WT, wild-type.

endogenous levels is also observed in HEK-293 cells and brain homogenates (Fig. 2a and Supplementary Fig. 4b). The binding seems to be direct, because purified ARRB1 tagged with glutathione-S-transferase (GST-ARRB1) binds to p53 *in vitro* (Fig. 2b). To examine the effect of  $\beta_2$ -adrenoreceptor stimulation on this complex, we treated untransfected HEK-293 cells, which endogenously express only the  $\beta_2$  subtype of  $\beta$ -adrenoreceptors (Supplementary Fig. 2b, c), with isoproterenol. Stimulation of  $\beta_2$ -adrenoreceptors does not affect the binding of ARRB1 to p53 (Supplementary Fig. 4c). Subsequently, we mapped the binding sites in ARRB1 and p53 by performing sequential deletions, followed by immunoprecipitation from HEK-293 cells (Supplementary Fig. 4d, e). We identified the amino terminus of ARRB1 (amino acids 1–186) as critical for binding to p53. In p53, a domain comprising amino acids 101–186 is required for binding to ARRB1. Consistent with these results, a synthetic ARRB1-binding peptide (ARRB-BP), which binds to the N terminus of ARRB1 and induces a conformational change<sup>26</sup>, disrupts the interaction between ARRB1 and p53 (Supplementary Fig. 4f).

Co-immunoprecipitation experiments after subcellular fractionation show that more than 90% of the binding between ARRB1 and p53 occurs in the nucleus (Supplementary Fig. 4g). Additionally, confocal analysis reveals that endogenous ARRB1 and p53 co-localize in the nucleus (Fig. 2c) and a ternary complex between ARRB1, MDM2 and p53 was observed in p53-null NCI-H1299 cells transfected with wild-type p53 (Supplementary Fig. 4h). The potential effects of nuclear ARRB1 on MDM2 binding to p53 were investigated in U2OS cells transfected with either *Arrb1* or *Arrb1-Q394L*, in which a single amino acid, Gln 394, has been mutated to Leu to create a nuclear export signal in ARRB1<sup>22,23</sup>. Overexpression of ARRB1 facilitates the binding of MDM2 to p53, enhancing basal  $\beta_2$ -adrenoreceptor-stimulated ARRB1 signalling (Fig. 2d); however, the effect is abolished with ARRB1-Q394L (Fig. 2e). This result indicates that ARRB1 facilitates an MDM2–p53 interaction in the nucleus. The role of endogenous ARRB1 as a facilitator of MDM2–p53 complex formation under isoproterenol-stimulated conditions is further demonstrated in *Arrb1*<sup>−/−</sup> MEFs (Fig. 2f), in which loss of ARRB1 prevents the increased interaction of MDM2 and p53 after isoproterenol stimulation, when compared to wild-type cells.

Next we examined whether ARRB1 expression affects p53 levels by comparing different clonal populations of wild-type and *Arrb1*<sup>−/−</sup> MEFs. *Arrb1*<sup>−/−</sup> MEFs show increased p53 levels (Supplementary Fig. 5a). Furthermore, rescuing ARRB1 expression in *Arrb1*<sup>−/−</sup> MEFs decreases p53 levels in a dose-dependent manner (Fig. 3a). Differences in p53 levels under basal conditions seem to be the result of decreased p53 ubiquitination in *Arrb1*<sup>−/−</sup> MEFs (Fig. 3b, lanes 1 and 3). Furthermore, consistent with  $\beta_2$ -adrenoreceptor-induced degradation of p53, isoproterenol stimulation promotes p53 ubiquitination, but the effect is markedly decreased in *Arrb1*<sup>−/−</sup> MEFs (Fig. 3b, lanes 2 and 4). To address further whether ARRB1 facilitates the ubiquitination of p53 by MDM2, we conducted *in vitro* ubiquitination assays (Supplementary Fig. 5b). Addition of ARRB1 facilitates MDM2-mediated ubiquitination of p53 and the effect is abolished with ARRB-BP. Together, these data indicate that upon catecholamine stimulation, ARRB1 promotes the interaction of MDM2 and p53 by acting as an E3 ligase adaptor that facilitates ubiquitination of p53.

Cytosolic ARRB1 mediates catecholamine-induced activation of AKT and MDM2, whereas nuclear ARRB1 serves as an adaptor for MDM2-dependent ubiquitination of p53. Consistent with these results, isoproterenol stimulation leads to a lowering of p53 levels (Fig. 3c, lane 2). By contrast, p53 levels remain constant in *Arrb1*<sup>−/−</sup> MEFs (Fig. 3c, lane 4). Furthermore, rescuing ARRB1 expression in *Arrb1*<sup>−/−</sup> MEFs by transient transfection restores isoproterenol-stimulated degradation of p53 (Fig. 3c, lane 6), and suppression of ARRB1 by RNA interference results in suppression of isoproterenol-stimulated MDM2–p53 complex formation, and a lowering of p53 levels in U2OS cells (Fig. 3d, e).

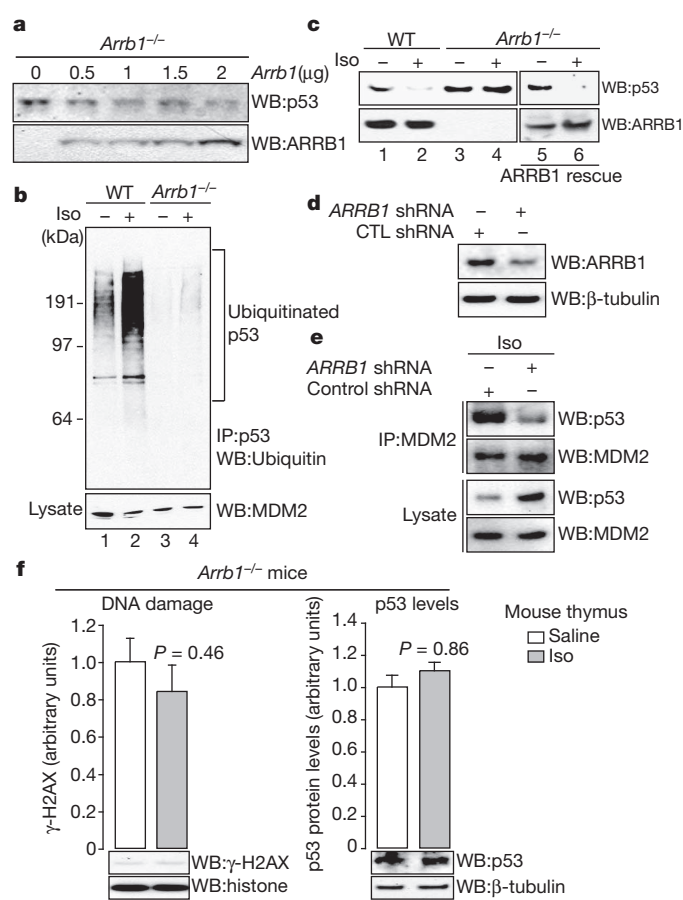


**Figure 3 | ARRB1 facilitates catecholamine-induced p53 degradation by MDM2.** **a**, Rescuing ARRB1 expression in *Arrb1*<sup>−/−</sup> MEFs decreases p53 levels. *Arrb1*<sup>−/−</sup> MEFs were transiently transfected with *Arrb1* and cell lysates were examined by immunoblotting. **b**, Isoproterenol stimulation leads to ubiquitination of p53 in an ARRB1-dependent manner. Wild-type and *Arrb1*<sup>−/−</sup> MEFs were stimulated with 10  $\mu$ M isoproterenol for 24 h. Cell lysates were immunoprecipitated with an anti-p53 antibody (FL-393) and analysed by immunoblotting with an anti-ubiquitin (P4D1) antibody. **c**, Isoproterenol stimulation leads to ARRB1-dependent p53 degradation. **d**, Reduction in ARRB1 levels induced by small hairpin RNA (shRNA) in U2OS cells. **e**, Suppression of ARRB1 suppresses isoproterenol-induced binding of MDM2 to p53 and restores p53 levels in U2OS cells. U2OS cells were treated with either control shRNA or ARRB1 shRNA for 72 h, followed by 24 h stimulation with 10  $\mu$ M isoproterenol. **f**, Levels of p53 in isoproterenol-infused *Arrb1*<sup>−/−</sup> mice remain constant and there is no accumulation of DNA damage. *Arrb1*<sup>−/−</sup> mice ( $n = 3$ –4 for each condition) were treated as in Fig. 1a. All bars represent mean  $\pm$  s.e.m.

To differentiate the cytosolic (catecholamine-induced MDM2 phosphorylation) and nuclear (E3 ligase adaptor) functions of ARRB1 in this cascade, a phosphomimetic mutant of MDM2 (*MDM2-S166D*) was co-transfected with either *Arrb1* or *Arrb1-Q394L* into *Arrb1*<sup>−/−</sup> MEFs. This allowed us to focus on the nuclear function of ARRB1. Restoring ARRB1 expression with the wild type, but not with the Q394L mutant, facilitates the degradation of p53 (Supplementary Fig. 5c). Consequently, it seems that although the cytoplasmic pool of ARRB1 is sufficient to activate MDM2 through the PI3K/AKT pathway, the nuclear pool of ARRB1 is required to act as an E3 ligase adaptor for MDM2 towards p53.

To examine this cascade *in vivo*, we examined the effects of catecholamine on p53 levels and accumulation of DNA damage in the thymus of *Arrb1*<sup>−/−</sup> mice. The mice were infused for four weeks with either saline or isoproterenol. In contrast to wild-type mice (Fig. 1a), p53 levels are maintained upon isoproterenol infusion in *Arrb1*<sup>−/−</sup> mice, and accumulation of DNA damage is abrogated (Fig. 3f).

We have observed that isoproterenol infusion leads to lowering of p53 levels, and have elucidated a molecular mechanism whereby

ARRB1 regulates MDM2-dependent degradation of p53 upon  $\beta_2$ -adrenoreceptor stimulation. Next, we investigated further the effects of catecholamine-dependent p53 degradation on accumulation of DNA damage. To visualize the prevalence of DNA damage, we analysed the formation of  $\gamma$ -H2AX foci in both wild-type and *Arrb1*<sup>-/-</sup> MEFs. After chronic stimulation with isoproterenol, there is an increase in the formation of  $\gamma$ -H2AX foci (sevenfold) in wild-type MEFs, which is significantly reduced in *Arrb1*<sup>-/-</sup> MEFs (Fig. 4a, panels 2 and 4, and Supplementary Fig. 6a). Moreover, rescuing ARRB1 expression in *Arrb1*<sup>-/-</sup> MEFs restores the accumulation of isoproterenol-induced  $\gamma$ -H2AX foci (Fig. 4b, panels 5–8, and Supplementary Fig. 6a).

To examine how exposure to stress hormones initiates DNA damage, p53-null NCI-H1299 cells were chronically stimulated with isoproterenol. This leads to accumulation of DNA damage (Fig. 4c, panels 1–8), indicating that DNA damage is triggered by p53-independent mechanisms after isoproterenol stimulation. One of the prominent cascades leading to DNA damage is the generation of reactive oxygen species through Gs-PKA signalling<sup>27</sup>. Accordingly, accumulation of isoproterenol-induced DNA damage is suppressed by inhibition of PKA (Fig. 4d, lanes 1 and 3). Consistent with the idea that ARRB1-mediated effects on DNA damage are due to altered p53 levels, rescuing p53 expression (Supplementary Fig. 3l) decreases isoproterenol-induced  $\gamma$ -H2AX foci (Fig. 4c, panels 9–16; Fig. 4d, lanes 1 and 2) and the p53 effect is antagonized by co-expression of ARRB1 (Fig. 4c, panels 17–20, and Supplementary Fig. 6b). These G-protein-mediated and ARRB1-mediated pathways may synergistically affect the accumulation of isoproterenol-induced DNA damage. Thus, combining PKA inhibition with rescue of p53 expression abrogates accumulation of DNA damage (Fig. 4d, lanes 1 and 4). Catecholamine-induced lowering of p53 levels may lead to increased survival of cells

containing DNA damage, owing to an impaired DNA damage checkpoint and repair cascade<sup>28</sup>. This would then facilitate accumulation of DNA damage. Accordingly, U2OS cells were irradiated with ultraviolet light after isoproterenol stimulation. Chronic stimulation leads to increased FOS expression, an indicator of cell survival and proliferation (Supplementary Fig. 6c). Because DNA damage occurs under these conditions, FOS expression leads to proliferation of cells that contain DNA damage. Taken together, these data indicate that Gs-PKA-dependent signalling, which leads to the generation of reactive oxygen species<sup>27</sup>, and ARRB1-dependent p53 degradation, which results in impaired DNA checkpoint and repair mechanisms<sup>28</sup>, synergistically lead to accumulation of DNA damage and consequently may have effects on genomic integrity.

DNA damage may promote rearrangements in chromosomes. To quantify the occurrence of catecholamine-induced rearrangements, we analysed inter-chromosomal rearrangements between *Tcr $\gamma$*  (the T-cell-receptor- $\gamma$  locus) and *Tcr $\beta$*  (the T-cell-receptor- $\beta$  locus) in thymocytes (see Methods and Supplementary Fig. 6d). Both wild-type and *Arrb1*<sup>-/-</sup> mice were infused for four weeks with either saline or isoproterenol, and genomic DNA was isolated from the thymus. Consistent with the accumulation of DNA damage (Figs 1a, 3f), isoproterenol infusion leads to an increase in these *Tcr* rearrangements in wild-type mice; however, the effects are no longer observed in *Arrb1*<sup>-/-</sup> mice (Fig. 4e and Supplementary Fig. 6e). This indicates that catecholamine-stress-hormone-dependent accumulation of DNA damage promotes rearrangements in chromosomes.

Because chronic isoproterenol stimulation affects DNA damage and chromosomal rearrangements, we examined whether this cascade also affects genome integrity in the testes, in which paternal stress may affect the offspring's genome. Using the isoproterenol-infusion model of chronic stress<sup>7,13</sup>, we observed that isoproterenol stimulation leads

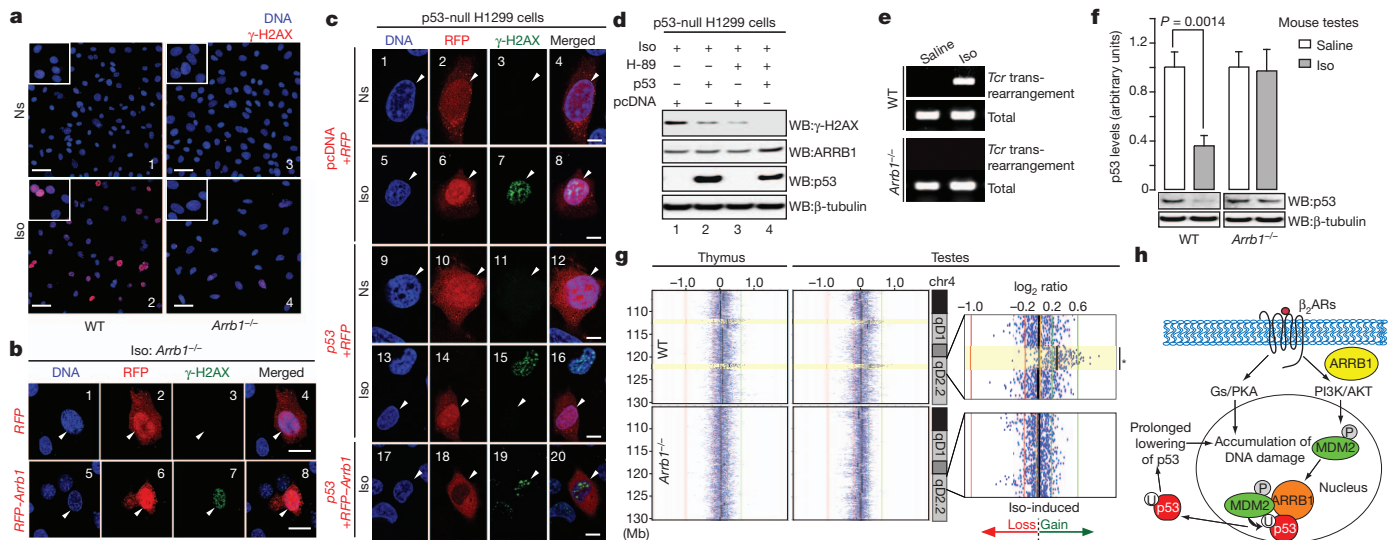


**Figure 4 | Chronic catecholamine stimulation leads to accumulation of DNA damage by an ARRB1- and p53-dependent mechanism.**

**a**, Isoproterenol stimulation leads to formation of  $\gamma$ -H2AX foci in wild-type but not in *Arrb1*<sup>-/-</sup> MEFs. Wild-type and *Arrb1*<sup>-/-</sup> MEFs were chronically stimulated with 10  $\mu$ M isoproterenol every 12 h for 3 days. Cells were immunostained and examined by confocal microscopy. Scale bar, 50  $\mu$ m. **b**, Rescuing ARRB1 expression in *Arrb1*<sup>-/-</sup> MEFs restores isoproterenol-induced  $\gamma$ -H2AX foci. Two days after transfection, cells were stimulated and examined as described in **a**. RFP, red fluorescent protein. Scale bar, 10  $\mu$ m. **c**, ARRB1-dependent regulation of p53 levels mediates the accumulation of isoproterenol-induced DNA damage. Two days after the transfection, cells were stimulated as in **a**. Transfected cells, indicated with arrowheads, were visualized with RFP. Scale bar, 10  $\mu$ m. **d**, Isoproterenol-induced accumulation of DNA damage is synergistically suppressed by PKA inhibition and by rescuing p53 expression. **e**, Isoproterenol stimulated, ARRB1-dependent accumulation of DNA damage promotes rearrangements in chromosomes.

Total indicates PCR amplification of a non-specific locus (see Methods).

**f**, Isoproterenol infusion leads to decreased p53 levels in the testes from wild-type, but not *Arrb1*<sup>-/-</sup>, mice. Wild-type and *Arrb1*<sup>-/-</sup> mice ( $n = 5$  for each condition) were treated as in Fig. 1a. All bars represent mean  $\pm$  s.e.m.

**g**, Isoproterenol-infused mice develop chromosomal rearrangements in an ARRB1-dependent manner. Wild-type and *Arrb1*<sup>-/-</sup> mice were infused as in Fig. 1a. Genomic DNA from each organ was examined in an array-CGH. The data represent log<sub>2</sub> ratio plots (isoproterenol/saline) of genomic content in chromosome 4 (chr4, 105–130 Mb), comparing isoproterenol-infused mice with saline-infused mice of a same genotype. \*, significance threshold of  $1.0 \times 10^{-7}$  (rank segmentation algorithm). The direction of isoproterenol-induced chromosomal gain (green arrow) or loss (red arrow) is indicated. Yellow highlights represent sites of isoproterenol-induced rearrangements. **h**, Schematic diagram of  $\beta_2$ -adrenoreceptor ( $\beta_2$ AR)-dependent regulation of DNA damage in response to prolonged secretion of catecholamines during chronic stress.



to a lowering of p53 levels in the testes. The effects are abolished in *Arrb1*<sup>-/-</sup> mice (Fig. 4f). To examine these phenomena in a genome-wide context, we conducted an array-comparative genomic hybridization (array-CGH). In the same model of chronic stress<sup>7,13</sup>, genomic DNA was isolated from the testes and thymus, which allowed us to eliminate any changes due to meiotic recombination by considering only rearrangements that occurred in both organs (see study design in Supplementary Fig. 6f). These studies show that the only such rearrangement occurring upon isoproterenol-infusion results in a duplication of more than 1 megabase (Mb) in regions 4qD2.2 and 4qD1 in wild-type mice; however, these events are not observed in the testes from *Arrb1*<sup>-/-</sup> mice (Fig. 4g and Supplementary Fig. 6f). Quantitative PCR (qPCR) of the testicular genome from each mouse also confirms isoproterenol-induced duplication at 4qD2.2 in an *ARRB1*-dependent manner (Supplementary Fig. 6g). Taken together, these data support the hypothesis that  $\beta_2$ -adrenoreceptor- and *ARRB1*-dependent signalling regulates catecholamine-induced degradation of p53, thus leading to the accumulation of DNA damage in both somatic and germline cells (Fig. 4h).

The stress response is conserved in mammals, and is probably required for survival. However, psychosocial stress in humans is not time-limited, because aspects of this type of stress response can be sustained over months or even years. This may lead to prolonged secretion of stress hormones and consequent adverse effects for the individual. Indeed, clinical studies have shown marked risk-reductions for prostate cancer, lung adenocarcinoma and Alzheimer's disease associated with chronic  $\beta$ -blocker ( $\beta$ -adrenoreceptor-antagonist) therapy<sup>4,29,30</sup>. It also seems plausible that such hormonal influences on DNA damage may not be limited to the  $\beta_2$ -adrenoreceptors.

## METHODS SUMMARY

**Experimental procedures.** Each experiment was repeated at least three times with comparable results, unless indicated otherwise.

**Cell culture conditions and treatments.** Isoproterenol was prepared fresh for each experiment by dissolving bitartrate salt (Sigma) immediately before stimulation. To study chronic  $\beta$ -adrenergic effects, U2OS cells and MEFs were cultured until confluent, then stimulated with 10  $\mu$ M isoproterenol for 24 h unless otherwise indicated. To study  $\gamma$ -H2AX formation, cells were cultured until 40–50% confluent, then stimulated with 10  $\mu$ M isoproterenol every 12 h for 3 days. To study phosphorylation of MDM2 at Ser 166 in MEFs, cells were serum-starved for 4 h, then stimulated with 10  $\mu$ M isoproterenol for 1 h. H-89 (10  $\mu$ M), leptomycin B (10 nM), ICI 118,551 (10  $\mu$ M), wortmannin (100 nM), 5-(2-benzothiazolyl)-3-ethyl-2-(2-(methylphenylamino)ethyl)-1-phenyl-1H-benzimidazolium iodide (AKT1, 1  $\mu$ M) or LY294002 (10  $\mu$ M, Sigma) were added to the media 30 min before stimulation with isoproterenol.

**Isoproterenol infusion.** Mice were subcutaneously implanted with ALZET osmotic pumps to administer saline or isoproterenol (30 mg kg<sup>-1</sup> d<sup>-1</sup>) continuously, dissolved in saline, for 28 days (mini-osmotic pump model 2004), following the manufacturer's procedure. After administration, animals were killed and the indicated organs were dissected out. All animals used in these studies were adult male mice of 8–12 weeks of age. Animals were handled according to approved protocols and animal welfare regulations of the Institutional Review Board at Duke University Medical Center.

**Full Methods** and any associated references are available in the online version of the paper at [www.nature.com/nature](http://www.nature.com/nature).

Received 16 July 2010; accepted 18 July 2011.

Published online 21 August 2011.

1. Selye, H. A syndrome produced by diverse nocuous agents. *Nature* **138**, 32 (1936).
2. Charmandari, E., Tsigos, C. & Chrousos, G. Endocrinology of the stress response. *Annu. Rev. Physiol.* **67**, 259–284 (2005).
3. Goldstein, D. S. Catecholamines and stress. *Endocr. Regul.* **37**, 69–80 (2003).
4. Antoni, M. H. *et al.* The influence of bio-behavioural factors on tumour biology: pathways and mechanisms. *Natl. Rev.* **6**, 240–248 (2006).
5. Flint, M. S., Baum, A., Chambers, W. H. & Jenkins, F. J. Induction of DNA damage, alteration of DNA repair and transcriptional activation by stress hormones. *Psychoneuroendocrinology* **32**, 470–479 (2007).

6. Lu, T. *et al.* Gene regulation and DNA damage in the ageing human brain. *Nature* **429**, 883–891 (2004).
7. Thaker, P. H. *et al.* Chronic stress promotes tumor growth and angiogenesis in a mouse model of ovarian carcinoma. *Nature Med.* **12**, 939–944 (2006).
8. Fratiglioni, L., Paillard-Borg, S. & Winblad, B. An active and socially integrated lifestyle in late life might protect against dementia. *Lancet Neurol.* **3**, 343–353 (2004).
9. Kinney, D. K., Munir, K. M., Crowley, D. J. & Miller, A. M. Prenatal stress and risk for autism. *Neurosci. Biobehav. Rev.* **32**, 1519–1532 (2008).
10. Nepomnaschy, P. A. *et al.* Cortisol levels and very early pregnancy loss in humans. *Proc. Natl Acad. Sci. USA* **103**, 3938–3942 (2006).
11. Ćikoš, S. *et al.* Expression of beta adrenergic receptors in mouse oocytes and preimplantation embryos. *Mol. Reprod. Dev.* **71**, 145–153 (2005).
12. DeWire, S. M., Ahn, S., Lefkowitz, R. J. & Shenoy, S. K.  $\beta$ -arrestins and cell signaling. *Annu. Rev. Physiol.* **69**, 483–510 (2007).
13. Ni, Y. *et al.* Activation of  $\beta_2$ -adrenergic receptor stimulates  $\gamma$ -secretase activity and accelerates amyloid plaque formation. *Nature Med.* **12**, 1390–1396 (2006).
14. Bonner, W. M. *et al.* GammaH2AX and cancer. *Nature Rev. Cancer* **8**, 957–67 (2008).
15. Freedman, D. A. & Levine, A. J. Nuclear export is required for degradation of endogenous p53 by MDM2 and human papillomavirus E6. *Mol. Cell. Biol.* **18**, 7288–7293 (1998).
16. Rainbow, T. C., Parsons, B. & Wolfe, B. B. Quantitative autoradiography of beta 1- and beta 2-adrenergic receptors in rat brain. *Proc. Natl Acad. Sci. USA* **81**, 1585–1589 (1984).
17. Zhou, B. P. *et al.* *HER-2/neu* induces p53 ubiquitination via Akt-mediated MDM2 phosphorylation. *Nature Cell Biol.* **3**, 973–982 (2001).
18. De Gregorio, G. *et al.* The p85 regulatory subunit of PI3K mediates TSH-cAMP-PKA growth and survival signals. *Oncogene* **26**, 2039–2047 (2007).
19. Goel, R., Phillips-Mason, P. J., Raben, D. M. & Baldassare, J. J.  $\alpha$ -Thrombin induces rapid and sustained Akt phosphorylation by  $\beta$ -arrestin1-dependent and -independent mechanisms, and only the sustained Akt phosphorylation is essential for G1 phase progression. *J. Biol. Chem.* **277**, 18640–18648 (2002).
20. Buchanan, F. G. *et al.* Role of  $\beta$ -arrestin 1 in the metastatic progression of colorectal cancer. *Proc. Natl Acad. Sci. USA* **103**, 1492–1497 (2006).
21. Kovacs, J. J., Hara, M. R., Davenport, C. L., Kim, J. & Lefkowitz, R. J. Arrestin development: emerging roles for  $\beta$ -arrestins in developmental signaling pathways. *Dev. Cell* **17**, 443–458 (2009).
22. Scott, M. G. *et al.* Differential nucleocytoplasmic shuttling of  $\beta$ -arrestins. Characterization of a leucine-rich nuclear export signal in  $\beta$ -arrestin-2. *J. Biol. Chem.* **277**, 37693–37701 (2002).
23. Wang, P., Wu, Y., Ge, X., Ma, L. & Pei, G. Subcellular localization of  $\beta$ -arrestins is determined by their intact N domain and the nuclear export signal at the C terminus. *J. Biol. Chem.* **278**, 11648–11653 (2003).
24. Wang, P. *et al.*  $\beta$ -arrestin 2 functions as a G-protein-coupled receptor-activated regulator of oncoprotein Mdm2. *J. Biol. Chem.* **278**, 6363–6370 (2003).
25. Boularan, C. *et al.*  $\beta$ -arrestin 2 oligomerization controls the Mdm2-dependent inhibition of p53. *Proc. Natl Acad. Sci. USA* **104**, 18061–18066 (2007).
26. Nobles, K. N., Guan, Z., Xiao, K., Oas, T. G. & Lefkowitz, R. J. The active conformation of  $\beta$ -arrestin1: direct evidence for the phosphate sensor in the N-domain and conformational differences in the active states of  $\beta$ -arrestins1 and -2. *J. Biol. Chem.* **282**, 21370–21381 (2007).
27. Yan, L. *et al.* Type 5 adenylyl cyclase disruption increases longevity and protects against stress. *Cell* **130**, 247–258 (2007).
28. Sengupta, S. & Harris, C. C. p53: traffic cop at the crossroads of DNA repair and recombination. *Nature Rev. Mol. Cell Biol.* **6**, 44–55 (2005).
29. Schuller, H. M. Mechanisms of smoking-related lung and pancreatic adenocarcinoma development. *Nature Rev. Cancer* **2**, 455–463 (2002).
30. Khachaturian, A. S. *et al.* Antihypertensive medication use and incident Alzheimer disease: the Cache County Study. *Arch. Neurol.* **63**, 686–692 (2006).

**Supplementary Information** is linked to the online version of the paper at [www.nature.com/nature](http://www.nature.com/nature).

**Acknowledgements** R.J.L. is a Howard Hughes Medical Institute investigator. This work was supported by HL16037 and HL70631 (R.J.L.). We thank D. Addison and Q. Lennon for secretarial assistance; S. H. Snyder and M. A. Koldobsky for providing p53 deletion constructs; B. K. Koblick and H. A. Rockman for providing *Adrb2*<sup>-/-</sup> mice; M. C. Hung for providing the MDM2-S166D plasmid; A. K. Shukla, A. Kahsai, J. Kim, J. Sun, S. M. DeWire and N. Odajima for discussion and comments.

**Author Contributions** M.R.H. and R.J.L. designed experiments, directed the study and wrote the paper. M.R.H. performed most of the experiments, analysed the data and prepared the figures. R.J.L. supervised the study and provided financial support. J.J.K. performed some experiments, helped to analyse the data and helped to write the paper. E.J.W., S.R., K.X., S.K.S. and S.A. helped to analyse the data. E.J.W., S.R., R.T.S., B.W., C.M.L. and S.A. performed some experiments. A.J.T. and S.G.G. performed the array-CGH and helped to analyse the data. W.G. and D.R.D. helped to characterize the functionality of p53 and to analyse the data.

**Author Information** Reprints and permissions information is available at [www.nature.com/reprints](http://www.nature.com/reprints). The authors declare no competing financial interests. Readers are welcome to comment on the online version of this article at [www.nature.com/nature](http://www.nature.com/nature). Correspondence and requests for materials should be addressed to R.J.L. ([lefk001@receptor-biol.duke.edu](mailto:lefk001@receptor-biol.duke.edu)).

## METHODS

**Reagents.** Unless otherwise noted, chemicals were purchased from Sigma.

**Antibodies.** Antibodies used were as follows, indicated WB for western blotting, IP for immunoprecipitation and CM for confocal microscopy. PARP-1 (WB, 1:500 dilution, Alexis Biochemicals). FOXO3a (WB, 1:500), MDM2 phosphorylated at Ser 166 (WB, 1:1,000), FOS (WB, 1:500), PUMA (WB, 1:500), p21 (WB, 1:500), all from Cell Signaling. Mouse p53 (FL-393; IP, 2 µg; WB, 1:200; CM, 1:50), human p53 (DO-1; WB, 1:5,000), MDM2 (SMP14; IP, 1 µg), ARRB1 (K-16; IP, 1 µg), ubiquitin (P4D1; WB, 1:200), human  $\beta_2$ -adrenoreceptor (H-20; WB, 1:3,000), mouse  $\beta_2$ -adrenoreceptor (M-20; WB, 1:200), anti-goat IgG-HRP (WB, 1:10,000), all from Santa Cruz. ARRB1 (10; WB, 1:200; CM, 1:50; BD Biosciences). LDH (WB, 1:300; Calbiochem). Mdm2 (HDM2-323; WB, 1:200),  $\beta$ -tubulin I (SAP.4G5; WB, 1:10,000), both from Sigma. Histone H2B (WB, 1:5,000), histone H2B phosphorylated on Ser 14 (WB, 1:5,000),  $\gamma$ -H2AX (WB, 1:1,000; CM, 1:100), all from Millipore. 53BP1 (WB, 1:1,000; Novus). p21 (WB, 1:200; Rockland). Anti-mouse IgG-HRP (WB, 1:10,000), anti-rabbit IgG-HRP (WB, 1:10,000), both from GE Healthcare. Rabbit polyclonal ARRB1 antibody (A1CT; WB, 1:20,000) was generated as previously described<sup>31</sup>.

**Primers.** *Tcrp* a1: 5'-ACCATACACTGGTACCGGCA-3', *Tcrp* b1: 5'-ACCCC TACCCATATTTCTTAG-3', *Tcrb* a2: 5'-TCTACTCCAACTACTCCAG-3', *Tcrb* b2: 5'-CCTCCAAGCGAGGAGATGTGAA-3', non-specific locus (chr 7) forward: 5'-AGGCCTGGCTAGGCTTTTGAATCTTTC-3', non-specific locus (chr 7) reverse: 5'-TGCCAGTGCTGGTGCCTGTGCACGGCTGT-3', qPCR chr4 qD2.2 forward: 5'-TGGTGTCTGGCACAACCTGGCA-3', qPCR chr4 qD2.2 reverse: 5'-TGACGGTGTCTTTTGCCTTACAGAAGC-3', qPCR control (chr1) forward: 5'-CCTCCCATCAACGTTTCAGGAGCC-3', qPCR control (chr1) reverse: 5'-ACTGCTTCTGCTCCAAACCTGC-3', *p21* promoter forward: 5'-CCAGAGGATACCTTGAAGGC-3', *p21* promoter reverse: 5'-TCTCTGT CTCCATTCATGCTCTCC-3'.

**Peptides.** The synthesis of ARRB1-binding peptide (ARRB1-BP; V<sub>2</sub>Rpp) has been described elsewhere. The sequence of the peptide, with phosphorylation sites underlined, is: ARGTRPPSLGPQDESCTTASSSLAKDTSS (ref. 32).

**Plasmids.** The *MDM2*-S166D plasmid<sup>17</sup> and *p53* deletion constructs<sup>33</sup> and were gifts from M. C. Hung and S. H. Snyder, respectively. Plasmids encoding shRNAs against *p53* (psiRNA-mp53 and psiRNA-hp53), and the control psiRNA-LucGL3, were purchased from InvivoGen.

**Experimental procedures.** Each experiment was repeated at least three times with comparable results, unless indicated otherwise.

**Immunoblotting.** SDS polyacrylamide gel electrophoresis (SDS-PAGE) was performed on 1.0-mm-thick NuPAGE 4–12% Bis-Tris gels (Invitrogen) and separated proteins were transferred to nitrocellulose membranes by semi-dry transfer, using trans-blot transfer medium (Bio-Rad). Blots were blocked with blocking buffer (5% skimmed milk in PBS with 0.02% Tween-20) before incubation at 4 °C overnight with primary antibodies, diluted in blocking buffer as described above. Blots were washed three times for 5 min each in PBS with 0.02% Tween-20, and then incubated with secondary antibodies in blocking buffer. Blots were washed three times for 5 min each in PBS with 0.02% Tween-20, and developed by SuperSignal West Pico/Femto solution (Pierce). Each protein band of interest on the immunoblot was quantified by densitometry using the GeneTools program (SynGene).

**Co-immunoprecipitation.** Cells were lysed in a lysis buffer (50 mM Tris (pH 7.4), 150 mM NaCl, 0.1% CHAPS buffer, 0.1 mg ml<sup>-1</sup> BSA, 1 mM PMSF and 1 mM EDTA, with Halt protease and phosphatase inhibitor cocktail (Pierce)), and homogenized by passing through a 28-gauge needle 20 times. Crude lysates were cleared of insoluble debris by centrifugation at 14,000g. Extra lysis buffer was added to 100–500 µg of cell lysate to bring samples to a total volume of 1 ml. Immunoprecipitating antibody (1–2 µg) was added and incubated on a rotator at 4 °C overnight. On the following day, 25 µl (50% slurry) of the appropriate TrueBlot IP beads (eBioscience) was added and incubated on a rotator at 4 °C for 1 h. The beads were washed five times with the lysis buffer and quenched with 30 µl of SDS sample buffer (×2). For detection of p53 ubiquitination (Fig. 3b), 10 mM *N*-ethylmaleimide and 20 µM MG132 were added to the lysis buffer. Co-immunoprecipitation after cell fraction was conducted as previously described<sup>34</sup>. Briefly, cells were lysed in RIPA A buffer (0.3% Triton X-100, 50 mM Tris (pH 7.4) and 1 mM EDTA), with rotation at 4 °C for 30 min. Cell lysates were centrifuged at 14,000g for 10 min and the supernatant was used as the cytosolic fraction. The nuclear fraction was extracted from the pellet with RIPA B buffer (1% Triton X-100, 1% SDS, 50 mM Tris (pH 7.4), 500 mM NaCl and 1 mM EDTA), affinity-precipitated with the indicated antibodies, and subjected to SDS-PAGE.

**Subcellular fractionation.** U2OS cells from a 10-cm plate were resuspended in 300 µl of buffer B (0.25 M sucrose, 10 mM Tris (pH 7.4), 10 mM MgCl<sub>2</sub>, 10 mM KCl, 1 mM DTT and protease inhibitor cocktail without EDTA) and homogenized with 150 strokes in a 1-ml dounce tissue grinder (Wheaton) using a tight pestle on

ice. After centrifugation at 750g for 10 min, the supernatant was isolated to separate the cytosolic fraction. The pellet was washed twice with buffer B, and resuspended in 100–200 µl of buffer B. The suspension was analysed as the nuclear fraction. Cytosolic fractions and nuclei were also prepared by using Nuclei EZ prep nuclei isolation kit (Sigma), following the manufacturer's protocol, and comparable results were obtained. To detect the effects of PI3K inhibition by LY294002 on isoproterenol-induced p53 nuclear export, U2OS cells were pre-incubated with 10 µM LY294002 for 30 min, and then stimulated with 10 µM isoproterenol for 1 h. To detect the effects of nuclear export on decreased nuclear p53, U2OS cells were pre-incubated with 10 nM leptomycin B for 30 min, and then stimulated with 10 µM isoproterenol for 1 h. To prepare a total-cell extract, cell pellets were lysed in a lysis buffer (50 mM Tris (pH 7.4), 150 mM NaCl, 0.1% CHAPS, 0.1 mg ml<sup>-1</sup> BSA, 1 mM PMSF and 1 mM EDTA, with Halt protease and phosphatase inhibitor cocktail (Pierce)) and homogenized by passing through a 28-gauge needle 20 times. Crude lysates were cleared of insoluble debris by centrifugation at 20,000g.

**Cell culture conditions and treatments.** Wild-type MEFs (passage number ~72), *Arrb1*<sup>-/-</sup> MEFs (passage number ~76) and *Arrb2*<sup>-/-</sup> MEFs (passage number ~49) were prepared according to the 3T3 protocol<sup>35,36</sup>. Established MEF cultures and RAW264.7 cells were maintained in Dulbecco's modified Eagle medium (DMEM) with 10% FBS and 2 mM L-glutamine at 37 °C with a 5% CO<sub>2</sub> atmosphere in a humidified incubator. U2OS, HEK-293 and NCI-H1299 cells were maintained in modified Eagle medium (MEM) with 10% FBS and 2 mM L-glutamine, with the same conditions as above. U2OS and NCI-H1299 cells were transfected with FuGENE6 transfection reagent (Roche) following the manufacturer's protocol. For RNA interference for ARRB1, the vector system shRNA was used as previously described<sup>37,38</sup>. Briefly, U2OS cells in 10-cm plates were transfected with either 10 µg control shRNA plasmid (5'-ACGTGACACGTTCCGAGAATTGATATCCGTTTC TCCGAACGTGTACAGTTT-3') or 10 µg *ARRB1* shRNA plasmid (5'-ATTCT CCGCGCAGAAGGCTTT GATATCCG AGCCTTCTGCGCGGAGAATTT-3'), and incubated for 72 h. HEK-293 cells and MEFs were transfected with lipofectamine 2000 (Invitrogen) following the manufacturer's protocol. Briefly, 2 µg of DNA was dissolved in 35 µl of serum- and antibiotic-free medium per well, in a 6-well plate. Lipofectamine 2000 (10 µl) was mixed with 25 µl of serum- and antibiotic-free medium, and incubated for 5 min. The prepared DNA and lipofectamine 2000 solutions were mixed and the mixture was incubated for 20 min at 18–23 °C. During the incubation, normal cell-culture medium was replaced with serum- and antibiotic-free medium. The transfection mixture was added to the cells in serum-free culture, and incubated overnight. On the following day, the medium was replaced with normal serum- and antibiotic-containing growth medium, and the cells were incubated for 48–72 h before testing.

Isoproterenol, epinephrine and norepinephrine were prepared fresh for each experiment by dissolving the bitartrate salts (Sigma) immediately before stimulation. To study chronic  $\beta$ -adrenergic effects, U2OS cells and MEFs were cultured until confluent, then stimulated with 10 µM isoproterenol for 24 h, unless otherwise indicated. To study  $\gamma$ -H2AX formation, cells were cultured until 40–50% confluent, then stimulated with 10 µM isoproterenol every 12 h for 3 days. H-89 (10 µM), leptomycin B (10 nM), ICI 118,551 (100 nM), wortmannin (100 nM), 5-(2-benzothiazolyl)-3-ethyl-2-(2-(methylphenylamino)ethenyl)-1-phenyl-1H-benzimidazolium iodide (AKTi, 1 µM) or LY294002 (10 µM, Sigma) were added to the media 30 min before stimulation with isoproterenol. To study the effects of isoproterenol stimulation on cell proliferation after DNA damage, cells were ultraviolet-irradiated (50 J per m<sup>2</sup>) and incubated for 6 h, followed by stimulation with 10 µM isoproterenol every 12 h for 3 days. Cell lysates were examined by immunoblotting for FOS, an indicator of cell survival and proliferation<sup>39</sup>. To study phosphorylation of MDM2 at Ser 166 in MEFs, cells were serum-starved for 4 h, then stimulated with 10 µM isoproterenol for 1 h. To study this phosphorylation event in U2OS cells, cells were serum-starved for 36 h, then stimulated with 10 µM isoproterenol for 10 min.

**In vitro ubiquitination assay.** 10 nM His-p53 (ProteinOne) was mixed with 200 ng E1 (BostonBiochem), 200 ng UbcH5b (BostonBiochem), 5 µg ubiquitin (BostonBiochem) and 25 nM MDM2 in 20 µl of reaction mixture (40 mM Tris (pH 7.6), 2 mM ATP-Mg<sup>2+</sup>, 1 mM dithiothreitol and 5 mM MgCl<sub>2</sub>). Purified recombinant ARRB1 (0, 50 or 500 nM) was added to the reaction mixture in the presence or absence of 300 nM ARRB1-BP. The sample was incubated for 60 min at 30 °C, resolved by SDS-PAGE and analysed by immunoblotting with anti-p53 antibody (DO-1).

**Isoproterenol infusion.** Wild-type (C57BL/6), *Arrb1* knockout (*Arrb1*<sup>-/-</sup>)<sup>40</sup> or  $\beta_2$ -adrenoreceptor knockout (*Adrb2*<sup>-/-</sup>)<sup>41</sup> mice were subcutaneously implanted with ALZET osmotic pumps to administer saline or isoproterenol (30 mg kg<sup>-1</sup> d<sup>-1</sup>) continuously, dissolved in saline, for 28 days (mini-osmotic pump model 2004), following the manufacturer's procedure. After administration, animals were killed and the indicated organs were dissected out. For protein preparation, dissected organ tissues were lysed and sonicated in RIPA buffer (50 mM Tris



(pH 7.4), 500 mM NaCl, 1% SDS, 1% Triton X-100 and 1 mM EDTA, with Halt protease and phosphatase inhibitor cocktail). Genomic DNA was prepared from dissected organ tissues by DNeasy blood & tissue kit (Qiagen), following the manufacturer's protocol. All animals used in these studies were adult male mice of 8–12 weeks of age. All mouse strains were backcrossed to the C57BL/6 background for  $\geq 10$  generations. Animals were handled according to approved protocols and animal welfare regulations of the Institutional Review Board at Duke University Medical Center.

**Quantitative real-time PCR (qPCR).** qPCR was performed with Power SYBR Green PCR Master Mix (Applied Biosystems) and StepOne Real-time PCR system (Applied Biosystems) following the manufacturer's protocol. To validate the array-CGH analysis, relative genomic content (copy number) was determined with the comparative  $C_T$  ( $\Delta\Delta C_T$ ) method<sup>42</sup>.

**GST pulldown assay.** Wild-type rat *Arrb1* or human *MDM2* were subcloned into the pGEX4T1 vector and prepared according to the manufacturer's recommendations (Amersham Biosciences). The GST tag was cleaved with thrombin protease (Hematologic Technologies Inc.). p53 (1 nM) was co-incubated overnight with 10 nM of GST-ARRB1 or 10 nM of GST at 4 °C in 1 ml binding buffer (50 mM Tris (pH 7.4), 150 mM NaCl, 0.1 mg ml<sup>-1</sup> BSA and 10  $\mu$ M D-myo-inositol 1,2,3,4,5,6-hexakisphosphate), and 20  $\mu$ l of 50% glutathione-sepharose was then added to the mixture. The mixture was further incubated at 4 °C for 1 h with rotation. The beads were washed once with 1 ml binding buffer, separated by SDS-PAGE and analysed by immunoblotting.

**Immunofluorescence experiments.** Immunofluorescence using confocal microscopy was carried out as previously described<sup>43</sup>. For detection of  $\gamma$ -H2AX foci, we captured images of more than 20 fields per preparation, which were randomly chosen in a blind manner. Cells positive for  $\gamma$ -H2AX foci in each field were tallied and added together to determine the percentage. The total number of cells was counted with 4',6-diamidino-2-phenylindole (DAPI) nuclear staining. For rescue experiments using the expression of RFP-ARRB1 (or RFP as a control) in MEFs, RFP-positive cells were counted for  $\gamma$ -H2AX foci. For p53 rescue experiments in NC1-H1299 cells, RFP-*Arrb1* (or RFP) and p53 were co-transfected in a 1:3 ratio.

**Detection of interchromosomal rearrangements between *Tcrg* and *Tcrb*.** The trans-rearrangement between *Tcrg* and *Tcrb* loci were detected by nested PCR, using first the 'a' set of primers and then the 'b' set of primers, as previously described<sup>44</sup> (Supplementary Fig. 6d). The number of rearrangements is expressed as the reciprocal of the highest dilution of DNA yielding an amplified product (for example, the number of trans-rearrangements per  $1.5 \times 10^5$  cells (1  $\mu$ g of DNA) is 1,000, yielding an amplifiable fragment at a 1:1,000 dilution (1 ng of DNA))<sup>44</sup>.

**DNA preparation.** DNA was prepared from the testes and thymus by using the DNeasy blood & tissue kit (Qiagen) following the manufacturer's protocol. To enrich sperm from excised testis grafts, the testis was minced and the epithelial tissue, containing leydig and sertoli cells, was removed.

**Array-comparative genomic hybridization (Array-CGH).** A tiling-path CGH array for the genome analysis in mouse (UCSC Build mm9) was designed and constructed by NimbleGen Systems (NimbleGen). The resulting array contained 720,000 probes with a median probe spacing of 3,537 base pairs. Probes were synthesized using an isothermal format (melting temperature 76 °C), and varied in length from 50 to 75 base pairs. Genomic DNA from five mice for each experimental condition was pooled and examined. Genomic DNAs (1  $\mu$ g) from test (isoproterenol-treated) and reference (saline-treated) mice were differentially labelled with 5'-Cy3 and 5'-Cy5 random nonamers (TriLink Biotechnologies), respectively, and hybridized to the oligoarray for 72 h using the MAUI hybridization station (BioMicro Systems Inc.). Image-capture of the hybridized arrays for fluorescent intensity extraction was performed using a Genepix 4100A scanner (Molecular Dynamics) and normalized using NimbleScan v2.5 microarray software (Nimblegen) before importing into Nexus Copy-Number (BioDiscovery) for analysis.

**Array-CGH analysis.** BioDiscovery's rank segmentation algorithm, which is similar to circular binary segmentation<sup>45</sup>, was used to identify genomic rearrangements. The significance threshold was set as  $1.0 \times 10^{-7}$ . The calling algorithm used cluster values and defined  $\log_2$  thresholds of  $\pm 0.2$ . We applied a cutoff of ten oligomer clones showing the same trend in copy-number change to define chromosomal rearrangements. Black lines in the plot indicate a 'cluster value', which is the median log-ratio value of all the probes in that region. Isoproterenol-induced rearrangements in the testes were determined, and identical rearrangements were detected in the thymus (see study design in Supplementary Fig. 6f).

**Radioligand binding experiments.** For ICI 118,551 and CGP 20712A affinity measurements, subtype-selective ligand affinities were determined from competition radioligand binding experiments, conducted according to previous works<sup>46,47</sup>. Briefly, 25  $\mu$ g of cell membranes, prepared via differential centrifugation, were resuspended in assay buffer (50 mM Tris-HCl (pH 7.4), 12.5 mM MgCl<sub>2</sub>, 2 mM

EDTA and 1 mM ascorbic acid) containing 60 pM [<sup>125</sup>I]cyanopindolol (NEX189, 2,200 Ci mmol<sup>-1</sup>) and concentrations of ICI 118,551 or CGP 20712A ranging from 1  $\mu$ M to 1 pM. Nonspecific binding was determined in the presence of 10  $\mu$ M propranolol. After incubation at 25 °C for 90 min, membranes were collected and washed via vacuum filtration (Brandel) and the bound radioactivity was quantified using a Packard Cobra gamma counter (Perkin Elmer). Equilibrium inhibition constant ( $K_i$ ) values were calculated from nonlinear regression analysis (Graphpad) using the method in ref. 48.

**p53 reporter assay.** U2OS cells were transfected with the p53-luc reporter plasmid (Stratagene) in the presence of serum, using FuGENE6 transfection reagent (Roche). Three hours after the transfection, media were changed to serum-free media containing 100  $\mu$ M ascorbic acid and appropriate concentrations of isoproterenol. Cells were incubated for 24 h and lysed in  $\times 1$  passive lysis buffer (PLB, Promega). The firefly luciferase reporter was analysed with addition of luciferase assay reagent II (Promega).

**Chromatin immunoprecipitation assay (ChIP) and Re-ChIP.** ChIP was performed as previously described<sup>49</sup>. In brief, both wild-type and *Arrb1*<sup>-/-</sup> MEFs were incubated with 50  $\mu$ M etoposide for 20 h. After incubation, cells were treated with 2 mM disuccinimidyl glutarate (Pierce) to crosslink protein complexes, then treated with formaldehyde to link protein to DNA covalently. Cells were lysed and the nucleoprotein complexes were sonicated. DNA-protein complexes enriched by the initial immunoprecipitation with anti-ARRB1 (K-16) antibody were eluted from beads with elution buffer (1% SDS, 0.1 M NaHCO<sub>3</sub>), and further immunoprecipitated with anti-p53 (FL-393) antibody for Re-ChIP. The retrieved complexes were then analysed by PCR amplification of p53-binding elements in the *p21* promoter.

**Statistics.** Unless otherwise noted, *P* values were calculated with Student's *t*-test (two-tailed). Analysis of variance was performed with Prism (GraphPad).

- Attramadal, H. *et al.*  $\beta$ -arrestin2, a novel member of the arrestin/ $\beta$ -arrestin gene family. *J. Biol. Chem.* **267**, 17882–17890 (1992).
- Xiao, K., Shenoy, S. K., Nobles, K. & Lefkowitz, R. J. Activation-dependent conformational changes in  $\beta$ -arrestin 2. *J. Biol. Chem.* **279**, 55744–55753 (2004).
- Koldobskiy, M. A. *et al.* p53-mediated apoptosis requires inositol hexakisphosphate kinase-2. *Proc. Natl Acad. Sci. USA* **107**, 20947–20951 (2010).
- Hara, M. R. *et al.* S-nitrosylated GAPDH initiates apoptotic cell death by nuclear translocation following Siah1 binding. *Nature Cell Biol.* **7**, 665–674 (2005).
- Kohout, T. A., Lin, F. S., Perry, S. J., Conner, D. A. & Lefkowitz, R. J.  $\beta$ -Arrestin 1 and 2 differentially regulate heptahelical receptor signaling and trafficking. *Proc. Natl Acad. Sci. USA* **98**, 1601–1606 (2001).
- Todaro, G. J. & Green, H. Quantitative studies of the growth of mouse embryo cells in culture and their development into established lines. *J. Cell Biol.* **17**, 299–313 (1963).
- Brummelkamp, T. R., Bernards, R. & Agami, R. A system for stable expression of short interfering RNAs in mammalian cells. *Science* **296**, 550–553 (2002).
- Yu, J. Y., DeRuiter, S. L. & Turner, D. L. RNA interference by expression of short-interfering RNAs and hairpin RNAs in mammalian cells. *Proc. Natl Acad. Sci. USA* **99**, 6047–6052 (2002).
- Seshadri, T. & Campisi, J. Repression of c-fos transcription and an altered genetic program in senescent human fibroblasts. *Science* **247**, 205–209 (1990).
- Conner, D. A. *et al.*  $\beta$ -Arrestin1 knockout mice appear normal but demonstrate altered cardiac responses to  $\beta$ -adrenergic stimulation. *Circ. Res.* **81**, 1021–1026 (1997).
- Chruscinski, A. J. *et al.* Targeted disruption of the  $\beta_2$  adrenergic receptor gene. *J. Biol. Chem.* **274**, 16694–16700 (1999).
- Livak, K. J. & Schmittgen, T. D. Analysis of relative gene expression data using real-time quantitative PCR and the 2<sup>-</sup>(Delta Delta C(T)) method. *Methods* **25**, 402–408 (2001).
- Kovacs, J. J. *et al.*  $\beta$ -arrestin-mediated localization of smoothened to the primary cilium. *Science* **320**, 1777–1781 (2008).
- Lista, F., Bertness, V., Guidos, C. J., Danska, J. S. & Kirsch, I. R. The absolute number of trans-rearrangements between the *TCRG* and *TCRB* loci is predictive of lymphoma risk: a severe combined immune deficiency (SCID) murine model. *Cancer Res.* **57**, 4408–4413 (1997).
- Olshen, A. B., Venkatraman, E. S., Lucito, R. & Wigler, M. Circular binary segmentation for the analysis of array-based DNA copy number data. *Biostatistics* **5**, 557–572 (2004).
- Hausdorff, W. P., Hnatowich, M., O'Dowd, B. F., Caron, M. G. & Lefkowitz, R. J. A mutation of the  $\beta_2$ -adrenergic receptor impairs agonist activation of adenylyl cyclase without affecting high affinity agonist binding. Distinct molecular determinants of the receptor are involved in physical coupling to and functional activation of Gs. *J. Biol. Chem.* **265**, 1388–1393 (1990).
- Baker, J. G. The selectivity of  $\beta$ -adrenoceptor antagonists at the human  $\beta_1$ ,  $\beta_2$  and  $\beta_3$  adrenoceptors. *Br. J. Pharmacol.* **144**, 317–322 (2005).
- Cheng, Y. & Prusoff, W. H. Relationship between the inhibition constant ( $K_i$ ) and the concentration of inhibitor which causes 50 per cent inhibition ( $I_{50}$ ) of an enzymatic reaction. *Biochem. Pharmacol.* **22**, 3099–3108 (1973).
- Nowak, D. E., Tian, B. & Brasier, A. R. Two-step cross-linking method for identification of NF- $\kappa$ B gene network by chromatin immunoprecipitation. *Biotechniques* **39**, 715–725 (2005).



# Small molecule inhibitors reveal Niemann–Pick C1 is essential for Ebola virus infection

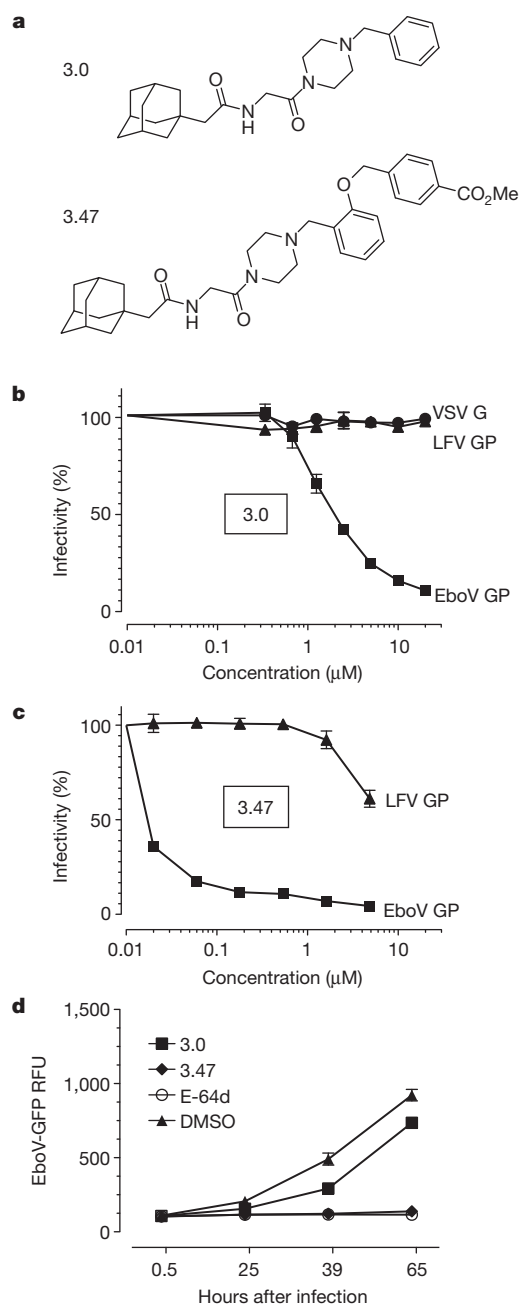
Marceline Côté<sup>1\*</sup>, John Misasi<sup>1,2\*</sup>, Tao Ren<sup>3\*</sup>, Anna Bruchez<sup>1\*</sup>, Kyungae Lee<sup>3</sup>, Claire Marie Filone<sup>1,4</sup>, Lisa Hensley<sup>4</sup>, Qi Li<sup>1</sup>, Daniel Ory<sup>5</sup>, Kartik Chandran<sup>1†</sup> & James Cunningham<sup>1,6</sup>

Ebola virus (EboV) is a highly pathogenic enveloped virus that causes outbreaks of zoonotic infection in Africa. The clinical symptoms are manifestations of the massive production of pro-inflammatory cytokines in response to infection<sup>1</sup> and in many outbreaks, mortality exceeds 75%. The unpredictable onset, ease of transmission, rapid progression of disease, high mortality and lack of effective vaccine or therapy have created a high level of public concern about EboV<sup>2</sup>. Here we report the identification of a novel benzylpiperazine adamantane diamide-derived compound that inhibits EboV infection. Using mutant cell lines and informative derivatives of the lead compound, we show that the target of the inhibitor is the endosomal membrane protein Niemann–Pick C1 (NPC1). We find that NPC1 is essential for infection, that it binds to the virus glycoprotein (GP), and that antiviral compounds interfere with GP binding to NPC1. Combined with the results of previous studies of GP structure and function, our findings support a model of EboV infection in which cleavage of the GP1 subunit by endosomal cathepsin proteases removes heavily glycosylated domains to expose the amino-terminal domain<sup>3–7</sup>, which is a ligand for NPC1 and regulates membrane fusion by the GP2 subunit<sup>8</sup>. Thus, NPC1 is essential for EboV entry and a target for antiviral therapy.

To identify chemical probes that target EboV host factors, we screened a library of small molecules and identified a novel benzylpiperazine adamantane diamide, 3.0, that inhibits infection of Vero cells by vesicular stomatitis virus particles (VSV) pseudotyped with EboV Zaire GP, but not with VSV G or Lassa fever virus (LFV) GP (Fig. 1a, b). To verify that 3.0 is a bona fide inhibitor, we measured EboV growth on Vero cells for 96 h and found it was reduced by >99% in the presence of 3.0 (Supplementary Fig. 1a). We synthesized and tested more than 50 analogues of 3.0 and found that the addition of a (methoxycarbonyl) benzyl group at the ortho position of the benzene ring (compound 3.47) increased the potency, as measured by a single cycle of EboV GP-dependent infection, and efficacy, as measured by growth of EboV on Vero cells (Fig. 1a, c, d).

## Figure 1 | Structure and function of Ebola virus entry inhibitors.

**a**, Compounds 3.0 and 3.47. **b**, **c**, Vero cells were grown in media containing increasing concentrations of 3.0 (**b**) or 3.47 (**c**) for 90 min before the addition of VSV particles encoding luciferase (**b**) or GFP (**c**) and pseudotyped with either EboV GP, VSV G or Lassa fever virus GP (LFV GP). Virus infection is reported as percent of luminescence units (RLU) or GFP-positive cells relative to cells exposed to DMSO vehicle alone. Data are mean  $\pm$  s.d. ( $n = 4$ ) and is representative of three experiments. **d**, Vero cells were grown in media containing 3.0 (40  $\mu$ M), 3.47 (40  $\mu$ M), vehicle (1% DMSO) or the cysteine cathepsin protease inhibitor E-64d (150  $\mu$ M) 90 min before the addition of replication competent Ebola virus Zaire-Mayinga encoding GFP (multiplicity of infection (m.o.i.) = 0.1). Results are mean relative fluorescence units (RFU)  $\pm$  s.e.m. ( $n = 3$ ).



<sup>1</sup>Division of Hematology, Department of Medicine, Brigham and Women's Hospital, Boston, Massachusetts 02115, USA. <sup>2</sup>Division of Infectious Disease, Department of Medicine, Children's Hospital, Boston, Massachusetts 02115, USA. <sup>3</sup>New England Regional Center of Excellence for Biodefense and Emerging Infectious Diseases, Harvard Medical School, Boston, Massachusetts 02115, USA. <sup>4</sup>United States Army Medical Research Institute of Infectious Diseases, Virology Division, Frederick, Maryland 21702, USA. <sup>5</sup>Diabetic Cardiovascular Disease Center, Washington University School of Medicine, Saint Louis, Missouri 63110, USA. <sup>6</sup>Department of Microbiology and Immunology, Harvard Medical School, Boston, Massachusetts 02115, USA. <sup>†</sup>Present address: Department of Microbiology and Immunobiology, Albert Einstein College of Medicine, Bronx, New York 10461, USA.

\*These authors contributed equally to this work.

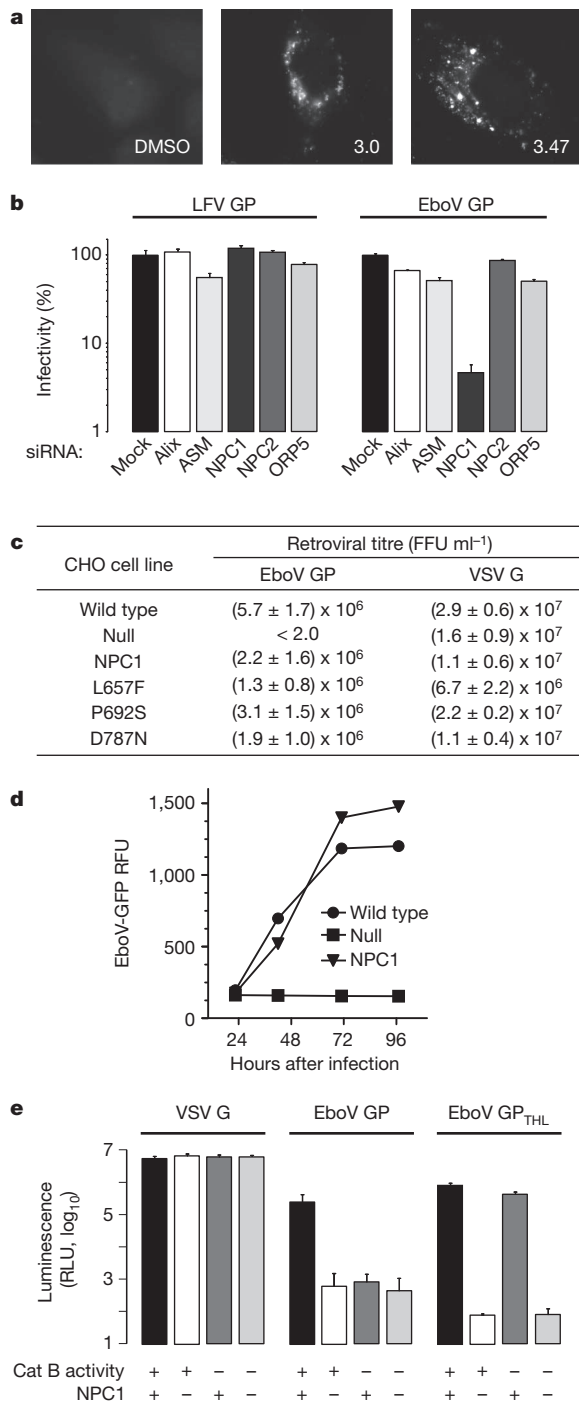


**Figure 2 | NPC1 is essential for Ebola virus infection.** **a**, HeLa cells were treated with 3.0 (20  $\mu$ M), 3.47 (1.25  $\mu$ M) or vehicle for 18 h, then fixed and incubated with the cholesterol-avid fluorophore filipin. **b**, HeLa cells were transfected with siRNAs targeting Alix, ASM, NPC1, NPC2 and ORP5. After 72 h, VSV EboV GP or LFV GP infection of these cells was measured as in Fig. 1c. Data are mean  $\pm$  s.d. ( $n = 3$ ) and is representative of three experiments. **c**, CHO<sub>wt</sub>, CHO<sub>null</sub> and CHO<sub>NPC1</sub> cells stably expressing mouse NPC1 (CHO<sub>NPC1</sub>) or NPC1 mutants L657F, P692S, D787N were exposed to MLV particles encoding LacZ and pseudotyped with either EboV GP or VSV G. Results are the mean  $\pm$  s.d. ( $n = 4$ ) and is representative of three experiments. FFU, focus forming units. **d**, CHO<sub>wt</sub>, CHO<sub>null</sub> and CHO<sub>NPC1</sub> cells were infected with replication competent Ebola virus Zaire-Mayinga encoding GFP (m.o.i. = 1). Results are mean relative fluorescence units  $\pm$  s.d. ( $n = 3$ ). **e**, CHO<sub>wt</sub> and CHO<sub>null</sub> cells were treated with the cathepsin B inhibitor CA074 (80  $\mu$ M) or vehicle. These cells were challenged with VSV G particles or VSV EboV GP particles treated with thermolysin (EboV GP<sub>THL</sub>) or untreated control (EboV GP). Infection was measured as in Fig. 1b. Data are mean  $\pm$  s.d. ( $n = 9$ ).

Previous studies revealed that the endosomal protease cathepsin B is essential for EboV infection because it cleaves the GP1 subunit of GP<sup>3,4</sup>. To address the possibility that 3.0 and 3.47 target this step, we measured cathepsin B activity in the presence of these compounds and found no effect *in vitro* or in cells (data not shown). Moreover, 3.0 and 3.47 inhibited infection by VSV EboV particles treated with thermolysin, a metalloprotease that faithfully mimics cathepsin cleavage of the GP1 subunit of GP (Supplementary Fig. 1b)<sup>4,9</sup>. These findings demonstrate that cathepsin B is not the target of 3.0 and 3.47.

HeLa cells treated with 3.0 or 3.47 for more than 18 h developed cytoplasmic vacuoles that were labelled by cholesterol-avid filipin (Fig. 2a). The induction of filipin-stained vacuoles by the compounds

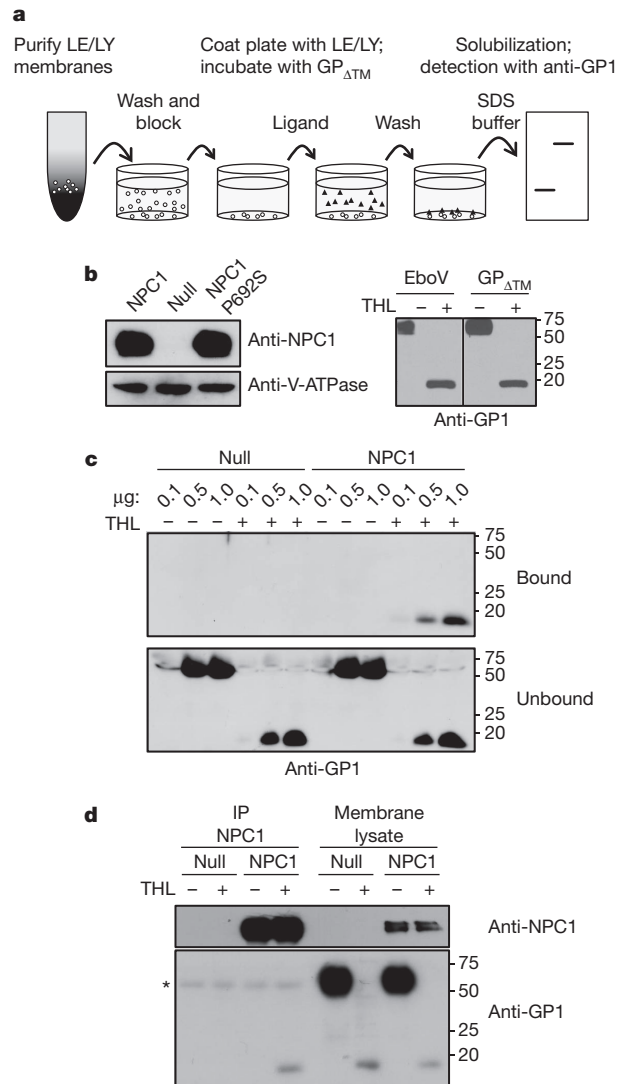


**Figure 3 | Protease-cleaved EboV GP binds to NPC1.** **a**, Schematic diagram of EboV GP1 binding assay used in panel c. **b**, left, LE/LY membranes from CHO<sub>NPC1</sub>, CHO<sub>null</sub> and CHO<sub>NPC1</sub> P692S cells were analysed by immunoblot using antibodies to NPC1 or V-ATPase B1/2. Right, VSV-EboV GP particles and EboV GP<sub>ATM</sub> protein were incubated in the presence or absence of thermolysin (THL) and analysed by immunoblot for GP1. **c**, EboV GP<sub>ATM</sub> or thermolysin-cleaved EboV GP<sub>ATM</sub> (0.1, 0.5, or 1.0  $\mu$ g) was added to LE/LY membranes purified from CHO<sub>null</sub> or CHO<sub>NPC1</sub> cells. Membrane bound and unbound GP1 were analysed by immunoblot. **d**, LE/LY membranes from CHO<sub>null</sub> or CHO<sub>NPC1</sub> cells were incubated with EboV GP<sub>ATM</sub> or thermolysin-cleaved EboV GP<sub>ATM</sub>. Following binding, membranes were dissolved in CHAPSO, NPC1 was precipitated using an NPC1-specific antibody, and the immunoprecipitate and the input membrane lysate were analysed by immunoblot for NPC1 (top) or GP1 (bottom). \* IgG heavy chain.

indicated that they target one or more proteins involved in regulation of cholesterol uptake in cells. To test this hypothesis, we used mutant cell lines and cells treated with small interfering RNA (siRNA) to analyse proteins for which loss of activity had been previously associated with cholesterol accumulation in late endosomes<sup>10–12</sup>. We found that EboV GP infection is dependent on the expression of Niemann–Pick C1 (NPC1), but not Niemann–Pick C2 (NPC2), acid sphingomyelinase (ASM), ALG-2-interacting protein X (Alix), or oxysterol binding protein 5 (ORP5) (Fig. 2b, Supplementary Fig. 2a–c). NPC1 is a polytopic protein that resides in the limiting membrane of late endosomes and lysosomes (LE/LY) and mediates distribution of lipoprotein-derived cholesterol in cells<sup>10,13</sup>. To analyse the role of NPC1 in infection, we studied Chinese hamster ovary (CHO)-derived cell lines that differ in expression of NPC1. We found that the titre of a murine leukaemia virus (MLV) vector pseudotyped with EboV GP on wild-type CHO cells (CHO<sub>wt</sub>) exceeded 10<sup>6</sup> infectious units per ml (Fig. 2c). Importantly, CHO cells lacking NPC1 (CHO<sub>null</sub>) were completely resistant to infection by this virus and infection of these cells was fully restored when NPC1 was expressed (CHO<sub>NPC1</sub>). Thus, NPC1 expression is essential for EboV infection.

In CHO<sub>null</sub> cells, LE/LY are enlarged and contain excess cholesterol (Supplementary Fig. 3)<sup>14</sup>. To determine if EboV infection is inhibited by endosome dysfunction secondary to the absence of NPC1, we studied a well-characterized NPC1 mutant P692S that is defective in cholesterol uptake and NPC1-dependent membrane trafficking<sup>13–15</sup> and found that expression of NPC1 P692S fully supports infection of CHO<sub>null</sub> cells (Fig. 2c). Conversely, gain-of-function mutants NPC1 L657F and NPC1 D787N (ref. 14) did not enhance EboV GP infection. Thus, EboV entry is strictly dependent on NPC1 expression, but not NPC1-dependent cholesterol transport activity. Consistent with the conclusion that NPC1 expression is essential for EboV

GP-dependent entry, we found that Ebola virus did not grow on CHO<sub>null</sub> cells (Fig. 2d). In addition, we tested a single round of infection by MLV particles bearing GPs from the filoviruses EboV Sudan, EboV Côte d'Ivoire, EboV Bundibugyo, EboV Reston and Marburg virus and found that all are strictly NPC1-dependent (Supplementary Fig. 4). Because these viruses are not closely related<sup>16</sup>, these findings indicate that the requirement for NPC1 as an entry factor is conserved among viruses in the *Filoviridae* family.

Because NPC1 and cathepsin B are both essential host factors, we analysed their relationship during infection. In our initial experiment, we measured cathepsin B activity in CHO<sub>null</sub> cells and found it was not significantly different from CHO<sub>wt</sub> cells (Supplementary Fig. 5). To determine if NPC1 is required for virus processing by cathepsin B, we tested whether thermolysin-cleaved particles are dependent on NPC1. As expected, we found that thermolysin-cleaved particles are infectious and resistant to inactivation of cathepsin B when NPC1 is present (Fig. 2e). However, thermolysin cleavage did not bypass the barrier to virus infection of NPC1 deficient cells. Taken together, these findings indicate that cathepsin B and NPC1 mediate distinct steps in infection.

Previous studies suggest that the product of cathepsin B cleavage of the GP1 subunit of EboV GP is a ligand for a host factor<sup>6,17–20</sup>. To test this hypothesis, we performed a series of experiments measuring binding of EboV GP to LE/LY membranes from CHO<sub>null</sub>, CHO<sub>NPC1</sub> and CHO<sub>P692S</sub> cells (Fig. 3a, b, left panel). The source of EboV GP is a purified recombinant protein that is truncated just before the trans-membrane domain (EboV GP<sub>ΔTM</sub>). EboV GP<sub>ΔTM</sub> is a trimer that is faithfully cleaved by thermolysin (Fig. 3b, right panel). We found that binding of EboV GP<sub>ΔTM</sub> to LE/LY membranes is concentration-dependent, saturable, and strictly dependent on both thermolysin cleavage of GP1 and membrane expression of NPC1 or NPC1 P692S (Fig. 3c and Supplementary Fig. 6a, b). To determine if cleaved GP

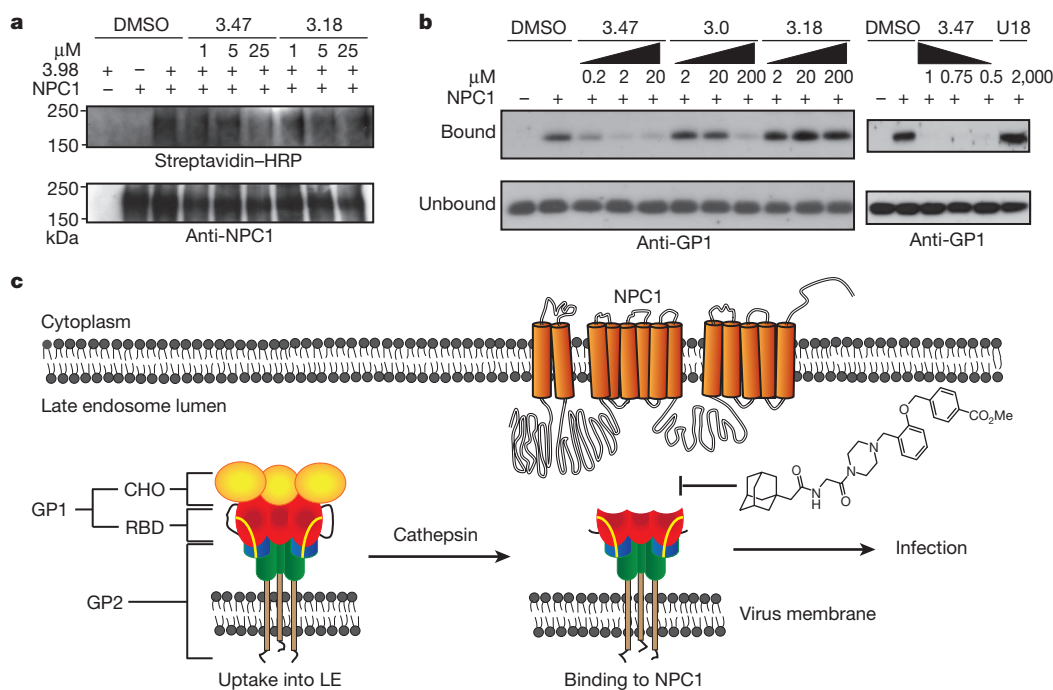


**Figure 4 | NPC1 is a target of the small molecule inhibitors.** **a**, LE/LY membranes from CHO<sub>null</sub> or CHO<sub>NPC1</sub> cells were incubated at the indicated concentrations of 3.47, 3.18 or DMSO (5%) before the addition of the photoactivatable 3.98 (25 μM). After incubation, 3.98 was activated by ultraviolet light and then conjugated to biotin. NPC1 was immunoprecipitated and analysed by immunoblot for conjugation of 3.98 to NPC1 using streptavidin–horseradish peroxidase (HRP) (top) and recovery of NPC1 (bottom). **b**, Thermolysin-cleaved EboV GP<sub>ΔTM</sub> protein (1 μg) was added to LE/LY membranes from CHO<sub>null</sub> or CHO<sub>NPC1</sub> cells in the presence of DMSO (10%) or

the indicated concentrations of 3.47, 3.0, or 3.18 (left panel), and 3.47 or U18666A (U18, right panel). Membrane-bound and unbound GP1 were analysed by immunoblot. **c**, Proposed model of EboV entry. Following EboV uptake and trafficking to late endosomes<sup>24,25</sup>, EboV GP is cleaved by cathepsin protease to remove heavily glycosylated domains (CHO) and expose the putative receptor binding domain (RBD) of GP1 (refs 6, 17–19). Binding of cleaved GP1 to NPC1 is necessary for infection and is blocked by the EboV inhibitor 3.47.



binds to NPC1, we performed a co-immunoprecipitation experiment. LE/LY membranes were incubated with EboV GP<sub>ATM</sub> and then solubilized in detergent. NPC1 was recovered from the lysate by immunoprecipitation and the immune complexes were analysed for GP1. The findings indicate that cleaved EboV GP<sub>ATM</sub> binds to NPC1 and that uncleaved EboV GP<sub>ATM</sub> does not (Fig. 3d).

Because the small molecules 3.0 and 3.47 inhibit infection of thermolysin-treated VSV EboV GP particles (Supplementary Fig. 1b) and inhibit cholesterol uptake from LE/LY into cells (Fig. 2a), both of which require NPC1, this suggests the possibility that these compounds directly target NPC1. To test this hypothesis, we synthesized the 3.47 derivative 3.98. This compound has anti-EboV activity and contains two additional functional moieties: an aryl-azide for photo-affinity labelling of target proteins and an alkyne for click conjugation with biotin<sup>21</sup> (Supplementary Fig. 7). Compound 3.98 was incubated with LE/LY membranes, activated by ultraviolet light and coupled to biotin. NPC1 was then isolated by immunoprecipitation and analysed using streptavidin–horseradish peroxidase. The findings show that NPC1 is cross-linked to 3.98 and that cross-linking is inhibited by the presence of 3.47 but not by the closely related analogue 3.18, which has weak antiviral activity (Fig. 4a and Supplementary Fig. 7). In addition, we observed that overexpression of NPC1 conferred resistance to the antiviral activity of 3.0 and 3.47 (Supplementary Fig. 8), thus providing additional functional evidence supporting the conclusion based on the results of the cross-linking experiment using 3.98 that NPC1 is a direct target of the antiviral compounds.

The evidence that NPC1 is the target of the 3.0-derived small molecules selected for anti-EboV activity indicated that these compounds may interfere with binding of cleaved GP to NPC1. Consistent with this hypothesis, we found that 3.0 and 3.47 inhibited binding of cleaved EboV GP<sub>ATM</sub> to NPC1 membranes in a concentration-dependent manner (Fig. 4b). Importantly, we observed a direct correlation between the potency of 3.47, 3.0 and 3.18 in inhibiting binding (Fig. 4b, left panel) and in inhibiting EboV infection (Supplementary Fig. 7). We also tested U18666A, a small molecule inhibitor of LE/LY cholesterol transport and membrane trafficking<sup>22,23</sup>, and found that it does not inhibit binding of cleaved EboV GP to NPC1 membranes (Fig. 4b, right panel). These results support the conclusion that the 3.0-derived compounds inhibit EboV infection by interfering with binding of cleaved GP to NPC1.

Previous studies show that cleavage of GP by endosomal cathepsin proteases removes heavily glycosylated domains in the GP1 subunit and exposes the N-terminal domain<sup>3–7</sup>. It has been proposed that binding of this domain to a host factor is essential for infection<sup>6,17–20</sup>. The most straightforward interpretation of the findings in this report is that NPC1 is this host factor. This conclusion is based on the observations that NPC1 is strictly required for infection, that cleaved GP1 binds to NPC1, and that small molecules that target NPC1 are potent inhibitors of binding and infection.

Analysis of the EboV GP structure shows that the residues in the N-terminal domain of GP1 that mediate binding to NPC1 are interspersed with the residues that make stabilizing contacts with GP2 (ref. 5). This structural feature is consistent with the possibility that binding of cleaved GP1 to NPC1 relieves the GP1-imposed constraints on GP2 and promotes virus fusion to the limiting membrane (Fig. 4c). The role of cathepsin proteases in cleavage of GP1 to expose the NPC1 binding site during EboV infection is analogous to the role of CD4 in inducing a conformational change in gp120 to expose the co-receptor binding site during human immunodeficiency virus infection<sup>8</sup>. An alternative possibility is that binding of protease-cleaved GP1 to NPC1 is an essential step in infection, but virus membrane fusion is not completed until an additional signal is received, possibly including further cleavage of GP by cathepsin proteases, as has been proposed<sup>3,4,9</sup>. These studies provide an example of how small molecules identified by screening and medicinal chemistry optimization can be used as molecular probes to analyse virus–host interactions.

## METHODS SUMMARY

Screening of small molecules was performed at the New England Regional Centers of Excellence for Biodefense and Emerging Infectious Diseases at Harvard Medical School. Infection was assayed using VSV pseudotyped viruses encoding green fluorescent protein (GFP) or luciferase. Experiments with native Ebola virus were performed under BSL-4 conditions at the United States Army Medical Research Institute for Infectious Diseases. Cells were infected with EboV Zaire-Mayinga GFP and growth was measured by mean fluorescence. EboV GP<sub>ATM</sub> is a derivative of EboV GP in which the transmembrane domain has been replaced by a GCN4-derived trimerization domain followed by a His<sub>6</sub> tag for purification. Late endosomes/lysosomes (LE/LY) were isolated by differential centrifugation and further purified by Percoll density gradient centrifugation. LE/LY were disrupted by incubation with methionine methyl ester and coated onto high binding ELISA plates. Following attachment, unbound LE/LY membranes were removed and plates were blocked. Bound membranes were incubated with the indicated amounts of native or thermolysin-cleaved EboV GP<sub>ATM</sub> protein. Unbound EboV GP<sub>ATM</sub> protein was removed, membranes were washed and bound EboV GP<sub>ATM</sub> protein was recovered in SDS loading buffer and analysed by immunoblot using GP1 antiserum. Where applicable, membranes were pre-incubated with 3.0, 3.47, 3.18 or vehicle before the addition of EboV GP<sub>ATM</sub>. To analyse EboV GP<sub>ATM</sub> binding to NPC1, LE/LY membranes were dissolved in 10 mM CHAPSO, NPC1 was recovered by immunoprecipitation, and the immune complexes were analysed by immunoblot using GP1 antiserum.

**Full Methods** and any associated references are available in the online version of the paper at [www.nature.com/nature](http://www.nature.com/nature).

**Received 19 March; accepted 19 July 2011.**

**Published online 24 August 2011.**

1. Zampieri, C. A., Sullivan, N. J. & Nabel, G. J. Immunopathology of highly virulent pathogens: insights from Ebola virus. *Nature Immunol.* **8**, 1159–1164 (2007).
2. Geisbert, T. W. & Jahrling, P. B. Exotic emerging viral diseases: progress and challenges. *Nature Med.* **10**, S110–S121 (2004).
3. Chandran, K., Sullivan, N. J., Felbor, U., Whelan, S. P. & Cunningham, J. M. Endosomal proteolysis of the Ebola virus glycoprotein is necessary for infection. *Science* **308**, 1643–1645 (2005).
4. Schornberg, K. *et al.* Role of endosomal cathepsins in entry mediated by the Ebola virus glycoprotein. *J. Virol.* **80**, 4174–4178 (2006).
5. Lee, J. E. *et al.* Structure of the Ebola virus glycoprotein bound to an antibody from a human survivor. *Nature* **454**, 177–182 (2008).
6. Dube, D. *et al.* The primed ebolavirus glycoprotein (19-kilodalton GP<sub>1,2</sub>): Sequence and residues critical for host cell binding. *J. Virol.* **83**, 2883–2891 (2009).
7. Hood, C. L. *et al.* Biochemical and structural characterization of cathepsin L-processed Ebola virus glycoprotein: Implications for viral entry and immunogenicity. *J. Virol.* **84**, 2972–2982 (2010).
8. Harrison, S. C. Viral membrane fusion. *Nature Struct. Mol. Biol.* **15**, 690–698 (2008).
9. Wong, A., Sandesara, R., Mulherkar, N., Whelan, S. & Chandran, K. A forward genetic strategy reveals destabilizing mutations in the ebolavirus glycoprotein that alter its protease dependence during cell entry. *J. Virol.* **84**, 163–175 (2010).
10. Kolter, T. & Sandhoff, K. Lysosomal degradation of membrane lipids. *FEBS Lett.* **584**, 1700–1712 (2010).
11. Du, X. *et al.* A role for oxysterol-binding protein-related protein 5 in endosomal cholesterol trafficking. *J. Cell Biol.* **192**, 121–135 (2011).
12. Chevallier, J. *et al.* Lysobisphosphatidic acid controls endosomal cholesterol levels. *J. Biol. Chem.* **283**, 27871–27880 (2008).
13. Ko, D. C., Gordon, M. D., Jin, J. Y. & Scott, M. P. Dynamic movements of organelles containing Niemann-Pick C1 protein: NPC1 involvement in late endocytic events. *Mol. Biol. Cell* **12**, 601–614 (2001).
14. Millard, E. E. *et al.* The sterol-sensing domain of the Niemann-Pick C1 (NPC1) protein regulates trafficking of low density lipoprotein cholesterol. *J. Biol. Chem.* **280**, 28581–28590 (2005).
15. Ohgami, N. *et al.* Binding between the Niemann-Pick C1 protein and a photoactivatable cholesterol analog requires a functional sterol-sensing domain. *Proc. Natl Acad. Sci. USA* **101**, 12473–12478 (2004).
16. Towner, J. S. *et al.* Newly discovered Ebola virus associated with hemorrhagic fever outbreak in Uganda. *PLoS Pathog.* **4**, e1000212 (2008).
17. Kuhn, J. H. *et al.* Conserved receptor-binding domains of Lake Victoria marburgvirus and Zaire ebolavirus bind a common receptor. *J. Biol. Chem.* **281**, 15951–15958 (2006).
18. Kaletsky, R. L., Simmons, G. & Bates, P. Proteolysis of the Ebola virus glycoproteins enhances virus binding and infectivity. *J. Virol.* **81**, 13378–13384 (2007).
19. Brindley, M. A. *et al.* Ebola virus glycoprotein 1: Identification of residues important for binding and postbinding events. *J. Virol.* **81**, 7702–7709 (2007).
20. Dube, D. *et al.* Cell adhesion-dependent membrane trafficking of a binding partner for the ebolavirus glycoprotein is a determinant of viral entry. *Proc. Natl Acad. Sci. USA* **107**, 16637–16642 (2010).
21. Ban, H. S. *et al.* Identification of HSP60 as a primary target of o-carboranylphenylphenoxyacetanilide, an HIF-1 $\alpha$  inhibitor. *J. Am. Chem. Soc.* **132**, 11870–11871 (2010).

22. Sobo, K. *et al.* Late endosomal cholesterol accumulation leads to impaired intra-endosomal trafficking. *PLoS ONE* **2**, e851 (2007).
23. Huynh, K. K., Gershenson, E. & Grinstein, S. Cholesterol accumulation by macrophages impairs phagosome maturation. *J. Biol. Chem.* **283**, 35745–35755 (2008).
24. Saeed, M. F., Kolokoltsov, A. A., Albrecht, T. & Davey, R. A. Cellular entry of Ebola virus involves uptake by a macropinocytosis-like mechanism and subsequent trafficking through early and late endosomes. *PLoS Pathog.* **6**, e1001110 (2010).
25. Nanbo, A. *et al.* Ebolavirus is internalized into host cells via macropinocytosis in a viral glycoprotein-dependent manner. *PLoS Pathog.* **6**, e1001121 (2010).

**Supplementary Information** is linked to the online version of the paper at [www.nature.com/nature](http://www.nature.com/nature).

**Acknowledgements** We thank B. Considine, A. Nilsson and S. Wilkes for assistance, S. Chiang for critical reading of the manuscript, G. Beltz, N. Gray, S. Grinstein, Y. Iannou, R. Infante, J. Kornhuber, F. Sharom and S. Whelan for discussion. This work was supported by grants from U54 AI057159, R01 CA104266 to J.C., PIDS-Sanofi-Pasteur Fellowship, K12-HD052896 and 5K08AI079381 to J.M., 5-T32-HL007623 to A.B., and

fellowship from Fonds de la Recherche en Santé du Québec to M.C.; C.M.F. was supported by the Postgraduate Research Participation Program at the US Army Medical Research and Materiel Command administered by the Oak Ridge Institute for Science and Education through an interagency agreement between the US Department of Energy and USAMRMC.

**Author Contributions** M.C., J.M., T.R. and A.B. equally contributed to this work. K.C. and T.R. performed the inhibitor screen. K.L. synthesized and purified 3.0 analogues and T.R. tested them. T.R., A.B., J.M., Q.L. and M.C. carried out infection assays with pseudotyped viruses. A.B. performed microscopy. J.M. purified recombinant glycoprotein. M.C. and J.M. designed and performed binding assays. M.C. performed immunoprecipitation. D.O. provided NPC1 constructs, antibodies and CHO cell lines. Ebola virus infections were performed in the lab of L.H. by C.M.F.; J.C. supervised the project and wrote the manuscript. All authors reviewed the manuscript.

**Author Information** Reprints and permissions information is available at [www.nature.com/reprints](http://www.nature.com/reprints). The authors declare no competing financial interests. Readers are welcome to comment on the online version of this article at [www.nature.com/nature](http://www.nature.com/nature). Correspondence and requests for materials should be addressed to J.C. ([jcunningham@rics.bwh.harvard.edu](mailto:jcunningham@rics.bwh.harvard.edu)).

## METHODS

**Cell lines.** Vero, 293T, HeLa (ATCC) and human fibroblasts<sup>26</sup> (Coriell) were maintained in DMEM (Invitrogen) supplemented with 5% FetalPlex, 5% FBS (Gemini) or 10% FBS (HeLa, human fibroblasts). All CHO derived cell lines were grown as previously described<sup>14,27</sup>. We have designated the CHO-K1 cell line as CHO<sub>wt</sub>, CHO-M12 as CHO<sub>null</sub>, CHO-wt8 as CHO<sub>NPC1</sub>, and the CHO-derived cell lines expressing NPC1 mutants as CHO NPC1 P692S, CHO NPC1 L657F, and CHO NPC1 D787N. CHO/NPC1-1, designated here as CHO hNPC1, expresses high levels of human NPC1 (ref. 27).

**Antibodies.** Rabbit polyclonal anti-serum was raised against a peptide corresponding to residues 83 to 98 of Ebola virus Zaire Mayinga GP1 (TKRWGFRSGVPPKVVC). Antibodies to NPC1 and V-ATPase B1/2 were obtained from Abcam and Santa Cruz, respectively.

**Expression plasmids.** Mucin domain-deleted EboV Zaire Mayinga GP (EboV GP) and VSV G were previously described<sup>3</sup>. Plasmids encoding Côte d'Ivoire-Ivory Coast GP, Sudan-Boniface GP, Reston-Penn. GP and Marburg-Musoke GP were obtained from Anthony Sanchez and the mucin domain-deleted ( $\Delta$ Muc) derivatives were created: Zaire $\Delta$ Muc GP (amino acids 309–489 deleted), Côte d'Ivoire $\Delta$ Muc GP (amino acids 310–489 deleted), Sudan $\Delta$ Muc GP ( $\Delta$ a.a. 309–490), and Reston $\Delta$ Muc GP amino acids 310–490 deleted). Bundibungyo-Uganda viral RNA was TRIzol-extracted and PCR was used to generate a construct that expresses a mucin-deleted GP (amino acids 309–489 deleted). A plasmid encoding Lassa fever virus GP1 was kindly provided by G. Nabel. A codon-optimized sequence encoding GP2 was generated and combined with the GP1 sequence in pCAGGS to complete a GP expression vector.

**Production and purification of pseudotyped virions.** VSV- $\Delta$ G pseudotyped viruses were created as described previously<sup>3</sup>. LacZ-encoding retroviral pseudotypes bearing the designated envelope glycoproteins were prepared as previously described<sup>28</sup>.

**Thermolysin digestion of EboV GP Virus and EboV GP<sub>ATM</sub>.** Purified EboV GP<sub>ATM</sub> (50  $\mu$ g ml<sup>-1</sup>) or VSV particles pseudotyped with EboV GP were incubated at 37 °C for 1 h with the metalloprotease thermolysin (Sigma, 0.2 mg ml<sup>-1</sup>) in NT buffer (10 mM Tris-HCl pH 7.5, 135 mM NaCl). The reaction was stopped using 500  $\mu$ M phosphoramidon (Sigma) at 4 °C. Cleaved EboV GP<sub>ATM</sub> was stored in phosphate buffered saline supplemented with 1 mM EDTA, 1 mM PMSF (Sigma) and 1 $\times$  EDTA-Free Complete Protease Inhibitor Cocktail (Roche).

**Infection assays with pseudotyped virus.** VSV pseudotyped viruses expressing GFP were added to cells in serial tenfold dilutions and assayed using fluorescence microscopy. An infectious unit (i.u.) is defined as one GFP-expressing cell within a range where the change in GFP-positive cells is directly proportional to the virus dilution. For VSV expressing the luciferase reporter, pseudotyped virus was added to cells and luciferase activity was assayed 6–20 h post-infection using the firefly luciferase kit (Promega). Signal was measured in relative luminescence units (RLU) using an EnVision plate reader (Perkin Elmer). In experiments involving inhibitors, stock solutions of 3.0 (20 mM) and 3.47 (10 mM) in DMSO were diluted to a final concentration of 1% DMSO in media. Inhibitory activity was stable in the media of cultured cells for more than 72 h as assessed using a single cycle entry assay. Infection of target cells with LacZ-encoding retroviral pseudotypes was performed in the presence of 5  $\mu$ g ml<sup>-1</sup> polybrene (Sigma). Seventy-two hours post-infection, cells were stained for LacZ activity and titre was determined by counting positive foci and expressed as focus forming units (FFU) per ml of virus.

**Ebola virus infections under BSL-4 conditions.** Vero cells or CHO cells were seeded to 96-well plates and exposed to EboV-GFP<sup>29</sup>. Vero cells were incubated with 3.0 (40  $\mu$ M), 3.47 (40  $\mu$ M), E-64-d (150  $\mu$ M) or 1% DMSO 90 min before the addition of virus (m.o.i. = 0.1). Virus was added to CHO cells at m.o.i. of 1 as measured on Vero cells. Virus-encoded GFP fluorescence was determined using a SpectraMax M5 plate reader (Molecular Devices) at excitation 485 nm, emission 515 nm, cutoff 495 nm at 22.5, 42, 71 and 97 h post-infection. An additional inhibitor experiment was performed using 3.0. Vero cells were treated with 3.0 (20  $\mu$ M) or 1% DMSO alone for 4 h, and then infected with EBOV Zaire-1995 (m.o.i. = 0.1). After 1 h, the virus inoculum was removed, cells were washed, and fresh media containing 3.0 or DMSO was added. Cell supernatant was collected at 0, 24, 48, 72, or 91 h post-infection. RNA was isolated from the supernatant using Virus RNA Extraction kits (Qiagen) and EboV NP RNA was measured using a real-time RT-PCR assay<sup>30</sup>. Virus titre was calculated using a standard curve obtained using a virus stock of known titre as determined by plaque assay.

**Screen for Ebola virus entry inhibitors.** Screening of small molecules was performed at the New England Regional Centers of Excellence for Biodefense and Emerging Infectious Diseases at Harvard Medical School. Vero cells were seeded in 384-well plates at a density of  $5 \times 10^3$  cells per well using a Matrix WellMate (Thermo Scientific). The ChemBridge3, ChemDiv4, ChemDiv5 and Enamine2 compound libraries were transferred by robotics to the assay plates using stainless

steel pin arrays. The compounds were screened at a constant dilution to achieve a final concentration between 10  $\mu$ M and 60  $\mu$ M. After incubation for 2 h at 37 °C, viruses were dispensed into each well (m.o.i. = 1) and incubated for an additional 6 h to allow virus gene expression. Cells were lysed by addition of Steady-Glo (Promega) and after 10 min at room temperature luminescence was measured using an EnVision plate reader. Each compound was tested in duplicate. Candidate compounds that inhibited EboV GP infection by more than 80% were analysed for potency, selectivity and absence of cytotoxicity (using Cyto-Tox assay, Promega) and 3.0 (2-((3r,5r,7r)-adamantan-1-yl)-N-(2-(4-benzylpiperazin-1-yl)-2-oxoethyl)acetamide) was identified. The antiviral activity of the inhibitors was verified on human cells (HeLa, A549, 293T), mouse embryonic fibroblasts and Chinese hamster ovary cells.

**Synthesis of 3.0 derivatives.** Compound 3.47 (methyl 4-((2-((4-(2-((3r,5r,7r)-adamantan-1-yl)acetamido)acetyl)piperazin-1-yl)methyl)phenoxy)methyl)benzoate) was prepared via a multi-step synthesis starting from N-Cbz-piperazine. Thus, coupling of N-Cbz-piperazine with N-Boc-glycine followed by removal of the Boc group under acidic conditions yielded 4-Cbz-piperazine glycineamide. After acylation of the terminal amine with adamantan-1-acetyl chloride, the Cbz group was removed by hydrogenolysis to give (1-(adamantan-1-yl)acetamido)acetyl piperazine. The piperazine was then benzylated via reductive amination with 2-(4-methoxycarbonyl)benzyloxybenzaldehyde using sodium triacetoxyborohydride to provide 3.47. Compound 3.18 was synthesized in a similar fashion. Compound 3.98 was prepared via a multi-step synthesis as follows. First, 2-hydroxy-5-nitrobenzaldehyde was alkylated by 4-ethynylbenzyl bromide in the presence of potassium carbonate in DMF. Resulting benzyloxy aldehyde underwent reductive amination with 2-((3r,5r,7r)-adamantan-1-yl)-N-(2-oxo-2-(piperazin-1-yl)ethyl)acetamide using sodium triacetoxyborohydride. The nitro group was then reduced to aniline (SnCl<sub>2</sub>), diazotized (NaNO<sub>2</sub>), and the diazonium finally converted to azide to yield 3.98. See Supplementary Information for detailed experimental procedures and characterization data.

**Protease inhibitors and protease activity assays.** The measurement of cathepsin B activity and the use of the inhibitor CA074 (Sigma) have been previously described<sup>3</sup>.

**Detection of intracellular cholesterol.** Cells were stained with filipin (50  $\mu$ g ml<sup>-1</sup>, Cayman Chemical) as previously described<sup>14</sup>. Images of stained cells were obtained using epifluorescence microscopy (Nikon Eclipse TE2000U). The images in the supplementary figures were processed using ImageJ software.

**Production and purification of EboV GP<sub>ATM</sub> soluble protein.** EboV GP<sub>ATM</sub> is a derivative of the mucin-deleted EboV Zaire-Mayinga GP in which the trans-membrane domain and carboxy terminus (amino acids 657–676) has been replaced by a GCN4-derived trimerization domain (MKQIEDKIEELISKIYHIEN EIARIKKLIGEV) and a His<sub>6</sub> tag. The expression plasmid encoding EboV GP<sub>ATM</sub> was transfected into 293T cells using lipofectamine2000. Eighteen to twenty-four hours later the culture medium was replaced with 293FSFMI (Invitrogen) supplemented with 1 $\times$  non-essential amino acids and 2 mM CaCl<sub>2</sub> and collected daily for 4 days. Media containing soluble EboV GP<sub>ATM</sub> was filtered and PMSF (1 mM)/1 $\times$  EDTA-Free Complete Protease Inhibitor Cocktail was added. EboV GP<sub>ATM</sub> was purified by affinity chromatography using Ni-NTA agarose beads (Qiagen), dialysed against PBS using a 3 kDa dialysis cartridge (Pierce) and stored at –80 °C. Purity and integrity of EboV GP<sub>ATM</sub> were analysed by SDS-PAGE.

**Membrane binding assay.** Indicated cells were washed with PBS twice, scraped in homogenization (HM) buffer (0.25 M sucrose, 1 mM EDTA, 10 mM HEPES pH 7.0), and disrupted with a Dounce homogenizer. Nuclei and debris were pelleted by centrifugation at 1,000g for 10 min. The post-nuclear supernatant was centrifuged at 15,000g for 30 min at 4 °C and the pellet, containing the LE/LY, was resuspended in a total volume of 0.9 ml composed of 20% Percoll (Sigma) and 0.4% BSA (Sigma) in HM and centrifuged at 36,000g for 30 min at 4 °C. Fractions (0.150 ml) were collected from the bottom to the top of the tube and those containing the highest  $\beta$ -N-acetylglucosamidase activity, as assessed by release of 4-methylumbelliferone from 4-methylumbelliferyl-N-acetyl- $\beta$ -D-glucosaminide (Sigma), were pooled and incubated in 20 mM methionine methyl-ester (Sigma) for 1 h at room temperature. Following LE/LY disruption, 1 $\times$  EDTA-Free Complete Protease Inhibitor Cocktail and 1 mM PMSF was added. The amount of purified LE/LY membranes used for the binding assay was normalized using the activity of the marker  $\beta$ -N-acetylglucosamidase and validated by immunoblot using V-ATPase B1/2 antibody (Supplementary Fig. 5).

Disrupted LE/LY membranes were coated on high-binding ELISA plates (Corning) overnight at 4 °C. Unbound membranes were removed and wells containing bound membranes were blocked for 2 h at room temperature with binding buffer (PBS, 5% FBS, 1 mM PMSF, 1 mM EDTA, 1 $\times$  Complete Protease Inhibitor Cocktail). The indicated amount of purified EboV GP<sub>ATM</sub>, pretreated or not with thermolysin, in binding buffer was added to each well and incubated for 1 h at room temperature. Unbound proteins were removed and wells were washed three



times with PBS. Membrane-bound EboV GP<sub>ATM</sub> was solubilized in SDS-loading buffer. Bound and unbound EboV GP<sub>ATM</sub> were detected by immunoblot using the EboV GP1 anti-serum. For binding assays in the presence of inhibitors, the immobilized membranes were pre-incubated at room temperature with the inhibitor or vehicle (10% DMSO) in binding buffer. After 30 min, thermolysin-cleaved EboV GP<sub>ATM</sub> was added in the continuous presence of compound and bound and unbound GP was measured as described above.

**Co-immunoprecipitation.** CHO<sub>null</sub> and CHO<sub>hNPC1</sub> cells were homogenized as described above. The 15,000g membrane pellet was resuspended in HM buffer and protein content was measured using the BCA assay (Pierce). The LE/LY membranes contained in the 15,000g resuspended pellet were disrupted by incubation with 20 mM methionine methyl-ester for 1 h at room temperature. Membranes of equal protein content were incubated with indicated amounts of EboV GP<sub>ATM</sub>, pre-treated or not with thermolysin, for 1 h at room temperature in the presence of Complete Protease Inhibitor Cocktail (Roche) and incubated for an additional hour on ice before the addition of membrane lysis buffer (12.5 mM CHAPSO, 150 mM NaCl, 1 mM EDTA, 10 mM Tris/HCl pH 7.4) for a final concentration of 10 mM CHAPSO. Proteins were solubilized on ice for 20 min and debris was removed by centrifugation at 12,000g for 10 min at 4 °C. The soluble membrane lysates were incubated with anti-NPC1 antibody for 1 h at 4 °C and then incubated with Protein A-agarose beads (Sigma) for an additional 4 h at 4 °C. Beads were then washed three times with 8 mM CHAPSO, 150 mM NaCl, 1 mM EDTA, 10 mM Tris/HCl pH 7.4 and immunoprecipitated product was eluted by incubation in 0.1 M glycine pH 3.5 for 5 min at room temperature. The eluted complex was then neutralized and analysed by immunoblot using the indicated antibody.

**Photo-activation and click chemistry.** Photo-activation and click chemistry were performed as described previously with some modifications<sup>21</sup>. Briefly, the 15,000g pellets from homogenized CHO<sub>hNPC1</sub> or CHO<sub>null</sub> cells were resuspended in PBS and incubated with the indicated concentrations of 3.47, 3.18 or DMSO for 10 min at room temperature. Membranes were then incubated with 25 µM of 3.98 for an additional 10 min and exposed to ultraviolet light (365 nm) for 1 min on ice. Proteins were solubilized in lysis buffer (1% Triton X-100, 0.1% NP-40, 20 mM HEPES pH 7.4) containing protease inhibitors and 150 µM of biotin-azide (Invitrogen) was added, followed by 5 mM L-ascorbic acid. The cycloaddition reaction (click chemistry) was initiated by the addition of 1 mM CuSO<sub>4</sub> and samples were incubated for 3 h at room temperature. NPC1 was immunoprecipitated and the product was resolved by SDS-PAGE, transferred to PVDF membrane, and analysed for conjugation of 3.98 to NPC1 using streptavidin–horseradish peroxidase (Sigma).

26. Gelsthorpe, M. E. *et al.* Niemann-Pick type C1 I1061T mutant encodes a functional protein that is selected for endoplasmic reticulum-associated degradation due to protein misfolding. *J. Biol. Chem.* **283**, 8229–8236 (2008).
27. Millard, E. E., Srivastava, K., Traub, L. M., Schaffer, J. E. & Ory, D. S. Niemann-pick type C1 (NPC1) overexpression alters cellular cholesterol homeostasis. *J. Biol. Chem.* **275**, 38445–38451 (2000).
28. Soneoka, Y. *et al.* A transient three-plasmid expression system for the production of high titer retroviral vectors. *Nucleic Acids Res.* **23**, 628–633 (1995).
29. Towner, J. S. *et al.* Generation of eGFP expressing recombinant Zaire ebolavirus for analysis of early pathogenesis events and high-throughput antiviral drug screening. *Virology* **332**, 20–27 (2005).
30. Weidmann, M., Mühlberger, E. & Hufert, F. T. Rapid detection protocol for filoviruses. *J. Clin. Virol.* **30**, 94–99 (2004).

# Evidence for several waves of global transmission in the seventh cholera pandemic

Ankur Mutreja<sup>1\*</sup>, Dong Wook Kim<sup>2,3\*</sup>, Nicholas R. Thomson<sup>1\*</sup>, Thomas R. Connor<sup>1</sup>, Je Hee Lee<sup>2,4</sup>, Samuel Kariuki<sup>5</sup>, Nicholas J. Croucher<sup>1</sup>, Seon Young Choi<sup>2,4</sup>, Simon R. Harris<sup>1</sup>, Michael Lebens<sup>6</sup>, Swapn Kumar Niyogi<sup>7</sup>, Eun Jin Kim<sup>2</sup>, T. Ramamurthy<sup>7</sup>, Jongsik Chun<sup>4</sup>, James L. N. Wood<sup>8</sup>, John D. Clemens<sup>2</sup>, Cecil Czerkinsky<sup>2</sup>, G. Balakrish Nair<sup>7</sup>, Jan Holmgren<sup>6</sup>, Julian Parkhill<sup>1</sup> & Gordon Dougan<sup>1</sup>

*Vibrio cholerae* is a globally important pathogen that is endemic in many areas of the world and causes 3–5 million reported cases of cholera every year. Historically, there have been seven acknowledged cholera pandemics; recent outbreaks in Zimbabwe and Haiti are included in the seventh and ongoing pandemic<sup>1</sup>. Only isolates in serogroup O1 (consisting of two biotypes known as ‘classical’ and ‘El Tor’) and the derivative O139 (refs 2, 3) can cause epidemic cholera<sup>2</sup>. It is believed that the first six cholera pandemics were caused by the classical biotype, but El Tor has subsequently spread globally and replaced the classical biotype in the current pandemic<sup>1</sup>. Detailed molecular epidemiological mapping of cholera has been compromised by a reliance on sub-genomic regions such as mobile elements to infer relationships, making El Tor isolates associated with the seventh pandemic seem superficially diverse. To understand the underlying phylogeny of the lineage responsible for the current pandemic, we identified high-resolution markers (single nucleotide polymorphisms; SNPs) in 154 whole-genome sequences of globally and temporally representative *V. cholerae* isolates. Using this phylogeny, we show here that the seventh pandemic has spread from the Bay of Bengal in at least three independent but overlapping waves with a common ancestor in the 1950s, and identify several transcontinental transmission events. Additionally, we show how the acquisition of the SXT family of antibiotic resistance elements has shaped pandemic spread, and show that this family was first acquired at least ten years before its discovery in *V. cholerae*.

Whole-genome analysis is perhaps the ultimate approach to building a robust phylogeny in recently emerged pathogens, through the identification of SNPs and other rare genetic variants<sup>4</sup>. Therefore, we sequenced the genomes of 136 isolates of *V. cholerae*, the causative agent of several million cholera cases each year (<http://www.who.int/mediacentre/factsheets/fs107/en/>). These sequences, including 113 isolates from the seventh pandemic, were added to 18 previously published genomes<sup>1,2,5</sup> to produce a global genomic database from isolates collected in the course of a century. We included representative El Tor isolates collected in the past four decades and compared these to previously reported and novel genome sequences of both classical and non-O1 types<sup>1,2</sup>.

The sequence reads were mapped to the reference sequence of El Tor N16961 (ref. 6), a seventh-pandemic *V. cholerae* that was isolated in Bangladesh in 1975 (see footnote to Supplementary Table 1) and the resulting consensus tree identified eight distinct phyletic lineages (L1–L8, see Supplementary Fig. 1 and Supplementary Table 1 for strain and lineage information), six of which incorporated O1 clinical isolates. The classical isolates formed a distinct, highly clustered group (L1), distant from the El Tor isolates of the seventh pandemic (L2). It is clear

from Supplementary Fig. 1 that the classical and El Tor clades did not originate from a recent common ancestor and instead seem to be independent derivatives with distinct phylogenetic histories, consistent with previous proposals<sup>2</sup>. Isolates of L4 share a common ancestor with previously reported non-conventional O1 isolates<sup>2</sup> (Supplementary Fig. 2), and are likely to have acquired the O1 antigen genes by a recombination event onto a genetically distinct genome backbone. Isolates of L7 also have a distinct backbone, whereas L2, L3 (USA gulf coast strains), L5, L6 and L8 share a more ‘El-Tor-like’ genome backbone, and the L1 backbone is of the ‘classical’ type.

Genome-wide SNP analysis showed that the 123 El Tor isolates in the L2 cluster (Supplementary Fig. 1) differed from the reference by only 50–250 SNPs. With this large sample size we were able to construct a high-resolution phylogeny that shows unequivocally that the current pandemic is monophyletic and originated from a single source, providing a framework for future epidemiological and phenotypic analysis of *V. cholerae*, including transmission-tracking and typing.

Predicted recombined regions were identified, and along with genomic islands and mobile genetic elements, these were initially excluded from the phylogenetic analysis of seventh-pandemic isolates, to determine the underlying phylogeny. Notably, analysis of the tree (Fig. 1; see Supplementary Fig. 3 for a tree with strain names) provides clear evidence of a clonal expansion of the lineage, with a strong temporal signature. This is most clearly illustrated by the fact that the most divergent isolates from the N16961 reference are represented by the oldest seventh-pandemic isolate in our collection, A6, collected in 1957, together with the most recent Haitian isolates<sup>5</sup> from late 2010. We performed a linear regression analysis on all the L2 isolates to calculate the rate of SNP accumulation on the basis of the date of isolation and the root-to-tip distance. The shape of the tree and temporal signatures in Fig. 1 show a very consistent rate of SNP accumulation, 3.3 SNPs year<sup>-1</sup> ( $R^2 = 0.73$ , Supplementary Fig. 4) in the core genome, emphasizing the tree’s robustness and utility for transmission studies. The only exception to this is *V. cholerae* A4, a repeatedly passaged laboratory strain that was originally isolated in 1973 (Supplementary Figs 3 and 4). The estimated rate of mutation for our seventh-pandemic *V. cholerae* collection was  $8.3 \times 10^{-7}$  SNPs site<sup>-1</sup> year<sup>-1</sup>: between 5 and 2.5 times slower than the rate estimated for recent clonal expansions of some other human-pathogenic bacteria<sup>4,7</sup>.

The seventh-pandemic tree can be subdivided into three major groups or clades by clustering using Bayesian analysis of population structure<sup>8,9</sup> (shown as waves 1–3 in Fig. 1); this clustering is mostly consistent with the cholera toxin (CTX) type of the three clades, which represent independent waves of transmission. Although examples of

<sup>1</sup>Wellcome Trust Sanger Institute, Wellcome Trust Genome Campus, Hinxton, Cambridge CB10 1SA, UK. <sup>2</sup>International Vaccine Institute, SNU Research Park, Bongcheon 7 dong, Kwanak, Seoul 151-919, Korea. <sup>3</sup>Department of Pharmacy, College of Pharmacy, Hanyang University, Kyeonggi-do 426-791, Korea. <sup>4</sup>Seoul National University, 1 Gwanak-ro, Gwanak-gu, Seoul 151-742, Korea. <sup>5</sup>Centre for Microbiology Research, KEMRI at Kenyatta Hosp Compound, Off Ngong Road, PO Box 43640-00100, Kenya. <sup>6</sup>Department of Microbiology and Immunology and University of Gothenburg Vaccine Research Institute, The Sahlgrenska Academy at the University of Gothenburg, Box 435, 40530 Göteborg, Sweden. <sup>7</sup>National Institute of Cholera and Enteric Diseases, P-33, CIT Scheme XM, Beliaghata, Kolkata 700 010, India. <sup>8</sup>University of Cambridge, Department of Veterinary Medicine, Madingley Road, Cambridge CB3 0ES, UK.

\*These authors contributed equally to this work.

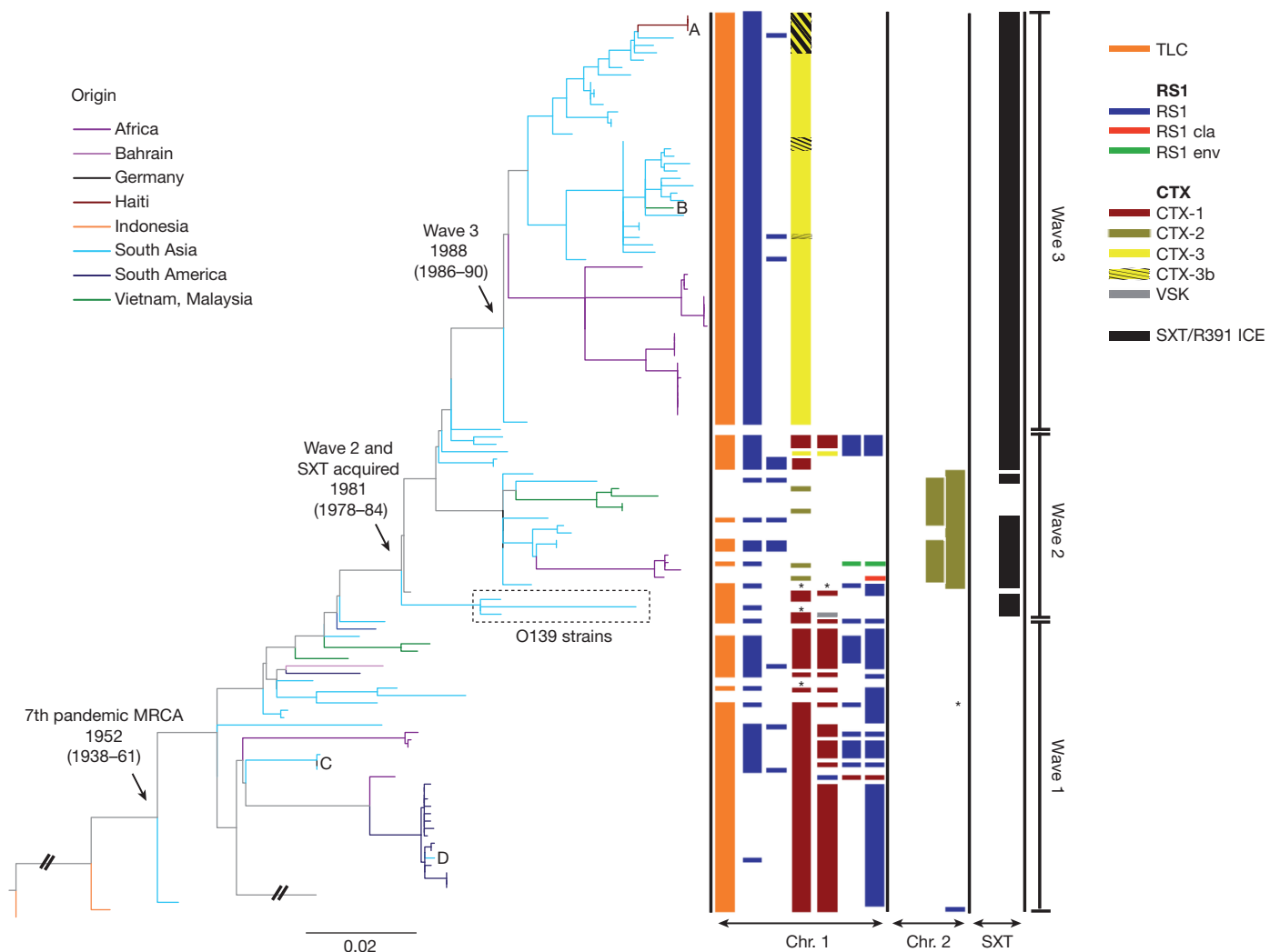


**Figure 1 | A maximum-likelihood phylogenetic tree of the seventh pandemic lineage of *V. cholerae* based on SNP differences across the whole core genome, excluding probable recombination events.** The pre-seventh-pandemic isolate M66 was used as an outgroup to root the tree. Branches are coloured on the basis of the region of isolation of the strains. The branches representing the three major waves are indicated on the far right. The nodes representing the MRCAs of the seventh pandemic, and subsequent waves 2 and 3, are indicated with arrows and labelled with inferred dates. The presence and

type of CTX and SXT elements in each strain are shown to the right of the tree. The presence of toxin-linked cryptic (TLC) and repeated sequence 1 (RS1) elements is shown, but their number and position, respectively, are arbitrarily assigned. Cases of sporadic intercontinental transmission are marked A–D. The dates shown are the median estimates for the indicated nodes, taken from the results of the BEAST analysis. The scale is given as the number of substitutions per variable site; asterisks indicate that no data were available.

genetic determinants differentiating these three CTX types have previously been published<sup>10</sup>, they have not been put into a phylogenetic context, undermining efforts to investigate the evolutionary aspects of their emergence. Perhaps as a result, there has been substantial uncertainty in naming new CTX types as they have been discovered. Our data shows that the first CTX type is canonical CTX El Tor and we propose that it is renamed CTX-1; for the other two we propose a new expandable nomenclature and class them as CTX-2 and CTX-3 (Supplementary Table 2).

Isolates spanning A18 to PRL5 (the lower clade in Fig. 1) represent wave 1, covering about 16 years (1977–1992). All isolates in this group lack the integrative and conjugative element (ICE) of the SXT/R391 family, encoding resistance to several antibiotics<sup>11,12</sup>. It is within this time period that seventh-pandemic cholera occurred in South America<sup>6</sup>. Our data show that the South American isolates form a discrete cluster, which also includes a single Angolan isolate collected in 1989. The position of the Angolan isolate at the base of the South American group indicates that transmission to South America may have been via Africa, as previously proposed<sup>13</sup>. We used BEAST<sup>14</sup> to translate evolutionary distance in SNPs into time (Supplementary

Fig. 5) and this indicated that transmission to South America is likely to have occurred between 1981 and 1985. The branch harbouring this West African–South American (WASA) clade is distinguished from all other *V. cholerae* by the acquisition of novel VSP-2 genes<sup>15</sup> and a novel genomic island that we have denoted WASA1 (Supplementary Table 3). Notably, the Angolan isolate A5 and all the South American isolates are discriminated by just ten SNPs. Based on the accumulation rate of 3.3 SNPs year<sup>-1</sup> (Supplementary Fig. 4), the 3-year time period between the isolation of A5 and the oldest South American isolate included in this study, A32, is consistent with previous studies indicating that cholera spread as a single epidemic<sup>13</sup>.

The first acquisition of an SXT/R391 ICE lies at the point of transition from the wave-1 cluster to the wave-2 cluster. Using our dated phylogeny (Supplementary Fig. 5)<sup>14</sup>, we were able to date this transition and the first acquisition of SXT/R391 ICE to 1978–84, ten years before its discovery in O139 strains, which also fits with the otherwise surprising discovery of SXT in a Vietnamese strain isolated before 1992 (ref. 16). This date would also correspond to the most recent common ancestor (MRCA) of the O1 and O139 serogroup isolates. Analysis of the diversity of the common regions of SXT/R391 ICEs in



our seventh-pandemic collection (Supplementary Fig. 6) shows that they are discriminated by 3,161 SNPs, compared to only 1,757 SNPs used to define the core whole-genome phylogeny in Fig. 1. This indicates either that there have been several recombination events within these ICEs, or that they have been acquired independently several times on the tree<sup>11</sup>. Isolates from wave 2 represent a discrete cluster that shows a complex pattern of accessory elements in the CTX locus (Fig. 1) and a wide phylogeographical distribution. It is also notable that isolates collected in Vietnam in 1995–2004 and strain A109 are the only wave-2 isolates studied from this time period that lack an SXT/R391 ICE. We examined the genomic locus in these clones that marks the point of insertion of SXT/R391 ICE in all other *V. cholerae* isolates and found no remnants of this conjugative element, which may have been lost from this lineage (no ‘scar’ in DNA sequence is expected after the precise excision of SXT/R391 ICE).

Ignoring the CTX-related genomic regions, the seventh-pandemic L2 isolates show relatively little evidence of recombination either within or from outside the tree. On the basis of the SNP distribution, 1,930 out of 2,027 SNPs (Supplementary Table 4) are congruent with the tree, leaving 97 homoplasies that could be due to selection or homologous recombination among the L2 isolates. Only 270 SNPs were predicted to be due to homologous recombination from outside the tree. The only two branches in which the SNP distribution indicated considerable recombination were those leading to the WASA cluster (Supplementary Fig. 7) and the O139 serogroup. Aside from the acquisitions of CTX and the SXT/R391 ICEs, we found evidence of gene flux affecting only 155 other genes (Supplementary Figs 8 and 9 and Supplementary Table 3).

Also represented in our collection are two isolates of serogroup O139, which are known to have arisen from a homologous replacement of their O-antigen determinant into an El Tor genomic backbone<sup>2,3,13</sup>. CTX types that are different from El Tor, classical, CTX-2 and CTX-3 have been reported for the O139 serogroup<sup>17–20</sup>; however, the phylogenetic position of the two strains included in this study shows that O139 was derived from O1 El Tor and therefore represents another distinct but spatially restricted wave from the common source.

We were also able to date the ancestor of the El Tor seventh-pandemic lineage, L2, as having existed in 1827–1936 (Supplementary Fig. 5), which is consistent with the predicted date of origin from the linear regression plot (1910, Supplementary Fig. 4). This also

corresponds well with the date of isolation of the first El Tor biotype strain in 1905 (ref. 21).

It is apparent from Fig. 1 that *V. cholerae* wave 1, which spread globally, was later replaced by the more geographically restricted wave 2 and wave 3, a phenomenon supported by local clinical observations and phage analysis<sup>10</sup>. This also reflects the fact that *V. cholerae* epidemics since 2003–2010 have been restricted to Africa and south Asia. Notably, the rates of SNP accumulation calculated independently for wave 1, wave 3 and wave 2 (2.3, 2.6 and 3.5 SNPs year<sup>-1</sup> respectively) are consistent with the rate calculated over the whole collection period (Supplementary Fig. 4).

The clonal clustering of L2 isolates, the constant rate of SNP accumulation and the temporal and geographical distribution support the concept that the seventh pandemic has spread by periodic radiation from a single source population located in the Bay of Bengal, followed by local evolution and ultimately local extinction in non-endemic areas. This is evidenced by the disappearance of wave-1 isolates, followed by the independent expansion of waves 2 and 3, both derived from the same original population, occurring within seven years of each other. These two waves are clearly distinguished from the first by the acquisition of SXT/R391 ICEs (Fig. 1). Plotting the intercontinental spread of each wave onto the world map (Fig. 2) clearly shows that the *V. cholerae* seventh pandemic is sourced from a single, restricted geographical location but has spread in overlapping waves. In these ancestral waves, there are at least four recent long-range transmission events (A–D in Fig. 1), in which isolates clearly share a common ancestor with recent strains at distant locations, indicating that such events are not uncommon. The most recent example of this is the Haitian outbreak, in which strains share a very recent common ancestor with south-Asian strains at the tip of wave 3. The number of SNP differences, even at whole-genome resolution, between the Haitian and the most closely related Indian and Bangladeshi strains is very low. This demonstrates that the Haitian strains must have come from south Asia, at most within the last six years. However, the limited discrimination means that it may prove challenging to make country-specific inferences as to the origins of the Haitian strains on the basis of DNA sequence alone. For such conclusions to be robust, great care must be taken in the selection of samples for analysis.

Despite clear evidence of sporadic long-range transmission events that are likely to be associated with direct human carriage, the overall pattern seen in our data is one of continued local evolution of *V. cholerae* in the

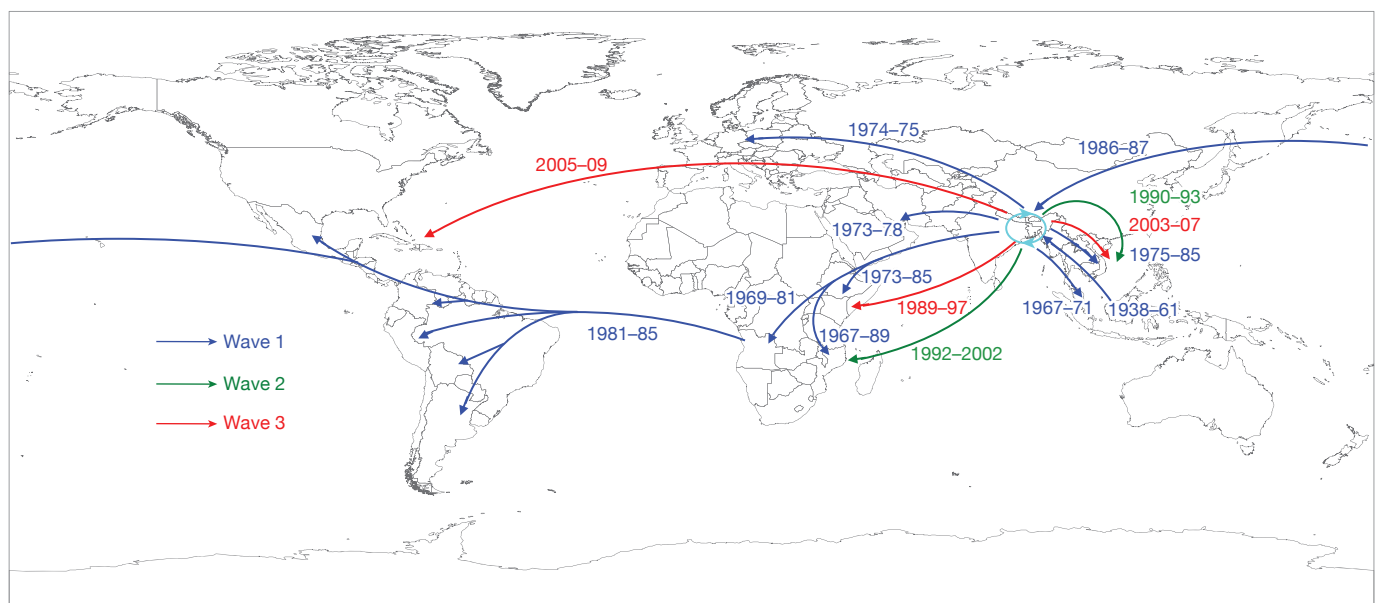


**Figure 2 | Transmission events inferred for the seventh-pandemic phylogenetic tree, drawn on a global map.** The date ranges shown for transmission events are taken from the BEAST analysis, and represent the

median values for the MRCA of the transmitted strains (later bound), and the MRCA of the transmitted strains and their closest relative from the source location (earlier bound).

Bay of Bengal, with several independent waves of global transmission resulting in short-term epidemics in non-endemic countries. Although our sample set is substantial, there are clearly areas where geographical coverage is limited. However, the structure of the tree, with deep branches between the major waves, means that increasing the number of strains and the resolution further should only identify further independent waves of transmission. Indeed, we cannot rule out the possibility of an El Tor population persisting or evolving as a new wave of the seventh pandemic; for example, in areas such as China that were not sampled in this study.

One notable factor in the ongoing evolution of pandemic cholera was the acquisition of the SXT/R391-family antibiotic resistance element. The clinical use of the antibiotics tetracycline and furazolidone for cholera treatment started in 1963 and 1968 respectively, about 15 years before our prediction of the first acquisition of an SXT/R391 ICE (1978–1984). Our analysis provides a robust framework for elucidating the evolution of the seventh pandemic further, and for studying the local evolution, particularly in the Bay of Bengal, that has such a key role in the evolution of cholera.

## METHODS SUMMARY

Genomic libraries were created for each sample, followed by multiplex sequencing on an Illumina GAIIX analyser. The 54-base paired-end reads obtained were mapped against N16961 El Tor as a reference and SNPs in the core genome were identified as described in Methods. The SNPs were used to draw a whole core-genome phylogeny as described in ref. 4. The final SNP alignment was used to perform BEAST<sup>14</sup> analysis and to confirm the output of linear regression analysis. The three cholera waves reported in the seventh-pandemic phylogeny were confirmed using BAPS<sup>8,9</sup>. The raw Illumina data were also assembled *de novo* (see Methods) so that pairwise genome comparisons could be made. A new and expandable nomenclature system describing the CTX trends seen in the last 40 years was proposed following the rationale described in Methods.

**Full Methods** and any associated references are available in the online version of the paper at [www.nature.com/nature](http://www.nature.com/nature).

Received 3 June; accepted 26 July 2011.

Published online 24 August 2011.

- Chin, C. S. *et al.* The origin of the Haitian cholera outbreak strain. *N. Engl. J. Med.* **364**, 33–42 (2011).
- Chun, J. *et al.* Comparative genomics reveals mechanism for short-term and long-term clonal transitions in pandemic *Vibrio cholerae*. *Proc. Natl Acad. Sci. USA* **106**, 15442–15447 (2009).
- Hochhut, B. & Waldor, M. K. Site-specific integration of the conjugal *Vibrio cholerae* SXT element into *prfC*. *Mol. Microbiol.* **32**, 99–110 (1999).
- Harris, S. R. *et al.* Evolution of MRSA during hospital transmission and intercontinental spread. *Science* **327**, 469–474 (2010).
- Update: cholera outbreak—Haiti, 2010. *MMWR Morb. Mortal Wkly Rep.* **59**, 1473–1479 (2010).
- Heidelberg, J. F. *et al.* DNA sequence of both chromosomes of the cholera pathogen *Vibrio cholerae*. *Nature* **406**, 477–483 (2000).
- Croucher, N. J. *et al.* Rapid pneumococcal evolution in response to clinical interventions. *Science* **331**, 430–434 (2011).

- Corander, J., Marttinen, P., Siren, J. & Tang, J. Enhanced Bayesian modelling in BAPS software for learning genetic structures of populations. *BMC Bioinformatics* **9**, 539 (2008).
- Corander, J., Waldmann, P. & Sillanpää, M. J. Bayesian analysis of genetic differentiation between populations. *Genetics* **163**, 367–374 (2003).
- Safa, A., Nair, G. B. & Kong, R. Y. Evolution of new variants of *Vibrio cholerae* O1. *Trends Microbiol.* **18**, 46–54 (2010).
- Garriss, G., Waldor, M. K. & Burrus, V. Mobile antibiotic resistance encoding elements promote their own diversity. *PLoS Genet.* **5**, e1000775 (2009).
- Wozniak, R. A. *et al.* Comparative ICE genomics: insights into the evolution of the SXT/R391 family of ICEs. *PLoS Genet.* **5**, e1000786 (2009).
- Lam, C., Octavia, S., Reeves, P., Wang, L. & Lan, R. Evolution of seventh cholera pandemic and origin of 1991 epidemic, Latin America. *Emerg. Infect. Dis.* **16**, 1130–1132 (2010).
- Drummond, A. J., Ho, S. Y., Phillips, M. J. & Rambaut, A. Relaxed phylogenetics and dating with confidence. *PLoS Biol.* **4**, e88 (2006).
- O'Shea, Y. A. *et al.* The *Vibrio* seventh pandemic island-II is a 26.9 kb genomic island present in *Vibrio cholerae* El Tor and O139 serogroup isolates that shows homology to a 43.4 kb genomic island in *V. vulnificus*. *Microbiology* **150**, 4053–4063 (2004).
- Bani, S. *et al.* Molecular characterization of ICEVchVie0 and its disappearance in *Vibrio cholerae* O1 strains isolated in 2003 in Vietnam. *FEMS Microbiol. Lett.* **266**, 42–48 (2007).
- Basu, A. *et al.* *Vibrio cholerae* O139 in Calcutta, 1992–1998: incidence, antibiograms, and genotypes. *Emerg. Infect. Dis.* **6**, 139–147 (2000).
- Faruque, S. M. & Mekalanos, J. J. Pathogenicity islands and phages in *Vibrio cholerae* evolution. *Trends Microbiol.* **11**, 505–510 (2003).
- Faruque, S. M. *et al.* The O139 serogroup of *Vibrio cholerae* comprises diverse clones of epidemic and non-epidemic strains derived from multiple *V. cholerae* O1 or non-O1 progenitors. *J. Infect. Dis.* **182**, 1161–1168 (2000).
- Nair, G. B., Bhattacharya, S. K. & Deb, B. C. *Vibrio cholerae* O139 Bengal: the eighth pandemic strain of cholera. *Indian J. Public Health* **38**, 33–36 (1994).
- Cvijetanic, B. & Barua, D. The seventh pandemic of cholera. *Nature* **239**, 137–138 (1972).

**Supplementary Information** is linked to the online version of the paper at [www.nature.com/nature](http://www.nature.com/nature).

**Acknowledgements** This work was supported by The Wellcome Trust grant 076964. The IVI is supported by the Governments of Korea, Sweden and Kuwait. D.W.K. was partially supported by grant RTI05-01-01 from the Ministry of Knowledge and Economy (MKE), Korea and by R01-2006-000-10255-0 from the Korea Science and Engineering Foundation; and J.L.N.W. was supported by the Alborada Trust and the RAPIDD program of the Science & Technology Directorate, Department of Homeland Security. Thanks to A. Camilli at Tufts University Medical School for providing the corrected N16961 sequence, to B.M. Nguyen at NIHE, Vietnam and M. Ansaruzzaman at ICDDR, Bangladesh for providing strains, and to M. Fookes at WTSI for training support.

**Author Contributions** A.M., D.W.K. and N.R.T. collected the data, analysed it and performed phylogenetic analyses and comparative genomics. J.H.L., S.Y.C., E.J.K. and J.C. analysed the CTX types. S.K., S.K.N. and T.R. were involved in strain collection and serogroup analysis. T.R.C. performed Bayesian analysis; N.J.C. and S.R.H. did the computational coding. J.L.N.W., J.D.C., C.C., G.B.K., J.H., N.R.T., J.P. and G.D. were involved in the study design. A.M., N.R.T., J.P., G.D., J.H., G.B.K., N.J.C., S.R.H., T.R.C., D.W.K. and M.L. contributed to the manuscript writing.

**Author Information** Reprints and permissions information is available at [www.nature.com/reprints](http://www.nature.com/reprints). All the genomic sequences have been submitted to the European Nucleotide Archive with the accession numbers listed in Supplementary Table 1. The authors declare no competing financial interests. Readers are welcome to comment on the online version of this article at [www.nature.com/nature](http://www.nature.com/nature). Correspondence and requests for materials should be addressed to J.P. ([parkhill@sanger.ac.uk](mailto:parkhill@sanger.ac.uk)).

## METHODS

**Genomic library creation and multiplex sequencing.** Unique index-tagged libraries for each sample were created, and up to 12 separate libraries were sequenced in each of eight channels in Illumina Genome Analyser GAI cells with 54-base paired-end reads. The index-tag sequence information was used for downstream processing to assign reads to the individual samples<sup>4</sup>.

**Detection of SNPs in the core genome.** The 54-base paired-end reads were mapped against the N16961 El Tor reference (accession numbers AE003852 and AE003853) and SNPs were identified as described in ref. 7. The unmapped reads and the sequences that were not present in all genomes were not considered a part of the core genome, and therefore SNPs from these regions were not included in the analysis. Appropriate SNP cutoffs were chosen to minimize the number of false-positive and false-negative calls; SNPs were filtered to remove those at sites with a SNP quality score lower than 30, and SNPs at sites with heterogeneous mappings were filtered out if the SNP was present in fewer than 75% of reads at that site. From the seventh-pandemic data set, high-density SNP clusters indicating possible recombination were excluded<sup>7</sup>. In total, 2,027 SNPs were detected in the core genome of the El Tor lineage. Of these, 270 SNPs were predicted to be due to recombination. Removing these provided a data set characterized by 1,757 SNPs: these were used to produce the final phylogeny.

**Comparative genomics.** Raw Illumina data were split to generate paired-end reads, and assembled using a *de novo* genome-assembly program, Velvet v0.7.03 (ref. 22), to generate a multi-contig draft genome for each of 133 *V. cholerae* strains<sup>4</sup>. The overlap parameters were optimized to give the highest N50 value. Because seventh-pandemic *V. cholerae* strains are closely related in the core, Abacas<sup>23</sup> was used to order the contigs using the N16961 El Tor strain as a reference, followed by annotation transfer from the reference strain to each draft genome<sup>4</sup>. Using the N16961 sequence as a database to perform a TBLASTX<sup>24</sup> for each draft genome, a genome comparison file was generated that was subsequently used in the Artemis comparison tool<sup>25</sup> to compare the genomes manually and search for novel genomic islands.

**Phylogenetic analysis.** A phylogeny was drawn for *V. cholerae* using RAXML v0.7.4 (ref. 26) to estimate the trees for all SNPs called from the core genome. The general time-reversible model with gamma correction was used for among-site rate variation for ten initial trees<sup>4</sup>. USA gulf coast strains A215 and A325, which have substantially different core genomes from all other strains in our collection, were used as an outgroup to root the global phylogeny (Supplementary Fig. 1), whereas a pre-seventh-pandemic strain, M66 (accession numbers CP001233 and CP001234), and strain A6 (from our collection), were used to root the seventh-pandemic phylogenetic tree (Fig. 1).

**CTX prophage analysis.** For each strain, the CTX structure and the sequence of *rstA*, *rstR* and *ctxB* was determined as in refs 27 and 28.

**Linear regression and Bayesian analysis.** The phylogram for the seventh pandemic was exported to Path-O-Gen v1.3 (<http://tree.bio.ed.ac.uk/software/pathogen>) and a linear regression plot for isolation date versus root-to-tip distance was generated. The same plot was also constructed individually for the three waves, but A4, being a laboratory strain, was excluded from the latter analysis.

The presence of three waves was checked, and their makeup was determined, using a BAPS analysis performed on the SNP alignment containing the unique SNP patterns from the seventh-pandemic isolates. The program was run using the BAPS individual mixture model and three independent iterations were performed using an upper limit for the number of populations of 20, 21 and 22 to obtain

optimal partitioning of the sample. The dates for the acquisition of SXT and the ancestors of the three waves were inferred using the Bayesian Markov chain Monte Carlo framework BEAST<sup>29</sup>. We used the final SNP alignment with recombinant sites removed and fixed the tree topology to the phylogeny produced by RAXML, as described above. We used BEAST to estimate the rates of evolution on the branches of the tree using a relaxed molecular clock<sup>14</sup>, which allows rates of evolution to vary amongst the branches of the tree. BEAST produced estimates for the dates of branching events on the tree by sampling dates of divergence between isolates from their joint posterior distribution, in which the sequences are constrained by their known date of isolation. The data were analysed using a coalescent constant population size and a general time-reversible model with gamma correction. The results were produced from three independent chains of 50 million steps each, sampled every 10,000 steps to ensure good mixing. The first 5 million steps of each chain were discarded as a burn-in. The results were combined using Log Combiner, and the maximum clade credibility tree was generated using Tree Annotator, both parts of the BEAST package (<http://tree.bio.ed.ac.uk/software/beast/>). Convergence and the effective sample-size values were checked using Tracer 1.5 (available from <http://tree.bio.ed.ac.uk/software/tracer>). ESS values in excess of 200 were obtained for all parameters.

**Nomenclature.** The seventh-pandemic cholera strains were clearly distinguished by three waves and we therefore propose their CTX types to be CTX-1, CTX-2 and CTX-3 under the new nomenclature scheme (see Supplementary Table 2). Our nomenclature system is expandable and would be suitable for naming any new seventh-pandemic *V. cholerae* strains. With CTX-1 representing canonical El Tor, we followed the rationale: (1) For CTX-1 to CTX-2, because there was a shift of *rstR*<sup>El Tor</sup> to *rstR*<sup>Classical</sup>, *rstA*<sup>El Tor</sup> to *rstA*<sup>Classical + El Tor</sup> and *ctxB*<sup>El Tor</sup> to *ctxB*<sup>Classical</sup>, we called it CTX-2; (2) for CTX-1 to CTX-3, because there was a shift of *ctxB*<sup>El Tor</sup> to *ctxB*<sup>Classical</sup>, we called it CTX-3; (3) for CTX-3 to CTX-3b, because there was only one SNP mutation in *ctxB*<sup>Classical</sup> from CTX-2 and rest was identical, we called it the next variant of CTX-3, which is CTX-3b.

In summary, if there is a shift of any gene from one biotype to another, the new CTX will be called CTX-n: thus the next strains fitting these criteria will be called CTX-4. However, if there is a mutation(s) that does not lead to a shift of the gene to another biotype gene, CTX-1b, CTX-1c or CTX-2b; CTX-2c or CTX-3b; CTX-3c and so on should be followed as appropriate.

22. Zerbino, D. R. & Birney, E. Velvet: algorithms for *de novo* short read assembly using de Bruijn graphs. *Genome Res.* **18**, 821–829 (2008).
23. Assefa, S., Keane, T. M., Otto, T. D., Newbold, C. & Berriman, M. ABACAS: algorithm-based automatic contiguation of assembled sequences. *Bioinformatics* **25**, 1968–1969 (2009).
24. Altschul, S. F., Gish, W., Miller, W., Myers, E. W. & Lipman, D. J. Basic local alignment search tool. *J. Mol. Biol.* **215**, 403–410 (1990).
25. Carver, T. et al. Artemis and ACT: viewing, annotating and comparing sequences stored in a relational database. *Bioinformatics* **24**, 2672–2676 (2008).
26. Stamatakis, A. RAXML-VI-HPC: maximum likelihood-based phylogenetic analyses with thousands of taxa and mixed models. *Bioinformatics* **22**, 2688–2690 (2006).
27. Lee, J. H. et al. Classification of hybrid and altered *Vibrio cholerae* strains by CTX prophage and RS1 element structure. *J. Microbiol.* **47**, 783–788 (2009).
28. Nguyen, B. M. et al. Cholera outbreaks caused by an altered *Vibrio cholerae* O1 El Tor biotype strain producing classical cholera toxin B in Vietnam in 2007 to 2008. *J. Clin. Microbiol.* **47**, 1568–1571 (2009).
29. Drummond, A. J. & Rambaut, A. BEAST: Bayesian evolutionary analysis by sampling trees. *BMC Evol. Biol.* **7**, 214 (2007).